# TOTAL CAVOPULMONARY CONNECTION HEMODYANAMICS AND THE SINGLE VENTRICLE: FUNCTIONAL RELATIONSHIPS AND TRANSLATIONAL POSSIBILITIES

A Thesis
Presented to
The Academic Faculty

by

Christopher Mark Haggerty

In Partial Fulfillment
of the Requirements for the Degree
Doctor of Philosophy in the
School of Biomedical Engineering

Georgia Institute of Technology
May 2013

**COPYRIGHT © BY CHRISTOPHER MARK HAGGERTY 2013**

# TOTAL CAVOPULMONARY CONNECTION HEMODYANAMICS AND THE SINGLE VENTRICLE: FUNCTIONAL RELATIONSHIPS AND TRANSLATIONAL POSSIBILITIES

Approved by:

Dr. Ajit P. Yoganathan, PhD, Advisor
Department of Biomedical Engineering
*Georgia Institute of Technology, GA*

Dr. Mark A. Fogel, MD
Division of Cardiology
*Children's Hospital of Philadelphia, PA*

Dr. Kirk R. Kanter, MD
Division of Cardiothoracic Surgery
*Emory University, GA*

Dr. Rudolph Gleason, PhD
Department of Biomedical Engineering
*Georgia Institute of Technology, GA*

Dr. John N. Oshinski, PhD
Division of Radiology
*Emory University, GA*

Date Approved: 19/12/2012

# ACKNOWLEDGMENTS

Where to begin?

I should first thank my advisor, Dr. Ajit Yoganathan, for the opportunity and privilege to be a part of the 'World Famous' CFM lab and for all the lessons I have learned through my 5½ years here at Georgia Tech. We have certainly had our moments… but looking back I can honestly say that we developed a very good and productive working relationship and I have the utmost respect for what he has accomplished in shaping the landscape of cardiovascular biomedical engineering.

I would like to thank the members of my committee: Drs. Fogel, Kanter, Oshinksi, and Gleason, who have all made significant contributions in my PhD training in various ways. I would like to particularly acknowledge Drs. Kanter and Fogel who were instrumental in pioneering the work that is presented in this thesis. It has been an honor and a pleasure to work with them so closely for the last several years.

I have also had the pleasure of working with many past and current members of the CFM lab who have been both great colleagues and good friends. I learned from many of these individuals the work ethic and dedication needed to conduct quality, impactful research, and I hope I have carried on in that example. In particular, I need to thank Kartik S. and Diane who are easily two of the smartest people I know and who continue to go out of their way to read papers and thesis chapters, or just discuss ideas long after they have moved on with their careers. I was given the opportunity to walk in their footsteps with my own research, and I am very grateful for that guidance. Speaking of reading thesis chapters, I must thank Lucia, Maria, and Elaine for all their time, effort, and contributions to the work presented here and their camaraderie through many long hours spent in meetings. Thanks also to Andrew for being a great friend, a trusted

associate, and a source of sanity through many long and stressful days. Finally, thank you to Keefe, who has been equal parts friend and mentor for the past 8 years, and I am tremendously grateful for both.

And then, of course, there's my family..

To my wife, Ally, who has been with me every step of the journey, I love you- your love and support got me here. You were there to pick me up when I was down and kept me grounded when I needed that too. The idea of work/life balance certainly seemed like a foreign concept at times along the way (particularly the past few months), but you kept me focused on what really matters in life. I cannot wait to see what the next chapter brings… (in life, not the thesis, I know what's there already).

To my parents, who have continuously sacrificed to lift me up and push me to succeed, thank you- I hope I am making you proud. To Sean and Casey, I love you guys, thank you for your constant support and love. And of course, I have been blessed with a great extended family of grandparents, aunts & uncles, cousins, and in-laws who have been a constant source of strength, encouragement, and support throughout my life; thank you.

# TABLE OF CONTENTS

# LIST OF TABLES

# LIST OF FIGURES

# LIST OF ANIMATIONS

# LIST OF ABBREVIATIONS

| | |
|---|---|
| ACGI | adaptive control grid interpolation |
| Ao | aorta |
| APC | atriopulmonary connection |
| Az | azygos vein |
| BC | boundary conditions |
| BSA | body surface area |
| BTS | Blalock-Taussig shunt |
| CFD | computational fluid dynamics |
| CHB | Boston Children's Hospital |
| CHD | congenital heart disease |
| CHOA | Children's Healthcare of Atlanta |
| CHOP | Children's Hospital of Philadelphia |
| CI | cardiac index |
| CMR | cardiac magnetic resonance |
| CO | cardiac output |
| CT | computed tomography |
| CVP | central venous pressure |

| | |
|---|---|
| DFI | divergence free interpolation |
| EC | extracardiac |
| EDV | end diastolic volume |
| ESV | end systolic volume |
| EF | ejection fraction |
| FE | frequency encoding |
| GFD | global flow distribution |
| HFD | hepatic flow distribution |
| HLHS | hypoplastic left heart syndrome |
| HR | heart rate |
| IA | intra-atrial |
| IB | immersed boundary |
| IVC | inferior vena cava |
| LPA | left pulmonary artery |
| LT | lateral tunnel |
| LV | left ventricle |
| MRI | magnetic resonance imaging |
| P | pressure |

| | |
|---|---|
| PA | pulmonary artery |
| PAVM | pulmonary arteriovenous malformations |
| PC MRI | phase contrast magnetic resonance imaging |
| PER | peak ejection rate |
| PFR | peak filling rate |
| PL | power loss |
| PLE | protein losing enteropathy |
| PVR | pulmonary vascular resistance |
| Q | flow |
| R | (TCPC) resistance |
| RF | radiofrequency |
| RPA | right pulmonary artery |
| RV | right ventricle |
| SI | stenosis index |
| SNR | signal-to-noise ratio |
| SSFP | steady-state free precession |
| StV | stroke volume |
| SV | single ventricle |

| | |
|---|---|
| SVC | superior vena cava |
| SVHD | single ventricle heart defects |
| SVR | systemic vascular resistance |
| TA | tricuspid atresia |
| TCPC | total cavopulmonary connection |
| TCPC-EDI | TCPC energy dissipation index |
| TE | echo time |
| TR | repetition time |
| VENC | velocity encoding |
| VF | ventricular function |
| VMTK | vascular modeling toolkit |

# LIST OF SYMBOLS

| | |
|---|---|
| $B_0$ | main magnetic field strength |
| $D_{max}$ | maximum vessel diameter |
| $D_{mean}$ | mean vessel diameter |
| $D_{min}$ | minimum vessel diameter |
| $M_0$ | effective magnetic moment |
| $\Delta P_{max}$ | maximum pressure drop |
| $PER_B$ | BSA-normalized peak ejection rate |
| $PER_V$ | volume-normalized peak ejection rate |
| $PFR_B$ | BSA-normalized peak filling rate |
| $PFR_V$ | volume-normalized peak filling rate |
| $Q_{LPA}$ | left pulmonary artery flow rate |
| $Q_P$ | pulmonary flow rate |
| $Q_S$ | systemic flow rate |
| $T_1$ | “spin-lattice” magnetic relaxation constant |
| $T_2$ | “spin-spin” magnetic relaxation constant |
| $\omega_0$ | angular rotation speed |

# SUMMARY

Single ventricle heart defects are a rare but serious form of congenital heart disease, which affect approximately 2000 children born in the United States each year. Staged surgical palliation, culminating with the “Fontan Procedure,” is typically required to achieve adequate supply of blood to both the pulmonary and systemic circulations while avoiding chronic ventricular volume overload. Thus, the surgery reroutes the systemic veins to the pulmonary arteries, forming a total cavopulmonary connection (TCPC), to completely bypass the right side of the heart and restore a series configuration to the cardiovascular circuits. Despite improved survival through this operative course in first weeks and years of life, Fontan patients are subjected gradual attrition and decreased life expectancy through a multitude of chronic complications. It is suspected that the adverse hemodynamics of this surgically altered physiology, including those specific to the surgical TCPC, play a role in determining patient outcome. However, the small and heterogeneous patient population has hindered decisive progress and there is still not a good understanding of the optimal care strategies on a patient-by-patient basis.

In recent decades, advances in medical imaging and image-based computational fluid dynamics (CFD) have redefined the realm of possibility for studying complex biomedical phenomena. Combined, these methods provide the means to create and evaluate patient-specific models of a wide range of cardiovascular structures, including the TCPC, with potentially high fidelity. Results from these models can then be used for a wide array of different analyses, such as identifying regions of flow separation or stagnation, calculating hemodynamic power loss, or quantifying local flow distribution patterns.

Through significant effort from numerous past investigators, a robust set of validated computational and image processing tools has been assembled, along with the largest

library of cardiac magnetic resonance (CMR) data of TCPC anatomy and flow. These tools are leveraged in this thesis to characterize the functional implications of TCPC power loss at an unprecedented scale: we report the largest CFD analysis of patient-specific TCPC hemodynamics to date with particular focus on identifying functional correlates. Combining these data with imaging-based analysis of ventricle function, we directly compare the CFD-derived hemodynamics to the performance of the single ventricle for the first time. Motivated by the physiologic significance of these findings, the same patient-specific CFD framework is used for the translational application of prospective surgery planning for hemodynamic optimization, including the first implementation of a novel TCPC connection design hypothesized to uniquely streamline the energetic performance. We conclude with a first look at the longitudinal evolution of patient functional status to begin understanding how factors such as TCPC hemodynamics contribute to poor long-term performance in these patients.

# Chapter 1. INTRODUCTION

Single ventricle heart defects are a rare but complex form of congenital heart disease in which there is only a single pumping chamber to move blood throughout the body. Surgery is often required to balance the distribution of blood between the pulmonary and systemic circuits, and it is typically done in stages to balance the need for ventricular unloading against the high vascular resistances in infants. In the first stage, a systemic-to-pulmonary shunt is introduced in the form of either a modified Blalock-Taussig shunt (right sub-clavian artery to pulmonary artery (PA)), or a right ventricle to PA shunt (Sano). Here, the systemic and pulmonary circuits are in parallel with the single ventricle supplying blood flow to both. The second procedure removes the shunt and replaces it with a superior vena cava (SVC) to PA connection; hence, the pulmonary circuit is placed in series with the superior half of the systemic circuit, while the inferior vena cava (IVC) remains connected to the heart. Finally, the Fontan procedure completes the right heart bypass by routing the IVC blood flow to the pulmonary arteries, which places the systemic and pulmonary circuits completely in series. In the modern era, a modified version of Fontan's procedure is typically performed, called the total cavopulmonary connection (TCPC).

The Fontan procedure has generally low operative mortality; yet, it is still considered palliative treatment given the fact that life expectancy is greatly reduced for single ventricle patients, and there are numerous long-term complications that reduce quality of life as well. These complications are the result of a complex combination of both ventricular and vascular dysfunctions, and frequently include arrhythmias, systemic hypertension, liver disease, poor exercise capacity, and protein-losing enteropathy. In

some of these cases, there is evidence to suggest that the surgical design of the TCPC and its associated hemodynamics may play a role in the cause or exacerbation of the disease. Hence, the TCPC has been the focus of a large body of research over the past two decades with the general goal of minimizing energy losses and balancing the distribution of hepatic blood flow in the IVC to the PAs.

Through multi-center collaborations with leading pediatric surgeons and cardiologists over the past 15+ years, the Cardiovascular Fluid Mechanics Laboratory at Georgia Tech has established an extensive set of validated engineering tools (e.g., medical image processing, computational fluid dynamics solvers) and a large library of cardiac magnetic resonance (CMR) data for single ventricle patients. Combined, these assets provide an unparalleled ability to study the patient-specific hemodynamics of the TCPC and identify generalizable trends.

In this thesis, this study of TCPC hemodynamics is expanded to an unprecedented scale. Rather than focusing on small sample sizes and test cases as many prior studies have done, we consider a large patient cohort with the complementary goals of establishing population averages for parameters of interest; relating the local hemodynamics to broader functional end points, such as ventricular function; and begin to observe how this complex physiology changes through time. In short, we seek to make functional connections to TCPC hemodynamics to being to understand its broader role and contributions to Fontan failure. At the same time, several promising strategies for systematically improving these hemodynamics (i.e., patient-specific surgical planning and bifurcated Fontan connection designs) will be investigated to demonstrate the translational engineering possibilities for improving patient outcomes.

# Chapter 2. SPECIFIC AIMS

Every year, approximately 2000 children are born in the US with a series of congenital heart defects that result in the functional use of only one ventricle[1]. In this pathology, the single ventricle (SV) is both volume loaded (supplying both pulmonary and systemic circuits in parallel) and inefficient with respect to oxygen transport; severe cyanosis and death likely ensue if left untreated. A series of staged, palliative surgical procedures are the most common clinical course, resulting in the total cavopulmonary connection (TCPC), which connects the venae cavae to the pulmonary arteries. Thus, the right side of the heart is bypassed, and the sole driving pressure behind pulmonary flow is the systemic venous return. The development of these surgical techniques has greatly extended the life expectancy of SV patients and decreased early mortality; however, gradual attrition with chronic complications, including ventricular dysfunction and diminished exercise capacity are common. The incidence of these complications can vary widely, suggesting a patient-to-patient dependence on the severity of ventricular dysfunction, altered vascular hemodynamics (including TCPC-mediated inefficiency), or both. Many previous studies have considered the single ventricle and TCPC components in isolation; few have sought to understand their connection. The cardiac magnetic resonance (CMR) database of SV patients at Georgia Tech (GT), which includes anatomy and flow information for both the TCPC and SV, provides a unique opportunity to address this shortcoming. We propose a two-pronged approach: a) elucidate the relationship between TCPC hemodynamics and ventricular function; and b) explore the clinical potential of promising means to improve these hemodynamics. ***The hypothesis for this study is that high TCPC power losses adversely affect vascular hemodynamics and***

***ventricular function in SV patients, with both deteriorating with time; surgical planning and novel surgical approaches may improve these hemodynamics.***

Aim 1- Characterize Fontan hemodynamics from a large patient series. Computational fluid dynamics (CFD) have become a popular standard means of evaluating local blood flow dynamics through patient-specific models of the TCPC. These studies, while valuable for exploring the connection between TCPC geometry and flows, are often hindered by small sample sizes making it difficult to identify population trends for important parameters of interest. In this aim, CFD from 100 patient-specific simulations will be analyzed to establish population baselines and relationships between variables, as well as make comparisons across anatomical templates. Metrics of interest include TCPC power loss (normalized as resistance and indexed energy dissipation), maximal pressure drop, hepatic flow distribution, cardiac index, and systemic venous flow rate.

Aim 2- Relate single ventricle function to TCPC hemodynamics. Short axis cine CMR data of the SV will be used to assess global ventricular function (VF) for a 40 patient subset of the patients from SA1. Parameters of interest include cardiac index, end diastolic and systolic volumes, stroke volume, ejection fraction, peak filling and ejection rates, and time to peak filling rate. Three comparisons will be drawn. First, the mean values for the 40 patients will be compared to literature values to assess their functional status. Second, the sample will be sub-divided based on ventricular morphology and VF measures compared to identify potential biases within the single ventricle population. Finally, the VF for each patient will be related to their corresponding hemodynamic efficiency metrics. Thus, we will be able to explicitly identify the impact that the TCPC, and specifically the hydrodynamic power it dissipates, has on global measures of VF.

Aim 3- Investigate the utility and reliability of prospective Fontan surgical planning for a wide array of single ventricle patients Pre-operative modeling of the Fontan procedure is a novel means of improving TCPC hemodynamics by identifying the optimal surgical approach before the operation. Preliminary investigations in a limited patient population have been promising, but comparison to post-operative hemodynamic outcomes have been lacking. We present our continuing experience of prospective surgical planning in 10 patients including expanded clinical indications and anatomical templates. Particular focus will be placed on the comparison to post-operative patient data to compare realized surgical outcomes to model predictions.

Aim 4- Evaluate the clinical feasibility of the Fontan Y-Graft for improving TCPC hemodynamics

An alternative proposal for systematically improving TCPC hemodynamics is the use of a bifurcated graft as the Fontan baffle. A total of 17 patients, including a consecutive series of 15 patients at a single center, have received such a connection, successfully demonstrating its technical feasibility. However, the associated hemodynamics of these *in vivo* Y-grafts must be evaluated to determine the actual effectiveness of their use. This objective will be accomplished in two parts: a) characterize the hemodynamics of the 15 patient series and compare them to population averages established in SA1; b) use the same virtual surgery paradigm as SA4 to create virtual extracardiac TCPC controls for 5 of the Y-graft patients to directly compare hemodynamic outcomes as a function of connection.

Aim 5- Analyze and compare longitudinal changes in VF and TCPC hemodynamics. Since most post-Fontan complications develop over the course of several years, a single snapshot of a patient's functional status cannot be expected to present the whole

picture. Rather, multiple time points' worth of data must be collected to observe the progression and dynamic change of these parameters. Therefore, in addition to the cross-sectional analyses conducted in SA1 and SA2, we propose a preliminary analysis of longitudinal changes in a small patient subsection (N=15) for whom CMR evaluations are acquired at multiple time points. Such an analysis will begin to elucidate the mechanisms of patient deterioration and failure.

# Chapter 3. BACKGROUND AND SIGNIFICANCE

## 3.1 Normal Cardiovascular Anatomy and Function

### 3.1.1 The Human Circulatory System

The cardiovascular system is the primary means of inter-organ transport in human physiology. Among its many functions, it serves as the vehicle for gas exchange, delivering oxygen to cells and removing carbon dioxide; and it is the means by which nutrients from food are distributed and waste products removed.

The driving force behind this system is the heart: a muscular structure divided into four functional chambers, two ventricles and two atria. The ventricles serve as the contractile blood pumps; whereas the atria serve as ventricular antechambers, and are integral in both the electrical conduction pathways of the heart and pumping function. As shown in Figure 3.1, the heart operates at the center of two distinct circulatory systems: the systemic and pulmonary circulations. Beginning in the right ventricle (RV), blood is pumped through the pulmonic valve into the pulmonary artery. Arteries are some of the largest blood vessels in the body serving the primary function of carrying blood away from the heart to the rest of the body. The pulmonary arteries carry blood from the RV to the lungs where, after successive vascular branching to a wide network of smaller arterioles and eventually capillaries, gas exchange occurs to increase blood oxygen content and extract carbon dioxide waste. The oxygenated blood is collected from the lungs by the venules, which eventually come together to form much larger veins. Veins are the vessels that return blood from the body tissues to the heart. In this case, the pulmonary veins deliver the blood into the left atrium before it passes through the mitral valve into the left ventricle (LV). The LV is the most muscular of the heart chambers since it must generate sufficient pressure to drive blood flow to the rest of the body

tissues (i.e., the systemic circulation). Blood from the LV passes through the aortic valve into the aorta, the body's largest artery, before following a similar branching pathway as the pulmonary circuit: arteries-arterioles-capillaries. In the capillaries, the oxygen absorbed in the lungs is delivered to the local tissues to facilitate cellular respiration, and respiratory by-products (e.g., carbon dioxide) are removed. From there, blood returns through the venules-veins-vena cava to the right atrium, through the tricuspid valve and back to the RV, thus completing the circuit. In a healthy adult circulation, the ventricles contract approximately 70-80 times and circulate 5 liters of blood per minute. Figure 3.2 shows a focused view of the heart, demonstrating the cardiac structures defined in the prior description.

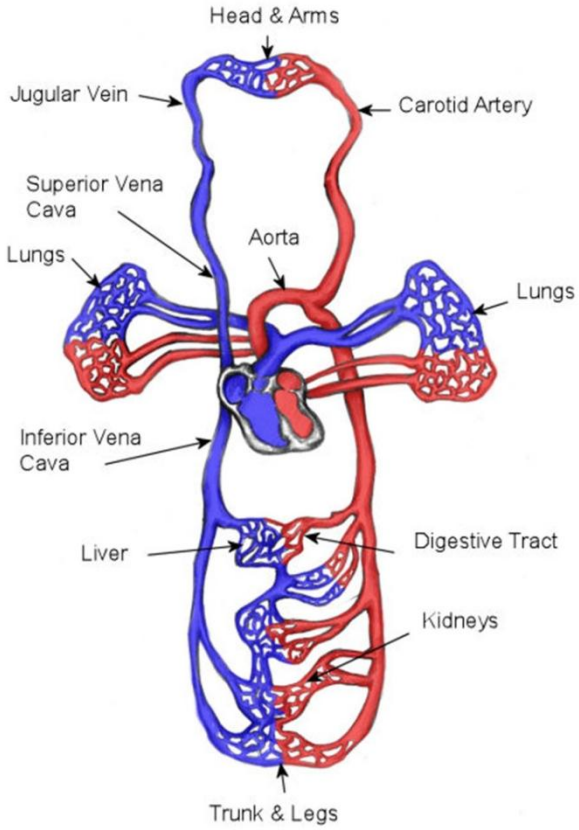


**Figure 3.1 Schematic of Human cardiovascular system comprised primarily of the heart and the systemic and pulmonary circulations. (Image credit- teachpe.com)**

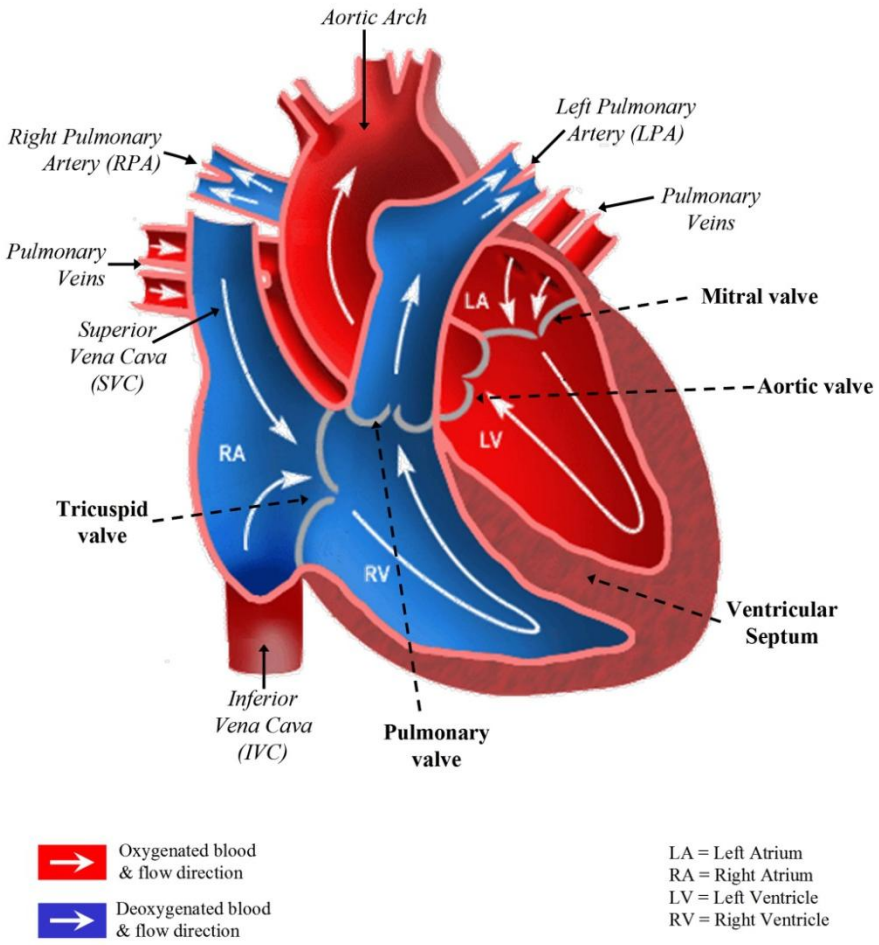


**Figure 3.2 Cardiac anatomy inclusive of two ventricles, two atria, four valves, the aorta, pulmonary arteries, and veins.**

### 3.1.2 Ventricular Function

The cardiac cycle can be broadly divided into two phases: systole (i.e., contraction) and diastole (i.e., relaxation) (see Figure 3.3). At the onset of systole, pressure increases within the ventricle and quickly surpasses the pressure of the atrium, closing the atrioventricular valve. A period of isovolumic contraction ensues in which ventricular

pressure continues to rise at a constant volume. Once the pressure surpasses that of the aorta (in the case of the LV), the aortic valve opens and blood is ejected from the ventricle into the aorta. The valve closes once ventricular pressure falls below that of the aorta, signaling the end of ventricular systole and the beginning of diastole. The ventricle relaxes isovolumically until the mitral valve opens and filling occurs. Near the end of diastole, the atrium contracts to force more blood into the passively filled ventricle just prior to the end of diastole and the start of the next systolic cycle.

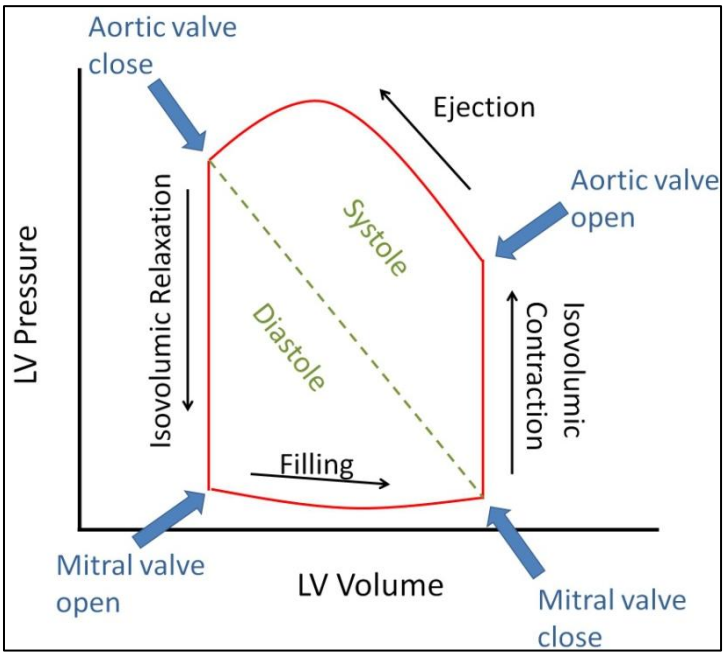


**Figure 3.3 Ventricular Pressure-Volume Relationship over the cardiac cycle. Cycle is divided into systole and diastole by diagonal dashed line; opening and closing of valves is highlighted by blue arrows.**

This function of the ventricles is highly specialized and responsive to the dynamic pressure and volume loads it encounters in the course of normal function. In particular, it is important to highlight three particular determining factors that help to govern cardiac functional output: *preload, afterload, and contractility*.

Preload is the stretching force imparted on the cardiac muscle cells in the 'relaxed' state prior to systolic contraction. It is related to the volume and/or pressure of blood contained within the ventricle (relative to its native size) at the end of diastole.

Afterload is the force opposing muscle cell shortening during systolic contraction. It is related to the resistance of downstream vasculature against which the heart is pumping.

Contractility is the inherent intensity of the contractile force the heart is capable of generating (independent of preload or afterload) as a function of the underlying muscle fiber structure.

Experimental muscle preparations[2] have consistently demonstrated that these forces have direct effects on the force generation and contractile velocity of the heart. For example, with increasing afterload, the tension placed on the cardiac muscle cells increases; however, the extent and velocity of muscle fiber shortening decreases (Figure 3.4). This inverse interplay is the so-called force-velocity relationship. Similarly, increasing the preload on the ventricle has a direct relationship with the force of muscle contraction through what is known as the Frank-Starling law (Figure 3.5).

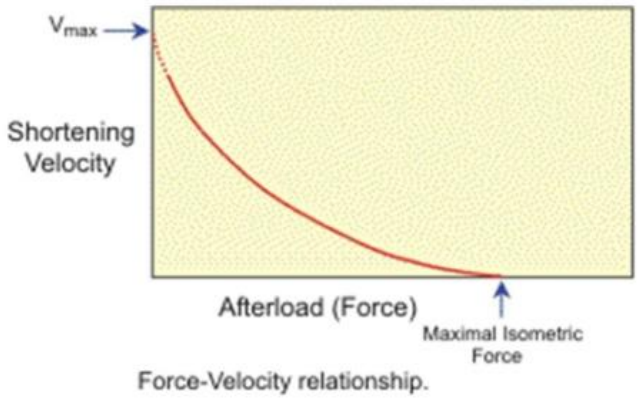


Force-Velocity relationship.

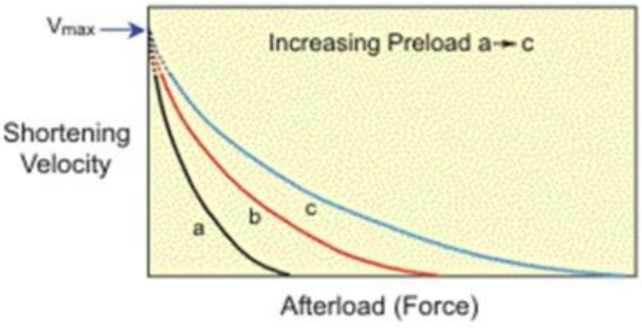


Effects of increasing preload (shift from curve a to c) on the force-velocity relationship.

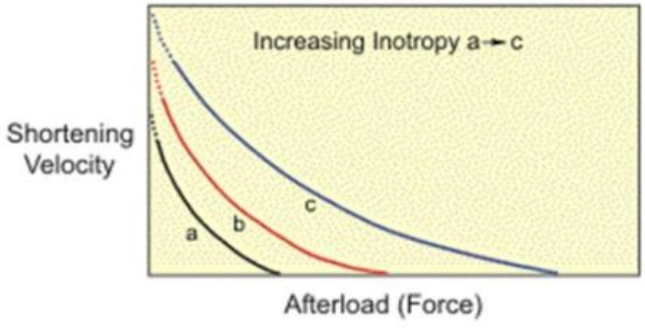


Effects of increasing inotropy (shift from curve a to c) on the force-velocity relationship.

**Figure 3.4 Plots demonstrating the force-velocity relationships with varying Preload [middle] and Inotropy [bottom]. Velocity of shortening decreasing with increasing afterload (force), but increases in preload and inotropy increase the velocity for a given force. (Image credit- cvphysiology.com)**

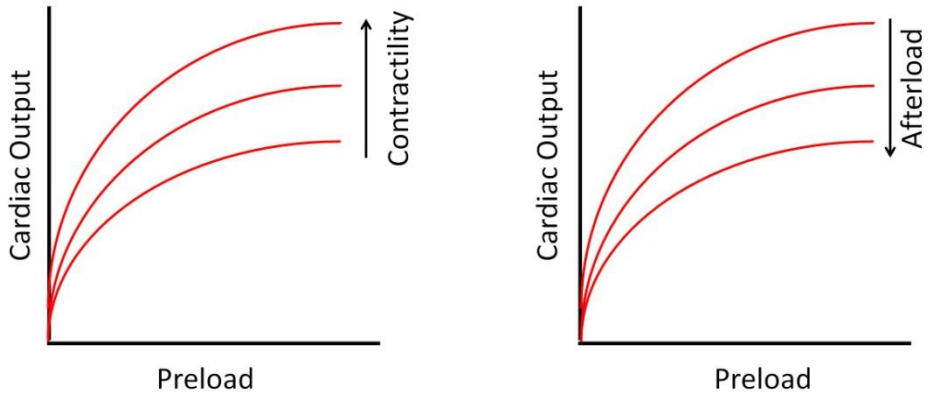


**Figure 3.5 Frank-Starling curves relating cardiac output with preload with the effects of changing myocardial contractility and afterload. Cardiac output rises (falls) with increasing contractility (afterload) at a given preload condition.**

In recent years, the study of diastolic function has grown in popularity and importance given appreciation for its role in congestive heart failure[3]. Normal diastolic function can be sub-divided into four phases: 1) isovolumic relaxation, 2) early filling (~80% of filling volume[4]), 3) diastasis (~5% of filling), and 4) atrial systole (~15% of filling). The process of ventricular relaxation (particularly the isovolumic stage) is a combination of active and passive processes[4], with the ultimate efficiency and effectiveness of ventricular filling dependent on mechanical properties, such as compliance, stiffness, and the end-diastolic pressure-volume relationship.

In summary, the biventricular heart is a highly specialized and functionally optimized muscle that has been evolutionally optimized, both in filling and ejecting, to respond to changing loads so as to maintain a stable homeostatic cardiovascular baseline.

## 3.2 Congenital Heart Disease

Congenital Heart Disease (CHD) is the generic term used to describe anatomical abnormalities of the heart present at birth. These defects could be as simple as an atrial septal defect, or a complex combination of multiple defects of both the ventricles, valves, and the great arteries. Approximately 8-10 per 1,000 births in the United States annually have some form of CHD[5, 6]. Table 3.1 provides estimates for the incidence of some of the more common forms of CHD[6].

**Table 3.1 Incidence of various CHD per 1,000 live births**

| CHD | Incidence |
|---|---|
| Ventricular Septal Defect | 3.6 |
| Patent Ductus Arteriosus | 0.8 |
| Atrial Septal Defect | 0.9 |
| Bicuspid Aortic Valve | 13.6 |
| Pulmonary Stenosis | 0.7 |
| Tetralogy of Fallot | 0.4 |
| Hyploplastic Left Heart | 0.3 |
| All cyanotic | 1.4 |

Some of the most severe forms of CHD are classified as ‘cyanotic’, which means that the delivery of concentrated, oxygen-rich blood to the systemic circulation is

compromised. For example, in Tetralogy of Fallot the combination of pulmonary stenosis, a ventricular septal defect, a mal-positioned aortic arch (over-riding the septal defect) and right ventricular hypertrophy leads to significant mixing of the oxygen-rich blood in the left ventricle (returning from the pulmonary circulation) and oxygen-poor blood from the right ventricle (returning from the systemic circulation). As a result, patients with cyanotic defects are typically born with blue-tinged skin (the color of de-oxygenated blood) indicative of poor blood oxygen saturation in their extremities. These defects often require surgery; in fact, more than 50% of children born with CHD require at least one invasive surgery during their lifetime[7]. The success of these treatment strategies has gradually improved over the past decades as evidenced by the fact that there are currently more adults than children living with CHD[8], but the long-term prognosis is still far from ideal in many cases. Cardiac-related morality 25 years post-operatively has been reported to be as high as 17% for certain defects[9].

### 3.3 Single Ventricle Defects

An important sub-class of CHD is characterized by the functional use of only a single ventricular pumping chamber, and are thus called single ventricle heart defects (SVHD). These defects occur in 7.7% of CHD[1]. SVHD is associated with an extremely high mortality rate without surgical intervention owing to: 1) hypoxic mixing of oxygenated and deoxygenated blood in the single ventricle, and 2) a likely imbalance of blood delivered to the systemic and pulmonary circuits (Figure 3.6). While the ultimate goal of surgical care is relatively consistent across SVHD (i.e., the restoration of a series configuration to the circulatory systems), this objective is often achieved in stages, which are very dependent on the underlying anatomic characteristics of the individual patient. The

following sections will therefore highlight some of the more common forms of SVHD and the common surgical treatment strategies.

### 3.3.1 Hypoplastic Left Heart Syndrome (HLHS; Figure 3.7)

HLHS is among the more common forms of SVHD and it is characterized by the severe under-development of left-sided heart structures (aorta, ventricle, etc), creating a significant deficiency of a systemic flow source after birth. In the neonatal period, the ductus arteriosus is medically kept patent to allow systemic flow to be shunted from right to left via the RV and pulmonary artery. However, within the first days to weeks of life, the neonate must undergo surgery to establish a more reliable source of systemic flow.

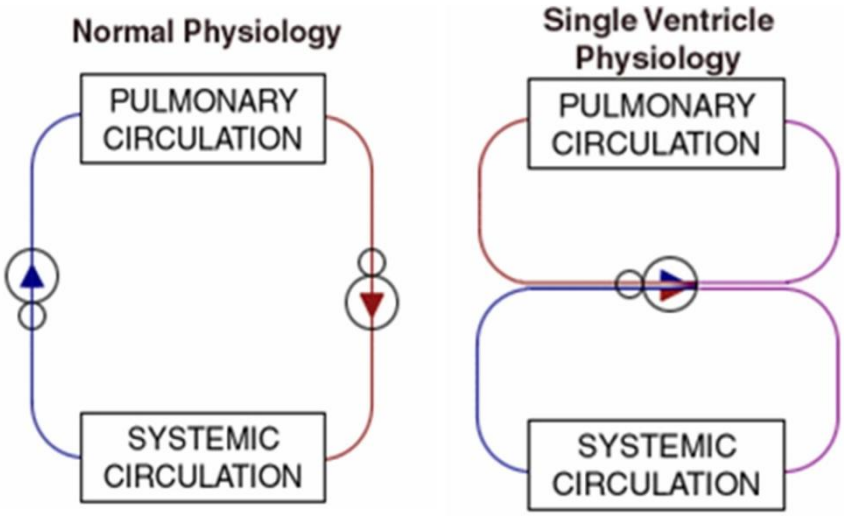


**Figure 3.6 Electrical circuit analog diagrams of normal (left) and single ventricle (right) cardiovascular systems. For single ventricles, the pulmonary and systemic circuits are in parallel with each other rather than a healthy series circuit.**

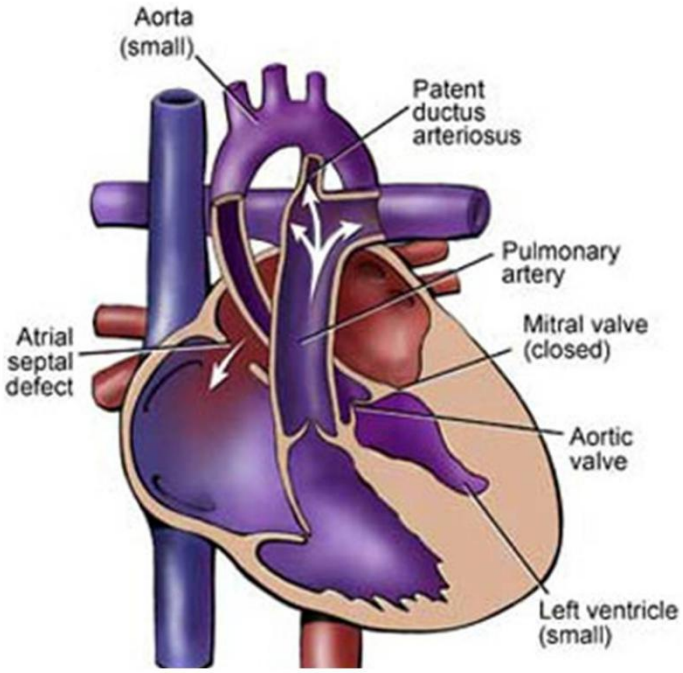


**Figure 3.7 Anatomy of Hypoplastic left heart syndrome. (Image credit- Mayo Foundation)**

### 3.3.2 Tricuspid Atresia (TA; Figure 3.8)

In this disease, the right atrioventricular valve (Tricuspid valve) is underdeveloped or absent, leading to an under-development of right-sided ventricular structures. Pulmonary blood flow at birth therefore depends on the presence of secondary defects (atrial and ventricular septal defects) to channel systemic venous flow from the right atrium to the pulmonary artery. The early palliative course for TA and other similar defects depends on numerous anatomic considerations, particularly the relative size of the great arteries and the ratio of pulmonary to systemic flow ($Q_p/Q_s$). For example, if $Q_p/Q_s$ is too high a PA band may be introduced to restrict the pulmonary artery size and promote flow to the aorta. On the opposite extreme, if the PA is under-developed a systemic-to-pulmonary

shunt (as in HLHS) may be required. If $Q_p/Q_s$ is naturally maintained in a healthy range, no immediate intervention may be necessary.

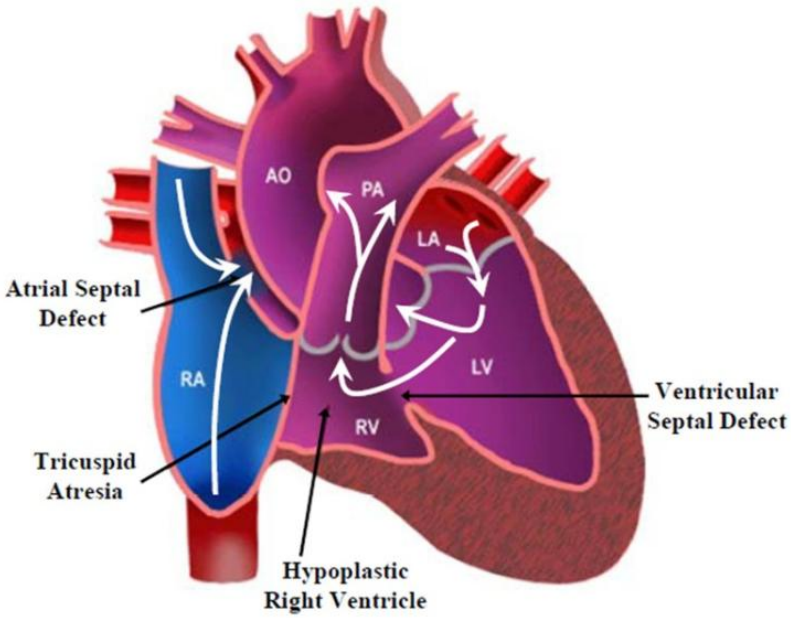


**Figure 3.8 Anatomy of Tricuspid Atresia.**

### 3.3.3 The Norwood Procedure

The Norwood involves (in many cases) a reconstruction of the hypoplastic aorta with the pulmonary artery (the Damus-Kaye-Stansel procedure) and a systemic to pulmonary shunt. If necessary, this procedure is performed within the first days or weeks of life (before the ductus arteriosus closes) to ensure adequate systemic and pulmonary blood flow. In the modern era, this shunt has taken the form of either the modified Blalock-

Taussig shunt (BTS; right subclavian artery to right pulmonary artery connection)[10], or the Sano procedure (right ventricle to pulmonary artery connection)[11]. The relative superiority between these options is a source of intense scrutiny since the Norwood procedure has among the highest mortality rates among common congenital heart procedures[12]. Comparative outcome results have been inconclusive: the first randomized, controlled study in pediatric cardiac surgery showed no difference in transplant-free survival after 12 months.

### 3.3.4 The Glenn Procedure

At 3 to 6 months of age, once pulmonary vasculature has developed and dropped vascular resistance from its high neonatal levels, the stage II procedure is performed. Here, the systemic to pulmonary shunt is removed and replaced by routing flow from the superior vena cava (SVC) to the pulmonary arteries (PA). The original Glenn procedure was a unidirectional connection of the SVC to the right PA; however, this has largely been replaced by several ‘bidirectional’ connection options: an SVC-PA end-to-side anastomosis (the Bidirectional Glenn; Figure 3.9 (left)) or a side-to-side anastomosis of the SVC (or right atrial appendage) to the PAs (the Hemi-Fontan; Figure 3.9 (right)).

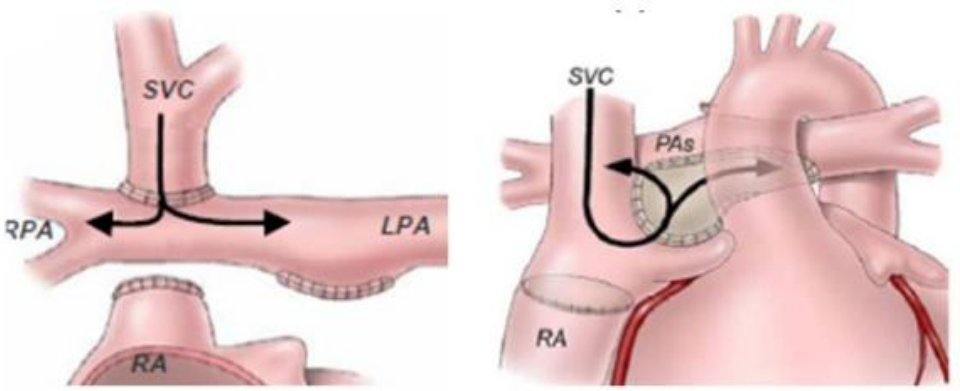


**Figure 3.9 Varying surgical approaches to superior cavopulmonary anastomosis. Left: Bidirectional Glenn connection (end-to-side anastomosis of SVC to RPA). Right: Hemi-Fontan connection (side-to-side connection of right atrium/SVC to pulmonary arteries).**

### 3.4 The Fontan Procedure

First proposed in 1971, the Fontan procedure completely restores a series circuit configuration to the cardiovascular system by routing systemic venous flow into the pulmonary arteries[13]. The connection proposed by Fontan and Baudet called for separate unions of the SVC to RPA and the IVC (through the right atrium with implanted valve conduits) to the LPA (Figure 3.10a). Two years later, Kreutzer *et al*. proposed a valveless atrio-pulmonary connection in which the SVC remained natively connected to the right atrium, while the atrial appendage was connected to the pulmonary arteries[14] (Figure 3.10b). The atriopulmonary connection (APC) remained the standard for this operation for almost 20 years, despite noted issues of atrial thrombus and arrhythmias[15, 16], among other issues. In 1988, de Leval *et al.* proposed the total cavopulmonary connection (TCPC) on the basis of hydrodynamic efficiency compared to dilated APCs[17] (Figure 3.10c). The TCPC was shown to decrease the incidence of arrhythmias compared to APC[18], and has since become the connection of choice for SVHD.

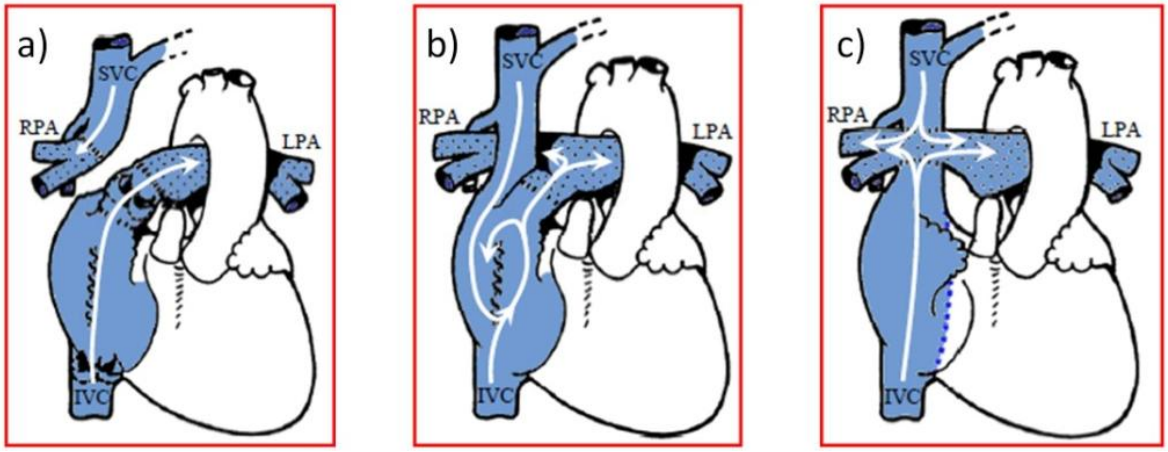


**Figure 3.10 The Evolution of the Fontan procedure. a) Unidirectional, valved end-to-end VC-PA connections originally proposed by Fontan and Baudet. b) Valveless atriopulmonary connection proposed by Kreutzer et al. c) Total cavopulmonary connection proposed by de Leval et al. which is the current standard.**

The actual connection described by de Leval was an intra-atrial lateral wall tunnel (Figure 3.11a) in which a synthetic patch was placed inside the atrium to direct IVC blood flow through the atrium to the pulmonary arteries (through the enlarged SVC-PA junction). An alternative TCPC design was proposed by Marcelletti *et al.*[19] that instead routed a synthetic baffle around the atrium from the IVC directly to the RPA (i.e., an extracardiac conduit; Figure 3.11b). The relative benefits of intra-atrial vs. extracardiac connection approaches are still the subject of debate and research in the present day; often the decision is based on patient size at the time of Fontan (since the lateral tunnel is believed to be more accommodating for growth) and surgeon preference. Perhaps one of the most compelling arguments for one connection over the other came from a recent review of over 2700 Fontan patients in the Society of Thoracic Surgeons Congenital Heart Surgery database that found the rate of in hospital death or Fontan

revision/takedown to be low (2.7%), but patients with an extracardiac connection had an adjusted odds ratio of 2.28[20].

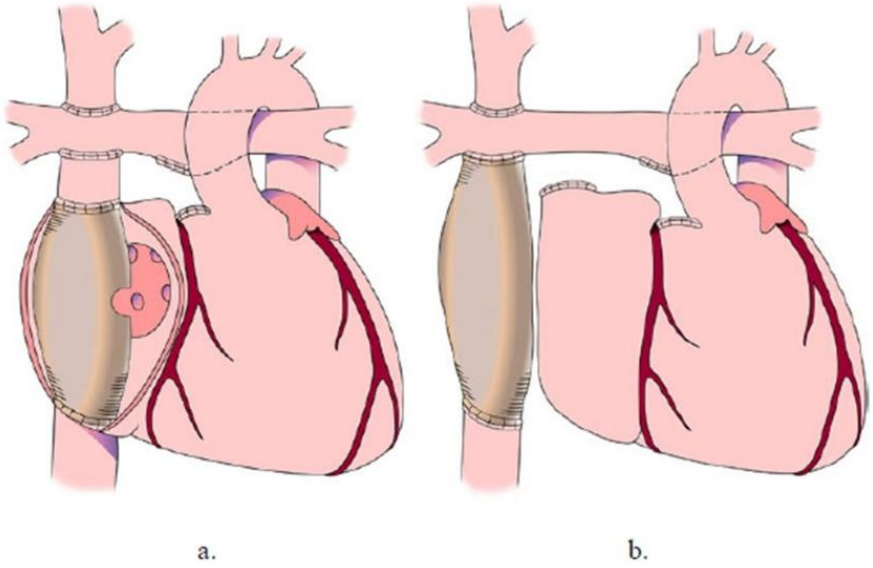


**Figure 3.11 Two primary methods of total cavopulmonary connection: a) intra-atrial lateral tunnel; b) extracardiac connection. (Image courtesy Children's Hospital Boston).**

It is important to point out that the Fontan procedure generally requires the surgical staging described in §3.3.3 and §3.3.4 (as opposed to a single operation at birth) because of high pulmonary vascular resistance (PVR) in the neonate. Since the lungs do not function *in utero*, PVR is very high at birth and decreases as the lungs develop. High PVR creates a preload limitation in the Fontan circulation, so neonatal resistances are not suitable for the Fontan and surgical staging is required. The use of mechanical circulatory support has been proposed as an alternative means to overcome high neonatal PVR[21], but such technology is not available.

## 3.5 Clinical Experience with the TCPC

Owing to significant advances in patient care and management, particularly with the development of effective surgical staging techniques, the short-term operative outcomes associated with the Fontan procedure are generally favorable. Patients are reaching adulthood with increasing frequency and with acceptable quality of life[22, 23]. Some acute issues may persist, such as sudden increases in central venous pressure leading to ascites, pleural effusions, decreased pulmonary compliance and increased pulmonary vascular resistance. Fontan takedown is one of limited options available in such instances[24], but is associated with drastically increased mortality[25].

Conversely, long-term complications and chronic failure are more commonly noted[26-29]. Among the most commonly cited chronic complications are ventricular dysfunction (both systolic and diastolic), atrial arrhythmias, liver fibrosis and dysfunction, atrioventricular valve regurgitation, pulmonary arteriovenous malformations (PAVMs), diminished exercise capacity, protein losing enteropathy (PLE), somatic growth retardation, thrombotic complications, and poor neurodevelopmental outcomes[27, 30, 31]. While many, if not all, of these issues are complex and multi-factorial in nature, they primarily reflect dysfunction of both the ventricle and the vasculature (inclusive of the TCPC).

### 3.5.1 Role of the Single Ventricle

As defects in the ventricle are the root cause of disease, it should come as no surprise that the function of the ventricle is integral to the long-term health and functional status of patients. It has been the focus of a large body of research to characterize SV function and understand the risk factors of poor outcomes. Kirklin *et al.* identified ventricular hypertrophy as a risk factor for death following the Fontan procedure[32]. Fogel *et al.* found that ventricular mass, volume, and contractile “vigor” decreased two years

following Fontan[33]. Cavalcanti *et al.* compared functionally healthy Fontans to failing patients and found a 51% decrease in cardiac index[34]. Eicken *et al.* reported a significant drop in ejection fraction (EF), a load dependent measure of systolic function, in patients 10 years post-Fontan (49.3% vs. 64.8% in a control group)[35] and thus the gradual development of heart failure is expected over time[36].

At the same time, appreciation for the incidence and importance of diastolic dysfunction is quickly growing. Anderson *et al.* reported abnormal diastolic function in 72% of a 500 patient cohort[30]. Cheung *et al.* reported ventricular relaxation times via echocardiography that were consistent with reductions in ventricular compliance[37].

The fact is that the physiology of SVHD is drastically altered from normal biventricular hemodynamics: the single ventricle must pump against increased afterload[38] (the systemic and pulmonary circuits in series) with decreased preload[39] (pulmonary driving pressure is decreased), which will inherently impair cardiac function (by the Frank-Starling relationships). Such afterload and preload reductions were noted by Szabo *et al.* in a canine model[40]. Furthermore, in many cases the ventricle itself may not even be optimally suited to handle systemic loads[41], particularly if it is a morphologically right ventricle. After years of working against these adverse conditions, it is perhaps not surprising that gradual attrition is the norm.

The ventricle may also have an important role to play in exercise intolerance. Work by Senzaki *et al.* showed a limited inotropic response and worsening diastolic filling with increased HR[39]. Hence, in response to exercise physiology, single ventricles have limited capability to improve stroke volume and must primarily meet the demands for increased cardiac output through higher heart rates.

### 3.5.2 Role of the Vasculature

To provide a theoretical framework for this discussion, it is first useful to review Guyton's isolated venous theory[42]. This theory says that the vascular compliance elements play the key role in mediating ventricular filling and cardiac output by providing the elastic potential energy needed to drive blood flow back to the heart. As such, Guyton demonstrated that changes to venous resistance had a more primary impact on cardiac output than arterial resistance because the venous resistance falls downstream of the vascular compliance. These observations are particularly relevant to single ventricle physiology (systemic and pulmonary circuits in series) because the systemic venous resistance, the TCPC, and the pulmonary vascular resistance are all downstream of the systemic vascular compliance. Thus, the sum of these resistive elements is the mediator of central venous pressure and the filling and output of the single ventricle.

Said another way, the differential of the central venous pressure (CVP) and the atrium is the sole driving force to move blood from the systemic veins back to the heart; any high resistors in that pathway will directly decrease the flow that can be achieved given that driving force. To maintain a reasonable cardiac output, chronic compliance remodeling (up to 400% decrease) occurs, which drastically increases CVP[43, 44]. de Leval best described this configuration as paradoxical: chronic systemic hypertension coupled with chronic pulmonary hypotension[45]. He also noted that the poor ventricular filling characteristics that result from this low driving pressure create a chronic preload-limited state analogous to mitral stenosis. In such an analogy, the degree of elevated PVR and/or TCPC resistance equates to the severity of the stenosis.

The chronic high CVP/low output state of the Fontan circuit may also explain the incidence of gastro-intestinal diseases, such as PLE and cirrhosis[46-48]. Vasodilating agents, such as sildenafil, have achieved some success in relieving these symptoms of

liver failure[49-51], but larger studies are needed to determine if it can effectively combat the 50% mortality rate within 5 years of PLE diagnosis[52].

### 3.5.3 Role of the TCPC

The importance of the TCPC in single ventricle hemodynamics is perhaps less straightforward and is still a source of controversy. It is important to recognize that the TCPC sits at a critical juncture of the single ventricle circuit at the transition of the systemic and pulmonary circuits such that all pulmonary flow (less collateral contributions) must first pass through the TCPC. Early experimental studies using idealized models of the TCPC demonstrated that the collision of caval flows at the junction was not optimally efficient for passive transport[53], and a large body of research has since sought better alternatives[54].

Using a mathematical model of the Fontan circulation, Sundareswaran *et al* predicted decreasing cardiac output with physiologic increases in TCPC resistance[55]. Furthermore, Sundareswaran *et al.* and Whitehead *et al.* showed how TCPC-mediated hemodynamic losses can become exacerbated with higher flow/simulated exercise conditions[55, 56]. Conversely, the other vascular resistances (SVR, PVR) typically decrease in response to physiologic exercise demands to improve ventricular filling and ejection characteristics[57]. Thus, the relative importance of the TCPC is perhaps accentuated under such conditions.

Finally, the TCPC has also been implicated for involvement in the development of pulmonary arteriovenous malformations (PAVM). These malformations are arterial-to-venous shunts that may develop in the pulmonary vasculature creating progressive hypoxemia as increasing blood volume bypasses blood oxygenation pathways in the lungs. Although the exact mechanism is unknown, it is widely believed that liver-derived

proteins present in the hepatic venous blood can prevent or counter-act their formation[58-60]. Duncan *et al*. reported that PAVMs develop in as many as 25% of patients following the Glenn procedure[58], presumably because the hepatic venous flow (along with the rest of the IVC flow) is still connected to the ventricle and does not pass through the lungs. Post-Fontan, the incidence of PAVMs drops off significantly; however, sub-optimal (i.e., unilateral) pulmonary flow distribution through the Fontan baffle has been shown to foster PAVM development in the contra-lateral lung[61]. At particular risk for such a scenario are patients with interruption of the IVC pathway[62], in which an enlarged azygos vein carries the majority of inferior venous blood flow to the SVC, and the hepatic veins natively drain into the atrium separately. With drastically decreased volume and flow momentum through the hepatic venous Fontan baffle, it can be particularly susceptible to poor distribution outcomes and is extremely sensitive to surgical positioning.

In summary, the Fontan procedure and its evolution over the past decades have given life to many patients with complex CHD who previously had little hope for survival. Yet, Fontan physiology is an imperfect palliation that drastically alters ventricular loads and vascular hemodynamics and so puts these patients on a course of gradual functional deterioration and attrition. *While the factors governing Fontan failure are complex and multi-factorial, isolating and understanding the contributions of the individual players (the ventricle, the vascular system, and the TCPC) may provide novel insights that empower caregivers to combat failure.*

### 3.6 Single Ventricle Function

Generally speaking, single ventricle function (VF) can be characterized by both systolic and diastolic dysfunction, owing in part to altered venous and arterial hemodynamics

and contractile abnormalities. These factors will be investigated in more detail in the following sections.

### 3.6.1 Systolic Dysfunction

Traditional measures of ventricular systolic function (i.e., cardiac index, ejection fraction) are generally reported to be lower in Fontan patients compared to normal, age-matched controls[33, 63-65]. Akagi *et al.* reported decreased cardiac index compared to normals[64]. On average, cardiac index in single ventricles is approximately 70% of normal values[66]. Parikh *et al* used radionuclide angiography in 15 patients going from BT-shunt to atriopulmonary connections and found that ejection fraction (EF) decreased from 52% to 39% over one year after surgery[65]. Similarly, Akagi *et al* used radionuclide angiography and found lower EF post-Fontan (50%) compared to controls (60%)[64]. However, in a contemporary cross-sectional study, EF was found to be normal in 73% of patients[30], perhaps reflective of improvements made in patient management over the past 20 years. Yet, it is worth noting that a difference in systolic function was seen in the more recent work based on ventricular morphology, with single LVs having a better function than single RVs[30]. Also, myocardial fibrosis, occurring in approximately 30% of patients, has been associated with decreased ejection fraction and may be a discriminating factor in these differing results[67].

There is a fair amount of uncertainty regarding the source of this systolic dysfunction, and it is likely the result of a combination of multiple altered states. While many early studies presumed that decreases in functional metrics were indicative of inherent contractile shortcomings (which still may be true for single LV vs. single RV considerations), their dependence on ventricular loading conditions is an important confounder. For example, Senzaki *et al* invasively measured vascular impedance in Fontan patients compared to BTS and normals[38], and found that elevated levels of

vascular impedance (i.e., afterload) caused by low frequency wave reflections were significantly correlated with decreased cardiac index. At the same time, Senzaki *et al.* used β-adrenergic stimulation to test the inotropic response of the single ventricle, and the expected (albeit limited) improvement in cardiac index was observed. Hence, the underlying contractile capabilities of the ventricle remain intact, but there was lack of sufficient reserve to augment output substantially, which is consistent with the fact that ventricular filling is more important than myocardial contractility in augmenting stroke volume[68].

Yet, it has been pointed out that a decrease in ventricular afterload in single ventricles (unlike in the normal circulation) will not increase cardiac output[66]. Instead, systemic resistance tends to increase to maintain blood pressure in chronically low output states[40], suggesting that afterload may be a result, not a cause, of diminished cardiac index in single ventricles[66].

### 3.6.2 Diastolic Dysfunction

In contrast to the 73% of patients with preserved EF, Anderson *et al* reported that diastolic function was abnormal in 72% of patients[30]. While that prevalence was an unexpected finding, it builds on a large body of literature demonstrating delayed[69, 70] or decreased peak rates[63, 64] of ventricular filling. Peak filling rates have been correlated with ventricular relaxation rate and atrial pressure at the onset of atrioventricular valve flow[71]; contributions of wall thickness and elastic properties (perhaps 'supranormal' compliance[69]), preload, and other extrinsic factors have also been suggested[4]. Again, progressive development of myocardial fibrosis, which has been correlated with increasing end diastolic volume, may play an important role in this process[67]. These are generally summarized as 'impaired relaxation.'

Here again, the significance of these findings is controversial. Penny *et al.* suggested there may be a significant impact of this delayed filling phenomenon on ventricular filling capacity[72]. Senzaki *et al.* instead claim their results (from primarily left morphological ventricles) show such impairment has minimal impact on overall diastolic filling at rest[39]. Finally, Gewillig *et al.* argue that ventricular preload may be the cause of abnormal diastolic function and the primary mediator of cardiac output in single ventricles[66], which suggests that Fontan failure may be as much a disease of the vasculature as of the ventricle itself.

## 3.7 TCPC Hemodynamic Investigations

Through the years, significant insights into the local fluid dynamics within the TCPC have been gained through combined use of experimental, computational, and clinical imaging methodologies. The primary focus of these works is traditionally related to the energy efficiency of the observed flow fields. The following sections provide a brief overview of some of the major contributions.

### 3.7.1 In Vitro and Computational Models

The study that arguably fathered this field of research was the groundbreaking work of de Leval *et al.*[17] in which experimental investigations demonstrated the efficiency benefits of flow streamlining through straight pipes. This observation served as a primary motivator for the proposed switch from the dilated atriopulmonary connections to the TCPC. Many subsequent studies similarly used very simplistic models of the connection to isolate the impact of key geometric factors. Khunatorn *et al* conducted an in depth analysis of CFD flow fields and pointed to the secondary flow structures in the PAs as an important source of energy dissipation[73]. Sharma *et al*. experimentally demonstrated

improved efficiency through the introduction of a caval offset (i.e., lateral displacement of the central axes of the SVC and Fontan baffle; Figure 3.12)[53]. Gerdes *et al.* showed similar effects with the introduction of baffle curvature[74], while Ensley *et al.* advocated for flaring of the caval connections to the PA junction[75]. DeGroff *et al* showed that even with simplified models and laminar flow, the presence of flow instabilities and secondary flow structures had important implications for the results of computational flow simulations and their agreement with experimental measures[76]. Wang *et al* later confirmed the presence of such instabilities in more complex, patient-specific models as well[77]. These early studies provided a valuable basis for understanding the connection dynamics; however, it was soon realized that simplified, uniform models did not sufficiently capture the complexities of actual patient anatomies, such as the importance of vessel size differences[78-80].

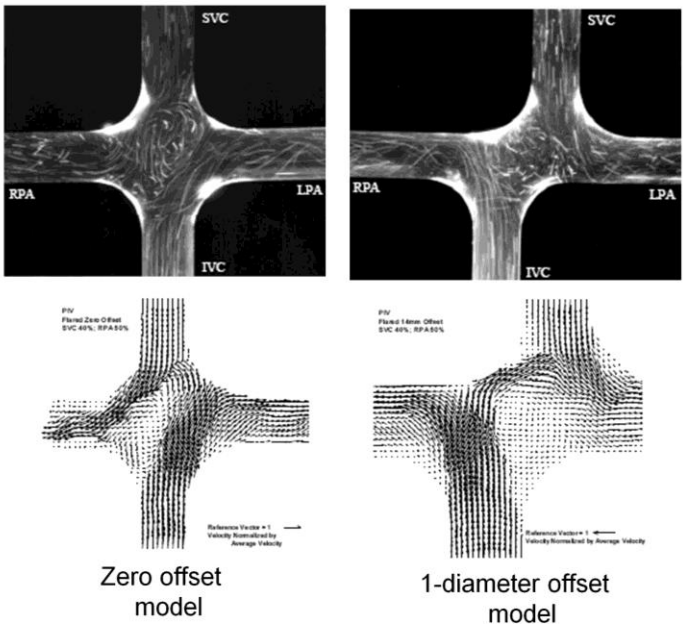


**Figure 3.12 Experimental comparison (via particle tracking (top) and particle image velocimetry vectors (bottom)) of idealized TCPC models with no offset (left) and a 1 diameter caval offset (right). Introduction of caval offset helps avoid flow collision to improve hemodynamic efficiency.**

Since that time, emphasis has shifted significantly toward the use of patient-specific geometries and computational modeling. Subsequent studies continued to reveal tight coupling between the geometric design of the connection and the resulting fluid mechanics[81, 82]. Through analyses of individual case studies or small patient samples, researchers investigated the effects of factors such as simulating LPA angioplasty[83], centrally positioning the Fontan between bilateral SVCs[81], and the results of different connections between the Fontan baffle and PAs[84].

Additionally, the relative ease of increased sample sizes afforded by CFD modeling allowed for broader physiologic insights to be derived. Whitehead *et al.* used CFD in 10 patients to demonstrate the non-linear increase in TCPC power loss that occurs with

simulated exercise flow conditions (Figure 3.13)[56]. Marsden *et al.* made similar observations in two patient-specific models with the inclusion of respiratory effects on time-varying flow conditions[85]. Sundareswaran *et al* showed potential linkages between CFD-derived power loss and cardiac output in 16 patients[55].

Other groups, such as Throckmorton *et al*[86], Rodefeld *et al*[87], and Lacour-Gayet *et al*[88] have leveraged the capabilities of CFD modeling to investigate mechanical support options for the single ventricle circulation.

### 3.7.2 Phase Contrast Cardiac Magnetic Resonance

A concurrent development in Fontan flow visualization and quantitative analysis is the increasing capabilities of medical imaging, particularly cardiac magnetic resonance (CMR), for making direct measurements of *in vivo* flow conditions. For CMR, such capabilities are achieved through the use of phase contrast sequencing, which are described in more detail in §4.1. Such methods are widely used to acquire cross-sectional velocity information in specific blood vessels to inform computational boundary conditions; however, the images themselves can provide valuable hemodynamic insight.

Be'eri *et al.* used planar, mutli-dimensional PC MRI to compare APC and TCPCs[89]. They reported regions of flow stagnation, reversal and recirculation in APC, while TCPC flows were less variable and more unidirectional. Conversely, Sharma *et al.* reported disturbed flow in the Fontan baffle[90].

Expansion of these imaging techniques into 4D provides improved visualization and analysis capabilities, as shown by more recent studies. Markl *et al.* demonstrated the feasibility of these volumetric techniques in 4 patients with an extracardiac connection[91]. Sundareswaran *et al.* used a novel interpolation scheme coupled with a stack of 4D

velocity slices in 16 patients to visualize differences between extra-cardiac and lateral tunnel connections (Figure 3.14)[92].

### 3.7.3 Lumped Parameter Modeling

Lumped parameter modeling has proved to be an effective tool for studying Fontan physiology. The relative simplicity of lower order modeling allows for the inclusion of a broader scope of the domain (i.e., modeling the entire cardiovascular system rather than just the local TCPC district). Such an approach has been used for a wide range of research objectives from prescribing TCPC boundary conditions[93-95], studying the effect of mechanical assist devices[96, 97], or relating TCPC resistance to broader physiology[55]. Some of these represent landmark studies that have provided key insights and motivation into ongoing work. The study by Pekkan *et al* was the first to demonstrate that a cavopulmonary pressure rise of 3-5 mmHg through the use of a mechanical assist device would be effective in reversing the Fontan paradox[96]. Many investigators have used this insight to motivate investigations into low pressure/high volume pumps for the specific application of single ventricles, as opposed to the high pressure design of traditional left ventricular assist devices. The study by Sundareswaran *et al* predicted that increasing TCPC resistance would have deleterious effects on single ventricle loads and function, such as increased afterload and central venous pressure, and decreased preload and cardiac output[55]. These findings served as important motivation for an ongoing NIH-funded study into hemodynamics and patient outcomes (HL098252), as well as much of the work presented in this thesis.

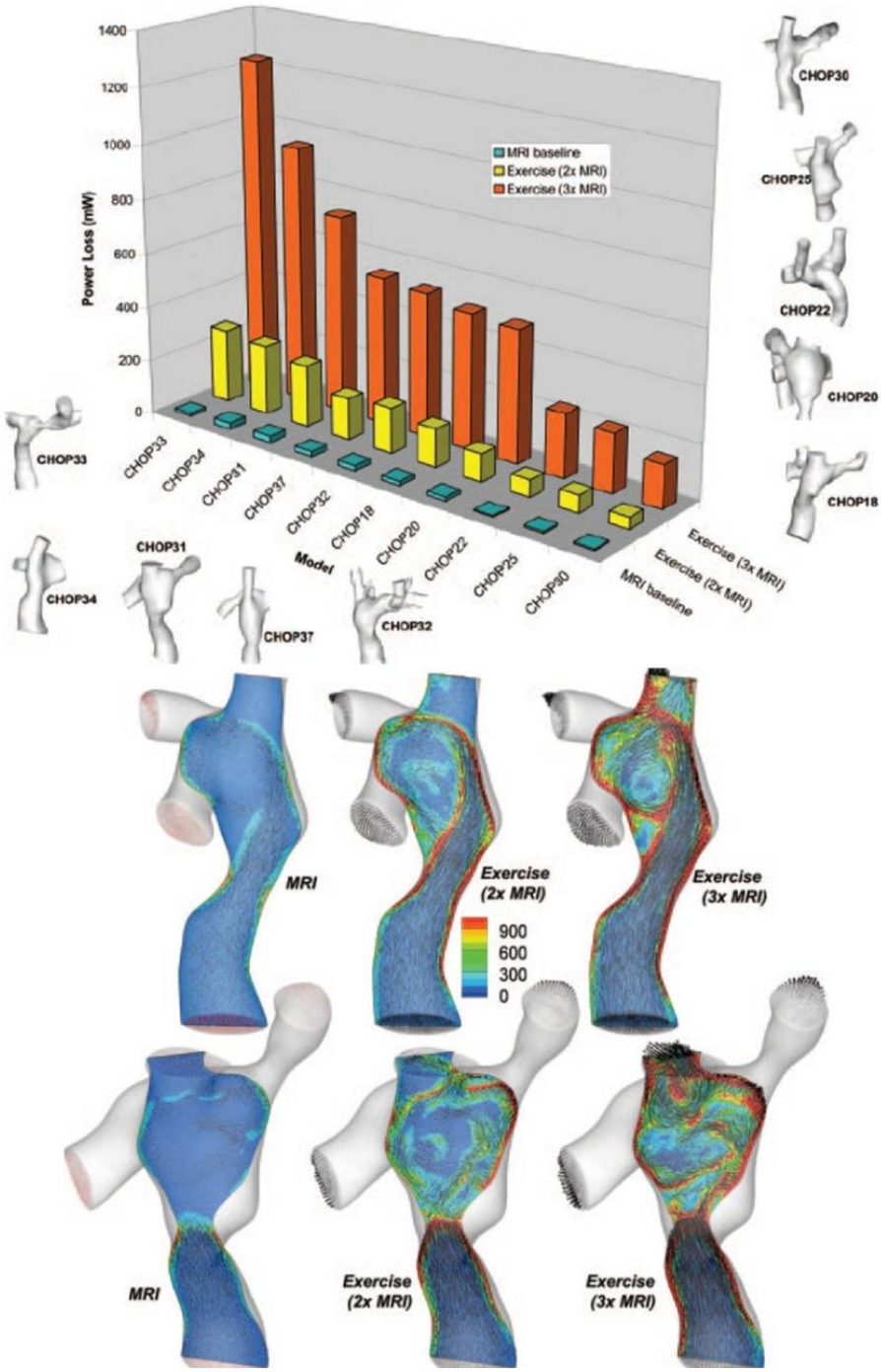


**Figure 3.13 Power loss increases non-linearly with increasing bulk flow rate (left) owing to increasing viscous energy dissipation (right), particularly close the walls. (Images adapted from Whitehead et al.[56])**

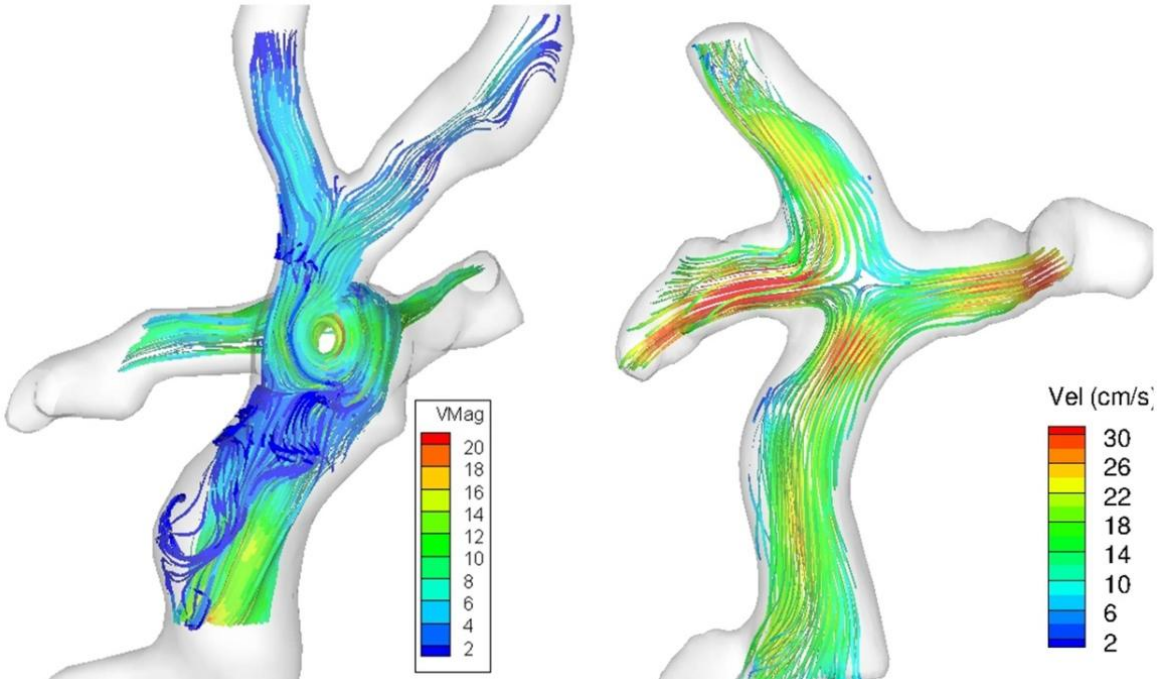


**Figure 3.14 Representative velocity streamlines reconstructed from 4D PC MRI in patient-specific lateral tunnel (left) and extracardiac (right) connections. Qualitative differences in flow patterns based on connection design are apparent. (Adapted from Sundareswaran et al.[92])**

### 3.7.4 Prospective Surgical Modeling

The unifying theme of many of these previous studies is the search for an 'optimal' TCPC geometry. However, patient-specific analyses have conclusively shown that a single, broadly applicable optimal surgical approach is not possible. Instead, the use of CFD methods coupled with anatomical editing capabilities affords the opportunity to prospectively indentify the optimal surgical approach on a case-by-case, patient-specific basis.

Surgical planning, by this definition, is the combination of 3D medical imaging, applied computer vision and computer-aided design capabilities to mimic and/or provide visual

guidance to surgical procedures. Since the first mention of such ideas almost 30 years ago[98], surgical planning is now a routine part of interventions in the fields of neurosurgery[99, 100], spine surgery[101], abdominal interventions[102], catheterization[103], and orthopedics[104]. Translating this paradigm to cardiovascular interventions provides the benefits of not only these enhanced 3D visualization abilities, but also the potential to interface with physics-driven computational solvers (e.g., CFD) to predict the hemodynamic outcomes associated with a given interventional approach.

Application of these principles to Fontan surgery began as theoretical exercises. Pekkan *et al*. showed a 50% improvement in energy efficiency through the virtual angioplasty of a diffuse left pulmonary artery stenosis in a patient-specific TCPC model[83]. de Zélicourt showed a 7% decrease in power loss and alleviation of flow stasis in a bilateral SVC TCPC by centrally positioning the Fontan baffle between the superior connections[81]. These studies provided valuable and useful insights, but did not tap into the fundamental promise of these techniques: to provide *prospective* clinical information.

A major turning point toward the use of surgical planning tools came with the report of Sundareswaran and de Zélicourt *et al.* who were the first to describe a case study of their prospective deployment[61]. In that work, a patient with interrupted IVC and azygos vein continuation had developed PAVM after inclusion of the hepatic venous flow by a Fontan connection to the enlarged Kawashima junction. Analysis by both PC MRI and CFD demonstrated that the hepatic venous flow was unilaterally streaming to a single lung, consistent with the PAVM diagnosis to the contra-lateral side. Multiple surgical options were investigated, and revision to a hepatic-to-azygos connection was ultimately found to produce the most desirable hepatic flow distribution characteristics of the potential options.

de Zélicourt *et al.* followed-up with a series of 5 prospectively modeled studies for patients with interrupted IVC who were surgical treated for PAVM with the use of surgical planning[105]. Trends were elucidated with regard to differences in connection hemodynamics on the basis of superior caval anatomy. Also, the authors reported an improvement in arterial oxygen saturations post-operatively, which anecdotally verified the results of the computational modeling insofar as increased hepatic flow was assumed to be reaching the diseased lung and helping to resolve the PAVM present.

These two studies represent critical proofs of concept for the potential of pre-operative modeling and planning. The linkage between PAVM and hepatic flow distribution is a rare instance in which the direct linkage between hemodynamics and disease is readily observable, making the application of these methods to that disease particularly straightforward. Critically, however, the lack of post-operative data has precluded the ability for more thorough validation of model predictions.

At the same time, Migliavacca and colleagues have also been working toward a surgery planning model through the retrospective study of individual test cases. Their approach has primarily targeted method development rather than application[93]. For example, Baretta *et al* used a coupled multi-scale solver to simulate different Fontan connections for a patient-specific connection and demonstrated efficiency differences among the various options[95]. Pennati *et al* used the same model to compare simulated post-operative physiology to actual acute patient measurements with mixed results, particularly with respect to the distribution of pulmonary flows[94].

### 3.7.5 Fontan Y-Graft

Another novel insight that has come from the extensive engineering analyses of the TCPC is the proposal of completely redesigned connections. While small changes to

positioning or angle of the Fontan baffle incrementally improved losses compared to head-on collision, such designs still mediated a complex flow transition from caval veins to pulmonary arteries with high potential for dissipative secondary flow structures[73]. This prompted the proposal by Soerensen *et al.* for the 'Optiflo' connection (Figure 3.15, right) in which the cavopulmonary connections were both bifurcated to allow for a streamlined, efficient transition of flow into the pulmonary circulation[106]. The authors reported between 23 and 40% decreases in power loss in a model with constant vessel cross-sections compared to the 1D offset TCPC model under increasing cardiac output conditions.

In a subsequent study, Marsden *et al*. designed a 'Y-Graft' bifurcation (i.e., half of the Optiflo) applied to patient-specific models and reported improved efficiency compared to an offset TCPC control[107]. This latter study also brought to light the importance of the choice of graft sizing for this bifurcated connection. Two different designs were modeled: one in which the cross-sectional area was maintained (18x12x12 mm), and one in which the branch diameters were held constant (18x9x9 mm). The former graft was the most efficient of the series, while the latter was actually slightly less efficient than the offset TCPC.

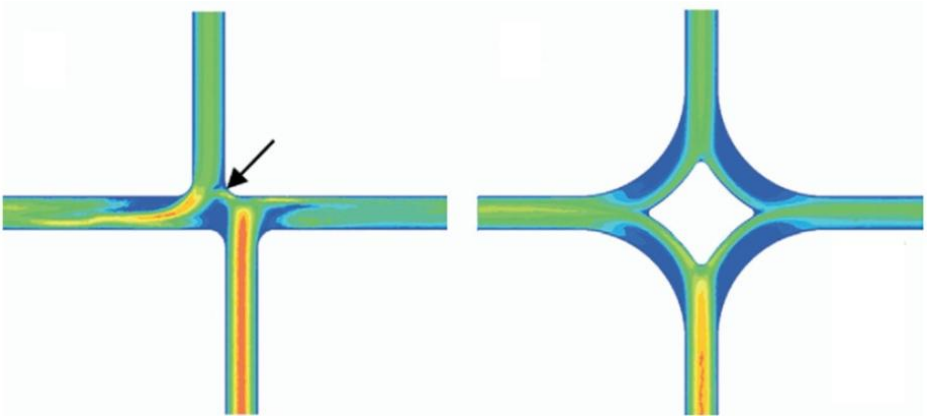

**Figure 3.15 Comparison of velocity fields via CFD for a 1D offset TCPC model (left) and a prototype of the Optiflo connection (right). The bifurcated design of the Optiflo is shown to streamline flow transition to the pulmonary arteries and avoid dissipative caval flow collision (arrow, left).**

Like surgical planning, the use of bifurcated grafts for the Fontan connection appears to a promising means of reducing the hemodynamic energy required to move blood from the systemic to the pulmonary circulations and thus improve circulatory function. However, the studies of Soerensen and Marsden did not address surgical feasibility, and so critical questions still remain as to the utility of this approach.

## 3.8 Summary and Significance of the Proposed Approach

Despite the relatively low incidence of single ventricle defects, the numerous complications have an impact on the whole healthcare system. With improved survival through their early care and operative course, single ventricle patients are living longer than ever before. In fact, there are now more adults than children living with congenital heart disease[8], and the number of adults is estimated to be growing at 5% per year in the US alone[108]. However, despite over 50 years of surgical experience with single ventricle defects, there is not yet a solution; instead, high early mortality has been

replaced by gradual attrition and onset of cardiac and gastrointestinal dysfunction. Thus, the cost of caring for these patients is also disproportionately large given their numerous chronic health issues[109].

These facts dictate that it is no longer sufficient to advance these patients through the early stages of surgical care and medical management with the 'simple' objective of short-term survival. Rather, every effort should be taken to understand and consider the long-term implications of these actions to help offset the compounding effects of an aging and chronically ill adult congenital heart disease population. The TCPC, as a central component in single ventricle management, serves as a prime target for detailed characterization. Past research has suggested numerous plausible functional hypotheses, but corroboration with patient data have generally been lacking.

For these reasons, the present study is designed to make several significant contributions to the field:

1) *Establish the functional importance of TCPC power loss*. Many studies have sought to evaluate TCPC hemodynamics; none have possessed sufficient sample size to make statistically powered observations. To date, the largest investigation of TCPC flows have only included sample sizes of 16[55, 92]. Similarly, many studies have considered the TCPC and the single ventricle in isolation, but none have sought to relate them using functional patient data. The proposed work contains both the statistical power and combination of endpoints to elucidate the relationship between the TCPC and single ventricle function, as well as the evolution of such metrics with time.
2) *Shift the surgical paradigm for TCPC design.* As a direct extension of the previous item, if, per the stated hypothesis, the magnitude of power loss is found to

significantly impact VF, then the use of pre-operative planning tools for TCPC design to minimize power losses will be justified. A recent National Heart, Lung, and Blood Institute working group on research in adult congenital heart disease recommended the development of technology to "support hemodynamic and functional modeling of individual patients to improve understanding of cardiac status, and to plan for future therapy"[8]. The framework for such a surgical planning system already exists[61, 110], but it lacks two critical inputs: 1) an understanding of which hemodynamic measures are clinically relevant at what thresholds; 2) verification that the pre-operative models reflect the post-operative hemodynamic results. Both of these points are addressed through this thesis.

3) *Establish the efficacy of new TCPC designs.* Again, with the importance of TCPC power loss established, the continued search for new means of systematically improving it would be justified. The Y-Graft/Optiflo paradigm is a theoretically promising one, but critical clinical questions (*in vivo* power loss performance, size selection) remain outstanding.

# Chapter 4. MATERIALS AND METHODS

## 4.1 Magnetic Resonance Imaging (MRI)

The studies performed in this thesis are entirely dependent on the use of MRI to extract patient-specific anatomic and physiologic information to inform subsequent modeling and/or analysis. Thus, a brief overview of the physics behind MRI is first presented before detailing the specific sequences used and post-processing performed.

### 4.1.1 Physics Background

At a basic level, MRI produces an image by manipulating the rotation of water molecules (comprising between 70-90% of most body tissues) by subjecting them to a series of controlled magnetic spatial gradients superposed on a strong homogeneous magnetic field. As opposed to other medical imaging modalities such as X-ray, which are limited in their means of signal generation (e.g., attenuation of x-rays) and thus their means of generating contrast between adjacent tissues, there are any number of different sequences of magnetic field excitation that will each change the signal received. This characteristic is one of the primary strengths of the method and so will be explored in more detail in this section.

Consider a single proton. This particle is naturally in constant rotational motion and thus, because of its positive charge, creates its own weak magnetic field. If placed in a strong external magnetic field, this proton will tend to align the main axis of its own magnetic field with the direction of the main field; however, quantum mechanical effects keep the proton from statically aligning and it instead precesses about the main magnetic field axis ($B_0$; Figure 4.1). The angular speed of this rotation, $\omega_0$, is directly proportional to the magnetic field strength according to the Larmor equation:

$$\omega_0 = \gamma B_0$$ **(Equation 4.1)**

where γ is a constant called the gyromagnetic ratio. Hence, in a given sample under the influence of the same magnetic field, all protons are precessing at the same frequency. The vector sum of these spins is the net magnetization vector of the sample (effective magnetic moment), $M_0$, which is still small with respect to $B_0$.

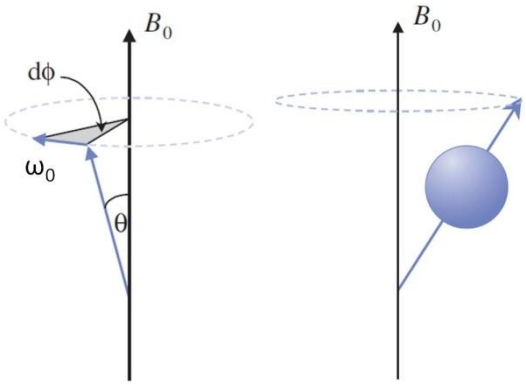


**Figure 4.1 Precession of proton about $B_0$ axis (adapted from[111]).**

In order to yield a measurable signal from $M_0$, it must be translated to the 'transverse' plane (90° from the direction of $B_0$) by a secondary magnetic field. This field is temporarily created by the so-called radiofrequency (RF) pulse ($B_1$, Figure 4.2) emitted by a separate transmitter coil. The angle swept by $M_0$ under the influence of $B_1$ depends on the duration of the RF pulse. For example, a "90° pulse" is timed to position $M_0$ on the

transverse plane. Additionally, the RF pulse induces phase coherence of the precessing protons (i.e., they all point in the same direction on the transverse plane). This rotating field thus induces a voltage in a receiver coil that is sensitive to magnetization only in the transverse plane.

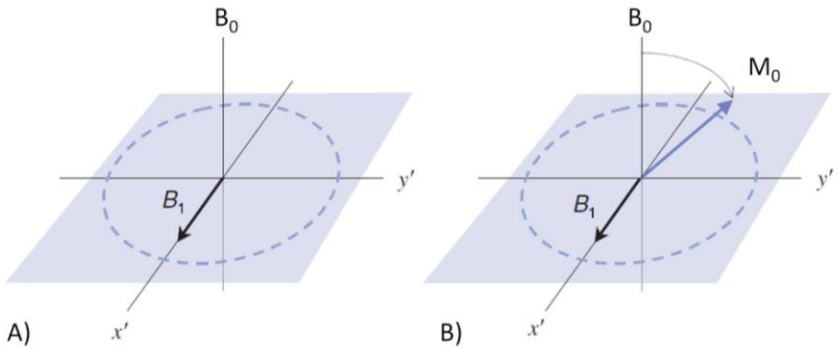


**Figure 4.2 A) Creation of RF pulse ($B_1$) to B) translate effective magnetic moment, $M_0$, from $B_0$ to the "transverse plane" (xy) to generate a measurable signal (adapted from[111]).**

Once the RF pulse is turned off, small inhomogeneities in the local magnetic field and proton-proton interactions cause the loss of phase coherence in the transverse signal amplitude, $M_\perp$. In fact, the signal decays exponentially (as the spins "fan out") in several milliseconds according to:

$$\frac{dM_\perp}{dt} = -\frac{1}{T_2} M_\perp \quad \textbf{(Equation 4.2)}$$

(note: this equation assumes a rotating reference frame), where $T_2$ is the experimental constant known as the "spin-spin" relaxation time constant. At the same time, the

magnetization component parallel to the main magnetic field is gradually restored as the energy imparted by the RF pulse is dissipated (as thermal energy) into the surrounding lattice. This can be expressed as:

$$\frac{dM_z}{dt} = \frac{1}{T_1}(M_0 - M_z) \quad \textbf{(Equation 4.3)}$$

where $M_z$ is the magnetization component parallel to the main magnetic field, $M_0$ is the equilibrium magnetization, and $T_1$ is the experimental "spin-lattice" relaxation constant. As a general rule, $T_1$ is much larger than $T_2$, therefore its relaxation is much slower. Together, Equation 4.2 and Equation 4.3 form the Bloch Equation for the time rate of magnetization (again presented in the rotating reference frame):

$$\frac{dM}{dt} = \frac{1}{T_1}(M_0 - M_z)\hat{z} - \frac{1}{T_2}M_{\perp}\widehat{xy} \quad \textbf{(Equation 4.4)}$$

While this temporary pulse and decay does create a readable signal (from what is known as Free Induction Decay), practically speaking this is not a signal of interest in clinical imaging. Instead, most images are built using "echoes" in the magnetization signal. The most common are gradient and spin echo sequences.

#### 4.1.1.1 Gradient echo

The Larmor equation dictates that angular frequency is dependent on magnetic field strength. While the frequency is therefore uniform under the sole influence of the main magnetic field, the superposition of a spatially-varying magnetic field will create heterogeneous frequencies within the sample as a function of position within the

smoothly varying field (Figure 4.3). As will be covered in a subsequent section, the ability to create these gradients is central to the spatial localization of images, but is also the basis for gradient echo sequencing.

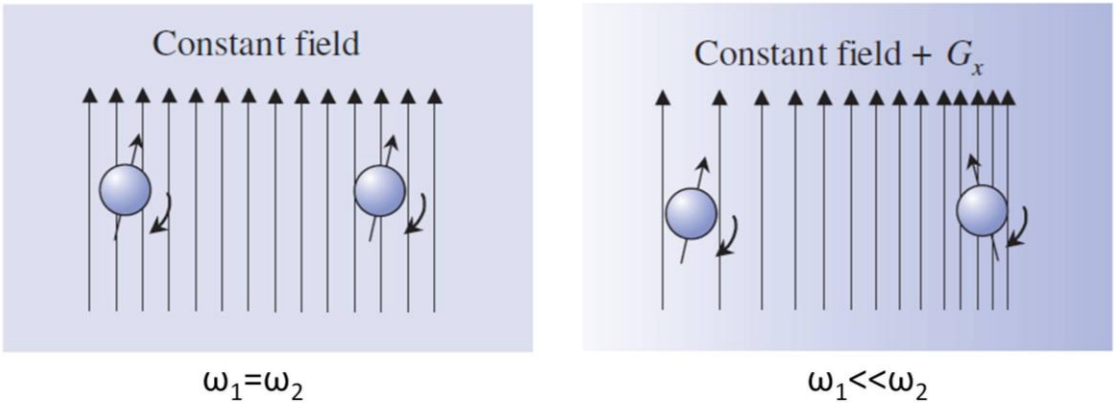


**Figure 4.3 Effect of local gradient superposition on proton spins. When the field was uniformly constant (left image), angular frequencies were the same. With spatially varying field (right), precession was slower in lower field strength and faster with higher field (adapted from[111]).**

A visual description of this process is illustrated in Figure 4.4. Following the RF pulse, a negative spatial gradient is briefly turned on causing a rapid dephasing of the transverse magnetization. The gradient is then reversed so that instead of dephasing, the spins rephase and eventually come back together into a coherent signal, called an echo. The signal associated with this echo is read by the receiver coil to build the image.

#### 4.1.1.2 Spin echo

A schematic of this process is illustrated in Figure 4.5. In this case, the spins are allowed to dephase naturally ($T_2$ decay) for a time following the RF pulse before a 180° pulse about the transverse plane is applied. With this latter pulse, the protons that had been dephasing faster (clockwise in the figure) are positioned “behind” the previously lagging protons, and vice versa. Thus, the natural dephasing will move the spins back toward coherence and, after a time equal to the delay between the 90° and 180° pulses, the echo occurs.

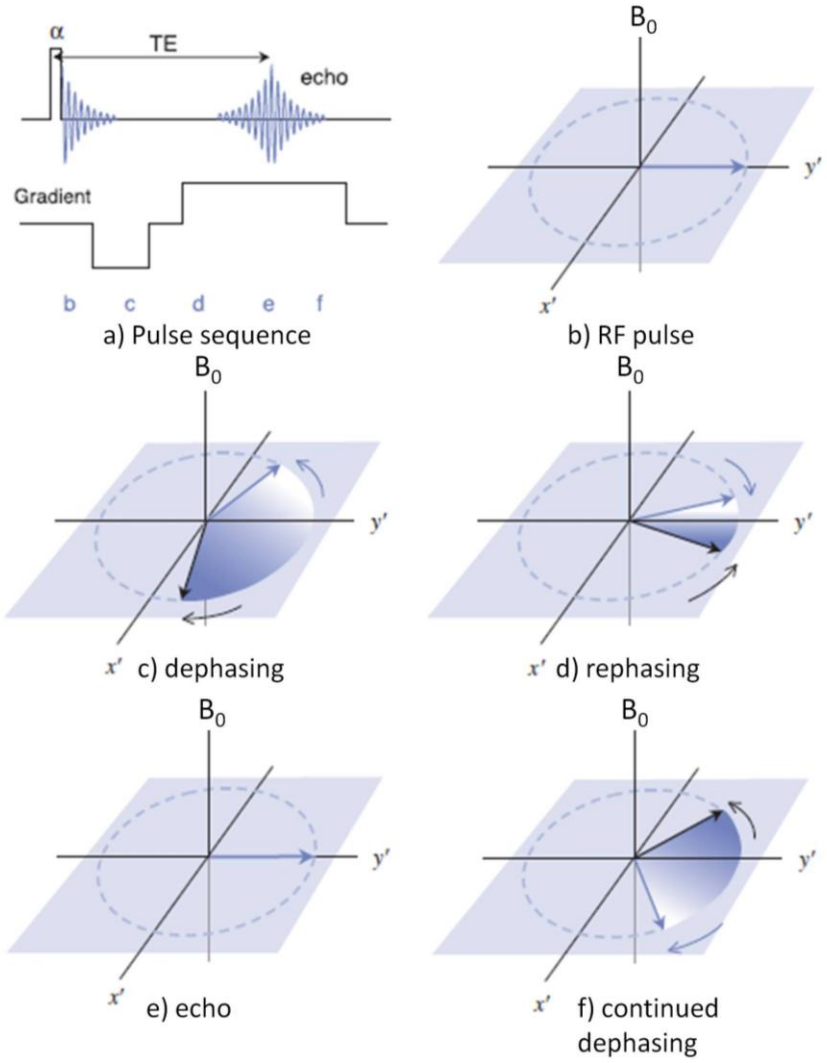


**Figure 4.4 Schematic of gradient echo sequence. a) Sequence diagram depicting relative timings of b) RF pulse, c) negative gradient lobe dephasing, d) rephasing under function of positive gradient lobe, e) formation of the echo, and f) continued dephasing (adapted from[111]).**

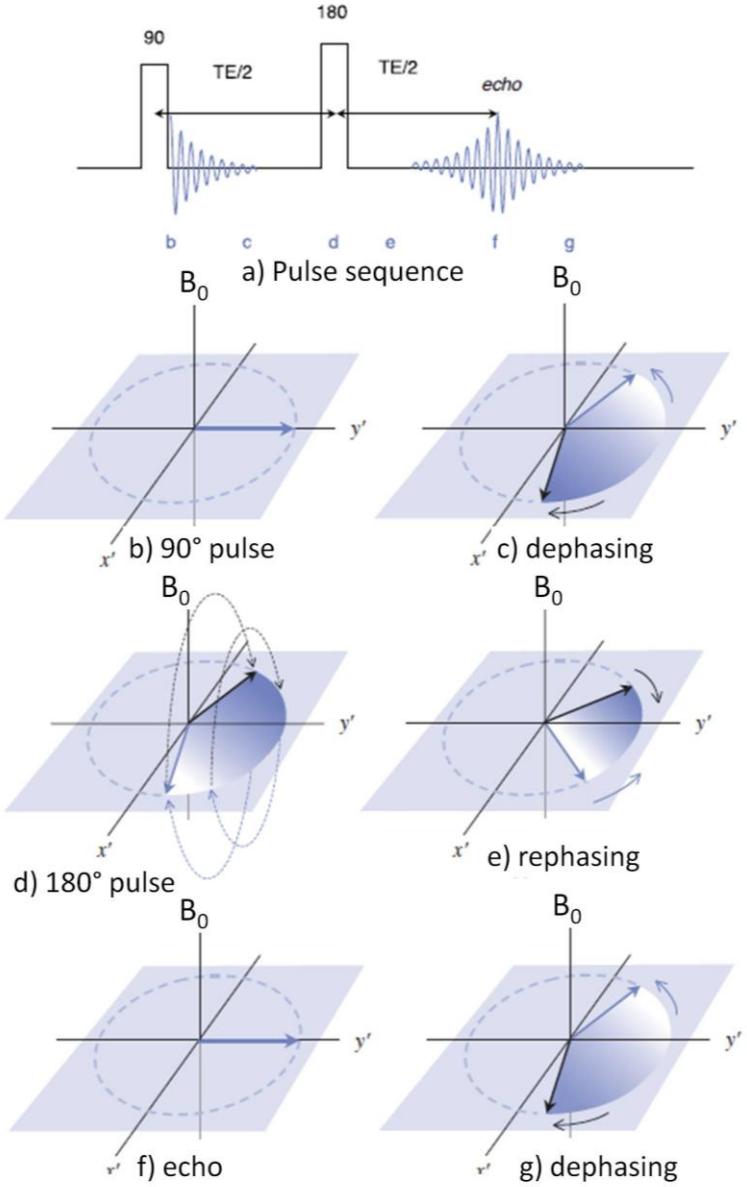


**Figure 4.5** ***Schematic of spin echo sequence. a) Sequence diagram depicting relative timings of b) 90°RF pulse, c) natural spin-spin dephasing, d) 180° pulse, e) natural spin-spin rephasing, f) creating an echo, and g) continued dephasing (adapted from[111]).***

#### 4.1.1.3 Image acquisition and k-space

Echoes are a key component in the methods of MR image acquisition, but they do not address the fundamental task of spatial localization. This process is achieved through the concerted application of multiple spatial gradients in addition to the “readout” gradient used to form the echo. This multi-dimensional gradient spectrum is ultimately what is built up, as “k-space”, to reconstruct the MR image using Fourier transforms. A generic representation of a 2D gradient echo-based image sequence is shown in Figure 4.6; the following paragraphs describe these constituent components in more detail.

The first step is slice selection: exciting a thin slab (for planar imaging) to image from the entire 3D volume of interest. This process involves two distinct components: a spatial gradient acting perpendicular to the desired slice (for an axial slice, this gradient would run from foot to head); and a specially tuned RF pulse with a narrow, specifically focused bandwidth corresponding (through the local gradient-induced Larmor frequency) to the location and thickness of the desired slice. The correspondence of these components with each other and the resulting slice selection is illustrated in Figure 4.7. The final step in slice selection is a rephrasing lobe (the negative portion of the slice selection signal in Figure 4.6). Just as the spatial gradient induces a spatial ‘spreading’ or spin dephasing in the creation of the gradient echo, the slice selection gradient has the same dephasing effect. The rephasing lobe therefore acts to refocus the spins to ensure a uniform distribution through the slice thickness.

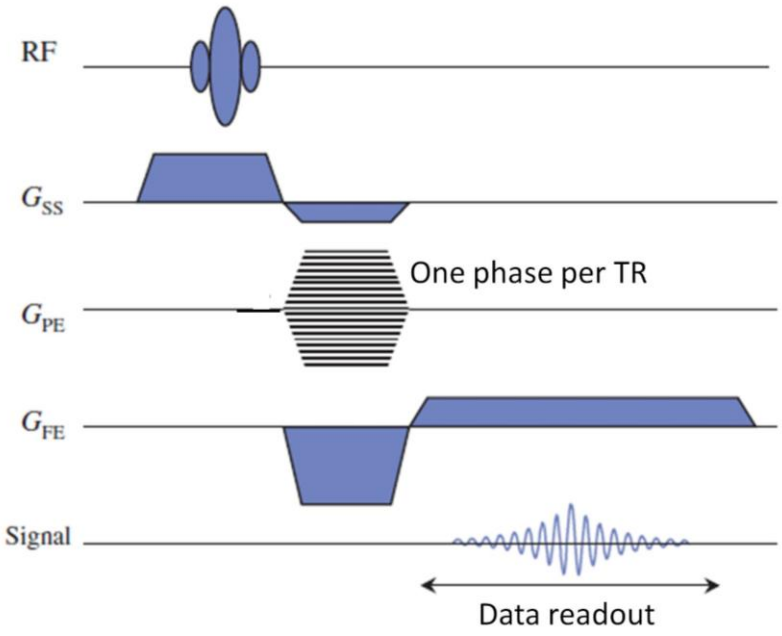


**Figure 4.6** ***Generic sequence schematic for gradient echo acquisition of a 2D slice with time positioned along the x-axis. $G_{SS}$- slice selection gradient; $G_{PE}$- phase encoding gradients (hashed lines denote coverage over sequential RF pulses); $G_{FE}$- frequency encoding (also known as "readout" direction)(adapted from [111]).***

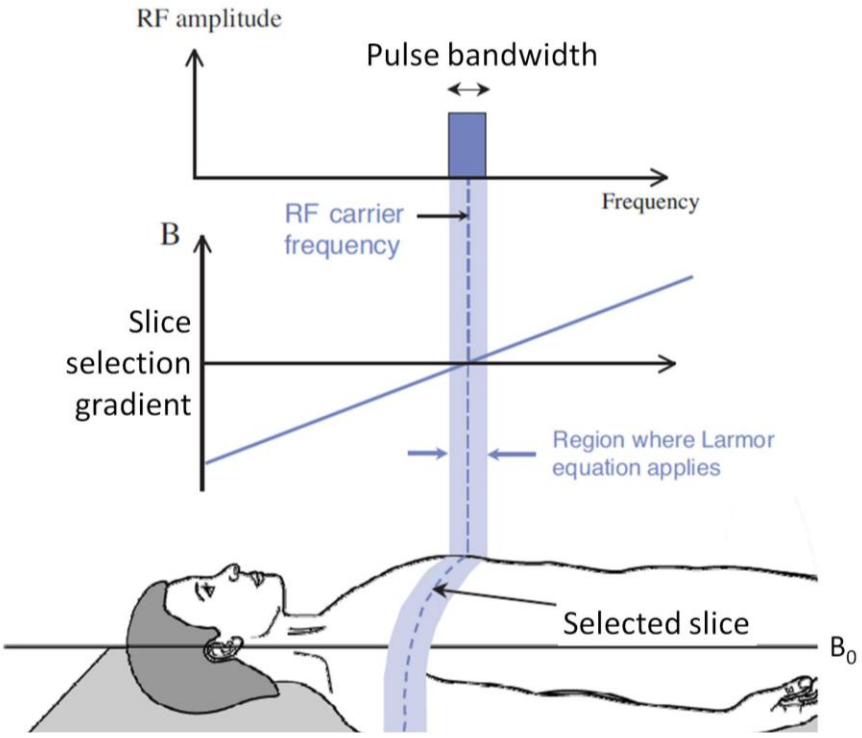


**Figure 4.7** ***Interplay of RF pulse and slice selection gradient to isolate a thin localized image slice. The specific frequency of the pulse is tuned to correspond to the Larmor frequency of the region of interest after application of the slice selection gradient. The RF bandwidth determines the slice thickness (adapted from[111]).***

With the slice localized, the next challenge is to spatially encode the information within that slice, which is done with a combination of frequency and phase encodings. For the phase encoding (represented by line 3 of Figure 4.6 and visually illustrated in Figure 4.8), a gradient is rapidly turned on and off in the phase encode direction. While the gradient is on, the frequencies vary spatially with the gradient such that, when the gradient is turned off and the spins are again precessing at a uniform frequency, the accumulated phase differences remain. This phenomenon is represented in Figure 4.8 by the fact that the arrows in the last column are at different phase angles even though they all have the same instantaneous frequency. Finally, the frequency encoding is

performed in the direction orthogonal to the phase encoding as described in the gradient echo section: a continuous gradient induces a spatially varying frequency profile that is detected by the receiver coil.

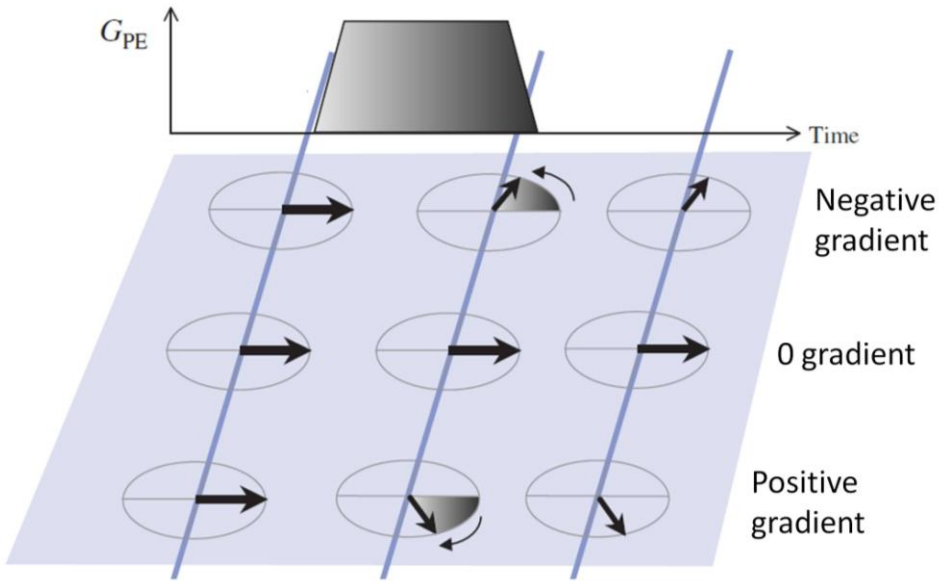


**Figure 4.8** ***Visual demonstration of the effect of phase encoding gradients. While gradient is on (middle column) the varying spatial frequencies dephase signals as usual such that, once the gradient is turned off (last column) the spins return to a uniform frequency but the acquired phase offsets remain (adapted from[111]).***

The process just described above pertains to a single RF excitation, which is insufficient for completely resolving an entire image. In fact, in the image spectrum matrix being measured (i.e., k-space), this sequence corresponds to a single measurement line. As represented by the discrete bans of the phase encoding excitation in Figure 4.6, this process of RF-slice selection-phase encoding-frequency encoding is repeated numerous

times (with varying magnitudes of the phase encoding gradient) to completely fill in the k-space matrix. Once completed, k-space looks like the top image of Figure 4.9a (with the corresponding magnitude image on the bottom). Interestingly, Figure 4.9b and Figure 4.9c reveal the distinct information encoded in the different parts of k-space: the low frequency central region carries most of the bulk image information (seen in the 'burry' bottom image), whereas the high frequency extremities of k-space carry most of the edge information.

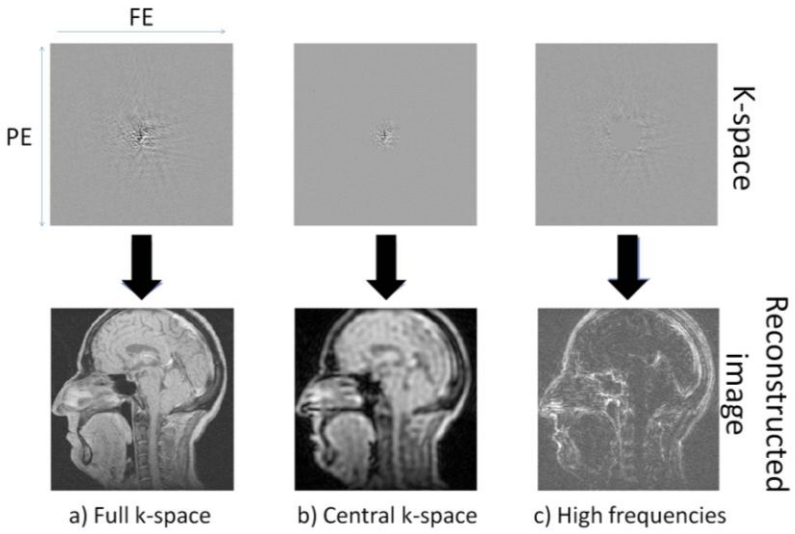


**Figure 4.9** ***Relationship of k-space to the resulting magnitude image. In b) only the low frequency center of k-space was used and the resulting image contains the bulk features but lacks edge definition. In c) only the high frequency regions of k-space were used and the reconstruction contained primarily the edge information missing from b)(adapted from)[111].***

Here it is worth noting that the spatial resolution of an MR image is dependent on the selections made regarding the frequency and phase encodings. At a basic level, the resolution depends on the size of the image and the number of sample measurements it contains. For a given field of view, the MR resolution depends on the matrix size, i.e., the number of frequency and phase encoded lines measured; the gradient magnitude (higher is better); and the sampling time (FE direction only; again, more is better). Conversely, decreasing the field of view at a constant matrix size requires increases in either the gradient strength or sampling time (FE direction).

Finally, the techniques herein described for acquisition of a 2D slice can be easily extended to a 3D volume. By simply phase encoding the third orthogonal direction and methodically covering a range of phase values for that component in addition to the planar phase encoding direction, the acquired slice is extended to a 3D (or 4D, with time) volume. Of course, the tradeoff with such an acquisition is the increased time needed to cover an additional phase encoding range for each of the original phase encoded lines.

#### 4.1.1.4 Contrast and Signal-to-Noise

In MR acquisitions, there is a finite signal available for each tissue in the field of view, which is dependent on the tissue properties and the sequence used. Ideally, a high contrast is achieved such that the tissue of interest generates a high signal while the signal from surrounding tissues is suppressed. This is done by leveraging inherent differences in tissue characteristics (proton density, $T_1$, or $T_2$) by manipulating sequence parameters such as repetition time (TR; the time between consecutive RF pulses) and the echo time (TE; the time from the RF pulse to the echo). Notably, the means of forming the echo (spin or gradient) does not matter as both can be used to generate $T_1$ or $T_2$-weighted images.

As an example of tissue dependent property values, fluids like cerebrospinal fluid and blood have higher proton densities than bones or tendons. For $T_1$, fluids (1500-2000 ms) have longer relaxation times than water-based tissues (400-1200 ms) or fat-based tissues (100-150 ms). The same is true for $T_2$ relaxation, even though the values are much smaller: times for fluids (700-1200 ms) are higher than those of water-based (40-200 ms) or fat-based (10-100 ms) based tissues[111].

For $T_1$-weighting, $T_2$ effects must be minimized to exploit only $T_1$ differences between tissues. Hence, both TR and TE are kept short (less than 40 ms for TE). With a short TR (less than 750 ms), tissues with longer $T_1$, such as blood, do not have enough time to completely relax before the 2$^{nd}$ RF pulse; thus, their transverse magnetization components are decreased compared to tissues with shorter $T_1$ after the subsequent RF. For this reason, fluids (like blood) usually appear dark in $T_1$-weighted images, unless they are flowing into the region of interest during the acquisition, which nullifies the effect of the short TR. When using gradient echo sequences to weight by $T_1$, the choice of flip angle (i.e., the angle traced out between the $B_0$ axis and the transverse plane as a function of the RF pulse) is also of profound importance as it will determine the component of magnetization that remains parallel to $B_0$ (and therefore does not have to 'relax' before the subsequent pulse. Hence, flip angles greater than 50° are generally required to achieve the desired $T_1$ weighting.

Conversely, $T_2$-weighting seeks to minimize $T_1$ effects using long TR (>1500 ms) and TE (>75 ms) values. For this reason, $T_2$ scans typically take much longer as scan time directly relates to TR. Fluid volumes tend to produce the strongest signal in $T_2$-weighted images, as the rapid dephasing of surrounding tissues is more apparent with longer TEs. This feature makes $T_2$-weighting a common selection in analysis of fluid-based pathological specimen surrounded by other soft tissues.

The final basic option is proton density weighting, which (as the name implies) relies solely on a higher number of protons present in a given tissue to produce a stronger signal than neighboring tissues. For these scans, both $T_1$ and $T_2$ effects must be negated. Notably, effects of proton density differences cannot be corrected in $T_1$- or $T_2$-weighted images and can act as a compounding factor, even though the relative proton densities of body tissues are fairly consistent. As may be guessed from the preceding paragraphs, long TR (to mitigate $T_1$ differences) and short TE (to negate $T_2$) scans are used to weight by proton densities.

The signal generated by these techniques is offset partially by the presence of noise: random differences in pixel values. In MR, these differences arise from fluctuations in electrical currents: those in the MR coils as well as the electrically conductive body tissues (containing ion channels) being imaged. The ratio of the signal strength to the noise magnitude is known as the signal-to-noise ratio (SNR). SNR is generally maximized through the use of dedicated body coils specific to the region of interest.

#### 4.1.1.5 Steady-State Precession and Coherent Echoes

The previous introduction of gradient echo and spin echo principles was very basic. In clinical reality, particularly in time-varying applications like cardiac imaging, time is limited and means of improving efficiency and speed of acquisition are highly sought. Perhaps the easiest way to cut down on scan times is to reduce TR. At short TR intervals, $T_1$ relaxation is incomplete and the longitudinal magnetization component exposed to the RF is reduced. However, after several RF pulses this component equilibrates such that the transverse magnetization completely relaxes between pulses. Equivalently, the longitudinal magnetization reaches a ‘steady-state’ and no longer varies with each RF pulse.

In many applications, TR may be reduced even below $T_2$. In such cases, remnants of transverse magnetization remain at the time of the following RF pulse that create ‘partial echoes’ in addition to the natural FID during the subsequent pulse period. Without properly accounting for these extra echoes, severe image artifacts and incorrect contrast characteristics ensue. There are three common strategies to handle the partial echoes: 1) “spoiling”, while removes these partial echoes; 2) “rewinding”, which uses them; and 3) “time reversing”, which exclusively depends on their formation.

Of these three, the rewinding option has become a predominant favorite for cardiac applications and Steady-State Free Precession (SSFP) sequences, which use this approach are considered a ‘workhorse’ of CMR owing to excellent contrast between blood and the myocardium. Figure 4.10 outlines a fully rewound, or ‘balanced’ SSFP acquisition. The defining characteristic of this pulse is that each gradient is reversed, i.e., the zeroth moment of all magnetization gradients about the RF pulse is 0.

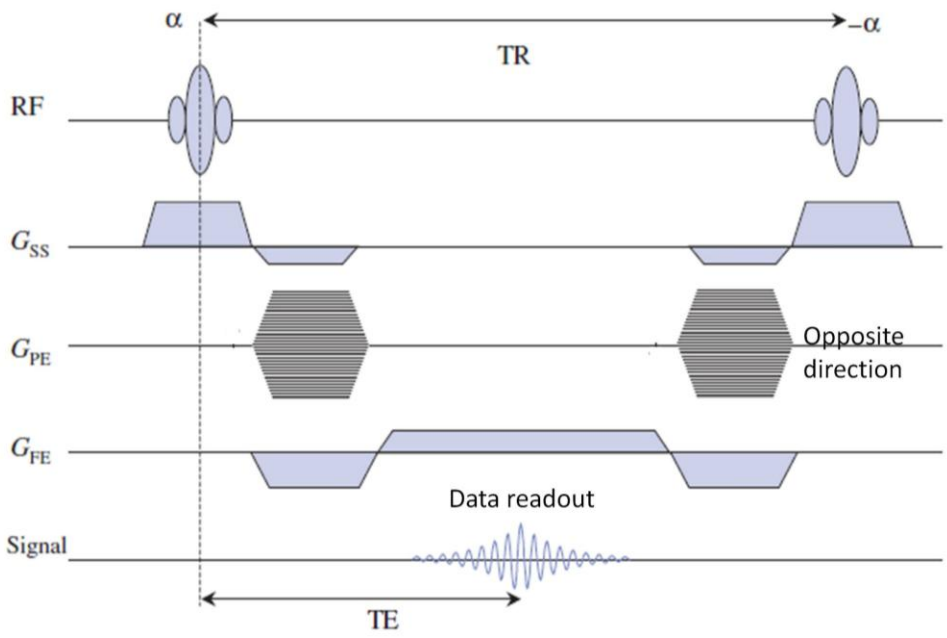


**Figure 4.10** ***Sequence diagram of a balanced, rewound steady-state gradient echo acquisition. It is noted that all gradients are reversed prior to the following RF pulse such that the net moment in every direction from pulse to pulse sums to zero (adapted from[111]).***

#### 4.1.1.6 Angiography and Phase Contrast Velocity Imaging

An implicit assumption made in reconstructing MR images from the basic spatially-varying phase encoding scheme is a lack of motion. In other words, changes in magnetization in a slice from pulse to pulse are expected to result only from changes in the phase encoding amplitude. Blood flow therefore presents an obvious violation of this assumption and in purely anatomical scans, it must be corrected for to avoid significant artifact formation. On the other hand, the signal disturbances resulting from blood flow can also be utilized to provide detailed functional information. This fact is another of the great strengths of MR in medical imaging and can be done in one of two ways: angiography (MRA) or phase contrast (PC MR).

Angiography is largely a qualitative approach to flow measurement, which relies on 'time-of-flight' (TOF) effects to generate flow signals related to the bulk flow velocity. MRA can be done using either spin echo or gradient echo sequences; however, because gradient echo methods produce bright blood images (preferable for image processors) compared to dark blood spin echoes, we will presently only consider the gradient echo situation. Figure 4.11 visually demonstrates the principle behind these acquisitions. First considering a case where the blood velocity is low (near 0) and assuming $TR<T_1$ for blood, the blood in the region of interest would become saturated by the short TR and produce little signal (Figure 4.11a). On the opposite extreme, if the blood is moving fast enough such that the volume in the slice is completely replaced (i.e., completely flows out of the volume) between successive pulses, the incoming blood would be unsaturated and produce a strong signal compared to the surrounding tissues (Figure 4.11c). In between (Figure 4.11b), the signal would be intermediate to these two cases as there would be a mixture of saturated and unsaturated blood signal within the volume. The critical velocity, Vc, distinguishing b from c is related to the slice thickness, z, and TR as:

$$\boldsymbol{Vc = \frac{z}{TR}} \quad \textbf{(Equation 4.5)}$$

such that $V \geq Vc$ produces the maximal signal of case Figure 4.11c.

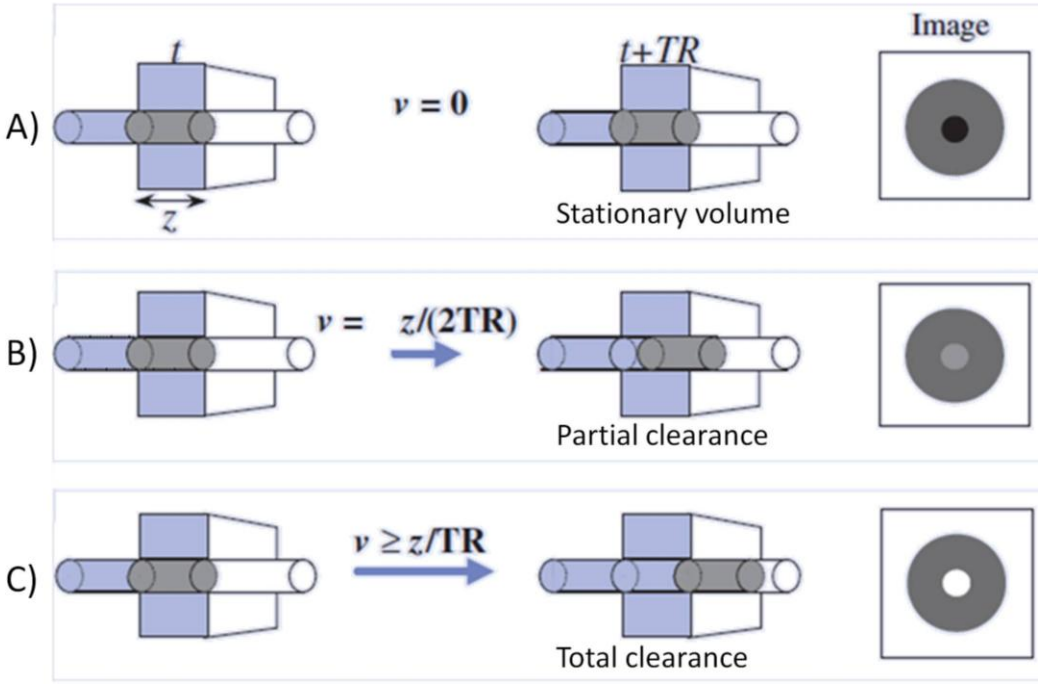


**Figure 4.11** ***Relationship between flow rate and image intensity for gradient echo MRA acquisitions. For slow moving or stagnant fluid (a), the spins become saturated and no fluid signal is produced. For high velocities (c), the fluid in the volume of interest completely moves out of the volume between successive pulses and the new fluid volume produces a high signal on the next pulse. For moderate velocities (b), the signal produced falls in between a) and c) because of partial spin saturation (adapted from[111]).***

By comparison, PC MRI is a quantitative means of measuring velocities in individual voxels in the region of interest. The underlying principle behind the method is that the phase shift acquired by moving spins under the influence of a bipolar gradient pulse is linearly related to the time rate of travel, i.e., its velocity, through a known dependency. The explanation is as follows. Phase is the time integral of precession frequency, $\varphi = \int \omega \, dt$, which is spatially dependent on the main magnetic field and the local gradient strength: $\varphi = \gamma \int (B_0 + G_x x) dt$. For spins moving at the constant velocity, v, this

relationship becomes: $\varphi = \gamma \int (B_0 + G_x(x + vt))dt$. Assuming a constant gradient, G, applied for a fixed time interval, T:

$$\boldsymbol{\varphi = \gamma \int_0^T Gvt\, dt = [\frac{1}{2}\gamma vGt^2]_0^T = \frac{1}{2}\gamma vGT^2 = \frac{1}{2}\gamma vM_1}$$ **(Equation 4.6)**

where $M_1$ is the "first moment" of the gradient. The negative gradient lobe creates a similar moment that cancels out all phase differences in stationary spins, but not the moving ones. Now, because phase contrast is usually imposed with gradient echoes, phase distortions due to local field inhomogeneities become important. It therefore becomes necessary to acquire a second image with the gradient lobes reversed to subtract the effect of the local distortions such that the only phase differences are the result of the desired motion:

$$\boldsymbol{\Delta\varphi = \gamma v \Delta M_1}$$ **(Equation 4.7)**

The relationship between the velocity and this magnetic moment must be encoded into the sequence prior to the acquisition, which is done by defining the velocity encoding, VENC, parameter. The VENC is the velocity that creates a 180° phase shift (π radians):

$$\boldsymbol{VENC = \frac{\pi}{\gamma M_1}}$$ **(Equation 4.8)**

Thus, by selecting the gradient strength and duration that corresponds to the desired VENC, the velocity of each voxel can be calculated following acquisition.

As is true with many of the sequences discussed in the prior sections, phase contrast acquisitions can be easily extended to cover three orthogonal directions and therefore resolve a three-dimensional velocity vector. An example of such a 3D PC MR acquisition is shown in Figure 4.12 along with the corresponding magnitude image.

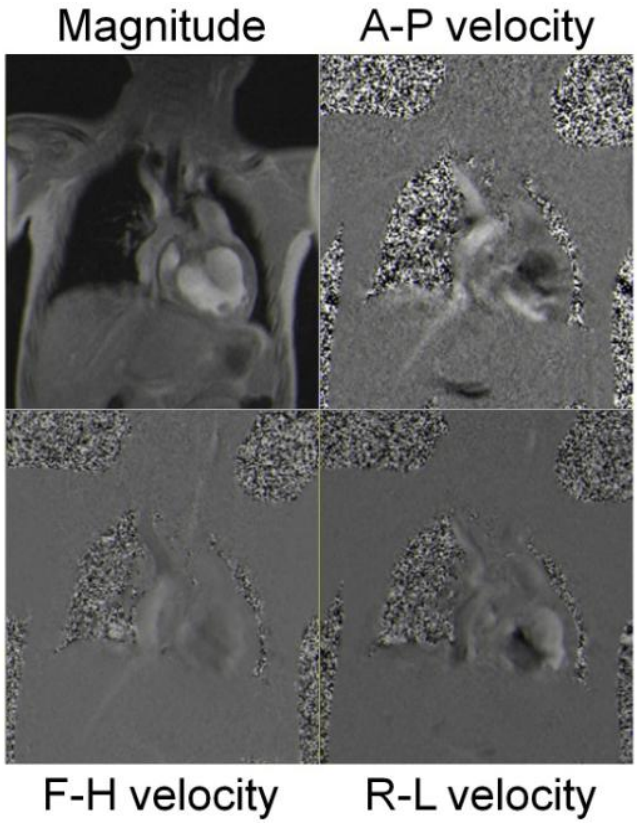


**Figure 4.12** ***Example of coronal slice acquisition of 3-component velocity vectors (plus magnitude image in top left) for a single ventricle patient with completed TCPC[92].***

From this basic MRI background, several strengths and attributes of the technology should be apparent, which make it the preferred method for hemodynamic investigations of the TCPC. First, the imaging data can provide both anatomic and functional (e.g., flow) information, critical boundary conditions for computational modeling. These features are unique among other standard medical imaging techniques (i.e., echocardiography and computed tomography (CT)), which either cannot provide quantitative flow information (CT) or are anatomically limited by severe depth dependence (echo). Second, MRI does not require ionizing radiation (like CT), which improves feasibility in young patients who may require many examinations over their lifetime. Finally, it can image in any arbitrary orientation in 2, 3 (static or 2+time), or 4 (3+time) dimensions and with reference to specific points of the cardiac cycle, if desired. For these reasons, and others, CMR was the cornerstone of these investigations.

### 4.1.2 Challenges of Pediatric CMR

Since the majority of subjects included in this thesis are pediatric patients, it is appropriate to make note of important challenges inherent to imaging pediatric patients. The most obvious issue is the smaller size of pediatric structures that necessitates greater spatial resolution compared to the same adult structures. Signal-to-noise ratio effectively sets a limit to how high this resolution can be set.

An additional challenge is related to the generally high pediatric heart rates, which necessitates high temporal resolution. This need requires that tradeoffs be struck between high temporal resolution acquisition schemes (reading one line of k-space per RF pulse) and clinically manageable acquisition times (typically achieved in adult

imaging through k-space 'segmentation'[112]: reading multiple k-space lines (typically 3-64[113]) per cardiac cycle).

In pediatrics, particularly for infants and young children, administration of sedation or anesthesia is often required to ensure the patient remains motionless throughout the study. The use of these drugs adds to the risk associated with performing the imaging study, which may limit the scan duration. Additionally, more clinical personnel are required to be present to administer these scans (e.g., cardiac anesthesiologist, cardiologist, etc.) and help avoid/address adverse events (at increased cost), and Institutional Review Boards (IRB) require stronger justification and direct patient benefit to offset the increased risk in cases where the scans are being performed for research purposes.

Finally, respiratory compensation is a particular challenge in pediatrics. The motion of the diaphragm and lungs induces time-varying motion in the adjacent cardiac structures being imaged; this motion must be accounted for in image acquisition to avoid blurring. Typically, through the use of shortened segmented acquisitions, adult respiratory compensation is typically done via short voluntary breath holds. Because of the frequent use of sedation/anesthetics in pediatric imaging, breath holding is not an option. Instead, signal averaging can be used, at the cost of increased scan time, to compensate for respiratory motion while the patient is freely breathing.

### 4.1.3 Acquisition Protocols and Image Processing

The patient-specific data investigated in this thesis were collected according to basic, yet specific protocols. The data were then post-processed and analyzed using previously

established methods specific to the application. These applications can be sub-divided into 3 categories: 1) anatomic, 2) flow, and 3) functional investigations.

#### 4.1.3.1 Anatomic

Patient-specific TCPC geometric information was primarily derived from a static axial stack of thin, 'trueFISP' (balanced SSFP) images (Figure 4.13). These acquisitions spanned the thorax region from diaphragm to upper torso in 35-50 images with 3-4 mm slice thicknesses. In plane resolution ranged from 0.55-1.88 $mm^2$.

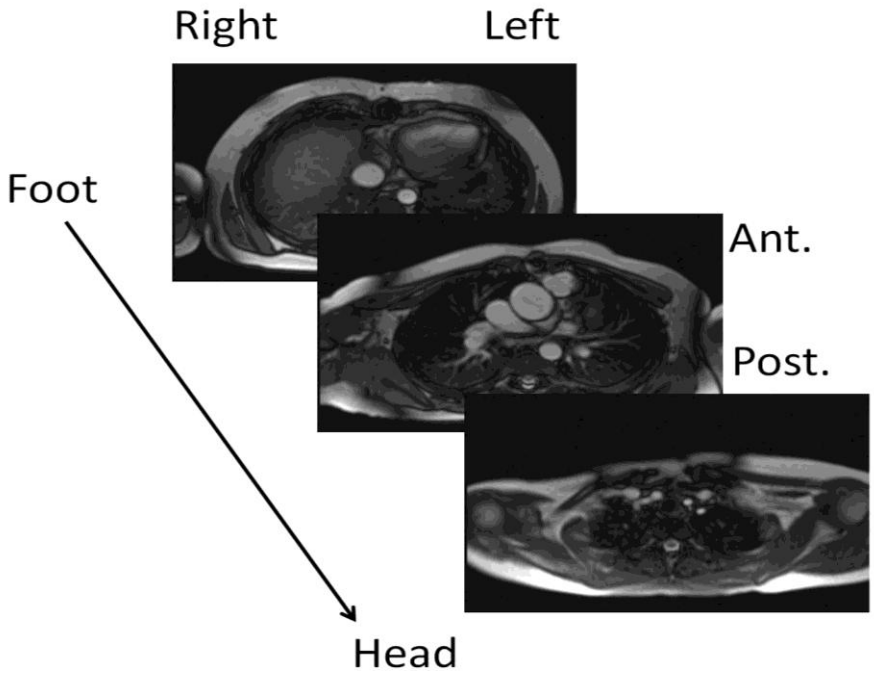


**Figure 4.13** ***Sample images from axial trueFISP image stack of single ventricle patient. Anatomical directions (right/left, anterior/posterior, foot/head) are indicated relative to the images.***

These images provide excellent cross-sectional views of the caval veins and Fontan baffle, which run perpendicular to the slice. Complete representation of the pulmonary arteries presents more of a challenge as they generally run parallel to the slice. Depending on the size of the arteries and the slice thickness, the PAs may be captured in only a few slices and the reconstruction of the cross-sectional profile may be less accurate.

The process for reconstructing the patient-specific anatomy from this image stack was as follows. To overcome the anisotropic resolution of the axial anatomic stack, the data were interpolated in the through-plane direction using adaptive control grid interpolation (ACGI)[114]. As can be appreciated in Figure 4.14, this technique smoothes the transition between slices, which helps to produce more realistic results (e.g., removing the appearance of piece-wise discontinuities). The interpolated stack was then semi-automatically segmented using a scaffolded shape-element (or 'bouncing ball') method[115]. With this technique, a threshold is applied to the image to remove noise, and the regions of interest for a given slice are selected. The program fills in the entire connected region for the location selected (Figure 4.15) and creates a binary mask of the segmentation. A 3D level set surface evolution algorithm was then used to smoothly and coherently deform the masked data, using gradient 'forces' derived from the raw images, to create a point-cloud representation of the 3D segmentation (Figure 4.16). Finally, Geomagic Studio (Geomagic, Inc., Research Triangle Park, NC) was used to fit a surface to the point cloud, perform any necessary smoothing or de-noising, crop the vessels, and prepare the model for CFD simulation.

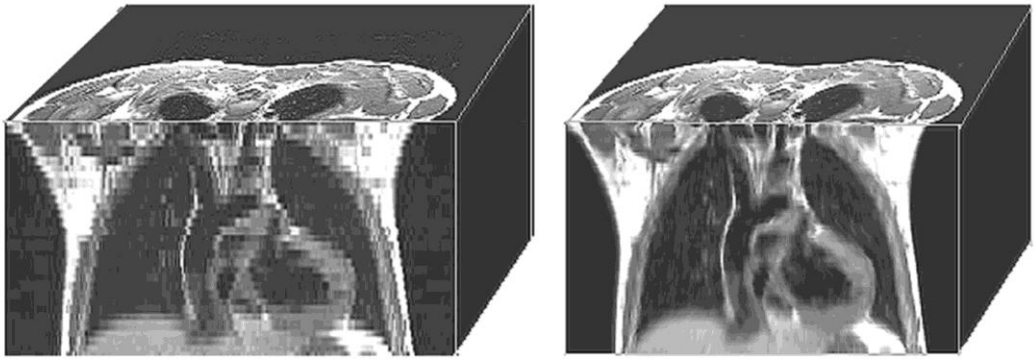

**Figure 4.14** ***Effect of ACGI on the anatomic data (in this case, shown as a 'black blood' image volume). The block on the left contains the raw data and the discrete, discontinuous steps between slices are apparent. The block on the right shows the interpolated data and is visually a much smoother and arguably more physiologic representation of vascular surfaces.***

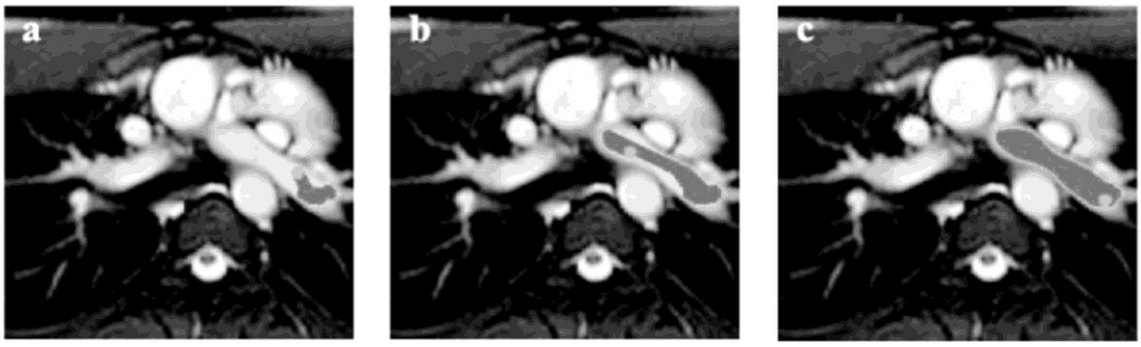


**Figure 4.15** ***Sequence of 'bouncing ball' segmentation. After shape-element initialization within the vessel (a), it moves within the vascular scaffold (b) until all the pixels internal to the structure are segmented (c).***

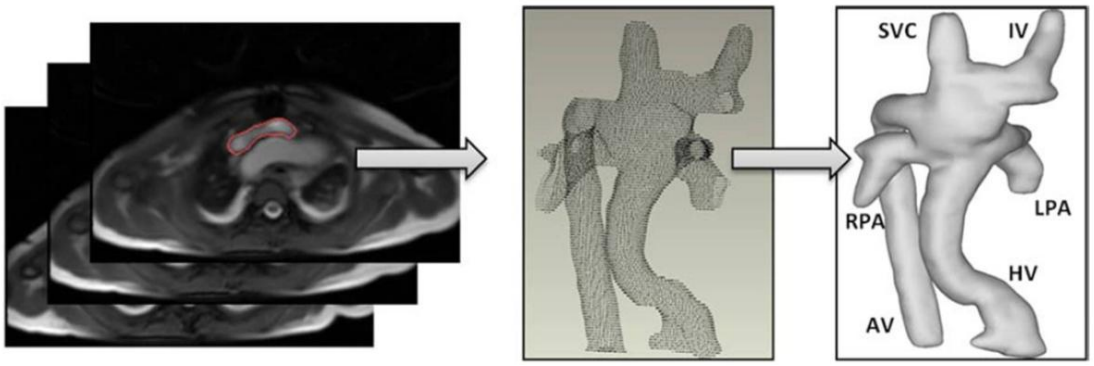


**Figure 4.16** ***Extraction of surface points from 3D level set evolution and wrapping in Geomagic Studio.***

While the trueFISP sequence was the standard input for anatomic reconstruction, several other methods were also employed, particularly from scans acquired at Children's Healthcare of Atlanta. The two most common were isotropic 3D volume acquisitions, and gadolinium-enhanced angiograms. Gadolinium is an MR-specific contrast agent that enhances $T_1$ relaxation and thus provides strong signal with short TR. The protocol for using these images was generally no different than the truFISP images, but the SNR and contrast characteristics varied.

#### 4.1.3.2 Velocity

The other critical input for patient-specific computational modeling of the TCPC is local flow information at the vessel (or system of vessels) inlets and outlets. This was obtained using a series of through-plane (i.e., one velocity component) cine (time-varying) PC MR slices. As shown in Figure 4.17, these planes were specifically positioned at the inlets (distal to relevant venous confluences) and outlets (proximal to major bifurcations) of the TCPC, as well as the ascending aorta to provide cardiac output information. Depending on patient heart rate, these data typically spanned the cardiac

cycle in 15-30 phases. The VENCs were tuned with consideration of patient-specific flow rates (often after a pilot acquisition), and generally ranged from 50 cm/s (in the VCs) to 150 cm/s (for the aorta). The VENC of PA slices was generally higher than those of the VCs.

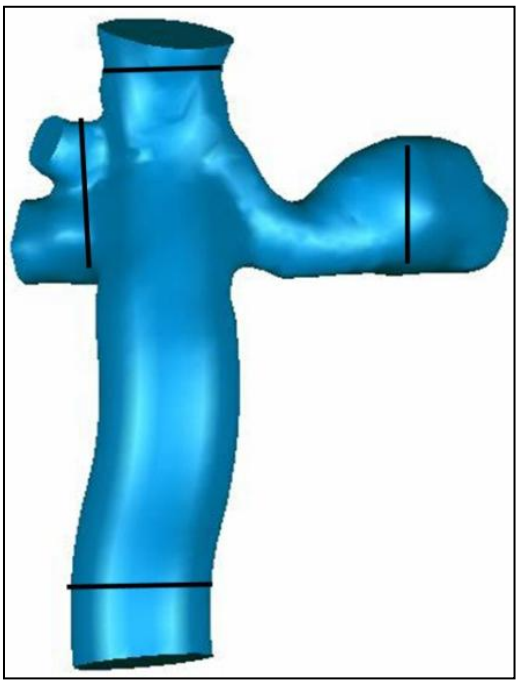

**Figure 4.17** ***Positioning of the PC MR planes (in black) on the TCPC inlets and outlets relative to a patient-specific anatomy.***

The cross-sectional PC MR data were segmented with an in-house algorithm using active contours[116]. In this method, the user initializes a contour around the vessel of

interest in a single magnitude image and that contour is then automatically evolved according to an image-based energy functional:

$$\boldsymbol{E = \int_0^1 \frac{1}{2}[\alpha\left|C'(s)\right|^2 + \beta\left|C''(s)\right|^2 + E_{ext}(C(s))]ds}$$ **(Equation 4.9)**

where E is the total energy of the evolution; C(s) is a parametric contour as a function of arc length, s; α is a constant that weights the curvature of the contour; β is a constant that controls rigidity in the through-plane direction (set to 0 for 2D); and $E_{ext}$ is the 'energy' of the image[117]. The image energy was defined using gradient vector flow (GVF)[118], which diffuses the gradient of the image contours throughout the image to both provide insensitivity to initialization location and noise and naturally handle vessel concavities. Additionally, a hybrid image was created based on a cross-correlation of the magnitude and phase images[119]. This hybrid image is particularly helpful when the vessel of interest is in close proximity to another anatomic structure, such as the SVC and the aorta in Figure 4.18, because the local phase discontinuities (stemming from the internal velocity differences) distinguish the structures in the hybrid representation. The active contour functional was then implicitly evolved with a level set-based formulation[120] to extract the region of interest for each phase of the cardiac cycle.

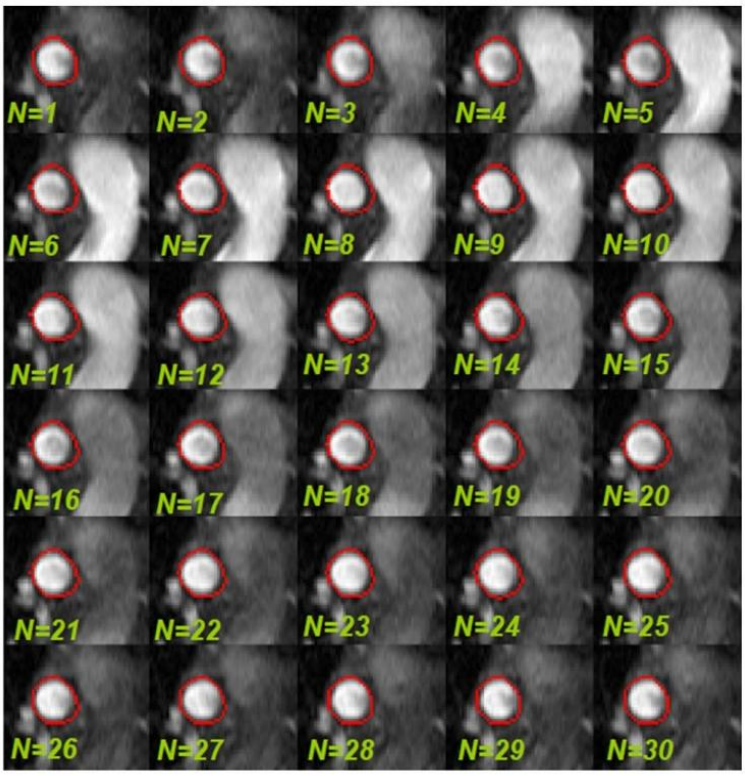


**Figure 4.18** ***Effectiveness of hybrid magnitude/velocity image energy functional for distinguishing different vessel structures in close proximity, such as the SVC (segmented in red) and aortic arch[119].***

Once the region of interest was segmented, a novel post-processing algorithm was used to filter the data and remove noise and spurious vectors. This approach is called Fuzzy Adaptive Vector Median Filtering[116]. Briefly, a median vector is defined from a subset of the sampled data and a set of fuzzy membership rules is used to determine if individual vectors are noise or true signal. If determined to be noise, the same filter selects a suitable replacement value based upon the same vector median. This methodology was previously shown to improve accuracy of segmented results[116].

From the segmented data, characteristics of vessel area, flow and velocity over the cardiac cycle, pulsatility and resistance indices, and cross-sectional quadrant flow profiles were extracted[119]. Of these, the time varying and time averaged flow rate values were retained to provide the flow boundary conditions for CFD simulations (see §4.3.4).

While the through-plane acquisitions were performed and analyzed in this way for the vast majority of patients enrolled in these studies, an additional 4D velocity protocol was acquired in a small subset to reconstruct of the full *in vivo* flow fields. These data were acquired as a coronal stack, usually comprising of 5-7 slices with 3 orthogonal velocity components acquired on each slice (as shown in Figure 4.12). VENCs were generally similar to through-plane values (as the velocities measured were the same). Because the data were acquired as anisotropic slices (as opposed to a volumetric slab[91]), an interpolation scheme was required to resolve velocities between slices.

This interpolation scheme, developed and implemented through the PhD work of Dr. Sundareswaran[119], is called Divergence Free Interpolation (DFI), and uses inherent properties of incompressible fluid flows (i.e., zero divergence, $\nabla \cdot \vec{V} = 0$) to improve the accuracy of interpolating flow-based vector fields[121]. A brief description of this method will be provided here; the interested reader is directed to Dr. Sundareswaran's thesis[119] for a more detailed derivation.

Helmholtz's theorem of vector calculus states that any sufficiently smooth 3D vector field can be resolved into the summation of irrotational (curl-free) and divergence-free vector fields. An experimentally measured incompressible 3D velocity field can therefore be thought of as the superposition of divergence-free (the true velocity field) and curl-free (noise) components. By projecting the measured data into a divergence-free space, the

true velocity field is recovered. It therefore becomes the challenge to define appropriate basis functions for this divergence-free space.

The works of Narcowich and Ward[122] and Lowitzch[123] introduced the concept of divergence free spaces defined using radial basis functions. This space has the general form:

$$\boldsymbol{\Phi}(\boldsymbol{x}) = \{-\boldsymbol{\nabla}^{\mathbf{2}}\boldsymbol{I} + \boldsymbol{\nabla}\boldsymbol{\nabla}^{\mathbf{T}}\}\boldsymbol{\Psi}(\boldsymbol{x}) \textbf{ (Equation 4.10)}$$

where I is the identity matrix, $\nabla^2$ is the Laplacian operator, $\nabla$ is the gradient operator, and $\Psi$ is a scalar-valued, infinitely supported radial basis function. In the scheme proposed by Narowich and Ward[122], $\Psi(x)$ was based on the Gaussian function:

$$\boldsymbol{\Psi}_{\boldsymbol{\alpha}}(\boldsymbol{x}) = \boldsymbol{e}^{-\boldsymbol{\alpha}\|\boldsymbol{x}\|^{\mathbf{2}}} \textbf{ (Equation 4.11)}$$

which produces a smooth, positive definite basis. The interpolation model is thus:

$$\boldsymbol{V}(\vec{\boldsymbol{x}}) = \sum_{\boldsymbol{j}=\mathbf{1}}^{\boldsymbol{P}} \boldsymbol{\Phi}\left(\left|\vec{\boldsymbol{x}} - \overrightarrow{\boldsymbol{x_j}}\right|\right)\overrightarrow{\boldsymbol{C_j}} \textbf{ (Equation 4.12)}$$

where V is the interpolating function, ($x_j$, j=1:P) is the set of stationary control points in the domain, $\Phi$ is the divergence free radial basis function and C is a vector valued set of

coefficients that are determined from a least squared error analysis from the measured velocity data.

With the interpolating scheme in place, the primary practical challenge in applying this method to the coronal TCPC data is in segmentation of the flow domain. Typically the spatial resolution and coverage of the axial data used for the anatomic reconstruction is much better than what the coronal magnitude images provide. Thus, rather than performing a *de novo* segmentation of the coronal data, the segmentation and flow domain identification is performed through a registration of the single axial segmentation mask to the time-varying velocity data (Figure 4.19). The velocity data are then interpolated to the anatomic grid providing a time varying volumetric reconstruction. This method has been successfully applied to numerous studies of *in vivo* TCPC flows[61, 92].

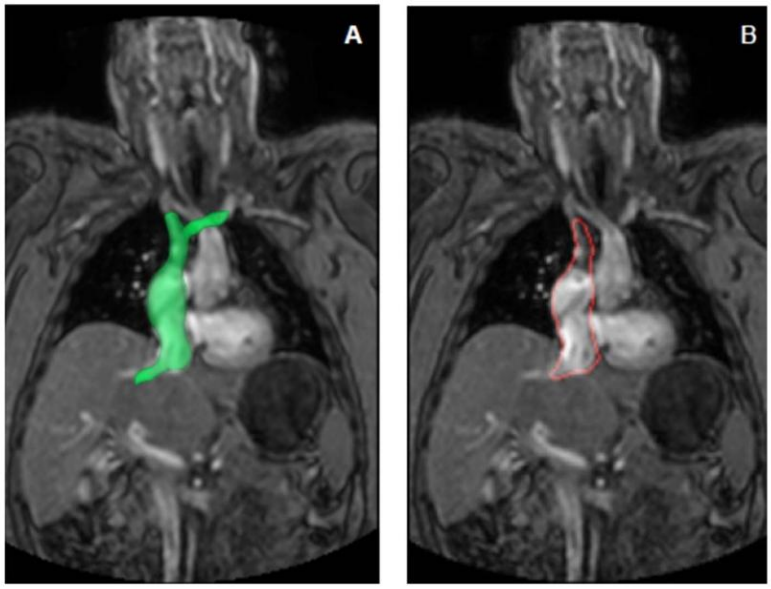


**Figure 4.19** ***Segmentation of coronal 4D PC MR data via A) registration with 3D anatomy reconstructed from axial stack and B) segmentation of vessel boundaries on each slice.***

From the reconstructed 4D velocity fields, the quantitative endpoints of interest were power loss and IVC flow distribution. Since there is no pressure information available from the MR data to calculate power loss using the traditional control volume approach, power loss was instead approximated based on viscous dissipation:

$$\dot{E}_{Loss} = \int \eta \cdot \left[ 2 \cdot \left( \left(\frac{\partial u}{\partial x}\right)^2 + \left(\frac{\partial v}{\partial y}\right)^2 + \left(\frac{\partial w}{\partial z}\right)^2 \right) + \left( \left(\frac{\partial v}{\partial x}\right) + \left(\frac{\partial u}{\partial y}\right) \right)^2 + \partial w \partial y + \partial v \partial x 2 + \partial u \partial z + \partial w \partial x 2 \right] \quad \textbf{(Equation 4.13)}$$

For flow distribution, the built-in temporal interpolation and particle tracking functionalities of the open-source ParaView data analysis and visualization application (version 3.12.0; paraview.org) was used. Credit for the development of this protocol belongs to Dr. Lucia Mirabella. Briefly, the procedure was as follows:

1. Import the set of 4D velocity fields (usually arranged as one time point per file), with the first time point duplicated and appended to the end of the set.
2. Perform temporal interpolation (Filters> Temporal Interpolator> Interval = 0.1)
3. Scale time to match MR acquisition (Filters> Temporal Shift Scale> Scale as appropriate; 3 periods; select periodic and periodic end correction).
4. Cache temporal data for particle tracking (Filters> Temporal Cache)
5. Select emitter source plane (select interpolator data in pipeline browser, Use ‘Slice’ Tool)
6. Particle release (select cache in browser, Filters> Particle Tracer)

#### 4.1.3.3 Ventricular Function

In the patient subset for which ventricular function was quantified, a short axis stack (6-12 slices) of cine SSFP (16-33 phases) images was acquired. The stack was positioned to span from ventricular apex through its base.

Segmentation was performed using a variation of the 2D level set active contours used for the velocity cross-sectional segmentation. A contour was initialized on the first phase for a given slice and propagated through the rest of the cine set. Manual corrections were made as necessary to ensure a visually appropriate segmentation. Once the stack was entirely segmented, the volume of each cardiac phase was calculated using a Simpson's rule approach.

The following measurements were derived from the segmented volumes:

- End diastolic volume (EDV)
- End systolic volume (ESV)
- Stroke volume (StV = EDV-ESV)
- Ejection Fraction (EF = StV/EDV)
- Maximum time rates of volume change (three point averaged)
    - Peak filling rate (PFR)
    - Peak ejection rate (PER)
- Time to PFR (difference between phase at which PFR occurred and end systolic phase)

## 4.2 CMR Patient Database

As it serves as the primary data source for all studies conducted in this thesis, a brief description of the Georgia Tech Single Ventricle CMR database is warranted. This

resource is the result of over 10 years of a multi-center collaboration between Georgia Tech, the Children's Hospital of Philadelphia (CHOP) and Children's Healthcare of Atlanta (CHOA). The database is comprised of complete CMR studies, both prospectively and retrospectively collected, for single ventricle patients in various stages of palliation, with particular focus on Glenn-stage patients and patients late after Fontan. All told, it includes data for 303 patients (at the time of this writing) and represents the largest known CMR library for TCPC hemodynamics. The investigations performed in this thesis drew primarily from the CHOP patient contributions to the database, specifically 100 such patients with a completed Fontan connection. However, the 15 patient Y-graft series from CHOA is also a notable component.

### 4.3 Computational Fluid Dynamics (CFD)

The CFD methods employed in this thesis are all based on the assumption of incompressible Newtonian fluid motion:

$$\frac{d\rho}{dP} = 0 \quad \textbf{(Equation 4.14)}$$

$$\tau_{ij} = \mu \frac{du_i}{dx_j} \quad \textbf{(Equation 4.15)}$$

where ρ is the fluid density, P is the static pressure, τ is the shear stress tensor, u is velocity, and μ is the fluid viscosity. The unsteady 3D velocity vectors were iteratively calculated through the solution of the incompressible continuity equation (Equation 4.16) and Newtonian form of the Navier-Stokes equations (Equation 4.17):

$$\nabla \cdot \vec{u} = 0$$ **(Equation 4.16)**

$$\rho\left(\frac{d\vec{u}}{dt} + \vec{u} \cdot \nabla\vec{u}\right) = -\nabla P + \mu\nabla^2\vec{u} + f$$ **(Equation 4.17)**

where f represents generic body forces (such as gravity), which were neglected. The numerical solver used extensively throughout this thesis was developed and implemented through the PhD work of Dr. de Zélicourt[124]. A broad overview of its details is provided here, but the interested reader is referred to her work for a complete description.

### 4.3.1 Solver Description

The fluid solver is fundamentally based on the hybrid Cartesian sharp-interface immersed boundary method of Gilmanov and Sotiropoulos[125]. Herein, the external surface of the fluid domain (e.g., the fluid in contact with the lumen of a blood vessel in the case of vascular flows) is meshed with unstructured triangular elements and registered within a structured Cartesian grid. The grid cells are thus classified into one of three groups (Figure 4.20): 1) the fluid cells internal to the boundary, 2) the wall cells external to the boundary, and 3) the immersed boundary (IB) cells immediately interior to the wall. From this classification, the Navier-Stokes equations were discretized and solved in the fluid cell; the wall nodes were excluded from the computation; and the velocity of the IB cells was reconstructed through quadratic interpolation, assuming a rigid no-slip condition on the wall. To further improve computational efficiency for complex vascular structures, which tend to be small with respect to the bounding Cartesian volumes, de Zélicourt *et al* recast the computationally expensive structured Cartesian data in an unstructured formulation by completely discarding the wall nodes[126].

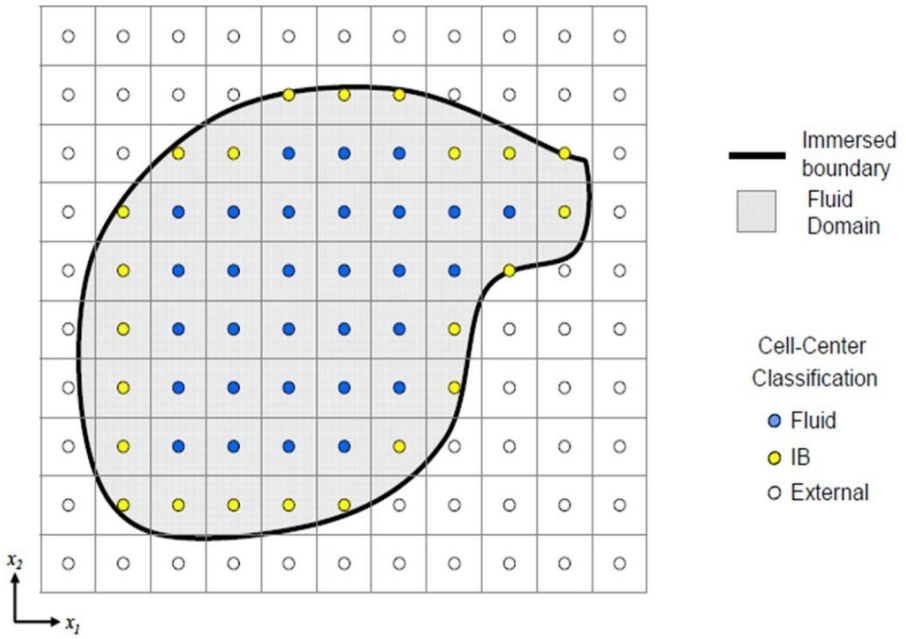


**Figure 4.20** ***2-dimensional representation of Cartesian grid cell classification with respect to the Immersed Boundary. External (Wall) cells (white) are external to the boundary. Immersed boundary (IB) cells (yellow) are internal and immediately adjacent to the boundary. Fluid cells (blue) are entirely enclosed by the boundary and IB cells[124].***

### 4.3.2 Spatial Discretization

With the geometry represented with an unstructured Cartesian grid, spatial derivatives are calculated using a basic three-point central differencing scheme:

$$\frac{du_i}{dx} = \frac{u_{i+1} - u_{i-1}}{2\Delta x} \quad \textbf{(Equation 4.18)}$$

where i denotes cell index, and Δx is the spacing between cell centers. While this scheme represents one of the simplest approaches, it is not without potential challenges

and instabilities. Most notable are known oscillations in the pressure field when the pressure and velocity data are collocated (i.e., stored at the same grid location) and symmetric differencing operators are used. The instabilities in this scheme arise from the fact that $P_i$ depends on $u_{i-1}$ and $u_{i+1}$, which depend on $P_{i-2}$, $P_i$, and $P_{i+2}$. Thus, the adjacent grid points are de-coupled and may evolve independently of each other.

The most common solutions to this problem are either the introduction of artificial damping terms or the use of a staggered grid arrangement; that is, storing pressure values at cell centers and velocity values at cell faces. To overcome challenges in synchronization of boundary condition prescription with this latter approach, Gilmanov and Sotiropoulos proposed the use of a hybrid staggered/non-staggered formulation in which the boundary conditions are imposed on a non-staggered layout, the velocity values are mapped to their staggered cell face locations, and the Navier-Stokes equations are solved in the staggered configuration[125]. Figure 4.21 visually demonstrates this varying variable storage scheme for a single cell domain. Away from vessel boundaries, the non-staggered velocity values (at the cell centers) are reconstructed from the staggered velocities using a QUICK interpolation scheme:

$$v_{1\,(i,j,k)} = \frac{3 \cdot u_{1\left(i-\frac{1}{2},j,k\right)} + 6 \cdot u_{1\,(i+1/2,j,k)} - u_{1\left(i+\frac{3}{2},j,k\right)}}{8}$$ **Equation 4.19.**

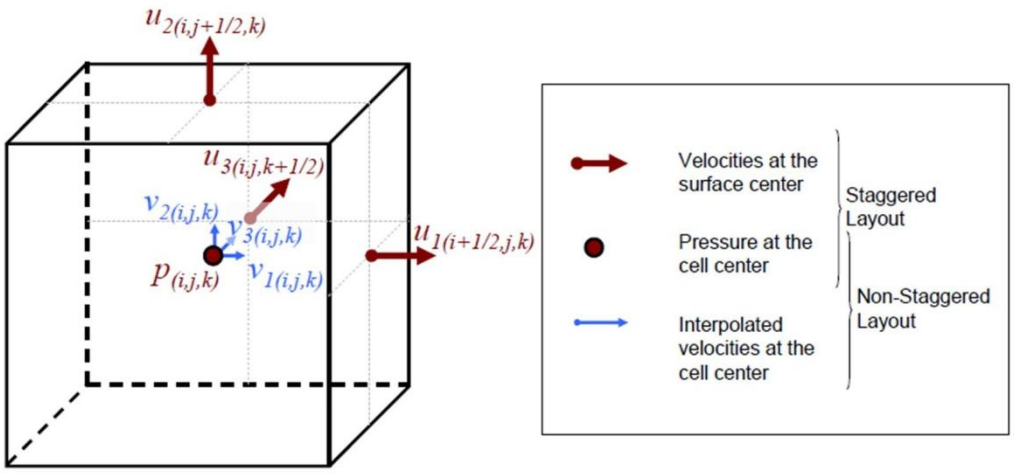


**Figure 4.21** ***Representation of the hybrid Staggered/non-Staggered variable storage scheme. Pressure (P) values are stored at cell centers while velocities (u) are stored at cell face centers. In the boundary condition prescription, velocities are interpolated to the cell center (v) to maintain temporal uniformity with the imposed pressure[124].***

### 4.3.3 Temporal Discretization

Time advancement was accomplished using a fractional-step integration method, a widely used approach for incompressible flows[127]. The method is comprised of three steps: a prediction step, where the fluid momentum equations are solved without enforcing continuity; a pressure correction step, which iteratively solves for the pressure correction term based on the intermediate velocity field obtained in the first step; and projection into divergence free space, which enforces continuity and advances the 'predicted' intermediate variables in time. The first step was performed using a 4$^{th}$ order explicit Runge-Kutta method to obtain the intermediate velocity prediction, u*, from:

$$\frac{u_i^* - u_i^n}{\Delta t} = -u_j^n \frac{\partial u_i^n}{\partial x_j} - \frac{1}{\rho}\frac{\partial P^n}{\partial x_i} + \nu \frac{\partial^2 u_i^n}{\partial x_j \partial x_j} \quad \textbf{(Equation 4.20)}$$

It is important to note that the pressure, P, in Equation 4.19 is the known pressure field from time, n, and only u* is advanced in time through that calculation. Because u* is not, by definition, divergence free, a correction must be applied to recast the result back into divergence free space. To do so, the incremental pressure field must be resolved. It can be shown that this incremental pressure, δP, is related to u* as:

$$\nabla^2(\delta P) = \frac{3}{2\Delta t}\nabla(u^*) \quad \textbf{(Equation 4.21)}$$

The solution of this Poisson equation (Equation 4.20) is non-trivial and is iteratively performed using the Flexible Generalized Minimal Residual (FGMRES) solver with a multi-grid pre-conditioner[124, 128]. With δP determined, $P^{n+1}$ and $u^{n+1}$ can be simply computed as:

$$P^{n+1} = P^n + \delta P \quad \textbf{(Equation 4.22)}$$

$$u^{n+1} = u^* - \frac{3}{2\Delta t}\nabla(\delta P) \quad \textbf{(Equation 4.23)}$$

### 4.3.4 Boundary Conditions

As previously mentioned, all simulations performed in this thesis assumed static and rigid vessels and a no-slip boundary condition along those walls. The handling of the inlet and outlet boundary conditions was more varied although was always based on the PC MR-derived flows, as described in §4.1.3.

#### 4.3.4.1 Velocity reconstruction at the Immersed Boundaries

Velocity values in the IB cells are handled differently than for fluid cells: rather than being calculated from the Navier-Stokes equations, the velocities are reconstructed based on wall normal vector and proximal fluid cell velocity. Figure 4.22 helps to visualize this protocol. The normal vector ($\overrightarrow{n_f}$) from the center (F) of the closest triangular surface mesh element (s) connects the immersed boundary cell center (G) to its respective fluid element (H). The value at G is then reconstructed via quadratic interpolation based on the known values at H and F (the latter being 0 for no-slip boundary conditions). The selection of quadratic interpolation has been shown to improve the results compared to simple linear schemes[125].

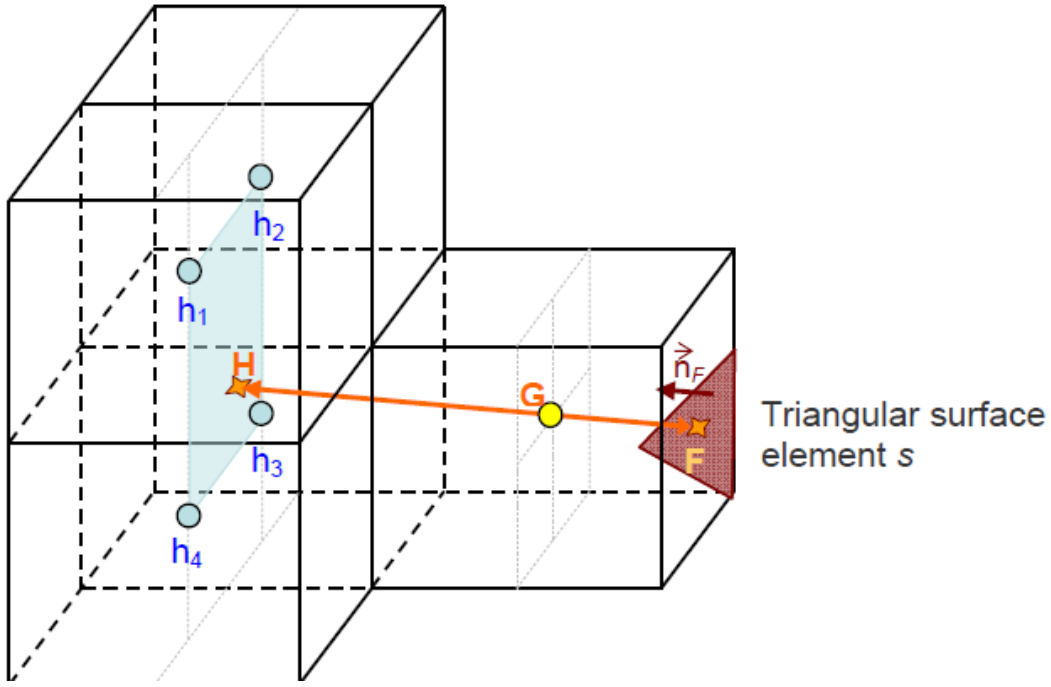


**Figure 4.22 Reconstruction of the solution at an IB-cell center (G) by interpolating between its projection onto the closest immersed-boundary and fluid elements (points F and H, respectively) along the local normal to the immersed-boundary. The light gray lines are provided for visual reference to help localize the centers of the fluid and IB cells[124].**

#### 4.3.4.2 Inlet boundary conditions

At the inlets (typically, only the SVC and IVC), either time-averaged ("steady") or time-varying ("pulsatile") flow conditions were imposed as either a flat, plug-like velocity profile or a fully-developed parabolic velocity profile. The preference was generally for time-averaged conditions (although each section will explicitly state which condition was used) based on the relative simplicity of simulation implementation, analysis, and communication of results. Recognizing this selection as a potential limitation, however, an explicit comparison will be conducted between the two boundary condition types in Chapter 5 to better characterize the bias introduced.

An example of retained steady (dotted line) and pulsatile (box markers) flow conditions from a patient-specific measurement is demonstrated in Figure 4.23. It is noted that the character of the time-varying flow curve varied significantly both by patient and vessel, so while the time-averaged value in the present example appears to be a poor representation of the dynamic curve, the steady flow assumption is commonly employed in TCPC CFD modeling. It is also apparent from Figure 4.23 that the MR-derived flow measures have very few sample points compared to the temporal resolution needed for CFD. Hence, the measured flow curve underwent Fourier decomposition and reconstruction to achieve sufficient temporal sampling for pulsatile simulations. A minimum of 2000 time steps per cardiac cycle were used for pulsatile simulations, giving a temporal resolution on the order of 0.5 ms.

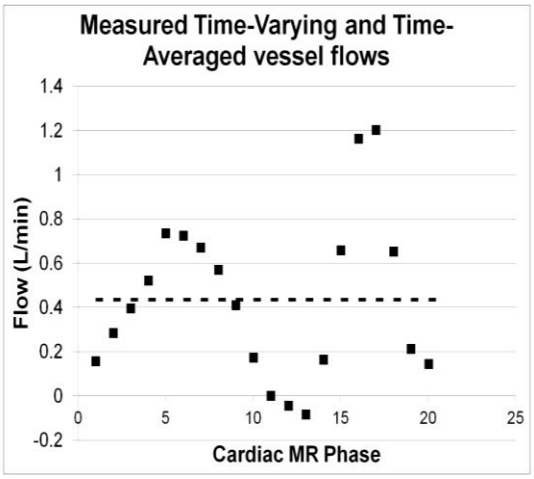


**Figure 4.23** ***Example of time-varying vessel flow curve (square markers) and associated time-averaged flow magnitude (dashed line) measured from through-plane PC MR and used to prescribe inlet flow boundary conditions for CFD.***

With respect to the selected velocity profile, the preference was generally for plug-like flow based on past-precedent[124], although the parabolic profile was selected in some cases based on good observed agreement with PC CMR measurements.

4.3.4.3 Outlet boundary conditions

At the outlets, flow boundary conditions were again enforced except, to ensure mass convergence (which factors such as Fontan fenestration flow, measurement noise, etc. tend to distort in the measured data), these flows were often imposed as the ratio of the outlet flows scaled to the inlet flow magnitude. That is:

$$\boldsymbol{Q_{LPA} = \frac{Q_{LPA}}{(Q_{LPA}+Q_{RPA})} \cdot Q_S}$$ **(Equation 4.24)**

where $Q_S$ is the sum of the measured caval flows. The velocities reconstructed/extrapolated at the outlet cell faces ($v_G$) are scaled to enforce these desired flow conditions and ensure mass conservation as follows:

$$\boldsymbol{\overrightarrow{v_G} = \overrightarrow{v_G} + \Delta Q \cdot \overrightarrow{n_f}}$$ **(Equation 4.25)**

where ΔQ is the difference between the desired mass flow rate, $Q_0$, and current value based on the extrapolated values, as:

$$\boldsymbol{\Delta Q = Q_0 - \sum_{G \in Outlet} \overrightarrow{v_G} \cdot \overrightarrow{n_f}}$$ **(Equation 4.26).**

### 4.3.5 Preparation of TCPC CFD Domain

A step-by-step guide for model creation was provided in the appendices of Dr. de Zélicourt's thesis[124] and so only a brief description is provided here. Beginning with the smoothed tetrahedral surface model discussed at the end of §4.1.3, each inlet and outlet vessel must be cropped to provide a flat surface for the prescription of the boundary conditions discussed in the preceding section. Traditionally, these cuts are placed perpendicular to the central axis of the vessel immediately distal to venous confluences (for the SVC, IVC) or immediately proximal to arterial branches (for the PAs). However, because of the proximity of the Glenn and Fontan connections to the branching of the right upper PA lobe, it was necessary in many cases to explicitly include that branch in the computational domain and crop both the main and upper PA branches distal to the bifurcation. Once cropped, the 'Exact Surfacing' functionality in Geomagic Studio is used to create a NURBS (Non-uniform rational B-spline) model of the geometry and export in .igs format to be read by the meshing software, GAMBIT (ANSYS, Inc.).

In Gambit, the vessel inlets and outlets were extended (by 10 and 50 mm, respectively) to ensure flow stability, minimize recirculation at the boundaries, and to reduce the effect of the chosen boundary condition profile on the hemodynamics in the domain of interest. The surface (including extensions and extended boundary faces) was then meshed with unstructured triangular elements and exported in the .FDNEUT format to be read by the IB solver pre-processor. Notably, a second mesh was also created and exported without the vessel extensions to be used in the post-processing steps such that only that actual domain of interest was used for the hemodynamic calculations.

Finally, the pre-processing step is performed to: a) read in the TCPC surface mesh; b) specify the Cartesian grid node density (typically 2% of IVC diameter for mesh independence[126]) and range; c) register the immersed boundary within the structured

Cartesian grid; d) classify the fluid, wall, and IB nodes; e) create the geometric 'Restart' files and boundary condition cell indices to be read by the solver.

### 4.3.6 Hemodynamic Metric Quantification

The primary quantities of interest to be derived from the CFD simulations were:

- Pressure drop: difference between cell centered running average pressure values at inlets and outlets of CFD domain (without flow extensions).
- Power loss (PL): based on a control volume energy balance assumption:

$$PL = \sum_{inlets} \int_A (p + \frac{1}{2}\rho v^2) v \cdot dA - \sum_{outlets} \int_A (p + \frac{1}{2}\rho v^2) v \cdot dA \quad \textbf{Equation 4.27}$$

where p is the same static pressure values retained for pressure drop calculation, dA is the differential area of the inlets and outlets, and ρ is fluid density (set to 1060 kg/m$^3$). Because of the known dependence of power loss on bulk flow rates and patient size, the use of an appropriate normalization framework for power loss is critical when performing across-patient comparisons. In this thesis, two such frameworks were used extensively.

  - Resistance: To create an analog to the common clinical measure relating pressure drop through a vascular bed to the local flow rate, a power loss-based pressure drop ($\Delta P_{TCPC} = \frac{PL}{Q_s}$) was defined (here, $Q_s$ is the systemic venous flow rate in units of $m^3 \cdot s^{-1}$) to calculate the connection resistance

($R = \frac{\Delta P_{TCPC}}{Q_s/BSA}$) in Wood Units (WU; mmHg·min·L$^{-1}$); here, $Q_s$ in units of L·min$^{-1}$.

- TCPC Energy Dissipation Index (TCPC-EDI): Based on the work of Dasi *et al.*[129, 130], PL was indexed ($\frac{PL}{\rho Q_s^3/BSA^2}$) to calculate the dimensionless TCPC-EDI, where $Q_s$ is the systemic venous flow (here, in units of L·s$^{-1}$), BSA is the body surface area [m$^2$].

- Hepatic (IVC) flow distribution (time-averaged simulations only): the running average velocity field was imported into Tecplot and streamlines are seeded at every point in a selected IVC cross-sectional slice. The streamlines are segregated based on the PA in which they terminate (i.e., they are classified as either LPA or RPA streamlines) and the fluxes (i.e., $Q_{LPA} = \sum_{p,LPA}(u_p dA)$) of the streamlines (p) are computed based on the velocity (u) of the IVC seed point and the differential area. The relative distribution ($\frac{Q_{LPA}}{(Q_{LPA}+Q_{RPA})}$) is then quantified and retained.
- Particle residence time (pulsatile simulations only): Using the in-house particle tracking program developed by de Zélicourt[124], post-processing of pulsatile simulations included an IVC particle tracking analysis. A cross-sectional slice at the base of the IVC was selected and uniformly seeded 50 times over 1 cardiac cycle[85]. A total of 5 cardiac cycles were then simulated to allow for particle advection through the connection. As with the streamline analysis, particles were categorized as either LPA or RPA particles depending on termination location, and the relative proportion of these particles were quantified to give the flow distribution. In addition, the 'temporal probability' output from the code was imported into Tecplot to quantify statistics about the particle residence times. The calculated values include:

- Minimum transit time (shortest time for a particle to reach an outlet)
- Mode transit time (residence time of the highest number of particles)
- Maximum transit time (longest time registered for more than one particle).

Figure 4.24 visually represents these points with respect to the residence time histogram. The selection for maximum time may be counter-intuitive; however, it was selected primarily for its objective repeatability in identification. As can be appreciated in Figure 4.24, many particles have longer transit times than the point marked as the maximum; yet, it cannot be conclusively said that even the highest (i.e., furthest to the right) point registered is the maximum without running many more cycles to capture very slow moving particles. Hence, that definition would introduce operator variability on the basis of selected cycle number and is arguably not representative of the higher end transit time experienced by 'most' particles. The times reported in each case were re-dimensioned by multiplication by the characteristic velocity ($V_{IVC}$) divided by the characteristic length scale ($D_{IVC}$) to give units in seconds.

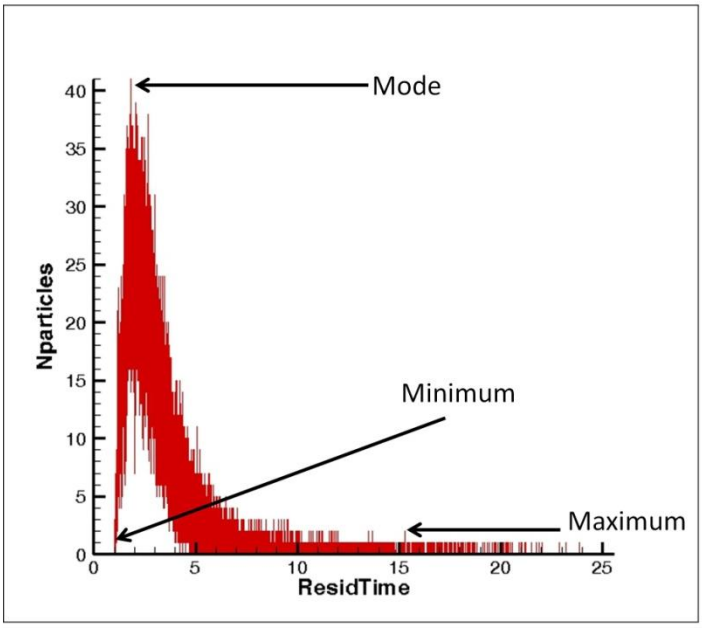


**Figure 4.24 Visual representation of retained particle tracking statistics (minimum, mode, maximum) from residence time histogram.**

## 4.4 Lumped Parameter Modeling

To help in relating the local effects of the TCPC to the broader single ventricle physiology, an electrical circuit analog model of the cardiovascular system was employed. This lumped parameter model was based on the circuit used by Pekkan *et al*[96] and Sundareswaran *et al.*[55]. In this scheme, the ventricle, arteries and veins are treated as time-varying compliance chambers while capillary beds are represented as lumped resistances. The TCPC is additionally modeled as a lumped resistance value in series between the systemic and pulmonary circuits.

The instantaneous flow and pressure from compartment i to compartment j of this model are thus evaluated by iteratively solving the following set of differential equations until convergence:

$$\boldsymbol{Q_{ij} = \left(P_j - P_i\right) \cdot \frac{1}{R_{ij}} \cdot S_{ij} - \frac{L_{ij} Q_{ij}}{R_{ij}} \cdot S_{ij}} \text{ (Equation 4.28)}$$

$$\boldsymbol{\frac{d(C_i P_i)}{dt} = \sum_{j-1}^{N} j(Q_{ij} - Q_{ji})} \text{ (Equation 4.29)}$$

where P, Q, and C are the pressure, flow and compliance in a given compartment; R, L, and S are the resistance, lumped impedance, and valves between compartments.

Based on the needs of the studies considered in this thesis, the previously developed models were amended by considering the superior and inferior systemic compartments as separate entities. A schematic of the model used is shown in Figure 4.25.

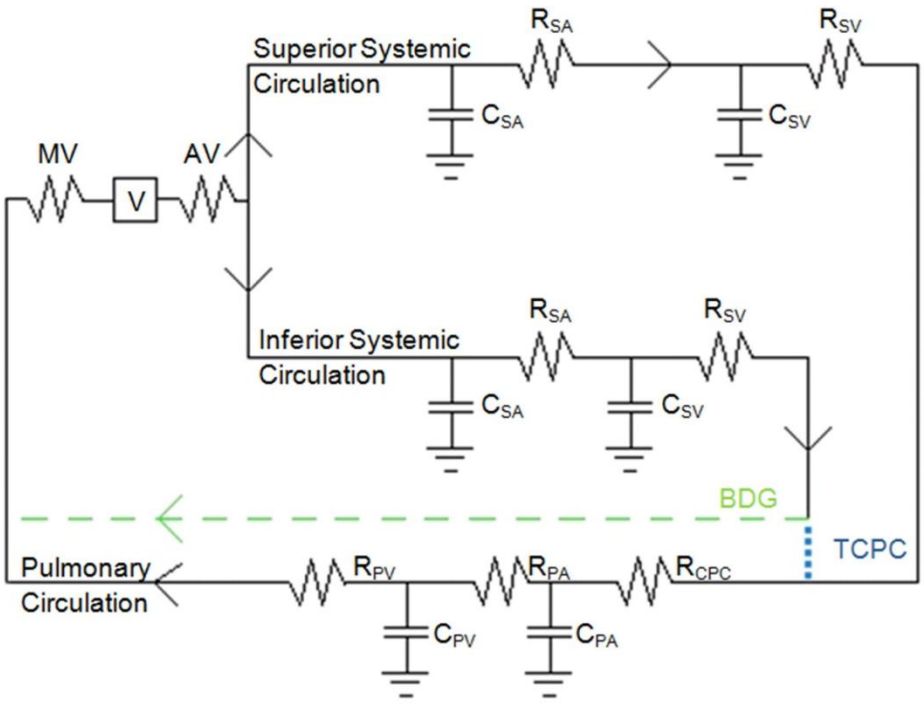


**Figure 4.25 Schematic of lumped parameter circuit for single ventricle cardiovascular system including separate compartments for the superior and inferior systemic circuits. MV- mitral valve; V- ventricle; AV- aortic valve; R- resistance; C- compliance; SA- systemic arteries; SV- systemic veins; CPC- cavopulmonary connection; PA- pulmonary arteries; PV- pulmonary veins**

## 4.5 TCPC Geometric Characterization

Understanding that there is a tight coupling between the geometric characteristics of the TCPC and its hemodynamics, there is a concurrent need to measure these features and relate them to the CFD-derived hemodynamics to gain a more explicit knowledge of this relationship. To this end, the vascular modeling toolkit (VMTK; vmtk.org) was used to extract geometric features of the reconstructed TCPC CFD models.

VMTK is an online and open-sourced collection of libraries and tools specifically tailored and designed to handle the 3D reconstruction, geometric analysis, mesh generation, and

surface data analysis for image-based models of blood vessels. It has been used extensively in the study of intra-cranial aneurysms[131]; however, many of the same principles apply to the study of the TCPC.

The geometric analysis in VMTK is based upon the identification of vessel centerlines, defined as the result of a functional minimization such that the minimal distance of the line to the vessel lumen is maximized. With the centerlines of each vascular branch of the connection identified, the characteristics of their union (i.e., the centerline bifurcation vectors, b) can also be identified. An example of the computed centerlines and bifurcations for a given TCPC reconstruction is shown in Figure 4.26. A full step-by-step protocol and custom script for TCPC analysis in VMTK is provided in the appendices. Credit for the development of this protocol belongs to Elaine Tang.

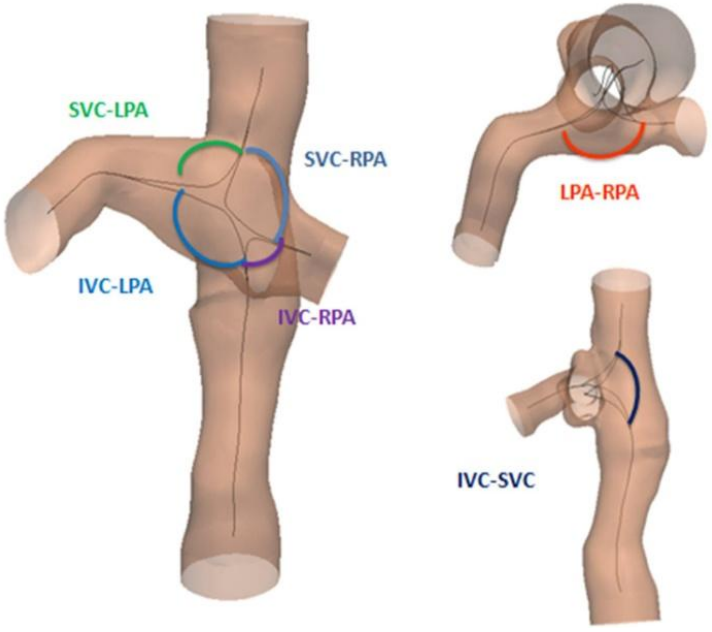


**Figure 4.26** ***Visual representations of angle definitions between (left) VC-PA connections, (top-right) the PA branches, and (bottom-right) vena cavae.***

The features of interest retained from the centerline calculation were as follows:

- At each point along the centerline, the maximum inscribed sphere radius was calculated by VMTK; the diameter (D) of each vessel was obtained by doubling this radius. The minimum, mean and maximum diameters were thus computed for all vessels. Additionally, the variation of diameter along vessel was defined as the stenosis index (SI):

$$SI = 1 - \frac{D_{min}}{D_{max}}$$ **(Equation 4.30)**

  An SI of 0 represents an ideal, uniform cylinder, a value of ~1 would indicate that $D_{min}$ is ~0.

- The angle (θ) between any 2 vessels (Figure 4.26) was quantified by computing the dot product of the corresponding bifurcation vectors (b):

$$\theta = arcos\left(\frac{b_1 \cdot b_2}{\|b_1\|\|b_2\|}\right)$$ **(Equation 4.31)**

- Caval offsets (Figure 4.27 were computed by projecting the displacement between the IVC and SVC vector onto (1) the anterior-posterior axis (AP offset; negative when the IVC is anterior to the SVC), and (2) the right-left axis (RL offset; negative when the IVC is to the right of the SVC). The VC-PA offset was defined as the shortest distance between the two centerlines from IVC to SVC and from LPA to RPA.

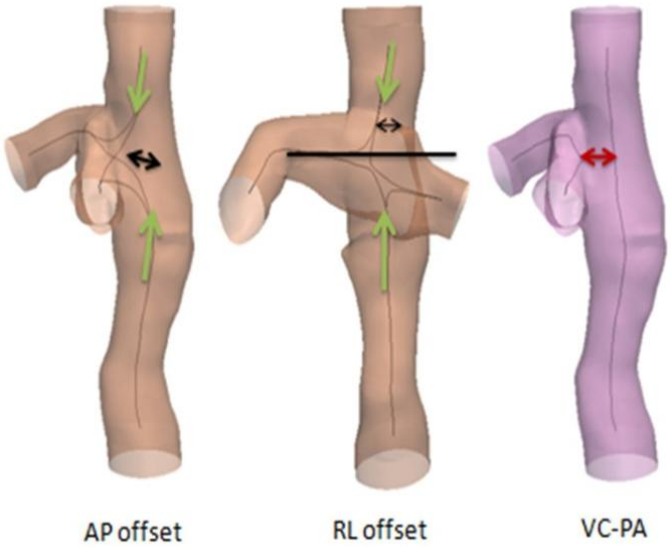


**Figure 4.27** ***Visual definition of caval offsets (left) in the anterior-posterior direction, (middle) in the right-left direction, and (right) with respect to the PA axis.***

## 4.6 SURGEM: Virtual Surgery Interface

The ability the accurately recreate the surgical interventions to successfully model procedures is a critical requirement for the development of virtual surgery tools. Pekkan *et al.* detailed SURGEM as the solution to this need[110]. Developed through collaborations between Drs. Yoganathan and Rossignac (GT College of Computing), SURGEM provides an interface for a user to re-create virtual surgical connections based on patient-specific templates using independent 3D spatial control via PHANTOM Omni haptic devices (Geomagic Inc.) (Figure 4.28). In other words, the reconstructed anatomy from CMR can be loaded into the software and a virtual cylinder can be registered to the anatomy to mimic the positioning of the surgical baffle.

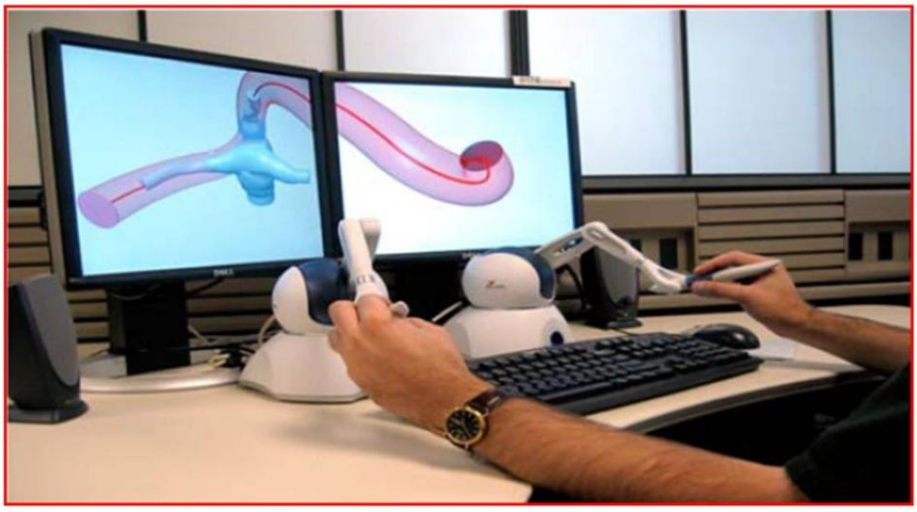

**Figure 4.28** ***Virtually interfacing a virtual surgical baffle (red) with reconstructed patient-anatomy (blue) using 3D haptic devices.*** ***youtube.com***

The realism of the output of this naturally depends on the proper constraint of the work space. For Fontan surgery, this means that simply visualizing a patient's Glenn connection and proximal IVC 'in a vacuum' is unlikely to yield satisfactory results. Instead, it is regular practice to incorporate those elements as well as surrounding anatomical structures into the interface in order to properly orient the virtual connection to realistic landmarks. An example is shown in Figure 4.29 wherein the Fontan pre-cursors (bilateral bidirectional Glenn and proximal IVC) are shown in blue, the surrounding anatomy (heart, aorta, pulmonary veins) are shown in orange, and the virtual Fontan baffle is shown in red. Control of the baffle is achieved at the three control points located distributed along its centerline, such that the cylinder can be elongated, shortened, or curved in any direction. Importantly, no material properties are introduced and the cylinder will contort to any shape imposed on the centerline.

Even with the inclusion of surrounding anatomy, it is important to appreciate common surgical landmarks to accurately replicate what is done in the operating room. For

example, extracardiac Fontan connections are typically positioned close to the junction of the pulmonary veins and the atrium, as shown in the right side of Figure 4.29. Lateral tunnel connections are more challenging to emulate with the current software; however, the ‘inside-out’ viewing mode does facilitate visualization of internal structures as needed. Thus, the SURGEM software provides all the basic tools necessary to cover a broad range of modeled interventions.

Alternative methods for virtual anatomic design have been proposed[132]; however, there are several key distinctions. SURGEM is user driven, as opposed to being an automatic framework, which makes it sub-optimal for robust optimization since the user would have to create each individual geometric alteration. However, this feature also means that the model designs are created visually, which is the way the surgery is performed, and so are more intuitive and natural than parametric representation of a curve, and can better conform to physical spatial constraints.

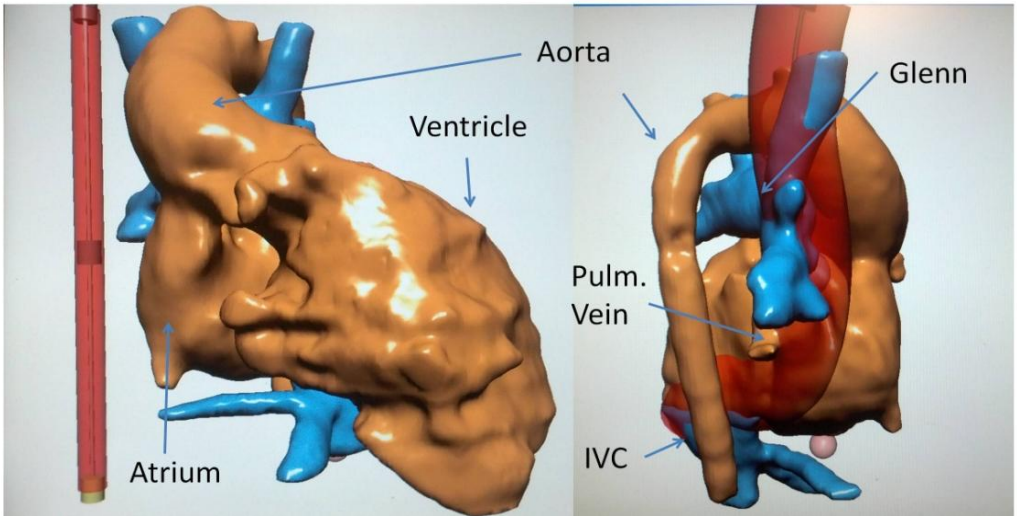


**Figure 4.29** ***Patient-specific reconstruction of bilateral bidirectional Glenn connection (blue) with surrounding anatomy (orange) in the SURGEM interface. The virtual surgical baffle is shown in red and can be seen being positioned from IVC to the right Glenn connection in the image at right.***

## 4.7 Section Summary

MRI is a diverse and robust clinical imaging modality whose numerous strengths made it an ideal basis for the acquisition of patient-specific anatomic and functional data for analysis in this thesis. Over the past decade, a diverse and powerful set of complementary tools have been developed in our group to make use of the potential of the MR images to extract valuable functional information at a patient-specific level and improve physiologic understanding. These include: TCPC anatomic reconstruction and geometric characterization; quantification of *in vivo* flows from PC MR, both in a single vessel and in a volumetric domain; and the computational simulation of local hemodynamics with very high temporal and spatial resolution.

The computational tools in particular represent a robust and valuable asset in the study of single ventricle palliation. Such methods, in addition to providing superior spatial and temporal resolution compared to CMR flow measurements (for improved quantification of metrics like power loss), CFD also allows for the parametric variation of specific variables to observe their individual impact. Such variables could be simple boundary condition adjustments, to model exercise physiology or changing pulmonary vascular tone, or could be complex modeling of entirely new patient-specific connections (as created with the SURGEM interface). These strengths are all leveraged in various ways throughout this thesis to better our understanding of TCPC hemodynamics and its role in single ventricle physiology.

A schematic of how these methodologies fit together to produce the study metrics of interest is provided in Figure 4.30. For the first time, this thesis builds upon each of these prior developments and deploys them in unprecedented study sizes to provide the best opportunity to date to relate TCPC hemodynamics to patient functional outcomes.

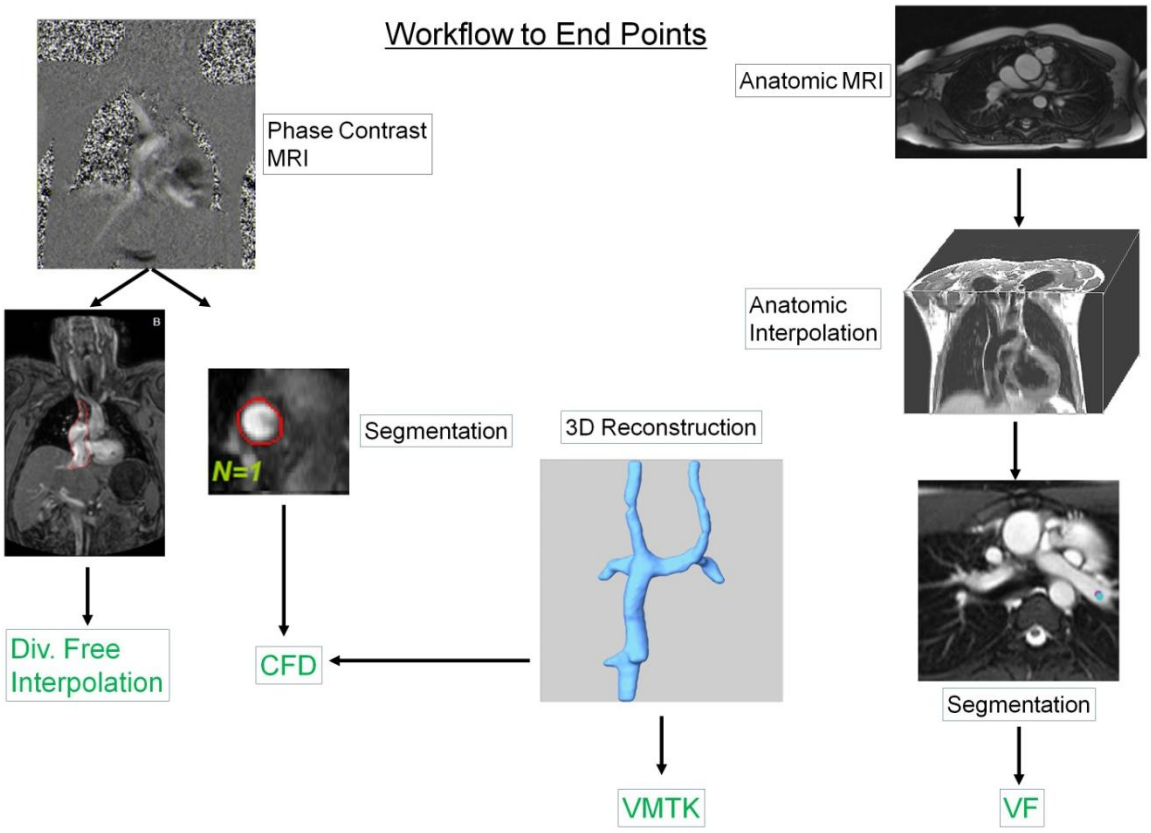


**Figure 4.30** ***Schematic of methodology workflow from MRI to the various investigational methods employed in this thesis.***

# Chapter 5. SPECIFIC AIM 1: ANALYSIS OF TCPC HEMODYNAMICS IN A LARGE PATIENT COHORT

## 5.1 Overview

In the present era, operative mortality for the Fontan procedure is low[22, 133], but gradual attrition is a significant problem[29]. The TCPC is known to mediate an adverse hemodynamic environment[45] and in some cases, strong hypothetical connections can be drawn between these adverse hemodynamics and the cause or exacerbation of chronic morbidities. For example, poor exercise tolerance may be related to non-linear power loss increases across the connection[134]; poor distribution of hepatic factors to the lungs is widely believed to be related to the development of pulmonary arteriovenous malformations (PAVM[58]). For these reasons, the TCPC has been the focus of a large body of research[54].

Early optimization studies using idealized models identified modifications to reduce venous collision and improve flow efficiency such as a caval offset and vessel flaring[75, 135-137]. However, it was soon realized that the 3-dimensional hemodynamics of patient-specific connections can be much more complex than can be appreciated with such simplified models[80]. A majority of studies over the past decade have therefore used medical imaging and/or computational fluid dynamics (CFD)[81, 85, 107, 134, 138, 139, 91, 92] to characterize TCPC flows at a patient-specific level. These investigations have been very successful in incrementally improving fundamental physiologic knowledge[55] and providing surgical insights[105].

There are inherent challenges to the use of patient-specific models. Considerable effort and resources are required to amass and analyze such data in significant quantities; the largest Fontan CFD study to date included only 16 patients[55]. Furthermore, the ability to draw generalizable conclusions based on small samples of patient-specific results is limited and must be approached with caution. If local dynamics and energetics of TCPC flows are an important determinant of patient functional health status and quality of life as they are hypothesized to be, larger sample sizes are needed to power the analysis of such outcome metrics.

The NIH-supported GT CMR Fontan database is therefore a valuable resource, which can provide significant sample sizes for these detailed hemodynamic evaluations. By leveraging these data, this study provides an unprecedented patient population for being able to answer these questions. The broad objective was therefore to use the image-based patient-specific data to perform numerical simulations and quantify hemodynamic parameters of interest. These parameters can then be used to: a) establish mean values for this population; b) statistically relate the findings to other functional measures, such as cardiac index or systemic venous flow; c) compare results across surgical (intra-atrial vs extracardiac) or anatomic (single RV vs. single LV) templates and observe biases.

The basic outline for the chapter is as follows. First, the protocol used for patient selection, CFD simulation, and statistical analyses will be discussed. Next, an in depth comparison of selected computational results against 4D PC CMR-derived velocity fields will be performed to provide verification for solver accuracy (in addition to the formal validation studies previously conducted). An explicit comparison of results from steady vs. pulsatile flow boundary condition simulations will provide further indication of the impact of limiting assumptions employed in the modeling effort. Finally, moving to the core of our study, we will detail the results for the entire patient cohort study, including

3D CFD results and statistical analyses of key hemodynamic metrics, followed by the VTMK geometric analysis and, finally, the comparison of geometric and hemodynamic metrics in order to identify potential predictors of global TCPC performance.

## 5.2 Study Protocols

### 5.2.1 Patient Selection

As discussed in §4.2, the GT Fontan CMR database contains results from over 250 patients with a single ventricle. From these, 114 patients consecutive patients were selected on the bases of: a) having a completed Fontan connection (i.e., excluding patients at the Glenn stage); and b) having been imaged at CHOP. Patients were then excluded on the bases of severe CMR artifacts in the available data, lack of sufficient phase contrast velocity data, or diagnosis of Ebstein's anomaly, reducing the number of investigated patients to 100. Basic demographic details for these 100 patients are provided in Table 5.1. The complete list of patient detail is provided in Appendix A.

**Table 5.1 Patient demographic details**

| | | | |
|---|---|---|---|
| **Age** (years) | 12.0 ± 6.8 | **Connection Type** (IA/EC/APC) | 64/33/3 |
| **Body Surface Area** ($m^2$) | 1.23 ± 0.46 | **HLHS vs. non-HLHS** | 31/69 |
| **Gender** (m/f) | 55/45 | **Bilateral SVC Connections** | 15 |

IA- Intra-atrial; EC- Extracardiac; APC- Atriopulmonary; HLHS- Hypoplastic Left Heart Syndrome; Continuous data reported as mean ± st. dev.; See Table 12.1 in Appendix A.

### 5.2.2 CFD Protocol

Simulations were divided among several investigators, with the candidate completing over 50% of the total. Unless otherwise indicated, simulations employed time-averaged boundary conditions based on the phase contrast velocity data for each vessel. At the inlet extensions, a flat velocity profile was imposed based on the vessel-specific flow rate measured. The presence of a fenestration was generally ignored, although in more recently acquired data in which PC MR planes were acquired above and below the fenestration, the flow rate from the acquisition above the fenestration was retained (see Appendix A).

Since the sum of the measured inflows usually exceeds the sum of the measured outflows (due in part to fenestration flow), imposing the measured pulmonary artery flow rates would typically violate conservation of mass compared the inlet flow rates. Accordingly, flow boundary conditions at the outlet extensions were not imposed based

on the measured outflow rates, but rather based on the ratio of these measured vessel flows to total pulmonary arterial flow. In a few selected cases, primarily when a stenosis was present in one branch pulmonary artery, the measured flow rate in the stenotic artery was retained for the simulation while flow through the contra-lateral branch pulmonary artery was assumed to be equal to the total caval return less the flow in the stenotic artery. It is known that connection 109nergetic are dominated by localized PA stenoses[140] so the above-described practice prevented the artificial increase in imposed flow across the stenotic region. For geometries in which the right upper lobe branch artery was retained in the computational domain, the measured RPA flow split (taken proximal to the branch) was divided between the lower and upper branches based on the ratio of their respective areas.

For all simulations, convergence at each time step was ensured by constraining the relative residuals of the Poisson solver to decrease by 8 orders of magnitude. Time was advanced (for steady simulations) until convergence of the running average to the instantaneous mean. This was assessed by tracking pressure and velocities at selected points within the computational domain, typically in the center of the connection and at proximal and distal (with respect to the artificial extensions) outlet points.

### 5.2.3 Statistical analyses

Statistical analyses were performed using Minitab (Minitab Inc., State College, PA). Continuous variables (e.g., TCPC-EDI, HFD) were tested for normality using the Anderson-Darling test. The Student's t-test and Mann-Whitney test were used for comparisons between groups, as appropriate, while Pearson's R or Spearman's ρ tests were used for correlations. P-values less than 0.05 were considered statistically significant in all cases. Partial correlation was used, as needed, to correct for the confounding effects of other independent variables. The analysis presented here is

exploratory in nature, and thus no adjustments were made for potential inflation of Type I error (i.e., rejection of a potentially true null hypothesis) due to multiple comparisons.

## 5.3 Modeling Verification

### 5.3.1 Comparison of 4D PC CMR with CFD

From the 100 patient CFD cohort, 8 patients had sufficiently high quality 4D PC CMR data (particularly in the PAs to allow for quantification of flow distribution) for a detailed cross-modality comparison. Such comparisons were performed to provide additional verification that the simulated results used for subsequent statistical and functional analyses are representative of the *in vivo* hemodynamics. Much of the credit for this section belongs to Dr. Kartik Sundareswaran who implemented the CMR interpolation scheme and reconstructed the flows for the 8 cases presented[119].

The following paragraphs present the analysis for the 8 patients; it is noted that multiple patient IDs are provided to reflect the identifiers in our three database entries; namely, the original bioengineering research partnership (BRP) grant database, the new designations of the 2010 R01, and surgical planning database (when applicable). It should also be noted that the power loss results from the CMR data are routinely an order of magnitude less than the CFD because the CMR values are calculated from viscous dissipation, thereby using velocity gradients, and their accuracy is hindered by the poor measurement resolution near the walls where gradients are typically the highest.

For each patient, the velocity fields are visually represented with: A) velocity streamlines from the time-averaged CFD; B) a representative series of instantaneous velocity

streamlines from CMR; C) streamlines from the time average of the CMR data; and D) instantaneous snapshots from CMR particle tracking.

#### 5.3.1.1 CHOP068/CHOP064A (Figure 5.1)

This patient had a lateral tunnel (LT) Fontan connection to a hemi-Fontan SVC anastomosis, resulting in a large ‘pouch’ anteriorly offset from the pulmonary arteries. Figure 5.1 shows a comparison of velocity encoded streamlines for the time-averaged CFD (A) and the instantaneous time points from the 4D PC CMR (B).

Focusing on the CMR results first (Figure 5.1B, Figure 5.1C), the clear defining characteristic of this connection is the large, dynamic central vortex in the LT pouch region. Owing to the right offset of the SVC anastomosis compared to the LT, as the SVC flow enters the connection it collides with the IVC flow, which has a right-to-left directionality from the LT curvature, creating a rapid direction change in the SVC flow and further constraining the IVC flow along the left lateral wall. The combined flow streams traverse right-to-left and anterior-to-posterior through the connection (giving the appearance of the central vortex with the incoming SVC flow) before colliding with the posterior wall of the connection and dividing between the right and left pulmonary arteries. Figure 5.1D shows an instantaneous snapshot of IVC particle tracings providing improved visualization of the IVC dynamics within the connection.

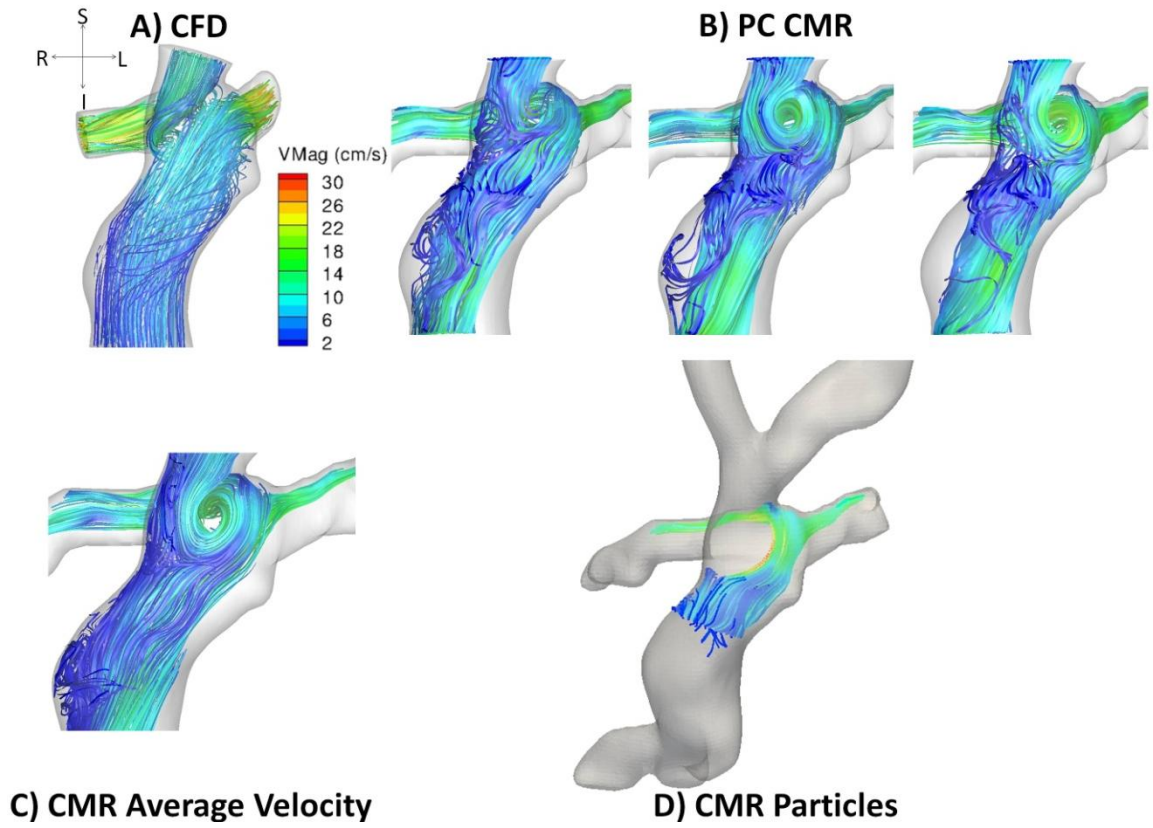


**Figure 5.1 CHOP064A (intra-atrial): Velocity streamlines from A) time-averaged CFD, B) instantaneous CMR reconstructions, and C) time-averaged CMR. D) IVC Particle tracing from CMR data. A large counter-clockwise recirculation is present in the center, formed by the right-to-left and anterior-to-posterior motion of the IVC and SVC flows at their collision point. The recirculation center is not as well defined in the CFD as in the CMR owing to differences in the cross-sectional velocity profile (best seen in the particle tracing).**

By comparison, the CFD streamlines (Figure 5.1A) demonstrate very similar characteristics. A counter-clockwise recirculation pattern is evident in the connection at the collision of the IVC and SVC flows and the local velocity magnitudes are in good agreement, despite the variations present in the time-varying results. There is a noticeable difference in the location of the center of recirculation, as well as the fact that, in the CFD, it is the SVC that is constrained along the right lateral wall more so than the IVC being constrained along the left wall. These minor differences likely reflect non-

uniformities in the inlet velocities, i.e., rather than uniformly distributed and perpendicularly directed (with respect to the vessel cross-section) velocities at the inlets, the *in vivo* distributions and angles vary, leading to small differences in the location and dynamics of flow collision.

Quantitatively, the flow distribution results were varied slightly (66% vs. 82% IVC to LPA for CMR and CFD respectively), likely reflecting the varied location of IVC-SVC interactions (more SVC flow exited the RPA in the simulations, consistent with the rightward constraint). Power loss quantities were 0.04 mW and 0.5 mW for PC MR and CFD, respectively.

5.3.1.2 CHOP073/CHOP069A (Figure 5.2)

As in the previous case, this patient had a lateral tunnel/hemi-Fontan connection and the local hemodynamics were again characterized by complex recirculation within the connection region. From the 4D PC CMR (Figure 5.2B and Figure 5.2C, results shown from a posterior perspective to facilitate visualization), the SVC flow is constrained to the right lateral wall upon entering the connection and primarily exits the RPA. The IVC flow appears to skew along the outer wall of the tunnel curvature and recirculate posteriorly and left to right within the connection (this is better seen in the instantaneous particle tracings in Figure 5.2D). The resulting IVC-to-LPA flow thus has a high degree of secondary flow apparent in the velocity streamlines.

The CFD streamlines are similar with respect to the constrained SVC-to-RPA flow; however, the complexities of the IVC flow within the connection appear to be slightly altered with decreased secondary flow magnitudes. Again, differences in the inlet velocity profile may mediate this discrepancy. It is noted that the streamlines in the

proximal IVC/Fontan baffle are more disturbed in the PC CMR results than the uniform distribution imposed on the CFD.

The flow distribution results compared favorably: 59% vs. 47% IVC-to-LPA (CMR vs. CFD). The reason for the slight difference is not immediately clear from the flow fields since the SVC flow appears to be entirely constrained to the RPA in both cases; small differences in volume flow rates to the respective vessels or limited PC CMR temporal resolution may play a role. The power losses were 0.1 mW vs. 0.8 mW for PC CMR vs. CFD, respectively.

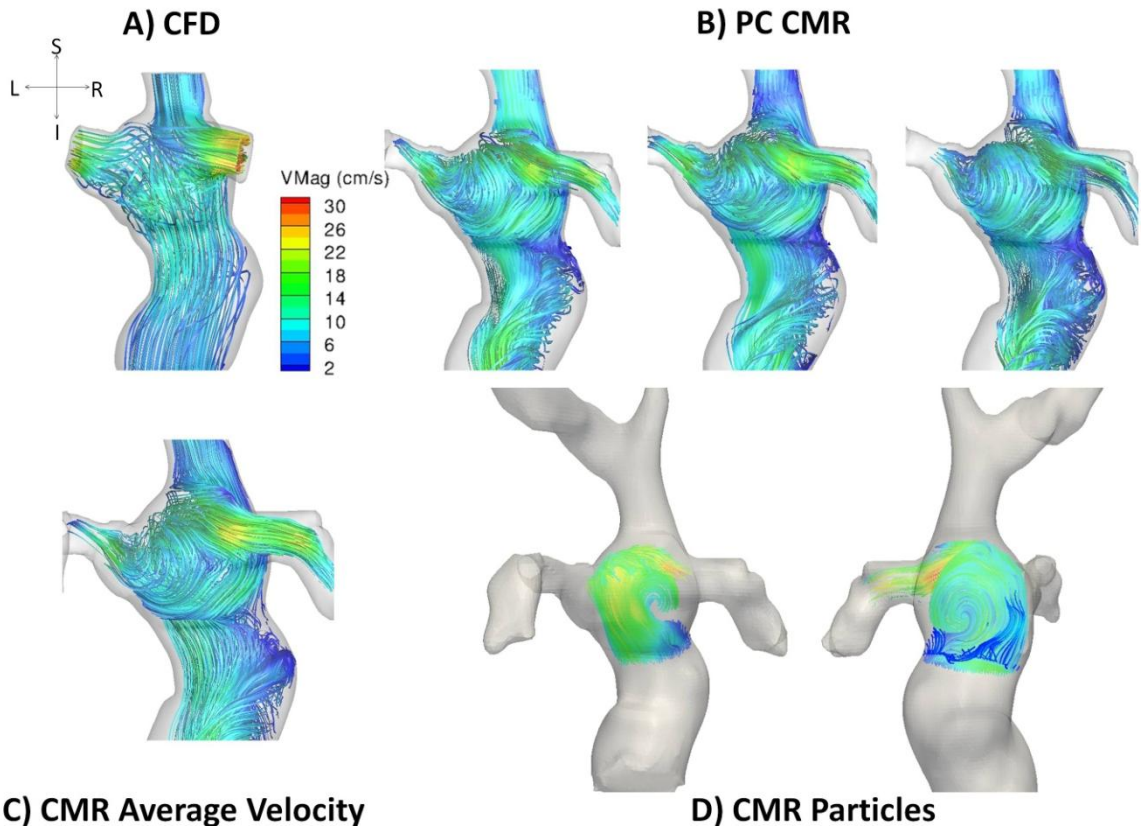


**Figure 5.2 CHOP069A (intra-atrial): Velocity streamlines from A) time-averaged CFD, B) instantaneous CMR reconstructions, and C) time-averaged CMR. D) Sequential (from left to right) IVC particle tracings from CMR data. As best seen from the particle tracings, the IVC flow is skewed along the outer wall of the lateral tunnel and recirculates posteriorly from left to right. The SVC flow is constrained to the RPA and a portion of the IVC flow continues a 360° (or more) rotation to exit the LPA. Not all of this complexity was captured by the CFD because of non-uniformity of the IVC velocity inlet profile.**

5.3.1.3 CHOP078/CHOP074A (Figure 5.3)

This patient has many of the same anatomic (LT) and hemodynamic features discussed in the previous two cases. Here, the PC CMR and CFD streamlines qualitatively reveal the same flow features: IVC flow is directed right-to-left, anterior-to-posterior as it enters the connection. Furthermore, the less “bulgy” nature of this connection compared to the previous examples, and more streamlined Fontan flow in the CMR data facilitated this

improved qualitative agreement. The posterior wall appears to act as a flow dividing point, splitting the IVC flow between the left and right PAs (Figure 5.3D). The SVC is entrained along the right lateral wall by the incoming IVC flow stream and exits entirely through the RPA.

Reasonable agreement was seen in comparing the IVC flow distributions (73% vs 60% LPA (CMR/CFD)). Power losses were 0.09 mW vs 1.3 mW, CMR vs. CFD.

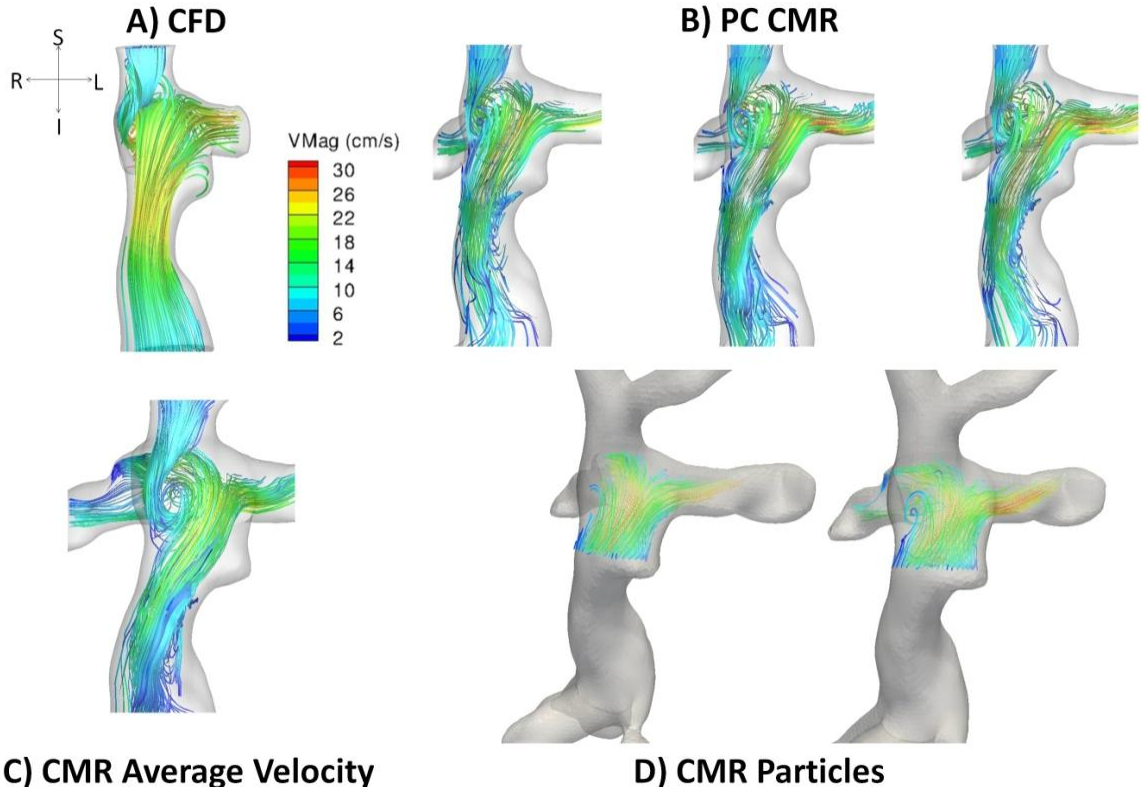


**Figure 5.3 CHOP074A (intra-atrial): Velocity streamlines from A) time-averaged CFD, B) instantaneous CMR reconstructions, and C) time-averaged CMR. D) Sequential (from left to right) IVC particle tracings from CMR data. The IVC flow dominates local dynamics, constraining the SVC flow along the right lateral wall and forcing a local recirculation zone as the SVC flow is redirected toward the RPA. The qualitative velocity streamlines were well conserved between CMR and CFD.**

#### 5.3.1.4 CHOP089/CHOP082A (Figure 5.4)

While the first three patients exposed above all had a lateral tunnel (LT), this patient and the 3 following ones featured the other common surgical approach to Fontan surgery; namely, an extracardiac conduit Fontan to a bidirectional Glenn SVC-PA anastomosis. In this patient, no offset was present between the inferior and superior caval connections, yielding direct collision of the IVC and SVC flows in the connection (as seen from both modalities, Figure 5.4A, B, and C). Despite the caval flow collision, flow in the PAs remains ordered and laminar with the IVC component fairly evenly distributed.

Here, the IVC flow distributions were different by only 3% (60% vs. 57% to the LPA for CMR and CFD, respectively) and power loss results were 0.14 vs. 1.4 mW, respectively.

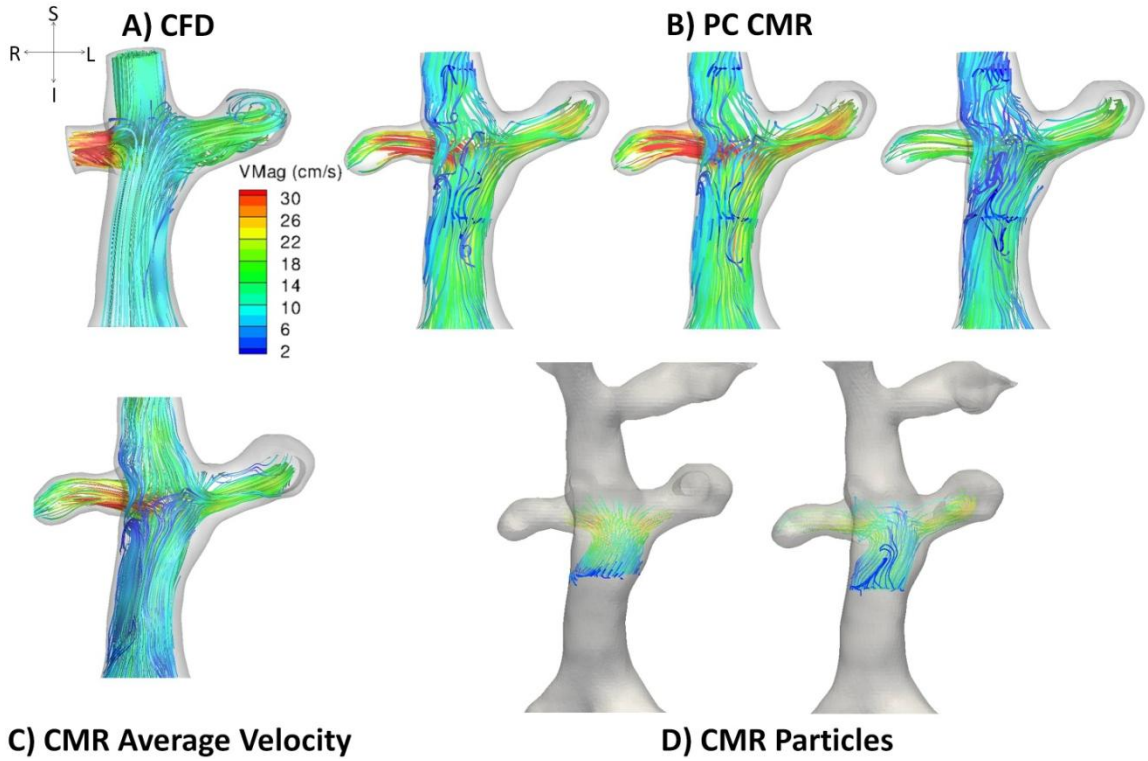


**Figure 5.4 CHOP082A (extracardiac): Velocity streamlines from A) time-averaged CFD, B) instantaneous CMR reconstructions, and C) time-averaged CMR. D) Sequential (from left to right) IVC particle tracings from CMR data. With no lateral offset between the SVC and IVC anastomosis locations, the caval flows collide and appear to both divide relatively evenly and smoothly transition laterally into the PAs. The qualitative velocity streamlines were well conserved between CMR and CFD.**

#### 5.3.1.5 CHOP090/CHOP083A (Figure 5.5)

A slight caval offset is seen with the extracardiac Fontan baffle offset to the RPA with respect to the bidirectional Glenn connection. As a result (as can be seen in both modalities, Figure 5.5 A, B, and C), there is a noticeable bias of SVC flow to the LPA. A significant secondary flow pattern develops in the IVC flow as it enters the connection through interactions with SVC flow and the superior wall of the PAs before primarily exiting the RPA.

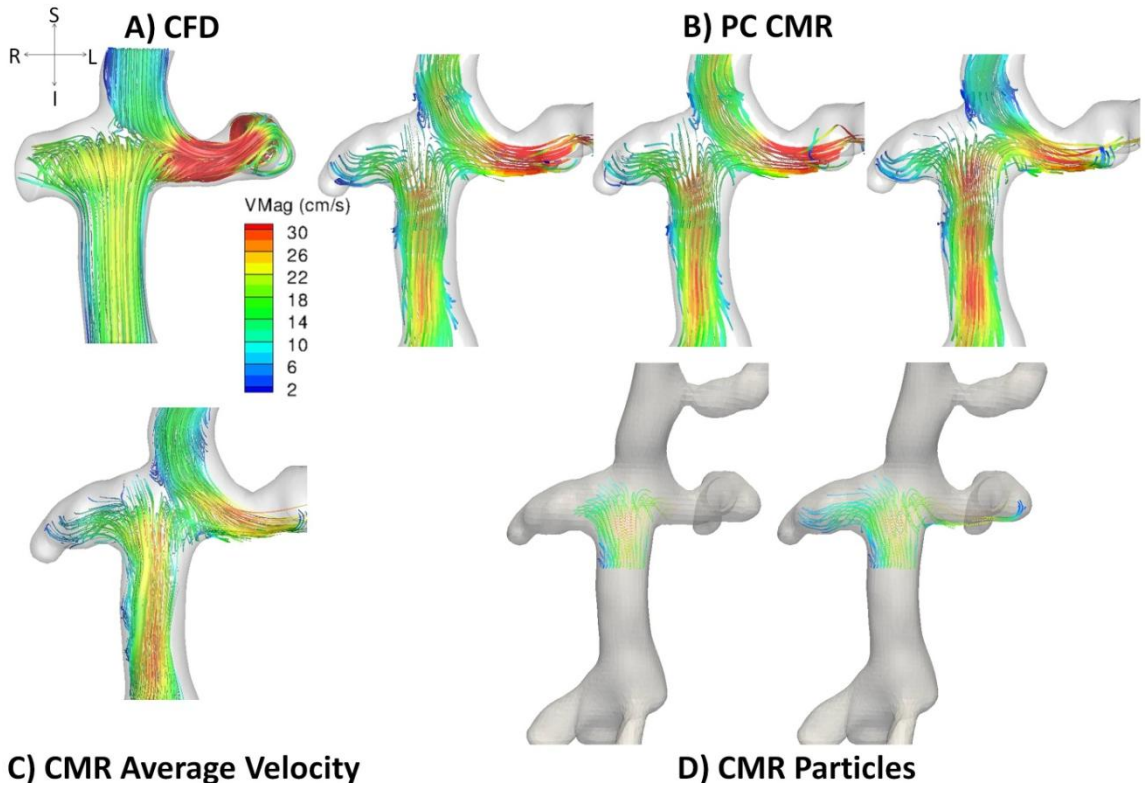


**Figure 5.5 CHOP083A (extracardiac): Velocity streamlines from A) time-averaged CFD, B) instantaneous CMR reconstructions, and C) time-averaged CMR. D) Sequential (from left to right) IVC particle tracings from CMR data. The Fontan baffle was positioned with roughly a half-diameter offset toward the RPA and as a result, the caval flow collision directs all the SVC flow exclusively to the LPA while the IVC flow perfuses both PAs with a high degree of secondary recirculation. The qualitative velocity streamlines have excellent agreement between CMR and CFD.**

In addition to the excellent agreement of local velocity magnitudes between the CMR and CFD flow fields, good agreement was seen between the IVC flow distribution results (32% vs 48% to the LPA for CMR and CFD, respectively). The power loss comparison was particularly weak (0.17 mW vs. 5.7 mW), perhaps owing to significant CMR signal drop off in the LPA distal to the sub-aortic narrowing (site of significant convective acceleration), as evidenced by the loss of streamlines (Fig 5.5B) and the constraining of IVC particles along the inferior vessel wall (Fig 5.5D).

#### 5.3.1.6 CHOP091/CHOP084A (Figure 5.6)

As another extracardiac connection without a visible caval offset, this connection is characterized by a direct collision of SVC and IVC flows. In fact, a distinct stagnation point is apparent in all figures across modalities. As was the case in CHOP089, the result of this collision is an apparently laminar and ordered transition from caval to pulmonary flows. The lack of large scale secondary flow structures in the CMR particle tracking (Figure 5.6D) particular supports this observation.

Quantitatively, the differences between CMR and CFD were on par with the prior cases: HFD was 61% vs 72% (CMR vs. CFD, respectively); power loss (0.11 mW vs. 1.4 mW).

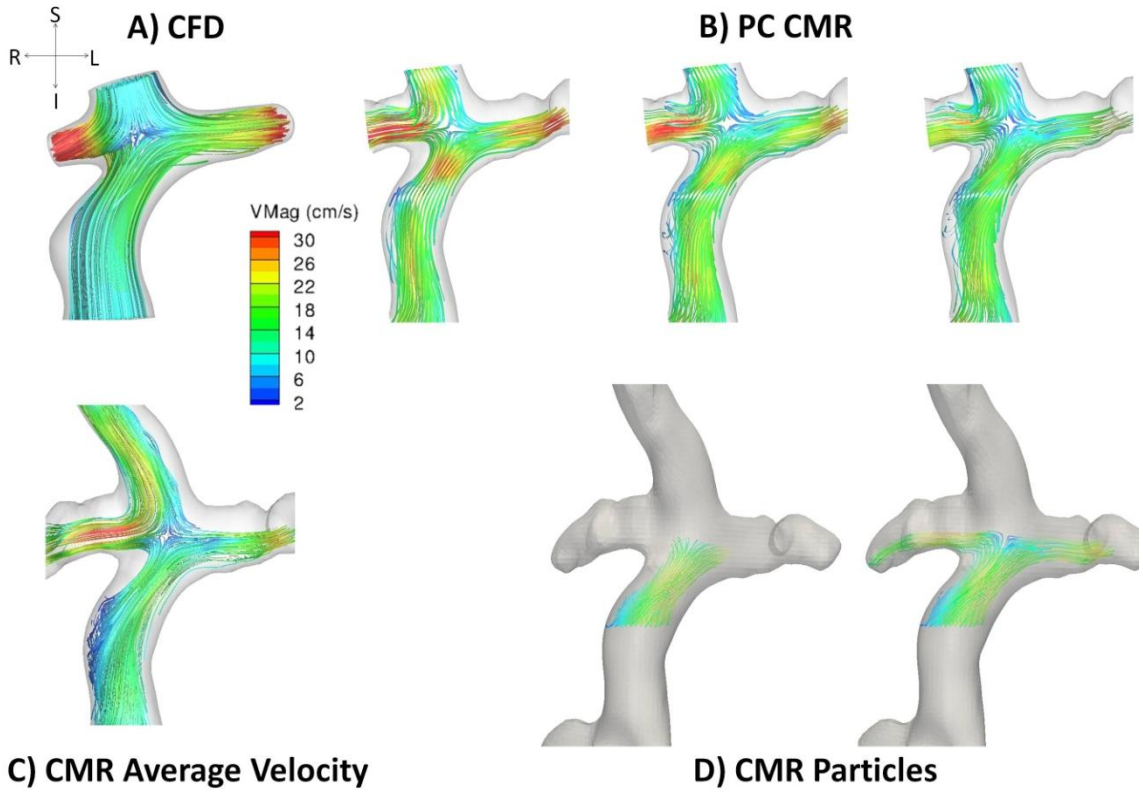


**Figure 5.6 CHOP084A (extracardiac): Velocity streamlines from A) time-averaged CFD, B) instantaneous CMR reconstructions, and C) time-averaged CMR. D) Sequential (from left to right) IVC particle tracings from CMR data. Despite curvature of the Fontan baffle, the hemodynamics do not demonstrate effects of a caval offset. Instead, the flows collide (forming a distinct stagnation point) and divide smoothly to the PAs. The qualitative velocity streamlines, particularly the stagnation point at the center of the connection have excellent agreement between CMR and CFD.**

5.3.1.7 CHOP095/CHOP088A (Figure 5.7)

The dynamics of this connection resemble those of CHOP090 owing primarily to the presence of a slight Fontan-to-RPA offset. Specifically, caval flow collision directs the majority of SVC flow to the LPA, while flow through the Fontan baffle tended toward the RPA with time varying magnitude. The time variation is perhaps best seen in the particle tracings (Figure 5.7D) in which the IVC particles are initially confined toward the RPA

(far left) before spreading through the connection and reaching both PAs (right two images).

HFD values were again in good agreement across modalities (20% vs. 27% LPA, CMR vs. CFD, respectively). Power loss agreement was much weaker (0.12 mW vs. 4.2 mW), perhaps because of low signal in the RPA where the CFD results predict significant convective acceleration.

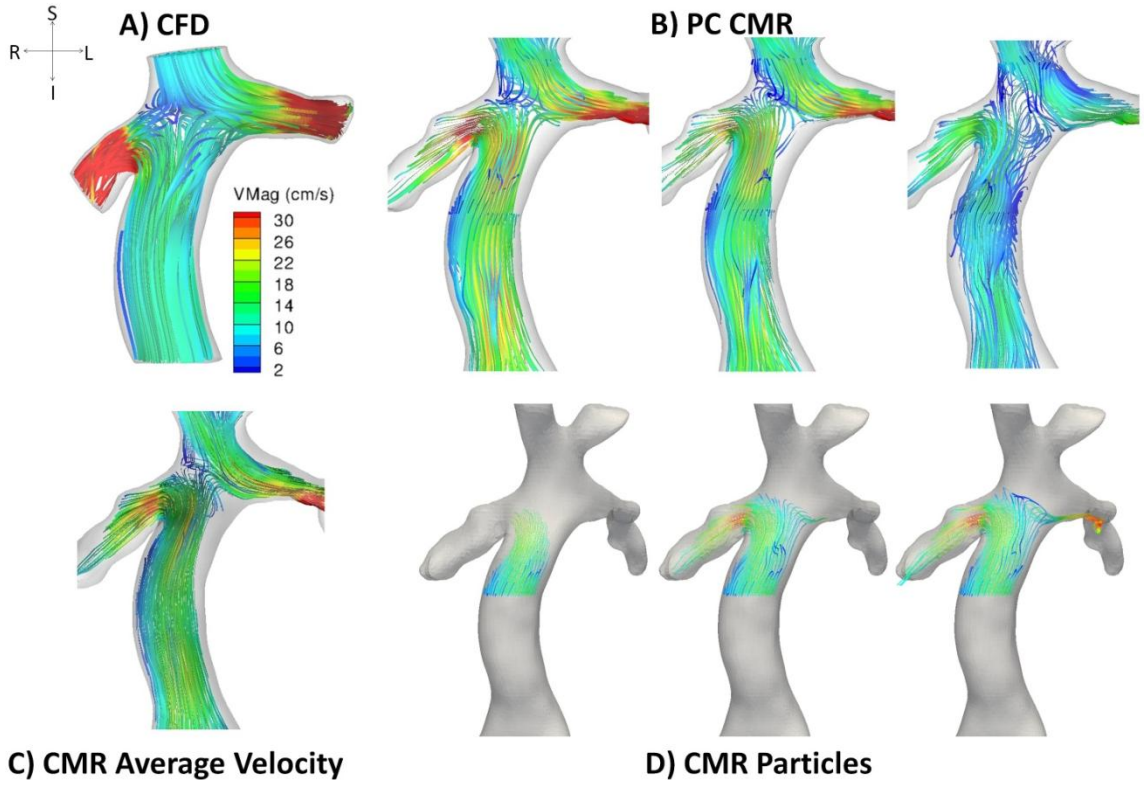


**Figure 5.7 CHOP088A (extracardiac): Velocity streamlines from A A) time-averaged CFD, B) instantaneous CMR reconstructions, and C) time-averaged CMR. D) Sequential (from left to right) IVC particle tracings from CMR data. The Fontan baffle was again offset toward the RPA, directing the SVC flow exclusively toward the LPA. The CMR results do reveal significant time-varying features (both in velocity magnitudes and direction of IVC flow), yet the CFD streamlines do appear to capture the general features well.**

#### 5.3.1.8 CHOP170/CHOP143A/CHOP_M1 (Figure 5.8)

This connection represents one of the most complex geometries and hemodynamic profiles in the GT database and was the focus of a recent manuscript discussing the use of surgical planning to correct pulmonary arteriovenous malformations[61]. This patient has a complex anatomical configuration characterized by interruption of the IVC with continuation of the azygos vein to the SVC. In other words, the inferior venous blood flow is carried not by the IVC but by an enlarged azygos vein, leaving only the hepatic veins natively connected to the inferior side of the right atrium. In addition, the connection of the innominate vein and the right SVC in this patient occurred at the level of the cavopulmonary anastomosis, effectively creating 4 distinct inlets to the connection.

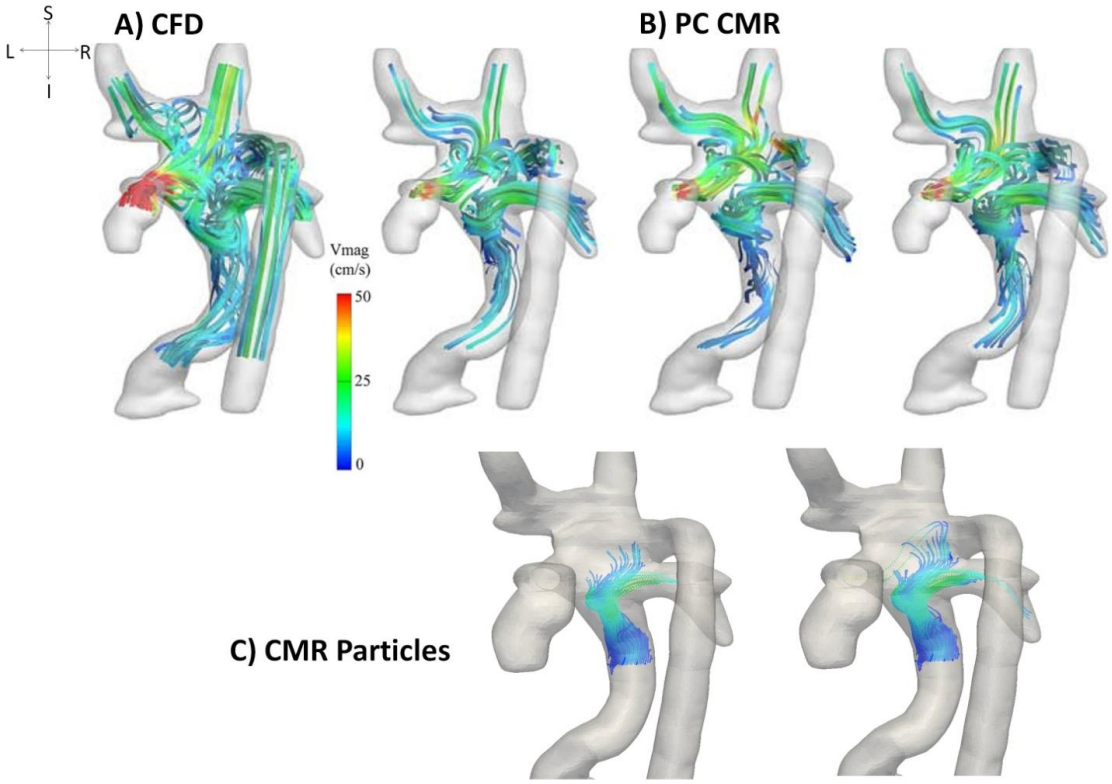


**Figure 5.8 CHOP143A (Interrupted IVC-extracardiac hepative venous connection): Velocity streamlines from A) time-averaged CFD and B) instantaneous CMR reconstructions. C) Sequential (from left to right) hepatic vein particle tracings from CMR data. Complex interactions among the superior (SVCs plus Azygos) venous flows preferentially direct hepatic flow to the RPA. The qualitative velocity streamlines, particularly in the complex patterns of the hepatic venous flow have excellent agreement between CMR and CFD. Image modified from Sundareswaran and de Zelicourt[61].**

The local hemodynamics were equally complex. The majority of systemic venous flow exited the LPA (as witnessed by the very high velocities in that vessel), and based on the streamlines (from both modalities) the SVC, innominate vein, and azygos flows were the primary contributors to LPA flow at the exclusion of the hepatic venous flow. In fact, as best seen by the particle tracings (Figure 5.8C) the hepatic flow, despite a preferential right-to-left curvature of the Fontan baffle, became entrained in higher momentum superior venous flows at the distal end of the baffle and made a nearly 180° turn and

exited the RPA. These hemodynamic findings are consistent with the diagnosis of left lung PAVMs, as mentioned.

Despite the complexity of these flow patterns, flow distributions across modalities were very well conserved: 13% vs. 12%, CMR vs. CFD, respectively. Power loss results in this case were very divergent (0.3 mW vs. 30 mW for CMR and CFD, respectively) because the high velocities through the stenosed LPA were not captured by the CMR data.

#### 5.3.1.9 Section Limitations and Summary

The preceding section provided direct comparisons, both qualitative and quantitative, between TCPC hemodynamics separately derived from computational simulations and medical imaging reconstruction for a series of 8 patients. The objective of the comparison was to provide support, in addition to formal and successful past validation studies[61, 124, 126], for the realism and validity of the computational results for capturing the *in vivo* hemodynamics characteristics.

It is first important to point out the significant limitations inherent to comparing CMR and CFD in the context of the quantitative discrepancies seen. First, the specific comparison made was between dynamic, interpolated results acquired and averaged over numerous cardiac cycles and static simulations whose boundary conditions were obtained from a separate CMR acquisition. Thus, there is a significant dependence on the stability and repeatability of the patient's cardiac and respiratory function to ensure consistency between both the through plane and coronal acquisitions and during the potentially lengthy coronal stack acquisition.

Another significant issue is the large inherent difference in the spatial scales of the two modalities, which has profound implications on the ability to assess power loss via CMR. Fontan 4D PC CMR studies have reported voxel sizes ranging from 5.8-17.5 $mm^3$ [91, 92], while the grid size for the solver in our study was on the order of 0.05 $mm^3$. These differences have significant implications for the ability of each method to resolve velocities close to vessel boundaries and accurately evaluate spatial derivatives of the velocity fields, both of which are crucial for hemodynamic power loss evaluation. Table 5.2 summarizes the relative merits of these two modalities for studying TCPC flows.

**Table 5.2 Relative merits of 4D PC CMR and CFD for studying patient-specific TCPC hemodynamics**

| | 4D PC CMR | CFD |
|---|---|---|
| **PROS** | • Velocity fields include effects of respiration, cardiac cycle variation, and vessel motion/elasticity<br>• No assumptions needed for inlet/outlet boundary conditions<br>• No assumptions needed for blood rheology | • High spatial and temporal resolution<br>• Results naturally adhere to laws of fluid mechanics, including mass conservation<br>• Needed input from imaging limited to short, basic sequences |
| **CONS** | • Requires specialized CMR sequences not universally available<br>• Limited spatial and temporal resolution<br>• Requires long scan times<br>• Data acquired piece-wise and averaged over many cycles | • Must prescribe boundary conditions at inlets and outlets<br>• Typically neglect respiration and wall motion<br>• Typically assume Newtonian rheology |

Hence, the CMR power loss values were almost uniformly an order of magnitude lower than the corresponding CFD power losses (Table 5.3). It can therefore not be claimed that the CMR provides the desired verification in this aspect of the numerical results; however, this limitation is not unique to the present study and thus most prior power loss validation studies have relied on other experimental methods and produced much better matches to control volume computational analyses[141].

Rather than power loss, the appropriate focus is therefore on the qualitative velocity comparisons and the quantitative HFD differences. With respect to the former, the agreement was generally very strong, as evidenced from Figure 5.1, Figure 5.2, Figure 5.3, Figure 5.4, Figure 5.5, Figure 5.6, Figure 5.7, and Figure 5.8. While some subtle variations and dependencies were noted as a function of the detailed inlet cross-sectional velocity profiles (as in CHOP064A and CHOP069A), the defining flow characteristics of each connection were well conserved across modalities. Specifically, the three intra-atrial connections were all characterized by 3-dimensional vortical patterns (anti-clockwise and anterior-to-posterior recirculation) within the large connection regions based on the interactions of the SVC and IVC flows with relation to the PAs. For the extracardiac connections, the effects of caval offset were apparent and consistent between CMR and CFD: either creating a head-on collision of the incoming flows (as in CHOP082A and CHOP084A) or preferentially directing SVC flow to the LPA in the presence of a Fontan-RPA offset (CHOP083A and CHOP088A).

This consistency translates into reasonably good agreement with respect to quantitative HFD calculations (Table 5.3). Keeping in mind that mass conservation is not present in the CMR-measured data nor globally enforced after divergence free interpolation (i.e., only the individual interpolating kernels are divergence free), the consistency with simulated results is promising (considering neither modality is a true gold standard for

this measurement). As seen in the Bland-Altman plot in Figure 5.9, the average difference is close to 0, despite the small sample size, and the maximum difference was on the order of 16%. While it is difficult to exactly dictate the accuracy needed for clinical utility of these methods (given the uncertainty surrounding the clinical thresholds of the metric itself), it is important to note that the hemodynamics of the patient who did experience an adverse flow distribution outcome in this series were consistently and properly characterized by both modalities. These findings therefore provide assurance that the simulated results analyzed through the rest of this aim and the rest of the thesis are reasonably accurate despite assumptions and limitations inherent to the methodology.

***Table 5.3*** **Summary of CMR and CFD Quantitative Comparisons.**

| | HFD (%LPA) | | Power Loss (mW) | |
|---|---|---|---|---|
| | **CMR** | **CFD** | **CMR** | **CFD** |
| **CHOP064A** | 66 | 82 | 0.04 | 0.5 |
| **CHOP069A** | 59 | 47 | 0.1 | 0.8 |
| **CHOP074A** | 73 | 60 | 0.09 | 1.3 |
| **CHOP082A** | 60 | 57 | 0.14 | 1.4 |
| **CHOP083A** | 32 | 48 | 0.17 | 5.7 |
| **CHOP084A** | 61 | 72 | 0.11 | 1.4 |
| **CHOP088A** | 20 | 27 | 0.12 | 4.2 |
| **CHOP_M1** | 13 | 12 | 0.3 | 30 |

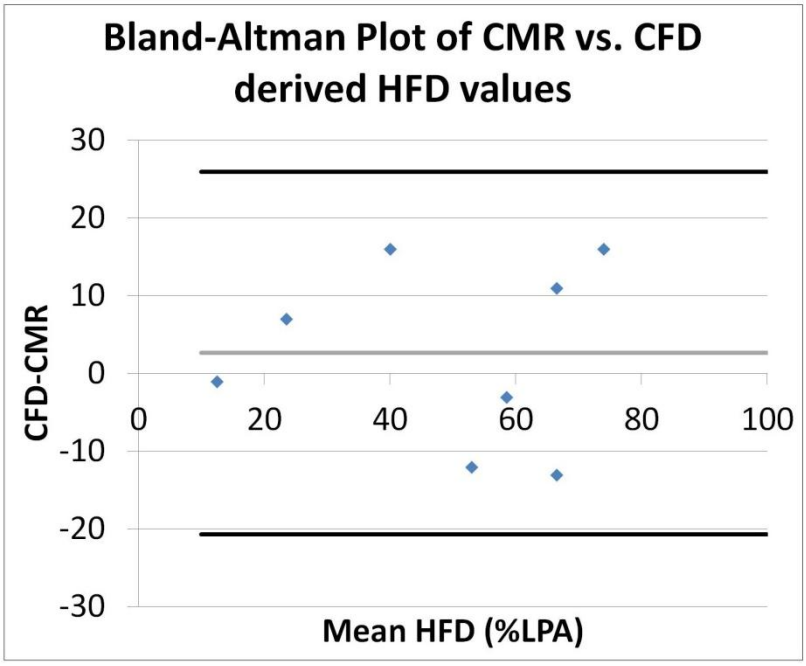


**Figure 5.9 Bland-Altman Plot of differences between CMR- and CFD-derived HFD values. In this small sample, the mean difference (gray horizontal line) was close to zero and maximum difference was 16%.**

### 5.3.2 Pulsatile vs. Time-Averaged Boundary Condition Results

For a subset (n=35) of the 100 patient cohort, simulations were performed using both PC CMR-derived time averaged and time-varying (pulsatile) flow boundary conditions. Paired comparison of the results of this set of simulations thus provides an indication of the impact that the steady flow assumption has on the quantitative simulation results. The results are considered separately below based on metrics of interest.

#### 5.3.2.1 Power loss

Table 5.4 summarizes the power loss findings as a function of imposed flow conditions. Of note, one of the patients (CHOP033A) was excluded from the power loss comparison because the RPA phase contrast measurement revealed flow reversal for a small portion

of the cycle that, because of the rigid wall assumption, created an unrealistic and unmeasured spike in LPA flow and inflated the pulsatile power loss result. In the remaining 34 patients, the pulsatile power losses were significantly higher on average (6.4 mW vs. 5.6 mW, $p<0.01$ by Wilcoxon signed rank test), which is consistent with the preliminary findings of de Zélicourt[124]. However, there were three cases in which the pulsatile power loss was less than the steady value. On an individual patient basis, this difference translated into a 16.2% average absolute error.

***Table 5.4*** **Summary of steady vs pulsatile flow power losses**

| | Steady flow power loss (mW) | Pulsatile flow power loss (mW) | Absolute error (%) |
|---|---|---|---|
| **Mean** | 5.6 | 6.4 | 16.2 |
| **Standard Deviation** | 4.5 | 4.8 | 11.4 |
| **Median** | 4.0 | 5.3 | 15.7 |

See Table 12.8 in Appendix B.

Figure 5.10 shows a Bland-Altman plot for these data demonstrating the agreement between the two simulation conditions. There is a positive bias in the mean differences (0.86 mW) and the top and bottom horizontal lines represent two standard deviations from the mean. The majority of data points fall within these standard deviation bounds, although there are two instances where the differences were greater: one steady flow over-estimate (CHOP080A) and one steady flow under-estimate (CHOP082B). In the former case, as will be discussed in more detail with regard to HFD in the next sub-

section, the relative phase shift in the incoming pulsatile flows alter their interactions (particularly the IVC and RSVC). For CHOP082B, the reason for the under-estimatation is the large amplitude of the flow pulsations, which ranged from 1 L/min to 5.5 L/min, resulting in significantly altered flow dynamics and power losses compared to the time-averaged conditions. Similar factors were present in many of the other cases with large differences between pulsatile and steady results, as noted by de Zélicourt[124].

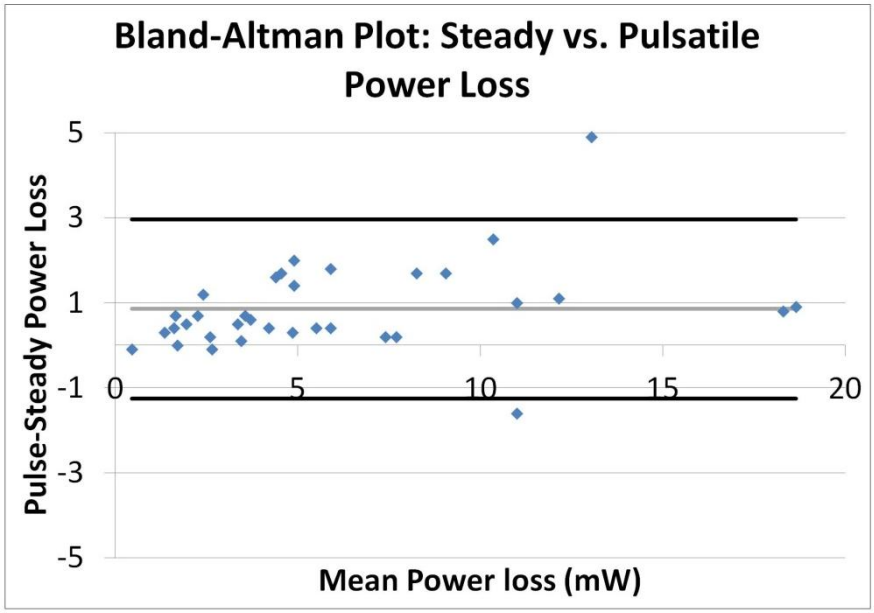


**Figure 5.10 Bland-Altman plot of power losses derived from pulsatile and steady boundary condition simulations. A positive bias is apparent (gray horizontal bar; pulsatile higher than steady), with 2 data points falling outside two standard deviations from the mean (black horizontal bars).**

From these data, the steady flow assumption appears to consistently undershoot pulsatile power loss values by 15-20%. Here, two points are worth noting. Firstly, this difference cannot be viewed as difference from truth as the pulsatile flow models were still limited by significant assumptions, particularly the use of rigid vessel walls. Second, without a fundamental understanding of the clinically significant thresholds of TCPC power loss, it is difficult to know the significance of these error margins and thus draw any decisive conclusions regarding the significance of the steady vs. pulsatile flow assumption.

#### 5.3.2.2 HFD

Table 5.5 summarizes the HFD findings from the steady and pulsatile flow simulations. The means of the two sets of simulations are nearly the same (43 vs. 44, steady vs. pulsatile, respectively) and there was no statistical difference between them (p=0.35 by Wilcoxon signed rank test); however, the average absolute deviation for a given patient was 5. In other words, a steady HFD to the LPA of 43% was, on average, 5 percentage points higher or lower under pulsatile conditions.

**Table 5.5 Summary of steady vs pulsatile flow HFD**

| | Steady HFD (%LPA) | Pulsatile HFD (%LPA) | Absolute difference |
|---|---|---|---|
| **Mean** | 43 | 44 | 5 |
| **Standard Deviation** | 18 | 17 | 4 |
| **Median** | 43 | 45 | 4 |

See Table 12.8 in Appendix B.

Figure 5.11 shows the Bland-Altman difference plot for these data. Unlike the power loss plots, the HFD differences are tightly grouped around zero with a mean bias of 1.1. All but two points fall within the two standard deviation bounds, and in fact they are all within a difference of 10.

Notably, the two outlier points (CHOP080A, CHOP091A) are cases of bilateral SVCs with a right-sided Fontan connection in which the steady flow conditions under-predicted the IVC perfusion of the left lung, while the pulsatile flow conditions yielded much more balanced IVC distributions. These findings suggest that dynamic vessel flow rates for these cases played an important role. Figure 5.12 shows the imposed pulsatile flow curves over one cardiac cycle for those two cases. The superposed vertical lines are provided to help relate the timing of the peak IVC flow rate to the concurrent changes in PA flows. For CHOP080A (Figure 5.12A), an increase and peak of IVC flow rate is closely synced with the increase and peak of the LPA flow rate. It is also noted that the amplitude of LPA pulsatility is much greater than that of the LSVC. These two observations imply that the IVC flow is primarily responsive to changes in LPA flow dynamics since the LSVC is comparatively static and the RSVC is more dynamically synced to RPA flow. This results in a more balanced IVC distribution than is obtained from the steady flow simulations, which (as seen in Figure 5.13) instead produced greater mixing of IVC and RSVC flows and thus a greater contribution of RSVC flow (shown in red) to the LPA. For CHOP091A (Figure 5.12B), the peak of the highly pulsatile IVC flow nearly coincides with the peaks of both LPA and RPA flows, while both superior caval flow curves are nearly flat over the entire cycle. Hence, the IVC flow is dynamically responsive to changes in flows to both PAs, and is thus more balanced than predicted by the steady flow simulation.

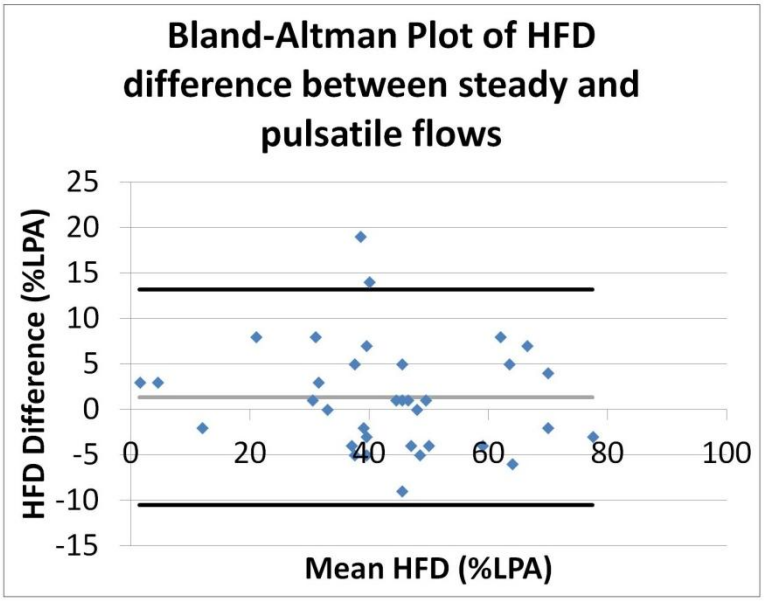


**Figure 5.11 Bland-Altman plot of flow distributions derived from pulsatile and steady boundary condition simulations. There was a slight positive bias in the measurement differences, with 2 data points falling outside two standard deviations from the mean (black horizontal bars). The remaining data points were all within 10%.**

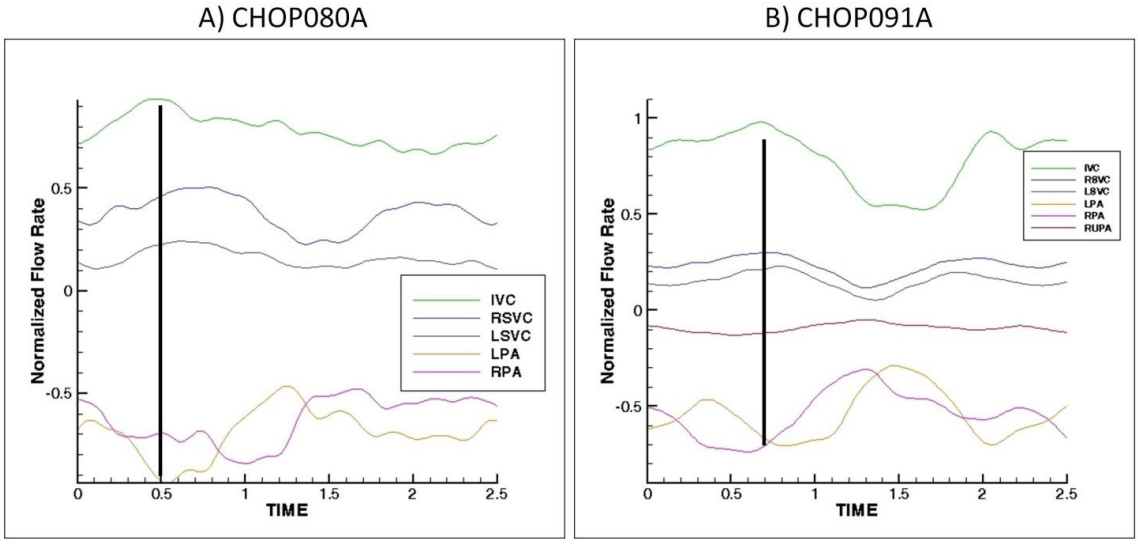


**Figure 5.12 Imposed pulsatile flow curves by vessel of one cardiac cycle for A) CHOP080A and B) CHOP091A. The vertical lines are provided as a visual correspondence between the pulmonary flows and the peak of the IVC flow rate.**

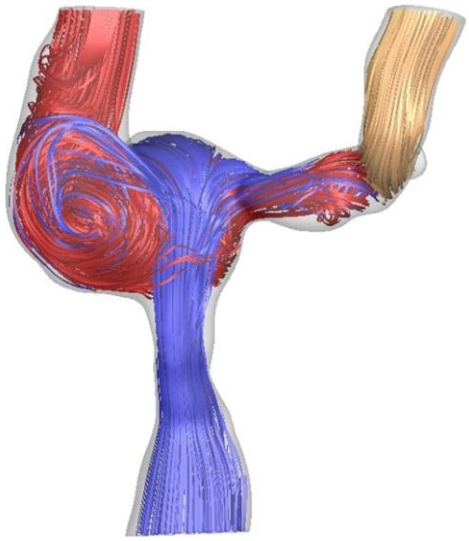

**Figure 5.13 Time-averaged velocity streamlines color coded by vessel of origin (blue- IVC, red- RSVC, yellow- LSVC) for CHOP080A. Mixing of IVC and RSVC flows within the large hemi-Fontan connection promotes distribution of RSVC flow to the LPA, which is apparently reduced with the use of the measured pulsatile flows in favor of a higher IVC-to-LPA percentage.**

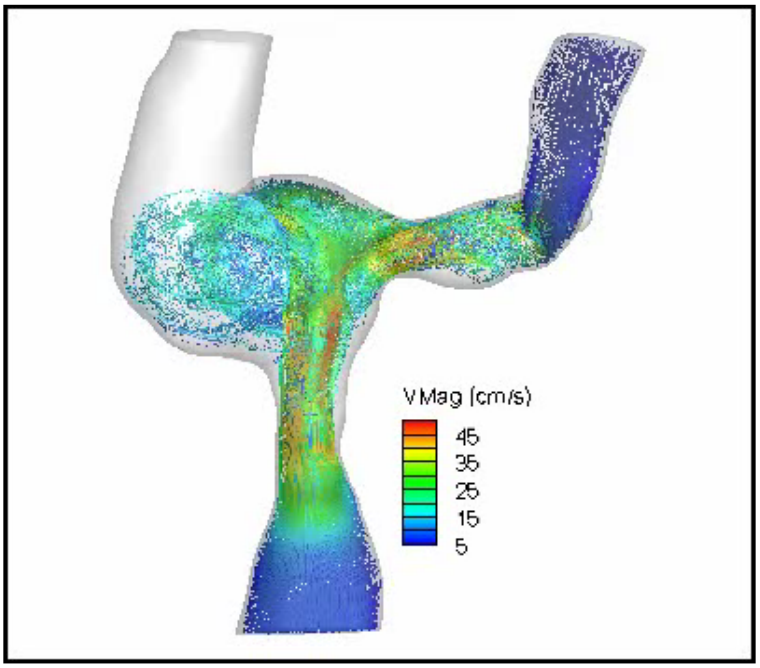


**Animation 5.1 Particle tracking for pulsatile simulation of CHOP080A.**

Returning to the more important question at hand, Figure 5.11 suggests that the steady flow assumption has little impact on hepatic flow distribution results. Clinically speaking, there is very little (if any) difference between an HFD value of 60 vs. 50 or even 40 vs. 30. Thus, considering the average values achieved and the average differences observed, the same information will be achieved using either set of flow conditions in TCPC simulations. That said, in more complex anatomic (such as the bilateral SVC outliers described) and physiologic (e.g., highly pulsatile or asynchronous flow curves) cases, it may be advisable to specifically select pulsatile flow boundary conditions.

#### 5.3.2.3 Section Summary

Directly comparing the quantitative outcomes of pulsatile and steady flow simulations in a 35 patient subset provided insights into the potential impact of the use of time-averaged boundary conditions for the cohort analysis. The impact with respect to IVC/hepatic flow distribution is clinically negligible as the average difference was close to 0 and in absolute terms was ±5 percentage points, generally no more than 10. For power loss, the impact is more difficult to gauge as a) there was a definite, but consistent bias toward higher power loss values under pulsatile flow conditions (17% on average); b) the effect of assuming rigid walls on the energetic of pulsatile flows is unknown; and c) the clinically relevant power loss thresholds are unknown, so it cannot be determined if a 15-20% underestimation is meaningful or not. For the purposes of this study, these results do not suggest that the use of time-averaged flows is a bad assumption (again, pulsatile results do not represent truth in this case), so they will be retained in the cohort analysis and the merits of the assumption can be revisited at the end of this chapter.

## 5.4 Cohort Results

Much of the credit for the data presented in this section belongs to Dr. Diane de Zélicourt for implementing and validating the numerical scheme used, Maria Restrepo and Elaine Tang for considerable assistance in performing and analyzing the simulations, and countless other past students who contributed to the anatomic and velocity CMR segmentations.

### 5.4.1 Flow Summary

Flow data derived from the PC MRI acquisitions are summarized in Table 5.6. All values were indexed to BSA. The full case-by-case results are provided in Appendix A, where it can be seen that not all vessel measurements were available for all patients. The collateral flow was calculated as the difference between cardiac output and $Q_s$, while fenestration flow was estimated based on the difference between $Q_s$ and pulmonary arterial flows. On average, fenestration flow was less than 10% of $Q_s$. This low value is significant given that fenestration flow was systematically neglected in the computational simulations. It therefore appears this limiting assumption was acceptable.

These numbers are in very close agreement with those reported by Whitehead *et al* although that was somewhat expected given the considerable overlap in the patients included in both works[142]. From that study, we learned that the IVC blood flow fraction in Fontan patients is a function of age and BSA; that the LPA fractional flow is 45% on average (consistent with the present data), and that this overall pulmonary flow distribution was not significantly affected by the type of SVC anastomosis type.

**Table 5.6 Average flow data [L/min/m$^2$] by vessel from PC MRI**

| Vessel | Flow rate [L/min/m$^2$) |
|---|---|
| **IVC** | 1.72 ± 0.55 |
| **SVC** | 1.00 ± 0.53 |
| **LSVC*** | 0.64 ± 0.35 |
| **Azygos Vein*** | 0.92 ± 0.37 |
| **$Q_s$** | 2.89 ± 0.81 |
| **LPA** | 1.21 ± 0.63 |
| **RPA** | 1.38 ± 0.50 |
| **Collateral** | 0.60 ± 0.78 |
| **Fenestration** | 0.30 ± 0.54 |

*Vessels not present in all patients; Data reported as mean ± st. dev; see Table 12.2 in Appendix A

### 5.4.2 Population Averages and Correlations

Hemodynamic findings from the CFD analysis are presented in Table 5.7. The mean HFD value was 44% (to the LPA) in close agreement with the average pulmonary flow distribution (45% LPA), and the two variables were significantly correlated (r= 0.36, p<0.001; Figure 5.14A). With respect to maximum pressure drop, the mean value was 1.5 mmHg (~10% of normal central venous pressures), with an inner quartile range of 0.5-1.9 mmHg. TCPC resistance (R) was 0.23 WU on average (~15-20% of normal pulmonary vascular resistance[55]) and TCPC-EDI was equal to 0.037 on average.

Pearson correlations revealed significant relationships between BSA and R (r=0.28, p<0.05), BSA and TCPC-EDI (r=0.37, p<0.05; Figure 5.14B), and age with TCPC-EDI (0.26, p<0.05). Additionally, because the power loss normalizing scheme used to

compute TCPC-EDI includes normalization by the cardiac output, scaling in $Q^3$, there is potential for a false positive correlation to develop between Q and $Q^{-3}$. After correcting for this confounder with partial correlation, the natural logarithm of TCPC-EDI was still significantly correlated with both $Q_s$ (r= -0.31, p=0.001; Figure 5.14C) and CI (r= -0.21, p=0.04; Figure 5.14D). Interestingly, there was also a negative correlation between age and CI (r=-0.37; p<0.05), which may have been a confounding factor in the TCPC-EDI vs. CI correlation: using partial correlation to correct for age effects weakened their relationship (r=-0.18, p=0.087). However, the TCPC-EDI vs. $Q_S$ partial correlation was still statistically significant (r=-0.23, p=0.023).

**Table 5.7 Cohort Hemodynamic Results**

| | **Cardiac Index** ($L/min/m^2$) | **Systemic Venous Flow** ($L/min/m^2$) | **Pulmonary Flow Dist. (GFD)** (%LPA) | **Hepatic Flow Dist.** (%LPA) | **$\Delta P_{MAX}$** (mmHg) | **R** (WU) | **TCPC-EDI** |
|---|---|---|---|---|---|---|---|
| **Mean** | 3.47 | 2.89 | 45 | 44 | 1.5 | 0.23 | 0.037 |
| **Standard Deviation** | 1.11 | 0.81 | 12 | 21 | 1.3 | 0.17 | 0.028 |
| **Median** | 3.43 | 2.85 | 43 | 44 | 1.1 | 0.19 | 0.031 |
| **25th Percentile** | 2.86 | 2.33 | 37 | 31 | 0.5 | 0.10 | 0.016 |
| **75th Percentile** | 3.85 | 3.36 | 52 | 57 | 1.9 | 0.28 | 0.047 |

HFD- Hepatic Flow Distribution; $\Delta P_{MAX}$- maximum pressure drop; R- TCPC Resistance; TCPC-EDI- Energy Dissipation Index; see Table 12.3 in Appendix A.

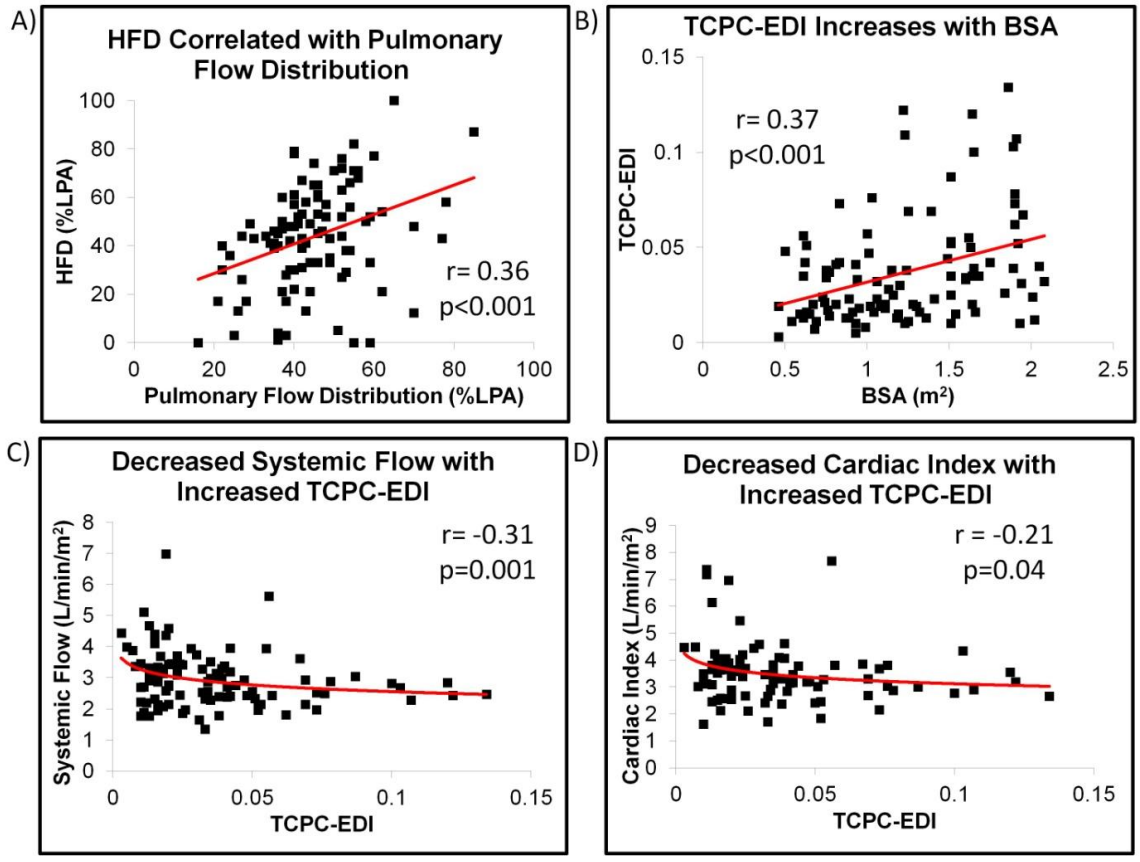


**Figure 5.14** ***Correlative relationships in cohort data between A) HFD and global pulmonary flow split, B) indexed power loss (TCPC-EDI) and BSA, C) TCPC-EDI and systemic venous flow (logarithmic), D) TCPC-EDI and cardiac index (logarithmic).***

### 5.4.3 Single vs. Bilateral SVC Connections (Table 5.8)

The presence of bilateral superior vena cava connections to the PAs (N=15) significantly increased the percentage of pulmonary flow to the LPA compared to single SVC connections (52% vs. 43%; p=0.02), but HFD to the LPA was comparatively decreased (34% vs. 45%; p=0.03). These observations can be simply explained by assuming that the composition of the LPA flow is: all of the left SVC flow and some combination of IVC and right SVC flows. Hence, the relative contribution of the superior venous flows to the

LPA is increased compared to single SVC cases in which some combination of SVC and IVC flows perfuse both lungs. It is noted that there was still a correlation of the pulmonary flow distribution with HFD in the bilateral patients ($\rho$=0.59; p=0.02), with a very similar coefficient, but with a shifted regression line compared to single SVC cases (Figure 5.15).

There were no differences with respect to connection efficiency between the two groups.

**Table 5.8 Comparison of Single and Bilateral SVC-PA Connections**

| | **Single SVC** (N=85) | **Bilateral SVCs** (N=15) | **p-value** |
|---|---|---|---|
| **Age** (years) | 12.3 ± 6.7 | 10.1 ± 6.9 | 0.19 |
| **BSA** ($m^2$) | 1.24 ± 0.44 | 1.14 ± 0.54 | 0.35 |
| **Cardiac Index** ($L/min/m^2$) | 3.49 ± 1.19 | 3.39 ± 0.59 | 0.81 |
| **GFD** (%LPA) | 43 ± 9 | 52 ± 15* | 0.02 |
| **HFD** (%LPA) | 45 ± 20* | 34 ± 26 | 0.03 |
| **$\Delta P_{MAX}$** (mmHg) | 1.5 ± 1.3 | 1.4 ± 0.6 | 0.57 |
| **R** (WU) | 0.23 ± 0.18 | 0.24 ± 0.10 | 0.21 |
| **TCPC-EDI** | 0.036 ± 0.029 | 0.038 ± 0.022 | 0.30 |

*Value significantly higher than other group; Data reported as mean ± st. dev.; See Table 12.4 in Appendix A

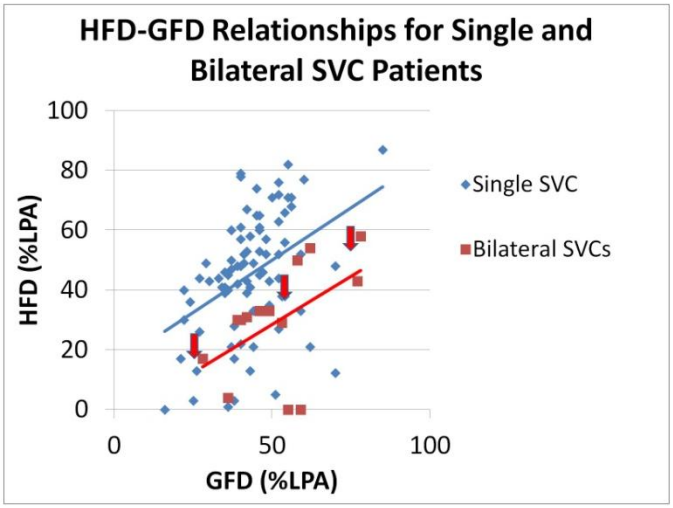


**Figure 5.15** ***Correlations between HFD and global pulmonary flow distribution (GFD) for single SVC TCPCs (blue) and bilateral SVC TCPCs (red). The slopes of the linear correlations are similar, but the bilateral line is shifted lower (toward more RPA flow).***

5.4.4 Intra-atrial (IA) vs. Extracardiac (EC) Connections (Table 5.9)

When comparing IA vs. EC (neglecting APC), IA patients were significantly older and had larger BSA, while there was a strong trend ($p=0.07$) toward higher CI in EC patients. Based on the negative relationship between age and CI noted in §5.4.2, these characteristics are likely coupled. There were no statistical differences in R or TCPC-EDI between groups ($p=0.48$ and 0.24, respectively); however, the flow distribution trends did show connection dependencies. The pulmonary flow distribution to the LPA was significantly higher in EC patients than IA, but there was a trend toward lower HFD to the LPA for EC ($p=0.08$). Finally, a breakdown of the pulmonary flow/HFD correlation noted in §5.4.2 revealed similar significant correlations for both connections ($p<0.05$), although the correlation was stronger for IA ($r=0.54$) than EC ($r=0.44$).

**Table 5.9 Comparison of Intra-atrial and Extracardiac Connections**

| | **IA** (N=64) | **EC** (N=33) | **p-value** |
|---|---|---|---|
| **Age** (years) | 13.5 ± 6.5* | 7.9 ± 4.8 | <0.001 |
| **BSA** ($m^2$) | 1.33 ± 0.43* | 0.96 ± 0.37 | <0.001 |
| **Cardiac Index** ($L/min/m^2$) | 3.30 ± 0.87 | 3.90 ± 1.41 | 0.07 |
| **Systemic Flow** ($L/min/m^2$) | 2.89 ± 0.89 | 3.10 ± 0.91 | 0.33 |
| **GFD** (%LPA) | 41 ± 9 | 51 ± 15* | 0.001 |
| **HFD** (%LPA) | 46 ± 18 | 37 ± 26 | 0.08 |
| $\mathbf{\Delta P_{MAX}}$ (mmHg) | 1.5 ± 1.1 | 1.4 ± 1.6 | 0.52 |
| **R** (WU) | 0.25 ± 0.19 | 0.20 ± 0.12 | 0.48 |
| **TCPC-EDI** | 0.040 ± 0.031 | 0.030 ± 0.017 | 0.24 |

*Value significantly higher than other group; Data reported as mean ± st. dev; See Table 12.5 in Appendix A.

### 5.4.5 Single Left vs. Right Ventricles

This section compares the TCPC hemodynamics between patients on the basis of the morphology of the single ventricle, excluding patients with mixed ventricular morphologies (N=17; e.g., complex heterotaxy syndrome or double outlet right ventricle). All physiological and hemodynamic comparisons are summarized in Table 5.10. There was no difference in cardiac index between the two groups, but there was a trend toward higher pulmonary flow percentage to the LPA for single LVs (p=0.10). The maximum TCPC pressure drop was significantly higher in single RV patients (1.7 vs. 1.1 mmHg; p=0.01) and there were also strong trends for higher R (p=0.10) and TCPC-EDI (p=0.07) in single RVs. These energetic differences are likely related to a significantly smaller (p=0.015) minimum PA diameter for single RVs than single LVs.

Dasi *et al* recently reported that the size of the reconstructed aorta, which is more frequently required for single RVs than LVs, is related to diminished LPA diameter[143]. Other studies have demonstrated the importance of minimum PA diameter in determining the TCPC energy dissipation[29]. It was therefore hypothesized that the vessel size and power loss differences noted in Table 5.10 might be mediated by the aorta. The patients (N=83) were sub-divided based on the presence or absence of aortic reconstruction; however, the patients without aortic reconstruction were significantly older than the patients with aortic reconstruction, which would confound the analysis since TCPC-EDI varies with age. To instead obtain two groups with comparable ages, a subset of patients (N=65) was selected consisting of RV patients with aortic reconstruction and LV patients without it. Results are shown in Table 5.11. The difference in total LPA flow became significant (p=0.025) and $\Delta P_{max}$ was significantly higher for the group with RV and aortic reconstruction; however, R and TCPC-EDI were statistically no different between these groups (p=0.42 and 0.28, respectively).

Considering the non-difference in normalized power losses, it is interesting that the minimum PA sizes were significantly different between these groups (p=0.04). However, the mean values (of the minimum diameters) for both groups were higher than the corresponding measures in Table 5.10 (i.e., LV < LV without aortic reconstruction). Given that power loss increases non-linearly with decreasing minimum PA size[140], it appears that this incremental diameter increase, particularly for the RV group, mediated enough of a decrease in TCPC-EDI to be statistically no different than the LV group.

These findings indicate that the differences in TCPC power losses between single LVs and RVs, noted in Table 5.10, were not caused by the reconstructed aorta compressing the LPA primarily in single RVs. If that were the case, than the RV with aortic reconstruction would have had significantly higher TCPC-EDI compared to the LV without reconstruction, and possibly a lower minimum PA diameter compared to entire RV group (assuming that RVs without reconstruction would have had generally larger diameters). Instead, it is possible that the fundamental differences between the morphologies with regard to pulmonary flow source and characteristics leading up to bidirectional cavopulmonary anastomosis (e.g., Norwood, PA banding, no palliation) may mediate different PA growth patterns, which manifest in long-term differences in TCPC power loss. Future work should investigate these potential effects.

**Table 5.10 Comparison of single left ventricles (LV) and single right ventricles (RV)**

| | **LV** (N=38) | **RV** (N=45) | **p-value** |
|---|---|---|---|
| **Age** (years) | 12.3 ± 7.6 | 11.9 ± 5.8 | 0.95 |
| **BSA** ($m^2$) | 1.22 ± 0.44 | 1.24 ± 0.45 | 0.88 |
| **Cardiac Index** ($L/min/m^2$) | 3.56 ± 1.02 | 3.30 ± 0.96 | 0.52 |
| **Systemic Flow** ($L/min/m^2$) | 2.95 ± 0.71 | 2.91 ± 0.99 | 0.53 |
| **GFD** (%LPA) | 45 ± 13 | 41 ± 10 | 0.1 |
| **HFD** (%LPA) | 45 ± 24 | 41 ± 19 | 0.47 |
| **$\Delta P_{MAX}$** (mmHg) | 1.1 ± 0.8 | 1.7 ± 1.2 | 0.01* |
| **R** (WU) | 0.20 ± 0.16 | 0.24 ± 0.16 | 0.10 |
| **TCPC-EDI** | 0.032 ± 0.026 | 0.040 ± 0.029 | 0.07 |
| **Minimum PA diameter** ($mm/m^2$) | 7.6 ± 2.4 | 6.5 ± 2.9 | 0.015* |

*Statistically significant difference; Data reported as mean ± st. dev; See Table 12.6 in Appendix A.

**Table 5.11 Comparison of left ventricles (LV) without aortic reconstruction and single right ventricles (RV) with aortic reconstruction**

| | **LV without Aortic Reconstruction** (N=31) | **RV with Aortic Reconstruction** (N=34) | **p-value** |
|---|---|---|---|
| **Age** (years) | 12.8 ± 7.7 | 10.5 ± 4.9 | 0.19 |
| **BSA** ($m^2$) | 1.27 ± 0.43 | 1.16 ± 0.41 | 0.31 |
| **Cardiac Index** ($L/min/m^2$) | 3.42 ± 0.87 | 3.28 ± 0.80 | 0.82 |
| **Systemic Flow** ($L/min/m^2$) | 2.92 ± 0.74 | 2.82 ± 0.80 | 0.65 |
| **GFD** (%LPA) | 46 ± 13 | 40 ± 10 | 0.03* |
| **HFD** (%LPA) | 47 ± 25 | 40 ± 18 | 0.21 |
| $\mathbf{\Delta P_{MAX}}$ (mmHg) | 1.0 ± 0.8 | 1.7 ± 1.3 | 0.03* |
| **R** (WU) | 0.21 ± 0.17 | 0.21 ± 0.12 | 0.42 |
| **TCPC-EDI** | 0.033 ± 0.027 | 0.035 ± 0.020 | 0.28 |
| **Minimum PA diameter** ($mm/m^2$) | 8.1 ± 1.9 | 7.0 ± 2.3 | 0.04* |

*Statistically significant difference; Data reported as mean ± st. dev.; See Table 12.7 in Appendix A.

### 5.4.6 Discussion

#### 5.4.6.1 Physiologic significance of TCPC power loss

TCPC design is one of the factors amenable to interventional/surgical manipulation in the care of single ventricle patients. From these data, it is seen that this patient-to-patient variation led to a two order of magnitude range in indexed power losses, so elucidating its role in patient functional status and outcomes is of practical relevance. A popular model of ventricular filling (i.e., diastolic function) and cardiac output says that resistance elements downstream of vascular capacitance have a drastic effect on limiting the ability of the ventricle to fill and thus provide adequate output[42]; in Fontan physiology the TCPC and pulmonary vasculature are two such resistive elements. Elevated power loss resulting from sub-optimal connection geometry may therefore contribute to restricted preload reserve[39, 66] of the single ventricle, which may limit long-term performance.

The significant negative correlations of iPL with $Q_s$ and cardiac index do in fact suggest such a relevant effect of elevated TCPC losses. A similar linear correlation between TCPC resistance and cardiac index has previously been noted[55]. The mean values of R and iPL were 0.23 WU and 0.037, respectively. To put these measures into context, normal pulmonary vascular resistance ranges for Fontan patients have been reported between 1.3-1.8 Wood units[27, 55], and Dasi *et al*. found that the Cardiovascular Energy Dissipation Index for single ventricles (i.e., indexed ventricular output power) based on published data ranged between 2.7 (for ~4.5 year old patients) and 8.1 (for ~11 year old patients)[129]. Since the TCPC and pulmonary vasculature are in series, the present results indicate that the TCPC resistance adds, on average, 15-20% to the total pulmonary vascular resistance, and that contribution is non-negligible.

#### 5.4.6.2 Extracardiac vs. Intra-atrial Connections

Despite significantly higher total LPA flow (51% vs. 41%), extracardiac connections had a strong trend (p=0.08) toward lower HFD to the LPA (38% vs. 47%). A recent study[144] found that HFD correlated with the total pulmonary distribution in intra-atrial connections but not in EC, presumably because of the more intense mixing of the caval flows within IA connections. Conversely, HFD in extracardiac connections only correlated with caval offset[144]. These observations agree well with the present findings. While HFD did correlate with the total flow distribution for extracardiacs, this correlation was weaker than for IA connections. Also, the significant influence of caval offset was still apparent as over 60% of IVC flow perfused the RPA (the predominant direction of caval offsetting for such connections) despite a nearly balanced total distribution (51% LPA). Most critically, the flow distribution results for EC and IA connections, representing the majority of Fontan patients, do not suggest an inherent risk factor for unilateral hepatic distribution and PAVM in either case[58].

Arguably the more interesting comparison between these connections is with regard to the energetics. Since the decision of one connection or the other is almost entirely at the discretion of the surgeon, determining the superiority of one approach over the other has been the subject of debate for a number of years[82, 145-148]. In this series, there were no energetic differences between connections. This finding is encouraging in that the selection of one connection or another, for reasons of either surgical preference or patient need, does not inherently bias the connection power loss. However, it is important to recognize that techniques and geometric details vary among centers and/or surgeons; since this was a single center study, extrapolating this finding to all patients may not be straightforward.

#### 5.4.6.3 Cohort Summary

From this largest computational analysis of the Fontan connection to date, several clinically relevant insights were gained. First, power loss varies widely (two orders of magnitude) among Fontan patients and may vary with age and development. Second, there is a significant correlation between indexed TCPC power loss and systemic venous flow, which supports the hypothesis that TCPC hemodynamics can impact diastolic ventricular function. Third, no energetic differences were observed between intra-atrial and extracardiac Fontan connections.

## 5.5 Factors Influencing Power Loss

In the absence of a meaningful difference between IA and EC energetics, but a physiologically meaningful impact of power loss, the critical question then becomes: what are the factors that discriminate among patients to create high losses in some cases, and negligible losses in others? The following sections will attempt to provide insight into that critical question through multiple means. First, hemodynamics of selected patients from both ends of the TCPC-EDI scale will be evaluated in detail to elucidate trends that distinguish efficient connections from inefficient ones. Second, results of a detailed TCPC geometric characterization will be presented and correlated with the hemodynamics. This latter investigation therefore builds upon the ‘classical’ engineering approach to studying the TCPC by extending the search for geometric/hemodynamic relationships to a broad patient-specific scale.

### 5.5.1 Most and Least Dissipative Connections

A total of 12 patients were selected from the 100 patient cohort on the bases of TCPC-EDI and age. Specifically, the 7 patients with the highest power loss (all with TCPC-EDI

> 0.08; average age of 16.6 years) and 5 of the 10 patients with the lowest power loss (average age of 13.8) were retained for this analysis. Five patients from this latter group were discarded to make the two groups similarly sized and as close in age as possible given the correlations between age and both cardiac index and TCPC-EDI noted in §5.4.2. The demographics and hemodynamics of these 12 patients are summarized in Table 5.12.

The hemodynamics of each patient will be considered on an individual basis in the following sub-sections starting from the highest power loss and ending with the lowest. Several different plots will be presented for each case: 1) standard velocity streamlines encoded either by local velocity magnitude or vessel of origin; 2) vortex iso-surfaces based on the Q-criterion (the second invariant of the deformation matrix)[149]; and 3) the magnitude of viscous dissipation (i.e., $\mu\left|\nabla^2 V\right|$; where μ is the viscosity and V the velocity). It is noted that the contour scaling of the viscous dissipation plots was held constant throughout to facilitate direct visual comparisons.

**Table 5.12 Patient data and hemodynamic metrics for the least (7 top rows) and most efficient (5 bottom rows) TCPCs analysis**

| | Connection Type | Age yrs | BSA [$m^2$] | CI [$L/min/m^2$] | $Q_s$ [$L/min/m^2$] | $\Delta P_{max}$ [mmHg] | R [WU] | TCPC-EDI |
|---|---|---|---|---|---|---|---|---|
| **CHOP103A** | IA | 22 | 1.86 | 2.65 | 2.46 | 3.0 | 0.72 | 0.134 |
| **CHOP023A** | IA | 12 | 1.22 | 3.19 | 2.43 | 2.3 | 0.66 | 0.122 |
| **CHOP032A** | IA | 18 | 1.64 | 3.55 | 2.84 | 3.0 | 0.76 | 0.120 |
| **CHOP080A** | IA | 17 | 1.91 | 2.91 | 2.28 | 2.4 | 0.54 | 0.107 |
| **CHOP034A** | IA | 14 | 1.89 | 4.35 | 2.67 | 2.7 | 0.61 | 0.103 |
| **CHOP072A** | IA | 14 | 1.65 | 2.78 | 2.81 | 3.1 | 0.63 | 0.100 |
| **CHOP005B** | IA | 19 | 1.51 | 3.01 | 3.03 | 3.3 | 0.58 | 0.087 |
| **CHOP191A** | EC | 16 | 1.25 | 3.13 | 1.88 | 0.2 | 0.05 | 0.011 |
| **CHOP203A** | IA | 16 | 1.93 | 3.45 | 2.69 | 0.3 | 0.06 | 0.010 |
| **CHOP188A** | IA | 17 | 1.51 | 3.49 | 2.21 | 0.4 | 0.05 | 0.010 |
| **CHOP089A** | IA | 10 | 0.93 | 3.12 | 3.45 | 0.5 | 0.08 | 0.010 |
| **CHOP128A** | IA | 10 | 0.93 | 3.97 | 3.97 | 0.5 | 0.05 | 0.005 |

#### 5.5.1.1 Comparison of Cardiac-Index and Flow Magnitudes

Despite the orders of magnitude differences in connection energetics (pressure drop, resistance, and TCPC-EDI), it is first interesting to note that the cardiac indices (3.2 ± 0.6 vs. 3.4 ± 0.3) and indexed systemic flow magnitudes (2.6 ± 0.3 vs. 2.8 ± 0.9) were not statistically different between high and low power loss groups, respectively. This finding runs counter to the noted correlation in Figure 5.14, which would instead predict that the higher power loss group would have lower systemic and cardiac flow rates. Assuming that the general correlation is true, this non-difference is likely the result of other confounding factors (e.g., PVR or underlying cardiac defect) and underscores the complexity and multi-factorial nature of these patients' physiology.

#### 5.5.1.2 Detailed Presentation of the 7 Most Dissipative Connections

CHOP103A

The velocity and vorticity fields associated with the most dissipative TCPC encountered in this study, CHOP103A, are shown in Figure 5.16 and Figure 5.17, respectively. The Fontan pathway in CHOP103A (a lateral tunnel) has a significant narrowing, particularly approaching the distal end of the lateral tunnel and the PA junction, and significant anterior/posterior curvature. The LT narrowing leads to a significant convective acceleration, which is further exacerbated by the anterior/posterior curvature that confines the IVC flow along the anterior wall. As a result, the IVC flow accelerates from an average inlet velocity of 8-9 cm/s to over 50 cm/s at the PA anastomosis. The elevated velocities and confinement along the wall lead to important energy dissipation within the LT itself. At the connection site, the IVC flow impinges against the superior aspect of the anastomosis resulting in significant secondary flows, and the strength of these recirculations is enhanced by the high kinetic energy of the impinging IVC flow.

The vortex cores (Figure 5.17A) reveal that this recirculation extends across the entire length of the PA domain as a single coherent structure. As the area surrounding the core decreases, the viscous energy dissipated by this vortex increases (Figure 5.17B).

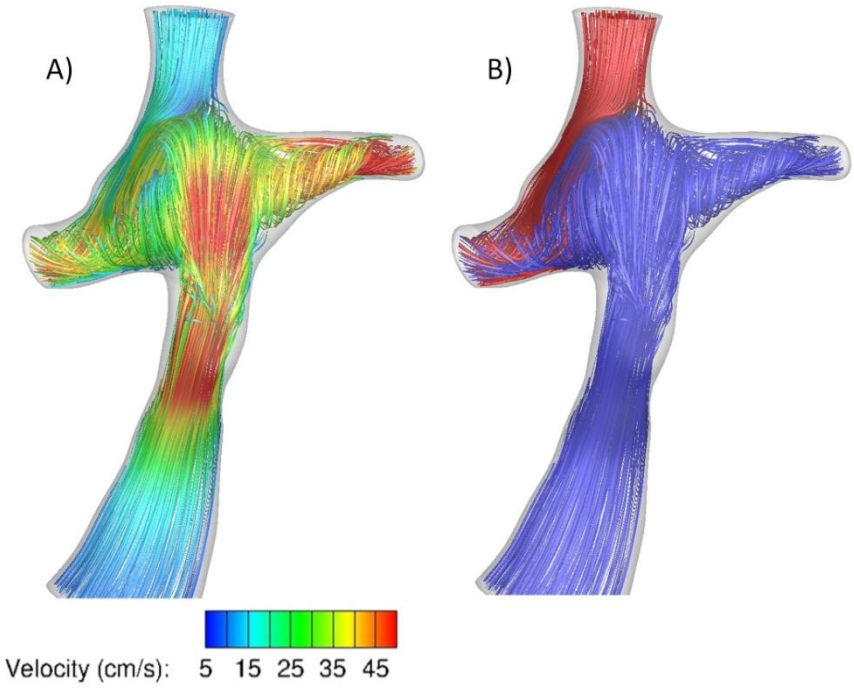


**Figure 5.16 Velocity streamlines for CHOP103A color coded by A) velocity magnitude and B) vessel of origin.**

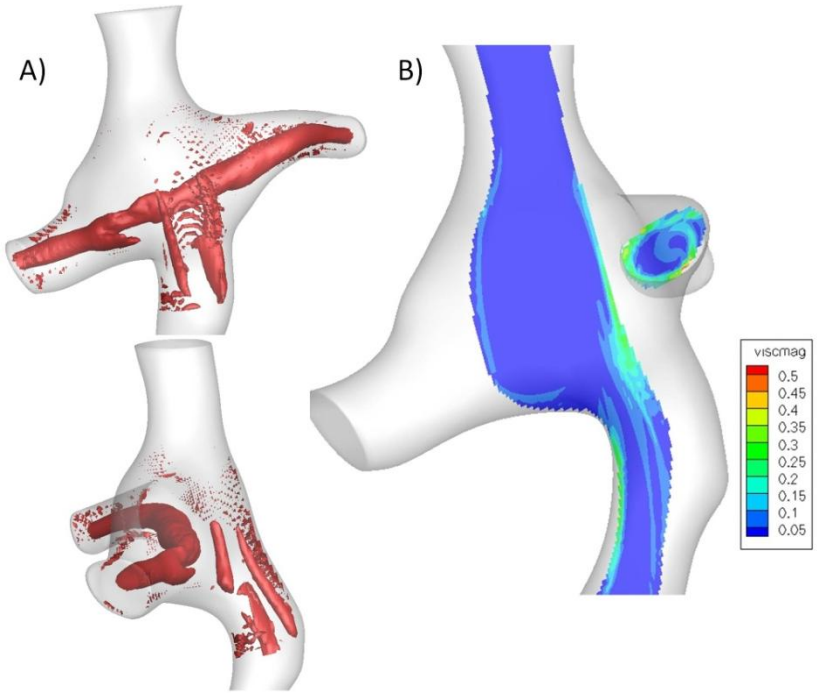


**Figure 5.17 A) Q-criterion vortex cores (Q=4000) and B) viscous dissipation contours for CHOP103A. Despite the expansive length of the vortex core in the PA, it only appears to contribute appreciably to viscous dissipation in the LPA.**

CHOP023A

This patient has an enlarged azygos vein (like CHOP_M1 as discussed in §5.3.1), but with no interruption of the IVC. Hence, the Fontan baffle (a lateral tunnel) still carries over 70% of the systemic venous return. The combination of apparent lateral tunnel stenosis, high Fontan flow rate, and enlarged hemi-Fontan connection result in a very high (~90 cm/s) IVC inlet velocity jet that is eccentrically oriented with respect the center of the connection (Figure 5.18). This jet induces extensive viscous dissipation within the lateral tunnel and at the entrance to the PAs (Figure 5.18C), then proceeds to impinge on the incoming SVC flow and create an extensive recirculation region within the

connection, leading to a very disturbed flow profile in the connection and PAs downstream. High viscous losses are also seen at the walls of the RPA, which is somewhat undersized while carrying 58% of the pulmonary flow.

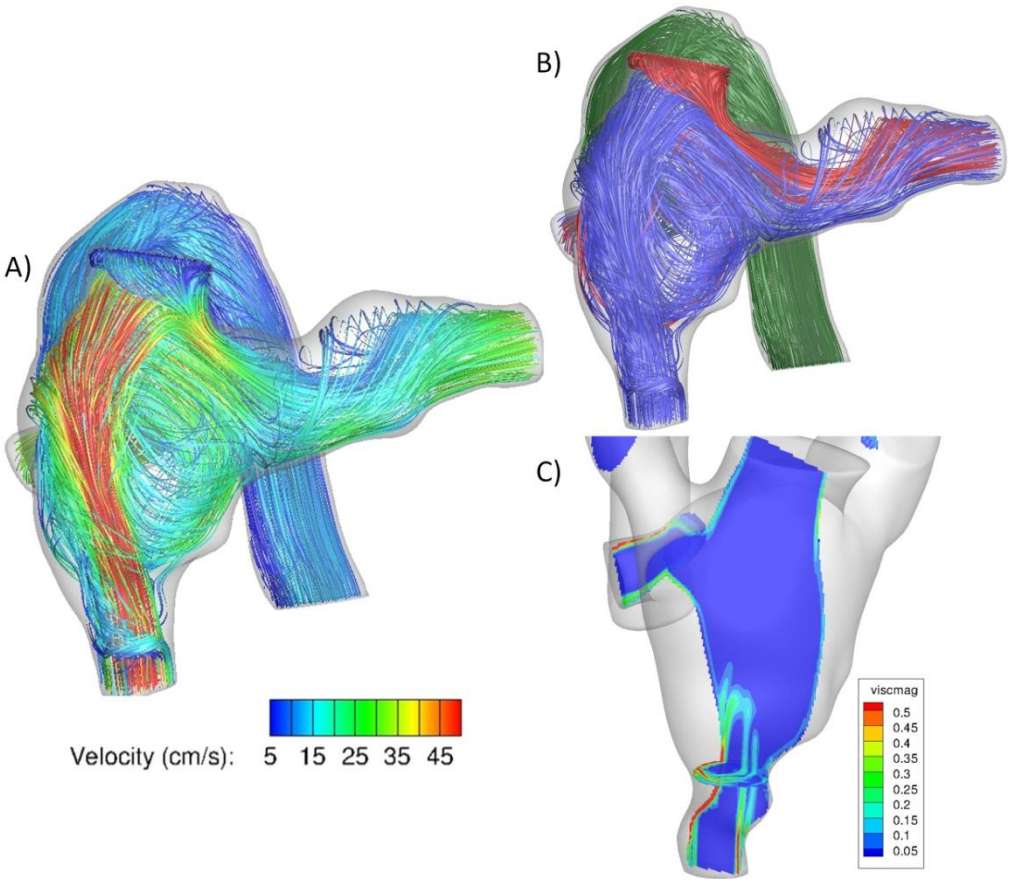


**Figure 5.18** ***Velocity streamlines for CHOP023A color coded by A) velocity magnitude and B) vessel of origin. C) Contours of viscous dissipation show the adverse effects of the high velocity IVC flow through the stenosed Fontan pathway.***

CHOP032A

In this case, the IVC undergoes a significant size reduction as it passes into the intra-atrial conduit, before again expanding within the hemi-Fontan connection. Thus, the IVC flow accelerates from ~10 cm/s to over 90 cm/s within the conduit (Figure 5.19). The Fontan connection was made posterior to the hemi-Fontan and thus the IVC flow impinges on the opposite superior PA wall (and partly into the SVC outlet) before inducing considerable secondary flow recirculation within the PAs. These recirculatory patterns are nicely demonstrated by the vortex cores (Figure 5.20A), which shows the posterior roll-up and extensive secondary recirculation into the LPA caused by the high velocity IVC jet. Viscous dissipation 'hot-spots' (Figure 5.20B) are evident along the lateral walls of the Fontan baffle, along the superior PA walls where the IVC jet impinges, and into the LPA from the complex secondary flow patterns present.

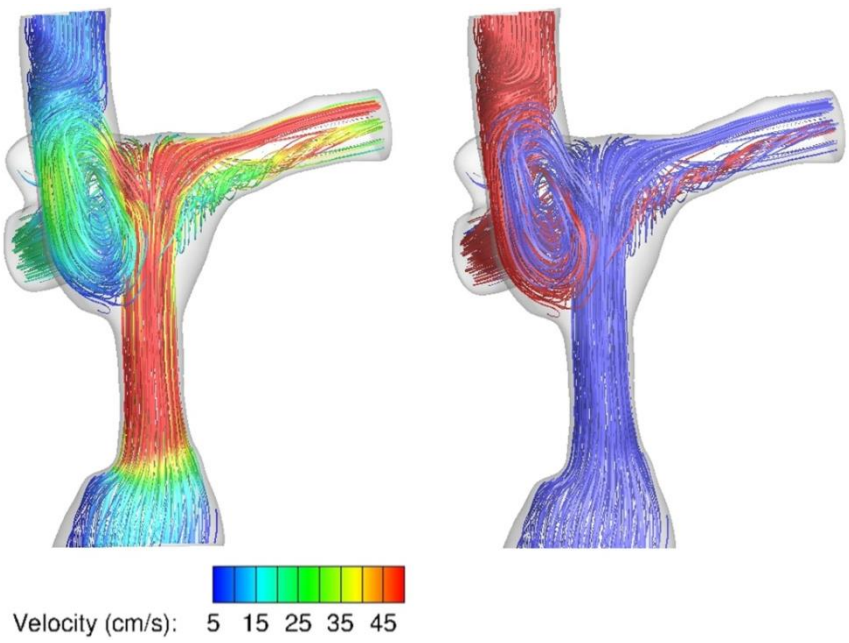


**Figure 5.19** ***Velocity streamlines for CHOP032A color coded by A) velocity magnitude and B) vessel of origin.***

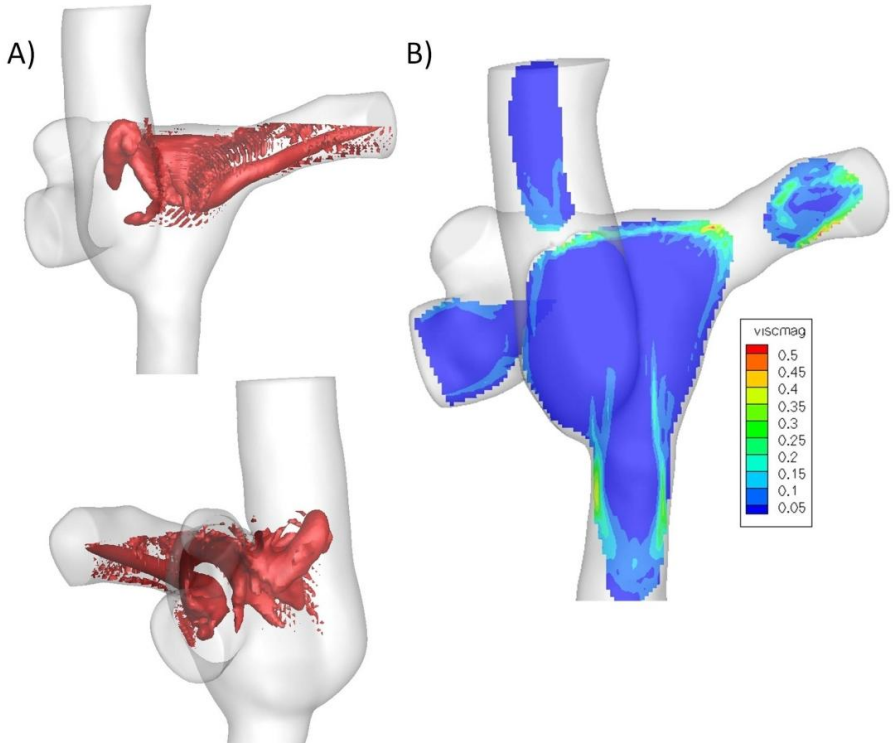


**Figure 5.20** ***B) Q-criterion vortex cores (Q=2000) and C) viscous dissipation contours for CHOP032A. IVC recirculation is largely contained on the left side of the connection, but numerous coherent cores and localized dissipation are visible.***

CHOP080A

In CHOP080A, another instance with an undersized intra-atrial Fontan conduit, many of the flow features resemble those of the previous case. IVC flow accelerates from an inlet average of 14 cm/s to over 60 cm/s before emptying into the large right-sided hemi-Fontan pouch; this case is complicated by the presence of bilateral SVC connections (Figure 5.21). A significant number of coherent vortex structures are visible (Figure 5.22A), particularly along the left lateral wall of the hemi-Fontan and through the mid-PA transition between the left and right SVC connections. The contribution of these structures to viscous dissipation within the connection is particularly evident in this case and shown by the overlay of the vortex cores on the viscous dissipation contours within the mid-PA section (Figure 5.22B).

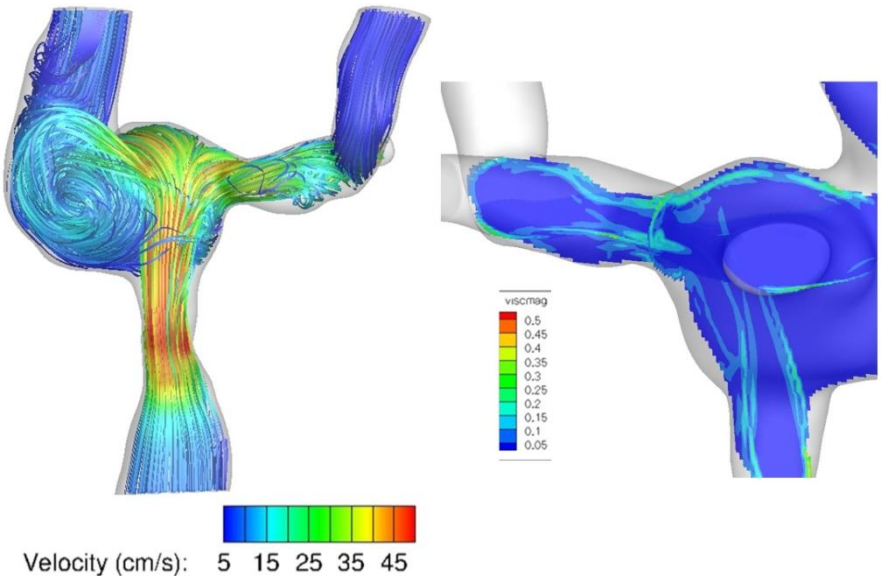


**Figure 5.21** ***CHOP080A: A) Velocity magnitude streamlines and B) viscous dissipation contours.***

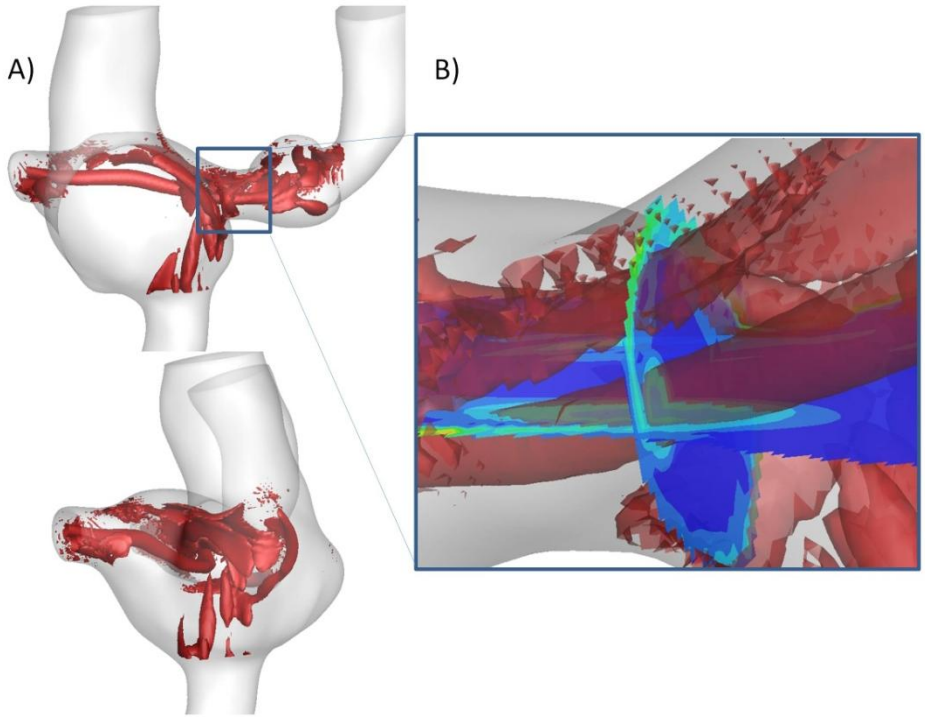


**Figure 5.22** ***CHOP080A: A) Q-criterion vortex cores (Q=2000) from anterior and right sagittal perspectives. B) Localization of vortex structures with high dissipation regions in the mid-PA segment.***

CHOP034A

This patient provides another example of a lateral tunnel connection with mild narrowing of the Fontan pathway, as evidenced by the local increase in velocity (Figure 5.23A) and viscous dissipation (Figure 5.23C) immediately proximal to the hemi-Fontan pouch. Impingement on the lower velocity SVC outlet flow and recirculation within the connection are again seen as in prior cases; however, it is the acceleration and mild flow separation through the mildly stenotic LPA that appears to yield the highest dissipation in the connection.

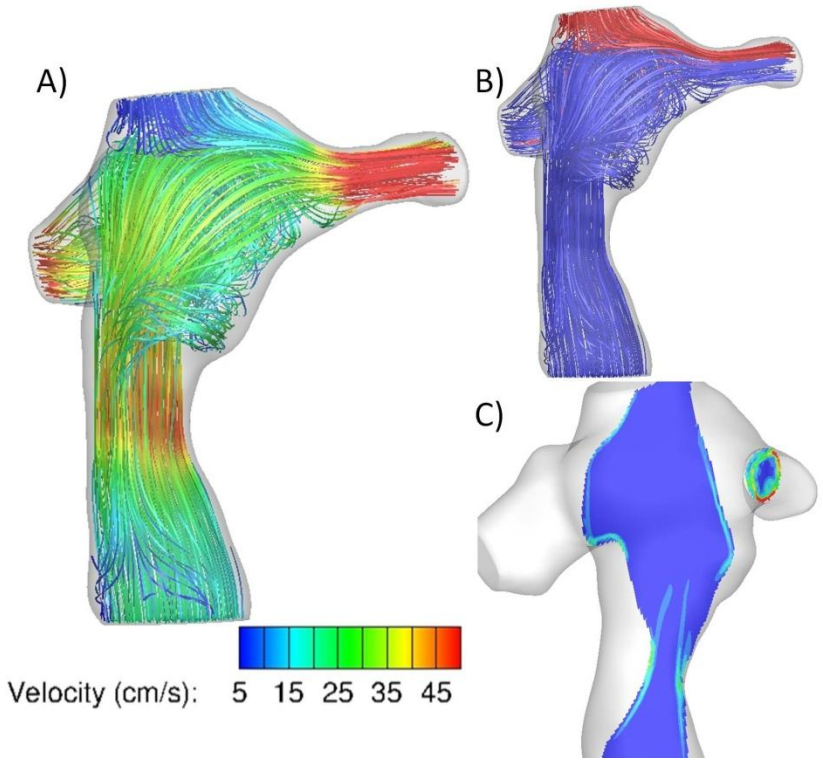


**Figure 5.23** ***Velocity streamlines for CHOP034A color coded by A) local magnitude and B) vessel of origin. C) Contours of viscous dissipation show 'hot spots' particularly concentrated in the LPA.***

CHOP072A

This lateral tunnel connection is characterized both by a moderate narrowing and right/anterior curvature, the combined effects of which create a high velocity, asymmetric jet that skews along the lateral/anterior wall before recirculating left/posteriorly within the connection (Figure 5.24A). The characteristic dissipation streaks can be observed along the lateral walls at the throat of the narrowing (Figure 5.24C). However, the more significant dissipation zones appear to again be located in the PAs, which are both small compared to the venae cavae, and thereby feature high velocities and dissipation via viscous friction along the arterial walls.

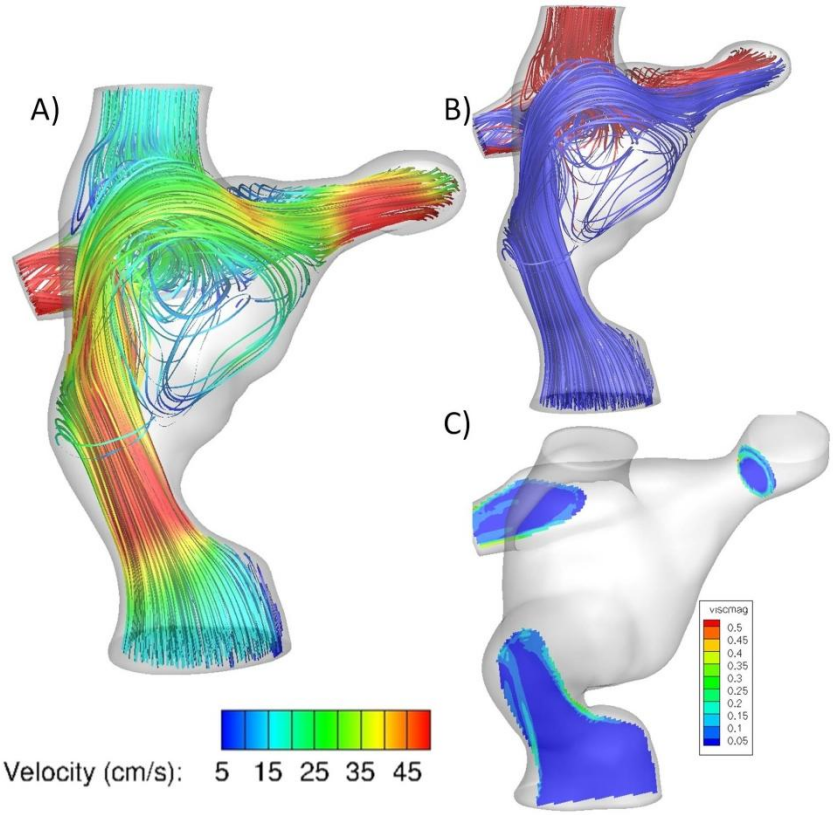


**Figure 5.24** ***Velocity streamlines for CHOP072A color coded by A) local magnitude and B) vessel of origin. C) Contours of viscous dissipation show 'hot spots' particularly concentrated in the PAs and within the stenosed lateral tunnel.***

CHOP005B

Unlike the previous six high power loss cases, there is no evidence of significant Fontan pathway narrowing in this patient. Instead, the losses appear to be largely, if not entirely related to flow through the LPA. In this vessel, the combination of narrowing and curvature lead to high velocities (maximum value of 107 cm/s), significant flow separation along the inferior distal wall of the LPA (Figure 5.25A), and extensive dissipation along the opposite superior distal wall (Figure 5.25C).

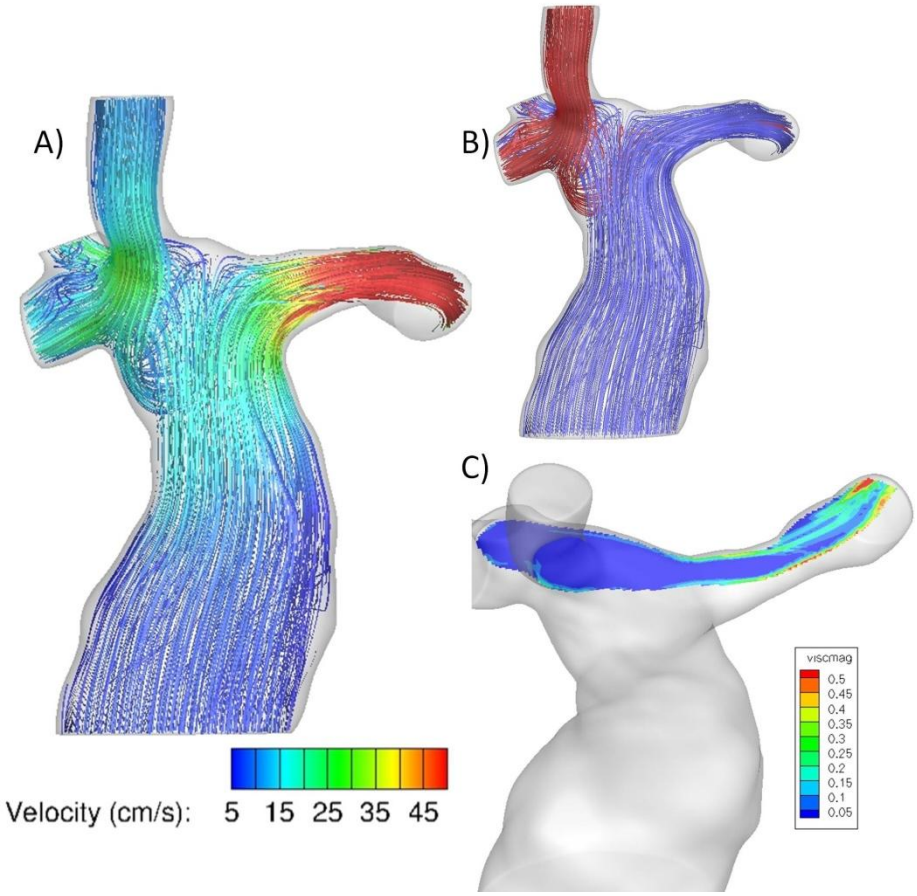


**Figure 5.25** ***Velocity streamlines for CHOP005B color coded by A) local magnitude and B) vessel of origin. C) Contours of viscous dissipation show extensive losses in the LPA related to the separations in the high velocity flow.***

5.5.1.3 Detailed Presentation of the Selected 5 Least Dissipative Connections

CHOP191A

This patient begins the series of lowest TCPC-EDI cases and represents the only extracardiac connection in either series (Figure 5.26). The most notable characteristic of this connection is its strong resemblance to the idealized caval offset glass models used in the early Fontan experimental investigations (Figure 3.15). Just as in those early

experiments, the use of a caval offset, here supplemented by a rightward angling of the SVC and a leftward flaring of the Fontan baffle, created a streamlined hemodynamic profile with little caval flow collision and a smooth cavopulmonary flow transition. Between these connection features and the generally large pulmonary arteries, very few focal points of viscous dissipation are apparent (Figure 5.26C).

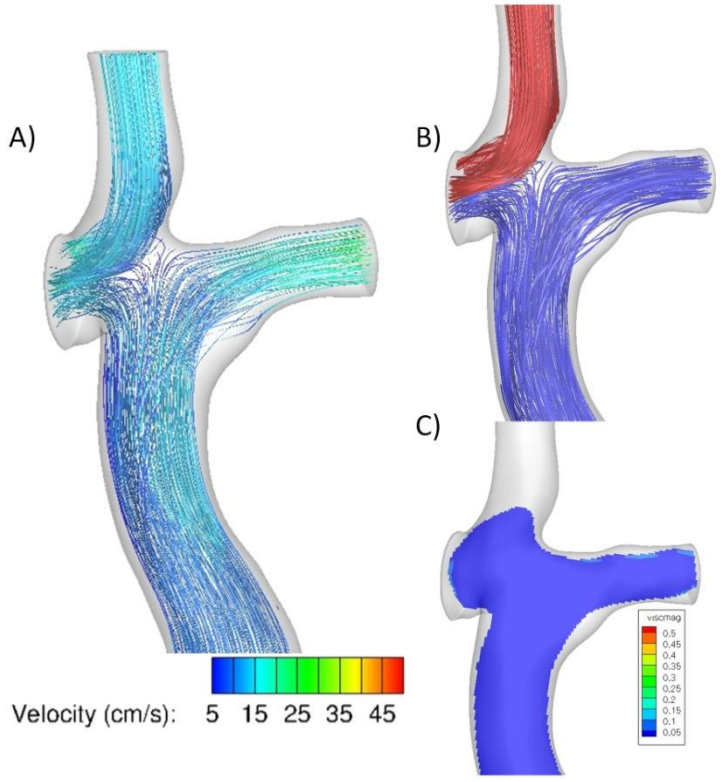


**Figure 5.26** ***Velocity streamlines for CHOP191A color coded by A) local magnitude and B) vessel of origin. C) Contours of viscous dissipation are lacking in any particular regions of interest.***

Remaining Cases

The remaining ‘most efficient’ cases are generally unremarkable in their geometric and hemodynamic features, which perhaps is what led to low power losses in each case. Thus, the results will be presented together and common features highlighted. The figure correspondences are as follows: CHOP203A in Figure 5.27, CHOP188A in Figure 5.28, CHOP089A in Figure 5.29, and CHOP128A in Figure 5.30.

Velocity magnitudes in these patients were in general lower and more uniform through the Fontan baffle than what was observed in the high loss group, although the total (non-normalized) systemic flows were also lower on average (3.6 vs. 4.4 L/min, respectively). While secondary flow patterns and coherent vortex structures were present in most cases, their associated energy dissipation was much lower in magnitude than the high loss cases (see Figure 5.28D). Although, in some instances coincidence of vortex cores with higher viscous dissipation zones suggests that further improvements in power loss may have been achievable with more streamlined flow. In Figure 5.29D, for example, the anterior offset of the IVC with respect to the PAs induced a vortex to form along the inferior/posterior PA wall that, at least in some regions, was highly dissipative. Redesigning the Fontan connection would have induced a different dynamic that may have reduced or removed these recirculations to maximize energy efficiency.

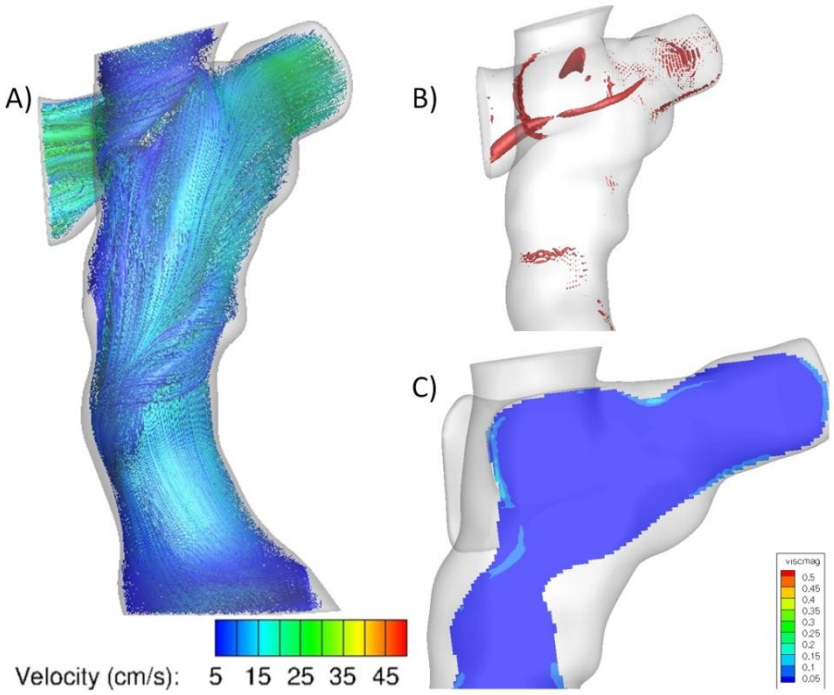


**Figure 5.27** ***Velocity streamlines for CHOP203A color coded by A) local magnitude and B) vessel of origin. C) Contours of viscous dissipation are lacking in any particular regions of interest.***

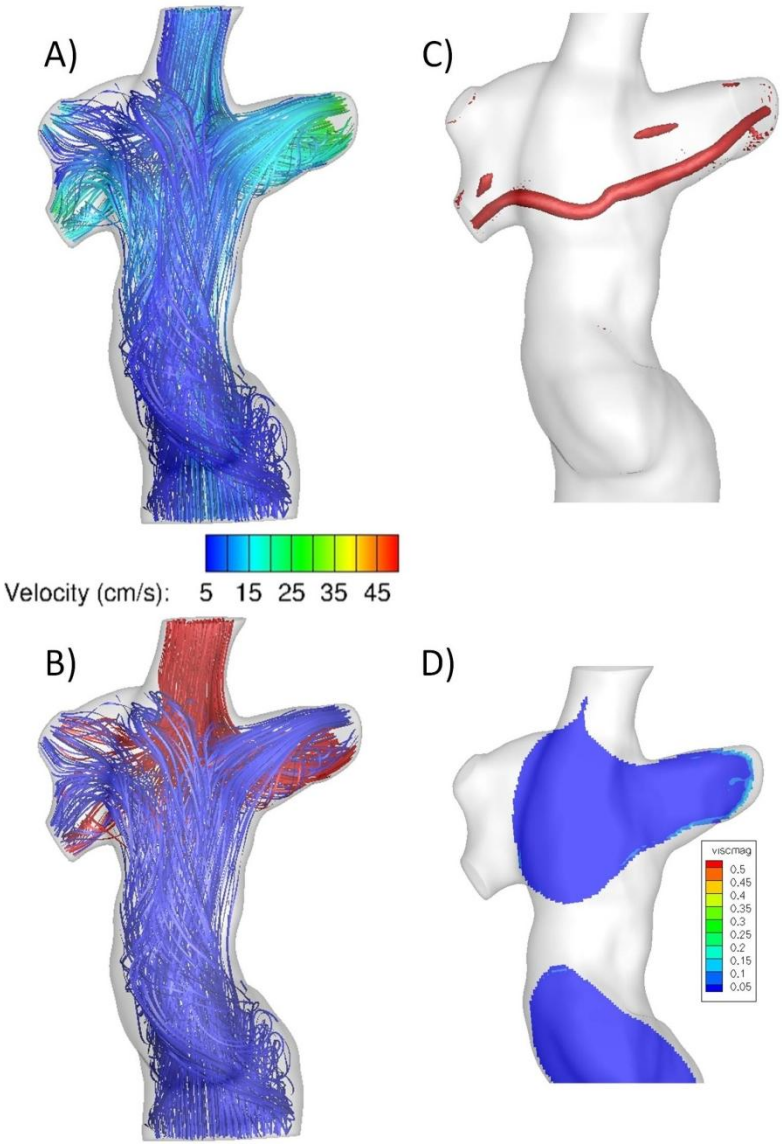


**Figure 5.28** ***Velocity streamlines for CHOP188A color coded by A) local magnitude and B) vessel of origin. C) Q-criterion vortex cores (Q=2000) and D) Contours of viscous dissipation are lacking in any particular regions of interest.***

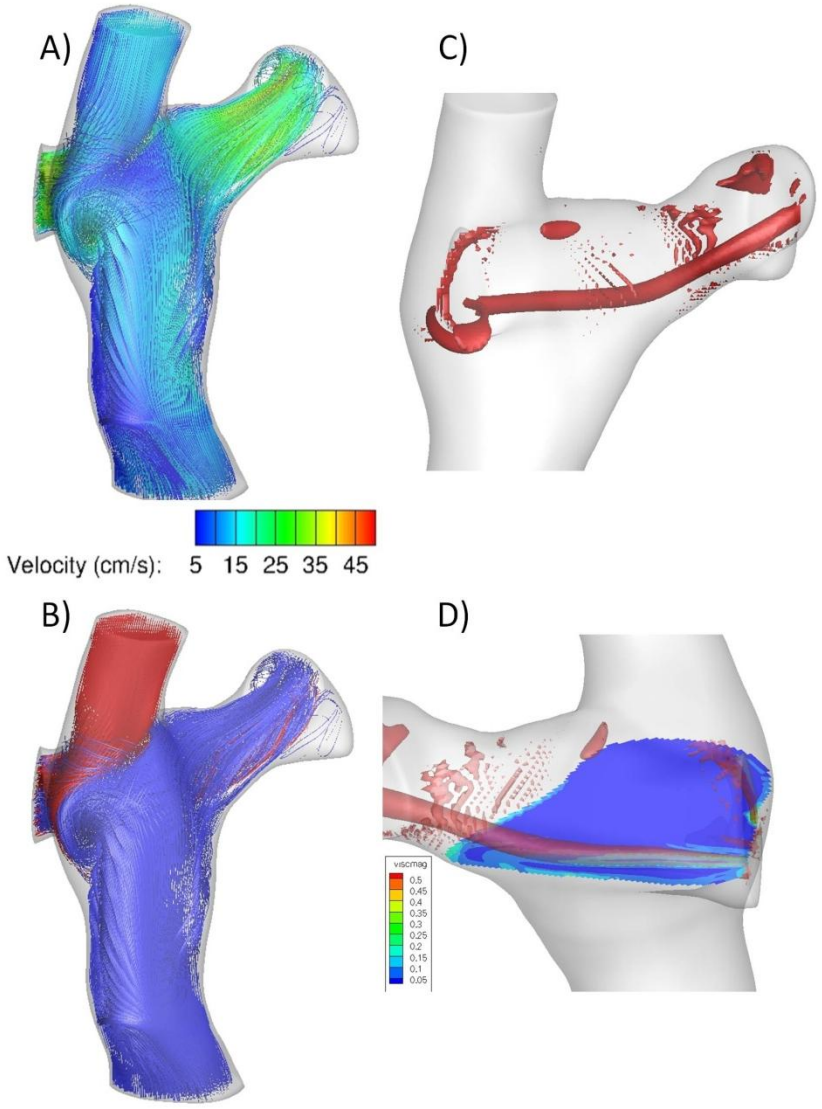


**Figure 5.29** ***Velocity streamlines for CHOP089A color coded by A) local magnitude and B) vessel of origin. C) Q-criterion vortex cores (Q=4000) and D) Contours of viscous dissipation overlaid on the vortex cores. Despite the low power loss associated with this connection, it appears that better streamlining (i.e., removal of complex secondary recirculation) may have led to further reductions.***

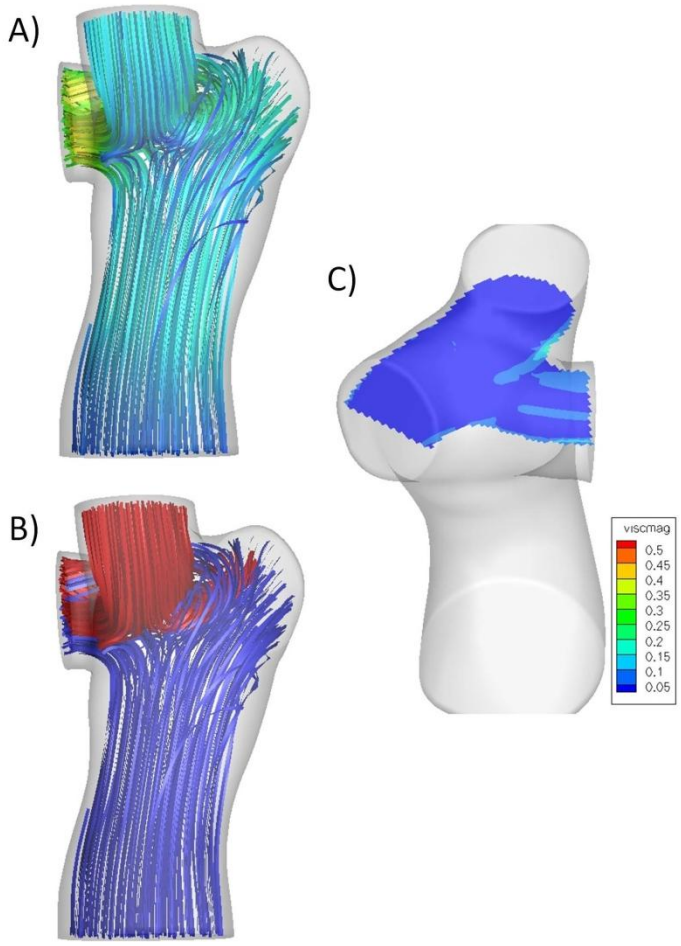


**Figure 5.30** ***Velocity streamlines for CHOP128A color coded by A) local magnitude and B) vessel of origin. C) Contours of viscous dissipation do show minor losses associated with secondary flow at the RPA outlet.***

### 5.5.2 TCPC Geometry and Hemodynamic Correlations

The 96 TCPCs of the 100 patient cohort (excluding 3 APC and 1 Y-Graft connection) were geometrically characterized using a centerline analysis with VMTK. There were two general measurements of interest: 1) vessel diameters and 2) relative connection orientations. These features and their relationships with TCPC hemodynamics, namely power loss and HFD, will be described in the following sections. Much of the credit for this work belongs to Elaine Tang for developing the VMTK protocol for TCPC analysis,

as well as Elaine and Maria Restrepo for performing the analysis on a large percentage of the TCPCs in the cohort.

#### 5.5.2.1 Vessel Diameters

For each vessel (IVC/Fontan baffle, SVC, LPA, RPA; neglecting the azygos, LSVC, and right upper lobe PA), there are four measurements of interest: mean, minimum, and maximum diameters (D), and stenosis index (SI; $1 - \frac{D_{min}}{D_{max}}$). An SI of 0 represents an ideal, uniform cylinder, a value of ~1 would indicate that $D_{min}$ is << $D_{max}$. The diameter values were all normalized by $BSA^{0.5}$.

Table 5.13, Table 5.14, Table 5.15, and Table 5.16 present the results for the IVC/Fontan, SVC, LPA, and RPA respectively. Notable trends include: IVC/Fontan pathway mean diameter was largest, followed by SVC, RPA, and LPA; LPA $D_{min}$ was significantly less than RPA $D_{min}$ (Mann-Whitney, $p<0.001$); and SI for LPA was significantly greater than all other vessels (ANOVA with Tukey post-hoc).

With respect to correlations with TCPC-EDI, all diameter dimensions (with the exception of the RPA $D_{max}$) were significantly correlated in the form of a Power Law relationship, similar to what Dasi *et al.* found for minimum PA size[130]. The strongest relationship in each case was with respect to the vessel minimum, as shown in Table 5.17 and Figure 5.31, except for the LPA in which case the mean diameter produced the same correlation coefficient as the minimum. For SI, only the IVC was significantly correlated with TCPC-EDI ($r=0.38$, $p<0.001$).

**Table 5.13 IVC/Fontan pathway Diameter Results**

| | $D_{mean}$ | $D_{max}$ | $D_{min}$ | SI |
|---|---|---|---|---|
| **Mean** | 18.1 | 22.1 | 15.2 | 0.30 |
| **Standard Deviation** | 4.2 | 6.1 | 4.2 | 0.13 |
| **Median** | 17.9 | 21.4 | 14.9 | 0.30 |
| **25$^{th}$ Percentile** | 15.1 | 18.6 | 12.2 | 0.20 |
| **75$^{th}$ Percentile** | 20.1 | 23.4 | 17.2 | 0.39 |

**Table 5.14 SVC Diameter Results**

| | $D_{mean}$ | $D_{max}$ | $D_{min}$ | SI |
|---|---|---|---|---|
| **Mean** | 13.7 | 16.5 | 11.9 | 0.26 |
| **Standard Deviation** | 3.0 | 3.9 | 2.8 | 0.14 |
| **Median** | 13.5 | 15.8 | 11.9 | 0.26 |
| **25$^{th}$ Percentile** | 12.0 | 14.5 | 10.0 | 0.14 |
| **75$^{th}$ Percentile** | 15.3 | 17.9 | 13.7 | 0.35 |

**Table 5.15 LPA Diameter Results**

| | $D_{mean}$ | $D_{max}$ | $D_{min}$ | SI |
|---|---|---|---|---|
| **Mean** | 11.0 | 16.4 | 7.9 | 0.49 |
| **Standard Deviation** | 2.5 | 4.5 | 2.3 | 0.19 |
| **Median** | 10.9 | 16.3 | 7.4 | 0.53 |
| **25$^{th}$ Percentile** | 9.1 | 14.0 | 6.4 | 0.35 |
| **75$^{th}$ Percentile** | 12.5 | 18.7 | 9.5 | 0.63 |

**Table 5.16 RPA Diameter Results**

| | $D_{mean}$ | $D_{max}$ | $D_{min}$ | SI |
|---|---|---|---|---|
| **Mean** | 12.0 | 15.8 | 9.9 | 0.35 |
| **Standard Deviation** | 2.5 | 4.2 | 2.2 | 0.17 |
| **Median** | 11.7 | 15.4 | 9.7 | 0.36 |
| **25$^{th}$ Percentile** | 10.4 | 13.2 | 8.5 | 0.21 |
| **75$^{th}$ Percentile** | 13.3 | 17.5 | 11.4 | 0.47 |

See Table 12.9 and Table 12.10 in Appendix C.

**Table 5.17 Power Law Correlations of Minimum vessel dimensions with TCPC-EDI**

| | Pearson correlation (r) | p-value | Multivariate Coefficient | p-value |
|---|---|---|---|---|
| **IVC $D_{min}$** | -0.59 | <0.001 | -1.30 | <0.001 |
| **SVC $D_{min}$** | -0.37 | <0.001 | | |
| **LPA $D_{min}$** | -0.51 | <0.001 | -1.11 | <0.001 |
| **RPA $D_{min}$** | -0.48 | <0.001 | -0.77 | <0.001 |

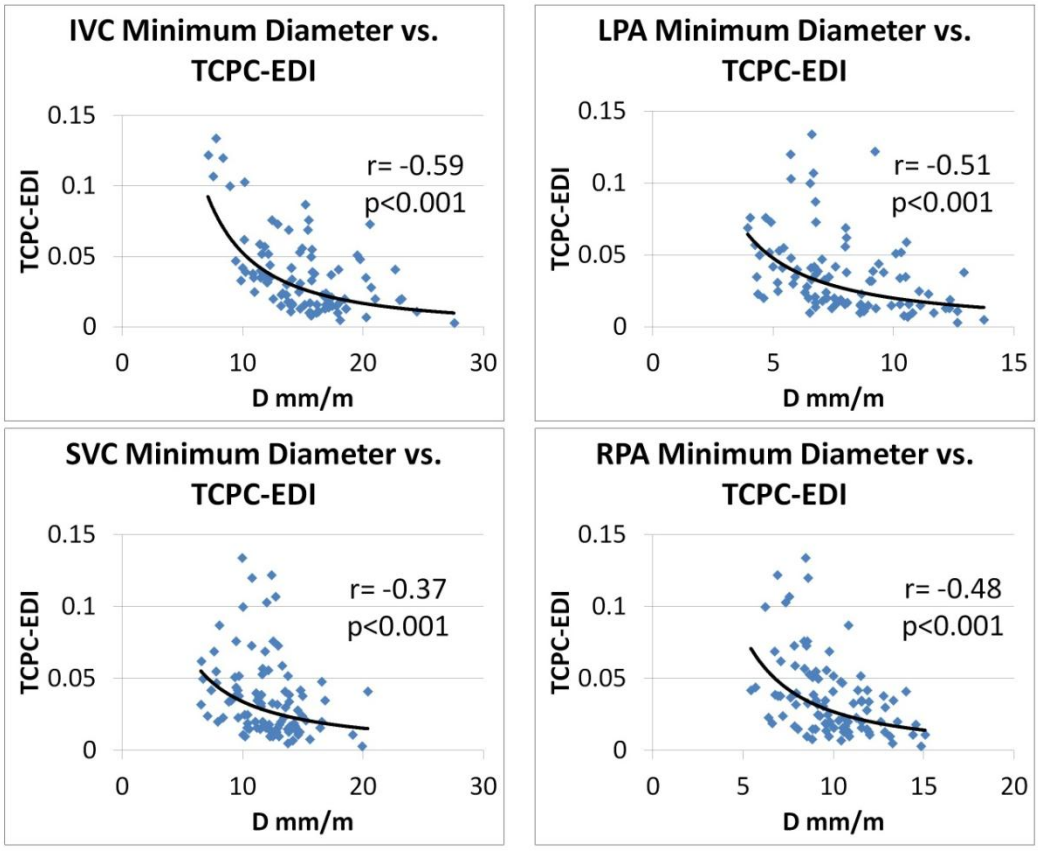


**Figure 5.31** ***Power law correlations of each TCPC vessel minimum diameter with TCPC-EDI. All correlations were statistically significant with correlation coefficients (r) shown.***

Focusing in more detail on the PA relationships, it is important to note that the hemodynamics are agnostic with respect to which PA is smaller. Thus, the TCPC-EDI correlation was repeated using the absolute minimum PA size for each patient (i.e., min[RPA $D_{min}$, LPA $D_{min}$]), and the strength of the correlation increased (r= -0.60, p<0.001). Finally, since the distribution of pulmonary flow can help to offset the effects of a stenosis on a single side, it was hypothesized that the average of the minimum diameters would be more descriptive. In fact, this comparison produced the strongest univariate correlation with TCPC-EDI (r= -0.66, p<0.001). These power law curves are shown in Figure 5.32.

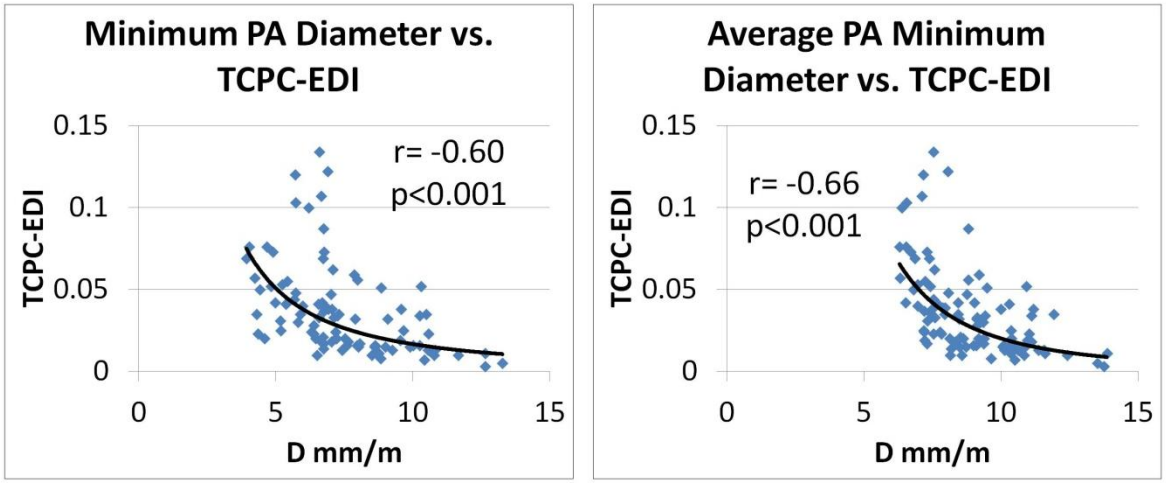


**Figure 5.32** ***Statistically significant power law correlations between (left) minimum PA diameter (either RPA or LPA) with TCPC-EDI and (right) average of PA minima with TCPC-EDI. The latter comparison provided the strongest power loss correlation (r=-0.66) of all univariate models.***

In a multivariate regression model with the four minimum vessel diameters, the IVC, LPA and RPA were all predictors of TCPC-EDI (r=0.78, p<0.001); the SVC was not significant and was thus not included in the multi-variate column of Table 5.17. The coefficients of

these values in the model are provided in Table 5.17, although it is noted that these coefficients correspond to the linearized form of the power law equation and so instead represent the exponents of the diameters.

With respect to HFD (represented as %LPA), only the mean (r=0.26, p=0.011) and maximum (r=0.21, p=0.045) LPA diameters were significantly correlated (linearly) with HFD. While it is not surprising that the caval sizes did not relate to this end point, it is interesting that an opposing trend was not seen with respect to RPA size. This suggests that, because the LPA was generally smaller, its size is a limiting and deterministic factor with respect to flow distribution.

Relative Connection Orientation (Angles and Offsets)

As shown in Figure 4.26 and Figure 4.27, there were six angles and three offsets of interest: the angles each VC makes with both PAs, the angle between the VCs, the angle between the PAs, the caval offsets in the right-left and anterior-posterior directions, and the shortest distance between the VC and PA axes. The offsets were all normalized by the mean IVC diameter given the traditional approach to describing the caval offset in terms of diameter (e.g., one-diameter offset or half diameter offset). Because the Fontan baffle could either be offset to the right or left of the SVC, the RL offset value is presented both in absolute and directional (positive when IVC to the right of the SVC) terms.

Table 5.18 presents the results for connection angles. Recall from Chapter 4 that a large angle denotes improving alignment of the vessel centerlines; a 180° angle would denote a straight cylinder. It is also important to recall that what is measured is a 3-dimensional angle between the centerlines of the respective vessels as opposed to the angle of the 2-dimensional coronal projection that may form the basis of the reader's visualization. Analysis of variance among the VC-PA angles (with a Tukey post-hoc) showed that the

IVC-RPA angle was significantly smaller than all the others; the IVC-LPA angle was also significantly larger than the SVC-RPA connection. None of these angles related to power loss results; instead, there were meaningful correlations with HFD. Specifically, the IVC-LPA, SVC-LPA (negatively), and SVC-RPA angles were all significantly correlated to HFD to the LPA, as shown in Figure 5.33. Interestingly, the correlation coefficients were higher for the SVC angles (-0.31 and 0.34 for the LPA and RPA angles, respectively) than the IVC-LPA angle (0.23), which suggests that the connection of the SVC may be as important in determining the flow distribution characteristics of a given connection as that of the Fontan connection.

**Table 5.18 Summary of Vessel Connection Angles**

| | IVC-LPA | IVC-RPA | SVC-LPA | SVC-RPA | IVC-SVC | LPA-RPA |
|---|---|---|---|---|---|---|
| **Mean** | 110 | 88 | 105 | 100 | 131 | 107 |
| **St. Dev.** | 16 | 15 | 15 | 15 | 23 | 27 |
| **Median** | 113 | 89 | 106 | 100 | 132 | 108 |
| **25$^{th}$ Percentile** | 102 | 78 | 94 | 91 | 119 | 89 |
| **75$^{th}$ Percentile** | 121 | 97 | 115 | 109 | 145 | 127 |

See Table 12.11 in Appendix C

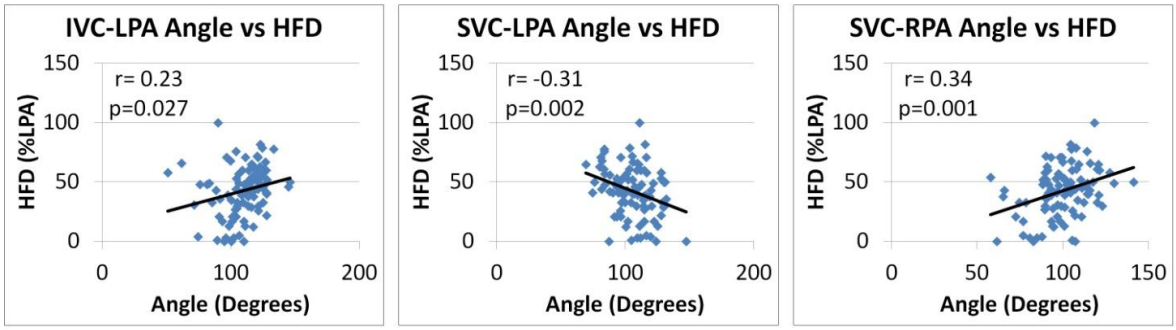


**Figure 5.33** ***Statistically significant linear correlations between (left) IVC-LPA angle, (middle) SVC-LPA angle, and (right) SVC-RPA angle with HFD. SVC correlations were stronger than the IVC.***

**Table 5.19 Summary of Vessel Offsets (mm/mm)**

| | RL | RL (abs) | AP | VC-PA |
|---|---|---|---|---|
| **Mean** | 0.09 | 0.23 | 0.05 | 0.27 |
| **Standard Deviation** | 0.41 | 0.35 | 0.13 | 0.23 |
| **Median** | 0.08 | 0.14 | 0.03 | 0.28 |
| **25$^{th}$ Percentile** | -0.01 | 0.05 | 0 | 0.02 |
| **75$^{th}$ Percentile** | 0.20 | 0.25 | 0.10 | 0.43 |

See Table 12.12 in Appendix C

For vessel offsets (Table 5.19), the population averages present several interesting insights. First, the mean of the right-left caval offset position was close to 0, while the absolute offset distance mean was 0.23, indicating that there is nearly equal preference for placing the Fontan baffle to the left (positive) or right (negative) of the SVC. Furthermore, it is apparent from these mean values that the 1-diameter to 1.5-diameter caval offset advocated by Sharma *et al*. is not a routine part of clinical practice[53, 135]. Yet, the lack of any correlation between RL offset and power loss (Figure 5.34A) indicates that its use may not be of critical importance. In fact, the only offset parameter that

related to power loss was the VC-PA distance (r=0.25, p=0.015) with higher offset related to higher losses (Figure 5.34B). This measure is effectively an indication of the size of the connection (e.g., the anterior extent of the hemi-Fontan connection), and the influence of the large, dissipative connections discussed in §5.5.1 (the points toward the top right of Figure 5.34B) is apparent. Flow distribution trends included positive significant relationships between HFD and SVC-AP (r=0.35, p<0.001; more posterior Fontan related to higher IVC-to-LPA flow) and SVC-RL (r=0.38, p<0.001; leftward Fontan baffle related to higher IVC-to-LPA flow). The AP trend is particularly interesting because it is counter-intuitive, but further analysis reveals that the AP offset is significantly correlated with a larger IVC-to-LPA angle (r=0.40, p<0.001 after neglecting CHOP_M7 and CHOP057A because they represent non-standard connections), which then explains why HFD to the LPA is facilitated.

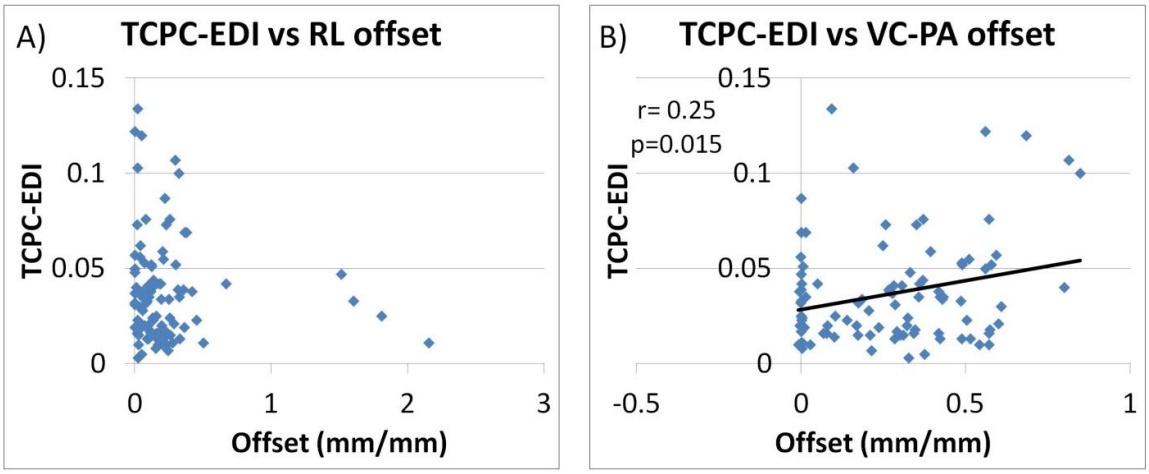


**Figure 5.34** ***A) No relationship between RL caval offset and TCPC-EDI. B) Significant linear correlation between VC-PA distance and TCPC-EDI.***

### 5.5.3 Section Summary

The preceding sections provided several important insights as to what factors mediate undesirable TCPC hemodynamics. The geometric characterization with VMTK showed the primary importance of vessel sizes, particularly the minimum diameter dimension in determining the connection power loss. The form of all of these relationships was a power law fit, which is consistent with the findings of Dasi *et al.*[130], and demonstrates that the impact of vessel size increases exponentially as it gets smaller. The collective effect of all of these dimensions (in the multivariate model) captured a large percentage of the power loss variation (r=0.78). By comparison, the finer details of connection angles and offsets were not found to be related to power loss (with the exception of distance of the caval axis from the pulmonary arterial axis) at a population level. This finding seems to contradict the earlier work of Sharma and Ensley[75, 135] that showed benefits associated with offsets and connection flaring; however, it is more likely that the influence of other patient-specific factors, such as vessel sizes (which were generally uniform in idealized models) is more important than caval offset. The fact that CHOP191A, which had a clear caval offset present, was among the lowest power loss cases in the cohort supports this idea that caval offset is not a poor concept, only a lower priority/lower impact feature.

The analysis of the most and least efficient patient cases provided strong visual support for quantitative trends elucidated by the geometric data. Specifically, the diameter of the Fontan baffle had a clear influence on the disturbed patterns seen in the high power loss patients (Figure 5.16-Figure 5.24). More precisely, the presence of a contraction or narrowing along the length of the baffle (i.e., the stenosis index) caused significant convective acceleration prior to collision with the SVC flow and transition into the PAs. A large cavopulmonary connection (as in the characteristic hemi-Fontan pouch; Figure

5.18, Figure 5.21) distal to such a narrowing appeared to exacerbate this phenomenon by facilitating large-scale recirculation of this high velocity flow. Still, the pulmonary arteries remain the predominant location of energy dissipation. Even in cases with elevated mixing within the dilated junction, the dissipation occurring at the edge of the vortex cores was still significantly lower than that occurring via friction against the pulmonary walls. It was only when the vortex cores extended into the narrower PAs where the recirculation created higher gradients that the dissipation became substantial. This PA-localized dissipation appears to be a confirmation of the work of Khunatorn *et al*[73] who noted increased power loss in idealized models with increased secondary flow in the PAs. Cross-referencing with the VMTK data shows that both PAs were relatively undersized in these patients given their leftward position in the average minimum PA size plot (Figure 5.32, right), a factor that would help to explain to concentration of losses in those regions.

With that said, there is an important distinction to be made here. The natural explanation for higher losses with smaller vessels is the result of increased velocity gradients and wall shear stresses assuming a Poiseuille-like flow profile; the presence of complex secondary flows does not factor into the this strictly geometric characteristic. In fact, what these particular cases represent is the superposition of negative geometric (small IVC and PAs) and hemodynamic (complex flow structures and recirculation) features; neither factor alone tells the whole story. So while vessel sizes alone may provide an excellent approximation of power loss (through the multivariate model) there is still significant room for variation due in large part to the local hemodynamics, which vessel dimensions alone cannot easily capture or anticipate.

A final observation of the patient analyses: although there were no statistical differences between intra-atrial and extracardiac Fontan connections in the broader cohort, it is

apparent from the makeup of these sub-groups that intra-atrial connections may provide an increased risk factor for variations in Fontan pathway diameter. While lateral tunnel connections provide the potential for growth with the patient by incorporating atrial tissue into the pathway, asymmetric growth of that pathway has the potential to create either stenoses or extreme dilations, which can adversely affect hemodynamics in various ways. Furthermore, intra-atrial conduit grafts tend to be smaller than extracardiac conduits (Figure 5.19 and Figure 5.21) and may be even more inclined to mediate high Fontan velocities. Thus, while extracardiac connections may not mediate improved hemodynamics as a general rule, they provide protection against adverse hemodynamics insomuch as they are less inclined to become stenosed.

Finally, the flow distribution trends deserve consideration. Perhaps the most interesting finding was the relationships between the SVC angles to the PAs and the HFD to the LPA. Briefly, the greater the angle between the SVC and RPA, the more the IVC flow tended to the LPA (presumably because SVC flow is primarily directed to the RPA). Conversely, a favorable (with respect to low flow resistance) SVC-LPA angle suppressed IVC to LPA flow. By comparison, the IVC angle relationships were weaker and the RPA angle was not significantly correlated. The most likely explanation for these trends is the fact that the SVC volume fraction is much lower than the IVC and it is therefore more likely to be unilaterally directed to a single lung, as was seen on numerous occasions in the comparison of CMR and CFD results in §5.3.1. These findings suggest that the general HFD trends are largely within surgical control at the times of the Glenn and Fontan procedures: by either angling the SVC preferentially to one PA, or offsetting the Fontan baffle preferentially to one side (based on the offset correlations).

## 5.6 Chapter Summary and Significance

### 5.6.1 Method Verification

Before highlighting the important physiologic findings, it bears repeating that the results presented in this chapter were based on computational simulations, which are subject to significant limitations such as assuming rigid vessel walls, time-averaged flow conditions, ignoring respiration and fenestration, etc. Computational validation is a critical component of any analysis although validation of patient-specific *in vivo* conditions is a significant challenge with no perfect gold standard. Hence, considerable effort was spent in providing support and verification (not necessarily 'validation') for the results obtained based on the best means available. First, a subset of 8 patients, covering several different connection templates and geometric complexity ranges, were selected for detailed comparisons of CFD and 4D CMR flow results. CMR is not bound by the numerical limitations: factors such as wall motion, breathing, and flow pulsatility are naturally incorporated into the results, thus providing an effective (although not conclusive) means to observe their impact. In light of the inherent limitations of CMR flow reconstruction itself (poor spatio-temporal resolution, the need for averaging of many cardiac cycles), the results of the comparison were very favorable both with respect to qualitative flow features and quantitative flow distribution outcomes, although there were instances where the lack of dynamic, time-varying data in the CFD posed potential limitations. In order to better quantify the error introduced by the time-averaged boundary conditions, we thus conducted a detailed, explicit comparison of time averaged vs. time varying boundary conditions. As expected, the use of pulsatile boundary conditions yielded higher quantitative values for power loss by about 15-20% consistently; flow distribution results were relatively unchanged. While this difference may one day prove untenable, our present understanding of the relationship between the absolute magnitude of power loss and clinical outcomes is not advanced enough

(even through the knowledge gained in this study) that the value itself is meaningful. Instead, conservation of relative relationships among patients with respect to other functional metrics of interest is presently the more important insight in initial attempts at elucidating physiologic impact. As such, while the retention of time averaged boundary conditions for the present aim was not ideal, it is an acceptable and pragmatic simplification that greatly facilitated subsequent aspects of the analysis, such as the most/least efficient connection comparison, that would have otherwise been much more difficult to carry out.

### 5.6.2 Physiologic Significance

TCPC design is one of the factors amenable to interventional/surgical manipulation in the care of single ventricle patients, elucidating its role in patient functional status and outcomes is therefore of practical relevance. In this specific aim, both the TCPC surgical geometry and local flow dynamics were explored from multiple scales: at the patient-specific level as well as a population level, with the emphasis and novelty primarily focused on the latter aspect. Most prior investigations into TCPC hemodynamics have focused on only a few patients with the goal of providing an incremental advance in general knowledge of the geometry/hemodynamic coupling through that relatively narrow focus. In contrast, the present work sought to leverage a large patient sample to provide statistical power for objective correlations and then allow for retrospective selection of individual patient cases to elucidate the functional mediators of the observed trends. As a result, we have gained new functional insights, as well as important explanations regarding their governing factors.

A popular model of ventricular filling and cardiac output says that resistance elements downstream of vascular capacitance have a drastic effect on limiting the ability of the ventricle to fill and thus provide adequate output[42]; in Fontan physiology the TCPC and

pulmonary vasculature are two such resistive elements. It is therefore reasonable to expect that elevated levels of TCPC power loss resulting from sub-optimal connection geometry contribute to restricted preload reserve[39, 66] of the single ventricle, which may limit long-term performance. In fact, this trend was observed in the relationships between TCPC-EDI and cardiac index and $Q_s$, in strong confirmation of the prior findings of Sundareswaran *et al.*[55] This finding, while far from a final answer to the problem, justifies past and continued investigations into TCPC hemodynamics at a time when some have claimed it is no longer an issue in single ventricle care[66].

The logarithmic shape of the modeled relationship between TCPC-EDI and flow (both $Q_S$ and CI) deserves specific attention. Table 5.7 shows that 75% of the TCPC-EDI values fall below 0.05 and Figure 5.14 reveals a large spread of flow values associate with that lower range of power losses; much of the strength of the correlation comes from its fit with the higher loss values. Contrastingly, the logarithmic curve dictates that the flows should be increasing in this lower range, and in most cases that is happening. However, it is important to keep in mind that the problem at hand is multi-factorial and perhaps these other factors (e.g., PVR, ventricular function) are more prominent at these low power loss levels. Correlation of these hemodynamics to patient outcomes is needed to determine if this observation is consistent with a meaningful threshold.

With confirmation of a physiologically meaningful relationship between TCPC power loss and systemic function, the question returned to the traditional engineering pursuit of what the important geometric factors are and how to optimize TCPC hemodynamics. Unequivocally, the most important factor in determining connection efficiency (from both the quantitative geometric analysis and the qualitative evaluation of patient flow fields) is vessel size, particularly the minimal dimension of each vessel in the connection. Even the one significant offset correlation observed (VC-PA distance) effectively reflects the

size of connection as opposed to the true offset in the mold of what Sharma *et al.*[135] proposed. No other geometric feature (IA vs. EC Fontan type, single or bilateral SVCs, connection angles or offsets, etc.) had a significant relationship, seemingly in contrast to the findings of many earlier studies. However, there is an important distinction to be drawn with past works. Parametric studies of singular variables, as many other works have done[82-84, 136, 146], artificially inflate the importance of the variable being studied (akin to selection bias) because all other variables are inherently held constant. In this study, by observing trends on a large patient cohort level the results obtained represent the effects strong enough to overcome the 'noise' patient-to-patient variability. The lack of significant relationships for other factors, like caval offsetting or flaring, does not invalidate those ideas nor preclude their prospective evaluation for use in a specific Fontan candidate, but suggests that their utility is sensitive to other geometric variables; there is no one-size-fits-all solution to the optimal TCPC design. This finding, in consideration for the role of power loss described in this aim provides excellent motivation for the continued development of patient-specific surgical planning methods, as will be discussed in greater detail later in this thesis.

Finally, as would be expected, there were significant relationships between connection angles and resulting flow distribution. The distribution of IVC flow to the PAs is of particular interest based on the importance of hepatic blood (assumed to be evenly distributed within the IVC blood) in the vascular health and development of the pulmonary circuit[58]. Three of the four cavopulmonary angles (IVC-LPA, SVC-RPA, and SVC-LPA) were significantly related to HFD, but more interesting is the fact that the respective SVC relationships were stronger (higher correlation coefficient) than the IVC angle correlation. This finding suggests that the SVC angle is a primary determinant of IVC flow distribution, which is not necessarily intuitive and suggests that for cases in

which HFD is a primary concern, proper planning of the Glenn connection is just as, if not more important that planning the Fontan connection.

# Chapter 6. Specific Aim 2: Assess single ventricle function and relate it to TCPC hemodynamics

## 6.1 Overview

In the present era, operative mortality of the Fontan procedure for single ventricle heart defects is low[22, 133], but gradual attrition is a significant problem[29]. Among the most commonly cited chronic complications are ventricular dysfunction (both systolic and diastolic), atrial arrhythmias, liver fibrosis and dysfunction, diminished exercise capacity, protein losing enteropathy (PLE), thrombotic complications, and poor neurodevelopmental outcomes[27, 30, 31]. While these issues are complex and multi-factorial in nature, extensive research in this field has pointed to the combined involvement of single ventricle function[33, 63, 150], the characteristics of the vasculature[43, 44] and the hemodynamics of the total cavopulmonary connection (TCPC)[55, 56]. While these factors are frequently considered in isolation, few studies have sought explicit connections, particularly with regard to the TCPC.

The NIH-supported Georgia Institute of Technology-Children's Hospital of Philadelphia cardiac magnetic resonance (CMR) Fontan database provides an excellent resource for investigating these functional connections. In this study, TCPC hemodynamics and ventricular function are characterized in a group of single ventricle patients late after the Fontan procedure. The results for these measures are first considered separately, with particular emphasis on the diastolic filling characteristics of the single ventricle given the prevalence of diastolic dysfunction in the single ventricle population[30]. Subsequently, TCPC hemodynamics and ventricular function will be correlated to observe functional relationships between the ventricle and TCPC for the first time.

## 6.2 Study Protocols

### 6.2.1 Patient Selection

A subset of forty-four consecutive functional single ventricle patients from the 100 patient cohort investigated in chapter 5 were selected for analysis on the basis of the retrospective availability of a ventricular short axis cine image stack for quantification of ventricular function (VF). Four of the patients were excluded on the basis of either severe image artifacts (3) or an inconsistent number of cine phases within the stack (1). In four other cases, the VF data were not available from the CMR scan included in chapter 5, but were present for a later scan for those patients; the VF and TCPC hemodynamics results from those later scans were used in those cases. The demographics of the remaining forty patients are shown in Table 6.1, while imaging details are provided in Table 6.2.

**Table 6.1 Demographic Details for (40) Patients in Function Analysis**

| | |
|---|---|
| **Age** (years) | 13.0 ± 5.0 |
| **Body Surface Area** ($m^2$) | 1.36 ± 0.42 |
| **Gender** (m/f) | 27/13 |
| **Ventricular Morphology*** (LV/RV/M) | 16/18/6 |

*LV- left ventricle, RV- right ventricle, M- 'mixed'; data presented as mean ± st. dev.; See Table 12.13 in Appendix D.

### 6.2.2 Segmentation Protocol

Details on the ventricular segmentation protocol and end point calculation were presented in §4.1.3.3. All analyses were performed at Georgia Tech. A sample output from the analysis showing two segmented volume phases and the time curves of ventricular volume and diastolic time rate of volume change is shown in Figure 6.1. It is noted that the ‘atrial kick’ was not always visualized in the filling curves.

To verify the precision of the segmented volumes, inter- and intra-user variability were assessed on a select number of patient data sets. For inter-user variability, another expert user separately segmented the end diastolic and end systolic phases for eight of forty patients using a modified version of the segmentation program. For intra-user variability, segmentations for five patients were repeated by the same user 7-8 months following the initial analysis. In either case, the errors associated with volume measurements were quantified.

**Table 6.2 Imaging Detail (mean ± st. dev.) for Ventricular Function CMR data**

| | |
|---|---|
| **Slices** | 7.9 ± 1.2 |
| **Slice Thickness** (mm) | 8.4 ± 1.4 |
| **Phases** | 25.5 ± 4.0 |
| **Phase dt (s)** | 0.03 ± 0.01 |
| **Spatial Resolution** (mm) | 1.35 ± 0.36 |

See Table 12.14 in Appendix D.

### 6.2.3 Statistical Analysis

Statistical analyses were performed using Minitab (Minitab Inc., State College, PA). Continuous variables were tested for normality using the Anderson-Darling test. The Student's t-test was used for comparisons between groups to test the null hypothesis of no differences in volume or function. Pearson's r was used for correlations between functional variables. P-values less than 0.05 were considered statistically significant in all cases. Partial correlation was used, as needed, to correct for the confounding effects of other independent variables. The analysis presented here is exploratory in nature, and thus no adjustments were made for potential inflation of Type I error (i.e., rejection of a potentially true null hypothesis) due to multiple comparisons.

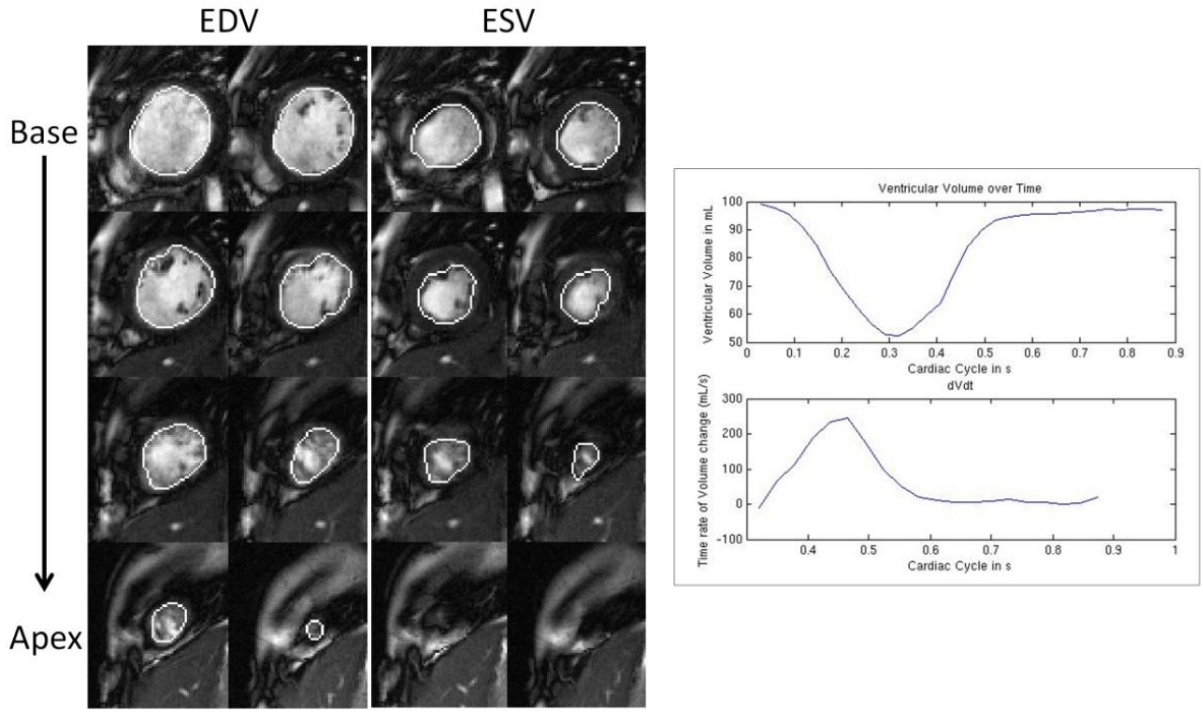


**Figure 6.1** ***Sample output from semi-automatic ventricular segmentation. Left: segmented overlays for two phases corresponding to EDV and ESV for CHOP033A (morphologic left ventricle). Right: Matlab-generated plots from ventricular segmentation showing (top) instantaneous volume curve over time and (bottom) three-point averaged time rate of volume change for ventricular filling (the peak corresponding to PFR).***

## 6.3 Results

This section is organized as follows: First, the summary of the entire forty patient sample will be presented with particular emphasis on dynamic functional measures; next, the single left and single right morphological ventricle groups will be compared; then the TCPC hemodynamic results (specifically TCPC-EDI given the physiologic relevance of that metric illustrated in the previous chapter) will be correlated with the ventricular function; finally, a multi-variate regression model will be constructed to predict cardiac index from the available data.

### 6.3.1 Ventricular Function (VF) Data

The traditional VF metrics for all forty patients are presented in Table 6.3. The volumes have all been normalized to BSA. The dynamic variables measured through the segmentation of cine data are summarized in Table 6.4. The peak filling and ejection rates (PFR, PER) are presented normalized to both BSA ($PFR_B$, mL/s/$m^2$) and EDV ($PFR_V$, EDV/s). Time to PFR was both presented as measured (s) and normalized to cardiac cycle time and reported as a 'Time Ratio'. There are fewer published studies to provide comparisons for these data. Akagi *et al.* reported that $PER_V$ and $PFR_V$ (via radionuclide angiography)[63] were significantly lower in single ventricles than for control subjects.

**Table 6.3 Summary of Traditional Ventricular Function Measures**

| | **End Diastolic Volume** (mL/BSA) | **End Systolic Volume** (mL/BSA) | **Stroke Volume** (mL/BSA) | **Ejection Fraction** (%) | **HR** (bpm) | **CI** [L/min/$m^2$] |
|---|---|---|---|---|---|---|
| **Mean** | 77 | 35 | 42 | 55 | 75 | 3.1 |
| **Standard Deviation** | 16 | 11 | 10 | 9 | 16 | 0.8 |
| **Median** | 80 | 35 | 43 | 55 | 76 | 3.1 |
| **$25^{th}$ Percentile** | 62 | 25 | 35 | 49 | 62 | 2.6 |
| **$75^{th}$ Percentile** | 90 | 42 | 48 | 59 | 88 | 3.4 |

See Table 12.15 in Appendix D.

**Table 6.4 Summary of Ventricular Dynamic Characteristics**

| | **$PER_V$** (EDV/s) | **$PER_B$** (mL/s/$m^2$) | **$PFR_V$** (EDV/s) | **$PFR_B$** (mL/s/$m^2$) | **Time to PFR** (s) | **Peak filling time ratio** |
|---|---|---|---|---|---|---|
| **Mean** | 2.87 | 220 | 2.73 | 209 | 0.16 | 0.20 |
| **Standard Deviation** | 0.64 | 59 | 0.72 | 66 | 0.04 | 0.06 |
| **Median** | 2.87 | 227 | 2.69 | 202 | 0.16 | 0.20 |
| **$25^{th}$ Percentile** | 2.41 | 179 | 2.15 | 165 | 0.13 | 0.16 |
| **$75^{th}$ Percentile** | 3.24 | 248 | 3.23 | 262 | 0.17 | 0.24 |

See Table 12.16 in Appendix D.

To provide a visual comparison, Figure 6.2 shows an example of volume vs. time and diastolic time rate of volume change vs. time for a normal left ventricle from a healthy volunteer. Of particular note is the characteristic shape of diastolic filling: rapid early phase, diastasis, and late atrial filling.

Figure 6.3 qualitatively compares a representative sampling of ventricular volume curves for nine patients. Several different modes were discernible: a) a ‘normal’ diastolic profile characterized by significant early filling, diastasis, and late active filling; b) a ‘parabolic’

diastolic profile with a short or absent diastasis period; or c) uniquely abnormal characteristics with prolonged or slowed relaxation/filling.

Table 6.5 summarizes the correlative relationships between PER/PFR and ventricular volumes. Both $PER_B$ and $PFR_B$ were significantly correlated to EDV and SV; however, none of these relationships were significant when EDV (preload) was instead used as the normalization factor. $PER_V$ was found to significantly correlate with ESV and EF, while $PFR_V$ only correlated with EF. There was also a strong relationship between $PER_V$ and $PFR_V$ and after using partial correlation to remove this effect, there was no longer a significant correlation between $PFR_V$ and EF. Finally, the EDV and peak filling time ratio were correlated ($r = -0.38$, $p=0.015$).

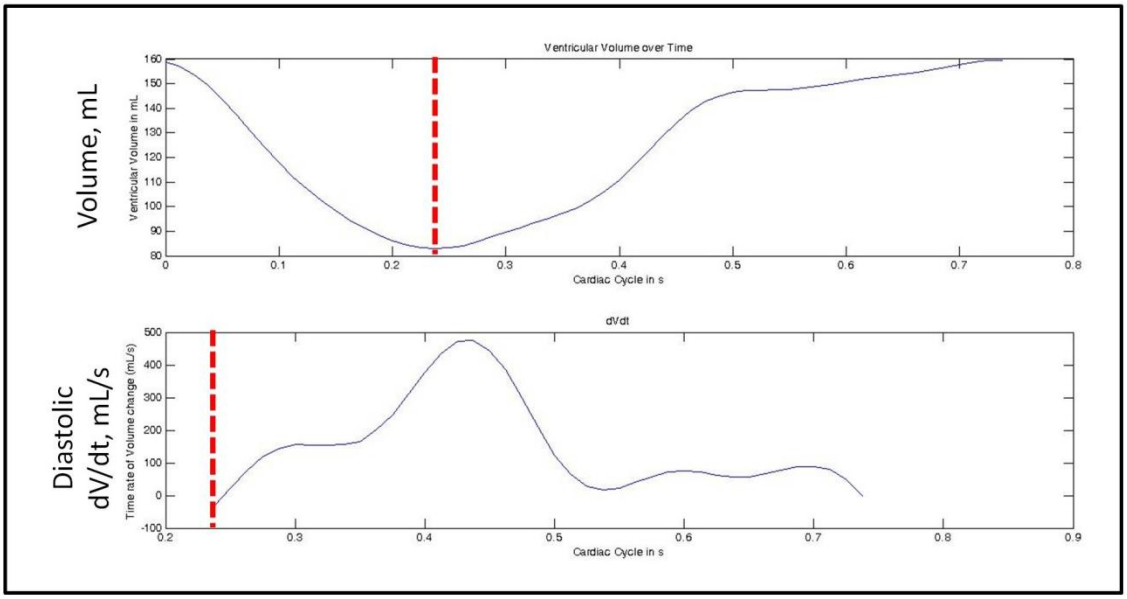


**Figure 6.2 Volume (top) and dVdt (bottom) curves for a normal LV from a healthy volunteer with the red vertical lines showing time relationship between the two plots.**

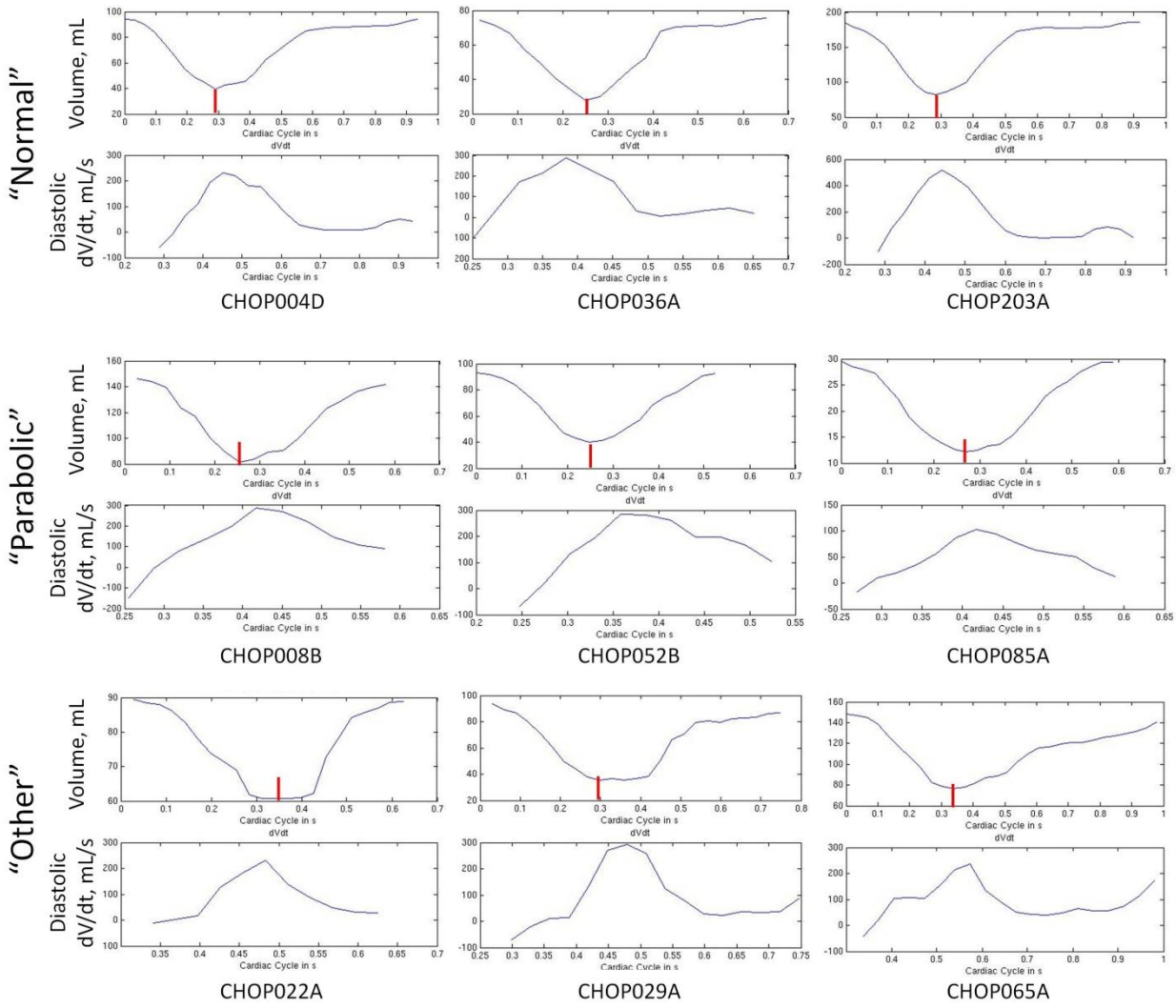


**Figure 6.3** ***Representative sampling of volume vs. time and time rate of volume change (diastole only) vs. time for nine patients. Red vertical lines on the volume curves denote the starting point of the associated dV/dt curve. Qualitatively, these samples either (top row) reflected a normal ventricular diastolic profile of early filling, diastasis, and late active filling; (middle row) had a parabolic filling profile with little to no diastasis; (bottom row) had an abnormal pattern characterized by either prolonged isovolumic relaxation or a shallow early filling phase.***

**Table 6.5 Statistical Correlations coefficients between PFR/PER and ventricular volumes**

| | EDV | ESV | StV | EF |
|---|---|---|---|---|
| **$PER_V$** (EDV/s) | NS* | -0.66 | NS | 0.74 |
| **$PER_B$** (mL/s/$m^2$) | 0.53 | NS | 0.82 | 0.49 |
| **$PFR_V$** (EDV/s) | NS | -0.42 | NS | 0.47 |
| **$PFR_B$** (mL/s/$m^2$) | 0.47 | NS | 0.62 | NS |

*NS- not significant

### 6.3.2 Single Left vs. Single Right Ventricles

The subset of patients with either a single left or single right morphological ventricle (excluding six cases with a 'functional' single ventricle in the form of two undersized ventricles) was analyzed to observe potential differences between groups. Table 6.6 shows the results of this comparison while Figure 6.4 visually demonstrates the volume differences. All variables were normally distributed based on the Anderson-Darling test, so the two-sample t-test was used for all comparisons.

None of the variables was significantly different between groups. This finding is in contrast to the findings of Anderson *et al.* who reported larger RV volumes (EDV, ESV, StV)[30], although the discrepancy appears to be largely related to RV results as the present LV volumes are statistically no different from the cross-sectional data reported therein (via Z-test). However, other investigators have similarly reported no differences between LVs and RVs[64], so these findings may just be a function of the relatively small sampling.

**Table 6.6 Comparison of Single LV and Single RV function**

| | **Single LV** (N=16) | **Single RV** (N=18) | **p-value** |
|---|---|---|---|
| **Age** (years) | 14.3 ± 5.1 | 12.2 ± 4.4 | 0.22 |
| **BSA** ($m^2$) | 1.37 ± 0.38 | 1.36 ± 0.43 | 0.94 |
| **EDV** (ml/BSA) | 79 ± 15 | 76 ± 19 | 0.68 |
| **ESV** (ml/BSA) | 34 ± 10 | 35 ± 14 | 0.72 |
| **StV** (ml/BSA) | 45 ± 10 | 41 ± 10 | 0.28 |
| **EF** (%) | 57 ± 8 | 55 ± 9 | 0.46 |
| **$PER_V$** (EDV/s) | 3.05 ± 0.72 | 2.79 ± 0.61 | 0.27 |
| **$PFR_V$** (EDV/s) | 2.91 ± 0.79 | 2.60 ± 0.67 | 0.23 |
| **Peak filling time ratio** | 0.19 ± 0.06 | 0.21 ± 0.06 | 0.24 |

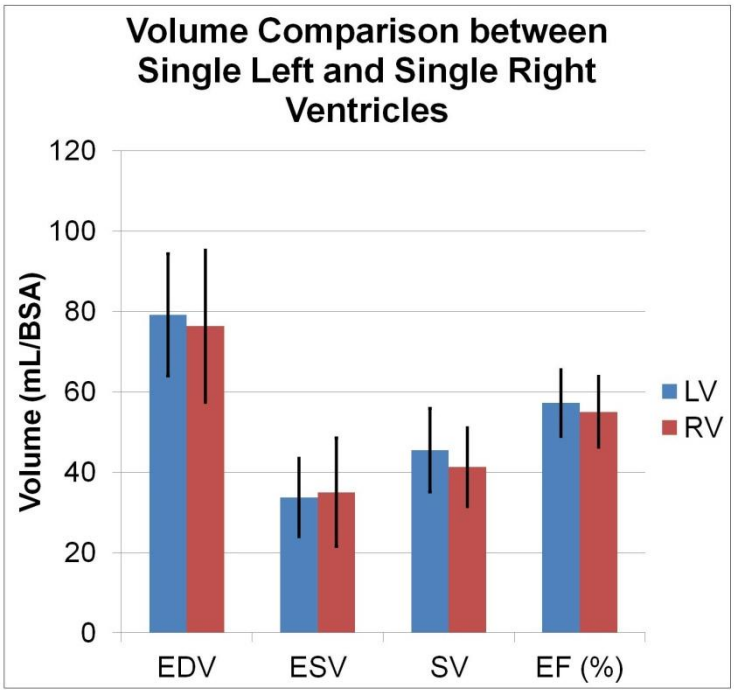


**Figure 6.4** ***Comparison of ventricular volumes and ejection fraction between single left and single right ventricle patients. There were no significant differences between groups in this analysis. See*** **Table 12.17** ***in Appendix D.***

### 6.3.3 Relationship to TCPC Hemodynamics

TCPC power loss (reported here as TCPC-EDI) was concurrently quantified for all patients using CFD with time-averaged flow boundary conditions as discussed in chapter 5. The average of this sub-group was statistically no different than the rest of the cohort (0.040 ± 0.028 vs. 0.037 ± 0.028). Table 6.7 shows the correlations of TCPC-EDI with VF. Significant results include correlations between the natural log of TCPC-EDI and EDV, ESV, and StV (p=0.054), and (linearly) with the time ratio to PFR. Table 6.7 also presents the linear regression coefficients between ventricular volume measurements and ln(TCPC-EDI) showing that the power loss relationship with EDV (Figure 6.5) was much stronger than for the other two measures. In fact, it was hypothesized that the

associations of TCPC-EDI with ESV and StV were secondary to the EDV/TCPC-EDI relationship. After using partial correlation to remove the effect of EDV, TCPC-EDI was no longer associated with ESV (r= -0.03; p=0.85) or StV (r=0.02; p=0.90).

### 6.3.4 Relationship to CI

The VF and TCPC hemodynamic variables were all individually compared to cardiac index with the results shown in Table 6.8. Notably, Figure 6.6 shows the logarithmic form of the EDV vs. CI relationship, which resembles the characteristic shape of the Frank-Starling relationship (see Figure 3.5). In addition, a multi-variate model was constructed by selecting the first four variables (limit for N=40) into a forward stepwise regression. The variable inputs to the regression were based on the significant uni-variate relationships; however, StV and PFR were left out because of co-linearity with other variables (EDV and PER, respectively). The resulting model had a very strong (r=0.82) correlation.

**Table 6.7 Correlations of TCPC-EDI with Ventricular function measures and results of linear regression with ventricular volumes**

| | ***Correlation with TCPC-EDI*** *(r)* | ***p-value*** | ***Linear Regression coefficient*** | ***t-statistic*** |
|---|---|---|---|---|
| ***Age*** [years] | 0.15 | NS | | |
| ***BSA*** [$m^2$] | 0.25 | 0.11 | | |
| ***ESV*** [mL/BSA] | -0.36* (lnTCPC) | 0.023 | -5.98 (lnTCPC) | -2.37 |
| ***EF*** [%] | 0.125 | NS | | |
| ***EDV*** [mL/BSA] | -0.43* (lnTCPC) | 0.005 | -10.49 (lnTCPC) | -2.96 |
| ***StV*** [mL/BSA] | -0.31 (lnTCPC) | 0.054 | -4.60 (lnTCPC) | -1.98 |
| ***$PER_V$*** [EDV/s] | 0.20 | NS | | |
| ***$PFR_V$*** [EDV/s] | -0.1 | NS | | |
| ***Time ratio to PFR*** | 0.32* | 0.044 | | |
| ***HR*** (bpm) | 0.11 | NS | | |

**Table 6.8 Correlation results with CI**

| | ***Correlation with CI*** *(r)* | ***p-value*** | ***Multivariate Coefficient*** | ***Multivariate p-value*** |
|---|---|---|---|---|
| ***Age*** [years] | -0.28 | 0.08 | | |
| ***BSA*** [$m^2$] | -0.21 | 0.19 | | |
| ***ln(TCPC-EDI)*** | -0.09 | NS | | |
| ***ESV*** [mL/BSA] | 0.05 | NS | | |
| ***EF*** **[%]** | 0.36* | 0.025 | | |
| ***ln(EDV)*** [mL/BSA] | 0.44* | 0.004 | 2.8 | <0.001 |
| ***StV*** [mL/BSA] | 0.61* | <0.001 | | |
| ***$PER_V$*** [EDV/s] | 0.52* | 0.001 | 0.73 | <0.001 |
| ***$PFR_V$*** [EDV/s] | 0.47* | 0.002 | | |
| ***HR*** [bpm] | 0.46 | 0.003 | 0.027 | <0.001 |
| ***Time to PFR*** | 0.12 | NS | | |

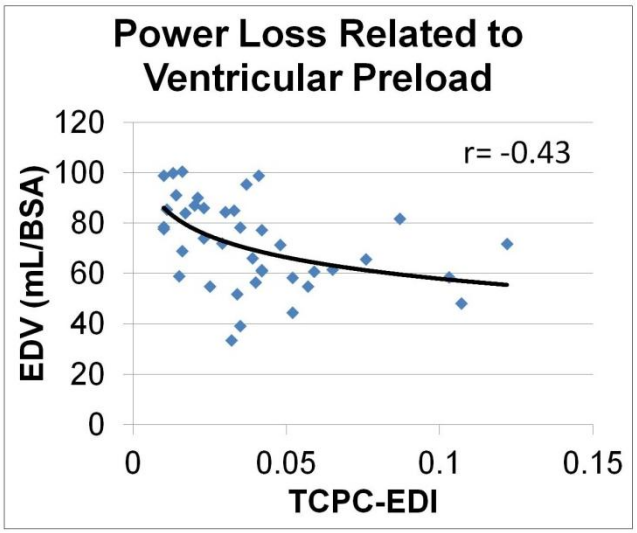


**Figure 6.5** ***Statistically significant correlation between the natural logarithm of indexed TCPC power loss and ventricular end diastolic volume (preload).***

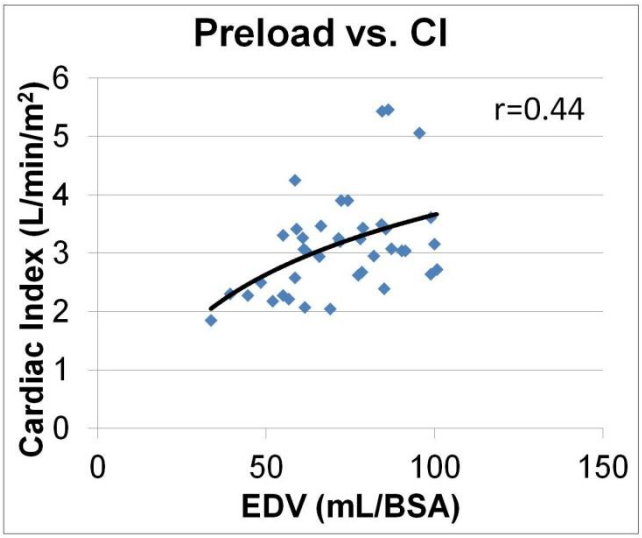


**Figure 6.6** ***Logarithmic relationship between EDV (as a surrogate of preload) and CI, reminiscent of the Frank-Starling relationship.***

### 6.3.5 Results Verification

Inter- and Intra-user variabilities were assessed through segmentations of 8 patients by two different individuals and 5 patients by the same operator on two separate occasions, respectively, to verify the precision of the reported results. The inter-user reliability was assessed using a two-way random intra-class correlation (ICC) model and combining the independent measures of EDV and ESV for the respective comparisons. The results are summarized in Table 6.9 as the average absolute errors among the various results. As expected, the EDV comparisons yielded the lowest error (since denominator is biggest), while the StV comparisons had the highest errors (compounding effects of individual errors in EDV and ESV). The inter-user variability was higher than desired, however it is reiterated that a different protocol was used and the segmented images are not available for review to understand the source of the differences. Conversely, the intra-user volume differences (from analyses 8-9 months apart) were all within 10% and provide greater confidence in data fidelity. The dynamic PER and PFR measurements both had an average error of 13%. The ICC coefficient for both measures was >0.9, indicating good reliability in the results.

**Table 6.9 Results precision/reliability analysis (Absolute % error)**

| | **EDV** | **ESV** | **StV** | **$PER_v$** | **$PFR_v$** | **ICC coefficient** |
|---|---|---|---|---|---|---|
| Inter-user (n=8) | 10 | 12 | 17 | N/A | N/A | 0.935 |
| Intra-user (n=5) | 4 | 8 | 10 | 13 | 13 | 0.993 |

See Table 12.18 and Table 12.19 in Appendix D

## 6.4 Discussion

### 6.4.1 Systolic Function

The ability to make conclusive statements regarding the functional status of the patients in this study is significantly hampered by the fact that this was a retrospective, observational study with no control group. Therefore, inferences must be drawn based on comparisons to past published data. It must be noted that ejection fraction and cardiac index are poor measures of ventricular function given their dependence on preload, afterload, heart rate, and contractility; yet, with limited measures available from this retrospective analysis, they must serve as a primary reference.

Ejection fraction (55 ± 9%) was on average lower in these patients than normal. Akagi *et al*. reported an EF of 60 ± 8% for controls, while Ingul *et al*. reported values of 64% and 57% for lean vs. obese healthy subjects, respectively[151]. In previous single ventricle studies (not age-matched to the present data), Parikh *et al* and Eicken *et al* both reported decreased ejection fraction post-Fontan compared to control[35, 65]. Finally, even though the PHN cross-sectional study reported preserved systolic function in 73% of patients (based on a Z-score for EF > -2), they similarly noted that the population mean (59% by echocardiography) was lower than that of normal subjects[30].

However, this decreased ejection fraction did not translate to suppressed cardiac index (3.1 ± 0.8 L/min/$m^2$). By comparison, Laird *et al.* reported a similar value (3.1 L/min/$m^2$) for healthy 14 year old subjects[152], while the results of Ingul *et al.* were between 2.6 and 3.0 L/min/$m^2$ for lean and obese normals, respectively[151]. These findings contrast with those of Akagi *et al.* and Senzaki *et al.* who reported suppressed CI in single ventricles compared to normals, although those studies were all done in much younger subjects[38,

[64, 150]. Perhaps age differences are significant in this regard with Fontan CI depressed early after surgical palliation, but normalizing by early adolescence.

Finally, PER provides another load-dependent assessment of systolic function. Akagi *et al.* quantified $PER_V$ via radionuclide angiography[63, 64] and without the use of three-point averaging, both of which preclude a direct comparison of the measured values. However, those authors noted a non-significant increase for single LVs compared to single RVs, with only the RV patients being significantly reduced from controls[64]. A similar non-significant difference on the basis of ventricular morphology was seen in this study (Table 6.6). Previous studies have shown an increase in ventricular afterload in single ventricle physiology[38], so a decreased PER with preserved ventricular contractility[66] likely reflects this adversity. Additionally, the strong correlation between $PER_V$ and EF is consistent with the findings of Rathod *et al.* who reported negative effects of myocardial fibrosis on ejection fraction in single ventricles[67]. In that study, patients with fibrosis had markedly decreased EF (45% vs. 56%), therefore a mean EF of 55% in the present study anecdotally suggests preservation of elastic properties.

### 6.4.2 Diastolic Function

With regard to diastolic function, it is more difficult to rely on other studies for comparison as diastolic dysfunction is typically assessed using echocardiographic measures of filling velocities (i.e., E-wave vs. A-wave). The qualitative comparison of rate of volume change vs. time profiles in Figure 6.3 provides anecdotal evidence of altered diastolic mechanics. Additionally, there are numerous reports of ‘delayed’, ‘altered’, and/or ‘impaired’ ventricular relaxation/filling[37, 69, 70, 72, 150] building upon the report of abnormal diastolic function in 72% of patients in the PHN cross-sectional study[30].

Broadly speaking, there are several factors that govern the diastolic filling of the ventricle: the driving head pressure (for single ventricles, that is the CVP), the ventricular compliance, and the cumulative resistance of the pathway between those two elements. Collectively, these factors determine the filling characteristics and ultimately the ventricular preload (the wall stress at end diastole). In the absence of ventricular pressure information, end diastolic volume can be used as a surrogate of myocardial stretch, and thus preload. The resemblance of the EDV/CI relationship (Figure 6.4) to the characteristic Frank-Starling relationship between preload and output (see Figure 3.5) supports this assumption. For single ventricles, the resistance between the CVP and the ventricle is the integration of the TCPC, the pulmonary vasculature, the atrium, and the AVV valve. Of these, the pulmonary vascular resistance is assumed to be the primary mediator, but the finding of a significant correlation between indexed TCPC power loss and EDV (Figure 6.5), the first time such a relationship has been explicitly shown, indicates that TCPC hemodynamics are also an important component of the pathway.

It is worth briefly considering an alternative interpretation of this relationship between TCPC-EDV. Poor ventricular compliance leading to decreased ventricular filling and transpulmonary flow rate in these patients could artificially increase the indexed power loss and produce a similar correlation between these variables. The data available cannot conclusively determine causality, so future studies will need to ultimately distinguish between these possibilities.

For the dynamic variables, the filling rate demonstrated inherent preload dependence as PFR was correlated to EDV when normalized by BSA; but after correcting for the preload dependence (normalizing by EDV), there were no longer relationships between with those variables. The PFR relationship to stroke volume was also preload dependent

by the same logic. Finally, the time ratio to PFR was significantly (negatively) correlated with EDV. This measure can be thought of as the percentage of the cardiac cycle required to accelerate atrio-ventricular flow to its peak rate and so the relationship to preload is reasonable. Furthermore, the (positive) correlation of this time ratio with indexed TCPC power loss is further evidence that the TCPC can contribute to decreased ventricular filling pressures.

Once corrected for preload, $PFR_V$ is partly a surrogate for ventricular relaxation. Ishida *et al.* showed that PFR (non-normalized) was associated with ventricular relaxation rate (τ, time constant of iso-volumetric pressure decline) and the atrial pressure at the onset of mitral flow in an animal model (head pressure)[71]. Senzaki *et al*. used $PFR_V$ to denote relaxation and found that, despite 'delayed filling' and decreased PFR, there were no chamber volume differences between single ventricles and controls[150]. A similar finding is noted here by the lack of a correlation between $PFR_V$ and ventricular volumes, particularly EDV.

Past studies have indicated that single ventricle mechanics are inherently altered from two ventricle hearts[153, 154], so altered or 'incoordinate'[72] relaxation is not an unexpected phenomenon. One potential hypothesis is, with decreased circumferential strain in single ventricles (with respect to both magnitude and uniformity)[153, 154], there is less elastic potential energy stored during systole to facilitate rapid diastolic filling through untwisting and "suction."[155, 156] However, the present findings and those of Senzaki *et al.*[150] suggest that secondary adaptations help to preserve the ultimate volumetric dimensions of the ventricle. The nature of those secondary changes is difficult to infer from the present data, but are perhaps related to resting heart rate or diastolic duration (i.e., allowance for extended filling time to overcome altered early filling mechanics).

Finally, the relationship between $PFR_V$ and $PER_V$ is a strong indication that the filling mechanics are not uniquely related to relaxation mechanics. Instead, that correlation is suggestive of a broader dependence on ventricular elastic/compliance properties[4], which have also been reported to be altered in single ventricles[67, 69]. No direct comment can be made on the 'normality' of the present data.

### 6.4.3 Predictors of Cardiac Index

A recent review by Gewillig pointed out that the factors mediating cardiac output for single ventricles are not entirely understood[66]. While output could be estimated in normal ventricles by some combination of heart rate, contractility, preload and afterload, the same is not true for single ventricles. Since cardiac index is a generic way of assessing overall cardiac function (while being very non-specific)[4], relating the present results to cardiac index through a multi-variate analysis is a worthwhile exercise.

Three variables were found to be predictive of CI: EDV, HR, and PER. Many parallels can be drawn from this list to the 'normal' predictors. EDV again serves as a surrogate for ventricular preload, while $PER_V$ represents some combination of afterload and ventricular compliance. While the findings of this model are perhaps academically interesting, from a clinical standpoint, the only worthwhile interventional target identified is the ventricular preload (EDV). While HR could theoretically be boosted by adrenergic stimulants, past experience has shown that single ventricle preload reserve limitations restrict the effectiveness of such therapies[150]. There is some disagreement regarding the importance of afterload, with Senzaki *et al*. finding negative relationships between low frequency arterial impedance and cardiac index[38] and Gewillig instead arguing that afterload increases as a consequence of low output (to maintain systemic arterial pressures) and is not a cause of it[66]. Regardless, there is far more evidence indicating

the importance of preload that it should be the primary target for increasing CI, either through PVR reduction or an efficient Fontan pathway.

### 6.5 Chapter Summary

Numerous studies have focused on single ventricle mechanics and function as a means to better understand and manage Fontan physiology. The general consensus from these works is that single ventricles post-Fontan experience both systolic and diastolic myocardial dysfunction concurrent with altered arterial and venous hemodynamics and potential disruption of electrical conduction[4]. While there was no control in this study to provide 'normal' bases for comparison, the quantitative findings were generally consistent with past observations and thus add to that body of literature.

The novelty of this study is instead focused on the relationship of the TCPC to the ventricle. While it has frequently been hypothesized that an inefficient TCPC could negatively impact the function and long-term cardiovascular health of the single ventricle, evidence to support such ideas has been lacking. This study therefore represents an important contribution as the first concurrent characterization and comparison of ventricular function and TCPC hemodynamics in single ventricle patients. Important findings include inverse relationships, as hypothesized, between TCPC power losses and ventricular volumes, most notably EDV as a preload surrogate. The correlation between power loss and the time ratio to the PFR provides additional evidence for the role of the TCPC in diastolic function. These findings are significant given the fact that the single ventricle output is largely mediated by preload (as confirmed by the multi-variate regression model), which is typically reserve limited[150], as well as the prevalence of diastolic dysfunction among the single ventricle population[30].

While it is not suggested that the TCPC is the primary factor or mediator of these problems, TCPC hemodynamics can be controlled via surgical intervention, thus providing at least one way to actively pursue better long term outcomes. In fact, as will be discussed in Chapter 7, the patient-specific hemodynamics could even be pre-selected through imaging-based surgical planning to minimize the need for re-intervention for hemodynamic optimization and further leverage these hemodynamic relationships into translatable improvements in patient functional status.

# Chapter 7. Specific Aim 3: Investigate the utility and reliability of prospective Fontan surgical planning for a wide array of single ventricle patients

## 7.1 Overview

Single ventricle patients following Fontan palliation with a TCPC are subject to gradual attrition with numerous morbidities. For a handful of these complications, there is strong evidence suggesting a link between the specific characteristics of blood flow through the TCPC and the cause or exacerbation of the complication. The most prominent example of such relationships is the development of pulmonary arteriovenous malformations (PAVM) (causing progressive hypoxia) because of the maldistribution of hepatic factors produced by the liver to the pulmonary vasculature[58]. Another example is impaired exercise capacity[157, 158] due in part to non-linear increases in the energy dissipated through the TCPC pathway with increased cardiac output[39, 55, 134]. Furthermore, in Chapters 5 and 6 of this thesis, statistically significant correlations were observed between TCPC power losses (TCPC-EDI) and systemic venous flow rate and end diastolic volume. Collectively, these findings suggest that ensuring an efficient TCPC design with a balanced hepatic flow distribution (HFD) may yield long-term benefits for patient health and quality of life.

A potential solution to this need may be found in the fact that it is currently possible to "virtually" mimic surgical interventions on patient-specific anatomies to assess the feasibility of a specific intervention or to explore various surgical approaches under consideration.[16,19] In addition, fluid-dynamic numerical solvers have progressed in complexity to the point of being able to accurately reflect *in vivo* function[126]. Together, these capabilities present a revolutionary way of approaching cardiac surgery in that the

functional implications of anatomic surgical decisions can be assessed and parametrically investigated preoperatively. Virtual surgical planning of the Fontan procedure has thus been proposed to help achieve desired flow characteristics on a patient-specific basis[110]. The potential for these methods is far-reaching across the field of cardiothoracic surgery, and single ventricle patients provide an ideal starting point for their development and evaluation for several reasons: (i) there is relative homogeneity in operative course and timing, while the surgical implementation details can vary widely; (ii) there is large variability in patient outcomes; (iii) an established and accurate computational model already exists; and (iv) our group has a large amount of preliminary data suggesting that the surgical decisions about Fontan geometry and connections directly impact outcome.

Previous reports have detailed the prospective use of such techniques for a limited number of single ventricle patients, primarily focused on addressing PAVM. In particular, the PhD dissertation of Dr. de Zélicourt included an evaluation of these methods toward the treatment of patients with interrupted IVC and azygos vein continuation[124]. The efficacy evaluations in these earlier studies were largely based on measures such as arterial oxygen saturations, which are clinically meaningful yet inconclusive for confirming modeled predictions because oxygen saturation levels are not explicitly included in the models[105, 159]. Thus, while a key assumption of these methods is the accuracy of preoperative predictions with respect to postoperative hemodynamic outcomes, detailed quantitative comparisons between pre- and post-operative hemodynamic metrics have not yet been reported.

Hence, the objectives of this specific aim are twofold: 1) expand the use of surgical planning for the Fontan procedure to include larger patient numbers, different anatomic characteristics, and different clinical end points of interest; and 2) use post-operative

follow-up CMR data to evaluate the efficacy and reliability of the surgical planning predictions. The hypothesis is that Fontan surgical planning can successfully delineate among the hemodynamic characteristics of various surgical options for a wide variety of patients with sufficient realism to recreate the post-operative physiologic state and thus assist in clinical decision making.

## 7.2 Study Protocols

This chapter consists of three primary sections. First, a retrospective review of the GT Fontan database was conducted to identify serial patient studies that could be used to provide preliminary insights, as the understanding of post-Fontan physiologic changes that are relevant to prospectively modeling the surgery (i.e., vena cava and pulmonary artery flow changes) is generally poor. Lumped parameter modeling was used to supplement these limited data sets. Second is the presentation of findings from prospective patient-specific surgical planning case studies. Finally, post-operative data collected for a limited number of these prospective cases will be characterized and compared to pre-operative models to assess the accuracy and reliability of these surgical planning methods.

### 7.2.1 Patient Selection

#### 7.2.1.1 Serial Flow Study

From a retrospective review of the Georgia Tech Fontan CMR database, 11 patients were identified based on the availability of CMR evaluations both prior to and shortly following their Fontan palliation. Three patients had interrupted IVC with azygos vein continuation and were excluded from this analysis. An additional patient was also excluded based on suspected obstruction of the RPA.

Clinical characteristics of the seven included patients are summarized in Table 7.1. Patient designations are provided with respect to the BRP patient designations due to the use of both CHOP and CHOA patients. Five patients had a bi-directional Glenn (BDG) procedure (including two with bilateral bi-directional connections), 1 had a hemi-Fontan, and 1 had a “one and a half ventricle” repair (i.e., the main pulmonary artery outflow was intact). The Fontan completion was performed using an extra-cardiac conduit in 5 cases and a lateral tunnel in the remaining 2 cases. The time from the Fontan operation to MRI follow-up ranged from 10 to 345 days (mean of 170 days).

**Table 7.1 Clinical Data for Serial Flow Study Patients**

| | BRP ID | Age (yrs) | BSA ($m^2$) | Δt Post-op (days) | Connection Type | Diagnosis |
|---|---|---|---|---|---|---|
| **Pt. 1** | CHOP053 | 4.7 | .63 | | BDG ECC | Heterotaxy and Dextrocardia |
| | CHOP055 | 4.7 | .63 | 35 | | |
| **Pt. 2** | CHOP057 | 2.8 | .43 | | BDG ECC | HLHS |
| | CHOP085 | 3.4 | .59 | 193 | | |
| **Pt. 3** | CHOP072 | 3.2 | .55 | | HF LT | HLHS |
| | CHOP111 | 4.2 | .61 | 345 | | |
| **Pt. 4** | CHOP120 | 3.5 | .56 | | 1.5V ECC | DORV with LV Hypoplasia |
| | CHOP148 | 4.1 | .65 | 224 | | |
| **Pt. 5** | CHOP_M5 | 1.3 | .49 | | BDG ECC | DORV with Pulmonary Stenosis |
| | CHOP_M5p | 2.0 | .58 | 227 | | |
| **Pt. 6** | CHOA014 | 1.8 | .53 | | BDG LT | LTGA, RV Hypoplasia |
| | CHOA027 | 2.4 | .58 | 153 | | |
| **Pt. 7** | CHOA029 | 2.2 | .46 | | BDG ECC | Pulmonary Atresia, DILV |
| | CHOA042 | 2.3 | .46 | 10 | | |

1.5V = One and a half ventricle repair; BDG = Bidirectional Glenn; DORV = Double Outlet Right Ventricle; ECC = Extracardiac Conduit; HF = Hemi-Fontan; HLHS = Hypoplastic Left Heart Syndrome; LT = Lateral Tunnel; LTGA = Levo Transposition of the Great Arteries; LV, RV = left, right ventricle

#### 7.2.1.2 Prospective Surgical Planning Studies

Patient selection was performed at the clinical level; that is, patients were referred by their cardiologist and/or cardiac surgeon to Georgia Tech for surgical planning on the basis of clinical need. No additional screening or inclusion/exclusion criteria were applied beyond that initial referral.

### 7.2.2 Procedures

#### 7.2.2.1 Serial Flow Study

An in-house program in Matlab (The Mathworks, Natick, MA) was used to process the MR images (see §4.1.3.2). An edge-based active contour algorithm was implemented for semiautomatic segmentation of the vessel of interest over all cardiac phases. An automatic noise removal algorithm was subsequently used to improve the accuracy of these velocity values. All flow rates were normalized by the patient body surface area at the time of the scan (i.e., the ascending aorta flow rate is reported as the cardiac index).

To supplement the patient data with theoretical baseline predictions, a lumped parameter model of the single ventricle circulation was used, which was based on the design of Peskin *et al.*[160] Details on the structure and formulation for this specific model were described in detail by Sundareswaran *et al.*[55]

One significant alteration that was made to the existing model design was to separate the systemic venous returns into superior and inferior sections. This change allowed for the creation of a BDG circuit configuration to complement the TCPC model. A schematic of these two designs is shown in Figure 7.1.

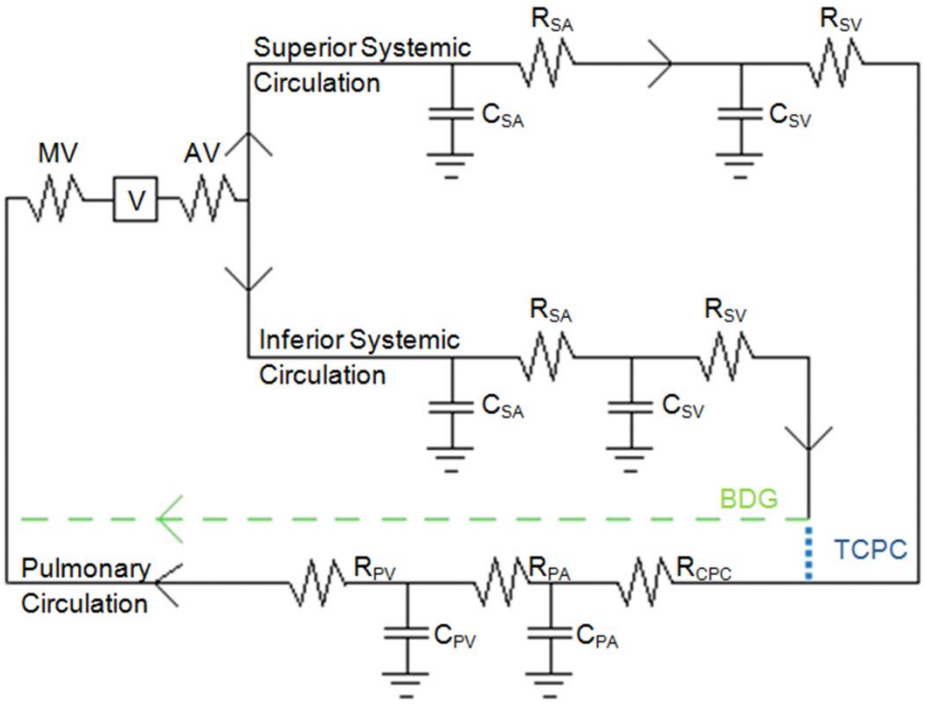


**Figure 7.1 Schematic describing the lumped parameter models used in this study. In the Glenn Stage model, the interior systemic circulation connected to the common atrium (green line, BDG). To simulate Fontan surgery, that connection was replaced by an IVC to PA connection (blue line, TCPC). AV = aortic valve; C = compliance; CPC = cavopulmonary connection; MV = mitral (atrioventricular) valve; PA, SA = pulmonary, systemic arteries; PV, SV = pulmonary, systemic veins; R = resistance; V = single ventricle.**

The modeling procedure for the lumped parameter study was as follows. The BDG model was run first to emulate the desired pressures and flows of typical Glenn-stage physiology (i.e., the simulations were not intended to be patient-specific as no pressure data were available). Subsequently, the TCPC model was run, using the BDG pressure and flow outputs as initial conditions, to characterize the physiologic response to the surgical reconfiguration. Both simulations were run for 200 cycles to ensure cycle-to-cycle consistency of the results. The model parameters (Table 7.2) were the same in

both cases (with the exception of BDG vs. TCPC resistance values) and were selected such that the BDG output represented typical Glenn-stage hemodynamics. These values of interest included: an approximate 45/55 SVC/IVC flow split (present data); SVC and IVC pressures of ~10-15 and ~6 mmHg, respectively (representative catheterization data); cardiac output ~2.7 L/min (from the average cardiac index value of the present data); stroke volume of 40 mL[36, 39] (and present data); ejection fraction between 50-60%[39, 153, 154, 161]; a maximum time rate of single ventricle pressure change (i.e., max(dP/dt)) of ~1350 mmHg/s[38]; and mean arterial pressure ~80 mmHg (representative catheterization data). The value for BDG resistance was derived from the results reported by Pekkan et al.[145], while the TCPC resistance was selected as the approximate midpoint of the range reported by Sundareswaran et al.[55] It is worth noting that the reported values for compliance of the systemic and pulmonary venous beds differ from earlier publications using this model[55, 96]. Since compliance is not a global physiologic parameter but a local one[44], the total compliance was prescribed based on the values of Kelly et al.[43], but those values were halved to account for the explicit representation of the superior/inferior, left/right circuits. Finally, all resistances are reported in Table 7.2 in terms of Wood units (WU ≡ mmHg*min/L).

The primary metrics of interest were the changes from Glenn to Fontan in the cavopulmonary pressures and flows, as well as the cardiac output.

**Table 7.2 Summary of Values Prescribed in the Lumped Parameter Model**

| Parameter | Lumped Parameter Value |
|---|---|
| $C_{SV}$, ml/mmHg | 332.5 (Total) |
| $C_{SA}$, ml/mmHg | 0.5 |
| $R_{SSV}$, WU | 50 |
| $R_{ISV}$, WU | 45 |
| $C_{PV}$, ml/mmHg | 80 (Total) |
| $C_{PA}$, ml/mmHg | 4.12 |
| $R_{RPV}$, WU | 6 |
| $R_{LPV}$, WU | 7 |
| $R_{CPC}$, WU | 0.1 (Glenn)<br>1.0 (Fontan) |
| $R_{MV/AV}$, WU | 0.01 |
| $C_V$(min), ml/mmHg | 0.05 |
| $C_V$(max), ml/mmHg | 6.5 |

C = Compliance; CPC = cavopulmonary connection; MV, AV = mitral, aortic valves; PA = pulmonary arteries; PV = pulmonary veins; R = Resistance; SA = systemic arteries; SSV, ISV = superior, inferior systemic veins; V = ventricle; MV, AV = mitral, aortic valves; RPV, LPV = right, left pulmonary veins; WU = Wood Units

#### 7.2.2.2 Prospective Surgical Planning

The basic surgical planning procedure consists of a number of steps, which were followed for all cases.

- Anatomic Reconstruction: As for the general CFD procedure described in §4.1.3.1, the patient-specific cavopulmonary vasculature is reconstructed from CMR images. However, there are additional requirements for these cases given the need to include surrounding anatomical landmarks (i.e., ventricle, atrium, pulmonary veins, and aorta) and, in some cases, the native IVC/hepatic veins

into the reconstruction to provide important inputs into the virtual surgery interface.

- Velocity Segmentation: This procedure was described in §4.1.3.2.
- Virtual Surgery: As described in §4.6, the state-of-the-art SURGEM software provides a robust interface to effectively mimic the Fontan procedure and investigate any number of patient-specific surgical options[110]. Following anatomic reconstruction, the engineering and clinical teams consult to discuss the particular details and challenges of a given case and formulate a modeling plan: what options are being considered for surgery and what other potential options exist. The patient anatomy is then loaded into SURGEM and the discussed options are created.
- "Stitching": One of the current limitations of the SURGEM software is the inability to automatically mate the virtual Fontan baffle to the underlying patient anatomy. Instead, the baffle creation step must currently be followed by a stitching step to manually perform this mating process using the Geomagic Studio software. Stitching can add considerable time to the model creation process as well as introducing an element of user dependence; it is important to ensure that the final result resembles typical Fontan connections (as from the database) and does not taken on unrealistic characteristics through the stitching process.
- Boundary Condition Prescription: Following the stitching phase, the CFD evaluation proceeds the same as in previous chapters with one important distinction. That is, the flow conditions at which the TCPC should be evaluated are not necessarily the same as what was measured with pre-operative PC CMR. In fact, the exact boundary conditions of interest are unknown given the generally poor understanding of post-operative physiologic changes, which is the

underlying motivation for the serial patient flow analysis. As such, the procedure for prescribing the boundary conditions of interest varied slightly from patient to patient, as will be detailed in the appropriate sections, but were based on the use of pre-operative measurements with hypothesis-based deviations.

In general, time-averaged flow conditions were used for patients undergoing their initial Fontan procedure since the measured pulsatility in the IVC was assumed to be largely dictated by its pre-operative connection to the atrium; cases requiring surgical revision were typically modeled with pulsatile flow boundary conditions. The PA split was parametrically varied (for the PAVM cases) based on the assumption that PAVM regression would increase resistance to the affected side and thus shift flow to the opposite lung. The effect of the Fontan baffle design on the internal connection resistance (insofar as it determines the PA split) was generally ignored; however, in select cases in which it was thought to be potentially non-negligible, a post-hoc resistance analysis was performed to estimate potential flow split changes.

### 7.2.3 Statistical Methods

Since this specific aim was primarily focused on small sample sizes and individual patient case studies, statistical evaluations were limited and generally descriptive in nature. Where appropriate, Pearson correlations and t-test comparisons were used to test for relationships between variables or groups.

## 7.3 Serial Flow Study Results

### 7.3.1 Patient Results

A statistically significant decrease in CI was observed (5.27 vs. 3.35 L/min/m$^2$; Figure 7.2). Figure 7.3 shows the averaged flows in each component of the Fontan pathway before and after TCPC. Consistent with the decrease in CI, significant decreases in both IVC (2.48 vs. 1.59 L/min/m$^2$) and SVC flows (2.07 vs. 1.35 L/min/m$^2$; after removing the patient with 1.5 ventricle repair) were observed. There was also a decrease in the IVC percentage of total caval flow in these patients (right side of Figure 7.3), although this difference was not statistically significant. With respect to pulmonary arterial flow, a significant increase in LPA flow was observed (0.88 vs. 1.40 L/min/m$^2$), while there was no significant change (despite a decreasing trend) in RPA flow.

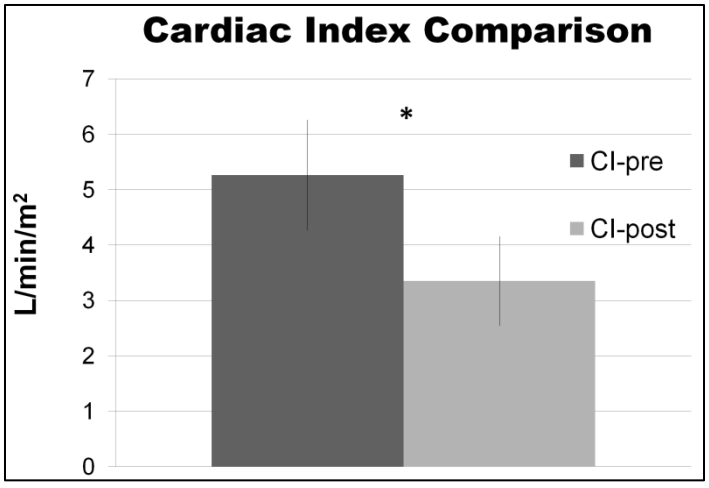


**Figure 7.2 Mean (± standard deviation) cardiac index values from phase contrast CMR data. Post-Fontan values were significantly less ($p<0.05$).**

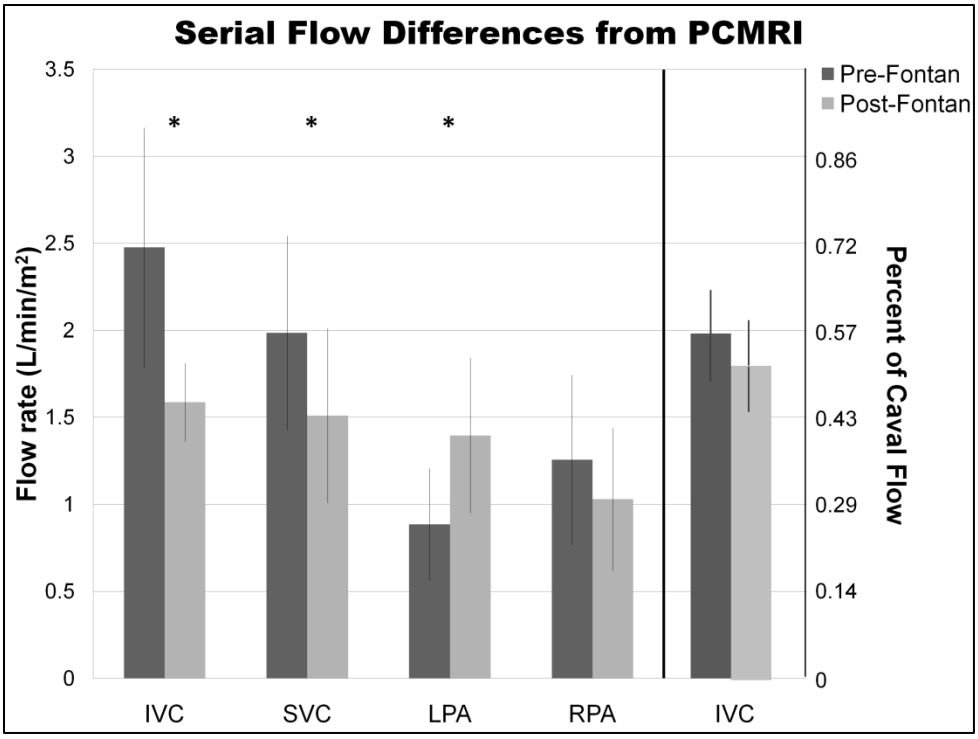


**Figure 7.3 Mean (± standard deviation) flows (left side of the figure), normalized by body surface area, through each of the vessels of the Fontan connection before and after surgery. A significant increase was seen in the LPA, while IVC flow change approached significance. Mean (± standard deviation) of the IVC percentage of total caval flow (right side of figure).**

To better assess the serial differences of caval flow distribution to the lungs, Figure 7.4 shows the changes in LPA percentage of total pulmonary flow for all 7 patients. The slope of each line is indicative of the degree of change for each patient with large slopes corresponding to large changes. Large variations across patients were seen in this regard, with only one instance in which the LPA percentage remained constant pre- and post-operatively.

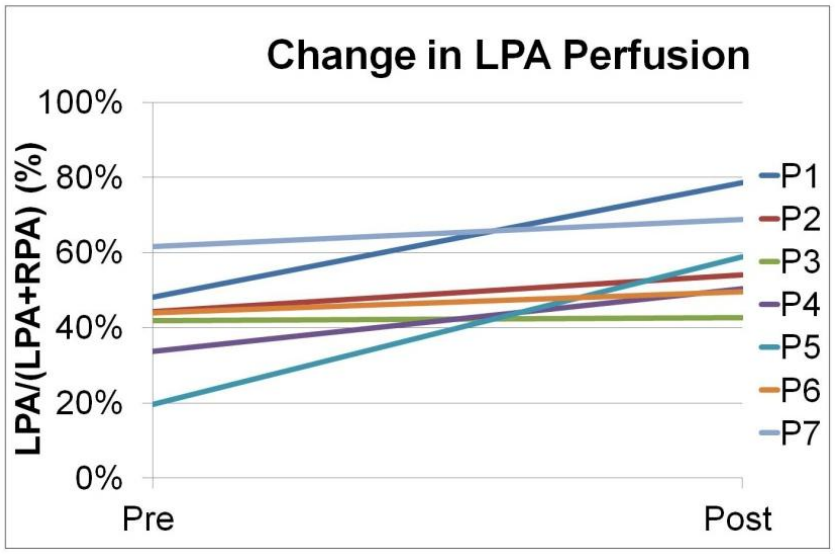


**Figure 7.4 Change in percentage of LPA flow (to total pulmonary flow) for each patient. Only one line appears to be flat, denoting changes in the left/right pulmonary flow distribution of all other cases.**

### 7.3.2 Lumped Parameter Results

The results of the lumped parameter simulations are presented in Table 7.3 and Table 7.4. The comparable values from the patient results are reported where appropriate. As with the patient data, there was a large (42%) decrease in cardiac output between the Glenn and TCPC models as a result of the altered ventricular loading conditions. This fact is most evident by the change in end diastolic volume, which decreased by 25%. By comparison, the end systolic volume decreased by ~6%. These results (i.e., near constant end systolic volume with decreasing end diastolic volume) agree well with the findings of Fogel et al.[33] The altered cardiac function resulted in decreases in caval flows- 44/40% for the IVC/SVC, respectively, while increases in both LPA and RPA flows

(27/26%, respectively) were observed. The percentage of IVC flow decreased from 54.2% to 52.6%, while the percentage of LPA flow was little changed (46.0% vs. 46.2%). Table 7.3 and Table 7.4 also show that pressures throughout the system (except in the IVC) decreased. It is important to note that no changes were made to the systemic arterial properties of the model from the BDG to TCPC configurations. Thus, while it is recognized that these pressure values are non-physiologic and not directly consistent with clinical observations, they are consistent with an increased circulating blood volume in the TCPC circuit[162], and the need for significant fluid loading in the acute post-operative period. Numerous other adaptive mechanisms are also likely to be involved.

**Table 7.3 Summary of ventricular function changes predicted by the mathematical model**

| Cardiac Function | Glenn | TCPC | % Difference | % Difference (Patient Data) |
|---|---|---|---|---|
| CO (L/min) | 2.99 | 1.73 | -42.1% | -31% |
| ESV (mL) | 32 | 30 | -6.3% | (NA)* |
| EDV (mL) | 69 | 52 | -24.6% | (NA) |
| SV (mL) | 37 | 22 | -40.5% | (NA) |
| EF (%) | 53.6 | 42.3 | -21.1% | (NA) |
| Ao $P_{max}$ | 98.1 | 61.8 | -37.1% | (NA) |
| Ao $P_{min}$ | 58.9 | 39.1 | -33.7% | (NA) |
| Ao $P_{mean}$ | 79.5 | 50.9 | -36.0% | (NA) |
| max(dP/dt) | 1360 | 813 | -40.2% | (NA) |

*NA- data not available

**Table 7.4 Summary of TCPC hemodynamic changes predicted by the mathematical model**

| Fontan Hemodynamics | Glenn | TCPC | % Difference | % Difference (Patient Data) |
|---|---|---|---|---|
| $Q_{IVC}$ (L/min) | 1.62 | 0.91 | -43.8% | -36% |
| $Q_{SVC}$ (L/min) | 1.37 | 0.82 | -40.1% | -35% |
| $Q_{LPA}$ (L/min) | 0.63 | 0.80 | 27.0% | 58% |
| $Q_{RPA}$ (L/min) | 0.74 | 0.93 | 25.7% | -18% |
| $P_{IVC}$ (mmHg) | 6.6 | 10.0 | 50.2% | (NA)* |
| $P_{SVC}$ (mmHg) | 11.2 | 9.9 | -11.1% | (NA) |
| $P_{PA}$ (mmHg) | 11.0 | 9.5 | -13.7% | (NA) |

*NA- data not available

### 7.3.3 Section Discussion and Summary

The insights provided by the novel combination of serial patient data with lumped parameter modeling in this study are twofold: 1) we see the mechanism by which the creation of the completed Fontan series circuit affects and impairs cardiac function; and 2) we see for the first time how such changes in cardiac output and ventricular function impact blood flow at the level of the TCPC. In the first case, it has been hypothesized that the altered ventricular function after the Fontan procedure is the result of significant changes to ventricular loading conditions, especially decreased preload[40, 55, 163], despite the fact that the single ventricle is already considered to be “unloaded” at the Glenn stage. The findings of lower end diastolic volume and stroke volume (model results) and the subsequent reductions in CI noted in both the patient and model results support this hypothesis. It also stands to reason based on this mechanism that the severity of these responses will be dependent on the resistance to flow through both the TCPC and the

pulmonary circuit, which supports the use of surgical planning or other hemodynamic optimization strategies for the TCPC to minimize its contributions in this regard.

With respect to TCPC flow changes, both caval flow rates significantly decreased, consistent with decreased cardiac output. Further, both the patient and modeling results suggest a redistribution of caval flow balance (with higher SVC percentages), which would be expected to have an impact on the local hemodynamics. The likely mechanism mediating this effect is the increased afterload resistance to IVC flow posed by the TCPC and pulmonary vasculature (just as they altered preload resistance to the ventricle).

For the pulmonary arteries, the additional source of flow (from the IVC) translated into a significant increase in LPA flow post-operatively; however, the finding of decreased RPA flow in the patient data is puzzling. The model results (showing an increase) agree with intuition in this case as there is no apparent reason that RPA flow should behave so differently from the LPA, nor why the percentage of LPA flow increased post-operatively in each case. Absent any geometric bias, uneven sampling of inherently large variations (i.e., type II error) could be a primary contributor. Alternatively, in a large patient series using the same acquisition protocol, Whitehead et al. noted challenges with RPA flow measurement related to the proximity of the measurement plane to the caval junction and right upper lobe branch point[142]. However, despite these potential uncertainties, it is difficult to completely dismiss the observed heterogeneity in PA flow distribution changes as an actual effect because of the possibility of complex physiologic adaptation to surgery or hemodynamic changes. Potential explanations include the confounding effects of residual pleural effusions or PAVM, or potential changes in right lung resistance post-Glenn. More research is needed to better understand these trends.

In large part, the significance of this work lies in how the results can be used to improve the accuracy of surgical planning results, given the rising interest in implementing such

methods. Until now, such changes have been neglected in prospective modeling studies, but the present data show that the relevant physiologic changes are not insignificant. Chief among such observations is the variation of PA flow distribution pre- and post-operatively (Figure 7.4). A similar observation was made in a recent study[94], but only in a single patient. These variations will obviously have a significant impact on the both dynamics of flow through the Fontan pathway as well as the distribution of the flow, particularly of the IVC (and thus hepatic) to the respective PAs[105]. Critically, the study by Pennati[94] also demonstrated, as is confirmed by the present results, that lumped parameter modeling may not be able to capture the entirety of pulmonary arterial adaptation following surgery because of the multi-factorial complexity of the response. Hence, while coupling CFD solvers to lower dimensional models[95, 164] is a positive strategy for anticipating *some* of the physiologic response to TCPC surgery and undoubtedly a necessary next step for the development of these surgical planning techniques, it is not entirely self-sufficient; user input, guided by past patient/clinical experience, is still required to ensure the surgical options are evaluated over the appropriate range of possible outcomes.

## 7.4 Prospective Patient Case Studies

### 7.4.1 Overview

In total, ten patient cases will be presented: seven patients from CHOP, two patients from Children's Healthcare of Atlanta (CHOA), and one from Boston Children's Hospital (CHB). The prospective Fontan surgical planning experience to date includes the contributions of multiple researchers among whom the work has been divided; the ten cases presented here (unless otherwise credited) represent the contributions of the PhD candidate (CMH) with no additional selection criteria. Furthermore, there is not yet a

formally established protocol for patient enrollment in surgical planning; instead, the recruitment is performed in the respective clinical centers on ad hoc, as needed basis. Details on the cases presented, including their 'M' designations in the surgical planning database are provided in Table 7.5. In half the cases, the planned surgery represented a revision of an existing Fontan connection, while for the other half it was the primary Fontan procedure. As discussed in §7.2.2.2, this factor played a primary role in dictating the boundary condition assumptions made for the study. A minimum of three surgical options were considered in each case (with one exception), with a maximum of eight. This number was primarily dictated by the number of viable options as well as the time available to perform the modeling study.

The data presented in the table as well as in the results sections indicated are in chronological order of the modeling studies, which were performed between August 2010 and June 2012. This order is not necessarily consistent with the applied numbering scheme of the patient identifiers. For a general summary of the surgical planning experience without the case-by-case detail, the reader is referred to §7.4.12.

**Table 7.5 Details for Surgical Planning Patients**

| | Age | Gender | Surgical Status | Reason for referral | PAVM location | Section |
|---|---|---|---|---|---|---|
| **CHOA_M2** | 18 | F | Post-Fontan | PAVM | Right | 7.4.2 |
| **CHOP_M9** | 2 | M | Kawashima | PAVM | Right | 7.4.3 |
| **CHOP_M10** | 3 | F | Kawashima | PAVM | Left | 7.4.4 |
| **CHOP_M12** | 2 | M | Bilateral BDG | PAVM | Left | 7.4.5 |
| **CHOP_M13** | 2.5 | F | Bilateral BDG | PAVM | Left | 7.4.6 |
| **CHOP_M8** | 8 | M | Post-Fontan | PAVM | Left | 7.4.7 |
| **CHB_M1** | 8 | M | Post-Fontan | PLE | N/A | 7.4.8 |
| **CHOA_M5** | 12 | F | Post-Fontan | PAVM | Right | 7.4.9 |
| **CHOP_M16** | 2 | M | Bilateral BDG | PAVM | Right | 7.4.10 |
| **CHOP_M17** | 14 | M | Post-Fontan | PAVM | Left | 7.4.11 |

### 7.4.2 CHOA_M2

This patient was an 18 year old female with interrupted IVC and azygos vein continuation to a ride-sided SVC who had developed right-lung PAVM even though the hepatic venous flow had previously been directed to the pulmonary arteries with a lateral tunnel Fontan. The pre-operative TCPC reconstruction is shown in Figure 7.5.

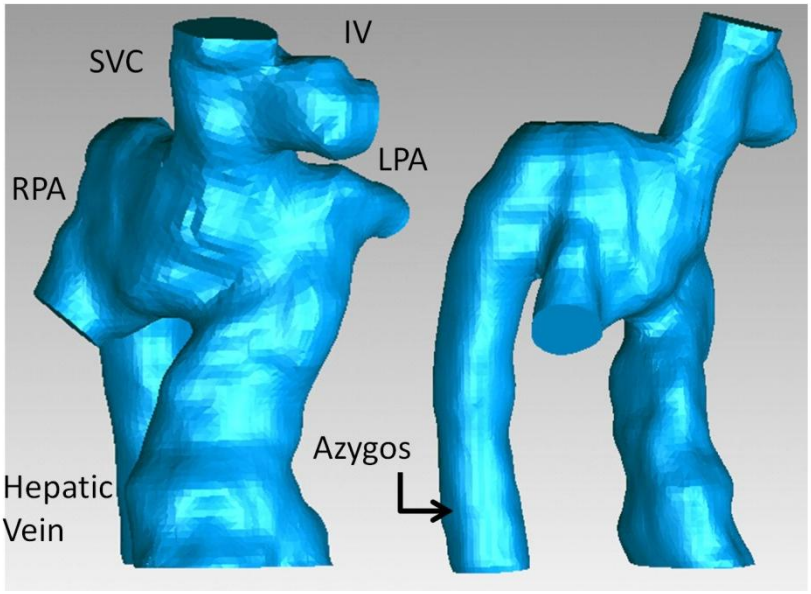


**Figure 7.5 Pre-operative anatomy for CHOA_M2 shown from anterior (left) and right sagitttal (right) perspectives.**

A significant challenge faced with the pre-operative modeling for this patient was the fact that the CMR images were not optimized for CFD modeling: the axial slice thicknesses were 10 mm. Additionally, there was significant signal dephasing at the PA junction, making it difficult to accurately resolve some connection features. Thus, the reconstruction shown in Figure 7.5 actually represents a manual combination of several different imaging acquisitions (i.e., axial, 4-chamber ventricular view, and a small sagittal 'Fontan' stack), which is far from optimal. These factors may have also contributed to the fact that the pre-operative simulations were never able to successfully recreate the unilateral hepatic flow-to-LPA streaming that would be consistent with the right lung PAVM diagnosis. Instead, as shown in Figure 7.6 the hepatic flow (yellow streamlines) was evenly divided between the LPA and RPA (50/50). This limitation was taken into

consideration in evaluating the hemodynamic performance of the subsequently modeled options.

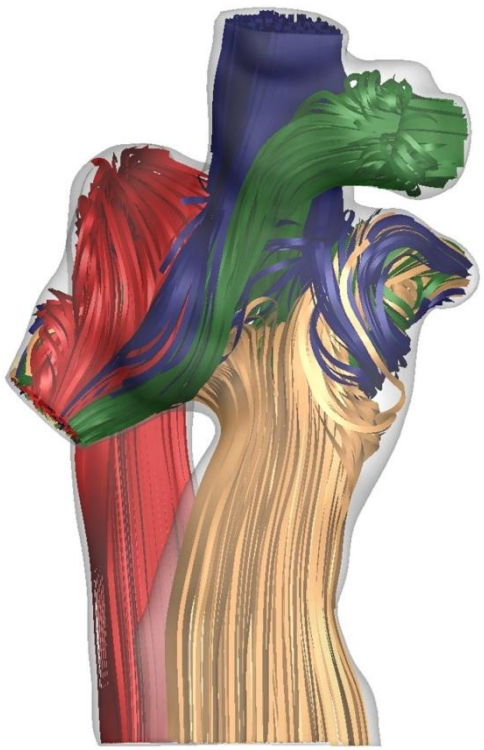

**Figure 7.6 Velocity streamlines color-coded by vessel of origin for pre-operative anatomy of CHOA_M2.**

The PC CMR-measured vessel flow rates are summarized in Table 7.6. The hepatic venous contribution to systemic return was low (17%), as expected, while the RPA carried 77% of the total pulmonary flow, which is consistent with right-sided PAVM given that it is a relatively unbalanced distribution.

**Table 7.6 Measured pre-operative flow rates for CHOA_M2**

| | Flow Rate (L/min) | Relative Distribution (%) |
|---|---|---|
| **Hepatic Vein** | 0.57 | 17 |
| **SVC** | 0.7 | 21 |
| **Az** | 1.61 | 49 |
| **Innom. Vein** | 0.43 | 13 |
| **LPA** | 0.97 | -23 |
| **RPA** | 3.3 | -77 |

A total of four different surgical options were modeled: three prospective designs and a fourth that was retrospectively considered (and constructed by modifying the post-operative anatomic reconstruction). For the three prospective designs, the rationale was that by either repositioning the Fontan connection 'centrally', anteriorly/centrally, or bifurcating the hepatic venous flow using a Y-graft, the HFD to the RPA would be improved while still maintaining an adequate distribution to the LPA. The final retrospective design was a hepatic-to-azygos connection, motivated by the studies of de Zélicourt *et al*.[105] and McElhinney *et al*.[62] These options are all shown in Figure 7.7.

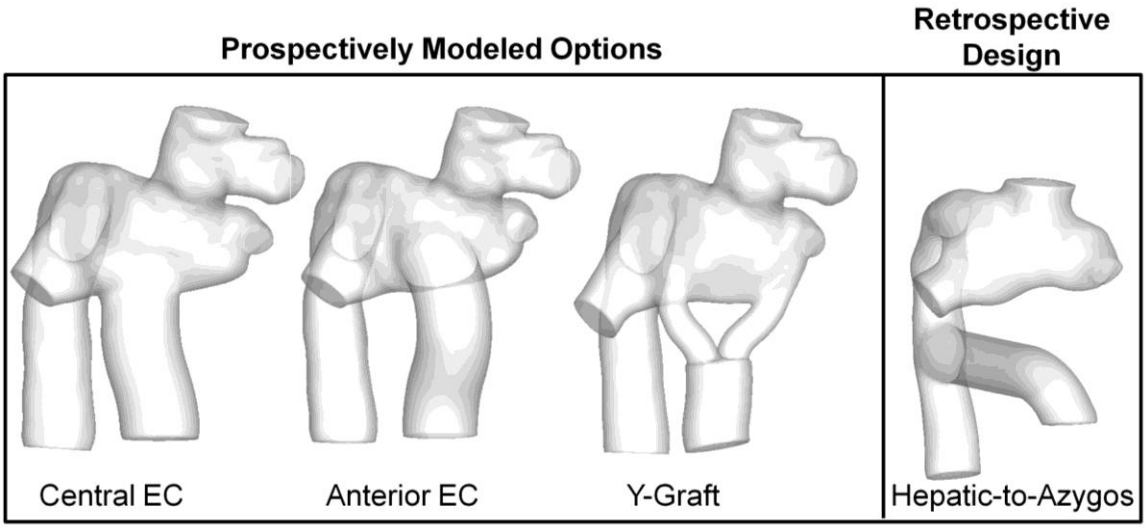


**Figure 7.7 Virtual surgical options investigated for CHOA_M2 representing two different placements of an extracardiac conduit ('Central' and 'Anterior'), a Y-Graft option, and a hepatic-to-azygos connection.**

To evaluate the prospective surgical options, three different simulations were performed with varying outflow boundary conditions, while maintaining constant inflow rates and using time-averaged conditions:

1. Pre-operatively measured conditions (23% LPA; Table 7.6)
2. 35%/65% LPA/RPA
3. 50%/50%.

Conditions 2 and 3 were intended to simulate a scenario in which the right lung PAVM regressed and the relative resistance through that lung increased, leading to a local redistribution of flow. In such a scenario, it is important to insure that a desirable flow distribution outcome can still be achieved over that range of possible conditions.

Figure 7.8 shows the results for the two EC options. As expected from prior experience[105, 124], the seemingly small change in baffle placement yielded very different quantitative outcomes because of the low flow momentum carried by the hepatic baffle

as compared to the superior venous returns. By moving the connection closer to the RPA, hepatic flow was biased toward the RPA; in fact, for two of the simulations performed for option A (without anterior curvature), the entirety of hepatic flow was directed to that lung. Introducing the anterior curvature to the baffle (option B) improved flow distributions slightly by removing the 'head-on' flow collisions with SVC flow; yet, the RPA bias was still present. Given this extreme sensitivity of results to baffle placement, these options were deemed to be undesirable.

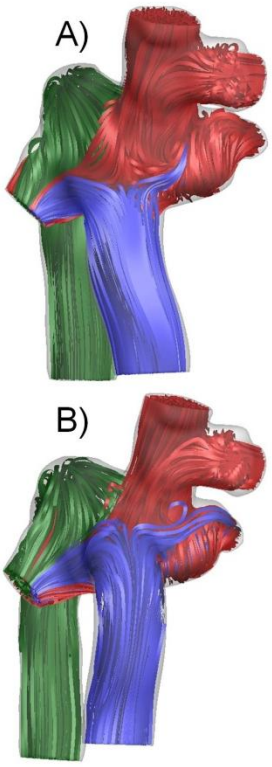


Represented by Figures

| | Sim. 1 | Sim. 2 | Sim. 3 |
|---|---|---|---|
| GFD | 23% LPA | 35% LPA | 50% LPA |
| HFD A (%LPA) | 6 | 0 | 0 |
| HFD B (%LPA) | 20 | 20 | 19 |

| | | | |
|---|---|---|---|
| Power Loss A (mW) | 4.7 | 1.9 | 2.3 |
| Power Loss B (mW) | 1.7 | 1.6 | 2.1 |

**Figure 7.8 Velocity streamline results from simulations under pre-operative BC (Sim. 1) for the extracardiac options for CHOA_M2. Hepatic venous flow is shown in blue. Tables at right provide quantitative results for HFD (top) and power loss (bottom).**

By comparison, Figure 7.9 shows the results for the virtual Y-Graft option. In this case, by placing the bifurcated branches on either lateral side of the SVC-Azygos connections, the hepatic flow (shown in blue) was predicted to distribute fairly evenly to both PAs (38% to the LPA under pre-operative flow conditions). For this reason, this approach was deemed to have improved stability and robustness compared to the extracardiac designs and was ultimately recommended and surgically implemented in August 2010.

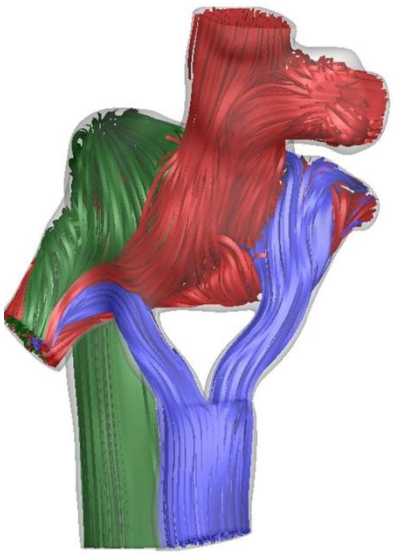

Represented by Figure

| | Sim. 1 | Sim. 2 | Sim. 3 |
|---|---|---|---|
| GFD | 23% LPA | 35% LPA | 50% LPA |
| HFD (%LPA) | 38 | 43 | 43 |
| Power Loss (mW) | 2.0 | 1.7 | 0.9 |

**Figure 7.9 Qualitative and Quantitative results for Y-Graft surgical Option for CHOA_M2. CFD predicted good HFD balance and low power losses.**

Finally, the result of the retrospective hepatic-to-azygos connection is shown in Figure 7.10, with the pre-operatively measured boundary conditions considered. This design promoted robust mixing of the inflows within the connection, leading to an HFD result

that was in close match to the global pulmonary flow split. While additional outflow splits were not explicitly modeled, this trend would be expected to lead to increased HFD-to-LPA flow with increased to total volume to that branch, making this connection potentially favorable. The two potential drawbacks are: higher power losses (3x higher than what was seen for the other options considered in Figure 7.8 and Figure 7.9), and potentially increased surgical complexity because of the posterior positioning of the azygos and its close proximity to the descending aorta.

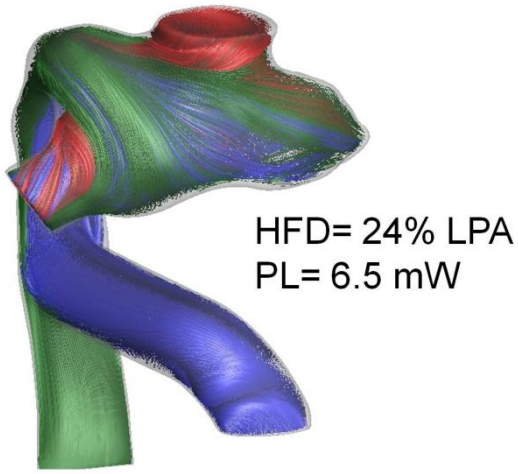


**Figure 7.10 Result from retrospectively considered hepatic-to-azygos connection for CHOA_M2 showing favorable flow distribution at the expense of higher power loss.**

### 7.4.3 CHOP_M9

This patient was a two year old male with Hypoplastic Left Heart Syndrome and Interrupted IVC who had an existing Kawashima connection, but did not have a Fontan

connection of the hepatic veins to the PAs. As a result, right lung PAVM had developed and the patient was referred for surgical planning to evaluate the possible operative options with respect to HFD. The anatomic reconstruction of the Kawashima connection is shown in red in Figure 7.11, while the measured flow rates are reported in Table 7.7.

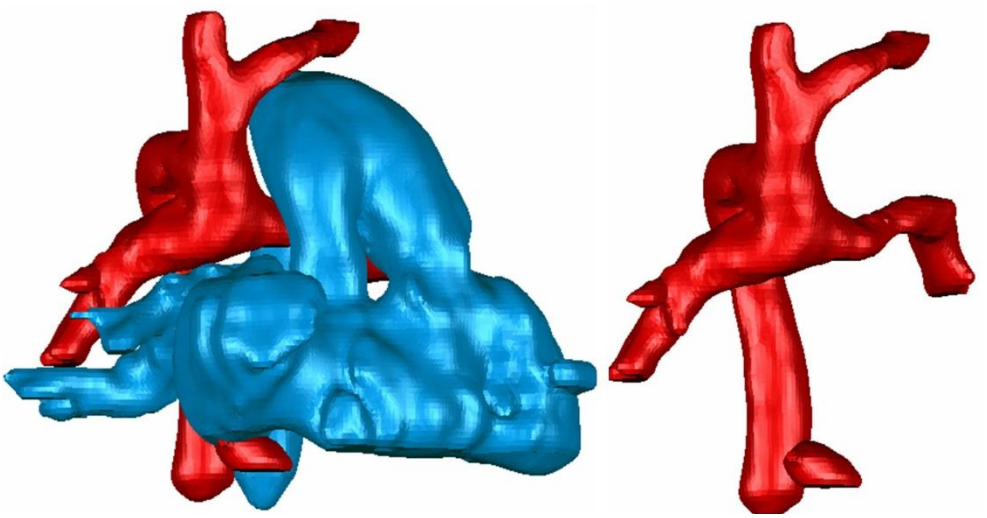

**Figure 7.11 Anatomic reconstruction for CHOP_M9 pre-operative connection with (left) and without (right) the surrounding structures (in blue).**

**Table 7.7 PC CMR-measured pre-operative flow rates for CHOP_M9**

| | Flow Rate (L/min) | Relative Distribution (%) |
|---|---|---|
| **Hepatic Vein** | 0.44 | 18 |
| **SVC** | 1.31 | 54 |
| **Az** | 0.68 | 28 |
| **LPA** | 0.5 | -34 |
| **RPA** | 0.97 | -66 |

A total of 9 surgical options were considered for this patient: three extracardiac conduits, two Y-grafts, three 'flow divider' options (one per extracardiac design), and one hepatic-to-azygos connection (retrospectively modeled). The first two extracardiac models employed a 20 mm conduit to the SVC and varied slightly by offset, with one option being positioned slightly closer to the RPA. A 5 mm cylindrical hole was created in the middle of the distal end of each of these baffles to create the first two flow divider options. The Y-graft was modeled as a 20x10 mm aorto-iliac graft. After this first round of options was modeled, it was determined that the 20 mm graft design was too large for this patient given that the hepatic venous baffle typically carries much lower volume than a typical Fontan. A second round of options was thus created using 14 mm grafts (including 14x7 mm Y-graft) and using a triangular-shaped insert for the flow divider option to minimize flow stagnation/separation points as would be expected with a circular profile insert. These options are shown in Figure 7.12.

As with CHOA_M2, the 20 mm-based options were all evaluated at a series of different pulmonary flow splits (34%, 50%, and 60% LPA; assuming regression of right PAVM) for a constant set of time-averaged inlet flow conditions based on the pre-operative measurements (Table 7.7). The second round of smaller options (14 mm-based) were only run under the pre-operatively measured conditions because of limited time constraints prior to surgery.

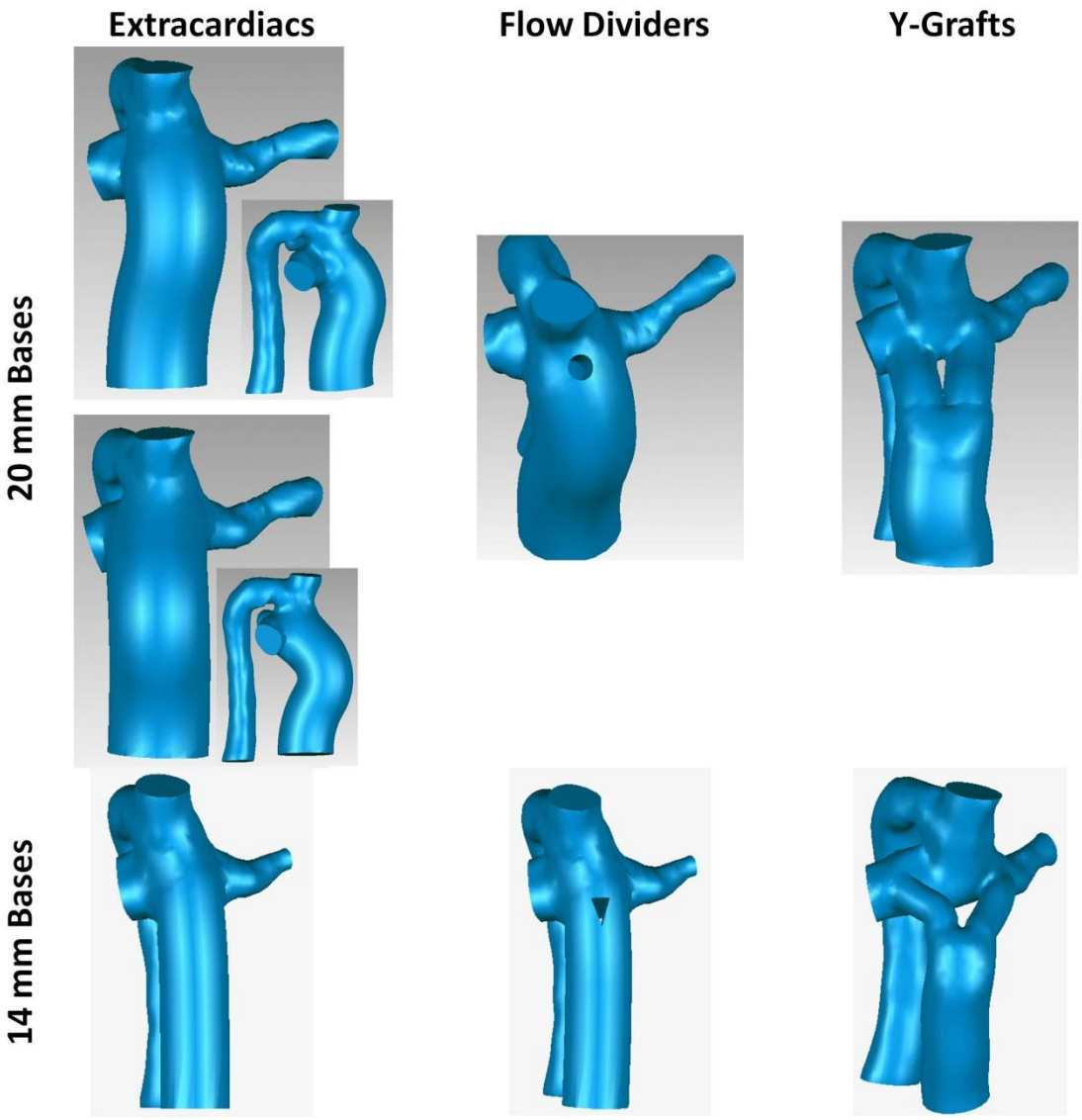


**Figure 7.12 Surgical options created and evaluated for CHOP_M9 encompassing extracardiac connections of different sizes (20 mm or 14 mm) and positions, flow dividers inserted in each associated extracardiac, and Y-Grafts of different sizes (20x10 mm and 14x7 mm).**

The results for the 20 mm extracardiac options with and without circular flow dividers are shown in Figure 7.13. Qualitatively, the flow in the hepatic baffle was very disturbed: the combination of low hepatic flow volume, large baffle size, and relatively high momentum SVC flow led to SVC penetration into the baffle and significant mixing. From the included plot it can be seen that even with a seemingly small difference in baffle placement between EC option 1 and EC option 2, the two options yielded HFD values at opposite extremes. Interestingly, the introduction of the flow dividers to both cases improved the HFD performance of both connections (i.e., moved the results closer to 50%), despite a similar qualitative appearance of disturbed flow within the Fontan baffle. While the mechanism for this improvement is not obvious from the visual results, it is likely that the presence of the divider actually helped to reduce SVC flow penetration into the baffle and subsequent constraining of hepatic flow preferentially to one side. Regardless, both options were extremely sensitive to placement and, considering the interactions with SVC flow, were extremely unpredictable.

By comparison, Figure 7.14 shows the results for the 14 mm extracardiac models. The smaller baffle improved hepatic flow momentum and reduced (but did not remove) SVC flow penetration. By virtue of a slight left offset, the non-divider option resulted in 73% hepatic flow to the left (measured flow conditions). Interestingly, the divider in this case did not moderate HFD as in the prior models (i.e., move it closer to 50/50). Instead, the flow characteristics changed completely because the SVC flow restricted passage through the left side of the divider and the distribution simply changed from one extreme (73% left) to the other (63% right).

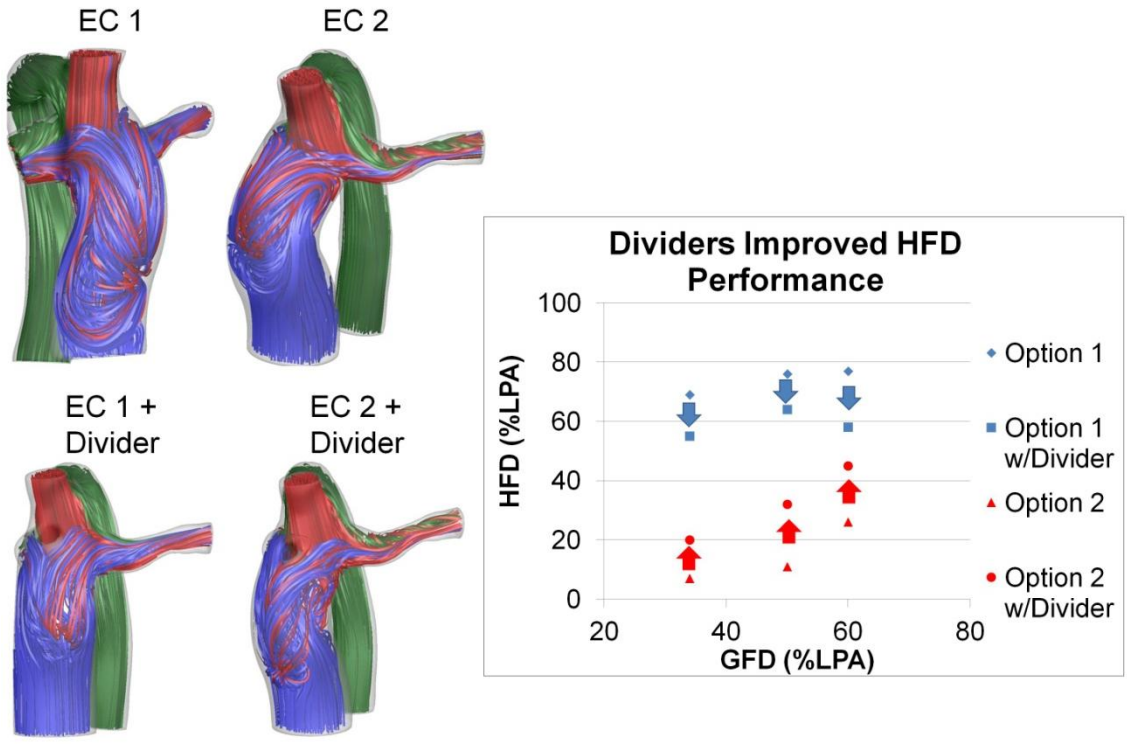


**Figure 7.13 Results for 20 mm extracardiac options for CHOP_M9 with and without flow dividers inserted. For these particular models, the presence of the flow dividers improved HFD performance for all investigated flow conditions.**

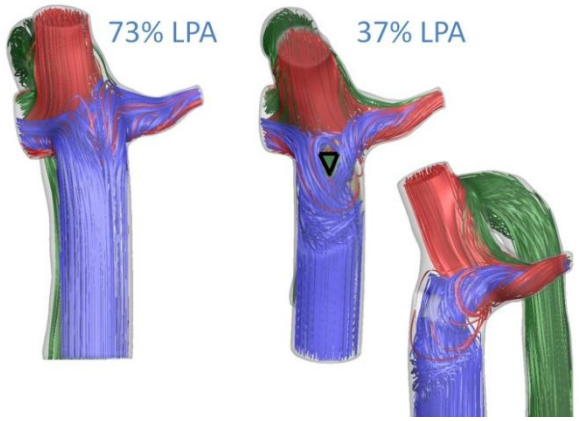


**Figure 7.14 Results for 14 mm extracardiac option for CHOP_M9 with (left) and without (right) a (triangular) flow divider (outlined in black). The flow divider result is additionally shown from the left (far right) to highlight the flow dynamic with the SVC. Rather than improving flow distribution in this case, the divider drastically changed qualitative performance and characteristics.**

The results of the two Y-Graft sizes investigated are shown in Figure 7.15. Because the SVC and azygos vein join the PAs at a single location, positioning the branches laterally to either side was deemed to be surgically feasible. For both options, SVC interaction with flow through the left branch is apparent (as with the left side of the flow divider in Figure 7.14), but appears to be more extensive with the larger (20-10) graft size. For the larger graft, increasing LPA flow also increased HFD to the LPA, a trend that was assumed would hold true for the 14-7 design. For these reasons, the 14-7 mm Y-Graft design was selected and surgically implemented in December 2010.

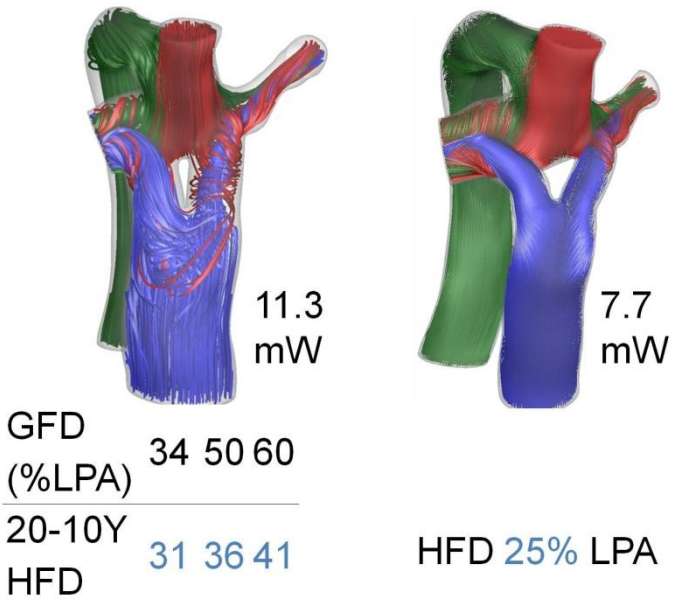


**Figure 7.15 Results from the 20-10 mm Y-Graft (left) and the 14-7 mm Y-Graft (right). HFD values listed in table below figures, power loss values (for 34% GFD condition) listed to the right.**

As a brief addendum, a hepatic-to-azygos connection was retrospectively modeled for this patient under pre-operatively measured flow conditions (as for CHOA_M2), with the result shown in Figure 7.16. The HFD result was comparable to the Y-Graft options, but with higher power loss.

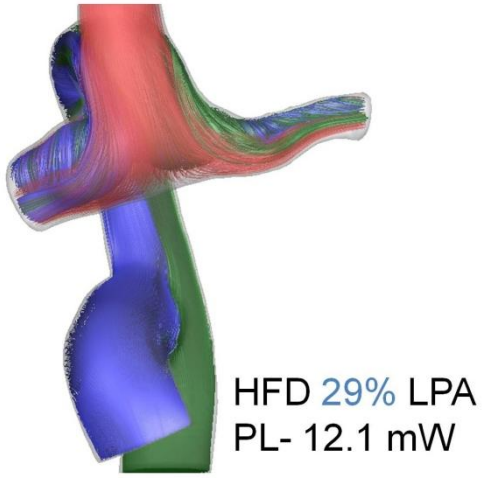


**Figure 7.16 Results of retrospective analysis of hepatic-to-azygos connection for CHOP_M9.**

### 7.4.4 CHOP_M10

This patient was a 3 year old female with pulmonary atresia with interrupted IVC and azygos vein continuation. Like CHOP_M9, she had a previous Kawashima connection but hepatic flow still drained into the atrium and left-sided PAVM had developed. Surgical planning was requested to investigate the flow distribution characteristics of the

available options. Reconstructed patient anatomy is shown in Figure 7.17 and measured flow rates are provided in Table 7.8.

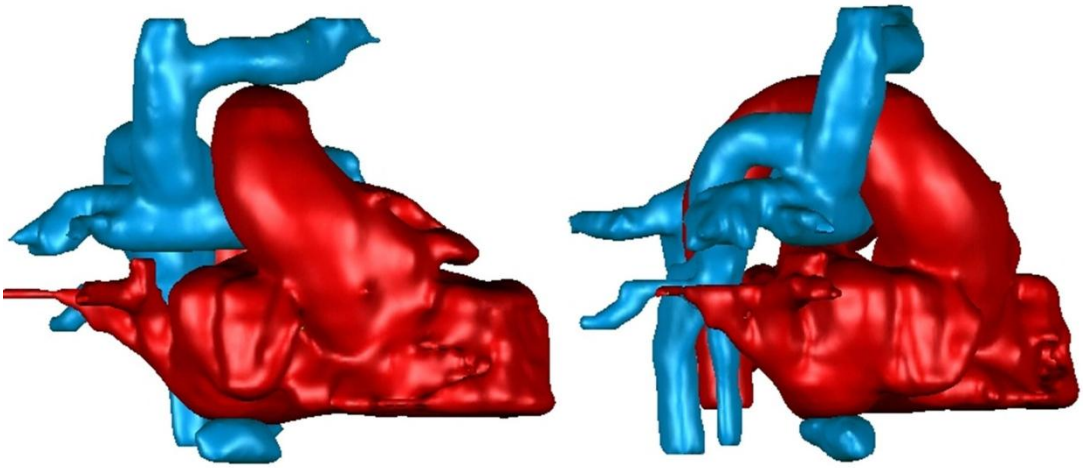

**Figure 7.17 Reconstructed Kawashima connection (in blue) and surrounding heart and vessels (in red) for CHOP_M10.**

**Table 7.8 PC CMR measured pre-operative flow conditions for CHOP_M10**

| | Flow Rate (L/min) | Relative Distribution (%) |
|---|---|---|
| **Hepatic Vein** | 0.35 | 18 |
| **SVC** | 1.09 | 56 |
| **Az** | 0.49 | 26 |
| **LPA** | 1.37 | -76 |
| **RPA** | 0.44 | -24 |

Six options were considered for this case, as shown in Figure 7.18: two extracardiac options, two Y-Grafts (18x9 mm and 14x7 mm), a hepatic-to-azygos, and a hybrid Y-Graft to azygos connection ('H-Graft'). In addition to the pre-operatively measured flow conditions (76% to the LPA), each of these options was also evaluated at 65/35% and 55/45% LPA/RPA flow splits (assuming regression of left-sided PAVM) with a constant set of time-averaged inflow conditions.

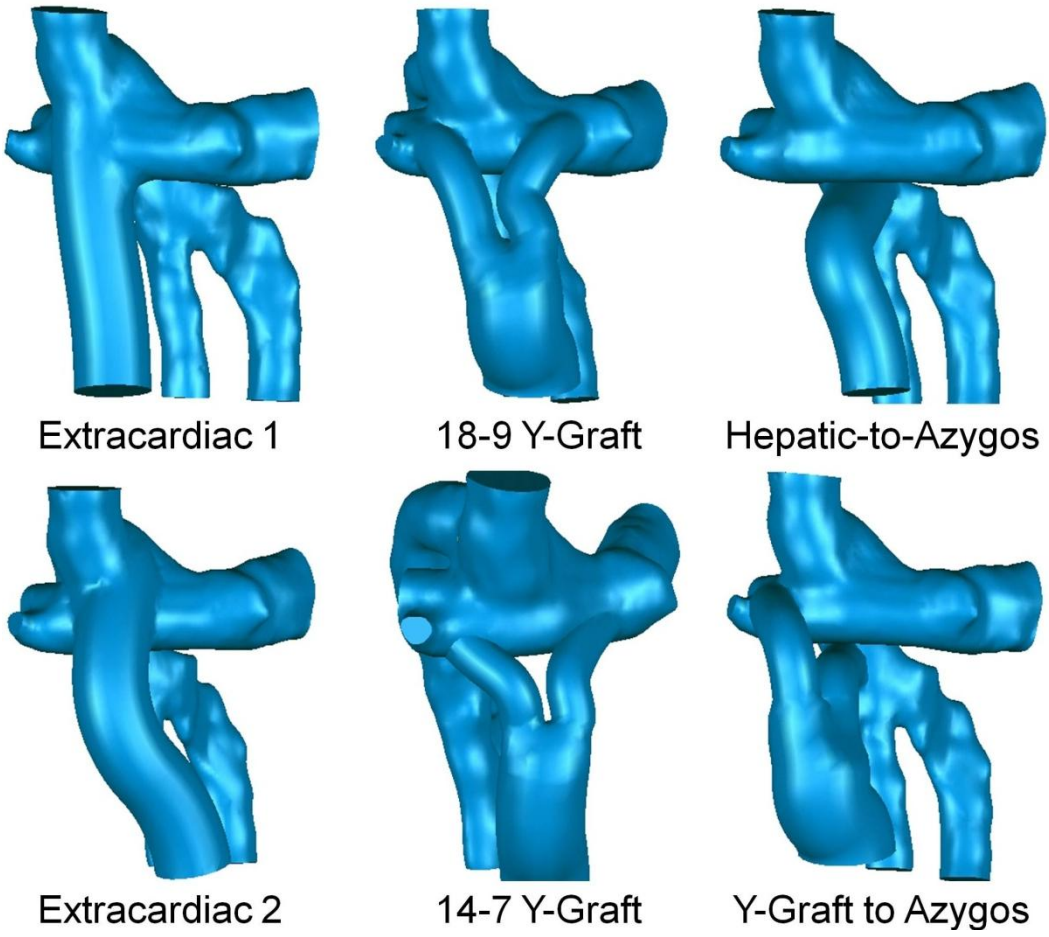


**Figure 7.18 Surgical options considered for CHOP_M10 encompassing two extracardiac models, two Y-Grafts of different sizes (18x9 mm and 14x7 mm), a hepatic-to-azygos and a Y-Graft to azygos.**

Results for the two extracardiac options are shown in Figure 7.19. As with CHOP_M9, flow through the hepatic baffle is seen to be adversely affected through direct collision with higher momentum superior flows, particularly for EC1 (Figure 7.19, left). Both options favored HFD to the LPA at all investigated flow splits (and were relatively consistent with respect to each other) despite the fact that attempts were made with the first option to introduce no offset of the baffle with respect to the SVC. Yet again, this finding underscores the placement sensitivity of extracardiac conduits in cases of interrupted IVC.

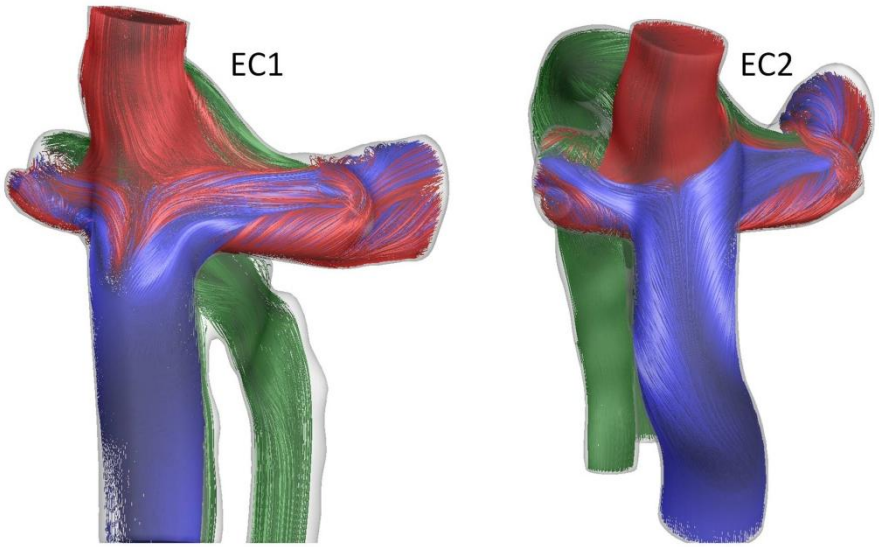


| GFD (%LPA) | 76 | 65 | 55 |
|---|---|---|---|
| HFD EC1 | 89 | 77 | 65 |
| HFD EC2 | 80 | 77 | 66 |

**Figure 7.19 Velocity for the two extracardiac options for CHOP_M10 and associated HFD performance over a range of PA flow splits. Images shown correspond to 76% LPA GFD condition.**

The Y-graft results are shown in Figure 7.20 and despite the size and (slight) positioning disparities, the velocity streamlines and HFD measures are very similar across options. Furthermore, the HFD values are nearly perfectly balanced and show relative insensitivity to changing global flow split. For these reasons, the 14x9 mm Y-graft was selected and surgically implemented in January 2011.

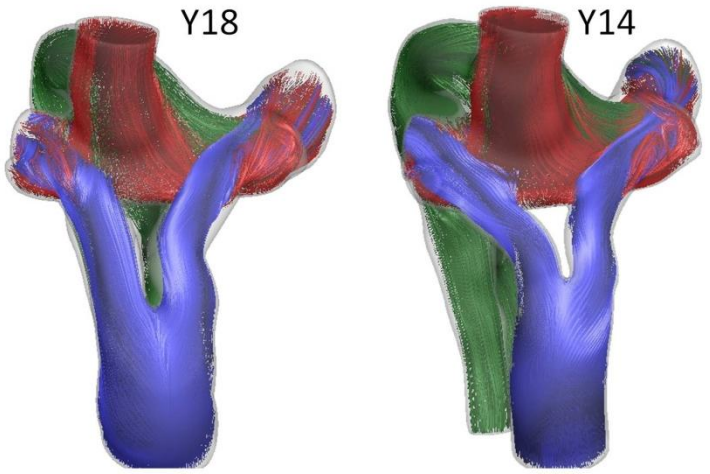


| GFD (%LPA) | 76 | 65 | 55 |
|---|---|---|---|
| HFD Y18 | 58 | 53 | 51 |
| HFD Y14 | 58 | 58 | 54 |

**Figure 7.20 Velocity for the two Y-Graft options (18x9 mm and 14x7 mm) for CHOP_M10 and associated HFD performance over a range of PA flow splits. Images shown correspond to 76% LPA GFD condition.**

Finally, Figure 7.21 shows the results for the H-Graft and hepatic-to-azygos connections. The H-Graft was by far the worst performer of the investigated options with respect to

HFD as all the hepatic flow (even the portion diverted through the azygos vein) was constrained to the RPA. However, it is worth noting that if the design had been reversed such that the PA-directed branch was connected on the left rather than the right, this option may have been more favorable with hepatic flow delivered to both lungs. However, these benefits would likely have been negligible as compared to the standard Y-Graft options. The hepatic-to-azygos connection again performed well, but was more sensitive to PA flow split and arguably more surgically challenging than the Y-graft, and so was not selected.

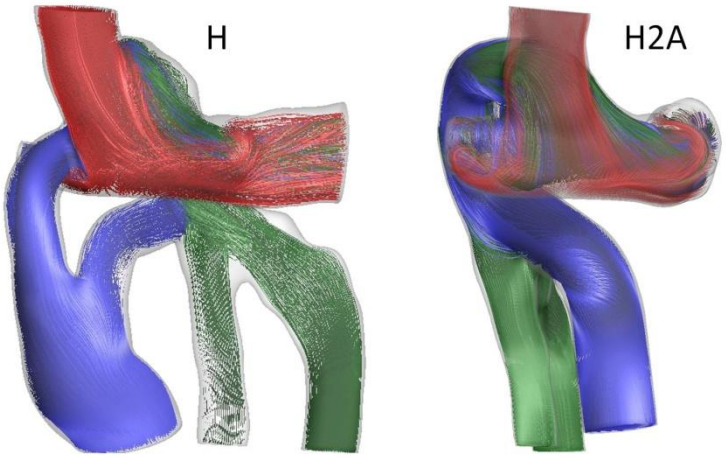


**Figure 7.21 Velocity for the H-Graft and hepatic-to-azygos (H2A) options for CHOP_M10 and associated HFD performance over a range of PA flow splits. Images shown correspond to 76% LPA GFD condition.**

### 7.4.5 CHOP_M12

It is noted that the credit for completing the study for this patient goes to Maria Restrepo (Georgia Tech); brief details are included here because of relevance to the later analysis for post-operative data.

This patient was a two year old male with bilateral bidirectional Glenn connections who had developed bilateral PAVM prior to Fontan completion. The patient-specific anatomic reconstruction is shown in Figure 7.22, while the measured flow conditions are in Table 7.9.

Figure 7.23 shows the four virtual options created for this patient consisting of two 20 mm extracardiac conduits and two 20x10 mm Y-Grafts. Differences of angles and offsets between like options were intentionally small based on the desire to evaluate option sensitivity to small perturbations in surgical implementation.

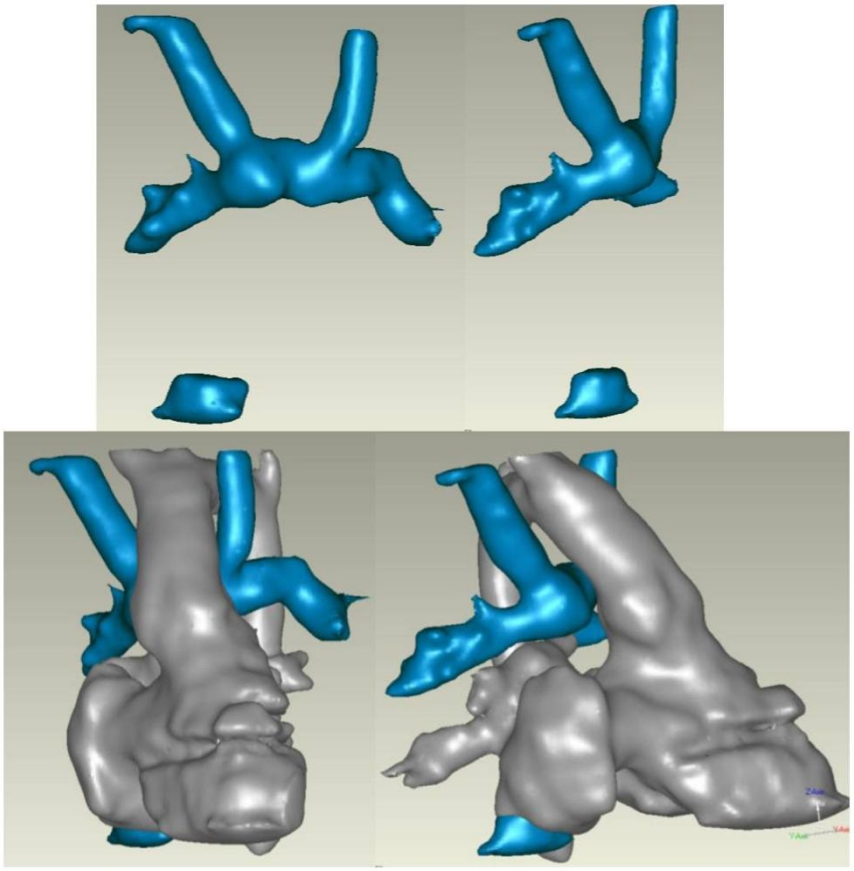

**Figure 7.22 Anatomic reconstruction of the bilateral bidirectional Glenn (in blue) and surrounding anatomy (in grey) for CHOP_M12.**

**Table 7.9 PC CMR measured pre-operative flow conditions for CHOP_M12**

| | Flow Rate (L/min) | Relative Distribution (%) |
|---|---|---|
| **IVC** | 1.27 | 56 |
| **RSVC** | 0.57 | 25 |
| **LSVC** | 0.42 | 19 |
| **LPA** | 0.61 | -62 |
| **RPA** | 0.38 | -38 |

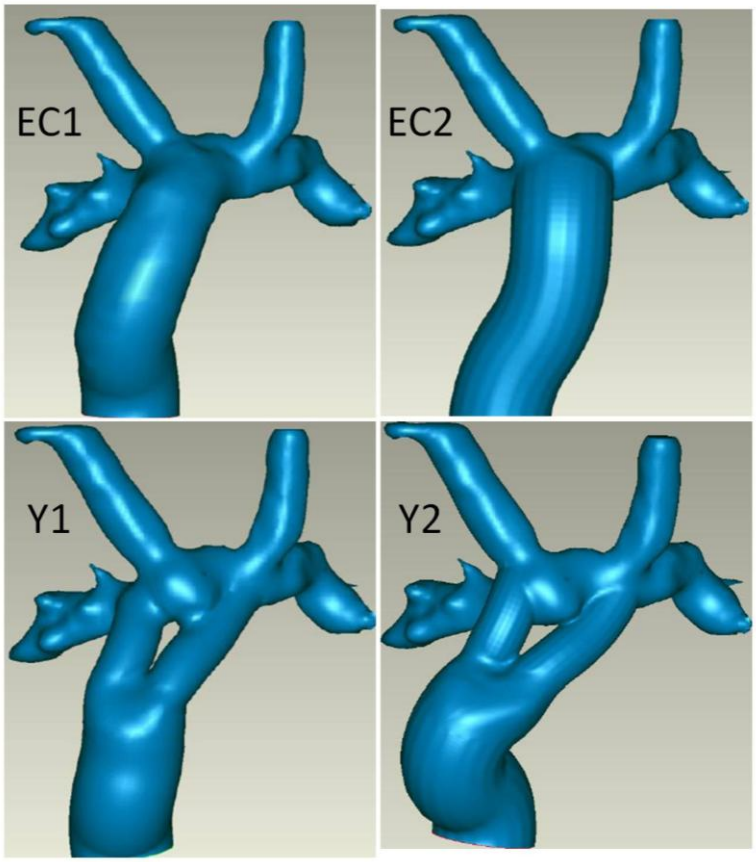


**Figure 7.23 Surgical options for Fontan surgery considered for CHOP_M12 consisting of two extracardiac connections and two Y-Graft connections varying primarily by baffle angles and offsets.**

Figure 7.24 shows the results for the extracardiac connections revealing very subtle qualitative differences in flow features. EC2 was positioned slightly further to the left but less angled to the left and as a result, its HFD-GFD curve is shifted up (note the location of the first point) relative to EC1. However, the slopes of the respective responses to changing GFD (40, 50, 70% LPA in addition to the pre-operative measurements) were fairly consistent.

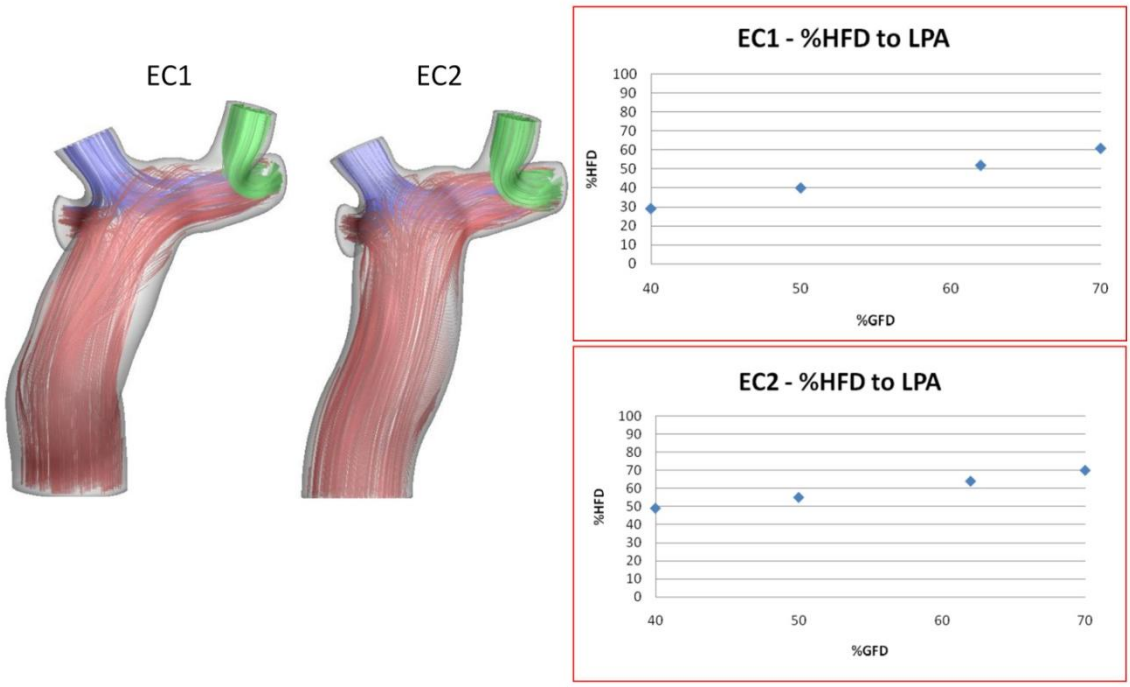


**Figure 7.24 Velocity streamlines and HFD results for the extracardiac options for CHOP_M12**

Differences between Y-Graft options (Figure 7.25) were qualitatively more apparent as Y2 exhibited much more complex mixing patterns both within the baffle itself because of the high degree of curvature as well as within the connection. By comparison, Y1 appeared to have a much more laminar profile in that the flow through the right Y-branch exited the RPA and vice versa. Thus, the HFD response for Y1 was relatively flat with respect to changing GFD; whereas, the response of Y2 varied considerably across conditions as a function of the mixing.

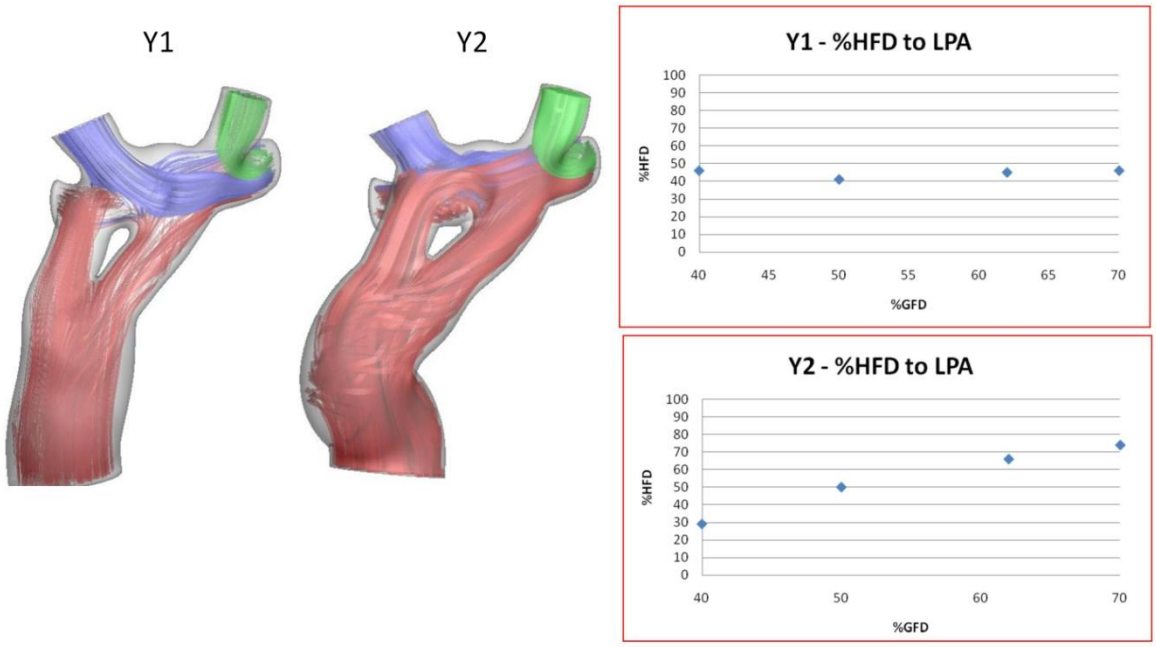


**Figure 7.25 Velocity streamline and HFD results for the two Y-Graft options for CHOP_M12.**

Finally, the summary of power loss measures across the range of investigated options is shown in Table 7.10. Values were generally consistent among the different connections, although a 55% difference was seen between the two Y-Graft options at the 40% LPA flow condition. Otherwise, power loss was not a strong discriminator.

**Table 7.10 Power loss summary for each option across investigated flow conditions.**

| %LPA | 40 | 50 | 62 | 70 |
|---|---|---|---|---|
| **EC1** | 3.9 | 2.9 | 2.3 | 2.1 |
| **EC2** | 3.6 | 2.7 | 2.3 | 2.2 |
| **Y1** | 3.1 | 2.7 | 2.3 | 2.4 |
| **Y2** | 4.8 | 3.1 | 2.5 | 2.2 |

In conclusion, because of the potential complexity and sensitivity of implementing a Y-Graft for a case of bilateral SVCs combined with the apparent stability and predictability of the extracardiac models, the surgeon opted for an extracardiac connection, which was implemented in April 2011.

### 7.4.6 CHOP_M13

This was an approximately 2 and a half year old female with the diagnosis of single ventricle in the form of heterotaxy syndrome, dextrocardia, malaligned atrio-ventricular canal (AVC), total anomalous pulmonary vein connections (TAPVC), infradiaphragmatic, double outlet right ventricle (DORV) with pulmonary stenosis (PS) after bilateral bidirectional Glenn reconstruction, TAPVC repair and main pulmonary artery (MPA) ligation and division. The patient was referred for surgical planning of the Fontan procedure with suspected PAVM in the left lung. Anatomic reconstruction is shown in Figure 7.26 where it can be seen that the case was complicated by the presence of separate IVC and left hepatic venous connections to the left atrium. PC CMR measured flow rates are listed in Table 7.11. In addition to those measured flow conditions,

simulations were also performed at pulmonary flow splits of 80/20 and 55/45 (LPA/RPA), and another assuming a 30% decrease in cardiac output (based on the finding of decreasing output during Glenn to Fontan conversion in §7.3), but at the measured pulmonary split.

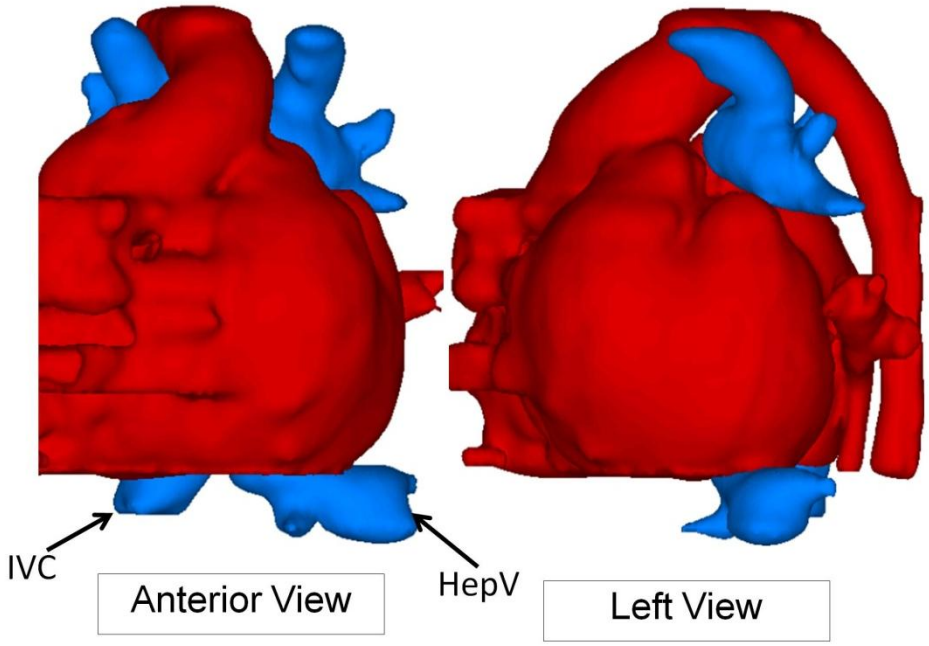


**Figure 7.26 Anterior (left) and left sagittal (right) views of anatomic reconstruction of bilateral bidirectional Glenn (in blue) and surrounding structures (in red) for CHOP_M13.**

**Table 7.11 Measured flow conditions for CHOP_M13**

| | Flow Rate (L/min) | Relative Distribution (%) |
|---|---|---|
| **IVC** | 0.56 | 24 |
| **HepV** | 0.1 | 5 |
| **RSVC** | 0.61 | 27 |
| **LSVC** | 1.0 | 44 |
| **LPA** | 0.93 | -68 |
| **RPA** | 0.44 | -32 |

A total of 8 options were investigated, as shown in Figure 7.27. The design breakdown is as follows: one option investigates two separate, bilateral baffles for the IVC and Hepatic vein, respectively (a). The next three options are intra-atrial baffles with the hepatic vein connecting in an end-to-side fashion to the IVC baffle inside the atrium. The distinction between the options is with respect to PA location: (b) sub-RSVC, (c) mid-PA, (d) sub-LSVC. The remaining options are variations of Y-grafts: (e) has a similar Hep-IVC connection and spans the two SVCs with the Y branches, (f) investigates the effect of offsetting the right Y branch of the previous option more centrally. The final two primarily vary the way in which the IVC and HepV are 'captured' by simulating part of the IVC baffle being sutured to the atrial 'floor' around the two venous entrance points and extending (g) left in an extracardiac approach and (h) right for an intra-atrial tunnel (using the same connection points as option e).

Note that options a-d used 18 mm baffles, while e-h used a 20x10 mm Y-graft.

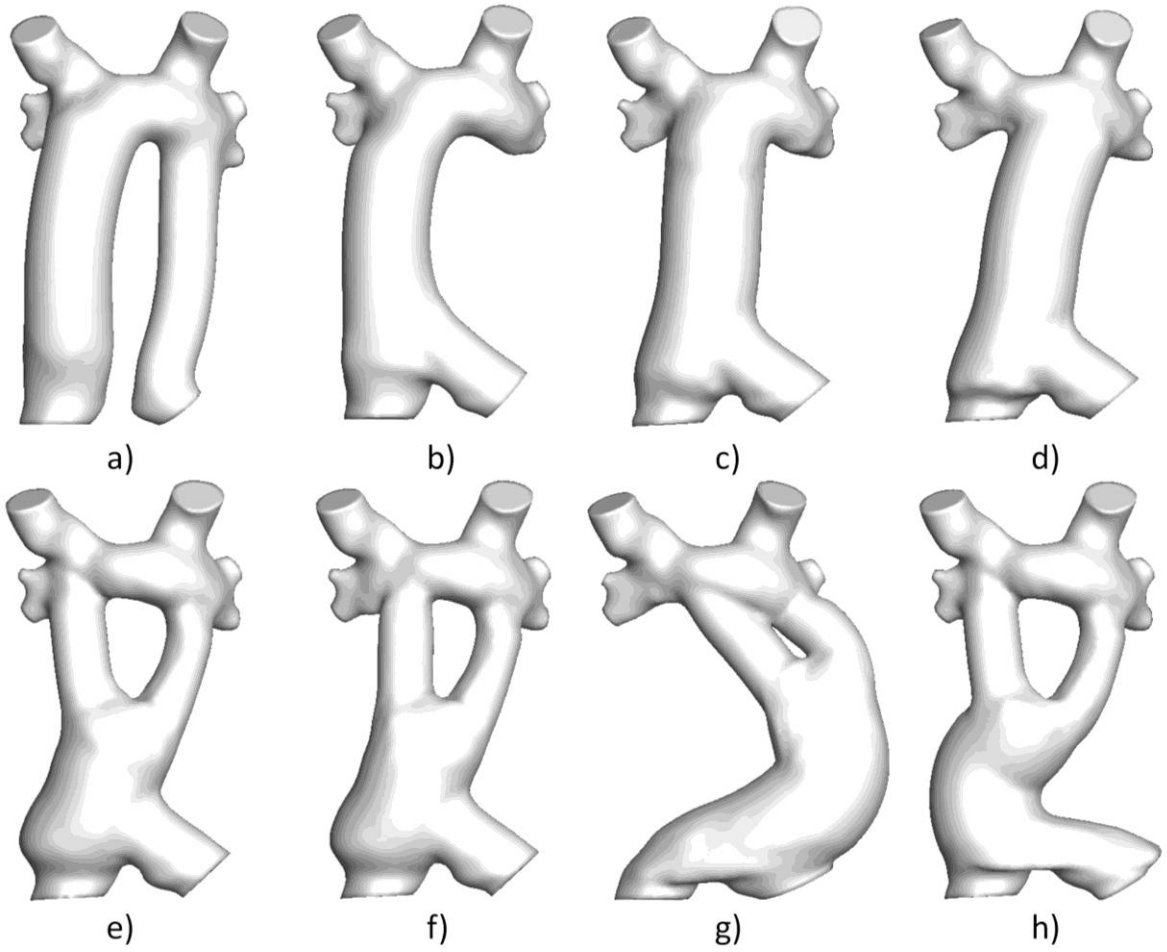


**Figure 7.27 Eight surgical options evaluated for CHOP_M13 representing (a) bilateral conduits for IVC and left hepatic vein, (b-d) intra-atrial conduits of varying connection locations, and (e-h) Y-Graft connections with varying placements and hepatic/IVC connection approaches.**

The HFD and power loss results for each option are detailed in Table 7.12 and Table 7.13, respectively for reference through the discussions of the individual options below.

**Table 7.12 HFD results by option for each investigated flow condition of CHOP_M13.**

HFD (%LPA)

| %LPA | a | b | c | d | e | f | g | h |
|---|---|---|---|---|---|---|---|---|
| 55 | 30 | 33 | 69 | 76 | N/A | 21 | 92 | 4 |
| 68 | 53 | 47 | 78 | 92 | 16 | 57 | 100 | 14 |
| 80 | 69 | 70 | 94 | 100 | 52 | 85 | 100 | 54 |
| | | | | | | | | |
| 70% CO | N/A | 52 | 77 | 91 | 17 | 59 | 99 | N/A |

**Table 7.13 Power loss results by option for each investigated flow condition of CHOP_M13.**

Power Loss (mW)

| %LPA | a | b | c | d | e | f | g | h |
|---|---|---|---|---|---|---|---|---|
| 55 | 5.2 | 3 | 11.5 | 6 | N/A | 11.7 | 5.8 | 3 |
| 68 | 5.4 | 3.3 | 7.4 | 6.6 | 6.9 | 9.1 | 7.5 | 3.4 |
| 80 | 8.4 | 5.4 | 8.6 | 9 | 7.4 | 11.1 | 10.5 | 5.4 |
| | | | | | | | | |
| 70% CO | N/A | 1.2 | 2.7 | 2.4 | 2.4 | 3.1 | 2.6 | N/A |

The first option that was eliminated from consideration was option (a) for the reason that significant concern was raised about the thrombus risk that the design posed given the extremely low flow rate present in the left hepatic veins. This would be especially exacerbated by the high velocity in the LSVC (44% of venous returns), which would be located opposite to the connection of that left hepatic baffle, and create significant resistance to forward flow. From the velocity plot in Figure 7.28, the difference in velocities (and thus momentum) between the LSVC and the IVC is readily apparent, which also came into play in the results of almost every option investigated.

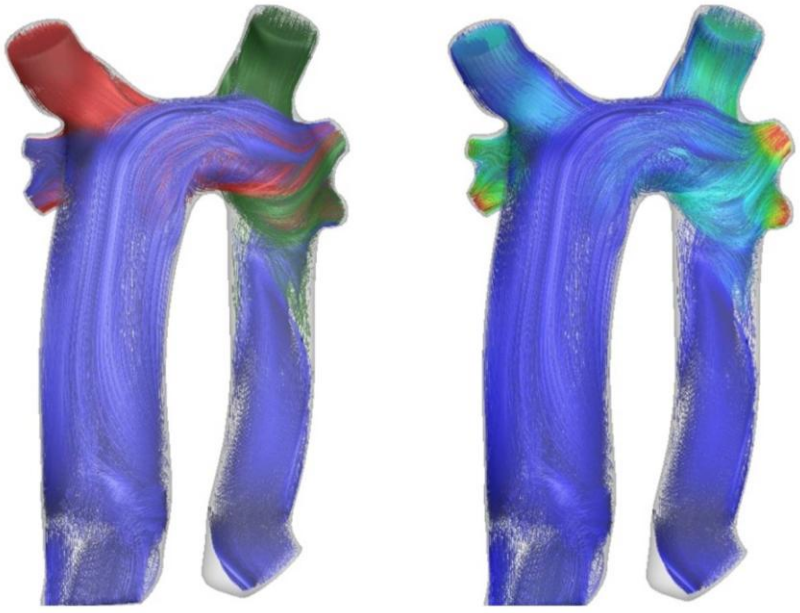

**Figure 7.28 CFD results for option (a). On the left, the streamlines are colored by vessel, on the right, by velocity magnitude**

Next considering the various Y-graft designs, it is evident from Figure 7.29 that for each of the 3 different Y-graft placements investigated (since e and h were the same with respect to placement), significant obstruction and disturbance of the flow in one branch occurred. Hence, even though some options produced reasonable flow distribution values (Table 7.12), the connections did not direct flow as intended, indicating energy inefficiencies. Furthermore, there was significant sensitivity to branch placement without a great indication from the modeled designs if an optimal placement could even be achieved. Therefore, no Y-graft approach was recommended for this patient.

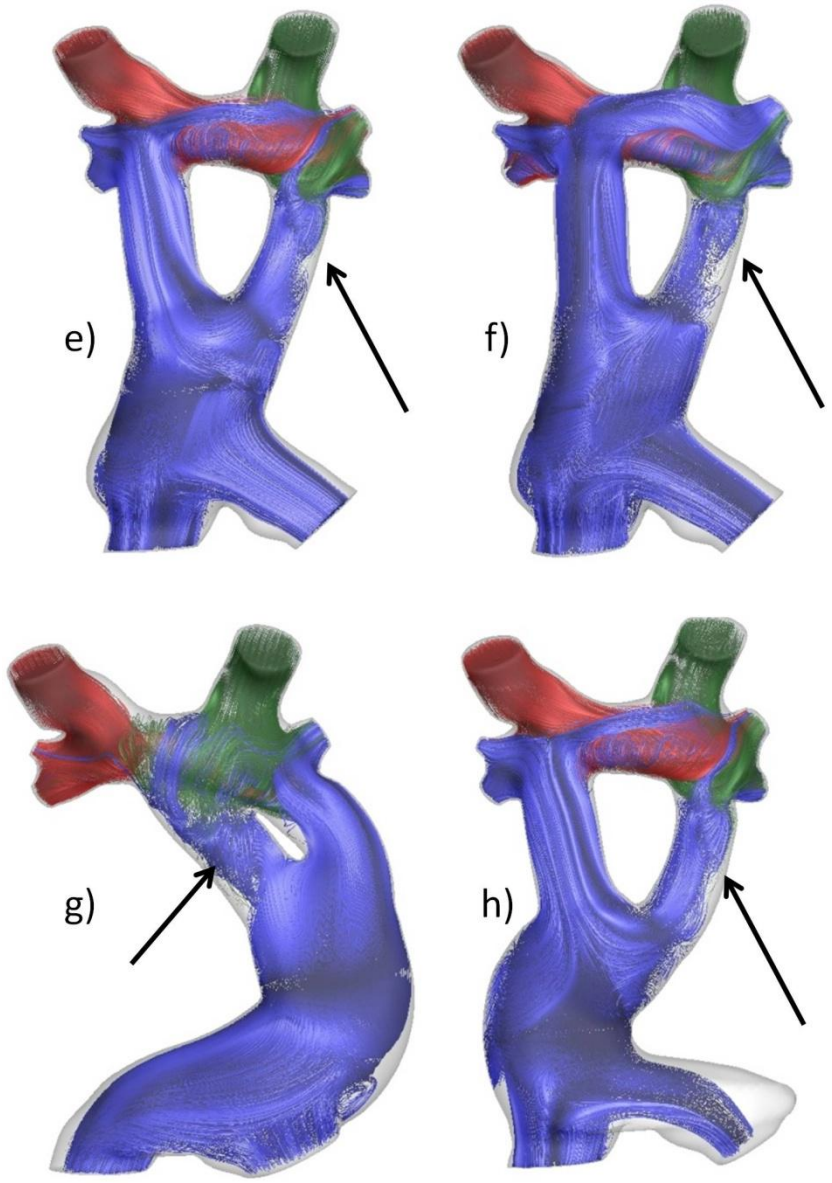


**Figure 7.29 CFD results for options (e-h). In each case (denoted by the arrows) one of the branches was significantly affected/obstructed by the superior caval flows, primarily the LSVC. As a result, the majority of IVC flow traveled through a single Y branch in each case.**

Finally, the intra-atrial tunnel designs (b-d) are shown in Figure 7.30. Perhaps owing to the fact that the bilateral SVCs were medially angled (i.e., forming a 'V'), these options (with the possible exception of option d) were consistently the best performers. There were significant interactions apparent between the Fontan and either of the SVC flows, particularly as the Fontan baffle moved left toward the dominant LSVC flow, but these interactions appeared to promote bidirectional flow distribution (Table 7.12), rather than unilateral (with the exception of option (d) when LPA flow was 80% of $Q_p$). By far the lowest power losses simulated in this study (Table 7.13) were seen in option b, which also had one of the most balanced flow distribution characteristics of any option. Thus, the recommended surgical approach was for a single, combined IVC-Hepatic intra-atrial baffle to be positioned medially with respect to the bilateral SVC, but closer to the RSVC than the LSVC. It was noted that positioning too far to the right would likely constrain the IVC flow primarily to the RPA, and so it was advised to err on the medial side rather than laterally on the right.

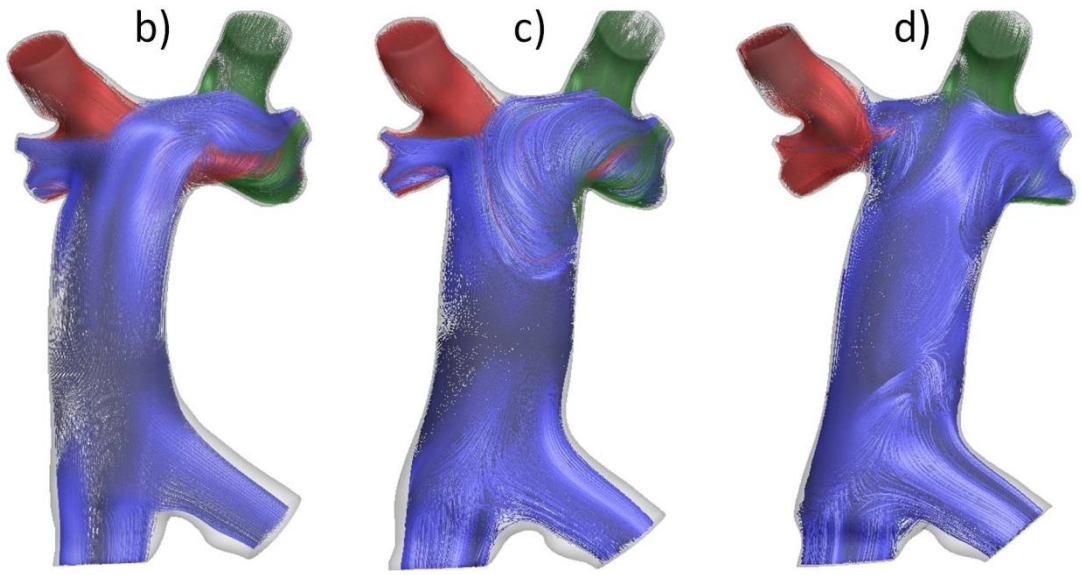


**Figure 7.30 CFD results for options (b-d). The major difference among these options was the position of the Fontan baffle, but the effect that difference has is noticeable by the smooth, streamlined look of b compared to the disturbed recirculation regions present in the latter two. Presumably this again owes to the fact that the IVC interactions with the LSVC are minimized in (b), which also provides energetic benefits.**

With respect to the means of connecting the left hepatic veins and IVC, a (roughly) direct comparison is possible with options e and h (Figure 7.29; although these are Y-graft models and not straight baffles). Of these two, there was minimal difference in the flow distributions; however, the power loss of option h (the one inclusive of the atrial wall) was considerably lower than option e. There is not an immediate visual clue as to why this is the case, although perhaps this configuration allows for a more natural streamlining of this combination rather than a blunt end to side connection. However, since this connection was never previously considered in these modeling studies, its geometric 'realism' was difficult to guarantee. Thus, no recommendation on that aspect of the connection was made.

Based on these findings, the surgeon opted to connect Fontan graft toward the left SVC in November 2011.

### 7.4.7 CHOP_M8

This was an 8 year-old patient with bilateral SVCs and interrupted IVC with azygos vein continuation to the left SVC. PAVMs were reported in the left lung even with an existing Fontan connection to include hepatic venous flow to the right SVC. The pre-operative reconstruction is shown in Figure 7.31. This case represents the most complex surgical modeling study to date.

This patient had previously been referred for CFD analysis as a risk assessment for PAVM development.[124] At that time, it was concluded there was a significant risk of left-sided PAVM because of a predicted imbalance in hepatic venous flow, as shown in Figure 7.32. As predicted, left lung PAVM developed and the patient was again referred for surgical planning. The updated average flow conditions are provided in Table 7.14.

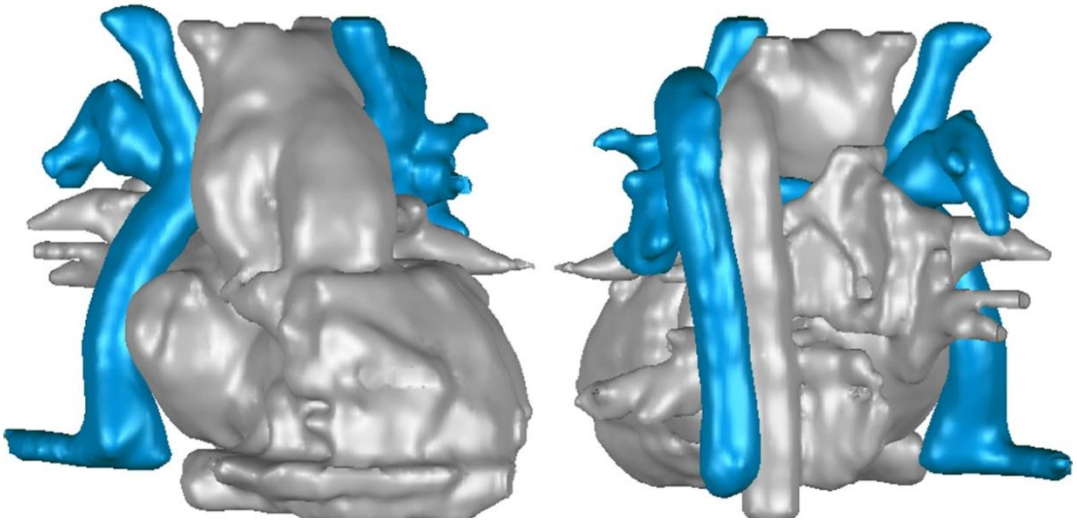

**Figure 7.31 Reconstructed TCPC (blue) and surrounding anatomy (gray) for CHOP_M8.**

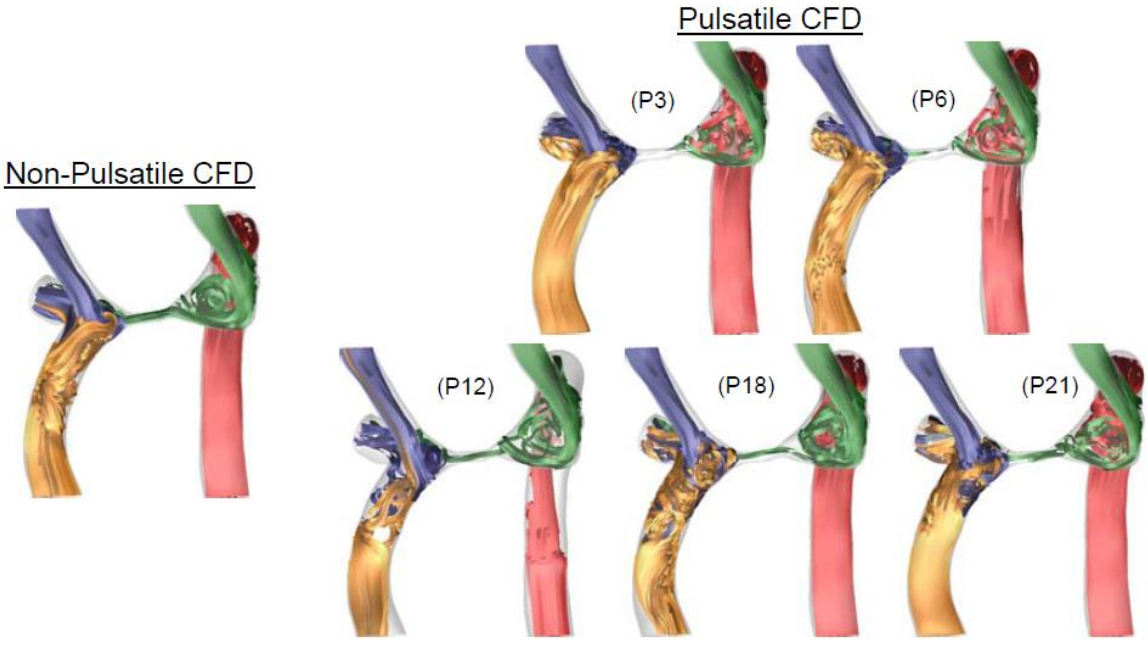


**Figure 7.32 Qualitative CFD results from original risk assessment study of CHOP_M8 to characterize distribution of hepatic flow (yellow streamlines). (Image taken from de Zélicourt[124])**

**Table 7.14 PC CMR measured average flow conditions for CHOP_M8 from 2nd (pre-surgical) scan.**

| | Flow Rate (L/min) | Relative Distribution (%) |
|---|---|---|
| **IVC** | 0.31 | 9 |
| **RSVC** | 0.72 | 22 |
| **LSVC** | 1.04 | 32 |
| **Az** | 1.21 | 37 |
| **LPA** | 1.48 | -55 |
| **RPA** | 1.23 | -45 |

Repeating the baseline simulations using the updated pulsatile flow conditions concurred with those previous findings, as there was still a significant lack (<1%) of hepatic flow reaching the LPA (Figure 7.33, Animation 7.1). Two important observations: 1) As before, there was a significant amount of pulsatility noted, particularly in the hepatic venous flow (see Figure 7.33; a significant portion of the cycle actually had flow reversal), so all simulations were done under pulsatile flow conditions; 2) There is a significant imbalance in left vs. right venous returns with the (average) sum of the LSVC and azygos accounting for 69% of the venous returns. This fact implies that simply re-positioning the Fontan connection medially between the bilateral connections is not sufficient; the severe mass imbalance must be overcome.

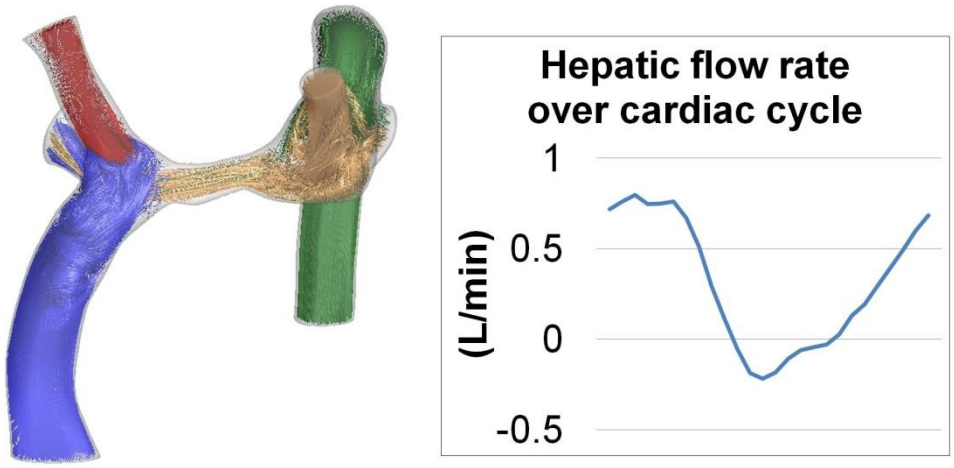


**Figure 7.33 Left- Instantaneous velocity streamlines based on most recent pre-operative CMR and PC MRC reconstructions for CHOP_M8 (HepV flow in blue). Right- time-varying flow curve for the hepatic baffle.**

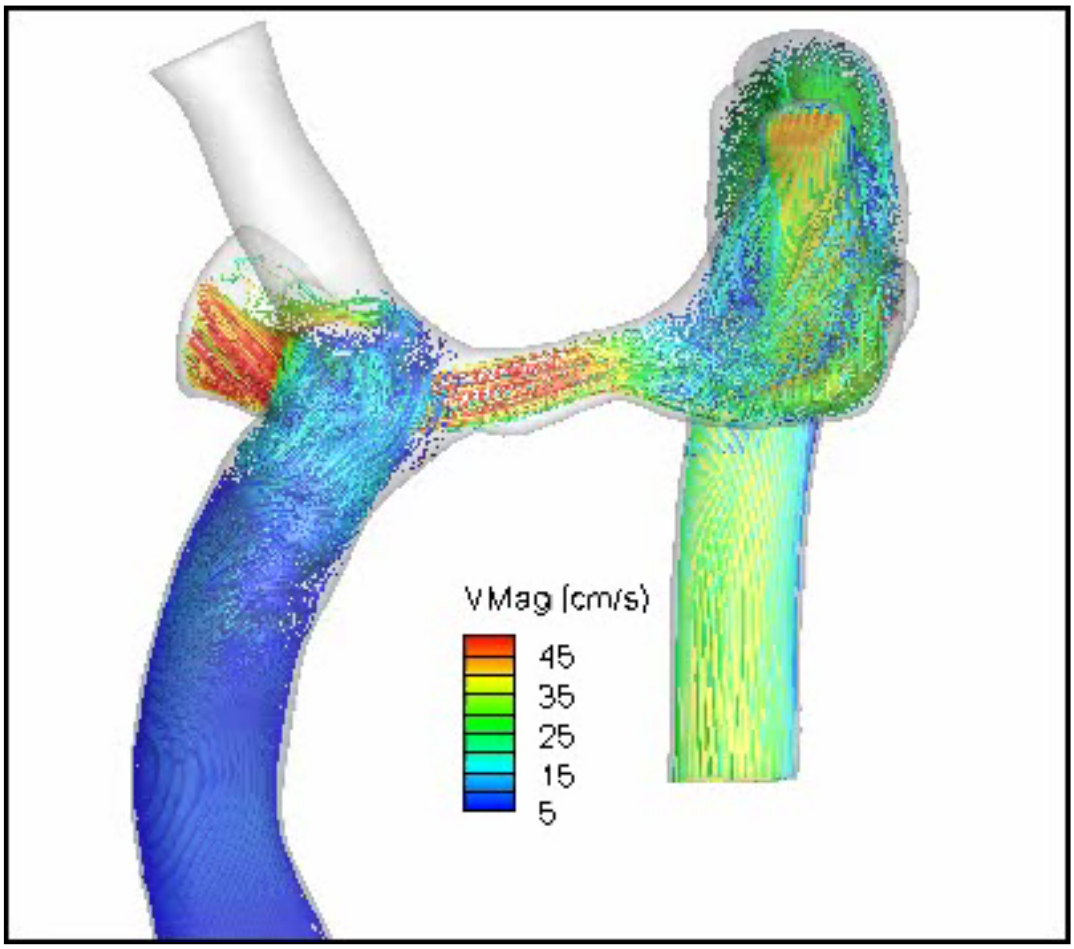


**Animation 7.1 Time-varying velocity streamlines for pulsatile simulation of post-operative connection for CHOP_M8.**

The six options considered for this patient are shown in Figure 7.34. Because of they are all non-standard and complex designs, a more thorough description of each is provided below.

- Option1: Intra-atrial graft routed to the LPA via the left atrial appendage.
- Option 2: Routing the LSVC around the aortic arch to the RSVC (as a normal innominate vein); no change to the existing Fontan connection.
- Option 3: Same as option 2 except the existing Fontan baffle was replaced with a Y-Graft.
- Option 4 (non-surgical): Based on an intervention that had previously been done for a similar patient (CHOP_M3), this option simulated a scenario in which a series of stents were deployed inside the MPA: one to dilate the whole segment, a covered stent to route hepatic flow through the first stent to the left side of the connection, and a third creating a space between the covered stent and the first stent to allow backflow to the RPA. Because this stent-in-stent design is not easily translatable to the design of the immersed boundary solver, this connection was instead simulated by connecting the hepatic baffle to the superior section of the left-sided Glenn connection and dilating the connection between left and right. The arrows drawn in Figure 7.34 denote the intended blood flow pattern through this design.
- Option 5: An extended Y-Graft design in which the left branch is routed through the atrium to the left side.
- Option 6: A Y-Graft in which the RSVC-MPA connection was ligated and anastomosed in an end-to-end fashion to the left branch of the graft.

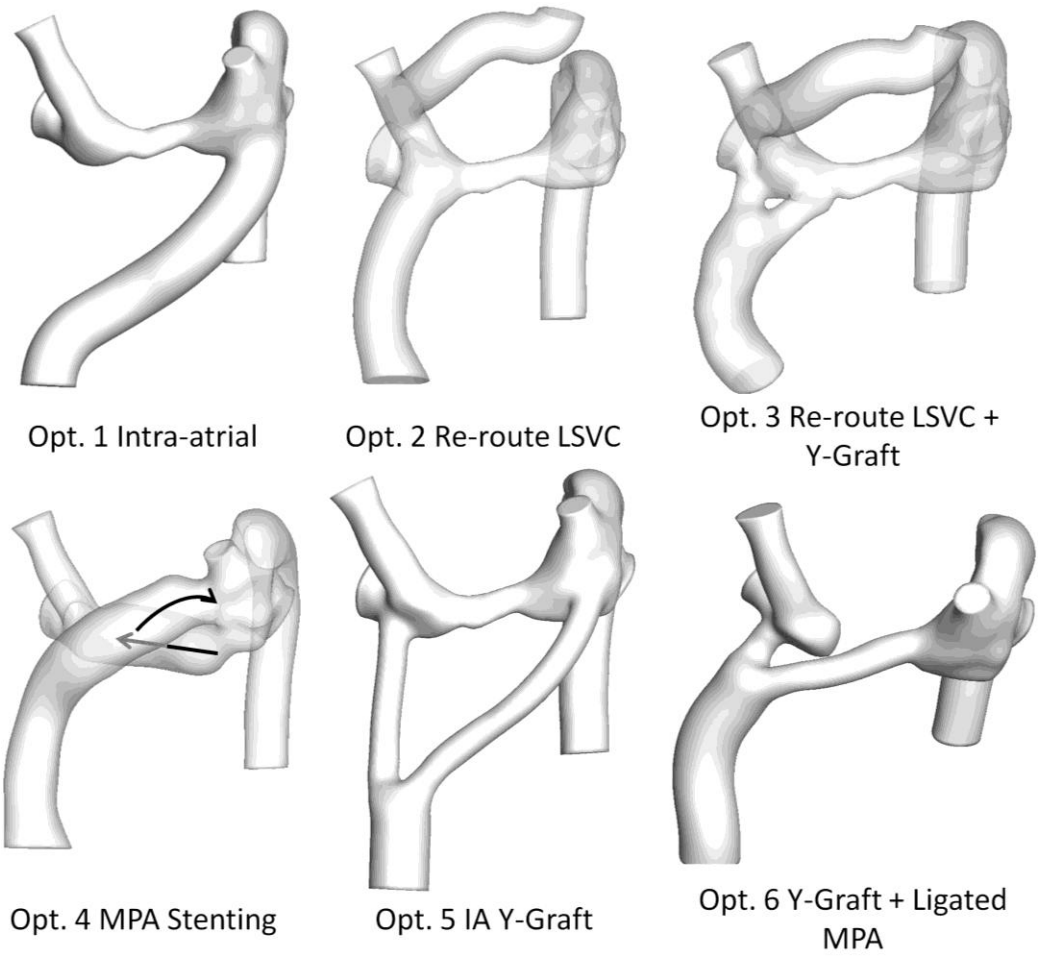


**Figure 7.34 Six surgical options modeled for CHOP_M8 to address LPA PAVM. Options included an intra-atrial connection to the left (1), re-routing the LSVC to the right without (2) or with (3) revising the Fontan baffle, a complex MPA stenting approach (4), and two potential Y-Graft approaches (5,6).**

A brief aside is now necessary regarding the handling of PA outflow conditions. As is standard, connection performance was assessed over a range of different outflow conditions because of the potential for future remodeling. However, the implicit assumption with these methods (since flow boundary conditions are imposed at the outlets) is that the surgical modifications do not significantly alter internal connection resistance. In other words, the flow split primarily dictated by the downstream pulmonary

vascular resistances, which are assumed to remain constant, would not be appreciably altered by the new connection. Given the anatomic complexity involved in this case, including the significant resistance imposed by the stenosed mid-PA segment, this assumption is very unlikely to hold true. Using option 2 in Figure 7.34 as an example, re-routing the LSVC flow to the right side of the connection would be expected to increase RPA flow because the relative pressure on the right side of the connection would increase, while the pressure on the left would decrease.

These concerns were addressed as follows: Using the original CFD results from the most recent scan, it was assumed that the hepatic venous pressure was 10 mmHg (value taken from cath report from CHOP_M3 prior to stent insertion). Then, using the CFD-derived differential pressure values through the connection, an estimate was obtained for the pulmonary vascular resistances (PVR) of each PA assuming a constant downstream atrial pressure. Based on the selection of 10 as the hepatic pressure, these values resulted in 2.2 mmHg·m$^2$·min/L total PVR, with independent L/R values of 4.5/4.6 mmHg·m$^2$·min/L as reference values. Assuming a constant hepatic venous pressure, this procedure was repeated for the surgical option results to retrospectively estimate branch PVR and compare to the references to estimate the likely PA flow splits following that intervention. That is, the pulmonary split for the subsequent surgical options that produced PVR values closest to the reference were assumed to be the likely post-operative result. To be clear, the simulations were still performed with flow boundary conditions; the PVR calculations were performed as a post-hoc assessment.

In addition to the 55% average LPA distribution measured pre-operatively, the alternative time-varying profiles for the PA splits were determined by: switching the measured left and right profiles (giving a 45% LPA condition), and by taking the LPA as

the instantaneous difference of the venous inflows and the RPA outflow (as there was a 0.6 L/min disparity in the measured values; giving a 63% LPA condition).

Finally, since time-varying flow conditions were used rather than time-averaged, the means of quantifying HFD were modified. Using the particle tracking algorithm described in §4.3.6, a hepatic baffle cross-section was seeded with particles at 50 evenly spaced time points across the cardiac cycle[107]. These particles were then advected through the time-varying velocity fields until they had been completely washed through the connection, at which time the relative distribution of particles to the left and right were summed. Additionally, instantaneous visualization of particle motion provides a more appropriate indication of the motion of blood elements as compared to instantaneous static streamlines.

For the first option (intra-atrial connection to the LSVC), results (Figure 7.35) indicate this design over-corrects: 99% of the hepatic flow goes to the LPA. While this would take care of the short-term problem, it is not a desirable long-term solution given the lack of hepatic flow to the RPA in that configuration. Further, such an approach is likely to be extremely sensitive to the exact positioning of the baffle with respect to the azygos and LSVC junction because of the momentum mismatch between the flow carried by these vessels and the hepatic baffle.

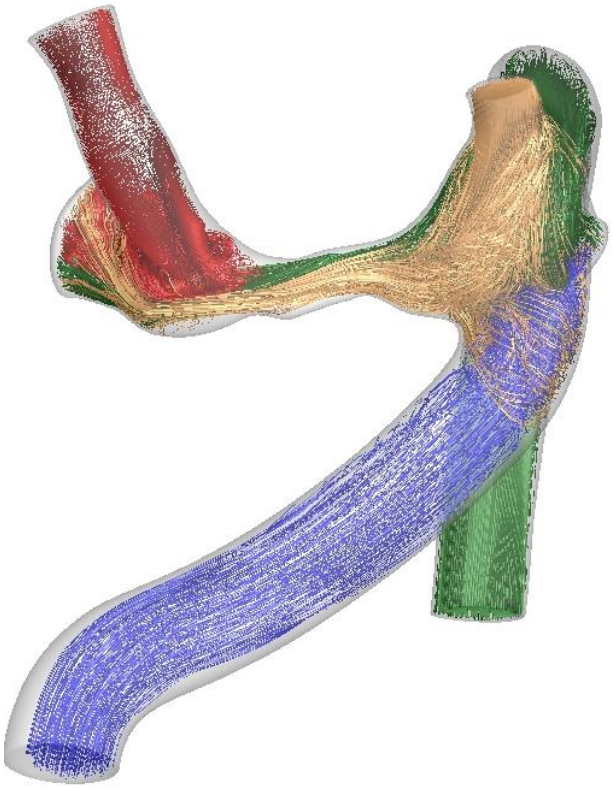

**Figure 7.35 Representative instantaneous velocity streamlines for the intra-atrial option for CHOP_M8.**

The results for option 2 (re-routing the LSVC) are shown in Figure 7.36 and Animation 7.2. From both the instantaneous streamlines and particle tracking, a qualitative improvement in hepatic flow to the LPA is seen. Effectively, this option redirected LSVC flow to the RPA rather than the LPA, allowing the hepatic flow to cross through the MPA to make up the difference. The quantitative results, as well as those of the pre-operative baseline connection, are shown in Table 7.15. HFD values ranged from 20-75% LPA across the various PA splits tested. Based on the estimated PVR values, LPA global flow percentage would be expected to decrease slightly from 55% as the calculated resistance (4.9 Wood unit PVR) was higher than the LPA reference (4.5 WU). However,

the change would not be drastic since the 45% LPA GFD condition produced a much lower PVR value (3.7 WU). Thus, the expected HFD result was ~40% (close to the 55% GFD result).

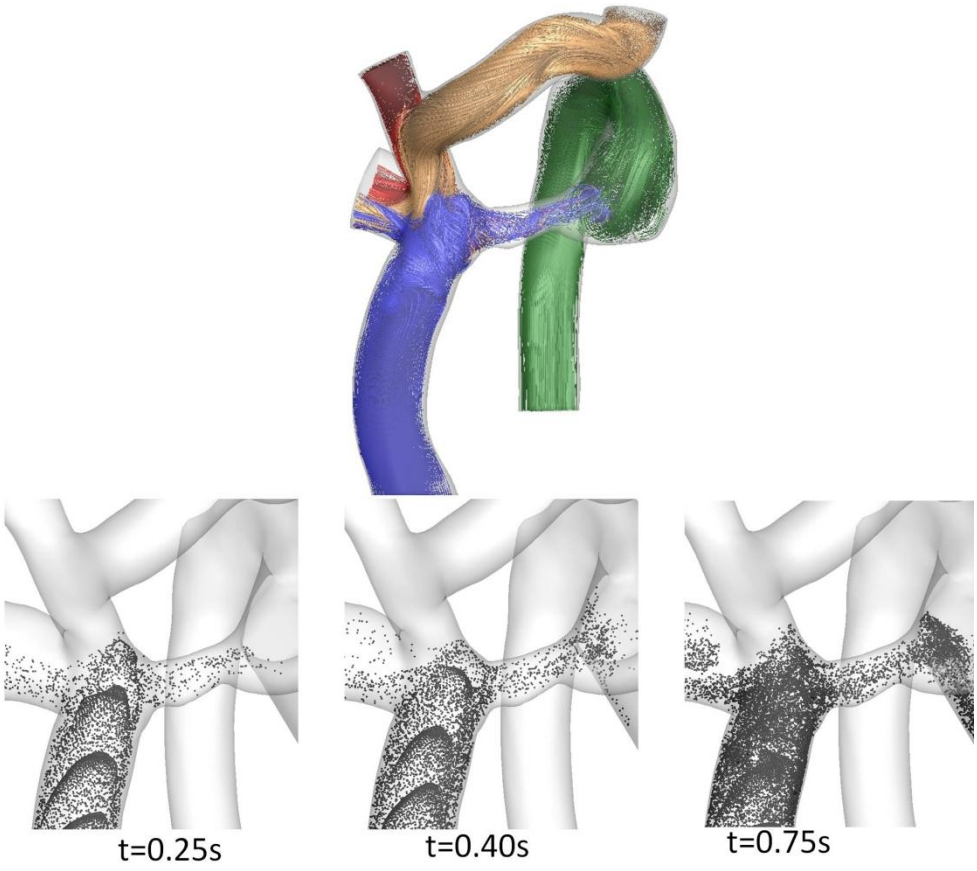


**Figure 7.36 Results for Option 2 (re-routing the LSVC). Top- instantaneous velocity streamlines at pre-operative flow conditions color-coded by vessel of origin (hepatic flow in blue). Bottom- A sequential series (from left to right) of hepatic particles traversing the connection with time from first release provided.**

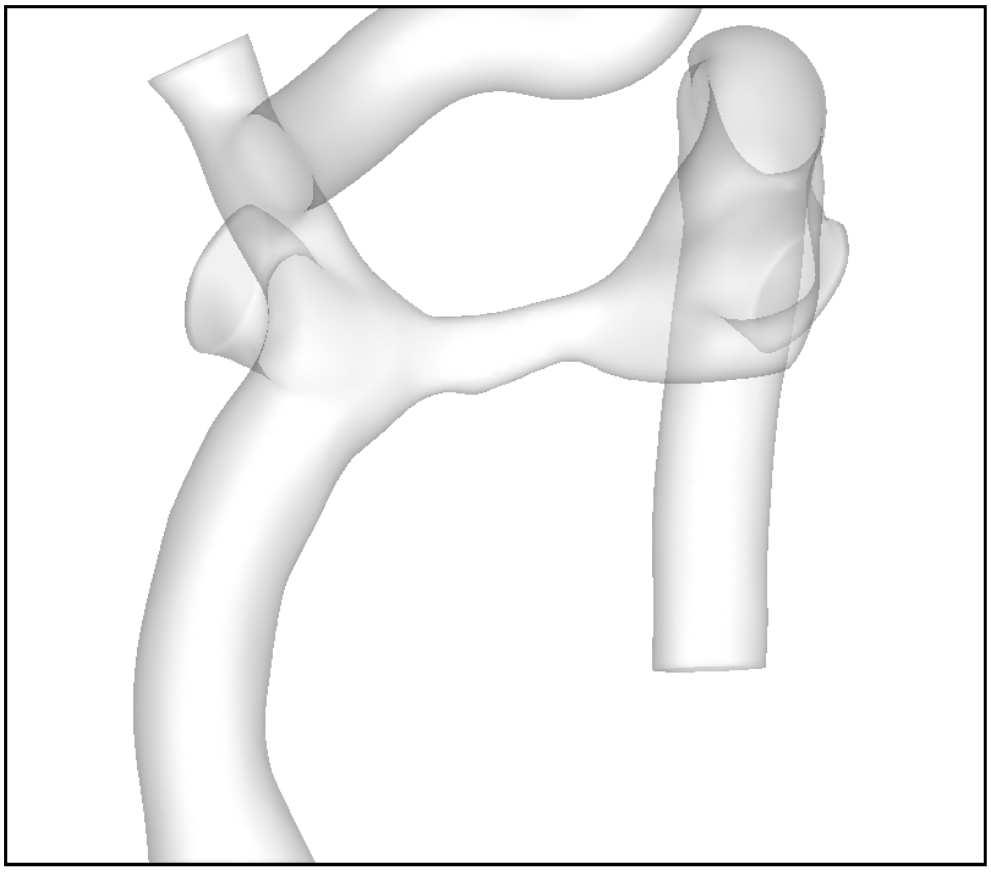

**Animation 7.2 Hepatic particle tracking for re-routed LSVC option (#2)**

**Table 7.15 HFD and Power loss results for CHOP_M8 Baseline (pre-operative) and Option 2**

| | HFD (%LPA) | Power loss (mW) | PVR (L/R) mmHg·min·$m^2$/L |
|---|---|---|---|
| **BASELINE** | 0 | 6.2 | 4.5/4.6 |
| 45% LPA | 20 | 11.1 | 5.4/3.7 |
| 55% LPA | 44 | 11.4 | 4.1/4.9 |
| 63% LPA | 75 | 16.7 | 3.4/6.6 |

Results for option 3 are shown in Figure 7.37 and Animation 7.3, and quantified in Table 7.16. As with option 2, improved HFD to the LPA was seen; however, expected additional improvements through bifurcating the hepatic baffle with a Y-Graft were not realized through this particular design. Instead, the results for the 55% LPA flow condition were fairly consistent between options 2 and 3 (HFD= 44 vs. 45%, respectively) with the primary difference being the more stable response of option 3 to changing PA splits (results ranged from 33-52% to the LPA). Still, based on the estimated PVR values, the expected ~50/50 post-operative PA split would still yield approximately 40% HFD to the LPA. The intentionally conservative design of the graft branches (i.e., short length, positioned close to the RSVC connection) contributed to these sub-optimal results as evidenced by the residual interaction between the hepatic flow through the left branch (blue) and superior venous flows (red) in Figure 7.37. Providing greater spatial separation at the left anastomosis (not investigated due to time constrains) would likely have improved performance and produced a more uniform 50/50 hepatic distribution.

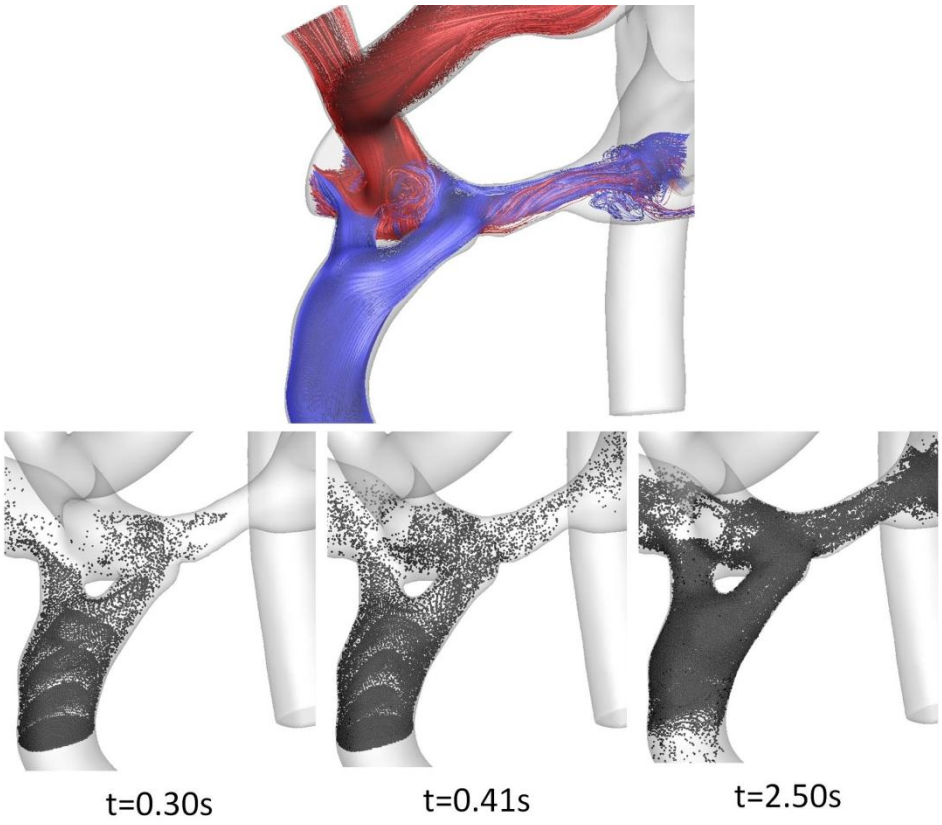


**Figure 7.37 Results for Option 3 (re-routing the LSVC + Y-Graft). Top- instantaneous velocity streamlines at pre-operative flow conditions color-coded by vessel of origin (hepatic flow in blue). Bottom- A sequential series (from left to right) of hepatic particles traversing the connection with time from first release provided.**

**Table 7.16 HFD and Power loss results for CHOP_M8 Option 3**

| | HFD (%LPA) | Power loss (mW) | PVR (L/R) mmHg*min/L |
|---|---|---|---|
| 45% LPA | 33 | 11.1 | 4.9/4.1 |
| 55% LPA | 45 | 12.2 | 4.0/4.9 |
| 63% LPA | 52 | 14.3 | 3.1/7.6 |

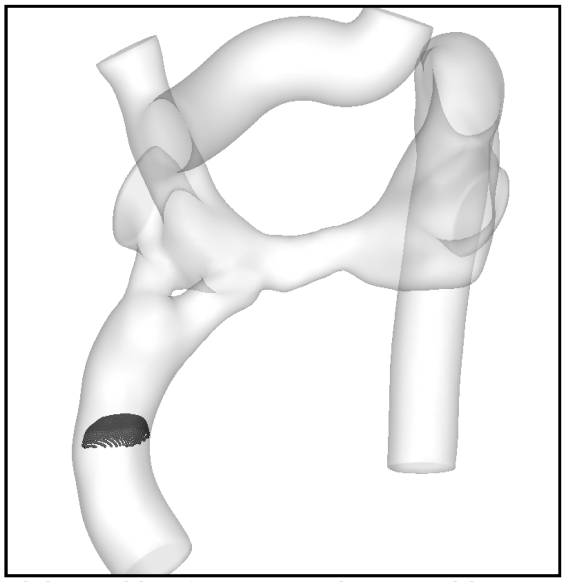

**Animation 7.3 Hepatic particle tracking for re-routed LSVC with Y-Graft Fontan option (#3)**

For option 4, because there was little confidence in the geometric realism of the model, going into extensive detail of its quantitative output would not have been a meaningful exercise. Instead, this option was treated simply as a proof of concept: that routing the hepatic flow to the left-sided LSVC and secondarily directing flow from left-to-right through the MPA could deliver hepatic flow to the left. This semi-quantitative assessment is shown in Figure 7.38 and, in fact, it is confirmed. Like option 1, this design would be expected to increase total LPA flow such that the result could fall in the range of the included table. The only potentially concerning finding from the results is that there was very little apparent mixing of hepatic flow with the LSVC/azygos flows, so depending on the geometry of the stented openings it is possible that the hepatic flow could traverse the MPA and be immediately redirected back to the right without reaching the LPA. Without accurate representation of that final geometry, the risk of this happening cannot be assessed and hence the brief treatment of this option.

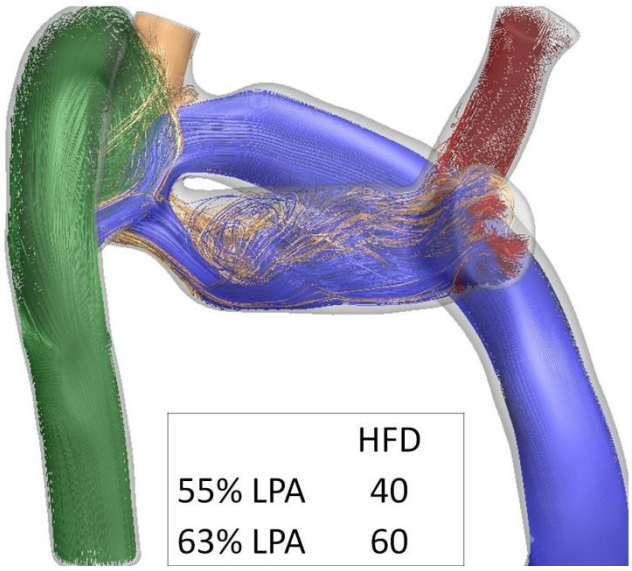


**Figure 7.38 Results for Option 4 (MPA stent) shown from the posterior perspective. Instantaneous velocity streamlines shown correspond to pre-operative flow conditions. HFD results provided in included table.**

Option 5 simulated a bifurcated design in which the left branch was routed through the atrium to the LSVC-Az junction. While promising in theory, the placement of the left branch (in opposition to the entrance flow of the LSVC+Az) impeded flow through that branch, as seen in Figure 7.39. Thus, the connection is still entirely biased to the RPA**.**

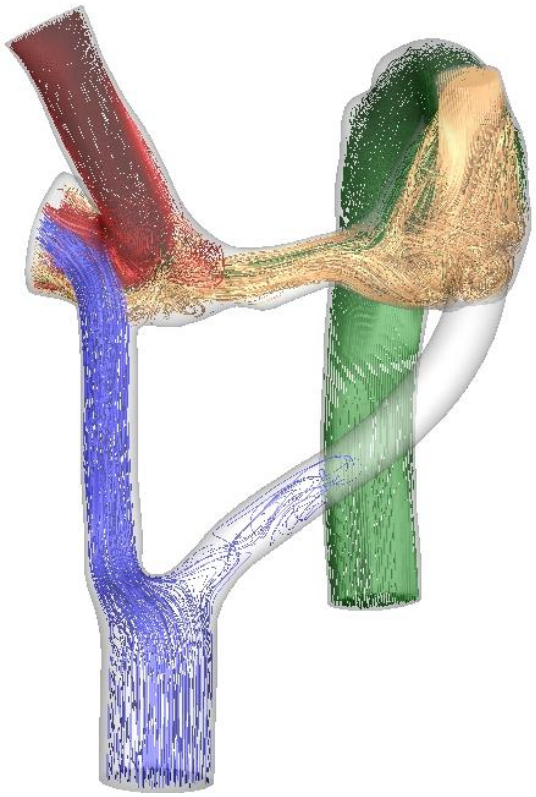

**Figure 7.39 Representative instantaneous velocity streamlines for the intra-atrial Y-graft option investigated for CHOP_M8.**

Option 6 simulated a Y-Graft design in which the MPA connection to the RSVC was mobilized and connected end-to-end to the left branch of the Y-graft. Evaluating such a connection exploits a weakness of using flow outlet conditions, as previously discussed, since the flow direction through that end-to-end connection is entirely dependent on the selected outlet conditions. It is clear that, with 69% of venous return coming from the LSVC and Az, if the *in vivo* flow split (55%) was imposed at the LPA, there would be a net flow from left to right through the connection (as in the original configuration) with the Y-branch simply taking the place of the MPA. Instead, an LPA flow split of 75% was set (which is enough to encompass all of the LSVC+Az flows, plus approximately half the

average contribution of the hepatic flow). To check the feasibility of this condition, the values of downstream PVR needed to produce these flow spits were computed, obtaining 2.7 Wood units for the LPA and 10.3 Wood units for the RPA. Both these values represent significant departures from the baseline values, meaning that the LPA resistance would have to drop considerably while the RPA resistance would have to increase considerably for this connection to produce the desired hemodynamic outcome. Since this is an unlikely scenario, this option was ruled out.

Ultimately, these results were not utilized as it was deemed that none of the modeled options was surgically feasible and a hepatic-to-azygos connection, which had been pre-operatively ruled out for feasibility concerns (see position of descending aorta in Figure 7.31), was implemented.

### 7.4.8 CHB_M1

Patient was a 9 year old male with an existing lateral tunnel Fontan and bilateral superior venous connections. He presented with suspected protein-losing enteropathy (PLE), fatigue, poor exercise tolerance, and frequent respiratory illness with desaturations into the mid-70s. He was referred for modeling for the dual purposes of 1) identifying if any streaming biases were present related to the desaturations; and 2) evaluate connection efficiency with respect to PLE and poor exercise tolerance, and determine if surgical revision might provide therapeutic benefit. The existing TCPC reconstruction is shown in Figure 7.40.

To complement the standard axial SSFP and through plane PC CMR data typically obtained, a coronal stack of 4D PC CMR data was also acquired to reconstruct the *in vivo* velocity fields and provide verification for the CFD results. A comparison of

instantaneous velocity streamlines between the two modalities is shown in Figure 7.41. Animation 7.4 shows the dynamic CMR results. Notably, it can be seen that the computational domain was extended inferiorly to explicitly include the distal IVC and hepatic veins before their confluence. This detail was added to the model based on the PC CMR findings to improve the qualitative match of the velocity profile entering the lateral tunnel.

From both analyses, the local hemodynamics were found to be very complex, particularly with respect to large-scale recirculation taking place within the dilated (up to 50 mm diameter) connection. However, both PAs were of good size, with no evidence of significant convective acceleration; thus, the connection power loss was low (2.7 mW). Furthermore, the IVC flow distribution was well balanced (65/35% LPA/RPA), which would not indicate a risk for PAVM.

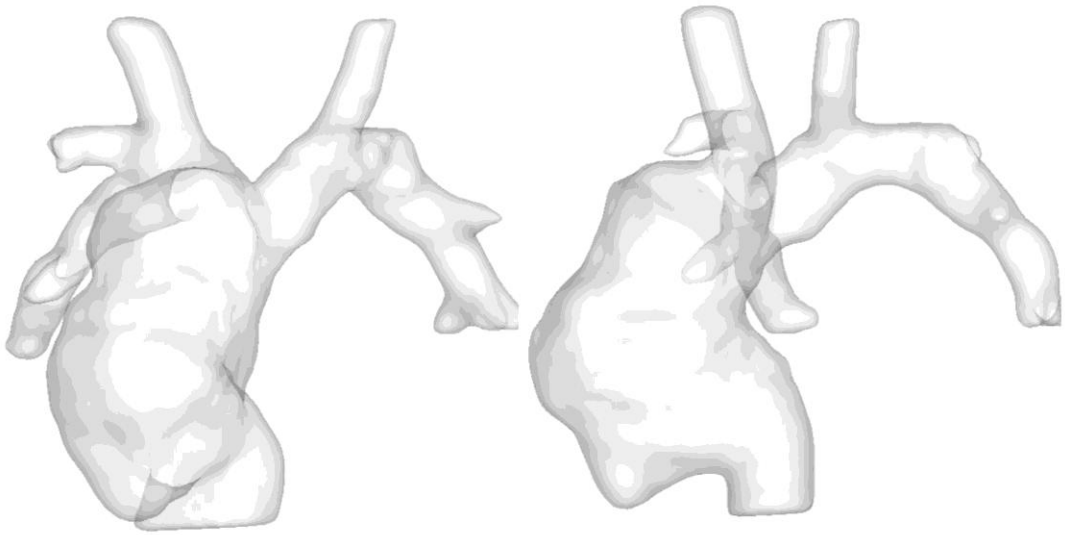

**Figure 7.40 Reconstructed TCPC anatomy for CHB_M1 shown from anterior (left) and left sagittal (right) views.**

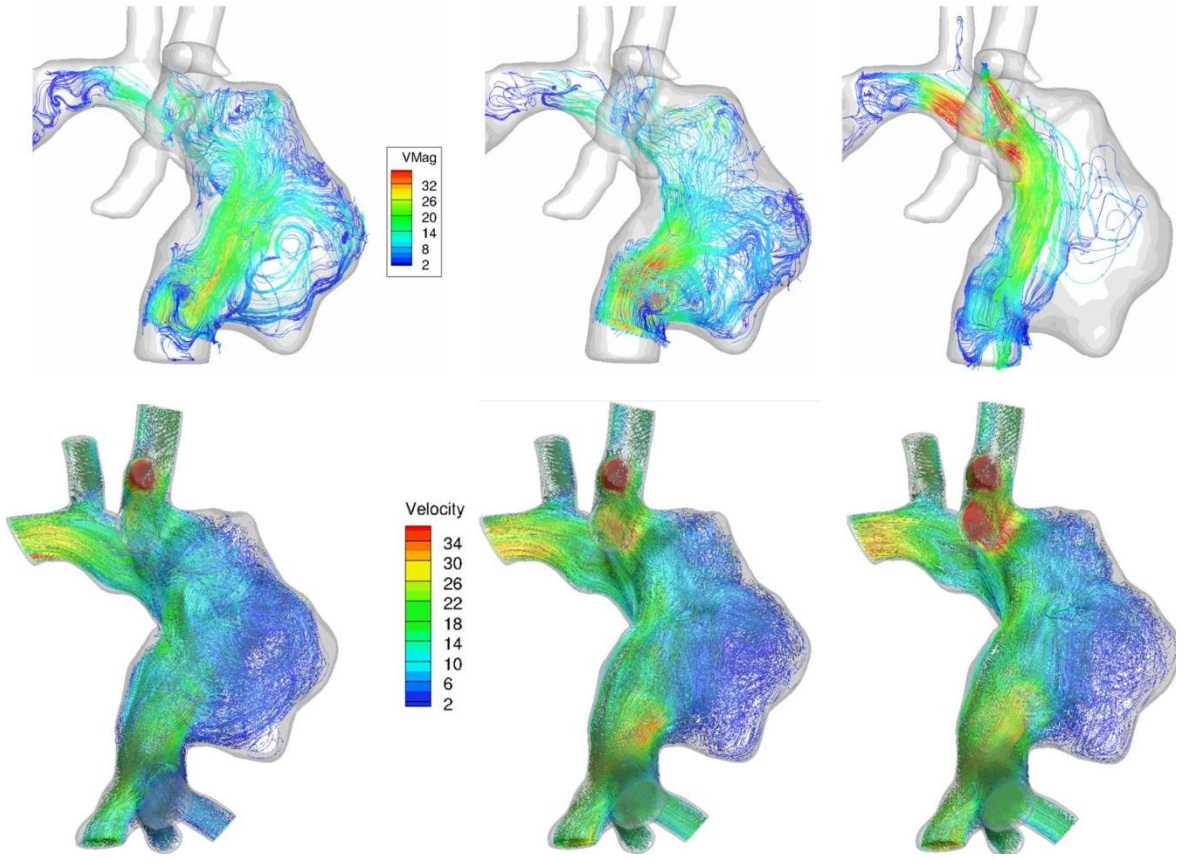


**Figure 7.41 Qualitative comparison of instantaneous velocity streamlines derived from 4D PC CMR (top row) and pulsatile CFD (bottom row).**

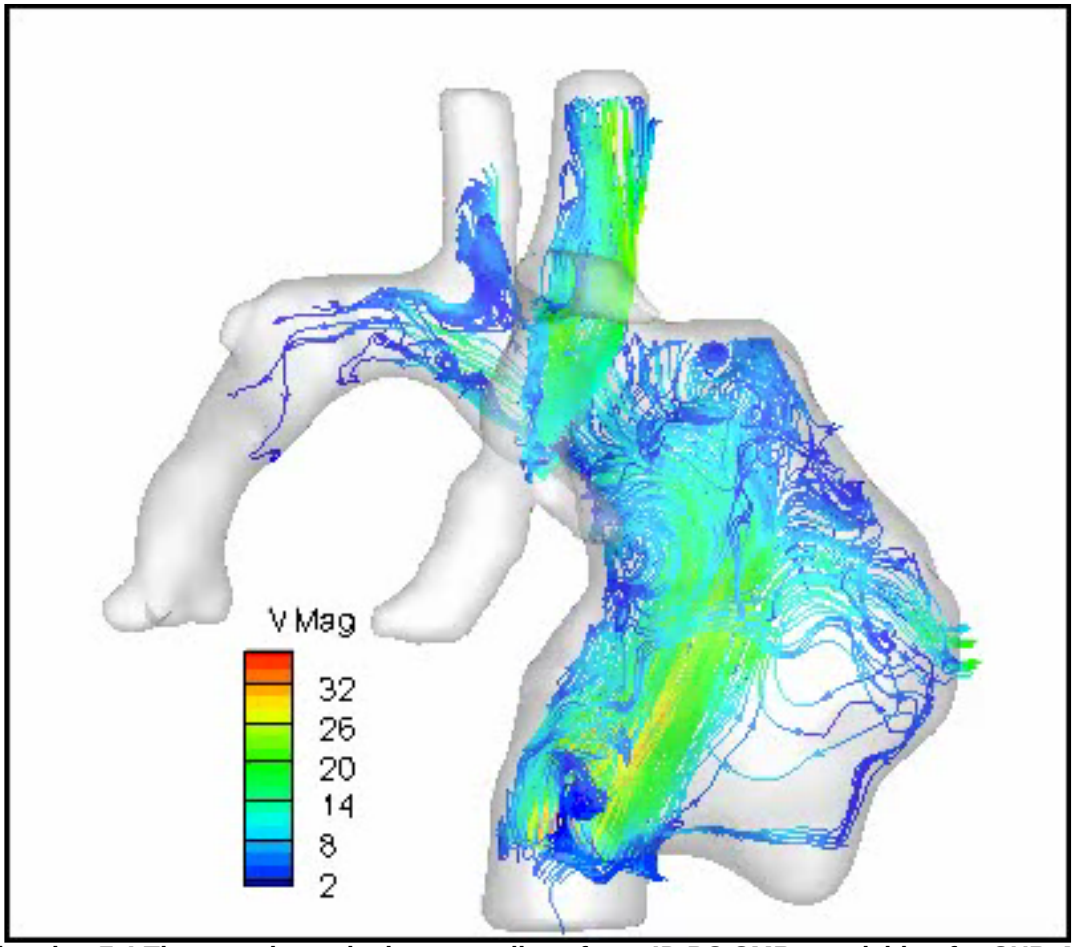


**Animation 7.4 Time-varying velocity streamlines from 4D PC CMR acquisition for CHB_M1.**

At the request of the clinical team, virtual surgery was performed to simulate a revision from the dilated lateral tunnel to a 22 mm extracardiac conduit, as shown in Figure 7.42. Comparison of resulting power losses under baseline and simulated exercise between the existing connection and virtual extracardiac model is shown in Table 7.17. Owing to the large PA size, there was no difference in power loss between connections, suggesting that surgical revision in this case would not yield meaningful benefit. On the surface, this finding is somewhat surprising in that it seems to contradict the work of de Leval that motivated the switch from atriopulmonary Fontan to TCPC[17], although important distinctions exist between the atriopulmonary connection and this lateral tunnel

connection, even with its dilated appearance (e.g., there is no collision and mixing with SVC within the connection for the lateral tunnel). The logical explanation for the finding, leveraging the geometric results presented in §5.5.2.1, is that vessel minimum and mean diameters are the strongest predictions of power loss for a given connection, not the maximum dimension. Hence, because the PAs for this patient are large, the resting power losses for the both the *in vivo* and virtual extracardiac connections were very low. With that said, this case may also exploit inherent shortcomings in the computational method related to the rigid wall assumption and the use of the same inlet flow conditions in the evaluation of the two surgical models. Revisiting this case in the future with such limitations may thus be a worthwhile exercise.

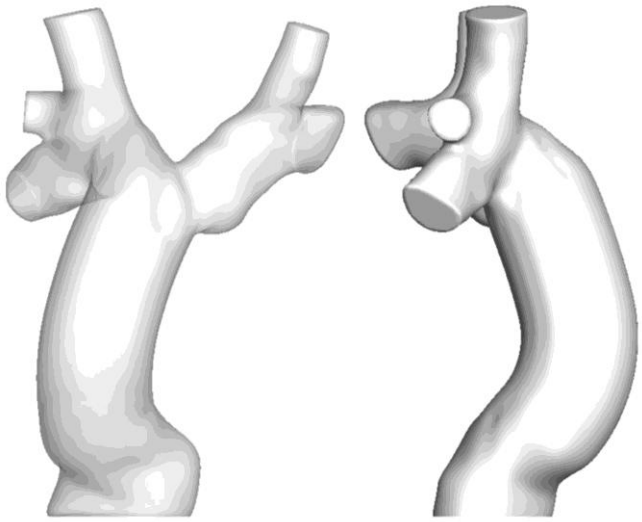

**Figure 7.42 Virtual extracardiac connection created and evaluated for CHB_M1 shown from anterior (left) and right sagittal (right) perspectives.**

**Table 7.17 Power loss (in mW) results at baseline and exercise for the two connections evaluated.**

| | Baseline | 2x exercise |
|---|---|---|
| **Current connection** | 2.7 | 12.5 |
| **Virtual Extracardiac** | 2.7 | 12.6 |

Finally, with limited hemodynamic resistance produced by the TCPC, we sought to quantify the potential therapeutic benefit of targeting/lowering PVR to relieve the high CVP (via Sildenafil use, for example). For this, the lumped parameter model (§4.4) was selectively tuned to approximate known values of this patient's physiology from catheterization (cardiac output - 3.2 L/min, PVR – 2.5 WU, arterial pressure 95/55 mmHg, atrial pressure 10 mmHg, CVP, 18.2 mmHg). With these baseline values established, the PVR parameter was arbitrarily decreased in steps of 0.5 units to observe the effect on CVP. Results are shown in Table 7.18.

**Table 7.18 Results of parametric lumped parameter analysis of PVR in CHB_M1**

| | From Cath. | Modeled Baseline | | | |
|---|---|---|---|---|---|
| **C.O. (L/min)** | 3.2 | 3.17 | 3.4 | 3.67 | 3.98 |
| **PVR (mmHg/L/min)** | 2.5 | **2.5** | **2** | **1.5** | **1** |
| **CVP (mmHg)** | 18 | 18.2 | 17.8 | 17.3 | 16.7 |

It was found that each step down in PVR dropped the CVP by increments of ~0.5 mmHg, as well as increased the cardiac output. For the extreme case tested (PVR =1) a maximal decrease of 1.5 mmHg was predicted along with a 0.8 L/min increase in cardiac output (which, again, is based on a non-specific model of the ventricle function).

Based in part on these findings, the patient was started on a Sildenafil regimen to attempt to lower PVR and CVP; however, at last follow-up, no change in baseline hemodynamics had been noted. Finally, it is worth noting that this patient was the focus of additional investigation and analysis by Mirabella *et al*[165].

### 7.4.9 CHOA_M5

Patient was a 12 year-old female with an existing lateral tunnel Fontan. Arterial oxygen saturations were in the low 90/high 80% range, but PAVM were diagnosed in the right lung on the basis of systemic venous bubble injections in the cath lab- patent bubbles observed in the pulmonary veins denote AVM as they would have been filtered out otherwise.

Most recent catheterization report was from 2009 at which time 2 Amplatzer ASD devices were inserted to close the fenestration. Pre-closure hemodynamics showed systemic saturation of 82%, systemic BP 100/67 with a mean of 79 mmHg, mean Fontan pressure 14 mmHg, LVEDP 11 mmHg, calculated Qp 1.71 L/min/$m^2$, calculated Qs 2.23 L/min/$m^2$, Qp:Qs 0.76:1, PVR 1.76 Wood units, SVR 29.11. Post-closure no further hemodynamics were performed except that the systemic saturation rose from 82 to 88%.

The CMR scan that served as the basis for this surgical planning evaluation was performed on 12/8/2011. No axial SSFP or cine sequences were acquired; however,

MRA data acquired in conjunction with lower extremity gadolinium injection were found to be sufficient for anatomic reconstruction. The results are shown in Figure 7.43; the defining characteristic is an apparent stenosis of the connection of the lateral tunnel to the PAs. As usual, phase contrast planes were acquired in both caval veins and proximal pulmonary arteries, with the results provided in Table 7.19.

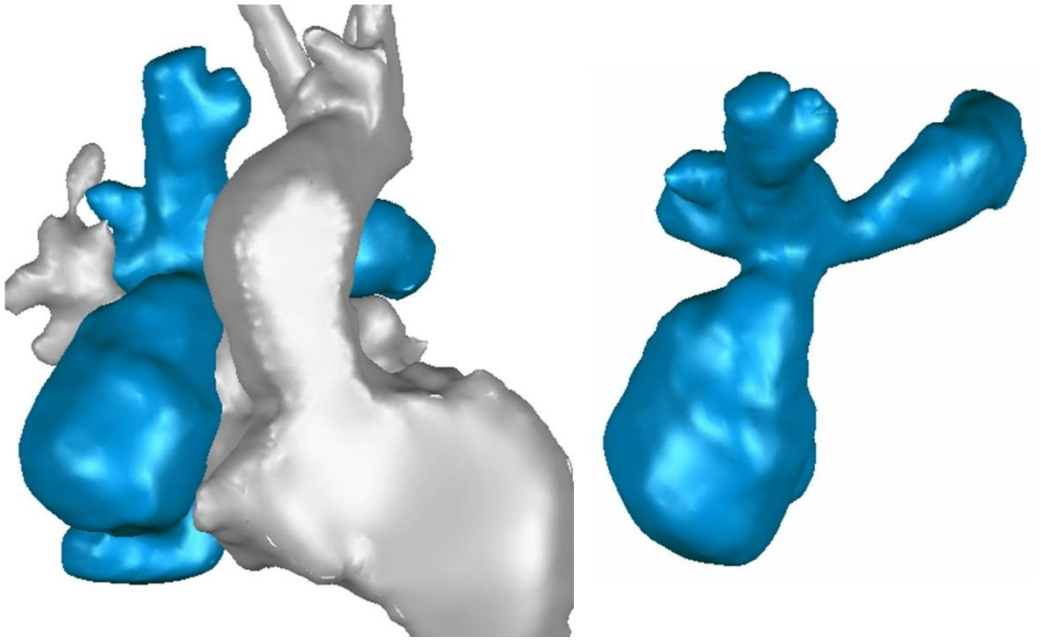

**Figure 7.43 Reconstructed TCPC (blue) and surrounding anatomy (gray) for CHOA_M5.**

**Table 7.19 Pre-operative vessel flow rates from PC CMR for CHOA_M5**

| | Flow Rate (L/min) | Relative Distribution (%) |
|---|---|---|
| **IVC** | 1.36 | 52 |
| **SVC** | 1.26 | 48 |
| **LPA** | 1.12 | -43 |
| **RPA** | 1.50 | -57 |

The results of simulating the pre-operative hemodynamics with time-varying boundary conditions are shown in Figure 7.44 and Animation 7.5. It is evident that the stenosed Fontan-PA attachment, which has a slight left offset with respect to the SVC, acts to direct the majority of the Fontan flow to the LPA; however, the acceleration (through the stenosis) and collision of Fontan flow against the posterior PA wall act to promote mixing and left/right division of Fontan flow such that there is a non-negligible fraction of that flow that appears to perfuse the right lung. By particle tracking over the cardiac cycle, this distribution was calculated to be 65/35% LPA/RPA. On the surface, this distribution does not appear to be consistent with the PAVM diagnosis, but perhaps neglecting wall motion through the lateral tunnel for this particular patient is a weak assumption. Energetically, both PAs were well-sized (with the possible exception of a small narrowing

of the sub-aortic section of the PA), so despite the large Fontan pathway and the stenosed junction, the total resistance was low- 0.30 Wood Units.

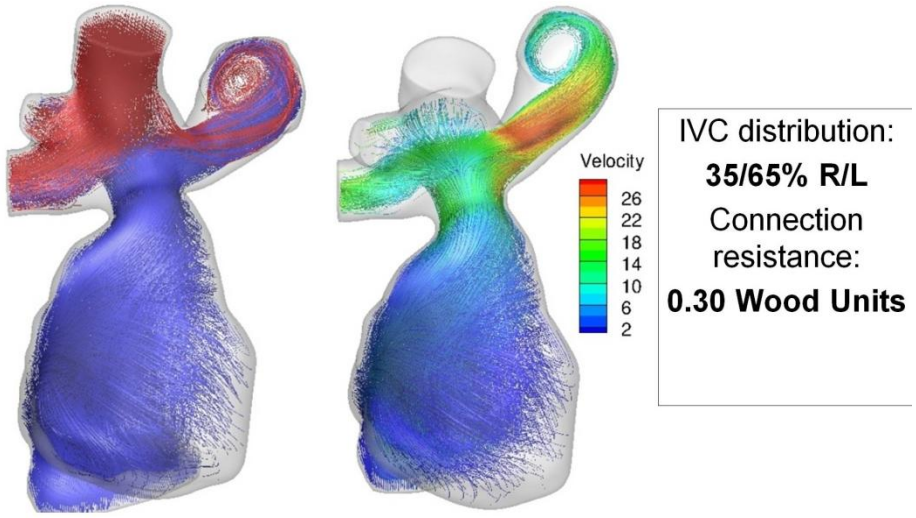


**Figure 7.44 Representative results from time-varying simulation of the pre-operative hemodynamics for CHOA_M5.**

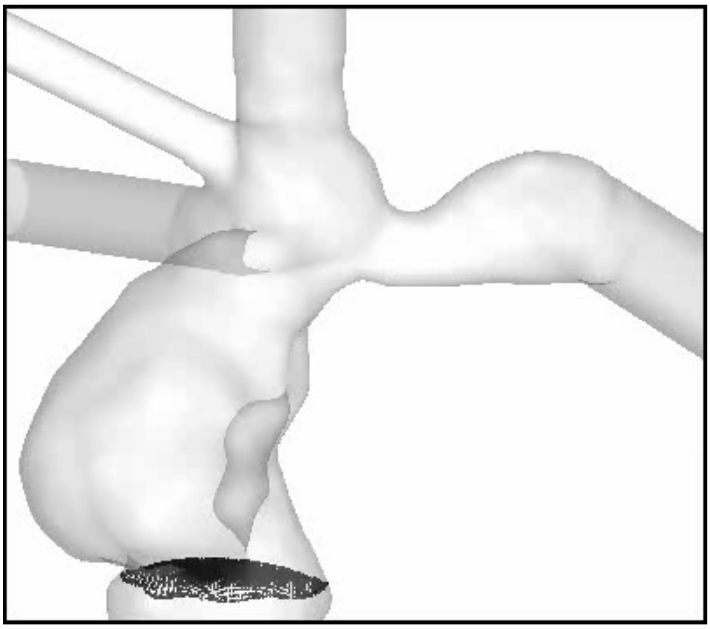

**Animation 7.5 Pulsatile IVC particle tracking for pre-operative simulation for CHOA_M5.**

All simulations for the surgical options were also performed by imposing time-varying flow conditions at the model inlet/outlets with rigid vessel walls. Because of significant compliance effects in the dilated lateral tunnel (peaks of ±10 L/min over the course of the cardiac cycle), the IVC flow conditions were imposed as the instantaneous difference among the other inlets/outlets. In addition to the measured flow conditions, two other scenarios were investigated for most options: an alternate PA outflow condition (65/35 RPA/LPA), and an alternate caval inlet distribution (65/35 IVC/SVC; with $Q_s$ held constant). The rationale for this latter condition was that changing $Q_S$ with constant vessel distributions (as was done for CHOP_M13) does not generally alter the results; whereas, changing the relative distributions (simulating increased IVC flow percentage with increasing BSA[142], for example) represented both a likely physiology scenario and a different data point at which the connection could be evaluated. HFD was quantified using the same particle-based method employed for CHOP_M8.

Given the relative simplicity of the patient anatomy compared to the previous cases presented, only two basic surgical revision approaches were envisioned: either an extracardiac conduit or a Y-Graft. However, as was done for CHOP_M12 (§7.4.5), multiple implementations of these two options were investigated to identify potential pitfalls and evaluate the robustness of each approach. These designs are shown in Figure 7.45. Briefly, three Y-Graft designs were tested: one ‘ideal’ implementation with both branches positioned laterally away from the Glenn anastomosis, and one option each with the left or right branch medially positioned with respect to the SVC (shown in red in Figure 7.45). The two extracardiac options explored the effects of no caval offset vs. a half diameter offset of the Fontan baffle toward the RPA.

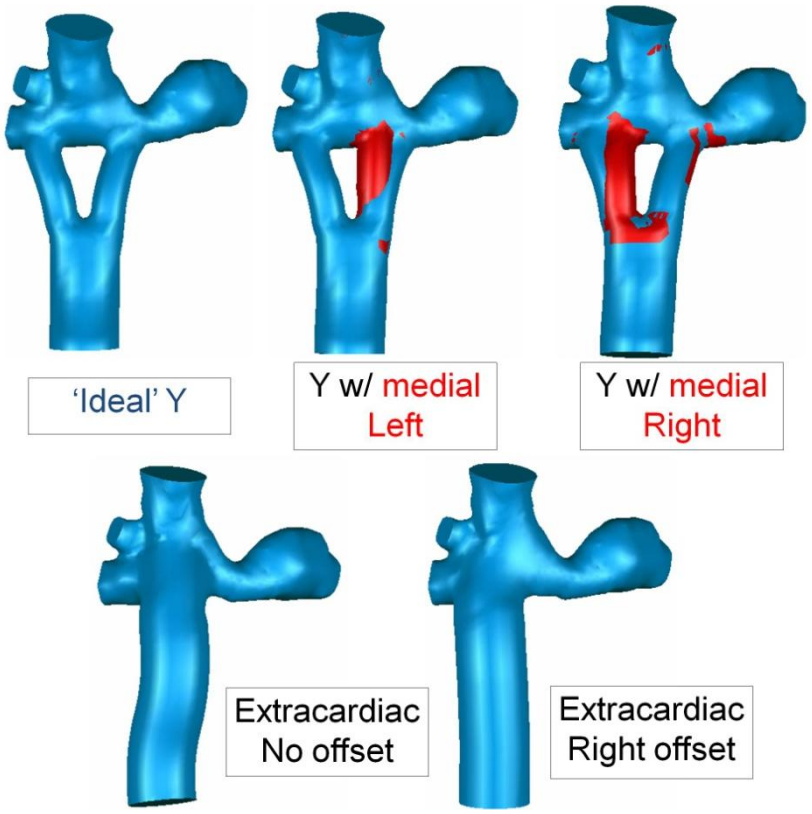


**Figure 7.45 Five surgical options investigated for CHOA_M5 representing three Y-Graft designs and two different placements of an extracardiac conduit. The medial Y-Graft designs are shown in red to highlight the difference with respect to the 'ideal' case.**

The results for the 'ideal' Y-Graft option are presented in Figure 7.46 and Table 7.20. Flow distribution results were well balanced (51/49% LPA/RPA) and presumably an improvement over the pre-operative condition (even though the simulated results were not particularly poor). Changes in imposed flow conditions did little to change these results. Connection resistance was equivalent to the pre-operative value (0.30 WU), likely because neither case relieved the slight narrowing of a sub-aortic PA stenosis. Positioning the left branch further to the left than what was modeled may have improved performance in this regard. Additionally, the convective acceleration through the

undersized Y-Graft branches likely reduced efficiency improvements, as evidenced by the fact that resistance increased at a higher IVC flow percentage.

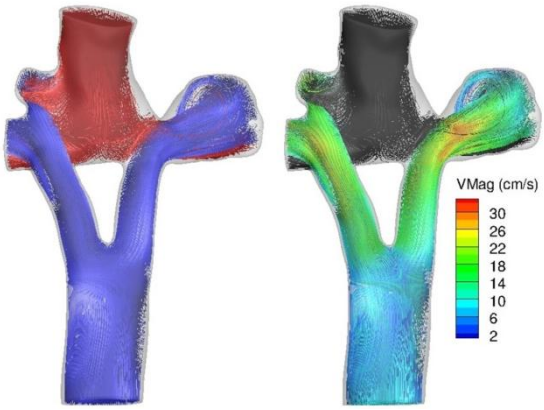


**Figure 7.46 Velocity streamlines for the 'ideal' Y-Graft option under pre-operative flow conditions. The left image shows the streamlines colored by vessel of origin while the right image shows the local velocity magnitude for the IVC flow.**

**Table 7.20 HFD and power loss (resistance) results for the 'ideal' Y-Graft option**

| | **Pre-operative** | **65/35 R/L split** | **65% IVC flow** |
|---|---|---|---|
| **Flow Distribution** (R/L) | 51/49% | 52/48% | 51/49% |
| **Connection Resistance** (WU) | 0.30 | 0.25 | 0.36 |

In comparison to the case where the branches were laterally positioned, Figure 7.47 shows the qualitative outcomes if either branch was instead placed medially. The quantitative data are provided in Table 7.21. As expected, medial offsets of the Y-graft limbs led to 1) slightly higher resistances; and 2) slightly higher flow distribution to the contra-lateral lung (as compared to the 'ideal' case). Fortunately, the outcomes with regard to flow distribution were all still generally balanced and favorable.

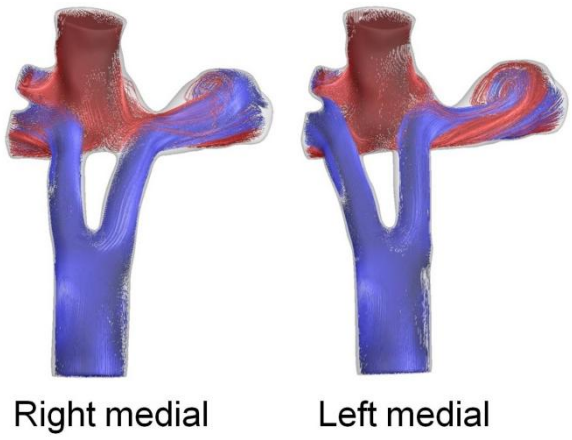


**Figure 7.47 Velocity streamlines (colored by vessel of origin) for the two medial Y-branch placement options. Interaction of the medial branch flow with the SVC flow is apparent, yet has little qualitative impact on the flow distribution.**

**Table 7.21 HFD and power loss (resistance) results for the two medial Y-Graft options.**

| | | Pre-operative | 65/35 R/L split |
|---|---|---|---|
| **Right medial** | **Flow Distribution** (R/L) | 47/53% | 50/50% |
| | **Connection Resistance** (WU) | 0.33 | 0.29 |
| **Left medial** | **Flow Distribution** (R/L) | 56/44% | 60/40% |
| | **Connection Resistance** (WU) | 0.34 | 0.28 |

Results for the extracardiac models are shown in Figure 7.48 and Table 7.22. With respect to flow distribution, both extracardiac options investigated produced favorable outcomes although 1) they demonstrated much greater sensitivity to the outflow splits than the Y-graft options (as expected); and 2) the introduction of a right offset biased flow much more to the right lung than any of the other options, which is again an expected outcome. Also noteworthy is the fact that these models were predicted to be slightly more efficient than the 20x10 mm Y-grafts.

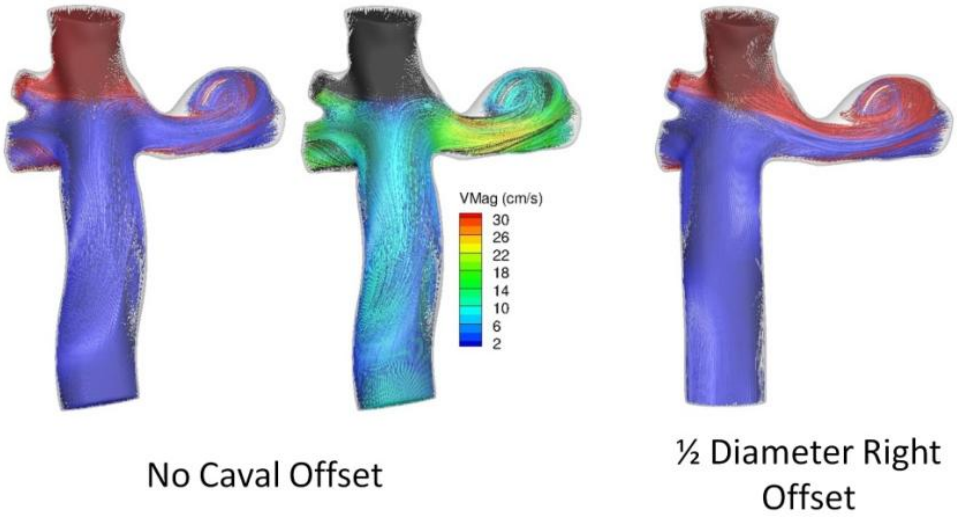


**Figure 7.48 Velocity streamlines for the (left two images) no offset extracardiac and (far right) right caval offset extracardiac options under pre-operative flow conditions.**

**Table 7.22 HFD and power loss (resistance) results for the two extracardiac options**

| | | **Pre-operative** | **65/35 R/L split** | **65% IVC flow** |
|---|---|---|---|---|
| **No Offset** | **Flow Distribution** (R/L) | 52/48% | 60/40% | 52/48% |
| | **Connection Resistance** (WU) | 0.28 | 0.2 | 0.28 |
| **Right Offset** | **Flow Distribution** (R/L) | 69/31% | 77/23% | N/A |
| | **Connection Resistance** (WU) | 0.3 | 0.22 | N/A |

Since this procedure was a Fontan revision (i.e., the patient was older than a normal Fontan recipient) and the small branch size in the 20x10 mm Y-Grafts was suspected to be a limiting factor in the lack of efficiency improvements compared to the virtual extracardiac and pre-operative connections, a final Y-Graft model with a 22x11 mm graft was created using the 'ideal' branch placement design. The results for this option are shown in Figure 7.49. Flow distribution results were still well balanced between LPA and RPA, although with a slightly greater preference for the RPA than the 20x10 graft. More importantly, the power loss was the lowest of any of the investigated options because of the decreased velocities through the branches owing to the larger graft size. Hence, this option was recommended (along with the suggestion that efforts be made to connect the left branch at the site of the LPA narrowing) and surgically implemented in April 2012.

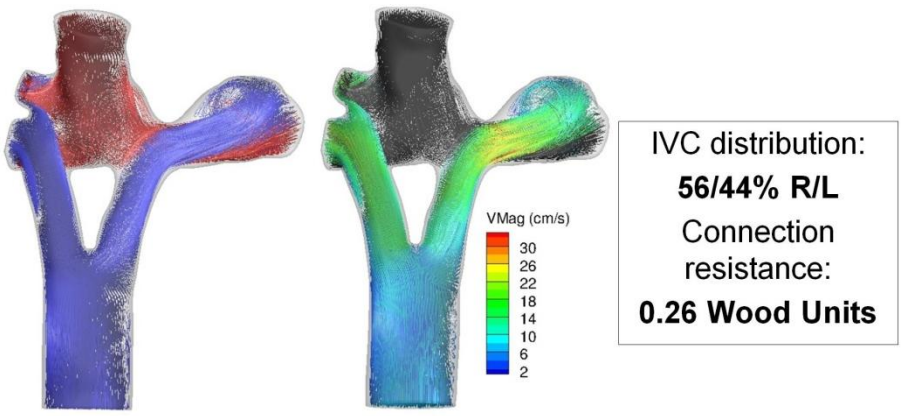


**Figure 7.49 Results from a 22x11 mm Y-Graft option with 'ideal' branch placement under pre-operative measured flow conditions.**

### 7.4.10 CHOP_M16

Patient was a 2 year-old male with heterotaxy syndrome of asplenia type status post bilateral bidirectional Glenn. PAVM were suspected in the right lower lobe and there was also a history of significant systemic-pulmonary collaterals.

The CMR scan that served as the basis for this surgical planning evaluation was performed on 8/8/2011. The imposed flow conditions for the computational simulations were taken directly from the MR report (included in the patient files) as there were some inconsistencies in the file labeling with regard to the acquisition VENC in the CMR dicoms.

The 3D anatomic reconstruction is shown Figure 7.50 (anterior and posterior views) in blue with the surrounding anatomy in gray. The IVC is located on the left, behind the heart, while the pulmonary veins primarily connect to the right atrium. The flow conditions used for the simulations are listed in Table 7.23.

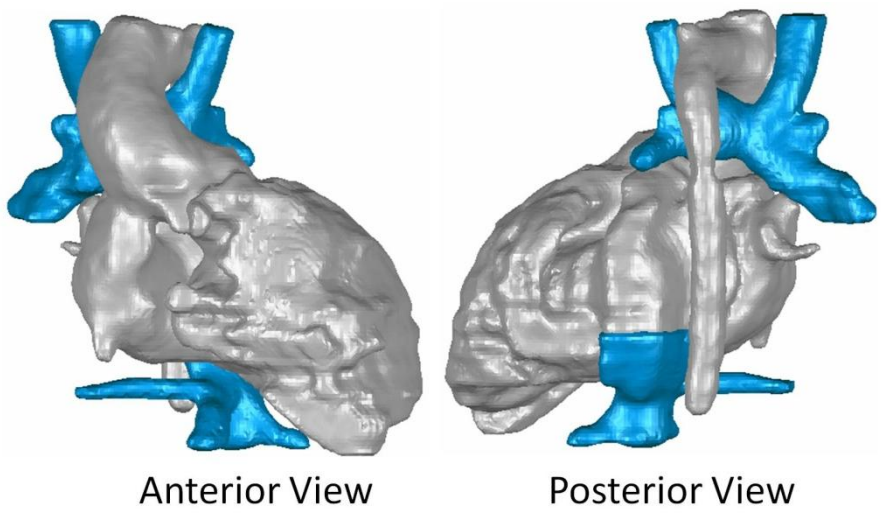


**Figure 7.50 Anatomic reconstruction of the bilateral bidirectional Glenn connection (blue) and surrounding anatomy (gray) for CHOP_M16.**

**Table 7.23 Flow rates from clinical CMR report for CHOP_M16**

| | Flow Rate (L/min) | Relative Distribution (%) |
|---|---|---|
| **IVC** | 1.09 | 55 |
| **RSVC** | 0.58 | 29 |
| **LSVC** | 0.32 | 16 |
| **LPA** | 0.22 | -22 |
| **RPA** | 0.74 | -78 |

All simulations were performed by imposing time-averaged flow conditions at the model inlet/outlets with rigid vessel walls. In addition to the measured flow conditions, two other scenarios were investigated: an alternate PA outflow condition (55/45 RPA/LPA) to simulate eventual PAVM regression and pulmonary redistribution; and a decreased IVC flow rate (0.68 L/min vs. 1.27 L/min) in anticipation of decreased cardiac output post-operatively. For this latter condition, the measured SVC flow rates were held constant to maximize the 'adversity' of this scenario, such that the IVC contribution dropped to 40% of the venous return. It is noted that these numbers (46% decrease in IVC flow pre- to post-operatively) were roughly based on the post-operative experience with CHOP_M12 (§7.4.5), which was anatomically very similar and had similar pre-op flow measures.

A total of 6 options were investigated. The first 5 modeled intra-atrial connections through the left atrium to the left/medial aspect of the connection based on the perceived difficulty of passing in front of the descending aorta. However, at the suggestion of the surgeon, a $6^{th}$ option was added simulating an extracardiac conduit running underneath the right atrium and up the right side of the heart, as per a normal connection. These options are shown in Figure 7.51.

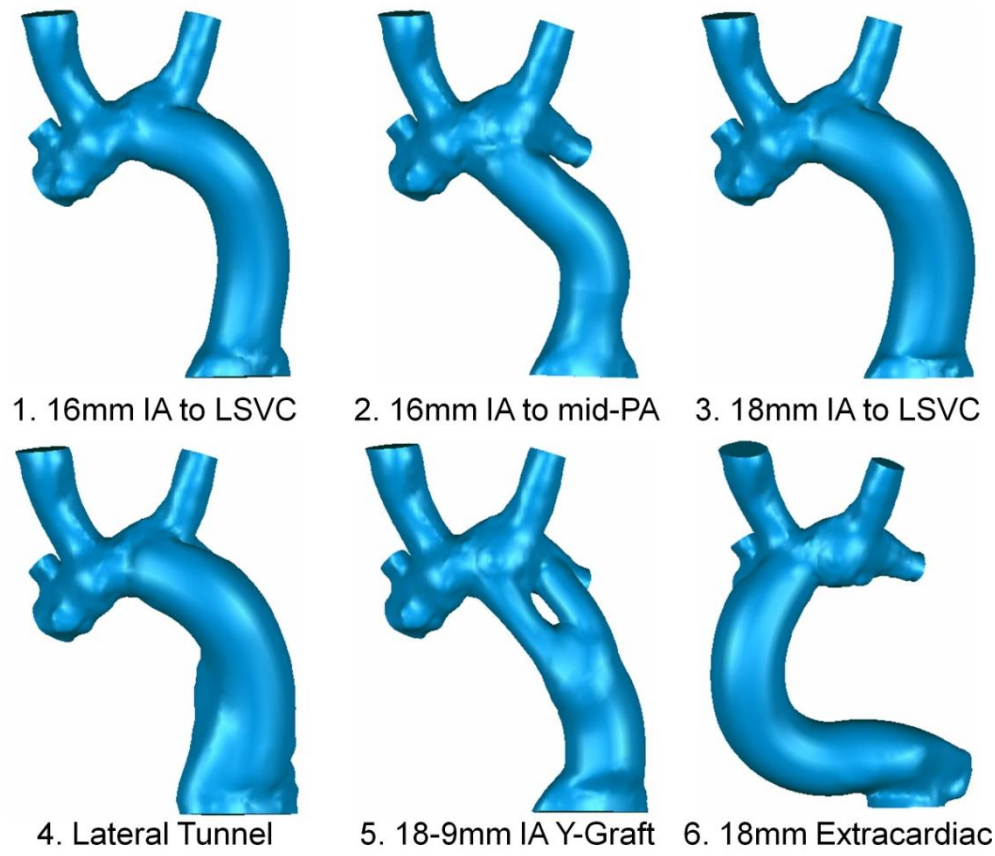


**Figure 7.51 Six surgical options investigated for CHOP_M16 including 5 intra-atrial approaches to the LSVC (#1-5) and an extracardiac connection to the right (#6).**

The characteristics of the 5 left-sided options were all very similar with respect to both flow distribution and resistance. The only design that clearly performed poorly was the Y-graft (Figure 7.52). The significant curvature imposed on the proximal (i.e., inferior) section of the conduit because of the IVC positioning (in addition to the angles of the SVCs) is not advantageous for angling the branches at the PA anastomoses. In the particular design modeled, for example, the left branch is angled to the right, away from the LPA rather than streamlining flow to that vessel; whereas the right branch runs inferior to the LSVC and (while this condition was not simulated) would have likely been

inhibited by LSVC flow at lower IVC flow conditions. The end result is a very chaotic flow profile that would intuitively not be very stable and robust and had the highest connection resistance (albeit, still not very high) of all evaluated options.

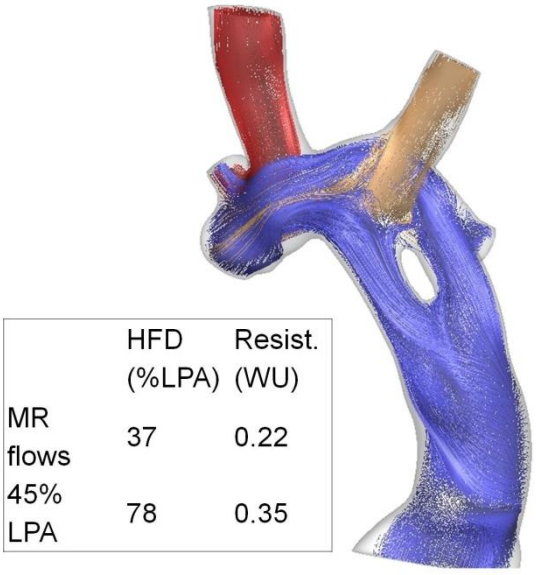

| | HFD (%LPA) | Resist. (WU) |
|---|---|---|
| MR flows | 37 | 0.22 |
| 45% LPA | 78 | 0.35 |

**Figure 7.52 Results for the intra-atrial Y-Graft connection investigated for CHOP_M16.**

For the remaining left-sided options, Figure 7.53 demonstrates that the results were all very consistent and there are very few qualitative distinguishing characteristics. Because of the medial angle of the LSVC, all four designs achieved approximately 60% HFD to the RPA (the side with suspected PAVM) at the pre-op MR flow conditions because both the LSVC and RSVC were carried across to the right side of the connection (Table 7.24). That is, the majority of LPA flow was IVC contribution. As a result, as the total LPA flow

increased, the IVC-to-RPA contribution dropped off quickly, with a bit more intra-option variation (Table 7.25). Furthermore, under lower IVC flow conditions, this behavior could be more problematic for getting IVC flow across the connection to the RPA as a larger percentage of the IVC flow will be required to meet LPA demands. For example, running option 1 at the 'low-IVC' conditions dropped the HFD from 59% RPA to 45% RPA. Depending on how severely the IVC flow decreases post-operatively, this difference could be even more pronounced.

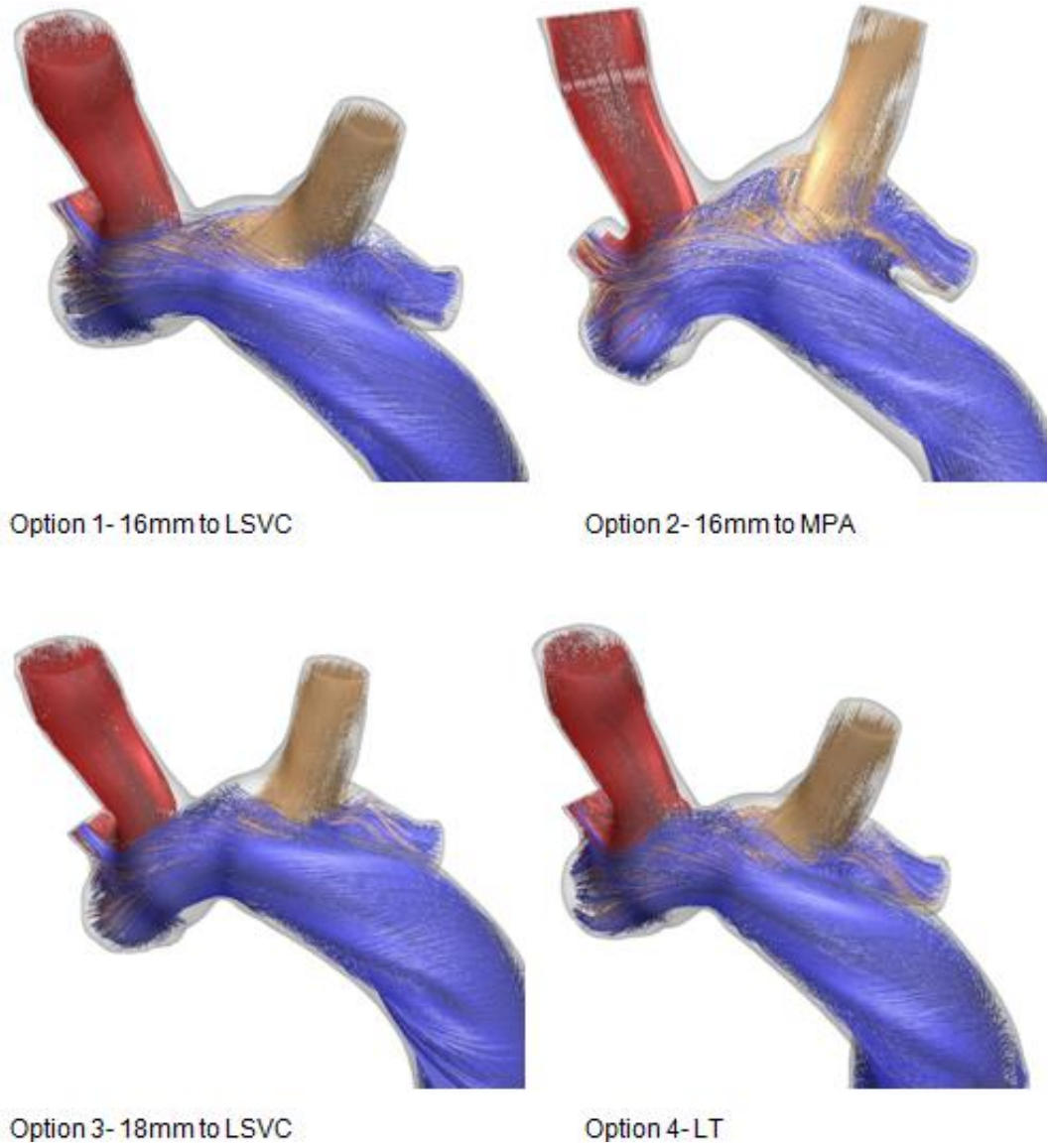


**Figure 7.53 Velocity streamlines (for the pre-operatively measured flow rates) for options 1-4 (intra-atrial connections) for CHOP_M16.**

**Table 7.24 Quantitative results for options 1-4 at the pre-operative flow conditions.**

| | HFD (%LPA) | R (WU) |
|---|---|---|
| **Opt1** | 41 | 0.15 |
| **Opt2** | 40 | 0.20 |
| **Opt3** | 40 | 0.16 |
| **Opt4** | 39 | 0.17 |

**Table 7.25 Quantitative results for options 1-4 for GFD=45% LPA**

| | HFD (%LPA) | R (WU) |
|---|---|---|
| **Opt1** | 71 | 0.3 |
| **Opt2** | N/A | N/A |
| **Opt3** | 62 | 0.27 |
| **Opt4** | 64 | 0.26 |

As compared to the left-sided options, the right-sided extracardiac connection (Figure 7.54) placed the Fontan in closer proximity to the RPA, leading to much high HFD-to-RPA values (which is the more immediate need with right-sided PAVM). Furthermore, for the design evaluated (conduit placed as far medially as visually possible) the Fontan flow does pass through the connection to the LPA suggesting that, as shown with the 45% LPA result, there does not appear to be a high risk of unilateral flow to the right. Finally, under low IVC flow conditions, the proximity of the baffle to the RPA provides a better hedge that IVC flow will still reach that limb.

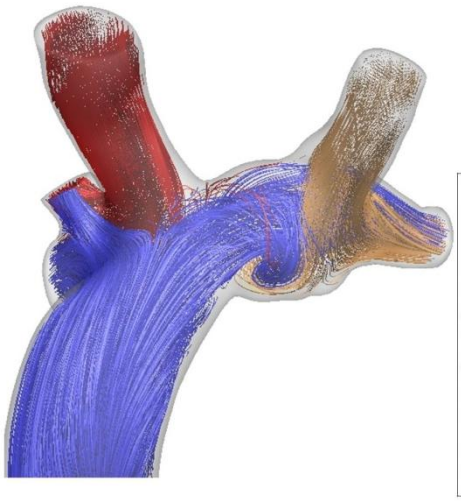

| | HFD (%LPA) | Resist. (WU) |
|---|---|---|
| MR flows | 87 | 0.13 |
| 45% LPA | 64 | 0.28 |
| Low-IVC | 95 | 0.21 |

**Figure 7.54 Results for the right extracardiac model investigated for CHOP_M16. Velocity streamlines shown correspond to the pre-operative flow conditions.**

The conclusion of this study was that, while none of the evaluated options except the Y-graft was a bad choice, the safest bet for ensuring distribution of flow through the Fontan baffle reached the RPA (assuming it is surgically feasible) was an extracardiac connection to the right. This design succeeds in perfusing both lungs, with a preference for the RPA obviously, and is more robust to decreases in IVC flow, as expected post-operatively. This option was selected and surgically implemented in June 2012.

### 7.4.11 CHOP_M17

Patient was a 14 year-old male with heterotaxy syndrome and a hypoplastic left ventricle. There was IVC interruption with azygos vein continuation to a left SVC. He had an existing Fontan connection of the hepatic veins to the RPA. He had progressing

systemic hypoxia because of substantial left lung PAVM with reported saturations in the upper 60s.

The patient was scanned via CMR on 6/8/2012 for surgical planning evaluation. Because of coil artifacts in the upper right chest, anatomic reconstruction was performed (by M. Restrepo, Georgia Tech) using a combination of SSFP and GRE sequences. The result is shown in Figure 7.55. The time-averaged vessel flow rates are provided in Table 7.26.

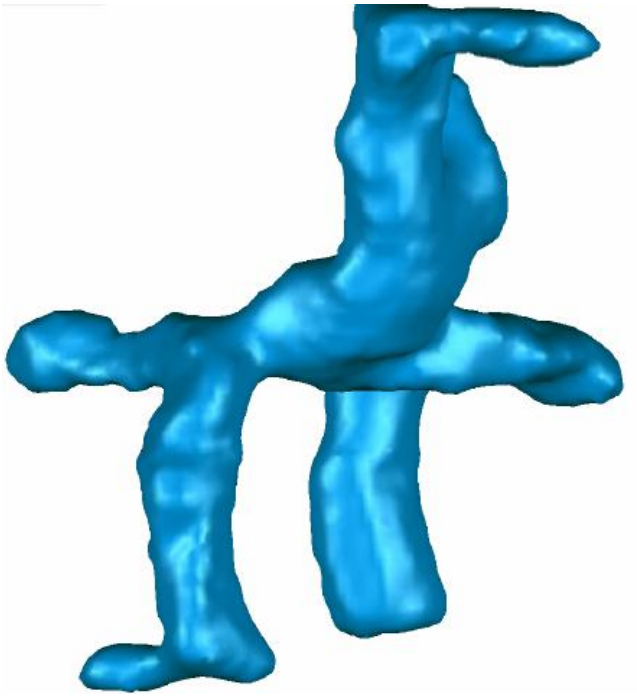

**Figure 7.55 Fontan reconstruction for CHOP_M17.**

**Table 7.26 Time-averaged flow data for CHOP_M17 measured from PC CMR.**

| | Flow Rate (L/min) | Relative Distribution (%) |
|---|---|---|
| **HepV** | 0.30 | 11 |
| **Az** | 1.40 | 50 |
| **LSVC** | 1.10 | 39 |
| **LPA** | 1.80 | -62 |
| **RPA** | 1.10 | -38 |

Simulations were run with pulsatile inflow conditions based on the measured vessel inflow conditions for hepatic vein, LSVC, and azygos vein. The HFD was quantified based on a pulsatile particle tracking method- massless particles were seeded across a specified cross-section of the hepatic venous inlet 50 times over 1 cardiac cycle and advected through the connection over the subsequent 4 cycles. Connection energetics are reported as power loss.

To confirm the diagnosis of left lung PAVM (by visualizing unilateral hepatic flow the right), the current patient-specific anatomy was simulated under the measured MR flow conditions. Representative flow streaming results are shown in Figure 7.56. Consistent with the clinical diagnosis, the hepatic flow (shown in blue) was entirely constrained to the right lung because of its extreme offset position with respect to the azygos and left SVC. Time averaged power loss for the connection was 2.0 mW.

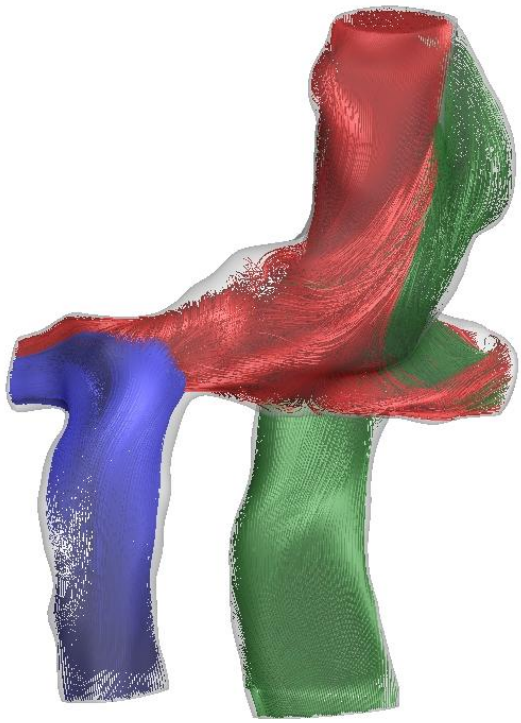

**Figure 7.56 Velocity streamlines for pre-operative Fontan connection of CHOP_M17.**

There was one minor inconsistency with these findings and other clinical reports- a catheterization report from 8/11 noted a 3 mm pressure drop between the azygos vein and LPA (18 mm Hg vs. 15 mm Hg). On average, there was only about 0.5 mm drop in simulations between those vessels- a 3 mm drop would require a severe obstruction or much higher flows, neither of which are present. The cath report also noted only a 1 mm drop from the azygos to the RPA (compared to 0.9 average drop from simulations). It is unclear how the distal vessel could have a smaller drop than the proximal one (again, without a severe obstruction present), so the LPA discrepancy is not overly concerning with respect to the model verification as it suggests a potential error in the data recorded in the catheterization report.

A total of 3 options were investigated, as shown in Figure 7.57. The first was simply an attempt to move the hepatic baffle to the site of the kawashima connection (as opposed to the current right offset). Next was a hepatic-to-azygos connection, which has been shown to be successful in past cases on interrupted IVC with a single SVC. Finally, an H-graft connection simulated hepatic venous connections to both the azygos and RPA.

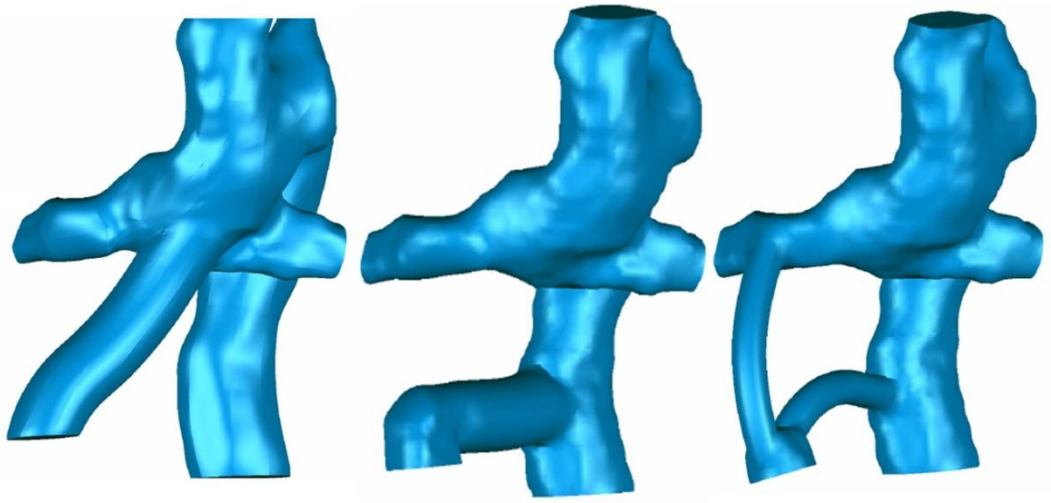

**Figure 7.57 Three surgical options investigated for CHOP_M17 representing (left) repositioning the hepatic venous baffle, (middle) hepatic-to-azygos connection, (right) and an 'H-graft' design.**

Simply re-positioning the hepatic baffle to the left did improve hepatic flow to the left slightly, as shown in Figure 7.58. However, the hepatic flow to the left was still only a small percentage of total hepatic flow volume (21% based on the pre-operative flows) and past experience (see §7.4.3) dictates that these connections are not very robust. In other words, they are extremely sensitive to baffle placement and the relative vessel flows. Thus, no other simulations were performed for this design.

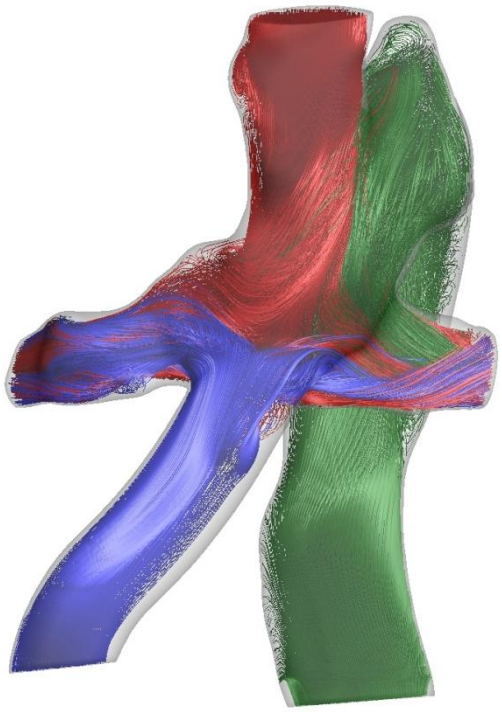

**Figure 7.58 Velocity streamlines for the re-positioned hepatic baffle (opposite the LSVC and azygos connection).**

The hepatic-to-aygos connection performed better for this patient given the natural tendency for azgos flow (green) to stream to the LPA (see Figure 7.59). Under the pre-operatively measured flow conditions ($Q_p$= 62% LPA), this led to HFD = 84% to the LPA (the side with PAVM). To evaluate this performance under varying outflow conditions, the PA splits were set to $Q_p$ =55% and 45% to the LPA in subsequent simulations to simulate progressive regression of left sided PAVM. HFD and power loss results for all these cases are shown in Table 7.27.

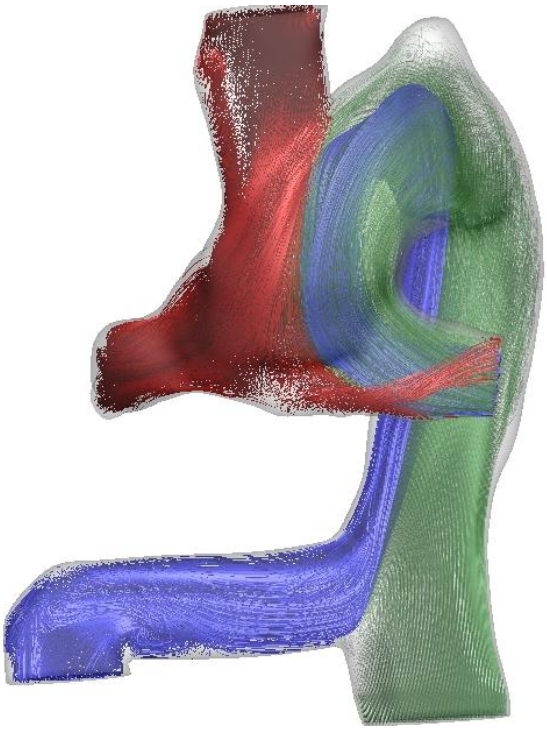

**Figure 7.59 Velocity streamlines from pre-operative flow conditions for the hepatic-to-azygos connection for CHOP_M17.**

**Table 7.27 Quantitative results for the hepatic-to-azygos connection at various boundary condtions**

| Imposed $Q_p$ Split | HFD (%LPA) | PL (mw) |
|---|---|---|
| **62% LPA (measured)** | 84 | 2.5 |
| **55%** | 76 | 2.1 |
| **45%** | 64 | 1.5 |

As total flow to the RPA increased, so did the hepatic flow, which was expected. Therefore, despite the fact that this connection biased hepatic flow to the left, pulmonary remodeling subsequent to PAVM regression would be expected to recruit hepatic flow to the RPA and so avoid future PAVM development in that lung. With respect to power loss, this connection is slightly less efficient than initial Fontan, consistent with prior findings regarding hepatic-to-azygos connections, although the magnitude still appears to be acceptably low.

Finally, to evaluate the impact of changing systemic venous returns in the acute post-operative period, one final simulation was performed with altered (time-averaged) inflow distributions. The new values were chosen based on measurements made from an 18 year old patient with similar venous anatomy (CHOA_M2) such that the total flow decreased from 2.8 to 2 L/min, and the relative distributions for the hepatic vein, svc, and azygos were set at 11%, 62%, and 27%, respectively. Despite these changes, 100% of hepatic flow was predicted to perfuse the LPA under those conditions, confirming the robustness of this connection design.

Since the hepatic-to-azygos option did bias flow to the LPA, one final option was considered that had potential to provide slightly better balance for HFD. However, as

seen Figure 7.60, the hepatic-to-RPA connection was energetically more favorable than the hepatic-to-azygos connection, so this option still favored hepatic flow to the right (24% HFD to the LPA).

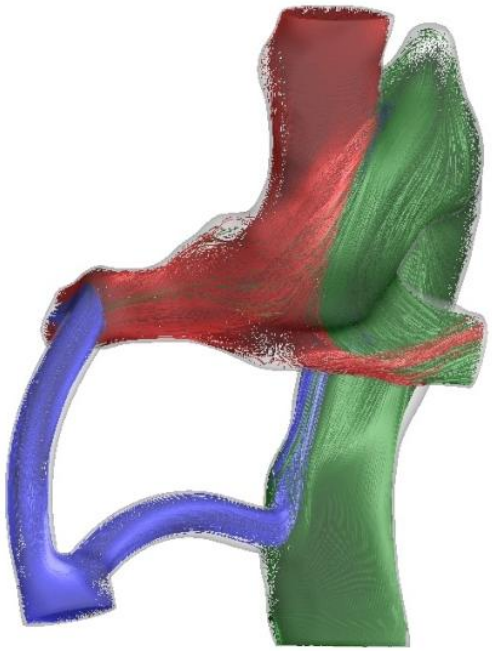

**Figure 7.60 Velocity streamlines for H-Graft connection under pre-operative flow conditions.**

The present results, in conjunction with past experiences, made this case rather straightforward. An extracardiac connection (further to the left) to the Kawashima junction was not a robust approach and could yield unpredictable outcomes. The left-sided SVC with a left-sided hepatic vein makes a 'traditional' Y-graft approach impossible, and the modified H-graft approach did not achieve the same flow distribution

effects. Therefore, the best approach was the hepatic-to-azygos connection, which was predicted to significantly improve hepatic flow to the left in a robust fashion with respect to expected physiologic remodeling. At the time of this writing, no information has been provided regarding the final surgical implementation.

### 7.4.12 Section Discussion and summary

#### 7.4.12.1 Approach for Patients with Interrupted IVC and Azygos vein continuation

Based on early experience of surgical planning for the Fontan procedure, de Zélicourt *et al*. proposed strategies for approaching the most anatomically complex single ventricle patients: those with interrupted IVC and azygos vein continuation[105]. These guidelines were separated based on superior venous anatomy with different advice for single versus bilateral SVC cases. Since the work presented in this thesis expands that experience considerably, it is worth revisiting those guidelines.

Figure 7.61 visually summarizes the conclusions reached for single SVC cases[105]. Namely, it was determined that the flow distribution within the connection was dictated by the directionality of the superior venous flows (SVC + azygos). Thus, standard extracardiac connections are very susceptible to unilateral distribution bias unless they are perfectly aligned with the center of momentum for the superior flows. Instead, the hepatic-to-azygos connection was suggested as a good default, an idea that has been independently advocated by others in the field[62]. The Y-Graft design has potential utility for these patients but is still susceptible to poor outcome in some cases (seen in the top row of Figure 7.61).

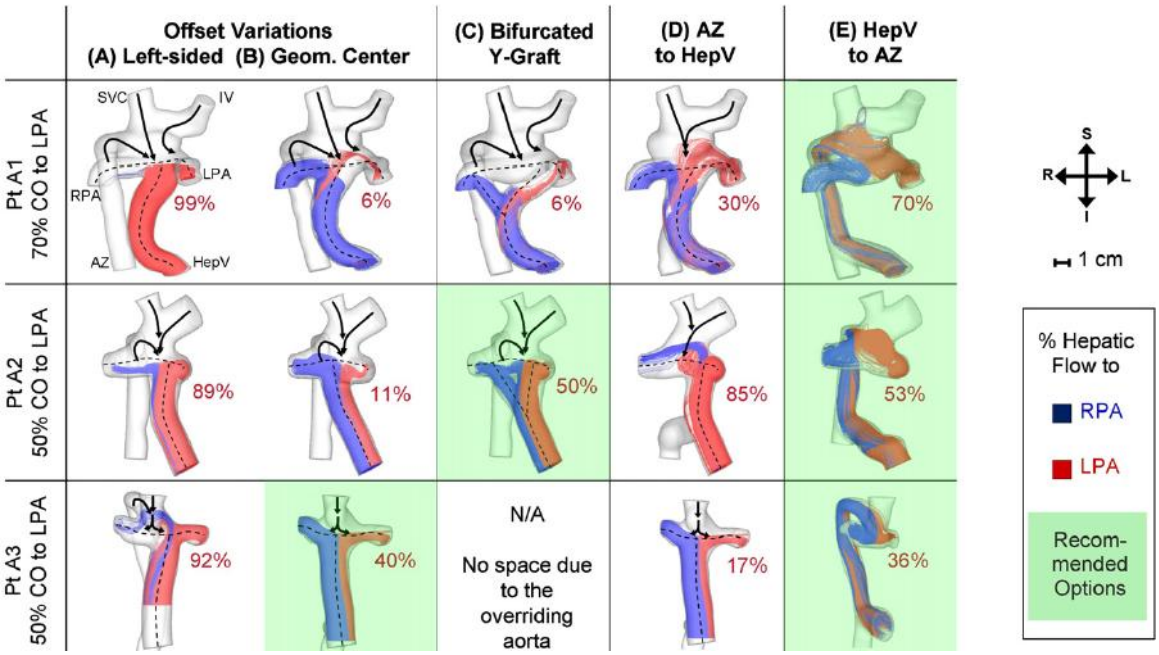


**Figure 7.61 HFD for selected TCPC options for the 3 patients with a single SVC, including intra-atrial or extracardiac options with (A) an offset to the LPA or (B) aiming to the center of the Kawashima connection, (C) bifurcated Y-grafts, (D) intra-atrial or extra-cardiac options combined with an AZ-to-HepV shunt, and (E) HepV-to-AZ shunts. Percentages indicate HFD to the left lung. Superimposed black arrows show the main flow direction of the superior inflows. Dashed lines denote vessel axes. Orientation axis: S ¼ superior; I ¼ inferior; L ¼ left; R ¼ right. AZ, Azygous; HepV, hepatic veins; N/A, not available; CO, cardiac output; LPA, left pulmonary artery; RPA, right pulmonary artery (Taken from [105])**

The conclusions regarding extracardiac connections were reaffirmed by the current experience; it is the guideline with respect to Y-Graft usage that must be revisited. Of the series of patients prospectively modeled in this thesis, four had this single SVC with interrupted IVC anatomy. Three received a Y-Graft hepatic baffle connection; a hepatic-to-azygos was recommended for the fourth. Clearly, the Y-Graft design is a good fit for this configuration.

The earlier hesitation for the Y-Graft was based largely on the experience with CHOP_M1[159] (see §5.3.1.8). In that case, a Y-Graft design was attempted despite an extremely large Kawashima connection and a dominant left-to-right directionality of the

superior venous flows. As a result, the Y-Graft option failed to effectively span the superior connections and thus deliver hepatic flow to both PAs. That patient was the first prospective Fontan surgical planning case and thus weighed heavily in the collective interpretation of the early cases; however, additional experiences have shown the connection geometry to be exceptionally complex even among other interrupted IVC cases. Putting aside the CHOP_M1 experience, the remaining single SVC cases are marked by relatively narrow and well-defined connections of the SVC and azygos to the PAs. Therefore, since the primary criterion for the Y-Graft to be successful in this configuration is the ability to laterally span the superior flows, having this narrow, focused center point is conducive for the Y-Graft.

None of these observations is to say that the prior conclusions regarding hepatic-to-azygos connections are invalid. To the contrary, these options continue to produce positive flow distribution results in all cases (including the retrospective modeling performed for CHOA_M2 and CHOP_M9 in this series). However, the caveat for these options remains the poor energetic performance: routing the hepatic flow through the extensive length of the azygos vein routinely created the highest power losses among the options modeled for each case (directly increasing hepatic pressures). Thus, if parity with respect to HFD can be achieved between hepatic-to-azygos and Y-Graft connections, it seems prudent to opt for the Y-Graft approach to reduce potential pressure build-up in the liver.

Unlike the case for single SVCs, for which we have strong evidence to suggest there are at least two viable surgical approaches, bilateral SVC connections in conjunction with interrupted IVC continue to present a significant challenge. de Zélicourt *et al.* proposed different strategies depending on the balance of flows between the left and right sides of the connection[105]; however, it would seem unlikely that the flows would be balanced (for the long term especially) with two inlets on one side of the connection and only one on

the other. The flow distribution results for CHOP_M7[124] and CHOP_M8 bear this out. For this scenario, H-Graft connections (which are extremely sensitive to flow split) or multi-step azygos-to-hepatic connections (questionable surgical feasibility) were recommended. Only one bilateral patient was modeled in this thesis, so conclusive statements cannot be made in this regard, except to say that the suggested approaches were not sufficient for that case. Instead, it is possible (and perhaps likely) that balanced HFD in these complex cases is simply not possible and the decision must be made as to which lung is in the most immediate need of hepatic flow unless other possible approaches (e.g., systemic to pulmonary shunts) are shown to be effective.

7.4.12.2 The Y-Graft Fontan

Soerensen *et al*[106] were the first to propose the use of flow bifurcation in constructing the TCPC to optimize flow efficiency. The model they investigated was both highly idealized and called for the bifurcation of both the IVC and SVC connections to form the 'Optiflo'. The Y-Graft patients presented in this study (CHOA_M2, CHOP_M9, CHOP_M10) were among the first to have this theory translated into practice, and the use of virtual modeling and patient-specific surgical planning were integral in that process. Furthermore, the success of these early cases motivated the use of the Y-Graft as a surgical standard for a consecutive series of Fontan patients at CHOA, which will be detailed in SA 4.

The fundamental motivation for the Y-Graft was to improve efficiency by reducing/removing caval flow collisions. Its merits in this regard will be explored in the next chapter; however, its use as a hepatic baffle for patients with interrupted IVC utilizes different strengths of the design based around the same concept: avoidance of flow collision allowing a greater degree of control over pulmonary flow distribution. Its

use for this purpose is irrespective of its energetic performance and should be widely considered moving forward in these complex cases, as discussed in §7.4.12.1.

There are two caveats based on the modeling experiences presented in this section. One is the issue of lateral placement away from superior anastomosis sites that has already been discussed. The second is the need to avoid significant lateral curvature. Reviewing the results for cases like CHOP_M12, CHOP_M13 (particularly option g), and CHOP_M16 showed that whenever a significant left-right curvature was imposed on the Y-Graft, the results were sub-optimal. Some of these results are compiled in Figure 7.62 as a reminder. There are multiple reasons for this observation, but the two factors most likely mediating the result are: a) the fact that the two branches are pointing in the same lateral direction at the anastomosis site rather than directing flow in opposite directions; and b) the curvature skews the velocity profile prior to the bifurcation such that the two branches no longer evenly divide the flow. Hence, it is advisable to avoid using a Y-Graft (regardless of whether there is IVC interruption or not) in cases where high lateral curvature will be required for desired branch positioning, due to the underlying anatomy.

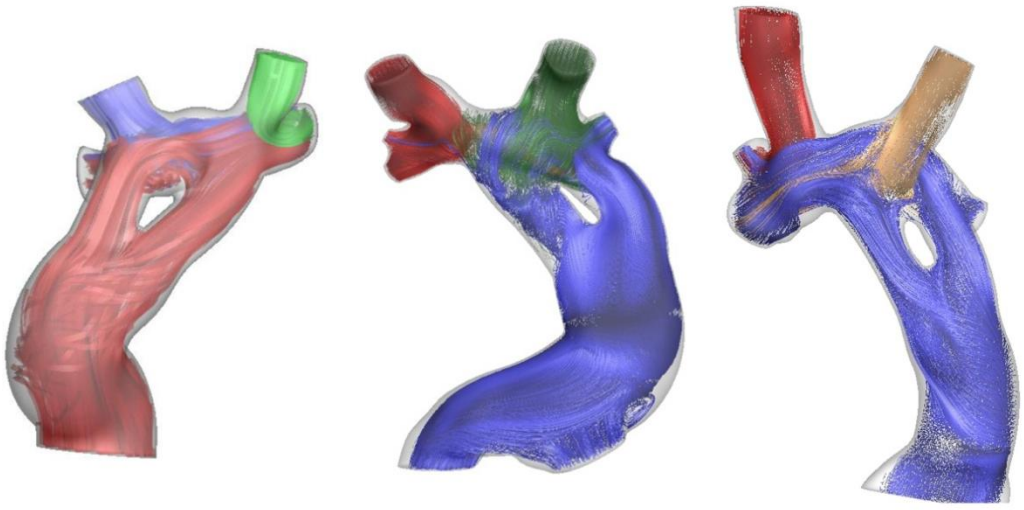


**Figure 7.62 Compilation of Y-Graft results for the specified cases in which significant lateral curvature limited Y-Graft effectiveness.**

## 7.5 Post-Operative Analyses[166]

The previous section as well as the work of de Zélicourt *et al.*[105] detailed the prospective use of surgical planning for a heterogenous group of single ventricle patients and based the estimation of their effectiveness on measures such as improving arterial oxygen saturations, which are clinically meaningful yet inconclusive for confirming modeled predictions[105, 159]. Thus, while a key assumption of these methods is the accuracy of preoperative predictions with respect to postoperative hemodynamic outcomes, detailed quantitative comparisons between pre- and post-operative hemodynamic metrics have been lacking.

The following section compares the pre- and post-operative hemodynamics for a small subset of cases for whom such data were available, and subsequently details

preliminary efforts to quantify the impact of the numerous unknown variables inherent to prospective surgical modeling (e.g., geometric agreement, adaptation of input and output boundary conditions) to assess the predictive power of the virtual surgery paradigm. In all cases, post-operative imaging occurred in the hospital prior to discharge (5-10 days following surgery).

### 7.5.1 Post-operative results

#### 7.5.1.1 CHOA_M2

Figure 7.63 shows a qualitative comparison of the post-operative TCPC compared to the virtual surgical model for CHOA_M2. In this case, the match was weakened by the fact that the pre-operative CMR data had a large slice thickness (10mm), while the post-operative CMR had only black blood images available for anatomic reconstruction, which provide different signal characteristics with regard to the vessel boundaries. Hence, there are significant visual differences between the two results, particularly with respect to the size (volume) of the SVC-Azygos-PA connection site.

Yet, the qualitative streaming results for these two connections (Figure 7.64) are remarkably similar. The flow through the Y-Graft, as predicted, is directly laterally to either side of the superior anastomoses and exits through the respective PAs. The quantitative results do show some disparity, although still within acceptable ranges: connection resistance was higher but still less than population means, while HFD was more balanced than predicted.

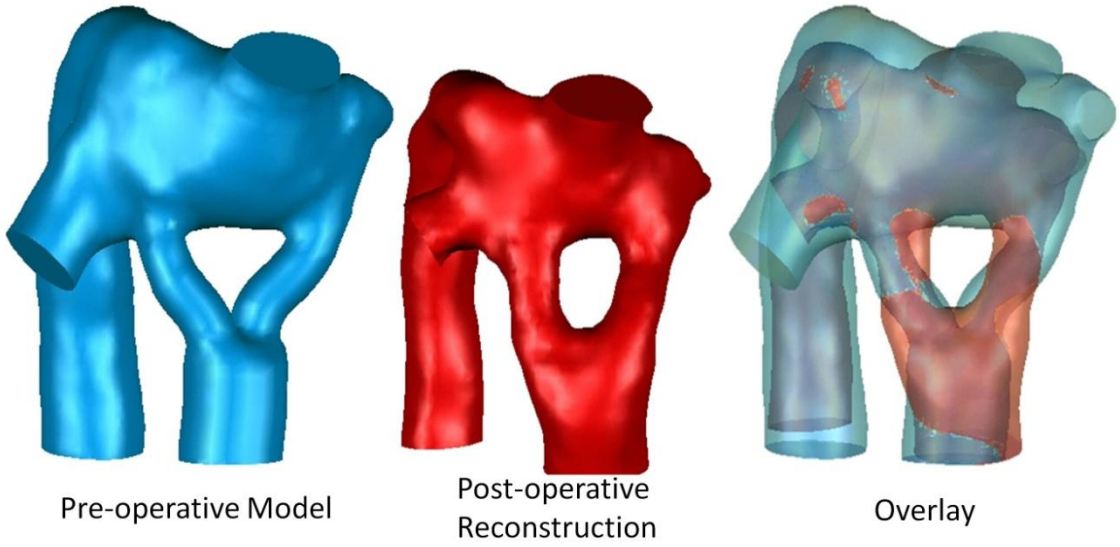


**Figure 7.63 Qualitative comparison of virtual model (blue) and post-operative reconstruction (red) for CHOA_M2.**

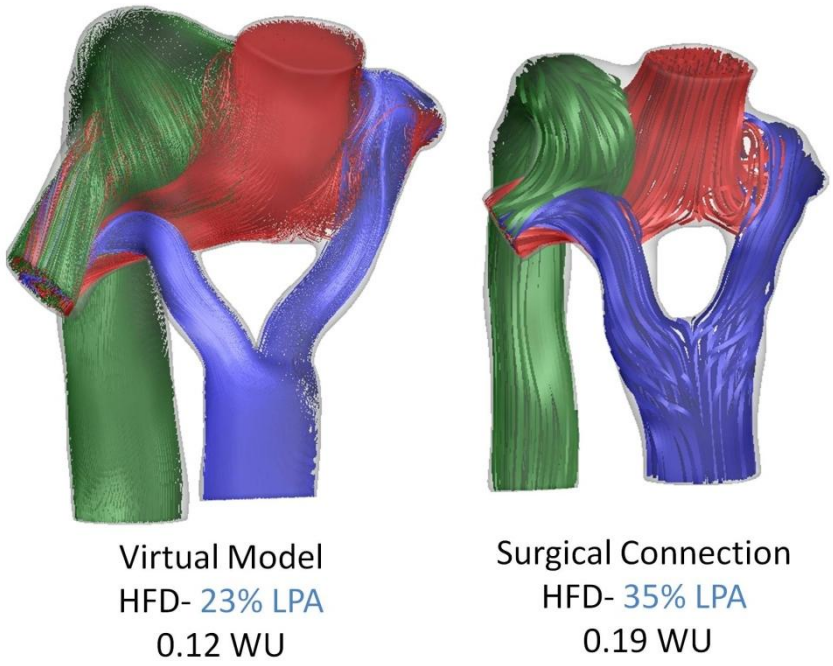


**Figure 7.64 Velocity streamlines and quantitative measures from the time-averaged pre-operative simulation (left) and time-varying post-operative simulation (right; representative streamlines) for CHOA_M2.**

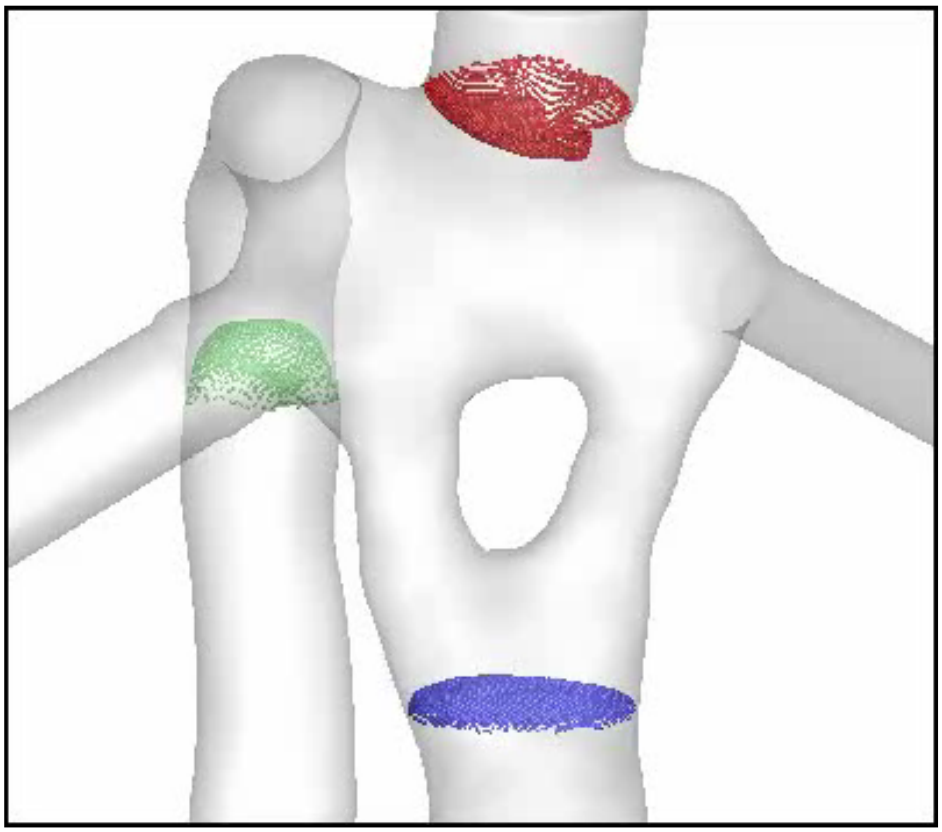

**Animation 7.6 Pulsatile particle tracing for post-operative simulation for CHOA_M2.**

#### 7.5.1.2 CHOP_M9

For this patient, post-operative arterial oxygen saturations improved from 85% to 95% 16.5 months after surgery. As argued by de Zélicourt *et al*., this finding suggests the surgical intervention was successful in addressing the PAVM.

Visual comparison of the pre-operative model and post-operative TCPC for CHOP_M9 is shown in Figure 7.65. There is a visible difference in the placement of the right graft branch (being more medially positioned in the actual connection), but the features of the connections are otherwise well-conserved.

The post-operative scan included a 4D PC CMR sequence, the results of which are shown in Figure 7.66 and Animation 7.7. The pre-dominance of RPA flow is apparent;

yet, bilateral hepatic distribution through the Y-Graft can be seen through most phases of the cardiac cycle. In fact, quantifying the particle tracking produced an HFD result of 24% to the LPA.

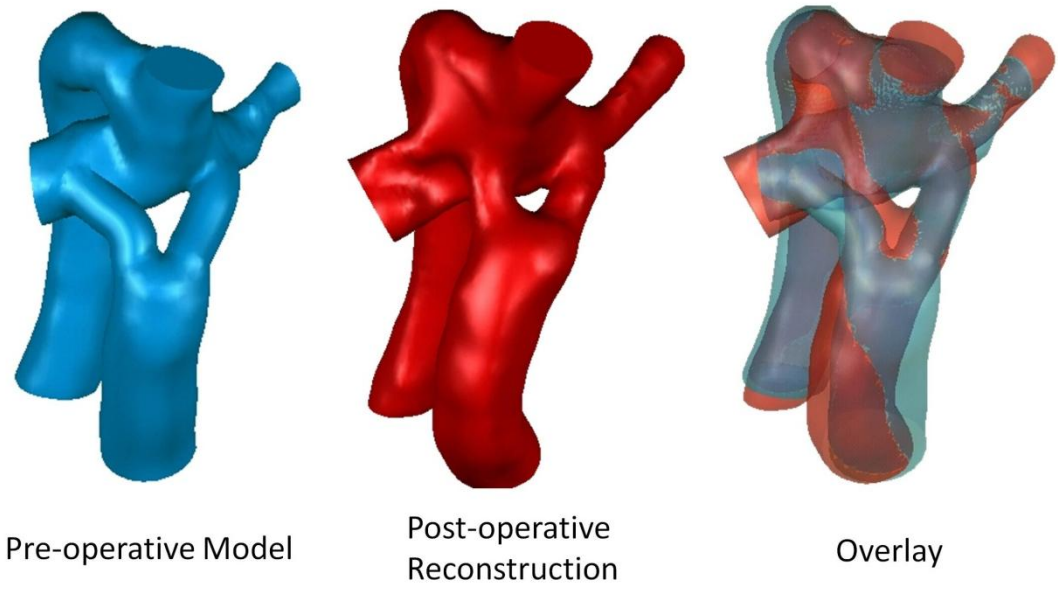


**Figure 7.65 Qualitative comparison of virtual model (blue) and post-operative reconstruction (red) for CHOP_M9.**

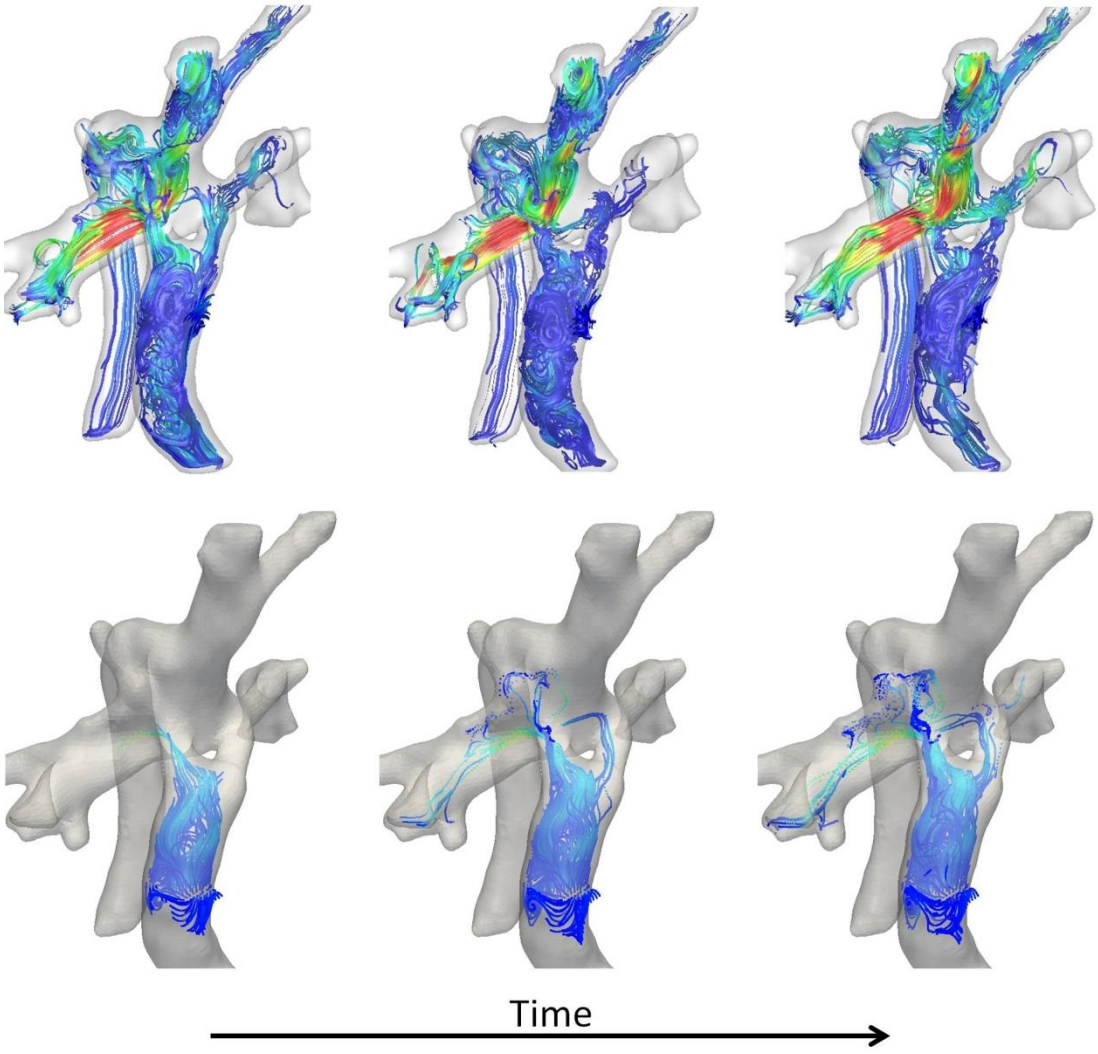


**Figure 7.66 4D Velocity data for post-operative reconstruction for CHOP_M9 derived from coronal PC CMR data with divergence free interpolation. Top row- instantaneous streamlines; Bottom row- sequence (left to right) of hepatic particle tracking.**

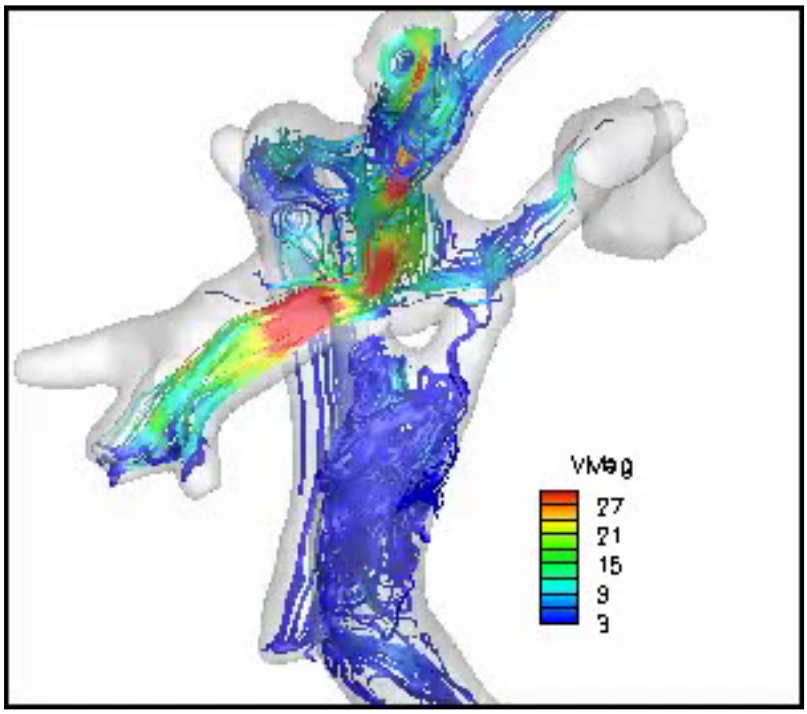


**Animation 7.7 Time-varying velocity streamlines from post-operative 4D CMR for CHOP_M9.**

Figure 7.67 compares the simulated velocity streamlines between the virtual model and post-operative result. Realized connection resistance was lower (likely because of less total flow to the LPA post-operatively), while HFD to the LPA was higher because the left branch of the Y-Graft was positioned further laterally than modeled. Still, the desired outcome of high HFD to the RPA with bilateral distribution was achieved.

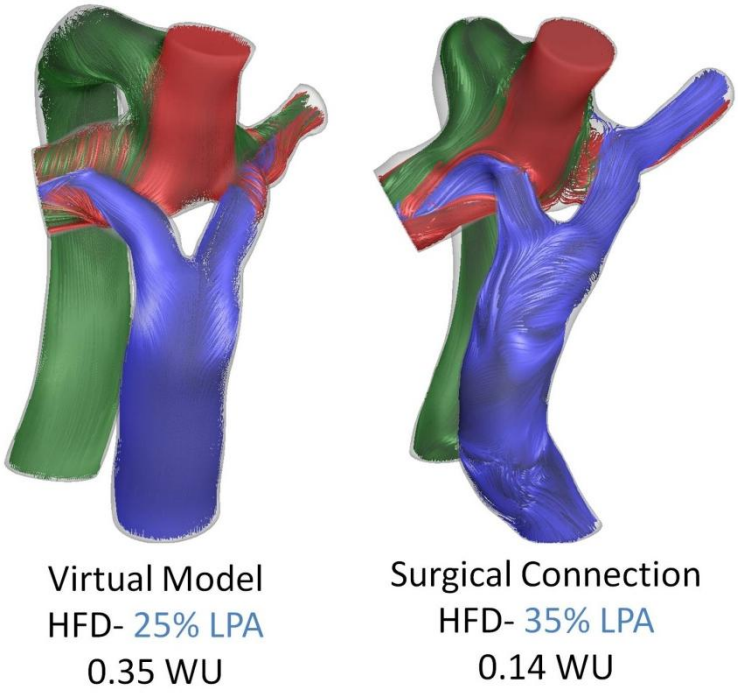


**Figure 7.67 Velocity streamlines and quantitative measures from the time-averaged pre-operative simulation (left) and time-varying post-operative simulation (right; representative streamlines) for CHOP_M9.**

#### 7.5.1.3 CHOP_M10

Post-operative arterial oxygen saturations had improved from 61% to 72% one month after surgery, with no updated report available since then. It is therefore difficult to conclude anything regarding the success of the surgery based on saturations over that short interval.

Anatomical comparison for CHOP_M10 is shown in Figure 7.68. The biggest difference is seen with respect to the placement of the right graft branch, which is more medial, anterior and superior in the actual connection compared to what was modeled. Otherwise, the models are very similar.

4D CMR data were again acquired and the results shown in Figure 7.69 and Animation 7.8. There is an appreciable bias of the superior flows for the LPA, and significant acceleration occurs as the SVC and azygos flow combine within the connection. Still, as particularly seen from the particle tracking images, hepatic flow is bilaterally distributed to both sides of the connection (76% to the LPA based on the particles).

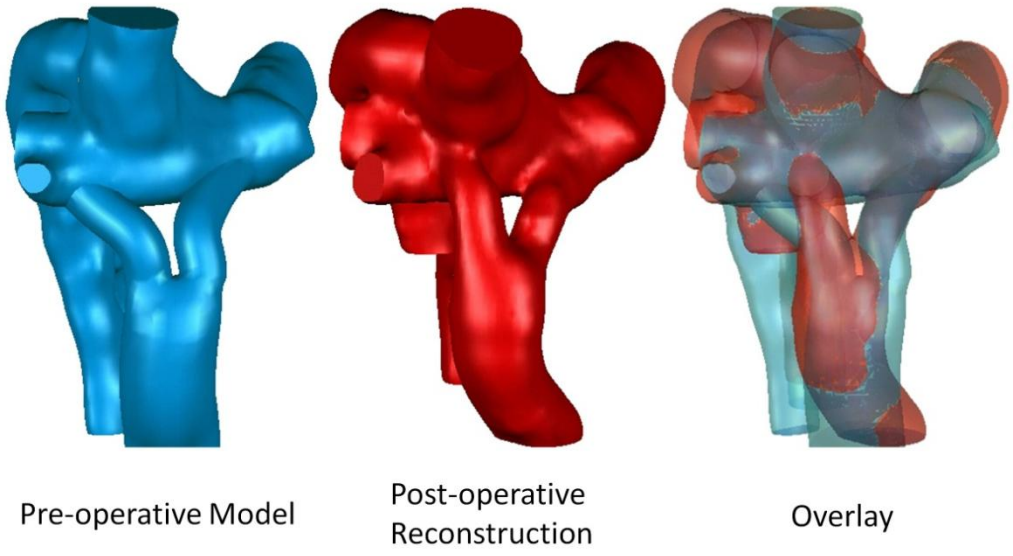


**Figure 7.68 Qualitative comparison of virtual model (blue) and post-operative reconstruction (red) for CHOP_M10**

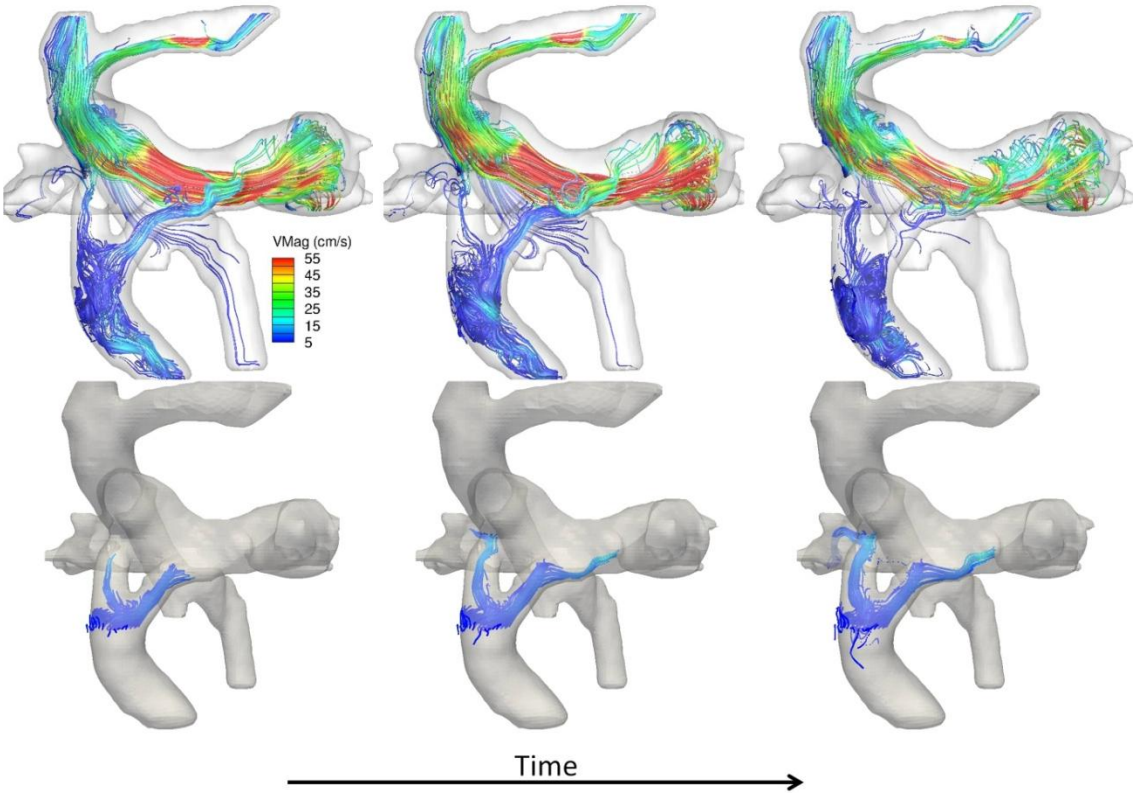


**Figure 7.69 4D Velocity data for post-operative reconstruction for CHOP_M10 derived from coronal PC CMR data with divergence free interpolation. Top row- instantaneous streamlines; Bottom row- sequence (left to right) of hepatic particle tracking.**

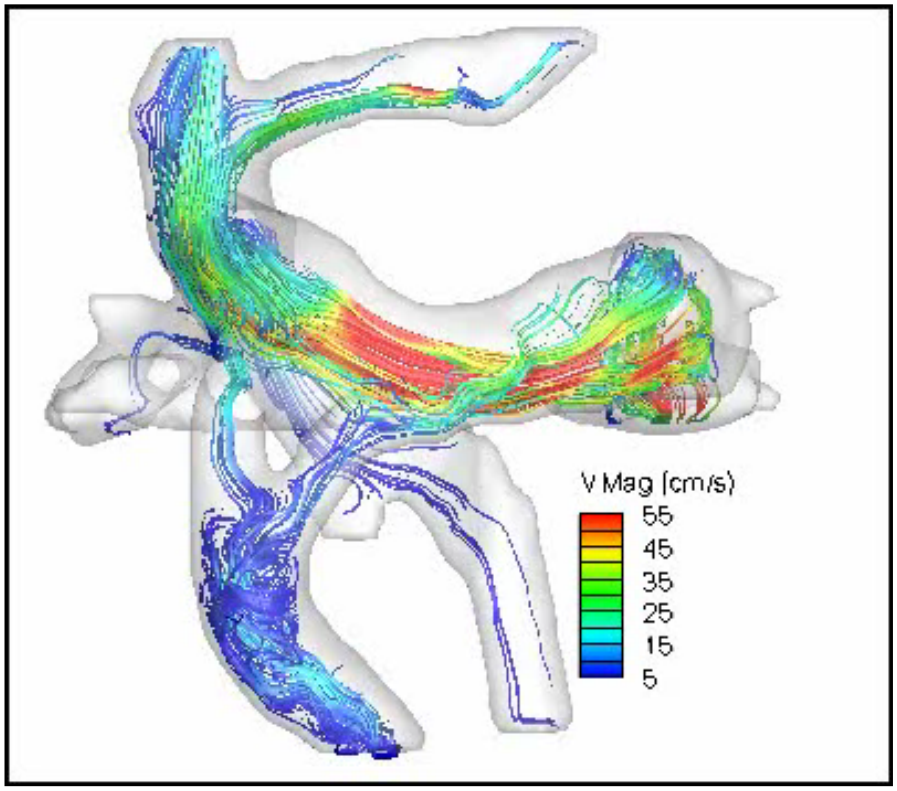


**Animation 7.8 Time-varying velocity streamlines from post-operative 4D CMR for CHOP_M10.**

Figure 7.70 shows the simulated velocity streamlines for the virtual and actual models, and a significant disparity can be seen. Owing to the difference in the placement of the right graft branch, hepatic flow through that pathway was markedly different between models, with significant collision with the superior venous flow simulated in the actual post-operative connection. However, that interaction was not apparent in the 4D CMR velocity fields, possibly because of a difference in cross-sectional velocity profile between what was numerically imposed (uniform profile) and what exists *in vivo* (with a significant skew to the left).

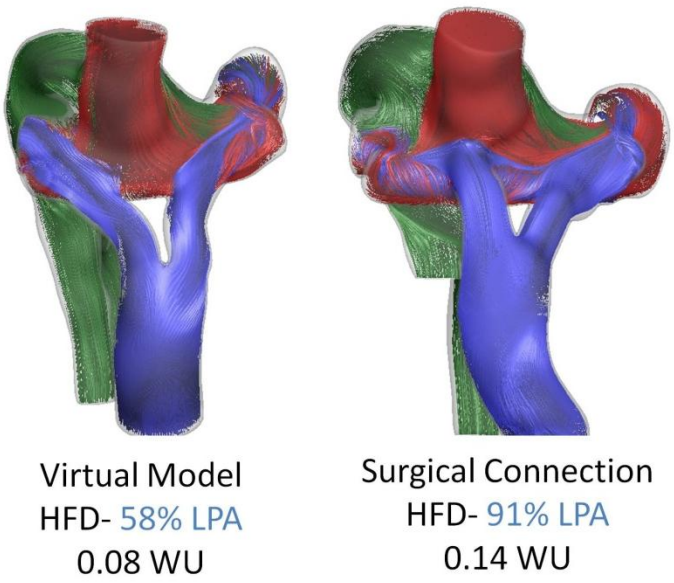


**Figure 7.70 Velocity streamlines and quantitative measures from the time-averaged pre-operative simulation (left) and time-varying post-operative simulation (right; representative streamlines) for CHOP_M10.**

#### 7.5.1.4 CHOP_M12

Arterial oxygen saturations had improved from 86% to 96% 8 months after surgery for this patient, suggesting a successful intervention with respect to PAVM.

The connection comparison for CHOP_M12 is shown in Figure 7.71. There is a clear difference in location of the Fontan connection as the model was medially positioned between the bilateral SVCs, while the actual connection was made further to the right without an offset to the RSVC.

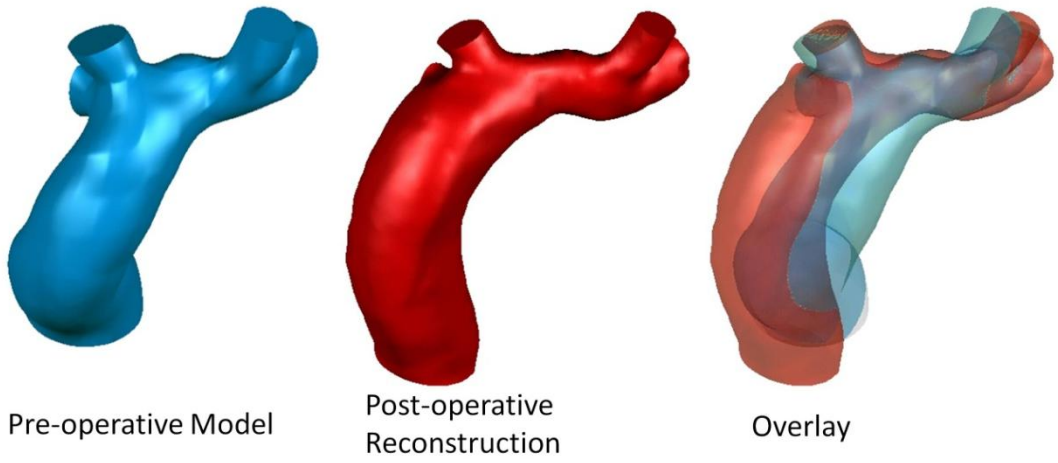


**Figure 7.71 Qualitative comparison of virtual model (blue) and post-operative reconstruction (red) for CHOP_M12**

Despite this anatomic difference, Figure 7.72 and Animation 7.9 show the reconstructed 4D CMR velocity data, in which the majority (75%) of IVC flow tends to the LPA despite a generally non-uniform and disturbed cross-sectional profile. By comparison, Figure 7.73 shows the simulated velocity fields (based on a uniform IVC inlet profile), which predict a more balanced IVC flow distribution from the post-operative connection in close agreement to the predicted value.

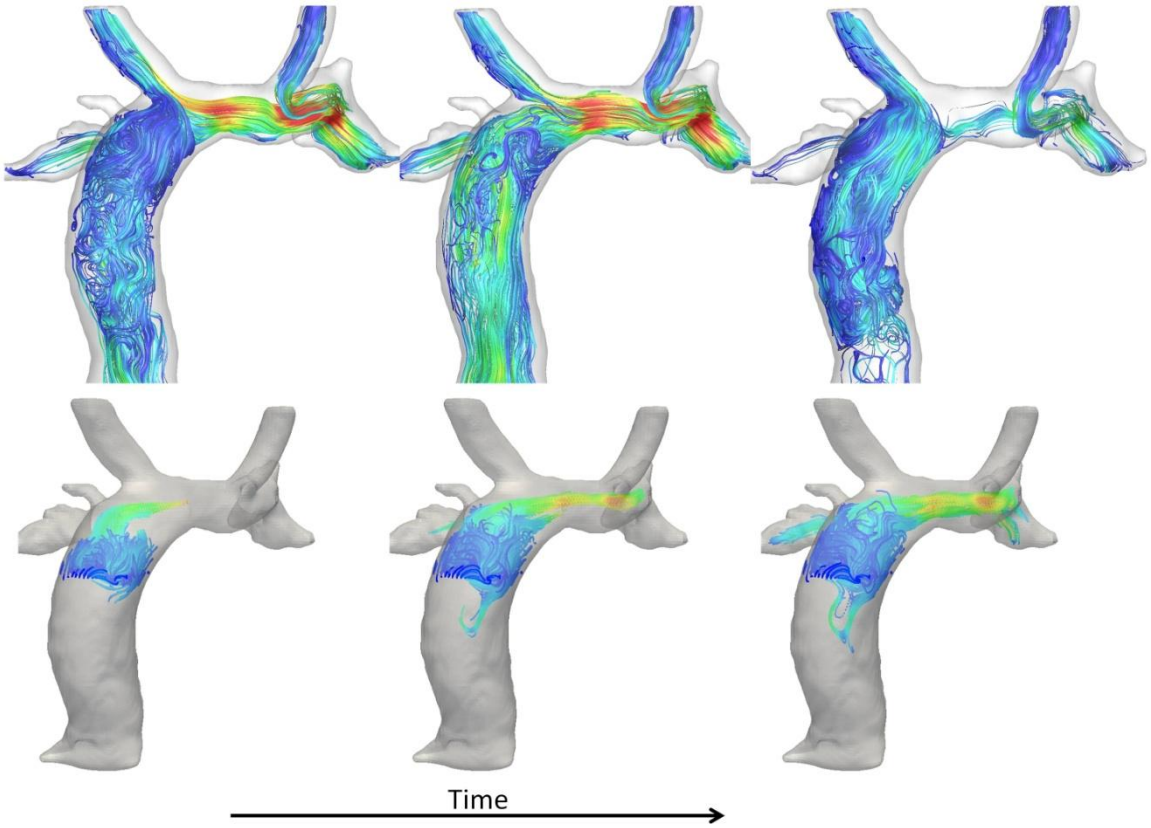


**Figure 7.72 4D Velocity data for post-operative reconstruction for CHOP_M12 derived from coronal PC CMR data with divergence free interpolation. Top row- instantaneous streamlines; Bottom row- sequence (left to right) of hepatic particle tracking.**

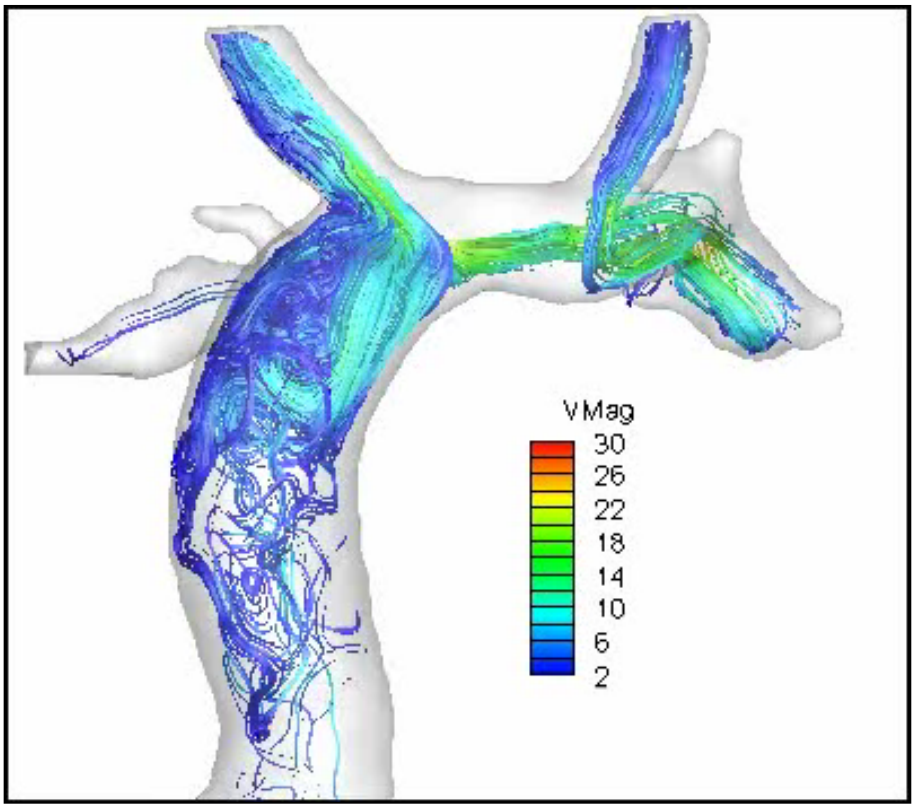


**Animation 7.9 Post-operative 4D CMR streamlines for CHOP_M12.**

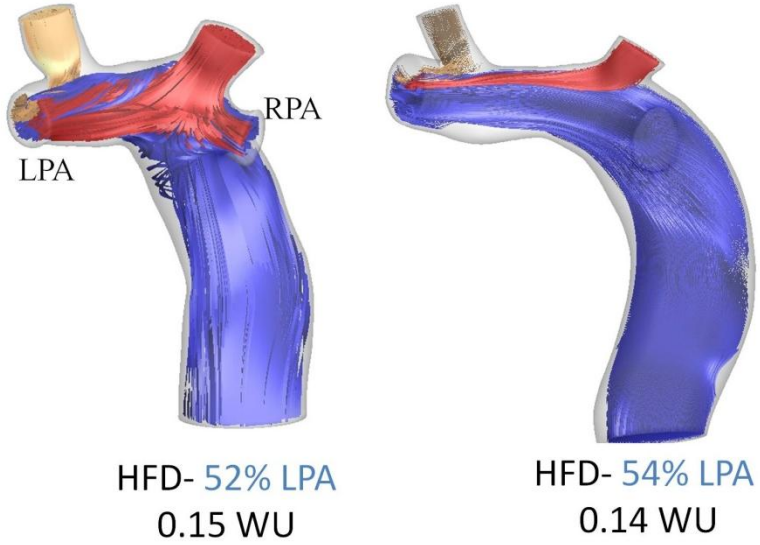


**Figure 7.73 Velocity streamlines and quantitative measures from the time-averaged pre-operative simulation (left) and time-varying post-operative simulation (right; representative streamlines) for CHOP_M12.**

#### 7.5.1.5 CHOP_M13

The anatomic comparison for CHOP_M13 is shown in Figure 7.74. The connection location to the PAs is consistent between the models (close to the LSVC); however, the curvature of the baffle was different. In the virtual model, the baffle was positioned in a straight path, resulting in a slight right-to-left bias. The actual surgical connection, by comparison, started further to the left and angled back toward the center of the connection.

Unlike the prior cases, the post-operative velocity results for this case did not show a net forward flow through the Fontan baffle (because of high fenestration flow). Hence, the results based on these data would not have been informative and no post-operative simulations were performed. Instead, longer term follow-up in this patient will be needed to evaluate the success of the prospective modeling.

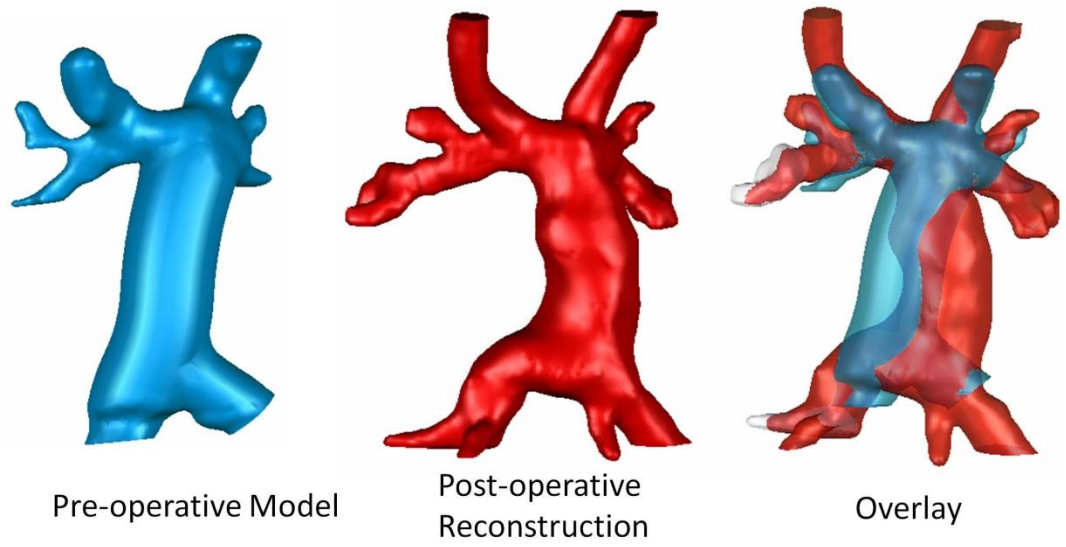


**Figure 7.74 Qualitative comparison of virtual model (blue) and post-operative reconstruction (red) for CHOP_M13**

#### 7.5.1.6 CHOA_M5

Geometric comparison of the virtual model and post-operative connection for CHOA_M5 is shown in Figure 7.75. While the general connection approach advocated by the model was used (22x11 mm Y-Graft), very little other similarities are present. The virtual model did not include much anterior-posterior displacement, while the actual surgery introduced significant anterior curvature before bilateral connection to the PAs. Also of note is the fact that the post-operative CMR data did not provide a clear enough signal to reconstruct the upper lobe branch of the RPA.

The simulated velocity and hemodynamic output results are shown in Figure 7.76. Resistance was higher than predicted, likely because of a decrease in RPA diameter, while HFD to the LPA was lower. Some interaction and cross-over can be seen with the flow through the left Y-branch, however, the absence of the upper RPA lobe is the bigger

reason for the HFD difference as the SVC flow was primarily directed to the LPA rather than having the upper RPA as an outlet.

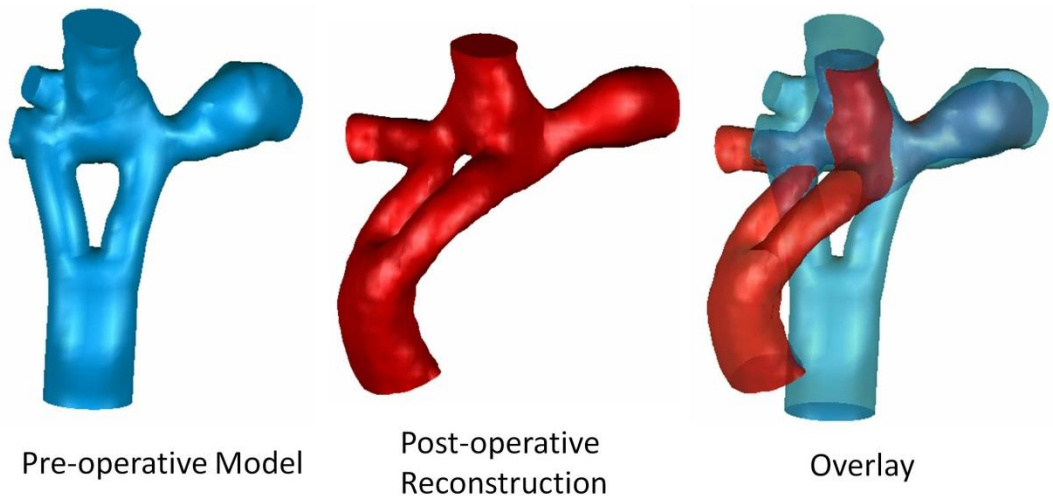


**Figure 7.75 Qualitative comparison of virtual model (blue) and post-operative reconstruction (red) for CHOA_M5**

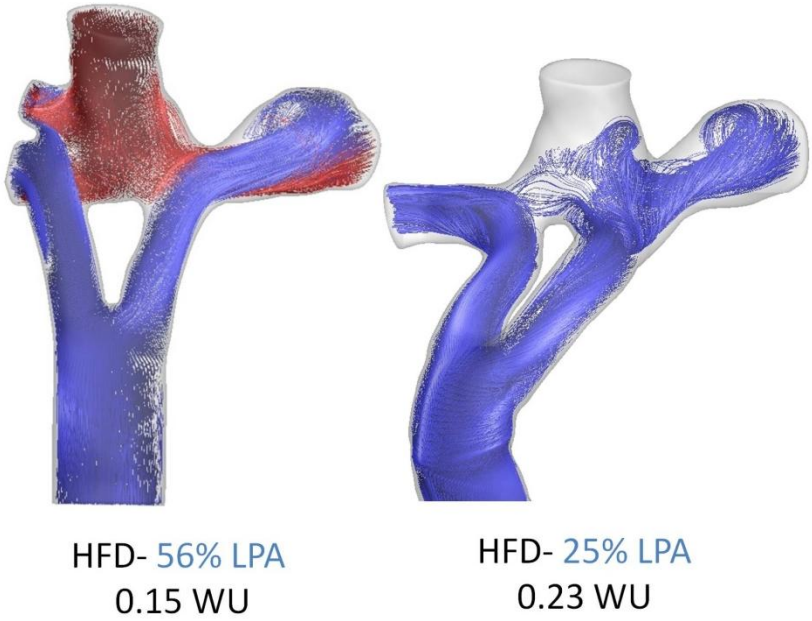


**Figure 7.76 Velocity streamlines and quantitative measures from the time-averaged pre-operative simulation (left) and time-varying post-operative simulation (right; representative streamlines) for CHOA_M5.**

### 7.5.2 Sensitivity Analysis

The previous section showed that, while agreement between pre-operative models and post-operative results (both simulated and imaged) was generally favorable, there were important differences in most cases. The objective of this study is to quantify the impact of the numerous unknown variables inherent to prospective surgical modeling (e.g., geometric agreement, adaptation of input and output boundary conditions) to assess the predictive power of the virtual surgery paradigm.

Because both patient-specific anatomy and flow conditions were variables in this analysis, multiple simulations were performed for each patient to isolate their effects.

Specifically, in addition to the time-averaged pre-operative analysis, which is simulation (1a), four simulations were run for each patient after the surgery:

1) The retained surgical planning model under:
    a) time-averaged pre-operative BCs
    b) pulsatile post-operative BCs
    c) time-averaged pre-operative inflows and time-averaged post-operative PA outflow split BCs
2) *In vivo* post-operative anatomy under:
    a) time-averaged pre-op BCs
    b) pulsatile post-op BCs (i.e., actual outcome)

Comparison of 1a vs. 2b was performed for each case in §7.5.1, and provides an assessment of the surgical planning predictive power with respect the primary planning endpoint of hepatic flow distribution. A comparison of 1c vs. 2b is instead used to assess connection resistance in order to remove the confounding effects of varying flow through a stenotic vessel (e.g., the LPA of patient 2). Comparing 1a vs. 2a and 1b vs. 2b provides insights into the impact of geometric variation; 1a vs. 1b vs. 1c and 2a vs. 2b was used to isolate the impact of the varying inflow and outflow BCs.

#### 7.5.2.1 Hemodynamic Changes from Geometric Variation

To isolate the hemodynamic impact of the observed surgical variations and image reconstruction differences, both the surgical planning and post-operative geometries were simulated under time-averaged, pre-operative boundary conditions (simulations 1a and 2a). The results (Figure 7.77, Table 7.28) demonstrated that the effects of geometric

mismatch (both surgically-mediated and image-processing related) can be significant. Previous studies have shown strong correlations between minimum PA size and power loss across the TCPC[140], and the present changes in power loss directly corresponded to variations in the minimum reconstructed PA sizes in each case. As a result, the errors in power loss values because of geometric differences ranged between 18-68% with an average of 39%. For HFD, differences ranged between 2-18%, with surgical baffle mismatch mediating the largest discrepancies (as for CHOP_M10 and CHOP_M12).

**Table 7.28 Geometry-Related Differences: Hemodynamics under Pre-Operative Flow Conditions (Comparison of Simulations 1a and 2a)**

| Patient | HFD [% LPA] (Surg. Planning/ Post-Op) | Hemodynamic Explanation | Power Loss [mW] (Surg. Planning/ Post-Op) | Hemodynamic Explanation |
|---|---|---|---|---|
| **CHOA_M2** | 23 / 14 | AZ flow impinging on Rt branch outlet | 1.9 / 3.2 | Pouch and PA size differences |
| **CHOP_M9** | 25 / 27 | | 7.7 / 5.1 | Different PA size |
| **CHOP_M10** | 58 / 72 | Medial placement of right Y-branch | 1.1 / 1.3 | Different PA size |
| **CHOP_M12** | 52 / 34 | IVC Offset | 2.3 / 1.5 | Different PA size |

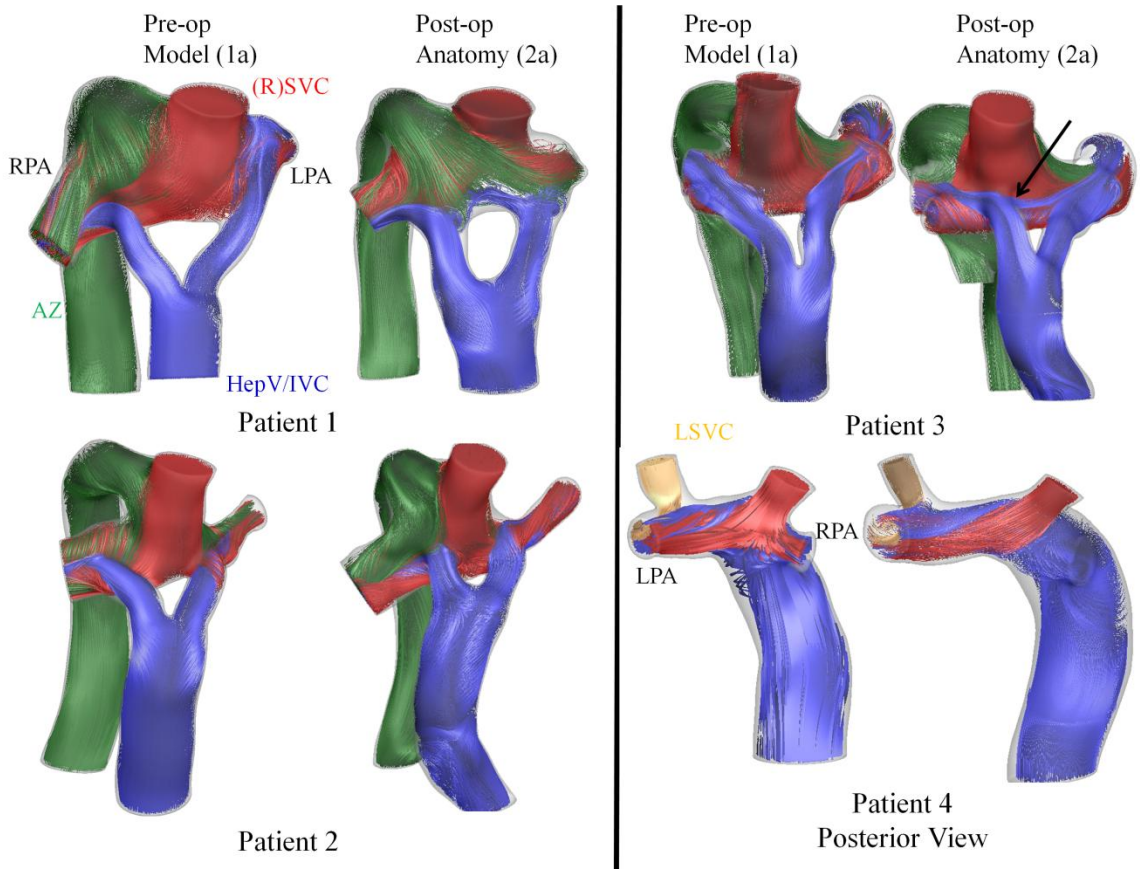


**Figure 7.77 Comparison of pre- and post-operative connections under steady, pre-operative flow conditions. Streamlines are color-coded by vessel of origin**

### 7.5.2.2 Post-operative flow conditions

Table 7.29 shows the phase velocity CMR-derived flows by vessel, plus the cardiac output (measured in the aorta) for each patient. Cardiac output decreased after surgery in 3 of the 4 cases. With respect to TCPC flows, the relative percentage distributions of each vessel were different following surgery; the magnitude of those changes ranged anywhere from 2 to 22%. Notably, the PA changes were all in favor of higher flow percentage toward the lung with PAVM.

**Table 7.29 CMR-derived flow rates**

| Patient | Scan | Ao* (L/min) | Percentage Distributions | | | | | |
|---|---|---|---|---|---|---|---|---|
| | | | HepV/IVC | Right SVC | Left SVC | AZ | LPA | RPA |
| **CHOA_M2** | Pre | 3.3 | 17 | 34 | | 49 | -23 | -77 |
| | Post | 2.4 | 21 | 52 | | 27 | -18 | -82 |
| **CHOP_M9** | Pre | 2.9 | 18 | 54 | | 28 | -34 | -66 |
| | Post | 1.8 | 30 | 47 | | 23 | -13 | -87 |
| **CHOP_M10** | Pre | 3.2 | 18 | 56 | | 26 | -76 | -24 |
| | Post | 3.7 | 16 | 72 | | 12 | -85 | -15 |
| **CHOP_M12** | Pre | 2.6 | 56 | 25 | 19 | | -62 | -38 |
| | Post | 1.8 | 58 | 20 | 22 | | -69 | -31 |

7.5.2.3 Hemodynamic Changes from Flow Rate Variations

Figure 7.78 shows representative, instantaneous streamlines for the CFD-derived post-operative flows (simulation 2b) for each patient. Despite the noted quantitative flow differences, the results for patients 2 and 3 are qualitatively very similar to their corresponding steady pre-operative flow results (simulation 2a) from Figure 7.77. For

patients 1 and 4, the impact of (decreased) azygos and (increased) IVC flow changes, respectively, are more evident in the 3D hemodynamic differences.

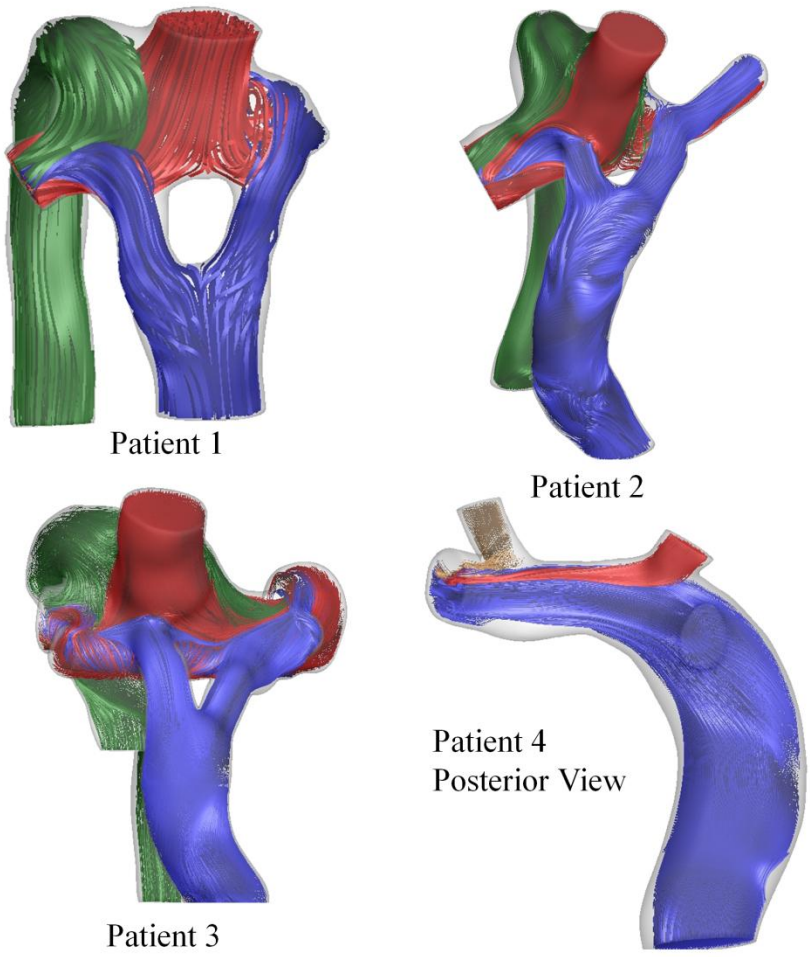


**Figure 7.78 Representative instantaneous velocity streamlines (color-coded by vessel of origin) from the time-varying post-operative flow simulations on the actual post-operative connections for all four patients.**

The hemodynamic results as a function of imposed flow conditions are reported for the surgical planning models and the post-operative anatomies in Table 7.30 and Table 7.31, respectively. To isolate the effect of varied PA splits from the total change in TCPC flow conditions, Table 7.30 also provides the results of combining post-operative outflow splits with pre-operative inflow conditions (simulation 1c). The HFD differences ranged between 3-19% (mean of 13%) and 8-21% (mean of 17%) for the virtual models and post-op anatomies, respectively.

**Table 7.30 Effect of Boundary Condition Variations: Surgical planning models (comparison of simulations 1a,1b,1c)**

| | HFD [%LPA] | | | Resistance [mmHg*min/L] | | |
|---|---|---|---|---|---|---|
| **Pt** | **Pre-op BC** | **Pre inflow; Post outflow** | **Post-op BC** | **Pre-op BC** | **Pre inflow; Post outflow** | **Pulsatile Post-op BC** |
| **CHOA_M2** | 23 | 19 | 40 | 0.26 | 0.28 | 0.19 |
| **CHOP_M9** | 25 | 17 | 28 | 0.77 | 0.27 | 0.2 |
| **CHOP_M10** | 58 | 58 | 77 | 0.18 | 0.21 | 0.24 |
| **CHOP_M12** | 52 | 61 | 66 | 0.2 | 0.18 | 0.14 |

**Table 7.31 Effect of Boundary Condition Variations: Post-operative Anatomy (comparison of simulations 2a and 2b)**

| Patient | HFD [%LPA] (Pre BC / Post BC) | Hemodynamic Explanation | Connection Resistance [mmHg*min/L] (Pre BC / Pulsatile Post BC) |
|---|---|---|---|
| **CHOA_M2** | 14 / 35 | Varied venous flow distributions | 0.44 / 0.22 |
| **CHOP_M9** | 27 / 35 | Varied venous flow distributions | 0.51 / 0.32 |
| **CHOP_M10** | 72 / 91 | Varied venous flow distributions | 0.22 / 0.35 |
| **CHOP_M12** | 34 / 54 | Increased Total LPA Flow | 0.14 / 0.18 |

Connection energetics in Table 7.30 and Table 7.31 are reported as resistance to partially correct for the noted changes in bulk flow rates. Generally minor variations were seen as a function of PA split (Table 7.30) owing to differences in vessel size. This effect

was substantial for CHOP_M9 because of the relatively small size of the LPA. Neglecting PA size effects and comparing only the 5th and 6th columns, the efficiency errors as a function of systemic flow variations ranged from 14-32% with an average of 24%.

#### 7.5.2.4 Predictive Accuracy

The explicit comparison of surgical planning predictions to simulated post-operative hemodynamics is shown in Table 7.32. For HFD, the predictive difference (pre-operative value vs. post-operative result) ranged between 2-33%, with a 90% confidence interval of 14.3 ± 4.3%. For connection resistances, the predictive comparisons (pre-operative inflows with post-operative PA splits vs. post-operative simulation) ranged between 0-40% error with a 90% confidence interval of 19.5 ± 4.8%.

**Table 7.32 Predictive Accuracy Summary**

| | HFD [%LPA] | | | Connection Resistance [mmHg*min/L]* | | |
|---|---|---|---|---|---|---|
| **Pt** | **Surgical Planning Model** | **Post-op Anatomy** | **Difference** | **Surgical Planning Model** | **Post-op Anatomy** | **% Error** |
| **CHOA_M2** | 23 | 35 | 12 | 0.28 | 0.22 | 22 |
| **CHOP_M9** | 25 | 35 | 10 | 0.27 | 0.32 | 16 |
| **CHOP_M10** | 58 | 91 | 33 | 0.21 | 0.35 | 40 |
| **CHOP_M12** | 52 | 54 | 2 | 0.18 | 0.18 | 0 |
| **90% #CInt.** | | | **14.3 ±4.3** | | | **19.5 ± 4.8** |

*Pre-operative values using post-operative outflow splits; #CInt. = Confidence Interval

### 7.5.3 Section Discussion and summary

This study compared the results from pre-operative virtual surgery modeling of the Fontan procedure to the simulated hemodynamic outcomes following the surgical implementation of those models in four patients. While the agreement was not exact, it is important to note that the hemodynamic outcomes with respect to what the patients ultimately needed (i.e., hepatic perfusion of the diseased lung) were achieved in each case, which is not a guarantee in such complex anatomical configurations. The improved/improving arterial oxygen saturation values further support this observation as they suggest the PAVMs are regressing and more blood is being properly routed through the lungs. Ultimately, that is the desired clinical endpoint.

These results suggest that the virtual models mimicked the interventions with sufficient realism to provide relevant insights to the cardiovascular surgeon and help in the decision-making process. The fact that these Y-graft patients were the first for either surgeon in this study provides strong testament that the modeling results were taken into account in their surgical strategy. Furthermore, providing the first assessment of prospective modeling comparisons is a milestone in the development of tools for engineering-based modeling of cardiothoracic surgery because it demonstrates the ability of the modeling to approximate the acute surgical result. Of equal importance, however, was the identification of key variables that dictate the error margins of the approximations. Such information will be critical to both prioritize and further motivate future developments to address these limitations.

HFD: As seen in Table 7.32, the confidence interval of pre-operative HFD predictions to post-operative results was 14.3 ± 4.3%. This finding is positive for several reasons. HFD is a primary consideration in patients with PAVM diagnoses based on the assumption that achieving desired flow streaming would successfully alleviate the immediate disease

state. However, there is a poor clinical understanding with regard to the critical values of HFD that mediate PAVM formation or regression, with the only clearly negative outcome being complete exclusion of hepatic flow from one lung. Interventional target values are therefore broad, ill-defined, and nearly impossible to dictate *a priori*. Providing a means to achieve a specific outcome, even with up to 19% uncertainty, thus represents a significant refinement of the current approach.

Surgical/model geometrical agreement is a critical mediator of flow streaming predictions and thus represents an important need to improve results. Unfortunately, surgical mismatch is currently an unavoidable factor of the process as consistently exact agreement would require: a) registered, simultaneous visualization of both the patient anatomy and virtual model in the operating room; b) a lack of intra-operative adjustments from the pre-determined plan by the surgeon; and c) simulation of the geometric changes that occur post-operatively (e.g., from chest closure or restoration of normal thoracic pressures). While none of these is impossible for future work to incorporate, they are not currently feasible. Rather than addressing this limitation on the surgical side, however, it would be easier to take preventative measures on the virtual design-side to minimize its impact. Such considerations were subjectively included in these present cases (see §7.4), but only on an ad hoc basis. Low sensitivity of desirable hemodynamic values to possible variations in exact implementation (i.e., option robustness) can also be mathematically formalized into a separate evaluation criterion to strengthen the analysis[167].

Connection Resistance: Prospective resistance predictions were not as strong as for flow distribution (19.5 ± 4.8%). Yet, even though the clinically relevant thresholds of TCPC power loss are currently unknown, it is assumed that the resistance values found in all cases were acceptably small. In fact, the low magnitudes (~0.3 WU) contributed to

the error magnitudes given the relatively small absolute differences observed (~0.1 WU or less). It is unlikely that the difference between 0.28 and 0.22, for example, would be clinically significant given that, from the work of Sundareswaran et al., a 3- or 4-fold increase in resistance would be required to drop cardiac output by ~12%[55]. Furthermore, power loss was only a secondary consideration in the decision making process for these patients (as seen from the pre-operative analyses) and only came into play when two options had similar flow distribution characteristics. In fact, the efficiency differences between the options for which power loss was a discriminator exceeded the 24% mean error margin, so it was still a useful metric in those pre-operative analyses. That said, the secondary importance of connection efficiency is not a permanent fixture, particularly given the physiologic impact of power loss demonstrated through the previous chapters; there are likely patients and disease states (e.g., poor exercise intolerance, high central venous pressure, severe diastolic dysfunciton) for which such metrics are of primary concern. Thus, while the present findings from this initial series provide a viable starting point, they are not sufficient for the ultimate promise of such analyses.

Based on the present data, one focal point for making improvements is minimizing the deviation of reconstructed vessel sizes, particularly of the small PAs, which were a primary contributor to predictive errors of efficiency. Uncertainties in vessel sizes were related to three primary sources: a) finite sampling of medical images; b) the possibility of actual changes occurring in the vessel sizes, as in response to changing flow conditions or surgical manipulation; and c) the reconstruction protocol itself (smoothing and surface fitting algorithms tend to shrink the segmented volume). Continuous advancements in imaging (particularly the growing use of 3D anatomic sequences) and image processing techniques will help address points (a) and (c); the effects of (b) will

need to be studied through future work with larger sample sizes, and may require fluid-structure interaction models to resolve if deemed critical to the result.

Flow boundary condition uncertainty: While surgical agreement and reconstruction errors were each found to impact pre-operative predictions in an isolated fashion (i.e., either HFD or power loss), changes in flow conditions was seen to mediate changes in both metrics of interest and thus deserves particular attention. Decreases in cardiac output post-Fontan have previously been noted by Fogel et al.[33] and in the work presented in §7.3. No similar report exists with respect to post-operative physiology of interrupted IVC patients. In this limited series, output decreased in 3 of 4 patient cases by as much as 1.1 L/min. Power losses are directly dependent on the total flow rate, so normalizing to express as a resistance better accounted for most of these changes, as evidenced by the similar orders of magnitude in the comparisons of Table 7.30, Table 7.31, and Table 7.32. Dynamic interactions among the various inlets, dictated by their relative flow rates, would have also contributed to the hemodynamic efficiency of the connection.

Relative vessel flow rates also impacted HFD. It is known that HFD is generally positively correlated to the pulmonary outflow split[144], so this finding was expected. In CHOP_M12, for example, pre-operatively varying the outflow split (Table 7.30) improved agreement with the result of the post-operative BC simulation. CHOA_M2 and CHOP_M9 (both with Y-graft conduits) diverged from this trend, which suggests that the inlet fluid momentum in bifurcated grafts may supersede the outlet conditions under certain conditions. More importantly though, the physiologic factors governing post-operative adaptation of pulmonary splits are not well characterized, and so parametric sensitivity studies should be a critical component of any surgical planning analysis.

Coupling lumped parameter models to 3D fluid solvers has been proposed and evaluated in hypothetical surgical planning studies as a means to mathematically predict physiologic changes and better account for such effects[94, 95, 164]. This is potentially a very powerful paradigm and certainly represents the future for these techniques. However, there is currently a lack of data in the literature characterizing patient-specific pre- and post-operative physiology for the models to be properly validated. Furthermore, the difficulty in obtaining the data needed to make such models truly patient-specific (e.g., explicit compliance characteristics throughout the various vascular beds) can be challenging. Perhaps the best approach for future protocols would be for these multi-modality approaches to be complemented by clinical experience of serial patient changes (both acute and chronic) to ensure the models have simulated all the relevant conditions. While this development continues, the controlled and hypothesis-driven deviation of the investigated outflow splits as part of our surgical planning analysis is worthwhile approach that, based on the presented findings, should be augmented and complemented with similar variations of the inlet BCs to ensure robust solutions with respect to physiologic changes.

## 7.6 Chapter Summary

In this specific aim, we have expanded our patient-specific Fontan surgical planning experience with respect to patient numbers, anatomical complexities, and physiologic indications. These techniques continue to be a promising and exciting new approach to the Fontan procedure with obvious implications for the broader field of cardiothoracic surgery.

Additionally, the unique contribution of this thesis is the preliminary investigations into post-operative outcomes through both theoretical lumped parameter modeling as well as detailed analyses of imaging data acquired after prospectively planned surgeries to compare the results to prospective virtual model predictions. This latter component in particular is a critical step for the advancement of the paradigm as it provides a first look at the fidelity of the modeling and its usefulness in representing the post-operative state. The results are promisingly positive while also indicating that more work is needed to ultimately achieve the desired utility. It was found that model predictions for flow distribution were within the range of clinically acceptable error margins (±14%), especially considering the fact that there are no existing means to quantify these measures without computational modeling, so the information provided is still better than what is otherwise available. On the other hand, the error margins for power loss predictions are on the order of the expected inter-option differences that surgical planning is expected to identify (this topic will be revisited in Chapter 10). Hence, continued advancement in the methods is needed to provide necessary confidence to make meaningful power loss assessments.

The largest need is clearly for a more robust means of arriving at the relevant post-operative boundary conditions to simulate, presumably through calculation with a coupled lumped parameter model. However, that alone is not sufficient since it is only providing a single result in what will be a transient physiology; the connection modeled needs to last a lifetime, not just in the acute post-operative period. Therefore, concurrent with the technological advancements is the need for continued medical research and longitudinal patient follow-up to understand how the physiology changes with time and what the important operational variables are to ensure a thorough modeling analysis.

# Chapter 8. Specific Aim 4: Evaluate the clinical feasibility of the Fontan Y-Graft for Improving TCPC Hemodynamics

## 8.1 Overview

While representing an energetic improvement over previous designs (APC), the TCPC creates an adverse hemodynamic environment due to the collision of the caval flows[53, 85, 168]. The idea of using a flow bifurcation in the Fontan connection was first proposed by Soerensen *et al.*[106] ("Optiflo"; U.S. Patent #7811244). The motivating concept was that by dividing and rerouting one or both of the vena caval flows, the inefficient collision and mixing at the PA junction can be avoided.

Subsequent studies have analyzed and sought to optimize the design of the Fontan Y-graft (half of the Optiflo) using virtually rendered models[107, 169]. However, the recent work of Kanter *et al.*[170] represents the first clinical report of Y-graft usage in a consecutive series of Fontan patients. Post-operative imaging data from these patients provide the unique opportunity to evaluate the hemodynamic outcomes of this series and compare them to what could have been realized with possible surgical alternatives.

We hypothesize that the use of a Y-Graft for the Fontan connection improves Fontan hemodynamics by both reducing power losses and providing a better balance of IVC flows to the left and right PAs. This hypothesis is evaluated in this section in two parts: 1) the results from a set of 15 consecutive Y-Graft patients will be presented and compared to the overall cohort as well as a sub-set of age-matched controls; and 2) five of the fifteen patients will be selected for more thorough numerical evaluation under resting and simulated exercise flow conditions, and comparing these performance characteristics to extracardiac TCPC models virtually created for the same patients.

## 8.2 Study Protocols

### 8.2.1 Patient Selection

Between August 2010 and July 2012, 15 consecutive patients receiving their Fontan connections under the care of Dr. Kirk Kanter at Children's Healthcare of Atlanta received a commercially available bifurcated aorto-iliac polytetrafluoroethylene (PTFE) graft (Goretex; W.L. Gore; Flagstaff, AZ) as their Fontan baffle. All patients were imaged post-operatively for clinical evaluation of their Fontan pathway and consented for the data to be used for research purposes. These patients are the focus of this study and their demographic information is summarized in Table 8.1. Two patients were excluded from the hemodynamic analyses: in one case (CHOA_Y7) the post-operative (3T) CMR data was not sufficient for anatomic reconstruction, while for the second (CHOA_Y15) the flow through the fenestration (as measured by PC CMR) was greater than the IVC flow such that net flow through the Y-Graft was negative, thus no CFD simulations were performed. Finally, it is noted that there is overlap between these patients and those presented in Chapter 8: CHOA_M2 was the first in this series ('CHOA_Y1'), while CHOA_M5 was the 11$^{th}$ patient ('CHOA_Y11').

**Table 8.1 Patient demographic detail for Y-Graft patient series**

| **Pt.** | **Age** (yrs) | **BSA** ($m^2$) | **Y-Graft size** (mm) | **Other comments** |
|---|---|---|---|---|
| CHOA_M2 (Y1) | 18 | 1.49 | 18 x 9 | Surgical revision; Interrupted IVC |
| CHOA_Y2 | 5 | 0.72 | 20 x 10 | Post-op CT |
| CHOA_Y3 | 2 | 0.53 | 18 x 9 | |
| CHOA_Y4 | 3 | 0.72 | 20 x 10 | Surgical revision |
| CHOA_Y5 | 2 | 0.47 | 20 x 10 | |
| CHOA_M3 (Y6) | 11 | 1.09 | 20 x 10 | Surgical revision; Post-op CT; bilateral SVCs |
| CHOA_Y7 | 2 | N/A | 20 x 10 | Poor CMR quality |
| CHOA_Y8 | 14 | 1.53 | 20 x 10 | |
| CHOA_Y9 | 3 | 0.51 | 20 x 10 | |
| CHOA_Y10 | 2 | 0.58 | 18 x 9 | |
| CHOA_M5 (Y11) | 12 | 1.40 | 22 x 11 | Surgical revision |
| CHOA_Y12 | 2 | 0.47 | 20 x 10 | |
| CHOA_Y13 | 4 | 0.6 | 20 x 10 | |
| CHOA_Y14 | 2 | 0.58 | 18 x 9 | |
| CHOA_Y15 | 2 | 0.5 | 18 x 9 | No net Fontan flow measured; bilateral SVCs |
| **Average** | **5.5 ± 5.2** | **0.78 ± 0.38** | | |

### 8.2.2 CFD Protocol

The computational simulation protocols were generally the same as has been used in the preceding chapters. Primary end points included TCPC power loss (TCPC-EDI) and HFD. There were several important distinctions from previous protocols that must be noted.

1. There was a preference for using time-varying flow boundary conditions in this study. The lack of CMR-measured velocities or the lack of a smoothly time-varying profile measured (from CMR) prevented their use in some instances. Hence, the BCs used (either time-averaged or pulsatile) will be noted during the presentation of the individual cases.
2. For the second half of the study involving the in depth analysis of five patient cases compared to extracardiac controls, simulated exercise boundary conditions were used per the method of Whitehead et al[56]. Specifically, the measured cardiac output was doubled (for "2x") or tripled (for "3x") with the difference imposed as an increase in IVC flow rate (simulating lower limb exercise). All of these exercise simulations were done using time-averaged flow values.
3. As seen for two cases in Table 8.1, only post-operative CT anatomic data were available to reconstruct the patient anatomy and no concurrent PC CMR measurements were available. Flow conditions to be used for the computational simulations therefore had to be derived from alternate sources.
    a. For CHOA_Y2, a pre-operative (Glenn-stage) catheterization report was used converting the $Q_P/Q_S$ ratio into the IVC and SVC flow rates (SVC= $Q_P$; IVC=$Q_S$-$Q_P$) and setting the pulmonary flow distribution on the basis of vessel sizes.
    b. CHOA_Y6 was a surgical planning patient (CHOA_M3; study performed by M. Restrepo) who had a pre-operative CMR performed; thus, the pre-operatively measured flows were used for the post-operative analysis.

### 8.2.3 Statistical Analyses

Statistical analyses were performed using Minitab (Minitab Inc., State College, PA). Continuous variables were tested for normality using the Anderson-Darling test. The Student's t-test and Mann-Whitney test were used for comparisons between groups. P-values less than 0.05 were considered statistically significant in all cases.

## 8.3 Results

### 8.3.1 Hemodynamic Summary

The TCPC reconstructions for the 13 included patients are shown in Figure 8.1. It is noted that the sizes shown are scaled consistently among the connections. There are two clear generations of surgical implementation that can be seen. The first 5 patients all exhibit relatively short branches with little curvature and generally connect to the PAs at right angles. Starting with the sixth case, branch lengths are all considerably longer and have greater curvature in an attempt to better direct flow smoothly into the PAs. It is clear, particularly considering patients 8-14, that achieving such an angle is easier for the left branch than the right. In fact, in many cases the right branch is angled away from the RPA outlet at the anastomosis, presumably because its proximity to the right lung limits the lateral space available.

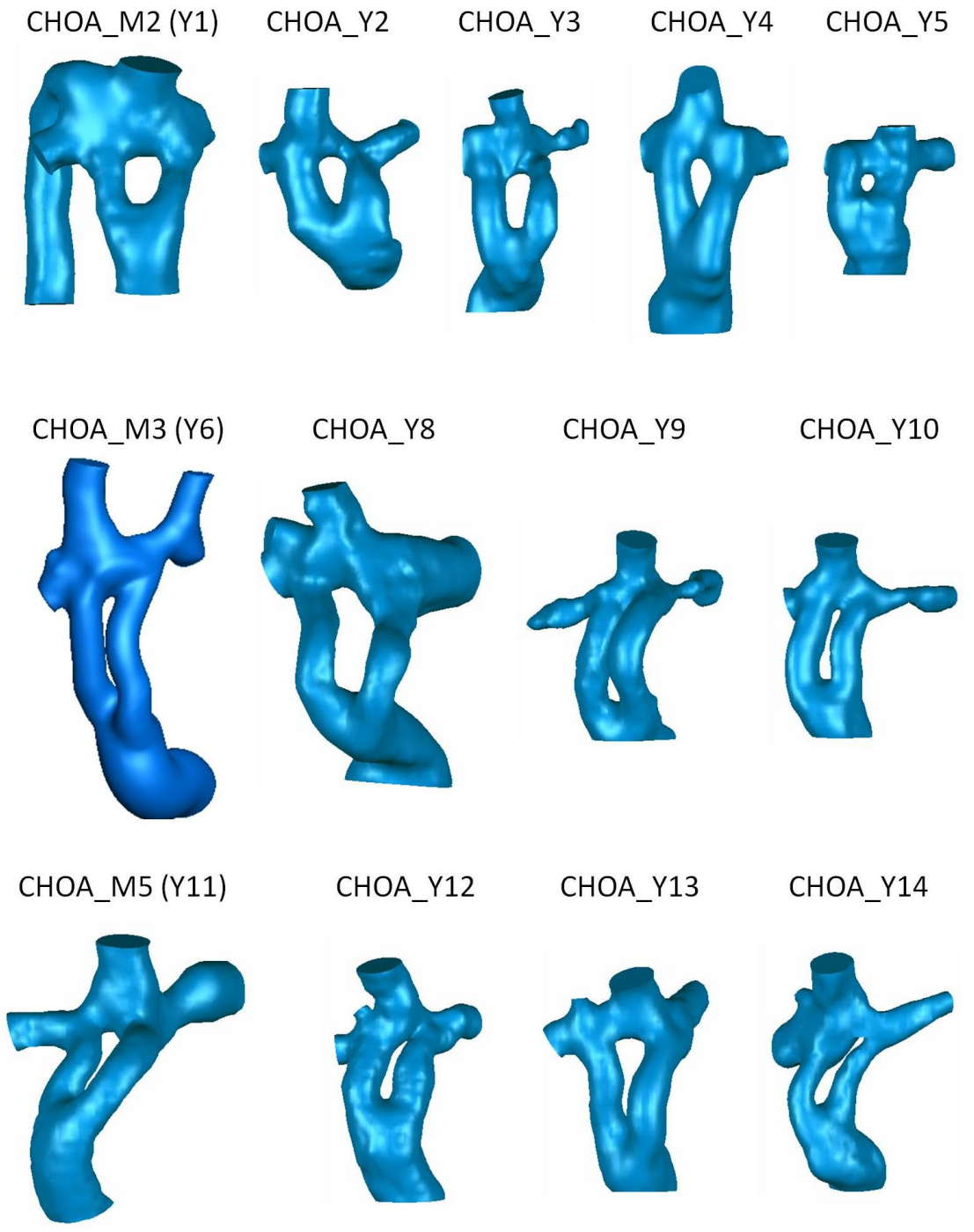


**Figure 8.1 Reconstructed Y-Graft patient connections (shown to relative size scale)**

A summary of the (non-normalized) flow rates used for each patient in the computational simulations is provided in Table 8.2. The flow rates were generally low, with 7 patients having cardiac outputs ≤ 2 L/min. Additionally, in most cases the IVC flow rate was lower than the SVC. Both of these observations are consistent with both the generally young age of the patients and the fact that the imaging studies were conducted in the acute post-operative period.

**Table 8.2 Vessel flow rates retained for each patient**

| **Pt.** | **CO** [L/min] | **IVC** [L/min] | **SVC** [L/min] | **LPA** [L/min] | **RPA** [L/min] |
|---|---|---|---|---|---|
| CHOA_M2 (Y1) | 5.0 | 0.5 (Hep) | 1.9 (+Az) | 0.4 | 2.0 |
| CHOA_Y2* | 2.7 | 1.5 | 1.2 | 1.3 | 1.4 |
| CHOA_Y3 | 2.0 | 0.3 | 0.5 | 0.2 | 0.3 |
| CHOA_Y4 | 2.5 | 0.6 | 0.8 | 0.3 | 0.6 |
| CHOA_Y5 | 1.4 | 0.4 | 0.5 | 0.6 | 0.2 |
| CHOA_M3 (Y6)† | 3.8 | 0.4 | 1.4 (+LSVC) | 0.8 | 0.4 |
| CHOA_Y8 | 4.1 | 2.1 | 1.3 | 1.6 | 1.7 |
| CHOA_Y9 | 1.5 | 0.5 | 0.9 | 0.4 | 0.9 |
| CHOA_Y10 | 1.5 | 0.5 | 0.9 | 0.4 | 0.7 |
| CHOA_M5 (Y11) | 4.1 | 1.0 | 1.5 | 0.8 | 0.9 |
| CHOA_Y12 | 1.1 | 0.4 | 0.7 | 0.8 | 0.2 |
| CHOA_Y13 | 1.0 | 0.4 | 0.8 | 1.1 | 0.3 |
| CHOA_Y14 | 1.8 | 0.6 | 1.0 | 0.5 | 0.7 |

*assumed from catheterization data; †assumed from pre-operative PC CMR

Representative velocity streamlines for all patients are shown in Figure 8.2 and Figure 8.3. General trends include low velocities (except in cases like Y3, Y9, Y10 with very small PAs); patient-specific variation in the dynamic interactions with SVC flow (recalling that SVC anastomosis angles were shown in Chapter 5 to be related to flow distributions); and IVC flow division between the two Y-Graft branches, as expected. Regarding this last point, however, static streamlines can be visually misleading in this regard, and Figure 8.4, Animation 8.1, and Animation 8.2 show that these dynamics varied among patients with some cases preferentially favoring IVC flow through one branch more than the other.

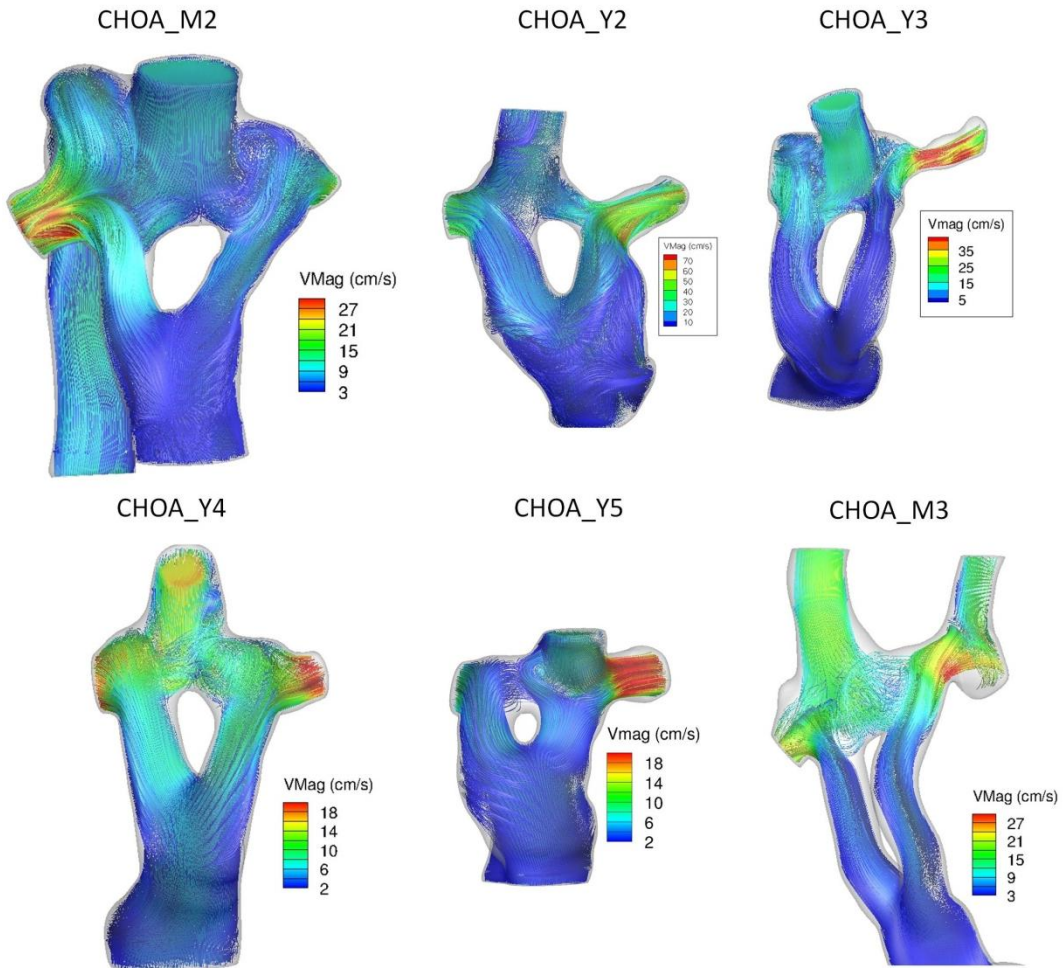


**Figure 8.2 Representative velocity streamlines color coded by local velocity magnitude for the first six Y-Graft patients**

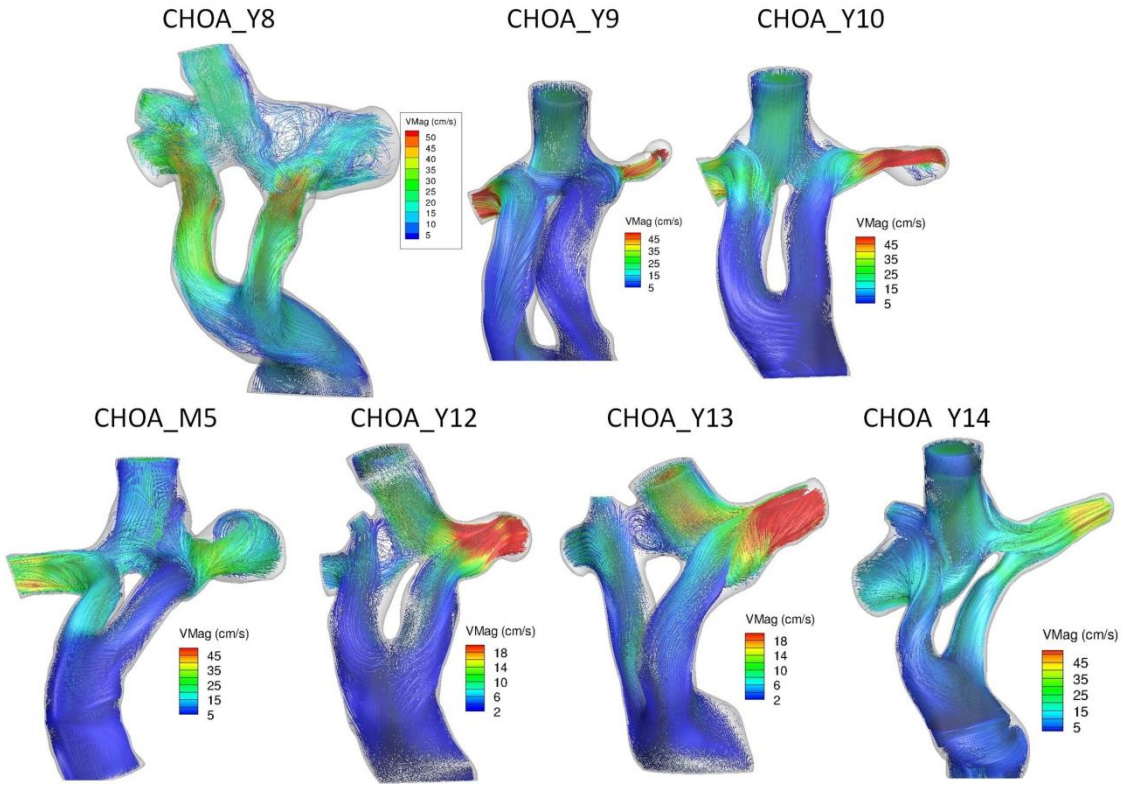


**Figure 8.3 Representative velocity streamlines color coded by local velocity magnitude for the Y-Graft patients 8-14.**

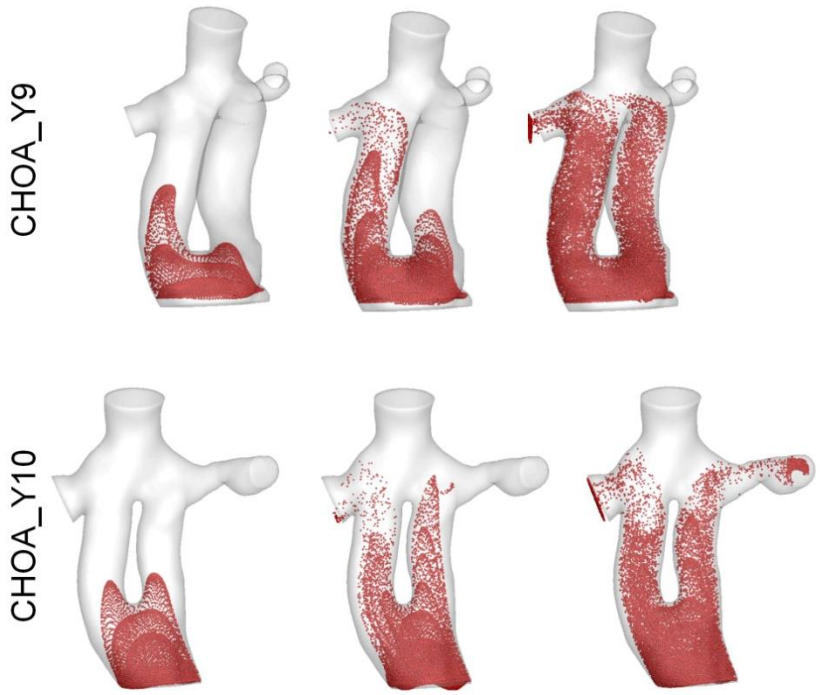


**Figure 8.4 Sequence of IVC particle tracking images for CHOA_Y9 (top) and CHOA_Y10 (bottom) contrasting cases in which branch velocities are approximately equal (Y10) and in which there is a significant disparity between left and right (Y9).**

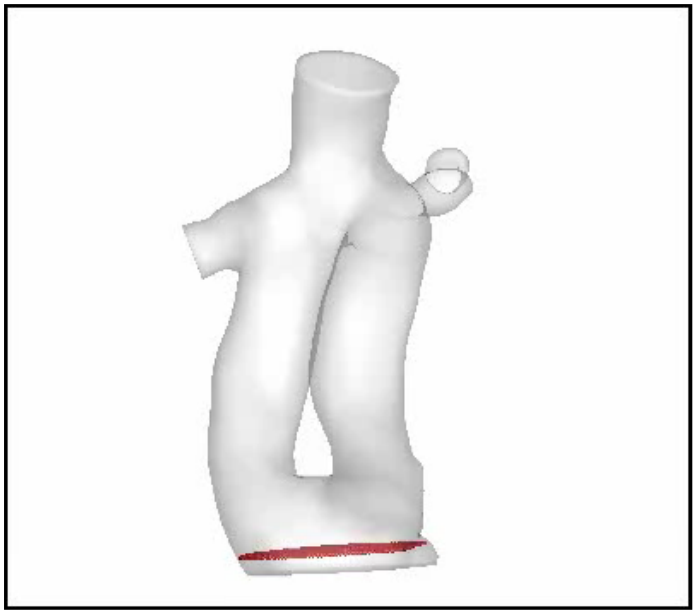

**Animation 8.1 Pulsatile particle tracking for CHOA_Y9**

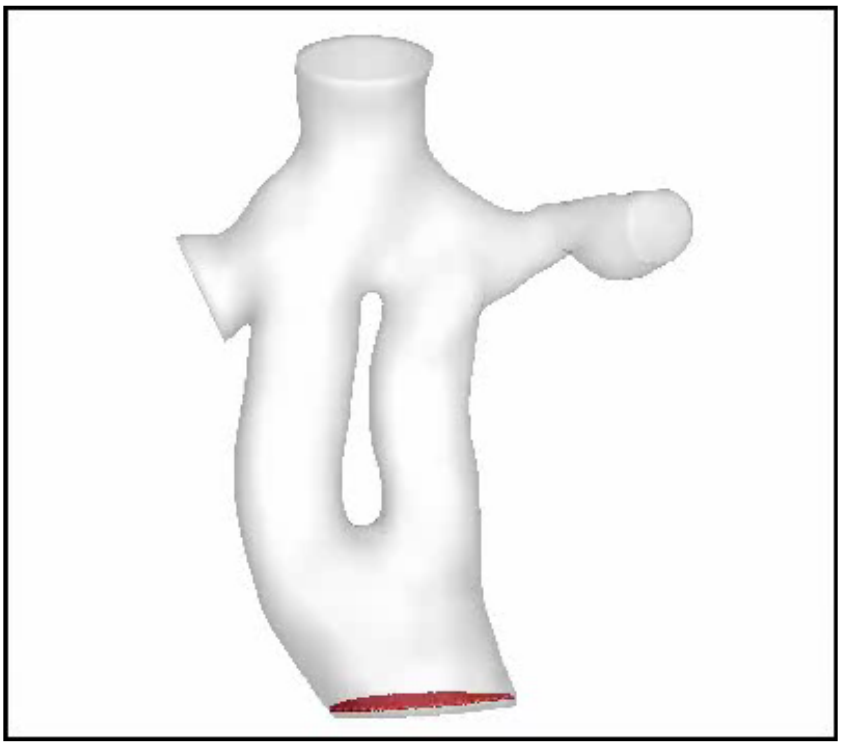

**Animation 8.2 Pulsatile particle tracking for CHOA_Y10**

The summary of the hemodynamic end points of interest derived from the computational simulations (as well as the type of BCs imposed for each case) is presented in Table 8.3. With respect to flow distribution, there is only one case that exhibits a significantly biased HFD result: CHOA_Y9 (7% LPA). Incidentally, this is the case highlighted in Figure 8.4 as having a significant bias for higher velocities through the right Y-branch. The LPA in that patient appears significantly stenosed and the SVC flow appears to add additional resistance to IVC flow tending to the left branch. Furthermore, the LPA carries only 30% of total pulmonary flow, so having a low hepatic contribution is expected.

For power loss (TCPC-EDI), there were three values > 0.090, which corresponds to the losses of the patients in §5.5.1 as being the highest power loss cases. In fact, CHOA_Y3 (0.244) has a value greater than any of those prior cases. All three of these patients are

marked by very small LPA diameters, which is the reason for the elevated energy dissipation.

**Table 8.3 Summary of CFD-derived hemodynamic data**

| **Pt.** | **BCs** | **TCPC-EDI** | **GFD** (%LPA) | **HFD** (%LPA) |
|---|---|---|---|---|
| CHOA_M2 (Y1) | Time-averaged | 0.027 | 18 | 35 |
| CHOA_Y2 | Time-averaged | 0.018 | 48 | 70 |
| CHOA_Y3 | Pulse | 0.244 | 33 | 28 |
| CHOA_Y4 | Pulse | 0.021 | 34 | 45 |
| CHOA_Y5 | Pulse | 0.029 | 74 | 34 |
| CHOA_M3 (Y6) | Time-averaged | 0.041 | 68 | 49 |
| CHOA_Y8 | Pulse | 0.052 | 49 | 38 |
| CHOA_Y9 | Pulse | 0.095 | 30 | 7 |
| CHOA_Y10 | Pulse | 0.133 | 35 | 41 |
| CHOA_M5 (Y11) | Time-averaged | 0.059 | 46 | 25 |
| CHOA_Y12 | Time-averaged | 0.027 | 80 | 62 |
| CHOA_Y13 | Time-averaged | 0.021 | 80 | 41 |
| CHOA_Y14 | Pulse | 0.034 | 46 | 52 |

### 8.3.2 Statistical Comparisons

The results in Table 8.3 were compared to those presented in Chapter 5 for the TCPC cohort to statistically evaluate the performance of this small Y-Graft series. With regard to HFD, Table 8.4 shows that the results were no different (p=0.49) with a mean of 44% LPA in both groups. Similarly, TCPC-EDI was statistically no different with respect to the median values (Mann-Whitney test; p=0.12) although the Y-Graft mean value was skewed considerably higher because of the high values reported in several cases.

**Table 8.4 Comparison of Y-Graft hemodynamics to TCPC cohort results**

| | TCPC Cohort (N=100) | Y-Graft Series (N=13) | p-value |
|---|---|---|---|
| **HFD** (%LPA) Mean ± SD | 44 ± 21 | 44 ± 20 | 0.49 |
| **TCPC-EDI** Mean ± SD (Median) | 0.037 ± 0.028 (0.032) | 0.057 ± 0.060 (0.034) | 0.12 |

## 8.4 Comparison to Patient-Specific Controls[139]

The cohort comparison for Y-Graft power loss is not necessarily the most appropriate because the Y-Graft patients were all imaged in the acute post-operative period, while the cohort data largely represent hemodynamics late after the Fontan procedure. Instead, a more appropriate way to evaluate the merits of an alternate Fontan connection (the Y-Graft) is to vary only the connection, while holding all other variables constant. This approach was the focus of the following section.

### 8.4.1 Methods

To provide this alternate basis for comparison, SURGEM was used to create two virtual extracardiac TCPC models for each of five Y-Graft patients (Y2-Y6) representing the possible alternative connections they may have received instead of a Y-graft[110]. This analysis was conducted early in the patient series, so the patients selected were those who had been recruited to that point. CHOA_M2 (Y1) was excluded from this analysis as the simulation of exercise physiology in the context of an interrupted IVC would not have evaluated the Y-Graft connection, as desired, but would instead increase azygos vein flows. The two extracardiac designs varied slightly in caval offset, and are thus

designated as the ‘t-junction’ and ‘offset’ models. Baffle diameters matched the diameter at the base of the Y-graft. Figure 8.5 shows the anatomical comparison of all connections.

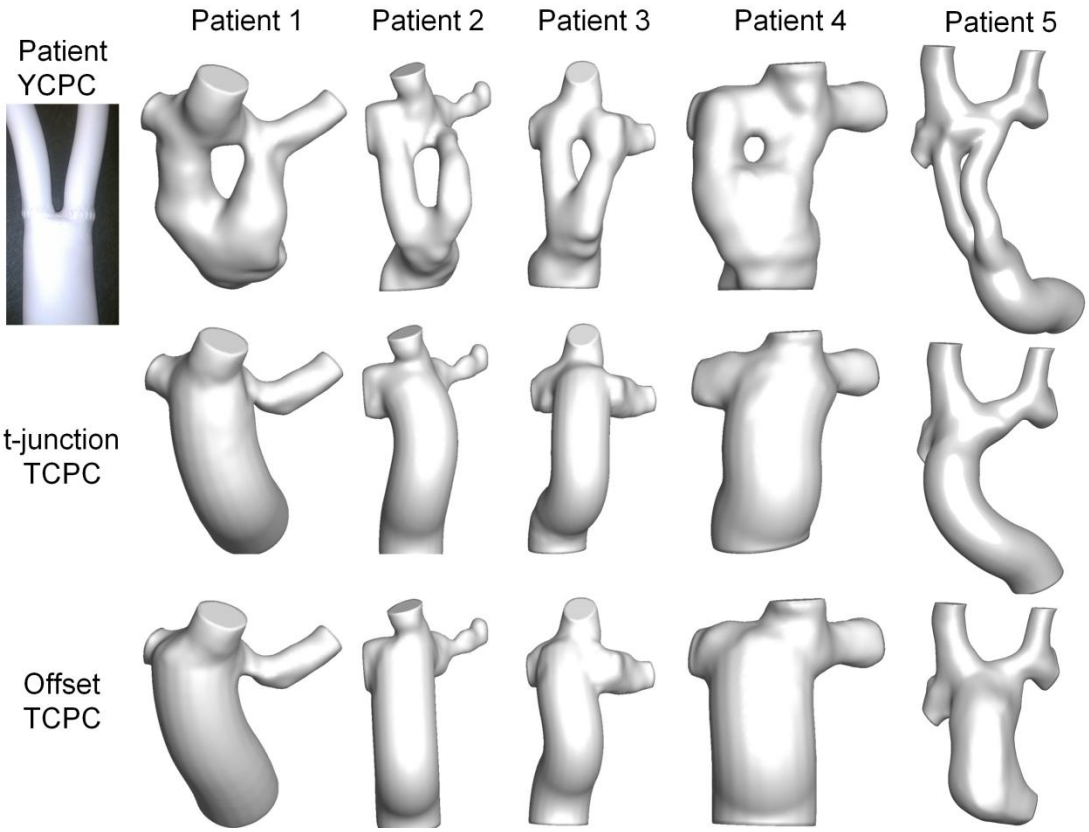


**Figure 8.5 Patient Y-Graft connections (top row; with photo of bifurcated PTFE graft) and virtually modeled t-junction (middle row) and offset (bottom row) TCPC controls for all 5 patients**

In addition to baseline (resting) flows, simulated exercise conditions were also investigated. Exercise limitations are a known chronic issue with Fontan patients[157, 158] and previous studies have shown that the non-linear increases in TCPC power loss with increased flow rates may be an important contributor[55, 134]. Further, since small inefficiencies under resting conditions may be amplified and exacerbated with higher flows, these simulations are a means to assess the hemodynamic characteristics and robustness for a given connection geometry. Per standard practice, simulated exercise conditions of two and three times baseline ('2x' and '3x') were numerically imposed by respectively doubling and tripling the measured cardiac output and imposing that difference as additional (time-averaged) IVC flow (approximating lower limb exercise)[107, 134]. The pulmonary flow splits were maintained constant across these varied conditions as suggested by previous studies[171].

The primary basis for comparison was the hemodynamic resistance (R) across the connection ( $R = \frac{\Delta P_{TCPC}}{Q_{VC} / BSA}$ ; where ΔP is pressure drop, $Q_{VC}$ is the sum of caval inflows, and BSA is the body surface area)[55]. Additionally, the IVC flow distribution to the PAs, (HFD) was quantified[144]. Further, to facilitate qualitative hemodynamic comparisons, the magnitude of viscous dissipation (i.e., $\mu\left|\nabla^2 V\right|$ ; μ is viscosity, V is velocity) and 3D vortex core visualization (via iso-surfaces of the second invariant of the deformation matrix, Q)[149] were also used, where appropriate.

### 8.4.2 Results

The resistance and HFD results are detailed in Table 8.5 and Table 8.6, respectively, and summarized in Figure 8.6. For resistance, the Y-Graft group had the lowest average

value. This trend was skewed by a single case (CHOA_Y2) for whom there was a significant improvement in efficiency with the Y-Graft. For the remaining patients, there were only minor differences. The non-linear response to simulated exercise was consistent among the connections (Figure 8.6A).

**Table 8.5 Connection Resistance Summary [mmHg*min/L] at Rest and Exercise**

| | Rest | | | 2x | | | 3x | | |
|---|---|---|---|---|---|---|---|---|---|
| **Pt.** | **Y** | **t-junction** | **Offset** | **Y** | **t-junction** | **Offset** | **Y** | **t-junction** | **Offset** |
| **Y2** | 0.33 | 1.26 | 1.21 | 0.74 | 2.57 | 2.29 | 1.22 | 3.95 | 3.43 |
| **Y3** | 1.6 | 1.6 | 1.5 | 2.63 | 2.42 | 2.60 | 3.93 | 3.83 | 3.83 |
| **Y4** | 0.17 | 0.15 | 0.23 | 0.40 | 0.32 | 0.46 | 0.68 | 0.51 | 0.62 |
| **Y5** | 0.2 | 0.19 | 0.19 | 0.57 | 0.55 | 0.67 | 0.89 | 0.90 | 1.08 |
| **M3** | 0.33 | 0.33 | 0.32 | 1.80 | 1.50 | 1.62 | 3.56 | 2.54 | 2.81 |
| **Mean** | 0.53 | 0.71 | 0.69 | 1.23 | 1.47 | 1.53 | 2.06 | 2.35 | 2.35 |

**Table 8.6 HFD Results [%LPA]**

| Pt. | Rest | | | 2x | | | 3x | | |
|---|---|---|---|---|---|---|---|---|---|
| | Y | t-junction | Offset | Y | t-junction | Offset | Y | t-junction | Offset |
| **Y2** | 70 | 65 | 42 | 51 | 56 | 38 | 47 | 52 | 42 |
| **Y3** | 32 | 16 | 4 | 30 | 14 | 9 | 30 | 24 | 20 |
| **Y4** | 49 | 57 | 28 | 45 | 47 | 42 | 44 | 43 | 41 |
| **Y5** | 52 | 46 | 35 | 58 | 56 | 60 | 66 | 65 | 69 |
| **M3** | 49 | 31 | 100 | 58 | 56 | 82 | 62 | 60 | 76 |
| **Mean** | 51 | 43 | 42 | 49 | 46 | 46 | 50 | 49 | 49 |
| **St. Dev** | 14 | 20 | 36 | 12 | 18 | 27 | 15 | 16 | 23 |

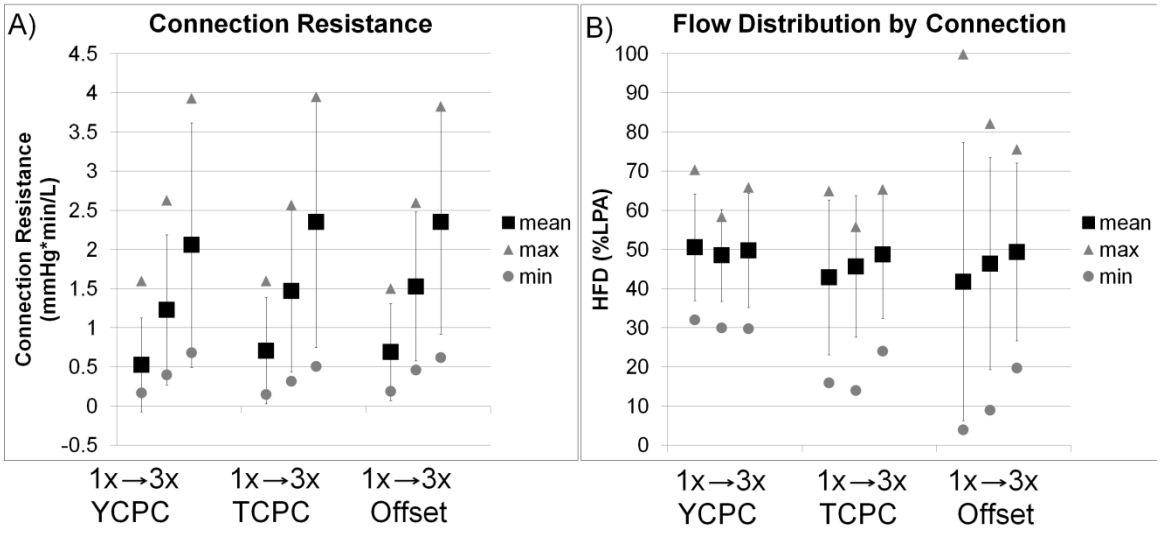


**Figure 8.6 Mean, maximum, and minimum values of connection resistance (A) and flow distribution (B) for each connection (YCPC (Y-Graft), TCPC, Offset) and flow condition (1x, 2x, 3x) investigated.**

With respect to HFD under baseline conditions, the Y-grafts had the smallest range and standard deviation among all patients (Figure 8.6B). By comparison, the TCPC offset models had a range of almost 100%, denoting significant patient-to-patient variation. Additionally, while there is no accepted 'optimal' value for HFD, the mean Y-Graft value (rest conditions) was closest to 50%, denoting desirable left/right balance.

### 8.4.3 Detailed Hemodynamic Analyses

As seen in Table 8.5 and Figure 8.6A, the resistance values varied considerably among patients. Thus, rather than focusing on the absolute magnitude of power loss, we seek to identify the factor(s) that mediated energy dissipation differences for a given patient across connection types, to then identify possible means for improvement. Two trends were discernible: dissipation through local vessel constrictions (Figure 8.7), and dissipation resulting from complex mixing and recirculation (Figure 8.8).

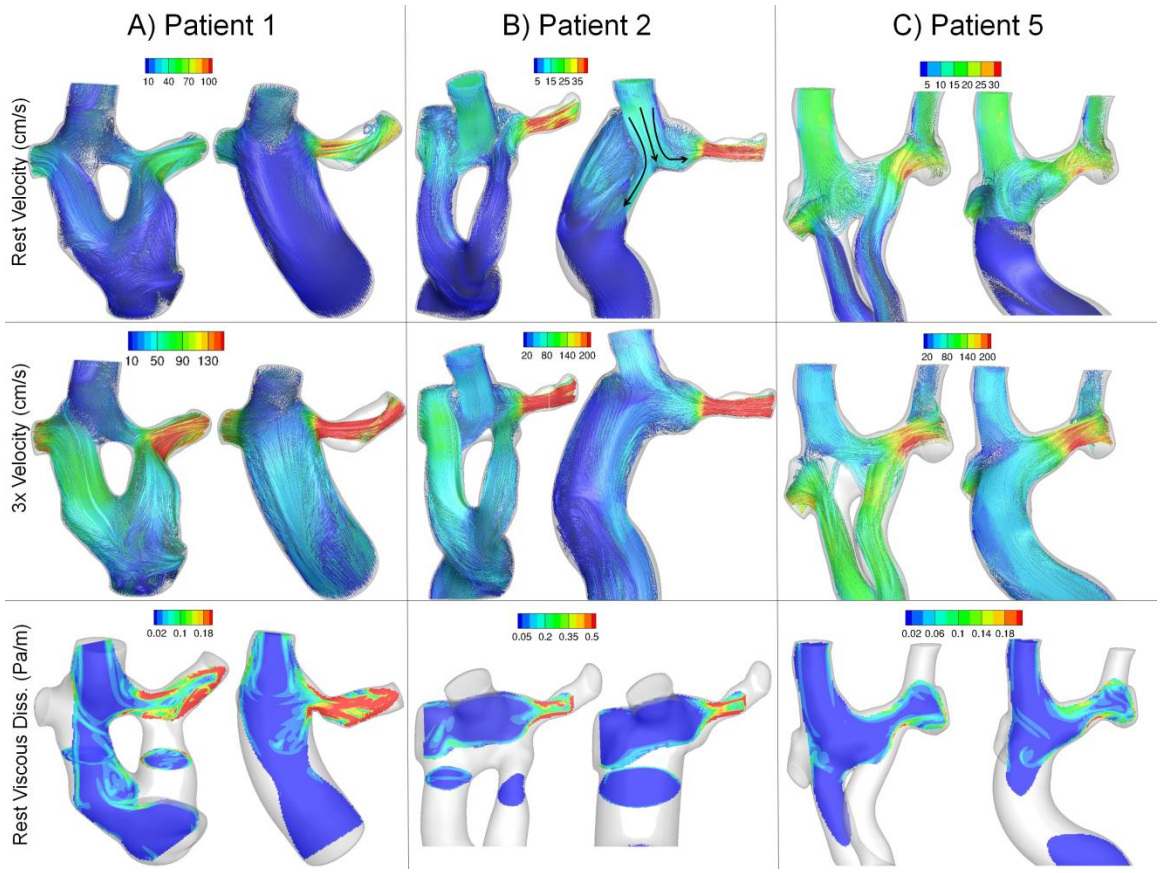


**Figure 8.7 Comparison of Y-Graft and TCPC hemodynamics for patients 1 (CHOA_Y2; A), 2 (CHOA_Y3; B), and 5 (CHOA_M3; C). The resting velocity streamlines (top row), 3x velocity streamlines (middle row), and viscous dissipation contours (bottom row) are shown in each case.**

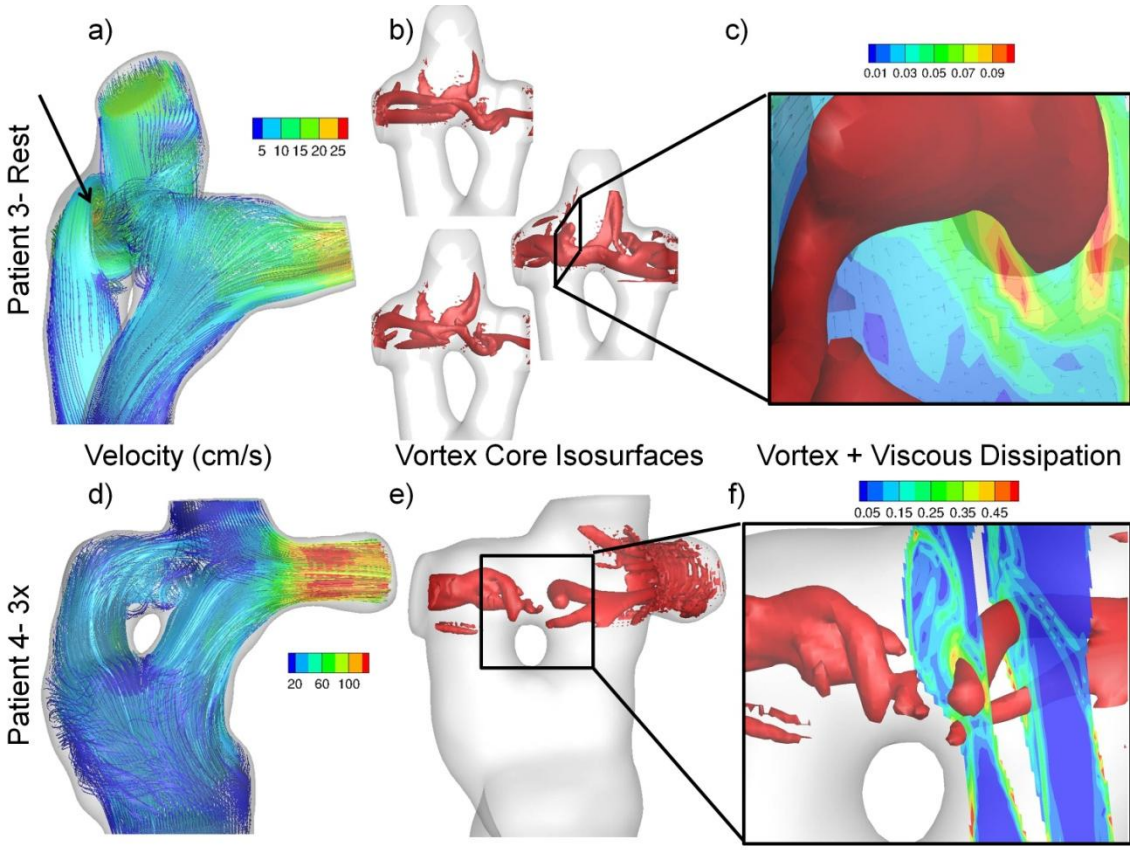


**Figure 8.8 Velocity streamlines (a,d), vortex core isosurfaces (Q=800 (top), 13000 (bottom)) (b,e), and viscous dissipation contours localized to the vortex isosurfaces (c,f) for Patients 3 (CHOA_Y4; top, rest) and 4 (CHOA_Y5; bottom, 3x).**

Figure 8.7 shows the resting (top) and 3x (middle) velocity streamlines, as well as resting viscous dissipation contours (bottom) for the Y-Graft and one TCPC option for CHOA_Y2, Y3, and M3. For CHOA_Y2, there was a section of the LPA that was mildly stenotic, which resulted in significant convective acceleration and dissipation of LPA flow for both connections, even under resting conditions. However, the position of the left branch of the Y-graft helped to augment the size of the vessel, bypass the throat of the constriction, and reduce flow separation in the distal LPA (particularly with exercise), as

compared to the t-junction results. These characteristics resulted in a significant reduction of the viscous losses (bottom row).

For CHOA_Y3 (Figure 8.7B), an acute stenosis in the LPA was again observed, except in this case it was distal to the Y-graft anastomosis. As a result, this patient consistently had among the highest resistance values in the study, irrespective of IVC baffle design (Figure 8.7, bottom row).

CHOA_M3 was unique in this series based on the presence of bilateral SVCs, and the use of numerical modeling to pre-operatively plan the procedure[105] and suggest surgical revision to a Y-graft. As seen in Figure 8.9a, the previous TCPC exhibited severely unbalanced HFD (blue) to the PAs (and thus right lung PAVMs developed) because of the unequal distribution of RSVC/LSVC flows (55% Qs vs. 21% Qs, respectively). In contrast, Figure 8.9b shows that the Y-graft delivers IVC flow to both PAs. However, the extended length of the Y-graft conduit caused significant acceleration and flow separation through the branches (Figure 8.7C) that increased energy losses.

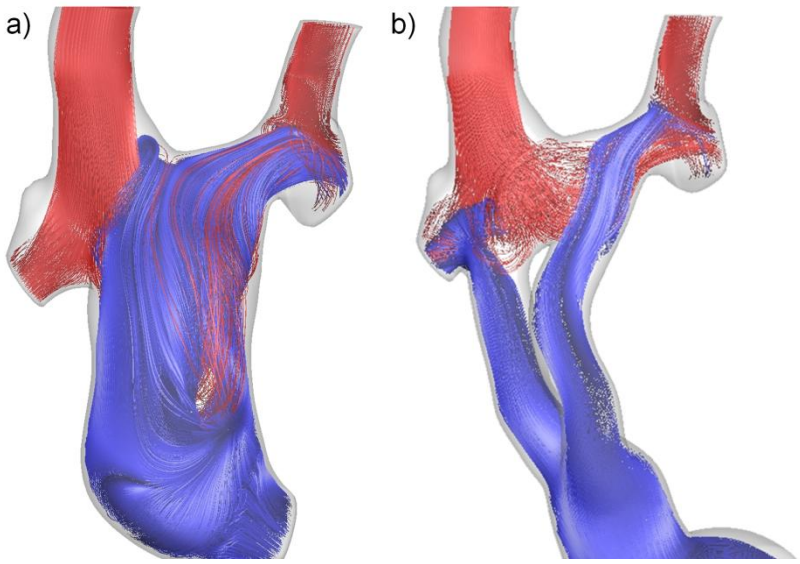


**Figure 8.9 Streamlines color coded by vessel of origin (red-SVC/LSVC, blue- IVC) for a) the CHOA_M3 offset TCPC (i.e., the failed connection prior to surgical revision) and b) the post-revision Y-Graft.**

For the remaining two patients (CHOA_Y4- top; CHOA_Y5- bottom), Figure 8.8 shows velocity streamlines (a) and coherent vortex cores (b), to facilitate appreciation of the complex flow recirculation. In these patients, both branches of the Y-graft were connected nearly perpendicularly to the PAs, resulting in significant flow recirculation at the anastomoses (arrow, Figure 8.8a). The vortex cores (Figure 8.8b) provide improved visualization of these rotational flow structures and show their expansive size. Rather than being local, contained phenomena, these vortices bilaterally originated in the high shear wake region distal to the IVC bifurcation and extended downstream into the PAs. As a result, Figure 8.8c shows that local regions of relatively high energy dissipation (from the color contours) were created at multiple downstream locations adjacent to these cores because of the complex fluid motion.

### 8.4.4 Section Summary

This study, in conjunction with the clinical report of Kanter, et al.[170], clearly demonstrates that the surgical implementation of the Fontan Y-graft is feasible. The additional contribution of this work is the identification and elucidation of the hemodynamic implications associated with the characteristics of the surgical design. In other words, the use of a Y-graft does not necessarily imply that it is as optimally efficient as in idealized studies[106, 107]. The following sections will analyze the numerically-derived 3D velocity fields in the context of the causative geometric design characteristics.

Hemodynamic Efficiency

The theoretical benefits of flow bifurcation in the cavopulmonary pathway originated with the experimental and numerical work of Soerensen et al.[106], in which the multiple bifurcations of the Optiflo were shown to outperform an idealized TCPC model. Rather than requiring a collision and 90° redirection of caval flows, the Optiflo efficiently redirected flow, ensuring a smooth and streamlined transition to the PAs. Marsden et al. followed with a numerical investigation in patient-specific models, focusing only on the bifurcation of the IVC[107], demonstrating again the potential for energetic improvements.

These hypothetical gains were not realized in the present *in vivo* implementations. In four of the five cases, Y-graft resistance was approximately equal to the resistances of the virtual TCPC controls. Clearly, since this is the first attempt at systematic, Y-graft use for the Fontan procedure, a learning curve to optimize the surgical implementation should be anticipated. In that regard, it is promising that there is no evidence in this series of diminished early outcome. These results suggest that the YCPC may be 'forgiving' enough to still be energetically equivalent to the TCPC when the design is

theoretically sub-optimal. Yet, there is also clear evidence from at least one case, that the energetics can be better than the TCPC.

In that case (CHOA_Y2), the decreased resistance is attributable to the fact that the Y-graft position augmented and bypassed an acute stenosis in the LPA that was otherwise a significant resistive element. Given the recent report showing the prevalence of sub-aortic PA stenosis[143] in single ventricle patients (particularly those with hypoplastic left heart syndrome), this potential strength of the Y-graft is something to consider for targeted use. However, this specific application does not tap into the fundamental characteristics of the Y-graft that theoretically make it efficient.

One possible reason for the efficiency differences compared to idealized models is the size selected for the Y-graft branches. Larger branches allow for lower fluid velocities and shear stresses, which would reduce losses. In fact, Soerensen explicitly evaluated Optiflo models of varying sizes, including a case in which the branch diameters summed to the base total as in the Gore grafts being used (20-10-10), and found higher power losses compared to the design in which the branch diameters equaled the base diameter (20-20-20, for example)[172]. Marsden *et al* reported similar findings comparing virtual models of 18x9 mm Y-Grafts vs. 18x12 mm Y-Grafts (constructed ad hoc)[107]. However, larger branches also impose increased spatial constraints, and are not available “off the shelf,” as the current grafts are. Without a pre-fabricated graft, the bifurcation must be constructed ad hoc, which creates an additional set of design variables and possible failure modes (e.g., thrombosis formation along additional suture lines). As such, a more pragmatic question to ask is, can the efficiency results be improved with the existing graft design to remove the need for pursuing size and construction alternatives?

A recent study by Yang et al. sought to parametrically optimize the Y-graft design (e.g., branch placement, angle, size, etc.)[169]. While, in theory, such an analysis would be helpful in directing surgical decision-making, insufficient mathematical constraint of the design variables limits the ability to translate those results into quantitative guidelines for surgical implementation. However, the demonstrated importance of tangential alignment of the bifurcation branches with the PA axis is a relevant message that was implicit in the original Optiflo design concept and provides an interesting perspective for the present results.

In this light, there were two primary shortcomings in these patient connections that limited hemodynamic efficiency and should be surgically addressed in future cases. The first was the near perpendicular angle of approach in most of the connections. This perpendicular connection creates a scenario in which the IVC flow enters the PA, impinges on the opposite (e.g., superior) vessel wall, and must undergo significant secondary recirculation to align with the PA axis of flow. As shown in Figure 8.8, this recirculation may create dissipative secondary flow structures that can extend to significant lengths downstream and decrease overall connection efficiency. By introducing an anterior curvature to the baffle may facilitate better angulation than a straight t-junction approach would allow. Beveling the distal ends of the graft is also suggested to achieve the efficiency benefits of a flared connection[75]. These features, particularly the anterior curvature, have been incorporated into the later patients in the Y-Graft series (as noted for Figure 8.1) and have generally helped to streamline flow through the left Y-Graft branch.

The second shortcoming was the close proximity or even medial (to the SVC) placement of the Y-Graft branches, which allows for continued interaction and mixing between the caval flows. In the extreme case where one branch was positioned exactly opposite the

SVC (as in CHOA_Y2 (Figure 8.7A) and CHOA_Y5 (Figure 8.8, bottom)), there is direct caval flow competition and the associated energy dissipation that a bifurcated design was intended to avoid. Placing the right branch distal to the right pulmonary upper lobe and the left branch immediately posterior to the ascending aorta provides the best means to avoid that scenario. Furthermore, positioning of the SVC at the Glenn stage could be adjusted in future Y-graft candidates to provide additional lateral space for the branches.

Importantly, these design factors are independent of graft size and, in fact, smaller branches would facilitate placement according to these guidelines. This provides additional support for the present choice in Y-graft design, and indicates that future studies should pursue these design optimization modifications in conjunction with parametric sizing studies to practically determine the best approach for Y-Graft implementation.

In addition to diameter, the length of the Y-Graft branches is another important variable with implications for its energy efficiency. Clearly, a length that is too short does not allow for lateral separation between the branches and instead approaches an extracardiac baffle with a cylindrical hole through the middle (see CHOA_Y5). On the other extreme, it is clear from basic fluid mechanics (Poiseuille flow) that pressure drop will increase linearly with the length of cylinder which, in conjunction with the longer length of higher wall shear dissipation with smaller diameter grafts, will contribute to increased power loss. Cases like CHOA_M3 and CHOA_Y8 show some of these deleterious effects of extensive graft length.

Clearly, there should be an optimal length in between these two extremes. A parametric evaluation could help to identify that solution; however, given the potential number of

variables involved (e.g., how discretely the range of lengths is sampled, the potential for anterior and/or lateral curvature), a basic parameter sweep could be computationally and time intensive. Instead, this type of question may be an ideal application for the surrogate management framework[169], or a similar optimization scheme assuming that the inputs are properly constrained within physiologic limits.

With regard to the originally posed hypothesis, this work shows that the Fontan Y-Graft *can* be effectively used in certain scenarios. Yet, this fact neither proves nor disproves the hypothesis with respect to energy efficiency because the question remains: can the suggested modifications ensure that the 'optimal' Fontan Y-graft is *consistently* realized under anatomic size constraints? The answer is likely to be patient-specific in that the position and size of the PA, pulmonary veins, SVC, and aorta are sure to be the critical determinants of whether or not the desired shape and position of the Y-Graft is achievable. Herein lies a potential application for patient-specific simulation-based surgical planning techniques for Fontan surgery[105, 159], which could be used to both select candidates for favorable Y-Graft implementation and visually provide the target landmarks for branch placement.

Caval Flow Distribution

Balanced HFD is an important consideration to prevent the formation of PAVM[58]. There is a lack of evidence to indicate the minimum thresholds to prevent PAVM formation; however, a split at or around 50/50 is a desirable target. In considering the HFD values of the various connections evaluated in this series, there was no clinical significance in the mean differences (Y-Graft vs. t-junction vs. Offset), as 40% vs. 50% HFD would not impact the patient outcomes. However, the smaller variance across the Y-Graft results is noteworthy because it demonstrates improved consistency and stability of that design.

By comparison, there were three instances with TCPCs that exhibited severely unbalanced HFD. So while, on average, the Y-graft may not significantly improve IVC flow distributions, these data suggest it could reduce the occurrence of outliers with poor streaming performance. Such outliers are far more prevalent in specific groups, such as cases of interrupted IVC[62], suggesting that these are additional patients who may benefit from targeted Y-Graft use over extracardiac baffles[105, 159].

In summary, the detailed hemodynamics of the Fontan Y-graft in an *in vivo* setting were investigated under a variety of relevant flow conditions and with direct comparison to patient-specific TCPC controls. Desirable IVC-PA flow distribution characteristics were found; however, the flow efficiency performance fell short of the outcomes predicted by previous models. A beneficial comparison was found when the Y-graft was able to offset the effects of acute PA stenosis, making such situations a potential for targeted usage. Further, detailed analysis of the surgical Y-graft implementation with respect to the resulting flow fields was used to identify strategies for improving performance on a broader scale.

## 8.5 Chapter Summary

This chapter provides an in depth hemodynamic analysis of a novel approach to Fontan surgery in a preliminary set of single ventricle patients. Motivated by fundamental engineering principles[106], the Y-Graft connection is hypothesized to improve the energy efficiency of the TCPC junction by avoiding caval flow collision and helping to streamline the transition from systemic to pulmonary flows.

Because of the need to two distinct connection sites instead of the one required for traditional Fontan connections, there were first concerns related to surgical feasibility

that needed to be addressed. As this series demonstrates, the Y-Graft can be surgically implemented with good short term outcomes[170]. The next important question was then: how do the hemodynamics compare of this connection compare to traditional approaches?

In Chapter 7 of this thesis, several cases were presented at length in which a Y-Graft connection was used to achieve a beneficial flow distribution result. Those anecdotal findings in addition to the balanced HFD reported in this series (44% LPA on average) demonstrate the ability of the connection in this regard. However, it is worth noting that balance did not represent an improvement over the average TCPC patient, so the need for the Y-Graft connection for that purpose is limited.

For power loss, results were much less conclusive as comparisons to the TCPC cohort as well as patient-specific controls both showed no difference with the Y-Graft. The size of these particular grafts are certainly a limiting factor[107, 172], but larger grafts may present a trade-off of improved efficiency at the expense of surgical feasibility. Detailed analysis of five patients prompted suggestions of modifications to surgical implementation, and those suggestions were incorporated in the latter series of recipients with respect to the placement of the left branch with respect to the LPA. Placement of the right branch still remains a significant challenge and potential limitation.

Ultimately, long term follow-up is needed to make strong conclusions from this experience. Issues such as PA growth and post-operative physiologic baseline hemodynamics are going to be critical mediators of the local connection hemodynamics that short-term follow-up does not capture. Additionally, a randomized clinical trial of the Y-Graft against extracardiac TCPCs, reminiscent of the recent single ventricle

reconstruction trial of the BT-shunt vs. the Sano shunt, would be another excellent method of evaluation.

# Chapter 9. Specific Aim 5: Compare longitudinal changes in VF and TCPC hemodynamics

## 9.1 Overview

In the first two specific aims (Chapters 5 and 6), the physiologic importance of TCPC power loss was indicated by significant correlative relationships with cardiac index, indexed systemic venous flow, and ventricular volumes (particularly end diastolic volume- a surrogate of preload). These findings are a confirmation of the long-held hypothesis regarding the potentially confounding role of the TCPC in broader single ventricle physiology. Concurrently, baseline ventricular function was characterized in a small patient subset.

These results, while novel and significant, represent only an instantaneous snapshot of each patient's functional status. By comparison, Fontan 'failure' is a gradual and progressive process, which often develops over the course of several years. The natural follow-up questions to ask are thus, how do these functional characteristics change with time, and what do the changes suggest about the mediators of Fontan failure?

The answers to such questions obviously require the use of serial patient analyses. While conclusive determinations would require extensive studies in a large patient sample, the lack of any such data (serial hemodynamics and function) means that a preliminary pilot study could provide novel insights to help inform and guide future, larger efforts. The aim of this chapter is to conduct such a preliminary analysis based on the availability of serial CMR data for a small subset of patients discussed in Chapters 5 and 6. It is hypothesized that TCPC power losses increase with time, ventricular function decreases, and the extent of that decrease in function may be related to the extent of hemodynamic losses.

## 9.2 Study Protocols

### 9.2.1 Patient Selection

Fifteen patients were selected from the 100 patient cohort analysis on the bases of having more than one CMR scan post-Fontan and having a ventricular short-axis cine acquisition as a part of at least one of those scan protocols. A total of thirty-three CMR scans were thus included for those fifteen patients (one patient having 4 different scans and another having 3) and TCPC hemodynamics were characterized from each. Twenty-six scans included ventricular function (VF) data; however, inconsistent cine phase numbers across slices invalidated three data sets and poor signal quality excluded two others. As a result, seven patients had serial VF data while only one did not have sufficient quality VF data at either time point. Table 9.1 summarizes the patients and VF data included and the time between scans in this analysis. The patient designations of A, B, C, etc. denote the sequential scans for a given patient (A being the first scan, B the second, etc.). The 'A' scans for some patients were excluded from this analysis on the basis of either the data being incomplete (missing VF or axial dicoms) or the presence of artifacts.

### 9.2.2 Statistical Analysis

Paired t-tests and Wilcoxon matched pairs tests were used to test for serial changes in hemodynamics and ventricular function. In the cases for which hemodynamics and function were characterized at multiple time points, Pearson correlations were used to elucidate relationships in the changes between time points.

**Table 9.1 Summary of Patients and data included in Serial Analysis**

| **Patients** | **Age at First Scan** (yrs) | **Time Between Consecutive Scans** | **Included Data** |
|---|---|---|---|
| CHOP005 (B,C) | 19 | 2 yrs, 1m | VF x2 |
| CHOP008 (B,C) | 16 | 2 yrs, 3m | VF x2 |
| CHOP017 (B,C) | 15 | 6 yrs, 4m | VF excluded |
| CHOP018 (A,B,C) | 7 | 3 yrs; 4 yrs | VF for C |
| CHOP019 (A,B) | 14 | 7 yrs, 6m | VF x2 |
| CHOP021 (A,B) | 11 | 3 yrs, 10m | VF for A |
| CHOP022 (A,B) | 7 | 3 yrs, 9m | VF for A |
| CHOP033 (A,B) | 10 | 7 yrs, 6m | VF x2 |
| CHOP036 (A,B) | 11 | 3 yrs | VF for A |
| CHOP052 (B,C,D,E) | 10 | 1 yr, 2m; 7m; 2 yrs, 10m | VF x2 (B,E) |
| CHOP065 (A,B) | 16 | 2 yrs, 4m | VF for A |
| CHOP080 (A,B) | 17 | 5 yrs | VF x2 |
| CHOP082 (A,B) | 7 | 5 yrs, 8m | VF for B |
| CHOP088 (A,B) | 8 | 5 yrs, 8m | VF for B |
| CHOP091 (A,B) | 18 | 5 yrs | VF x2 |

## 9.3 TCPC Changes

The average age at first scan for these patients was 12.4 ± 4.3 years and the average follow-up duration was 4.8 ± 1.9 years.

The results are organized as follows: first, case-by-case comparisons of TCPC geometric and hemodynamics changes will be presented followed by a summary and analysis of the combined trends. Next, the serial VF results will be analyzed for the seven eligible patients. Finally, an exploratory analysis will be conducted between the hemodynamic and functional data to understand if any preliminary trends or relationships are apparent from these data.

### 9.3.1 Patient-by-Patient Investigations

For each patient detailed in the following sub-sections, four primary comparisons are drawn: 1) a visual review of TCPC reconstruction differences; 2) a quantitative analysis of the geometrical results (obtained with VMTK analysis) by vessel; 3) quantification of changes in systemic and pulmonary flow rates and distributions; and 4) comparison of hemodynamic end points from serial CFD. For the visual TCPC comparisons, two points are noted: first, the registration was performed using the automatic registration features in Geomagic; second, the earlier geometry will be presented in blue in each figure with the more recent reconstruction surface provided as a translucent overlay. In most cases (unless more than one time point is presented) anatomic views are presented from both anterior (on left) and posterior views (on right). For the VMTK data, results are presented both non-normalized (in mm) and normalized to $BSA^{0.5}$ [mm/m] since that normalization scheme has been shown to be appropriate for vascular and valve diameters[173]. Based

on the strong hemodynamic correlations of the minimum and mean vessel diameters with power loss seen in Chapter 5, only those values will be reported.

#### 9.3.1.1 CHOP005

Figure 9.1 shows the resulting surface reconstructions while Figure 9.2 provides the VMKT results. The vessels generally increased in size with the notable exception of the LPA, which saw decreases in both the mean and minimum diameters.

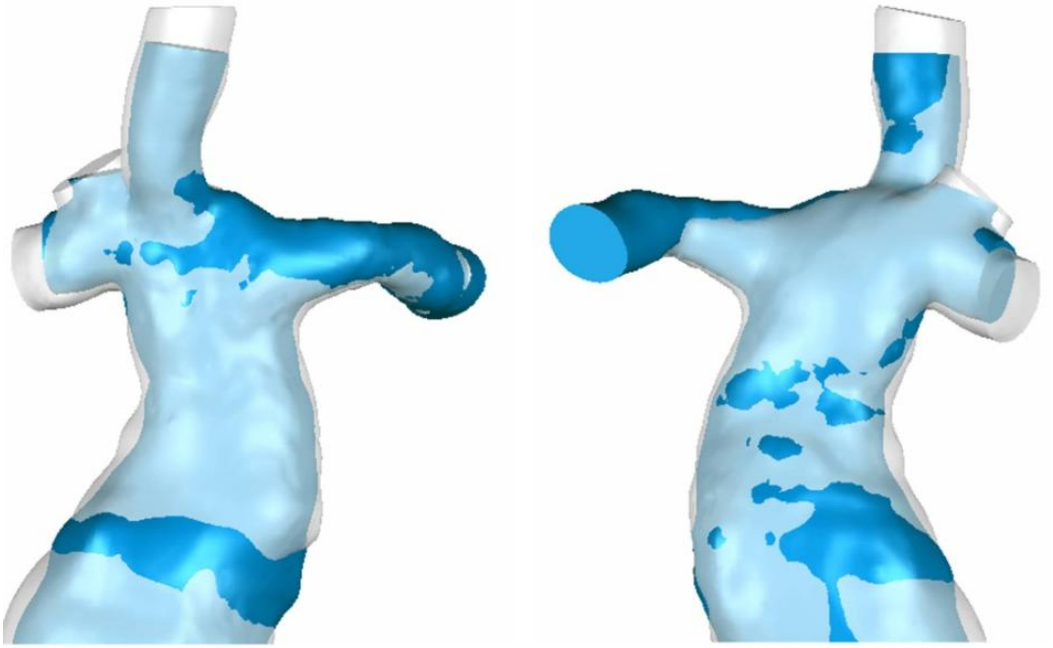

**Figure 9.1** ***Comparison of TCPC surface reconstructions for CHOP005B (blue) and CHOP005C (clear).***

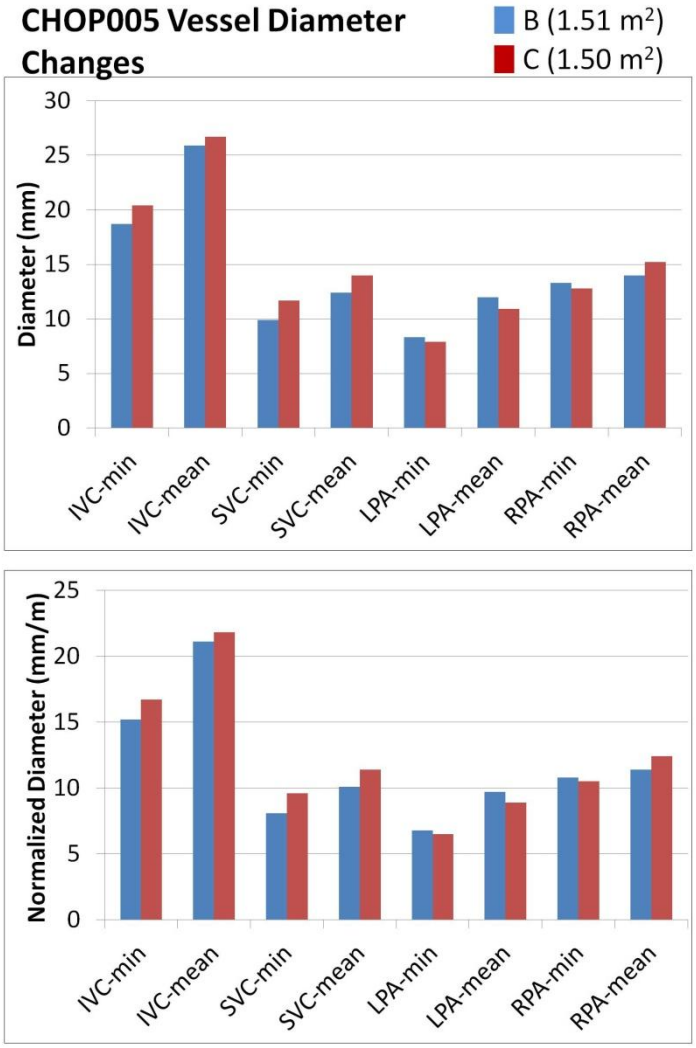


**Figure 9.2** ***Actual (top) and BSA-normalized (bottom) vessel minimum and mean diameters for CHOP005. The BSA values at each time point are provided in the color legend.***

The changes in vessel flow rates are shown in Table 9.2. For this patient the RPA measurements were not consistent and were discarded. The total cardiac output decreased in time leading to a subsequent decrease in IVC flow. The resulting time-averaged CFD flow fields are shown in Figure 9.3 and quantitative comparison in Table 9.3. High velocity LPA flow is seen at both time points. Fontan flow was decreased in

scan C through the combined effects of increased vessel size and decreased flow rate, thus the dynamics of the SVC/Fontan flow interactions were altered slightly, as evidenced by the change in HFD (increased in the later scan). The pressure drop and power loss decreased between scans (owing to the decreased flow rate); however, after indexing (as TCPC-EDI), the power loss was actually elevated at the later time point.

**Table 9.2 Measured flow rates (in L/min) for CHOP005 scans B and C.**

| | Ao | IVC | SVC | LPA | RPA |
|---|---|---|---|---|---|
| **B** | 4.5 | 3.6 | 1.0 | 2.6 | - |
| **C** | 3.6 | 2.1 | 1.1 | 1.9 | - |

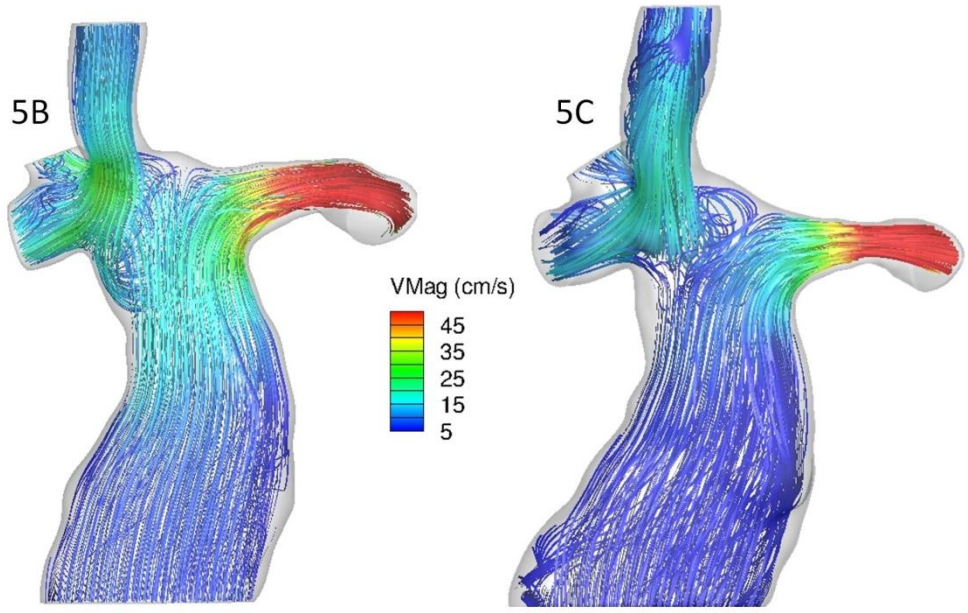


**Figure 9.3** ***Time averaged CFD velocity streamlines for CHOP005 B(left) and C(right).***

**Table 9.3 Hemodynamic measures for CHOP005 from serial CFD simulations**

| | HFD (%LPA) | $\Delta P_{MAX}$ (mmHg) | Power Loss (mW) | Resistance (WU) | TCPC-EDI |
|---|---|---|---|---|---|
| **B** | 68 | 3.3 | 17.9 | 0.58 | 0.087 |
| **C** | 93 | 2.2 | 8.1 | 0.54 | 0.116 |

9.3.1.2 CHOP008

Figure 9.4 and Figure 9.5 compare the surface reconstructions and vessel sizes, respectively, for CHOP008B and CHOP008C. All vessels decreased in diameter slightly, but the changes in the LPA and IVC/Fontan pathway are most visually apparent.

Table 9.4 provides the comparison of CMR-measured flows at the two time points. The total systemic flow remained constant despite minor shifts in cardiac output and superior/inferior distribution. The pulmonary flow split similarly varied slightly from 43% to 39% LPA, perhaps in response to the changes in vessel sizes. These minor flow changes did not create significant visual differences in the resulting flow fields (Figure 9.6); however, the quantitative results were very different, presumably owing to the small size of the LPA.

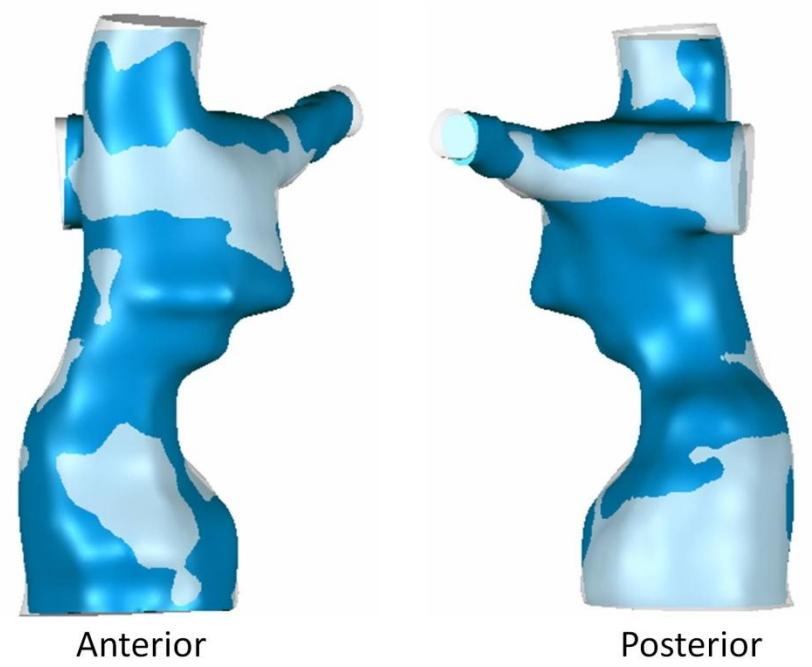


**Figure 9.4** ***Comparison of TCPC surface reconstructions for CHOP008B (blue) and CHOP008C (clear).***

In fact, the values for maximum pressure drop (>8 mmHg) and resistance (>1.1 WU) appear to be unphysiologically high, while the TCPC-EDI is more than double the highest value reported in Chapter 5. These findings suggest that because the minimum LPA diameter and through-plane spatial resolution of the anatomic CMR acquisition were of approximately the same dimension (both ~5 mm), the uncertainty in the vessel size may be large compared to the reconstructed dimension. If this size also corresponds to the high curvature region of the diameter/power loss Power Law relationship (Figure 5.31), which it likely does, then this uncertainty can produce large errors and the exact results reported here are likely inaccurate for that reason.

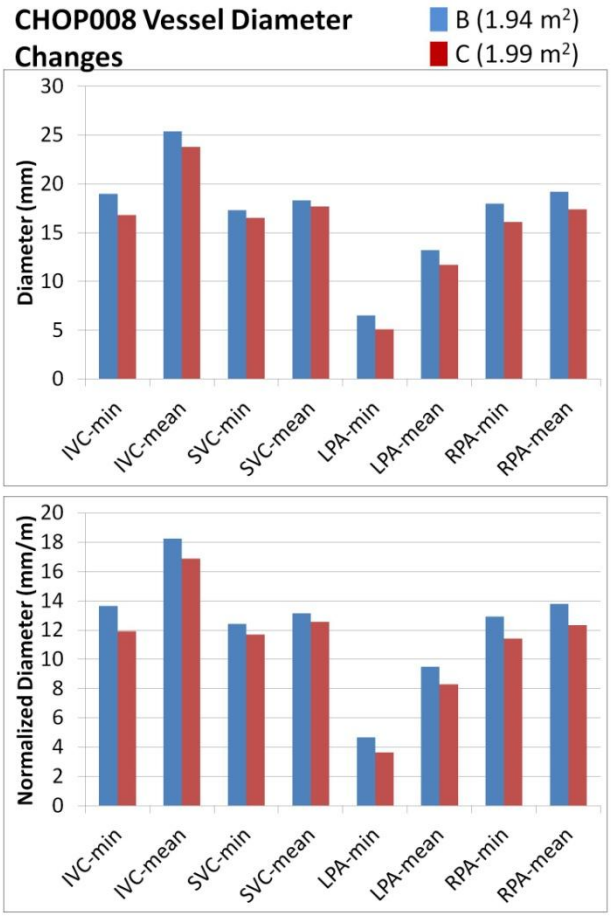


**Figure 9.5** ***Actual (top) and BSA-normalized (bottom) vessel minimum and mean diameters for CHOP008. The BSA values at each time point are provided in the color legend.***

**Table 9.4 Measured flow rates (in L/min) for CHOP008 scans B and C. PA percentages are shown in parentheses.**

| | Ao | IVC | SVC | LPA | RPA |
|---|---|---|---|---|---|
| **B** | 6.7 | 3.8 | 0.8 | 1.8 (43%) | 2.4 (57%) |
| **C** | 6.1 | 3.5 | 1.1 | 1.6 (39%) | 2.5 (61%) |

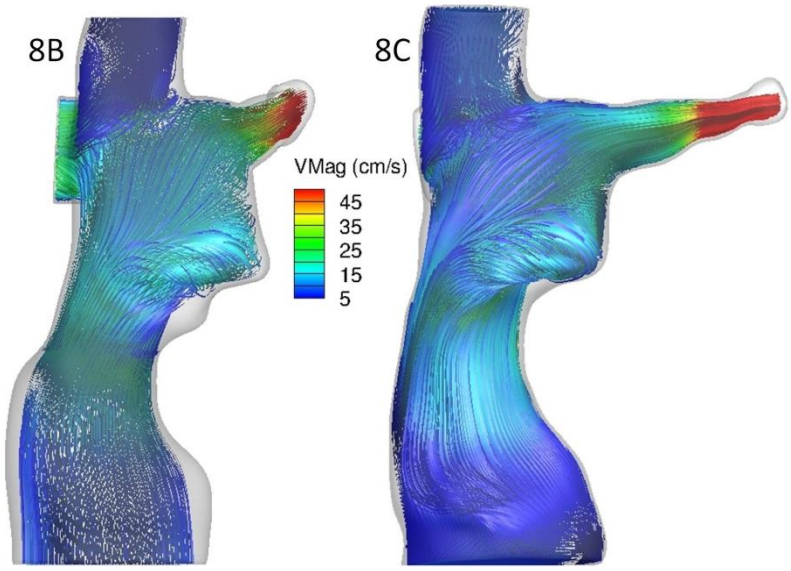


**Figure 9.6** ***Time averaged CFD velocity streamlines for CHOP008 B(left) and C(right).***

**Table 9.5 Hemodynamic measures for CHOP008 from serial CFD simulations**

| | **HFD** (%LPA) | **$\Delta P_{MAX}$** (mmHg) | **Power Loss** (mW) | **Resistance** (WU) | **TCPC-EDI** |
|---|---|---|---|---|---|
| **B** | 50 | 3.2 | 8.2 | 0.34 | 0.065 |
| **C** | 42 | 8.6 | 28.9 | 1.18 | 0.228 |

9.3.1.3 CHOP017

Figure 9.7 and Figure 9.8 show that the TCPC vessel sizes for CHOP017 were little changed between scans B and C. The most notable change was the slight decrease in LPA dimensions, which were already smaller than the other vessels. Table 9.6 shows the measured flows were also consistent between scans- cardiac output decreased (by

8%) but systemic venous return increased (by 5%) and total pulmonary flow (magnitude and distribution) was the same.

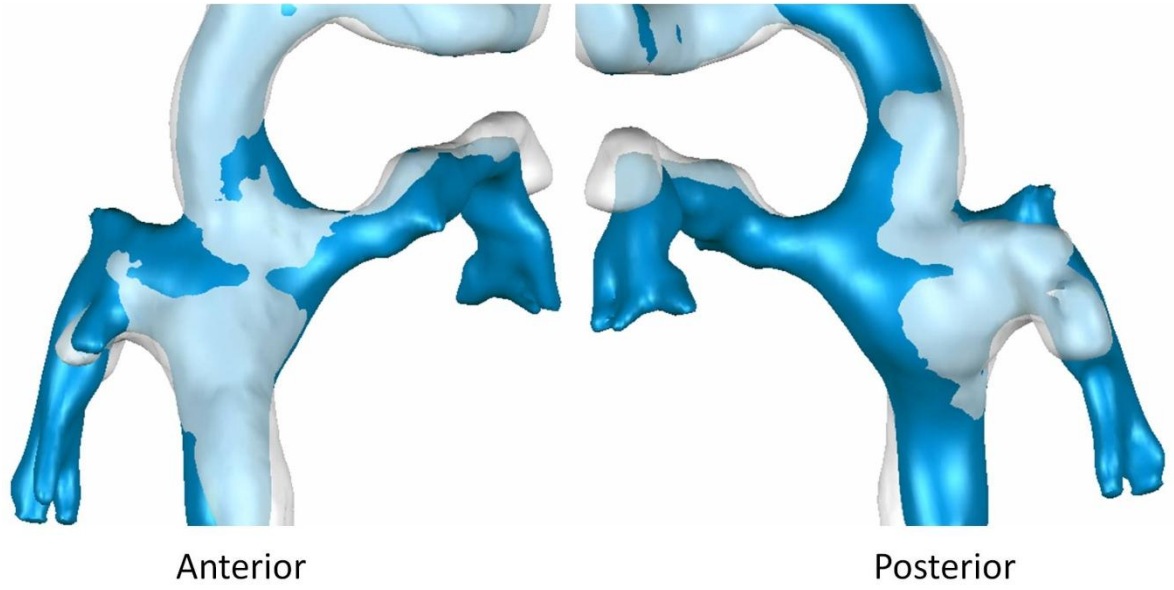


**Figure 9.7** ***Comparison of TCPC surface reconstructions for CHOP017B (blue) and CHOP017C (clear).***

Figure 9.9 shows the resulting CFD velocity fields, which were very consistent between time points: the SVC flow is pushed preferentially to the LPA, with a small portion recirculating and exiting the RPA, while the Fontan flow is primarily constrained to the RPA. Quantitative velocity differences (i.e., higher velocities in the later scan) in the Fontan baffle and LPA reflect increased IVC flow contribution and decreased LPA diameter, respectively. These changes, particularly in the LPA, led to a serial increase in power loss (raw and normalized), as seen in Table 9.7.

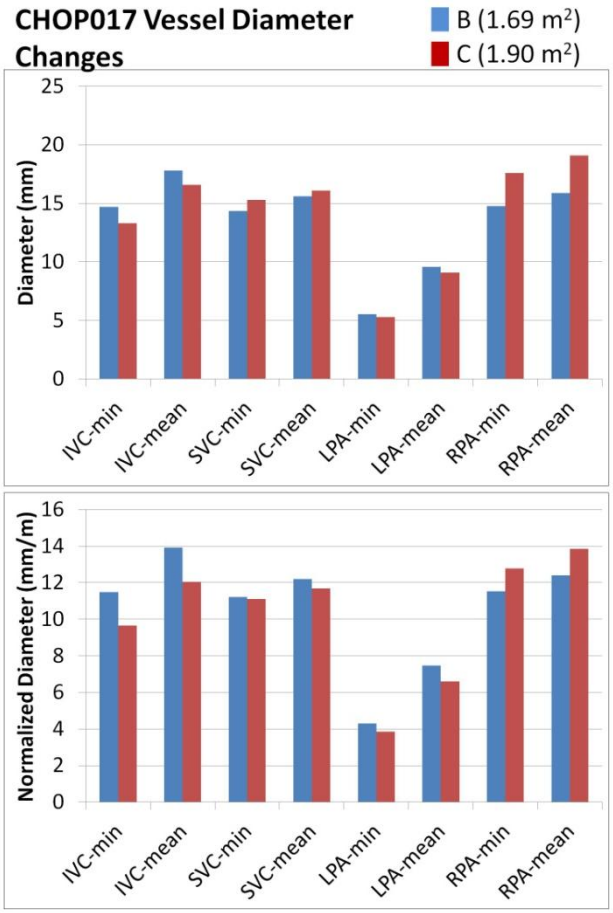


**Figure 9.8** ***Actual (top) and BSA-normalized (bottom) vessel minimum and mean diameters for CHOP017. The BSA values at each time point are provided in the color legend.***

**Table 9.6 Measured flow rates (in L/min) for CHOP017 scans B and C. PA percentages are shown in parentheses.**

| | Ao | IVC | SVC | LPA | RPA |
|---|---|---|---|---|---|
| **B** | 5.1 | 2.5 | 1.3 | 0.6 (16%) | 3.1 (84%) |
| **C** | 4.7 | 3.0 | 1.0 | 0.6 (15%) | 3.1 (85%) |

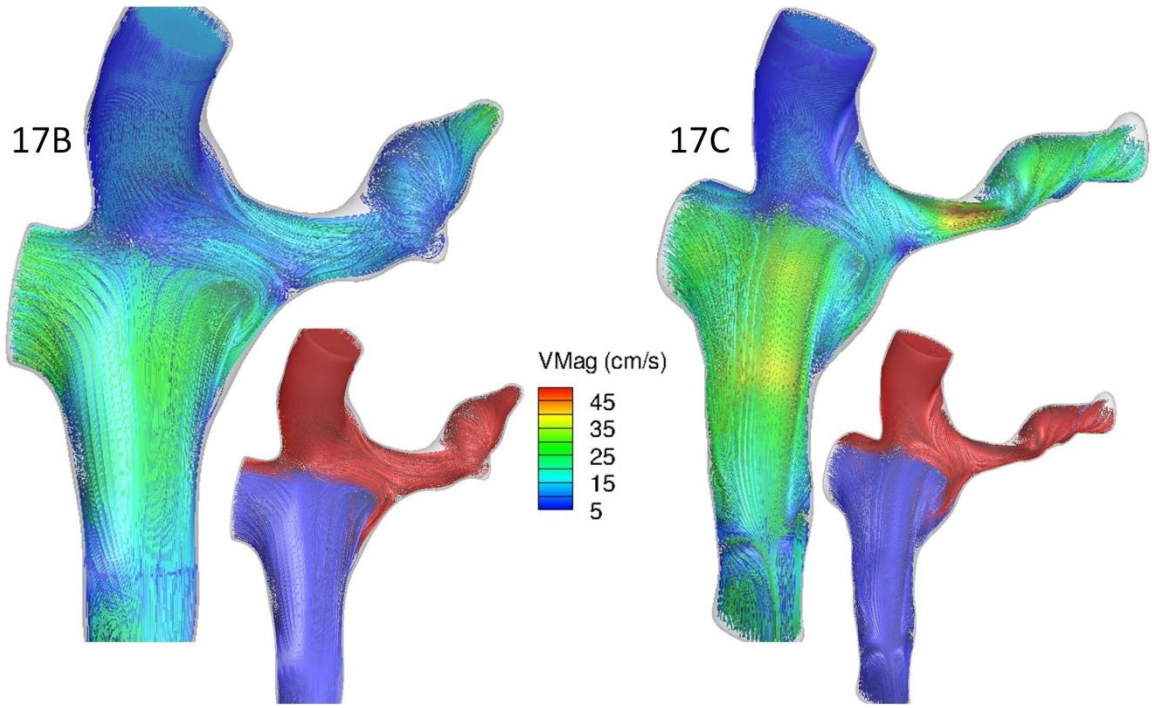


**Figure 9.9** ***Time averaged CFD velocity streamlines for CHOP017 B(left) and C(right). Inset images show streamlines color coded by vessel of origin (blue- IVC, red- SVC).***

**Table 9.7 Hemodynamic measures for CHOP017 from serial CFD simulations**

| | **HFD** (%LPA) | **$\Delta P_{MAX}$** (mmHg) | **Power Loss** (mW) | **Resistance** (WU) | **TCPC-EDI** |
|---|---|---|---|---|---|
| **B** | 0 | 0.8 | 3.4 | 0.18 | 0.035 |
| **C** | 2 | 1.0 | 5.0 | 0.28 | 0.061 |

9.3.1.4 CHOP018

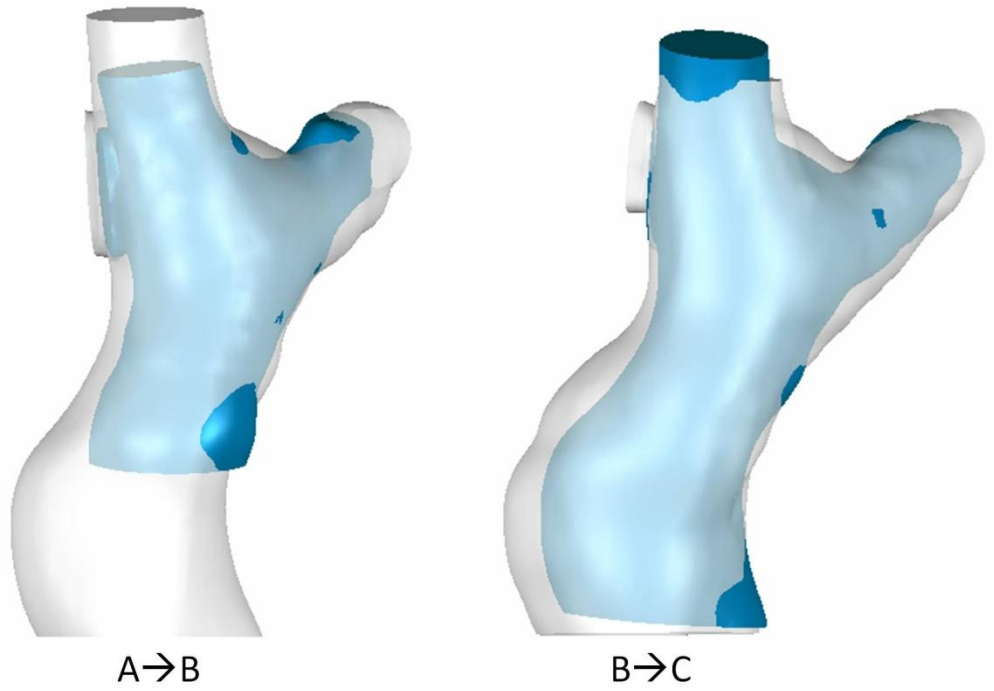


**Figure 9.10** ***Comparison of TCPC surface reconstructions for CHOP018A (blue, left) vs. CHOP018B (clear, left) and CHOP018B (blue, right) vs. CHOP018C (clear, right).***

From the three reconstructed TCPC geometries shown in Figure 9.10, significant growth and evolution can be observed in this patient across the series of 3 CMR scans. Moving from A→B resulted in appreciable increase in all vessel diameters (as also seen in Figure 9.11), although the fact that the A scan was reconstructed from black blood images is a confounding factor in this comparison, particularly the length of the Fontan pathway. Moving from scans B→C produced slightly smaller increases, although growth of the LPA and an increased size of the lateral tunnel (particularly where the native atrium is along the right lateral wall) are apparent. Despite the visible changes in size, on a BSA normalized basis (Figure 9.11bottom), the changes were much smaller and even

negative for some cases. The measured flows (Table 9.8) also increased, but only modestly over time (from 2.7 L/min to 3.3 L/min for $Q_S$); hence, connection velocities (Figure 9.12) were generally low and maintained a similar qualitative structure over time. TCPC-EDI and Resistance values (Table 9.9) were similarly low and consistent.

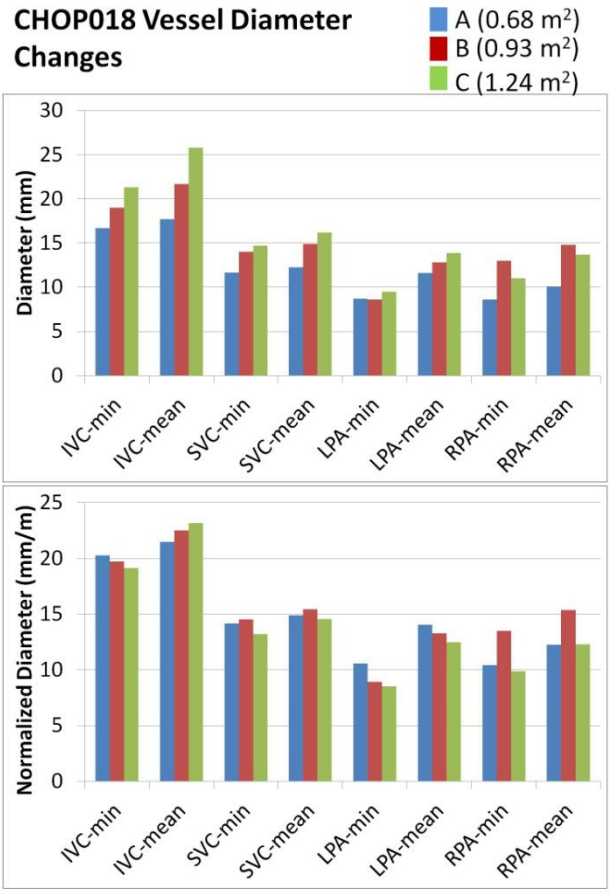


**Figure 9.11** ***Actual (top) and BSA-normalized (bottom) vessel minimum and mean diameters for CHOP018. The BSA values at each time point are provided in the color legend.***

**Table 9.8 Measured flow rates (in L/min) for CHOP018 scans A-C. PA percentages are shown in parentheses.**

| | Ao | IVC | SVC | LPA | RPA |
|---|---|---|---|---|---|
| **A** | 3.1 | 1.4 | 1.3 | 0.9 (42%) | 1.3 (58%) |
| **B** | 2.5 | 1.5 | 1.5 | 0.9 (51%) | 0.9 (51%) |
| **C** | 3.8 | 2.3 | 1.0 | 1.4 (40%) | 2.0 (60%) |

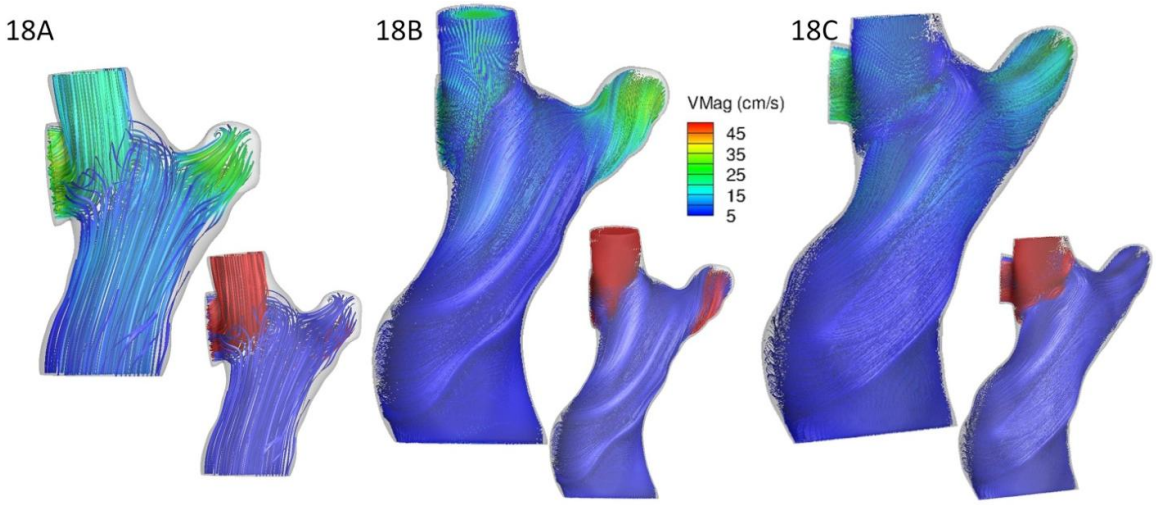


**Figure 9.12** ***Time averaged CFD velocity streamlines for CHOP018 A (left), B (middle) and C (right). Inset images show streamlines color coded by vessel of origin (blue- IVC, red- SVC).***

**Table 9.9 Hemodynamic measures for CHOP018 from serial CFD simulations**

| | HFD (%LPA) | $\Delta P_{MAX}$ (mmHg) | Power Loss (mW) | Resistance (WU) | TCPC-EDI |
|---|---|---|---|---|---|
| **A** | 67 | 0.4 | 1.4 | 0.06 | 0.008 |
| **B** | 63 | 0.9 | 1.5 | 0.07 | 0.010 |
| **C** | 69 | 0.5 | 1.1 | 0.06 | 0.010 |

#### 9.3.1.5 CHOP019

Figure 9.13 and Figure 9.14 show the surface reconstructions and vessel measures, respectively, for CHOP019A and CHOP019B. Growth in the lateral tunnel pathway and proximal LPA is visually apparent and only the RPA was found to marginally decrease in size between scans. Table 9.10 shows that, even though measured aortic flow decreased slightly, both systemic and pulmonary flow magnitudes increased with time, while keeping fairly consistent distributions.

As a result of the increased vessel dimensions, Figure 9.15 shows that the local TCPC velocity magnitudes generally decreased with time, with the possible exception of the RPA. The decreased magnitudes, in turn, correspond to decreased (normalized) power losses and pressure drop (Table 9.11). The dynamics with respect to the IVC/SVC flow interactions remained consistent (from inset images of Figure 9.15).

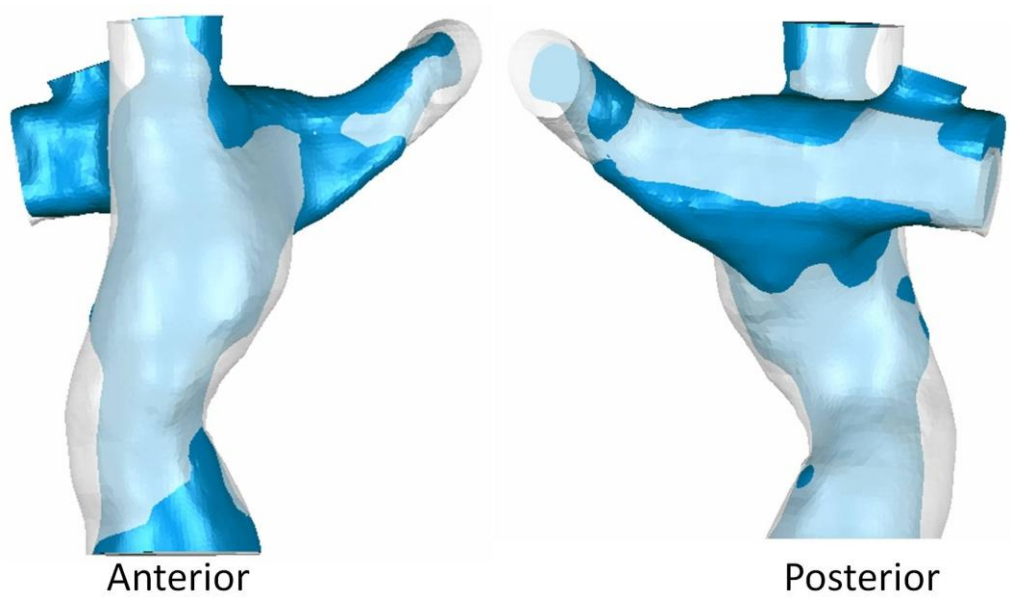


**Figure 9.13** ***Comparison of TCPC surface reconstructions for CHOP019A (blue) and CHOP019B (clear) The RUPA was included in the second scan, but cannot be readily seen in the reconstruction.***

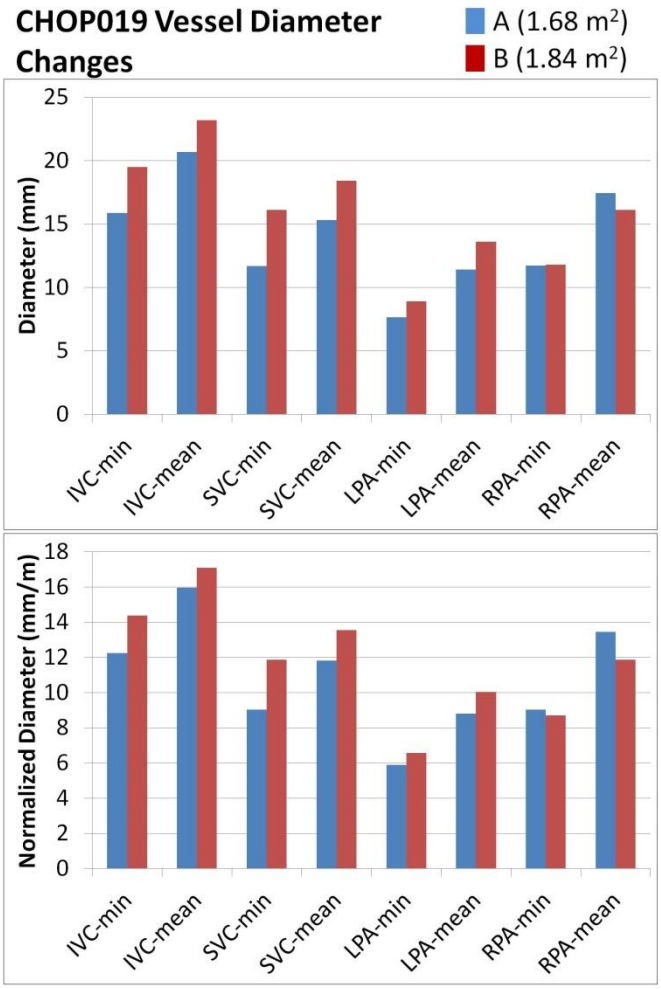


**Figure 9.14** ***Actual (top) and BSA-normalized (bottom) vessel minimum and mean diameters for CHOP019. The BSA values at each time point are provided in the color legend.***

**Table 9.10 Measured flow rates (in L/min) for CHOP019 scans A and B. PA percentages are shown in parentheses.**

| | Ao | IVC | SVC | LPA | RPA |
|---|---|---|---|---|---|
| **A** | 5.5 | 3.5 | 1.4 | 1.9 (41%) | 2.8 (59%) |
| **B** | 5.2 | 3.8 | 1.8 | 2.4 (42%) | 3.3 (58%) |

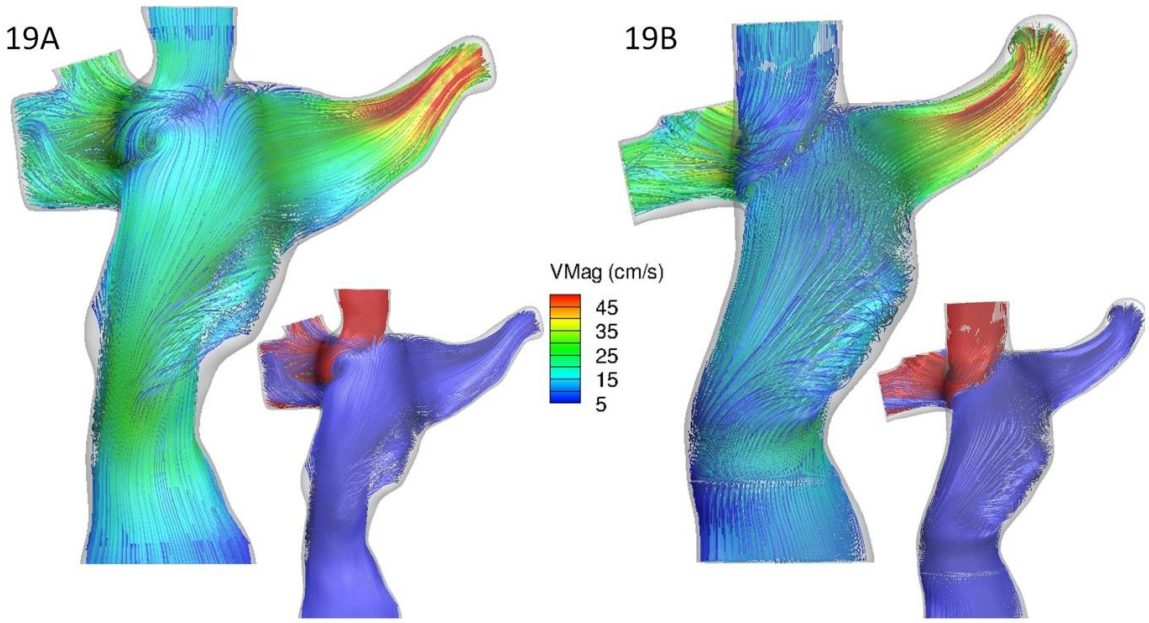


**Figure 9.15** ***Time averaged CFD velocity streamlines for CHOP019 A(left) and B(right). Inset images show streamlines color coded by vessel of origin (blue- IVC, red- SVC).***

**Table 9.11 Hemodynamic measures for CHOP019 from serial CFD simulations**

| | **HFD** (%LPA) | **$\Delta P_{MAX}$** (mmHg) | **Power Loss** (mW) | **Resistance** (WU) | **TCPC-EDI** |
|---|---|---|---|---|---|
| **A** | 52 | 1.8 | 7.4 | 0.23 | 0.034 |
| **B** | 60 | 1.3 | 7.5 | 0.20 | 0.030 |

#### 9.3.1.6 CHOP021

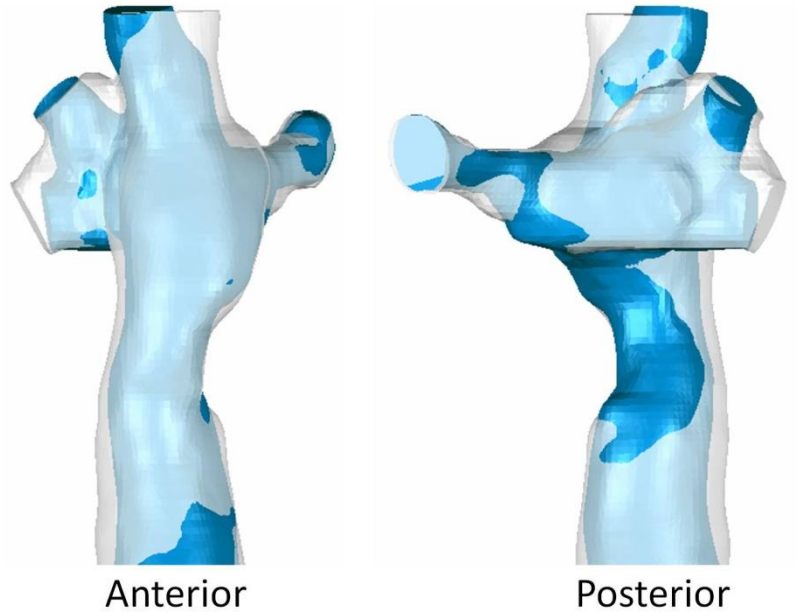


**Figure 9.16** ***Comparison of TCPC surface reconstructions for CHOP021A (blue) and CHOP021B (clear).***

Size comparisons for CHOP021A and CHOP021B are shown in Figure 9.16 and Figure 9.17. Visually (and with respect to non-normalized dimensions) all vessels increased in size between scans. After correcting for BSA change, the lateral tunnel/IVC and RPA were relatively unchanged, but the LPA and SVC still demonstrated large increases. CMR-measured vessel flow rates (Table 9.12) all increased, with the biggest relative change being an increase in RPA percentage of total pulmonary flow from 62% to 70%.

The CFD results (Figure 9.18) again show generally decreased velocity magnitudes, although significant acceleration and flow separation in the LPA is still apparent. As a result, the raw power loss value (Table 9.13) increased, but normalized values both

decreased (24% in the case of TCPC-EDI). HFD to LPA decreased, likely reflecting the overall decrease in LPA flow.

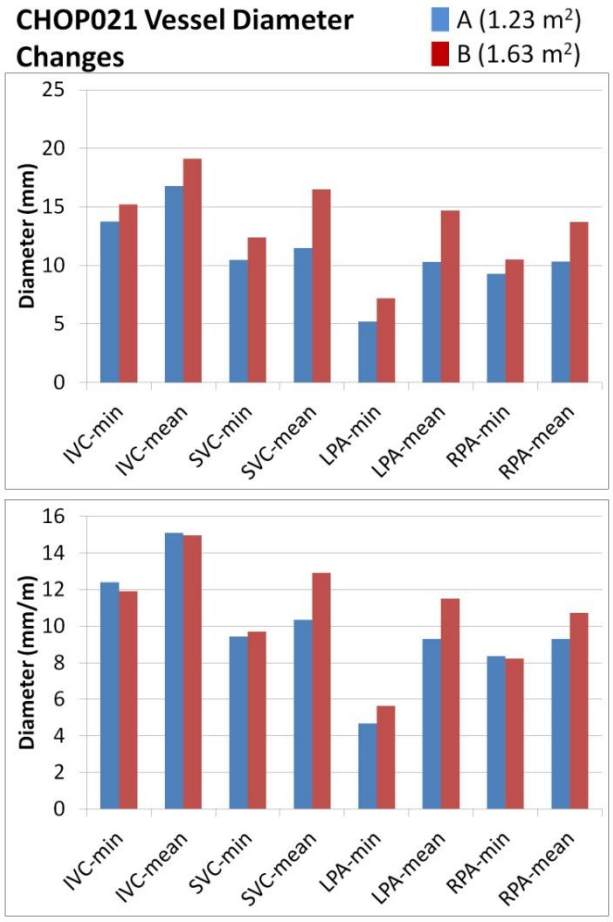


**Figure 9.17** ***Actual (top) and BSA-normalized (bottom) vessel minimum and mean diameters for CHOP021. The BSA values at each time point are provided in the color legend.***

**Table 9.12 Measured flow rates (in L/min) for CHOP021 scans A and B. PA percentages are shown in parentheses.**

| | Ao | IVC | SVC | LPA | RPA |
|---|---|---|---|---|---|
| **A** | 3.7 | 2.2 | 0.9 | 1.2 (38%) | 1.7 (62%) |
| **B** | 4.5 | 3.2 | 1.3 | 1.5 (30%) | 3.5 (70%) |

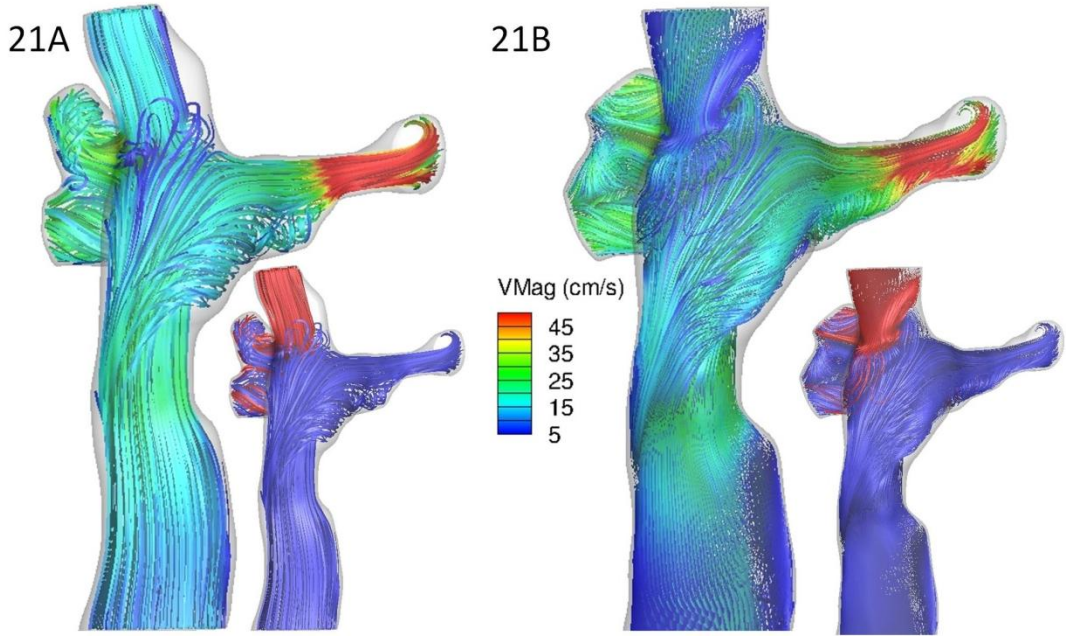


**Figure 9.18** ***Time averaged CFD velocity streamlines for CHOP021 A(left) and B(right). Inset images show streamlines color coded by vessel of origin (blue- IVC, red- SVC).***

**Table 9.13 Hemodynamic measures for CHOP021 from serial CFD simulations**

| | HFD (%LPA) | $\Delta P_{MAX}$ (mmHg) | Power Loss (mW) | Resistance (WU) | TCPC-EDI |
|---|---|---|---|---|---|
| **A** | 49 | 2.3 | 7.3 | 0.42 | 0.076 |
| **B** | 38 | 2.3 | 9.7 | 0.35 | 0.057 |

9.3.1.7 CHOP022

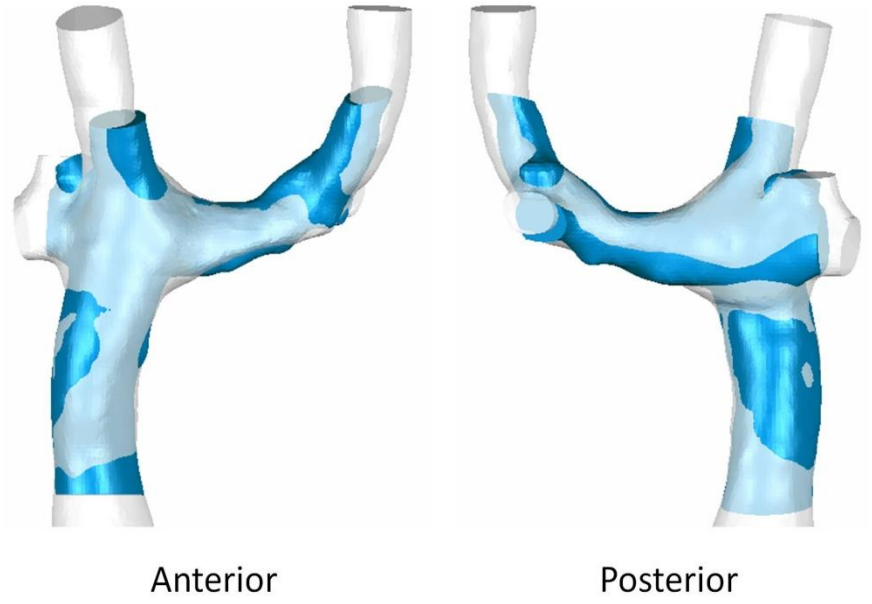


**Figure 9.19** ***Comparison of TCPC surface reconstructions for CHOP022A (blue) and CHOP022B (clear).***

Figure 9.19 and Figure 9.20 show the reconstruction and vessel sizes for CHOP022A and CHOP022B, which was a case with bilateral SVC connections. After correcting for BSA change, most dimensions were seen to decrease with time, particularly the minimum LPA dimension. The visual differences in the length of the bilateral SVCs are the result of segmentation differences and not an actual meaningful change, but such differences are expected to have minimal affect on power loss differences (only the additional pressure drop associated with moving blood through that additional length). In conjunction with across the board increases in local flow rates (Table 9.14), these changes resulted in substantial increases in local velocity magnitudes, as seen in the

CFD results in Figure 9.21. All energetic measures (Table 9.15) also increased substantially- maximum pressure loss nearly tripled, while TCPC-EDI increased by 100%.

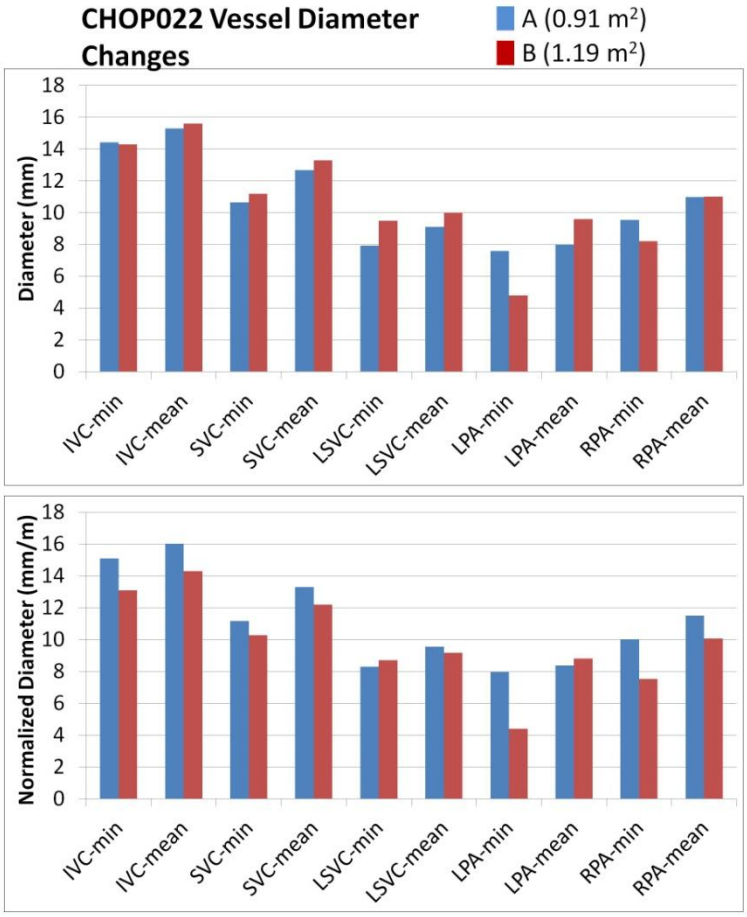


**Figure 9.20** ***Actual (top) and BSA-normalized (bottom) vessel minimum and mean diameters for CHOP022. The BSA values at each time point are provided in the color legend.***

**Table 9.14 Measured flow rates (in L/min) for CHOP022 scans A and B. PA percentages are shown in parentheses**

| | Ao | IVC | SVC | LSVC | LPA | RPA |
|---|---|---|---|---|---|---|
| **A** | 3.4 | 1.3 | 0.8 | 0.5 | 1.1 (49%) | 1.1 (51%) |
| **B** | 4.9 | 2.7 | 1.1 | 0.8 | 1.7 (43%) | 2.2 (57%) |

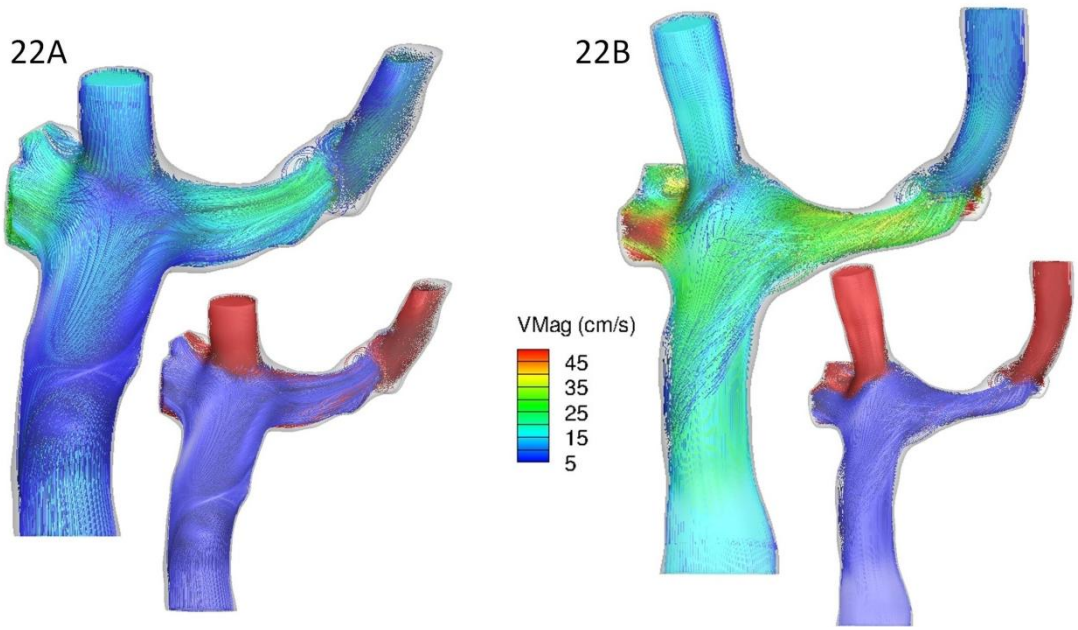


**Figure 9.21** ***Time averaged CFD velocity streamlines for CHOP022 A(left) and B(right). Inset images show streamlines color coded by vessel of origin (blue- IVC, red- both SVCs).***

**Table 9.15 Hemodynamic measures for CHOP022 from serial CFD simulations**

| | HFD (%LPA) | $\Delta P_{MAX}$ (mmHg) | Power Loss (mW) | Resistance (WU) | TCPC-EDI |
|---|---|---|---|---|---|
| **A** | 33 | 0.8 | 1.7 | 0.10 | 0.016 |
| **B** | 31 | 2.2 | 10.6 | 0.32 | 0.031 |

9.3.1.8 CHOP033

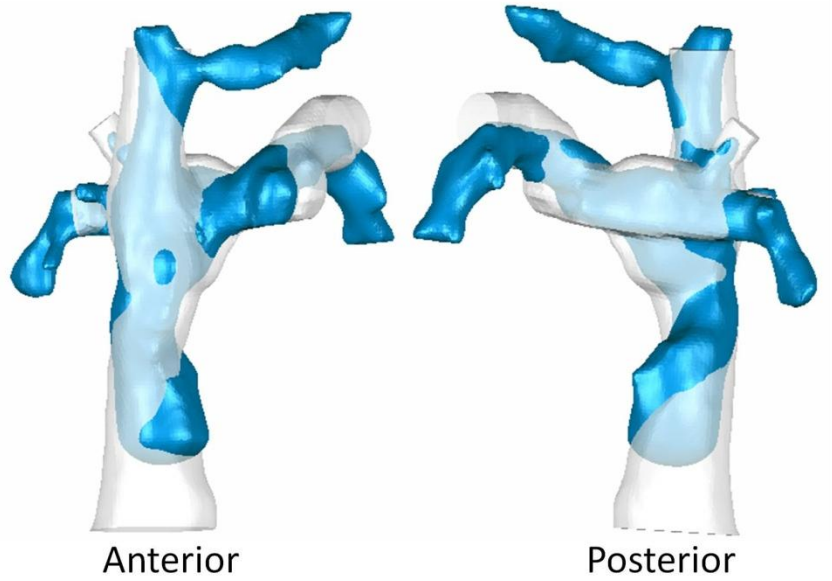


**Figure 9.22** ***Comparison of TCPC surface reconstructions for CHOP033A (blue) and CHOP033B (clear).***

For CHOP033 (Figure 9.22 and Figure 9.23), the change in caval dimensions kept pace with overall BSA change, while both PAs relatively decreased in size after normalizing. The flow rates (Table 9.16) increased, although local velocity magnitudes (Figure 9.24)

appear largely unchanged. Power losses increased by over 100% with respect to TCPC-EDI (Table 9.17), likely owing to decreases in PA diameter. The relative SVC-IVC dynamic interactions and HFD results remained largely unchanged.

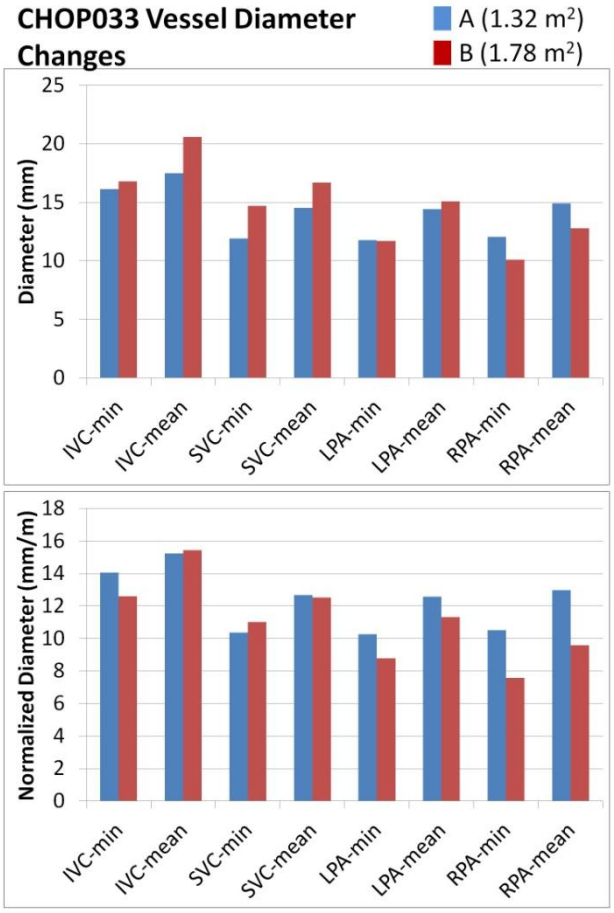


**Figure 9.23** ***Actual (top) and BSA-normalized (bottom) vessel minimum and mean diameters for CHOP033. The BSA values at each time point are provided in the color legend.***

**Table 9.16 Measured flow rates (in L/min) for CHOP033 scans A and B. PA percentages are shown in parentheses**

| | Ao | IVC | SVC | LPA | RPA |
|---|---|---|---|---|---|
| **A** | 3.4 | 2.3 | 1.5 | 1.7 (52%) | 1.6 (48%) |
| **B** | 5.5 | 2.9 | 1.2 | 2.1 (52%) | 2.0 (48%) |

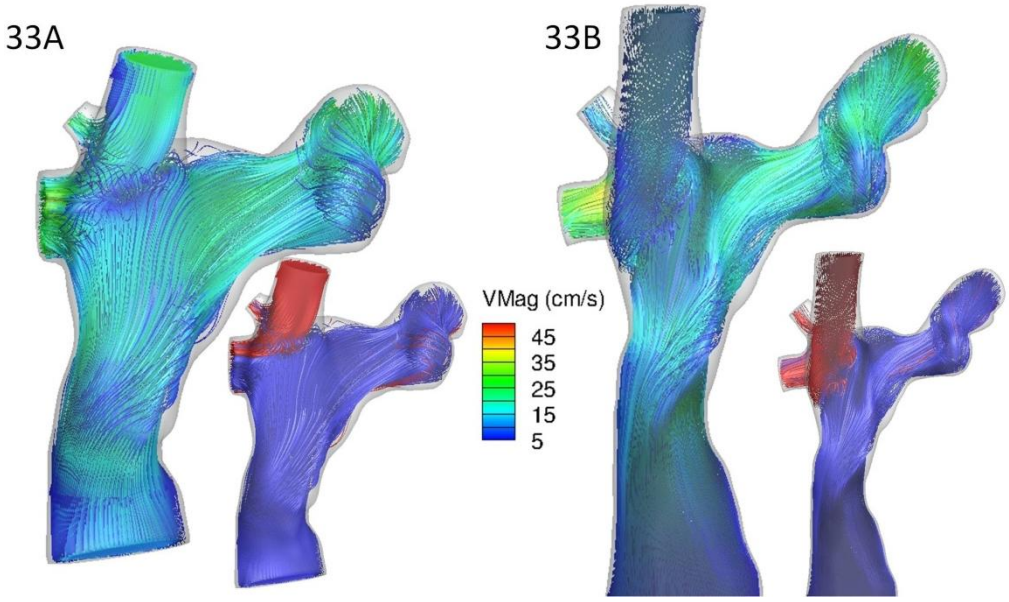


**Figure 9.24** ***Time averaged CFD velocity streamlines for CHOP033 A(left) and B(right). Inset images show streamlines color coded by vessel of origin (blue- IVC, red- SVC).***

**Table 9.17 Hemodynamic measures for CHOP033 from serial CFD simulations**

| | HFD (%LPA) | $\Delta P_{MAX}$ (mmHg) | Power Loss (mW) | Resistance (WU) | TCPC-EDI |
|---|---|---|---|---|---|
| **A** | 63 | 0.5 | 2.5 | 0.10 | 0.016 |
| **B** | 65 | 0.9 | 5.1 | 0.20 | 0.038 |

#### 9.3.1.9 CHOP036

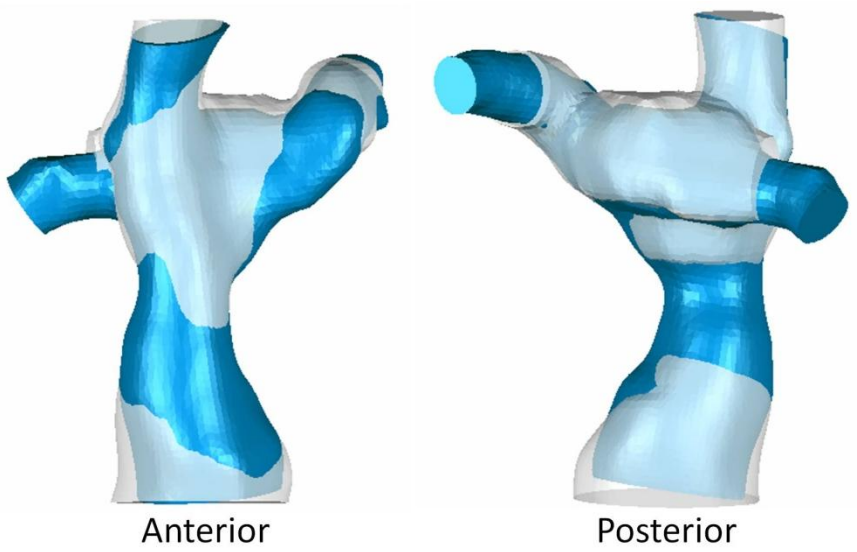


**Figure 9.25** ***Comparison of TCPC surface reconstructions for CHOP036A (blue) and CHOP036B (clear).***

Vessel sizes for CHOP036A and CHOP036B were largely unchanged, particularly after BSA-normalization (Figure 9.25 and Figure 9.26), with the exception of a decrease in the lateral tunnel dimension. Interestingly, the vessel flow rates (Table 9.18), particularly the IVC, decreased between scans; thus, even with minimal size changes, the local velocity magnitudes from CFD (Figure 9.27) generally decreased. Furthermore, the large drop in IVC flow led to a large shift in HFD measures (Table 9.19) with the increased SVC fraction taking a larger proportion of the RPA flow with very little change in the qualitative flow dynamics. Finally, despite a decrease in the raw power loss and pressure drop, TCPC-EDI increased owing to increased BSA and decreased systemic venous flow totals.

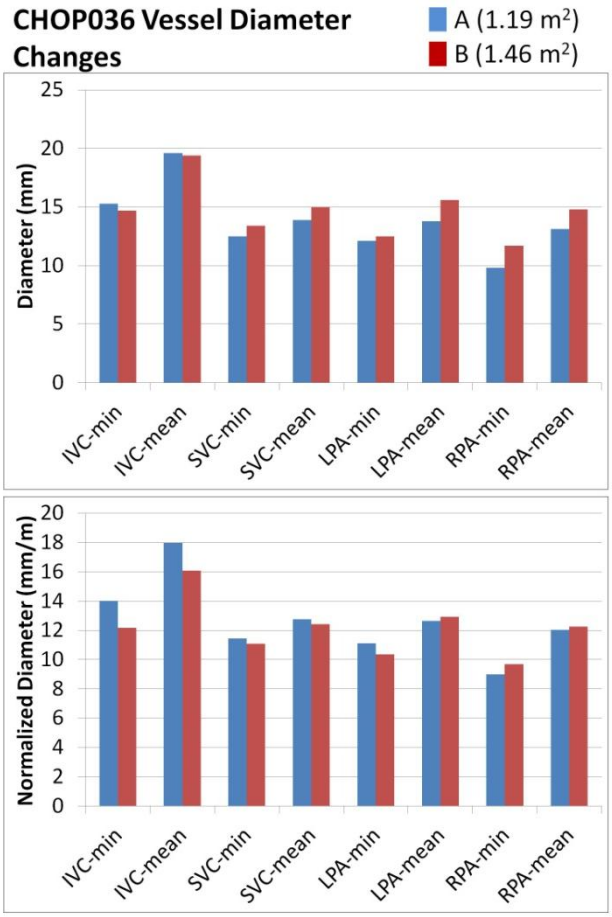


**Figure 9.26** ***Actual (top) and BSA-normalized (bottom) vessel minimum and mean diameters for CHOP036. The BSA values at each time point are provided in the color legend***

**Table 9.18 Measured flow rates (in L/min) for CHOP036 scans A and B. PA percentages are shown in parentheses**

| | Ao | IVC | SVC | LPA | RPA |
|---|---|---|---|---|---|
| **A** | 5.6 | 3.3 | 1.9 | 2.3 (55%) | 1.8 (45%) |
| **B** | 4.0 | 2.4 | 2.0 | 2.1 (62%) | 1.3 (38%) |

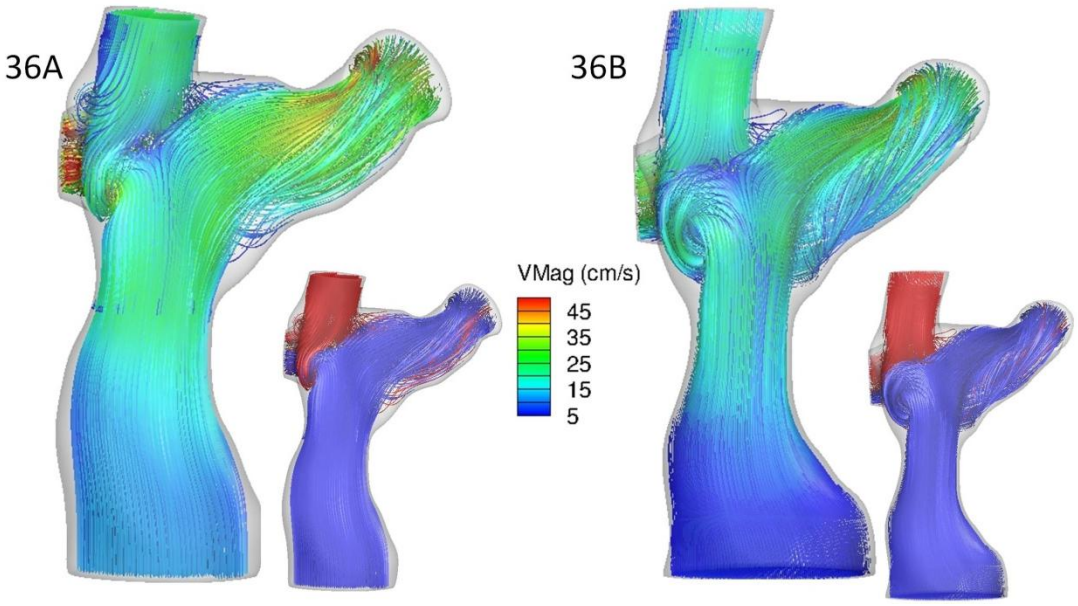


**Figure 9.27** ***Time averaged CFD velocity streamlines for CHOP036 A(left) and B(right). Inset images show streamlines color coded by vessel of origin (blue- IVC, red- SVC).***

**Table 9.19 Hemodynamic measures for CHOP036 from serial CFD simulations**

| | **HFD** (%LPA) | **$\Delta P_{MAX}$** (mmHg) | **Power Loss** (mW) | **Resistance** (WU) | **TCPC-EDI** |
|---|---|---|---|---|---|
| **A** | 71 | 1.2 | 7.6 | 0.15 | 0.016 |
| **B** | 90 | 0.8 | 4.5 | 0.15 | 0.023 |

9.3.1.10 CHOP052

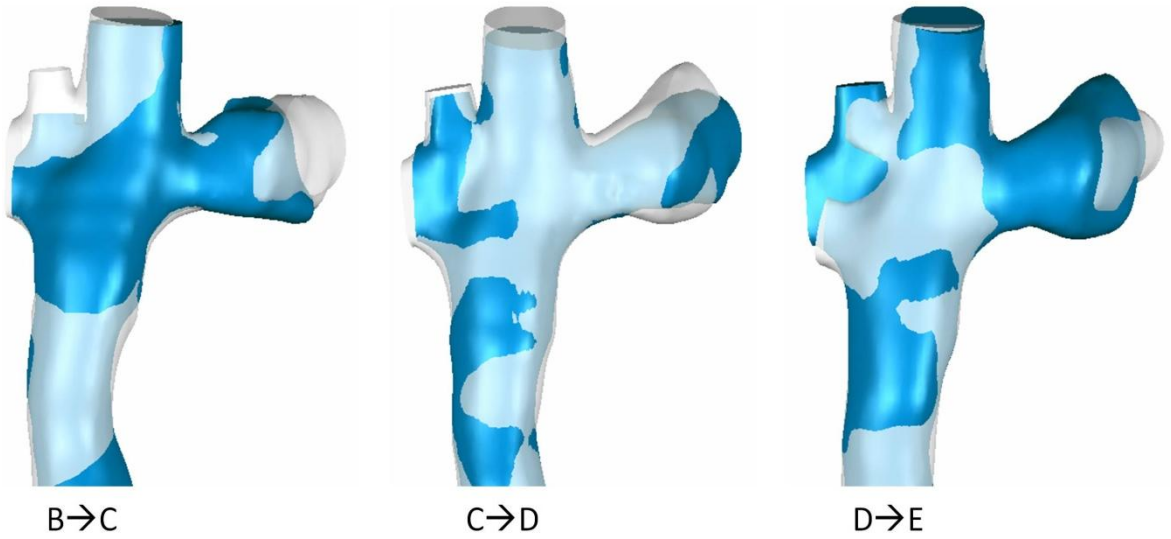


**Figure 9.28** ***Comparison of TCPC surface reconstructions for CHOP052B (blue, left) vs. CHOP052C(clear, left) and CHOP052C (blue, middle) vs. CHOP052D (clear, middle) and CHOP052D (blue, right) vs. CHOP052E (clear, right).***

CHOP052 is a very rare case in which four serial scans were available for analysis. The surface comparisons are shown in Figure 9.28 while the quantitative comparisons are shown in Figure 9.29. Unfortunately, small inconsistencies throughout the numerous scans limit some of the power of these rare data, but the picture is generally consistent with the other patients presented in this chapter. Geometrically, the inconsistencies are apparent in the PA reconstructions- IVC (extracardiac) and SVC dimensions were fairly consistent, and progressively decreased in size compared to BSA increases. By comparison, PA sizes fluctuated considerably between scans (particularly LPA min from scan D), and it is likely that limitations in through plane resolution impacted these results. Measured flow conditions (Table 9.20) were not much better: IVC and SVC magnitudes

were not properly encoded for scan C, while no aortic measure was available for scan E. Total pulmonary flow, which provided the most consistent measure, increased from 2.9 L/min to 3.9 L/min over time.

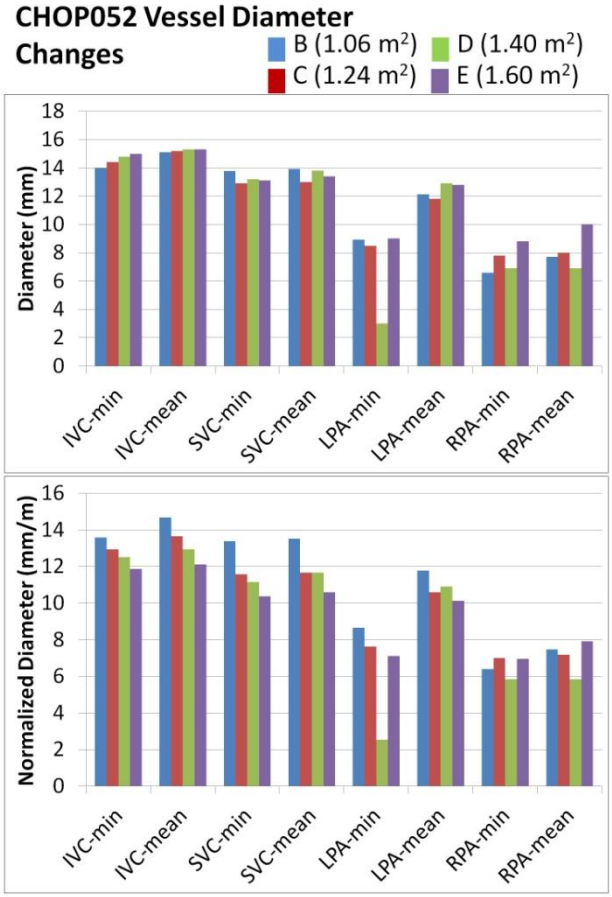


**Figure 9.29** ***Actual (top) and BSA-normalized (bottom) vessel minimum and mean diameters for CHOP052. The BSA values at each time point are provided in the color legend.***

**Table 9.20 Measured flow rates (in L/min) for CHOP052 scans B-E. PA percentages are shown in parentheses**

| | Ao | IVC | SVC | LPA | RPA |
|---|---|---|---|---|---|
| **B** | 5.8 | 2.1 | 1.2 | 1.4 (49%) | 1.5 (51%) |
| **C** | 6.5 | - | - | 1.5 (43%) | 2.0 (57%) |
| **D** | 5.9 | 1.9 | 1.5 | 1.7 (50%) | 1.7 (50%) |
| **E** | - | 2.4 | 1.6 | 2.0 (52%) | 1.9 (48%) |

The anatomic nuances are perhaps more apparent with respect to the CFD results (Figure 9.30) where, even though the presence of a right caval offset created a fairly consistent flow profile in each case, differences in the size and shape of proximal LPA have an appreciable impact, and the takeoff of the upper right lobe is seen to vary slightly based on limited contrast in the ‘E’ scan. Local velocity magnitudes stayed fairly consistent with the possible exception of acceleration through the sub-aortic PA in scan E. Quantitatively, (Table 9.21) TCPC-EDI increased marginally from scans B-D with a large jump to E, likely because of the higher flow rates.

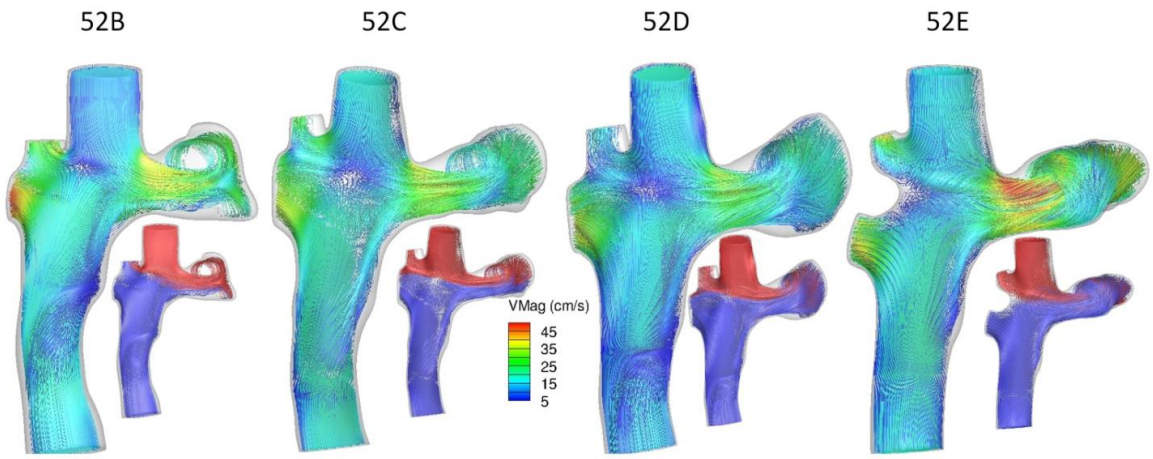


**Figure 9.30** ***Time averaged CFD velocity streamlines for CHOP052 B(far left), C(middle left), D(middle right) and E(far right). Inset images show streamlines color coded by vessel of origin (blue- IVC, red- SVC).***

**Table 9.21 Hemodynamic measures for CHOP052 from four serial CFD simulations**

| | **HFD** (%LPA) | **$\Delta P_{MAX}$** (mmHg) | **Power Loss** (mW) | **Resistance** (WU) | **TCPC-EDI** |
|---|---|---|---|---|---|
| **B** | 21 | 0.9 | 3.5 | 0.16 | 0.022 |
| **C** | 26 | 0.7 | 3.1 | 0.15 | 0.025 |
| **D** | 30 | 0.5 | 2.7 | 0.15 | 0.027 |
| **E** | 32 | 1.1 | 5.4 | 0.25 | 0.045 |

9.3.1.11 CHOP065

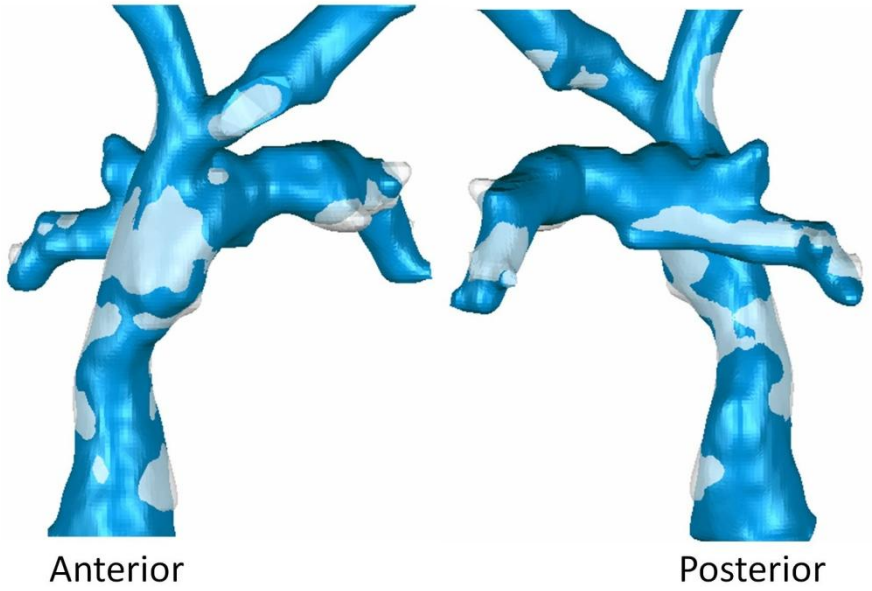


**Figure 9.31** ***Comparison of TCPC surface reconstructions for CHOP065A (blue) and CHOP065B (clear).***

Figure 9.31 and Figure 9.32 provide the serial geometric comparisons for CHOP065A and CHOP065B. Visually, very little growth was apparent from the surface reconstructions (i.e., Figure 9.31 shows mostly the blue elements from the A scan), despite the large increase (35%) in BSA between scans. That observation is generally borne out in the quantitative results and thus, after normalization, all diameter values were lower in the latter time point. For CMR-measured flows, (Table 9.22) despite constant cardiac output, the systemic and pulmonary flow magnitudes increased, including a shift toward much higher LPA flow in the latter time point, suggesting a decrease in the collateral flows between scans. The resulting CFD velocity fields (Figure

9.33) were therefore only visually different in the LPA magnitudes, and power losses increased considerably (Table 9.23).

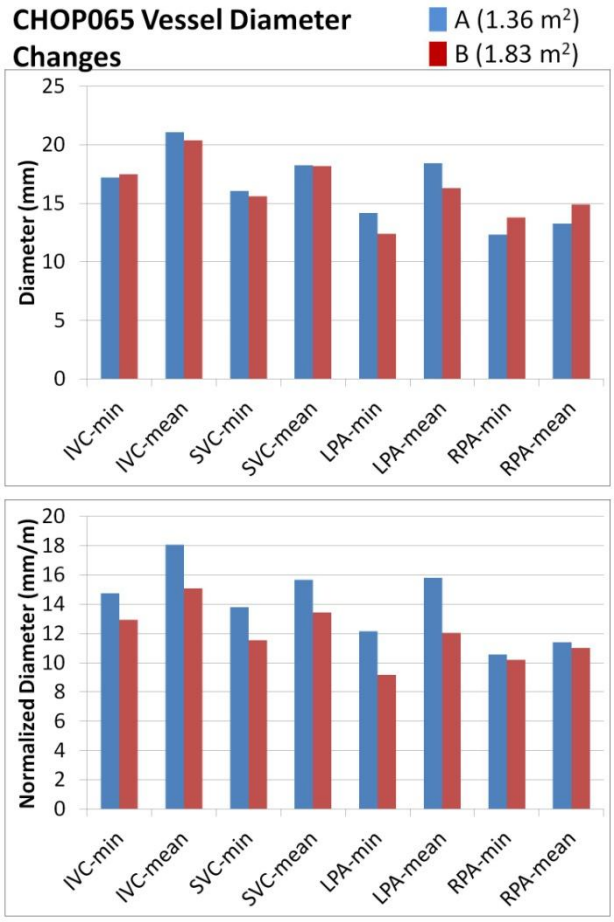


**Figure 9.32** ***Actual (top) and BSA-normalized (bottom) vessel minimum and mean diameters for CHOP065. The BSA values at each time point are provided in the color legend.***

**Table 9.22 Measured flow rates (in L/min) for CHOP065 scans A and B. PA percentages are shown in parentheses**

| | Ao | IVC | SVC | LPA | RPA |
|---|---|---|---|---|---|
| **A** | 3.3 | 1.9 | 0.5 | 0.8 (35%) | 1.5 (65%) |
| **B** | 3.3 | 2.2 | 1.1 | 1.8 (55%) | 1.5 (45%) |

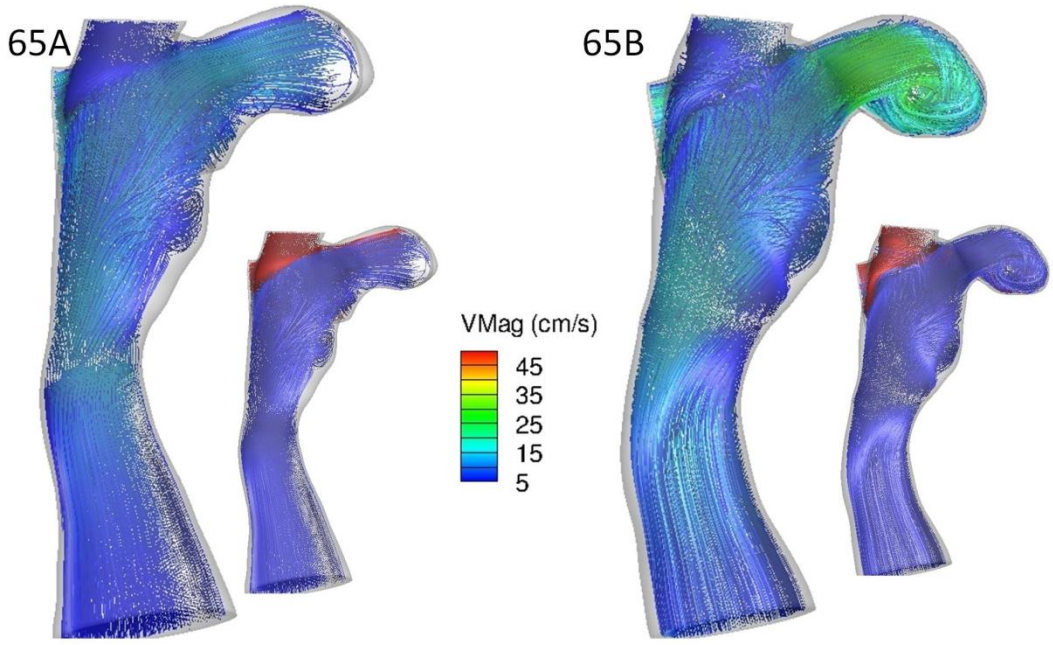


**Figure 9.33** ***Time averaged CFD velocity streamlines for CHOP065 A(left) and B(right). Inset images show streamlines color coded by vessel of origin (blue- IVC, red- SVC).***

**Table 9.23 Hemodynamic measures for CHOP065 from serial CFD simulations**

| | HFD (%LPA) | $\Delta P_{MAX}$ (mmHg) | Power Loss (mW) | Resistance (WU) | TCPC-EDI |
|---|---|---|---|---|---|
| **A** | 39 | 0.1 | 0.5 | 0.05 | 0.013 |
| **B** | 58 | 0.5 | 1.8 | 0.14 | 0.035 |

9.3.1.12 CHOP080

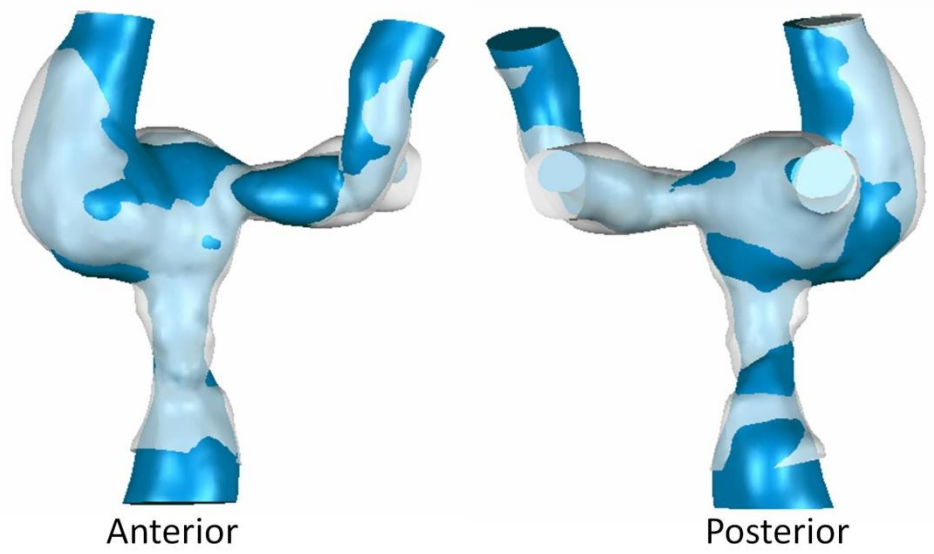


**Figure 9.34** ***Comparison of TCPC surface reconstructions for CHOP080A (blue) and CHOP080B (clear).***

This patient, CHOP080, was covered with the 'least efficient' cases in Chapter 5, thus providing some additional motivation for characterizing serial change. Regarding vessel sizes (Figure 9.34 and Figure 9.35), both PAs increased diameter substantially, as did the right SVC and right-sided hemi-Fontan connection. The Fontan connection, which was a major source of inefficiency at the first time point, visually appears to increase in size; however, as seen in the CFD results (Figure 9.36) there is still an obvious narrowing at the base of the connection that created significant acceleration through the pathway. Of course, the flow rates (Table 9.24) also increased between scan substantially, so the higher IVC velocities are also largely affected by that change.

Despite the higher flows and velocities, TCPC-EDI (Table 9.25) was basically unchanged (marginally lower) because of the offsetting effects of larger PA diameters.

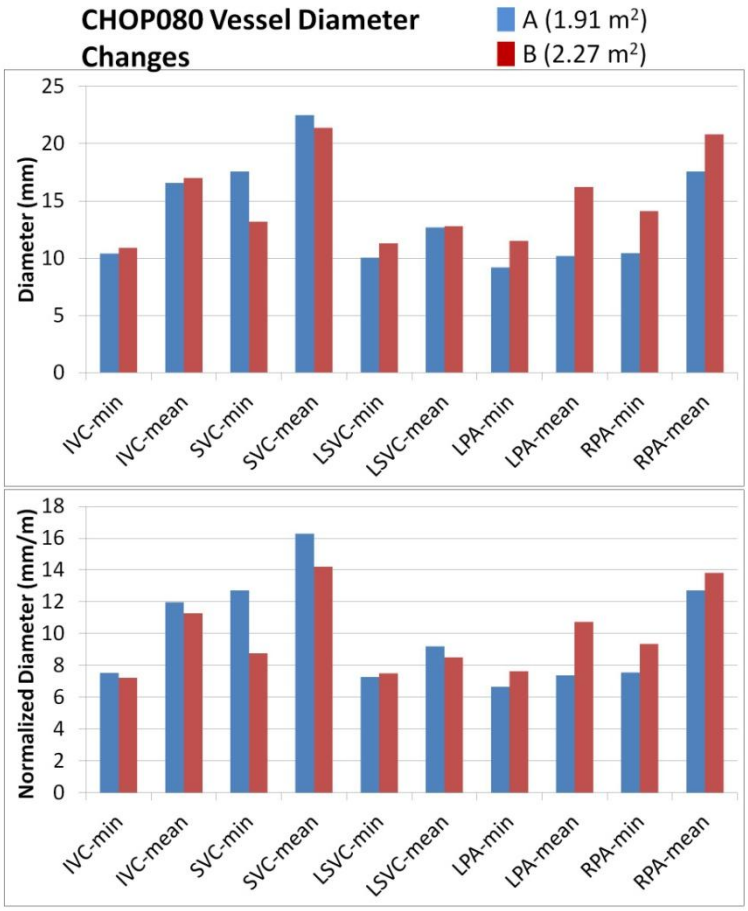


**Figure 9.35** ***Actual (top) and BSA-normalized (bottom) vessel minimum and mean diameters for CHOP080. The BSA values at each time point are provided in the color legend.***

**Table 9.24 Measured flow rates (in L/min) for CHOP080 scans A and B. PA percentages are shown in parentheses**

| | Ao | IVC | SVC | LSVC | LPA | RPA |
|---|---|---|---|---|---|---|
| **A** | 5.6 | 2.6 | 1.3 | 0.5 | 2.1 (53%) | 1.9 (47%) |
| **B** | 7.9 | 4.2 | 1.1 | 0.8 | 4.1 (49%) | 4.3 (51%) |

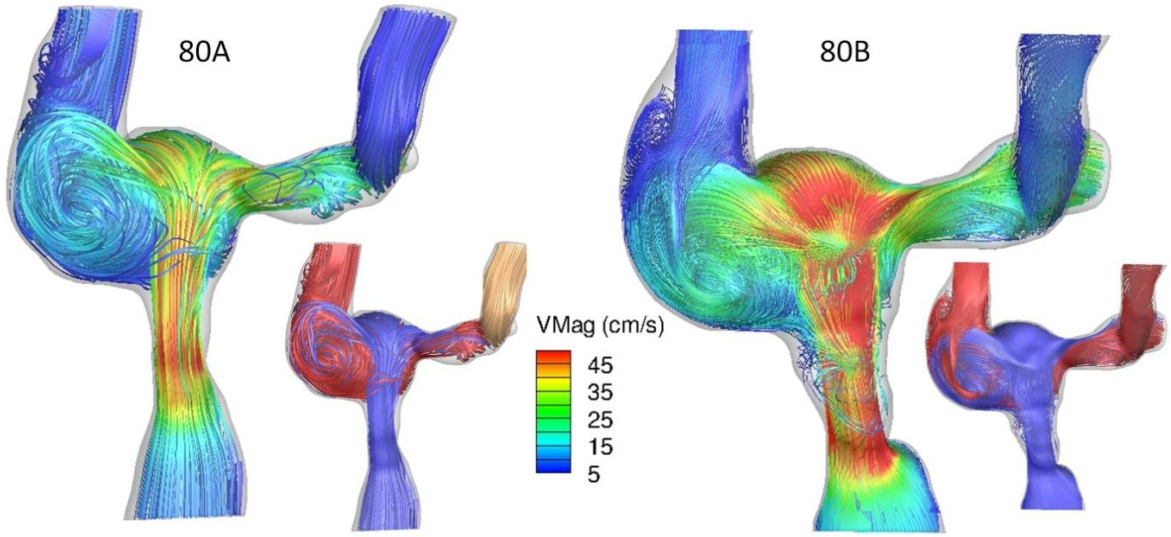


**Figure 9.36** ***Time averaged CFD velocity streamlines for CHOP080 A(left) and B(right). Inset images show streamlines color coded by vessel of origin (blue- IVC, red- SVC).***

**Table 9.25 Hemodynamic measures for CHOP080 from serial CFD simulations**

| | HFD (%LPA) | $\Delta P_{MAX}$ (mmHg) | Power Loss (mW) | Resistance (WU) | TCPC-EDI |
|---|---|---|---|---|---|
| **A** | 29 | 2.4 | 11.8 | 0.54 | 0.110 |
| **B** | 29 | 2.7 | 22.9 | 0.63 | 0.106 |

9.3.1.13 CHOP082

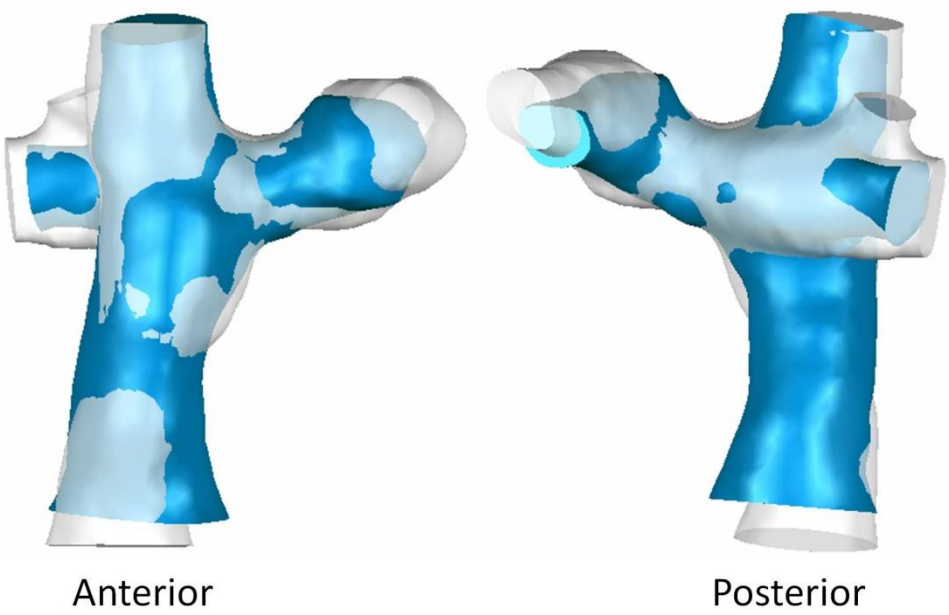


**Figure 9.37** ***Comparison of TCPC surface reconstructions for CHOP082A (blue) and CHOP082B (clear). The RUPA was not included in the A reconstruction.***

For this patient, CHOP082, the combination of minimal changes in vessel sizes (overall decreases on a normalized basis; Figure 9.37 and Figure 9.38), and significant increases in local flow rates (Table 9.26) yielded appreciable changes in TCPC velocities (Figure 9.39) and roughly 3-fold increases in pressure drop, resistance, and TCPC-EDI (Table 9.27); raw power loss increased by over 650%.

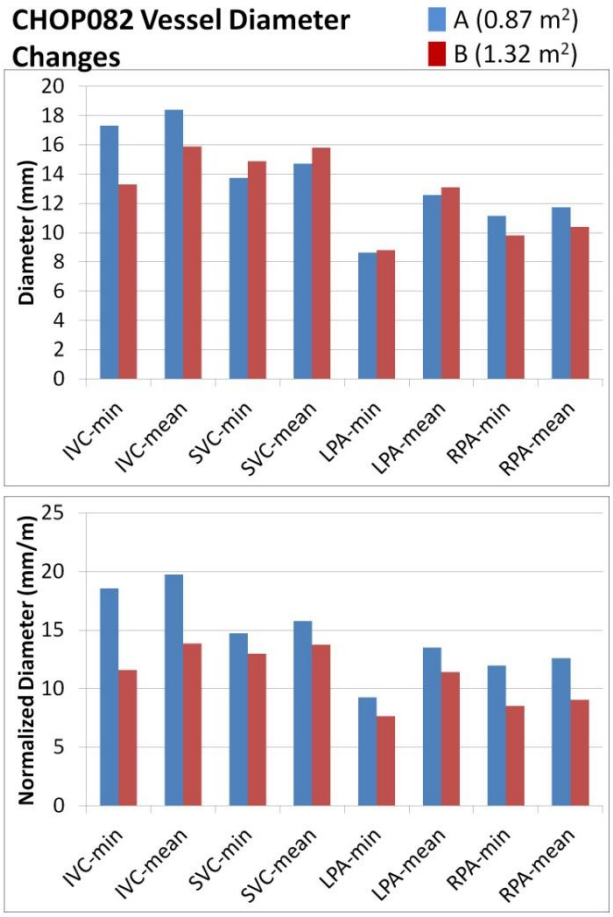


**Figure 9.38** ***Actual (top) and BSA-normalized (bottom) vessel minimum and mean diameters for CHOP082. The BSA values at each time point are provided in the color legend.***

**Table 9.26 Measured flow rates (in L/min) for CHOP082 scans A and B. PA percentages are shown in parentheses**

| | Ao | IVC | SVC | LPA | RPA |
|---|---|---|---|---|---|
| **A** | 2.7 | 1.6 | 1.0 | 0.8 (40%) | 1.2 (60%) |
| **B** | 5.0 | 3.2 | 1.6 | 1.6 (33%) | 2.3 (67%) |

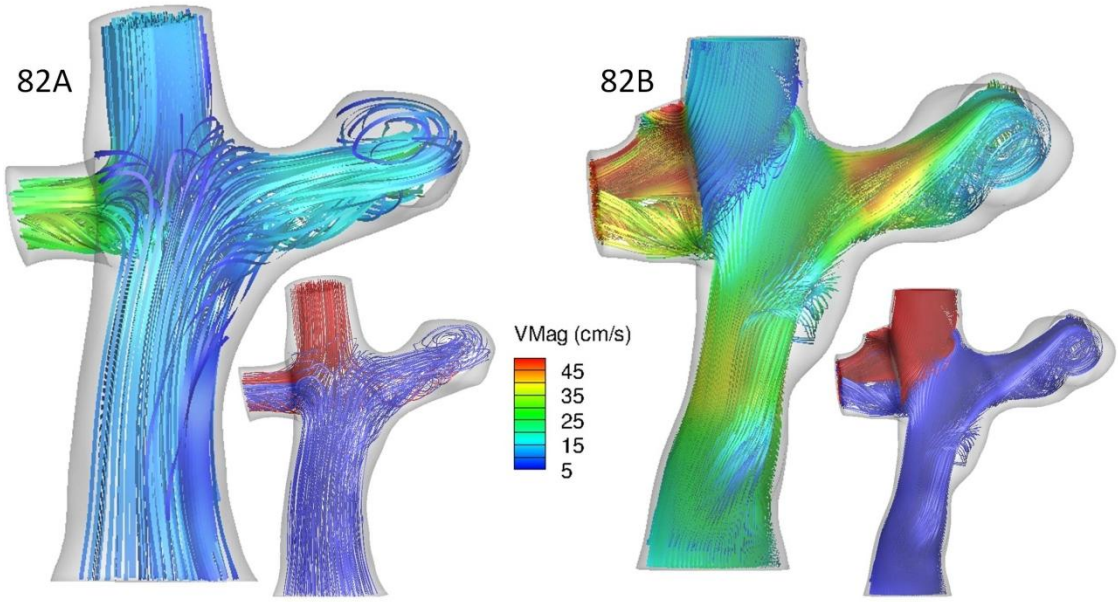


**Figure 9.39** ***Time averaged CFD velocity streamlines for CHOP082 A(left) and B(right). Inset images show streamlines color coded by vessel of origin (blue- IVC, red- SVC).***

**Table 9.27 Hemodynamic measures for CHOP082 from serial CFD simulations**

| | **HFD** (%LPA) | **$\Delta P_{MAX}$** (mmHg) | **Power Loss** (mW) | **Resistance** (WU) | **TCPC-EDI** |
|---|---|---|---|---|---|
| **A** | 57 | 0.4 | 1.4 | 0.08 | 0.012 |
| **B** | 51 | 1.3 | 10.6 | 0.27 | 0.033 |

9.3.1.14 CHOP088

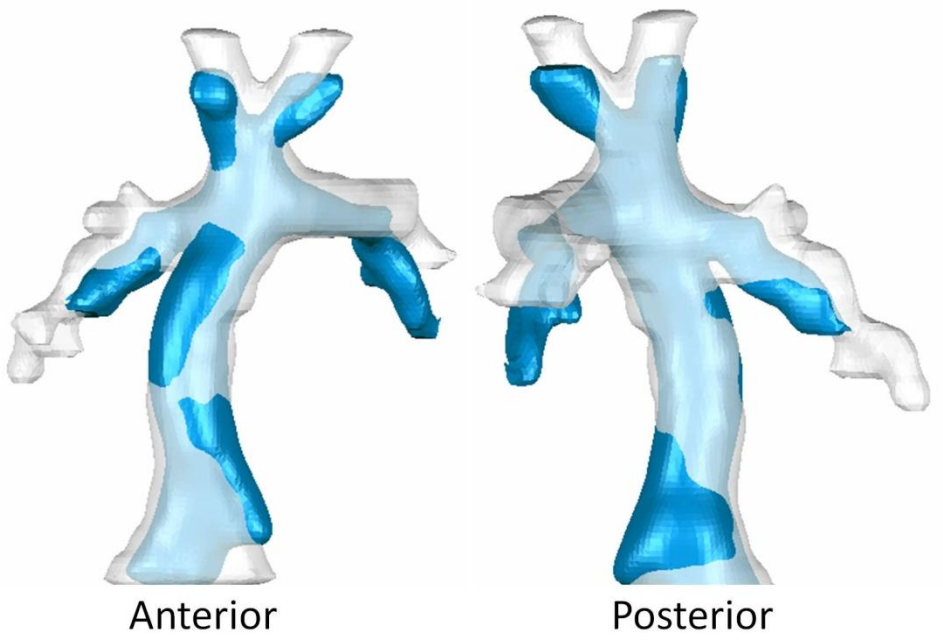


**Figure 9.40** ***Comparison of TCPC surface reconstructions for CHOP088A (blue) and CHOP088B (clear).***

Here, all diameter measures increased between scans (Figure 9.40 and Figure 9.41), but on a normalized basis, only the RPA increased. Despite the general increase in total volume flow rate through the connection (Table 9.28), that change (thanks in part to the fact that the RPA percentage increased substantially) was enough to mediate a decrease in normalized power losses (Table 9.29) as peak PA velocities (Figure 9.42) were actually decreased in the later data set.

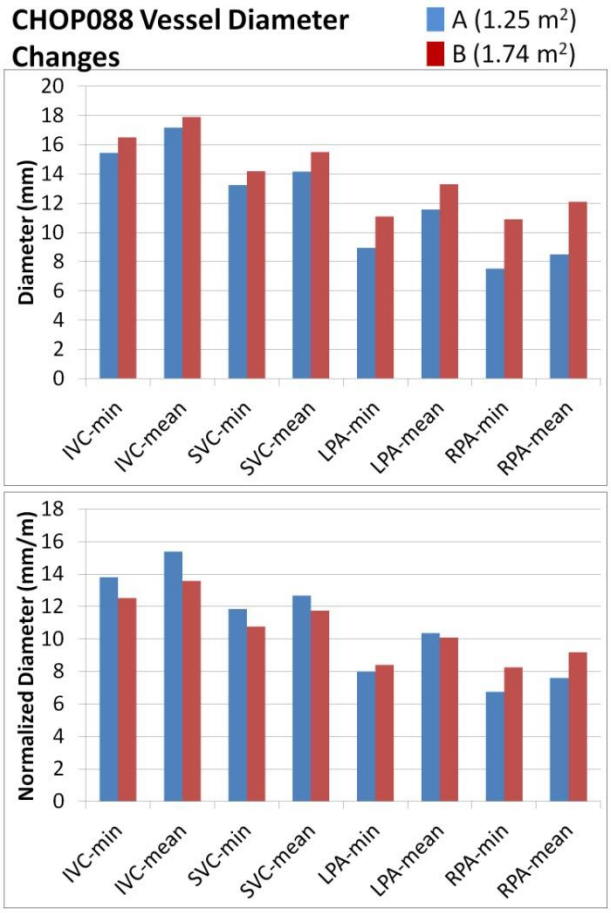


**Figure 9.41** ***Actual (top) and BSA-normalized (bottom) vessel minimum and mean diameters for CHOP088. The BSA values at each time point are provided in the color legend.***

**Table 9.28 Measured flow rates (in L/min) for CHOP088 scans A and B. PA percentages are shown in parentheses**

| | Ao | IVC | SVC | LPA | RPA |
|---|---|---|---|---|---|
| **A** | 3.4 | 1.8 | 0.9 | 1.6 (52%) | 1.5 (48%) |
| **B** | 6.1 | 3.6 | 1.3 | 3.0 (61%) | 1.9 (39%) |

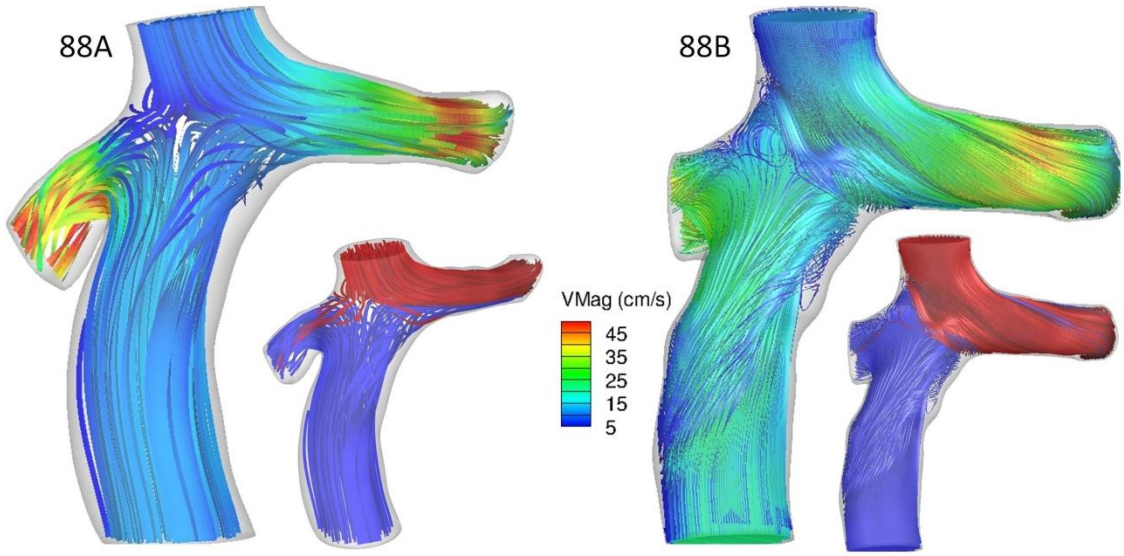


**Figure 9.42** ***Time averaged CFD velocity streamlines for CHOP088 A(left) and B(right). Inset images show streamlines color coded by vessel of origin (blue- IVC, red- SVC).***

**Table 9.29 Hemodynamic measures for CHOP088 from serial CFD simulations**

| | **HFD** (%LPA) | **$\Delta P_{MAX}$** (mmHg) | **Power Loss** (mW) | **Resistance** (WU) | **TCPC-EDI** |
|---|---|---|---|---|---|
| **A** | 27 | 1.2 | 4.2 | 0.33 | 0.068 |
| **B** | 50 | 1.0 | 5.6 | 0.18 | 0.029 |

9.3.1.15 CHOP091

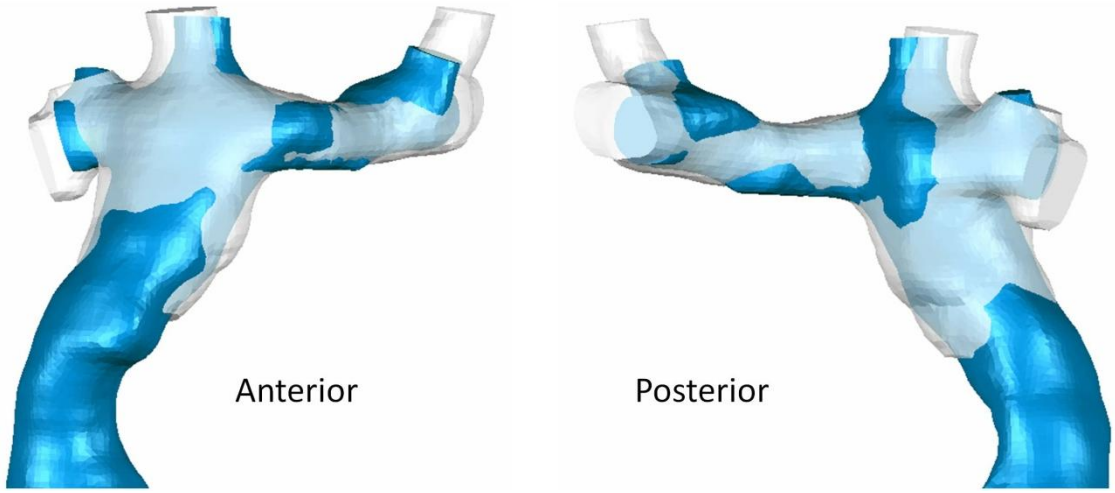


**Figure 9.43** ***Comparison of TCPC surface reconstructions for CHOP091A (blue) and CHOP091B (clear).***

For CHOP091, poor signal quality prevented a complete segmentation of the lateral tunnel pathway (Figure 9.43), but the serial reconstructions are otherwise quite similar with marginal increases in most normalized vessel dimensions (Figure 9.44). Flow rates (Table 9.30) were also generally consistent, but with a notable shift toward higher LPA flows. As a result, the qualitative CFD results (Figure 9.45) were very similar, and power losses decreased slightly (Table 9.31).

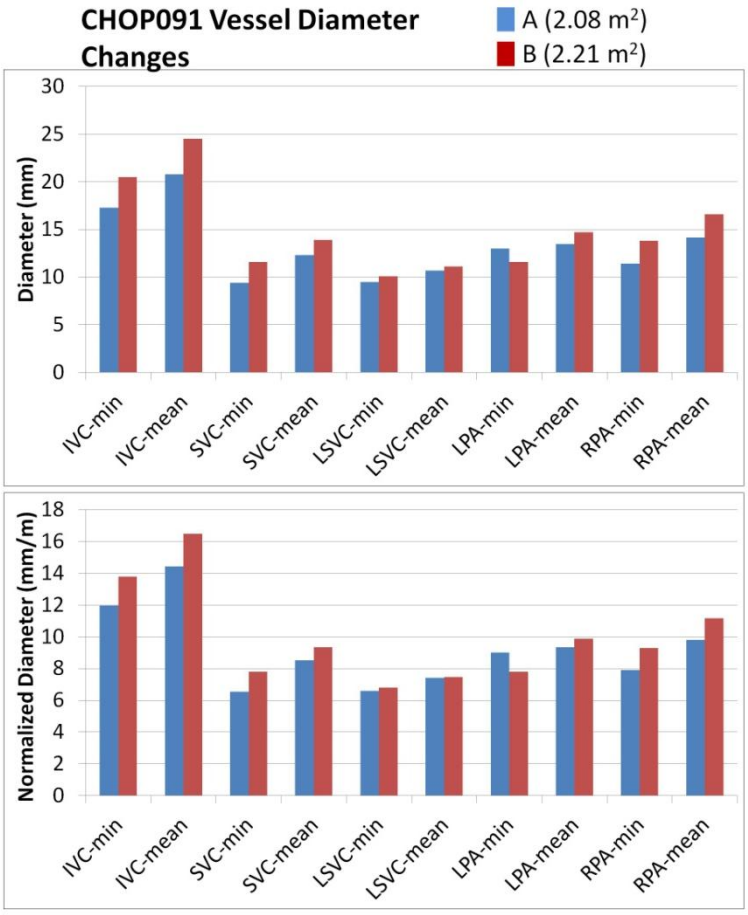


**Figure 9.44** ***Actual (top) and BSA-normalized (bottom) vessel minimum and mean diameters for CHOP091. The BSA values at each time point are provided in the color legend.***

**Table 9.30 Measured flow rates (in L/min) for CHOP091 scans A and B. PA percentages are shown in parentheses**

| | Ao | IVC | SVC | LSVC | LPA | RPA |
|---|---|---|---|---|---|---|
| **A** | 5.0 | 3.5 | 1.0 | 0.7 | 2.2 (46%) | 2.6 (54%) |
| **B** | 6.1 | 3.7 | 0.9 | 0.7 | 3.0 (55%) | 2.5 (45%) |

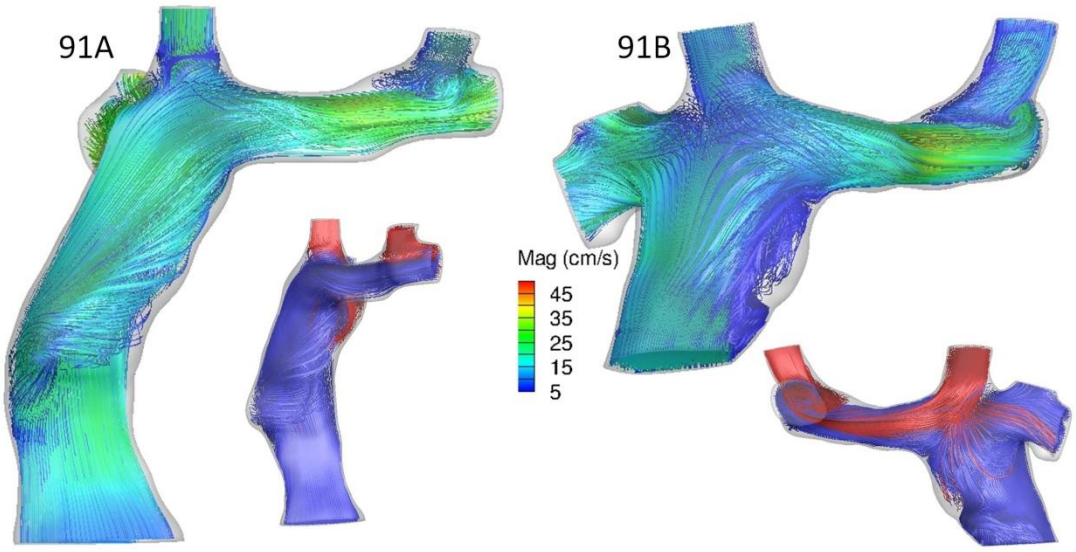


**Figure 9.45** ***Time averaged CFD velocity streamlines for CHOP091 A(left) and B(right). Inset images show streamlines color coded by vessel of origin (blue- IVC, red- SVC).***

**Table 9.31 Hemodynamic measures for CHOP091 from serial CFD simulations**

| | HFD (%LPA) | $\Delta P_{MAX}$ (mmHg) | Power Loss (mW) | Resistance (WU) | TCPC-EDI |
|---|---|---|---|---|---|
| **A** | 33 | 0.4 | 5.3 | 0.18 | 0.031 |
| **B** | 36 | 0.7 | 3.4 | 0.12 | 0.023 |

### 9.3.2 Summary and Analysis

Systemic Flow Rates (Table 9.32)

Both the IVC and SVC flows increased significantly ($p<0.05$) over time (using pair-wise comparisons). However, after normalizing by BSA, there were no significant differences in IVC, SVC, nor total $Q_s$ flow rates.

**Table 9.32 Summary (mean ± standard deviation) of serial systemic flow rate changes**

| | First scan | Last scan | p-value |
|---|---|---|---|
| $\mathbf{Q_{IVC}}$ (L/min) | 2.5 ± 0.9 | 3.0 ± 0.8 | <0.05* |
| $\mathbf{Q_{SVC}}$ (L/min) | 1.2 ± 0.4 | 1.4 ± 0.4 | <0.05* |
| **Norm.** $\mathbf{Q_{IVC}}$ (L/min/m$^2$) | 1.8 ± 0.4 | 1.8 ± 0.4 | 0.65 |
| **Norm.** $\mathbf{Q_{SVC}}$ (L/min/m$^2$) | 1.0 ± 0.4 | 0.9 ± 0.3 | 0.28 |
| $\mathbf{Q_S}$ (L/min/m$^2$) | 2.8 ± 0.7 | 2.6 ± 0.6 | 0.39 |

Vessel Sizes

As a first point, it is noted that the choice of $BSA^{0.5}$ as a normalization scheme for vessel dimensions was not entirely obvious. The ascending aortic diameter, for example, provides a logical alternative reference for Fontan vessel sizes in that it accounts for similar changes in alternate vascular structures. Sluysmans and Colan demonstrated that $BSA^{0.5}$ was linearly related to vascular and valvular diameters in normal children between 4 months and 20 years of age[173]. How that relationship translates to single ventricle anatomy or to patients over 20 (at which point the development of

cardiovascular structures could be expected to be completed while BSA could fluctuate with weight) is unknown. To verify that these choices of normalization would not provide independent information, Figure 9.46 shows that $BSA^{0.5}$ and ascending aortic diameter (in mm; assessed using the segmented phase contrast CMR cross-sectional slice, when available) were linearly correlated in these patients. Hence, we can conclude that the use of $BSA^{0.5}$ to normalize the vascular dimensions is appropriate.

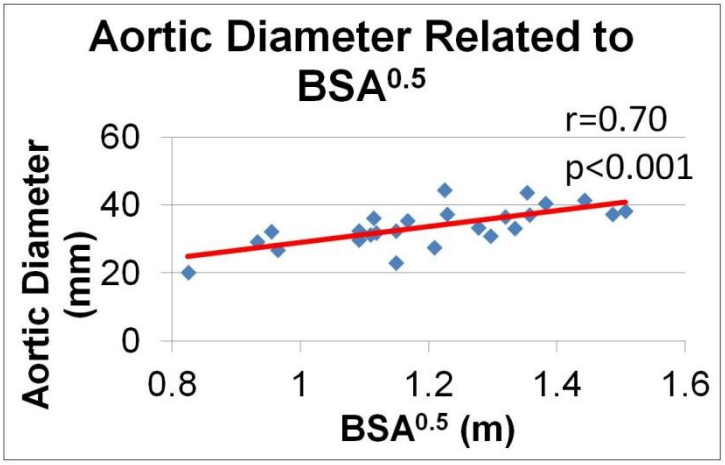


**Figure 9.46 Linear relationship between ascending aortic diameter and square root of BSA. See Table 12.20 in Appendix E**

Table 9.33 summarizes the BSA and normalized vessel diameter changes between serial scans. For the cases with more than two scans, the first and last were used in this comparison to capture the largest change. A paired two-sample t-test was used for statistical comparisons.

**Table 9.33 Summary (mean ± standard deviation) of serial BSA and vessel diameter changes**

| | First scan | Last scan | p-value |
|---|---|---|---|
| **BSA** ($m^2$) | 1.38 ± 0.42 | 1.7 ± 0.33 | <0.001 |
| **$D_{min}$ IVC** (mm/m) | 13.9 ± 2.9 | 12.8 ± 2.7 | 0.059 |
| **$D_{mean}$ IVC** (mm/m) | 16.6 ± 2.7 | 15.6 ± 3.3 | 0.08 |
| **$D_{min}$ SVC** (mm/m) | 11.3 ± 2.3 | 10.8 ± 1.5 | 0.18 |
| **$D_{mean}$ SVC** (mm/m) | 12.9 ± 2.2 | 12.5 ± 1.4 | 0.34 |
| **$D_{min}$ LPA** (mm/m) | 8.0 ± 2.5 | 7.1 ± 2.0 | 0.018 |
| **$D_{mean}$ LPA** (mm/m) | 10.7 ± 2.5 | 10.3 ± 1.7 | 0.42 |
| **$D_{min}$ RPA** (mm/m) | 9.6 ± 1.9 | 9.3 ± 1.6 | 0.48 |
| **$D_{mean}$ RPA** (mm/m) | 11.4 ± 2.0 | 11.2 ± 1.8 | 0.66 |

**See**

Table 12.21 in Appendix E

Two significant changes were observed in the serial comparisons (as highlighted in gray in the table): BSA increased and the normalized minimum LPA diameter decreased. There was also a strong trend ($p<0.1$) toward decreasing (normalized) diameters (both mean and minimum) for the Fontan pathway, reflecting the fact that all (for extra-cardiac) or part (for lateral tunnel) of that pathway is synthetic material. The remaining vessels grew at pace with the $BSA^{0.5}$.

Hepatic Flow Distribution

Results demonstrated there were significant changes in serial HFD values: the absolute differences between time points were greater than zero (9.8 ± 8.1; p<0.001). However, there was no directional bias to this change (i.e., the HFD did not preferentially increase to one PA or the other) since a (signed) paired t-test found no mean difference (p=0.112). Instead, as might be anticipated from the correlation noted in §5.4.2, HFD changes were more responsive to changes in the total pulmonary flow distribution. Figure 9.47a shows this relationship. Thus, the total pulmonary flow displayed very similar trends: the absolute pulmonary distribution differences were greater than zero (6.5 ± 5.2; p<0.001), but there was again no directional bias (means were 44.1 vs. 45.1 for first and second scans, respectively; p=0.68 via paired t-test). The inclusion of more patients for this analysis would be beneficial given the relatively small effect sizes to better determine if there are any significant trends.

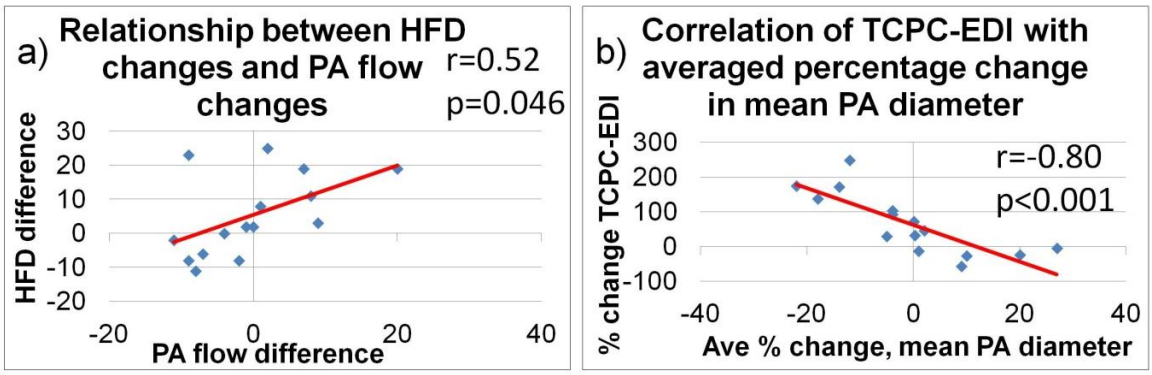


**Figure 9.47** ***Significant correlations between a) HFD differences and PA flow differences and b) % change in TCPC-EDI with average percent change of mean PA diameter. See*** **Table 12.22** ***and*** **Table 12.23** ***in Appendix E***

Power loss

In ten cases, TCPC-EDI increased between CMR scans (range: 29-249%); it decreased in the remaining five (range: 4-57%). Thus, a Wilcoxon paired ranks test found no significant difference in medians for TCPC-EDI between scans (estimated median change= 0.011; p=0.10). The primary determinant of this change was the geometric growth/change in each patient.

For these geometric growth changes, the magnitude of PA growth played a critical role. Figure 9.47b shows the very strong (r=-0.80, p<0.001) correlation between the averaged percentage change in PA mean diameters (i.e., average(% change $D_{mean}$ LPA, % change $D_{mean}$ RPA)) and the percentage change in TCPC-EDI. It is interesting to note that the y-intercept of the linear correlation is ~60%, which would suggest that in the absence of PA growth, TCPC-EDI will still tend to increase. Conversely the x-intercept value suggests that the PAs must increase their diameter by ~12% on a BSA-normalized basis to hold TCPC-EDI constant.

A similar negative correlation was present between normalized mean IVC/Fontan percentage diameter change vs. percent TCPC-EDI change (r=-0.52, p=0.047). However, in a multiple regression model with IVC and PA dimensions, only the PA change was a significant predictor for power loss change (Coeff=-4.7, t(12)=-4.13, p=0.001).

A natural question to then consider from these findings is: what factor(s) mediates, or is at least related to, the change in PA size and is thus also related to changes in TCPC-EDI? PA growth in the context of congenital heart defects is dependent on flow[174-176]. Figure 9.48a supports this idea based on a positive correlation from these data between serially averaged vessel flow rates (i.e., average($Q_{LPA}$ scan 1, $Q_{LPA}$ scan 2)) and the

percent change in normalized vessel mean diameter (r=0.46, p=0.012). It is also interesting to note that this association was much stronger for the LPA (Figure 9.48b; r=0.59, p=0.021) than the RPA (Figure 9.48c), for which the correlation was not significant (r=0.37, p=0.2). This difference could be related to the confounding issues of the right upper lobe branch: the measured RPA flow is not necessarily what is present at the site of the diameter measurement because of the upper lobe take-off. Further study is needed to confirm.

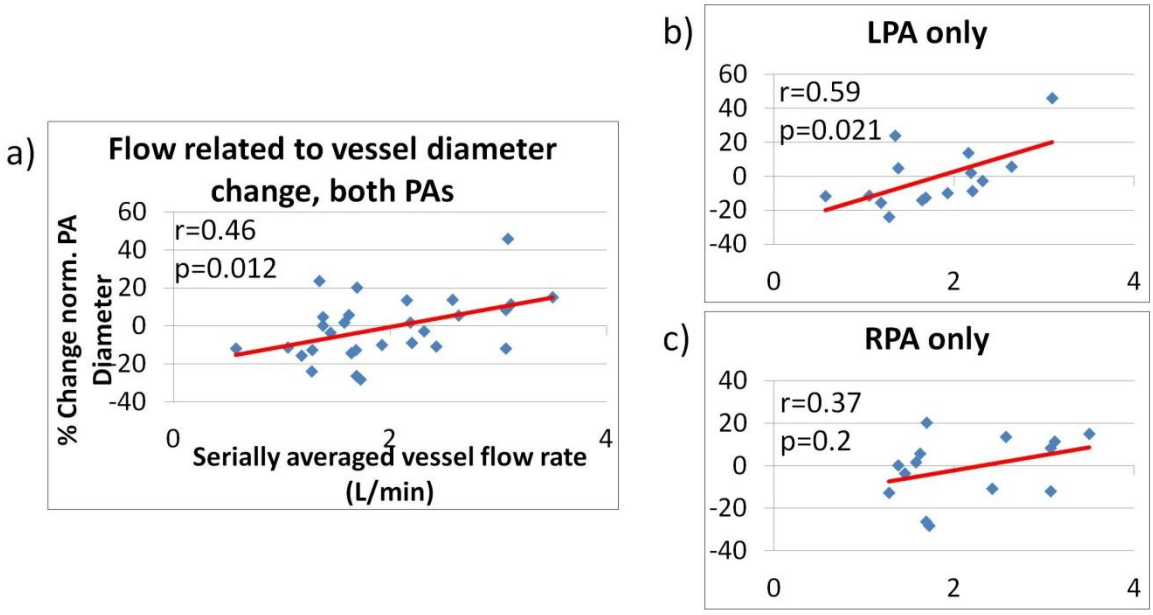


**Figure 9.48** ***a) Significant correlation between %change in PA diameter and serially averaged flow rate for all PAs. That correlation was asymmetric with respect to PA, however, given the stronger relationship for the LPA (b) than the RPA (c). See*** **Table 12.24** ***and*** **Table 12.25** ***in Appendix E.***

Pulsatility is another factor that could be expected to play an important role in PA size/growth. Time varying characteristics of pulmonary flows in SV patients are traditionally thought to be low compared to normal biventricular physiology with a pulsatile right ventricle. Yet, the combined effects of cardiac and respiratory variations do impart an appreciable pulsatile component to PA flows[177]. Figure 9.49 shows the comparison of serially averaged indexed pulsatility (PI) with serially averaged mean diameter and % diameter change by vessel. PI defined from phase contrast CMR measurements as:

$$PI = \frac{Q_{max} - Q_{min}}{2Q_{mean}}$$

where the maximum and minimum were defined from the instantaneous measures and mean is the time average. First considering the relationship of PI and vessel size, very divergent responses were seen by vessel with the LPA (Figure 9.49a) having a strong (r=0.63) positive correlation and the RPA (Figure 9.49b) having no relationship to PI. Similarly for the %change in diameter, the trends were very different for the two vessels: the LPA % change (Figure 9.49c) had a strong *negative* (r = -0.78) logarithmic relationship to PI, while the RPA % change was not related (Figure 9.49d).

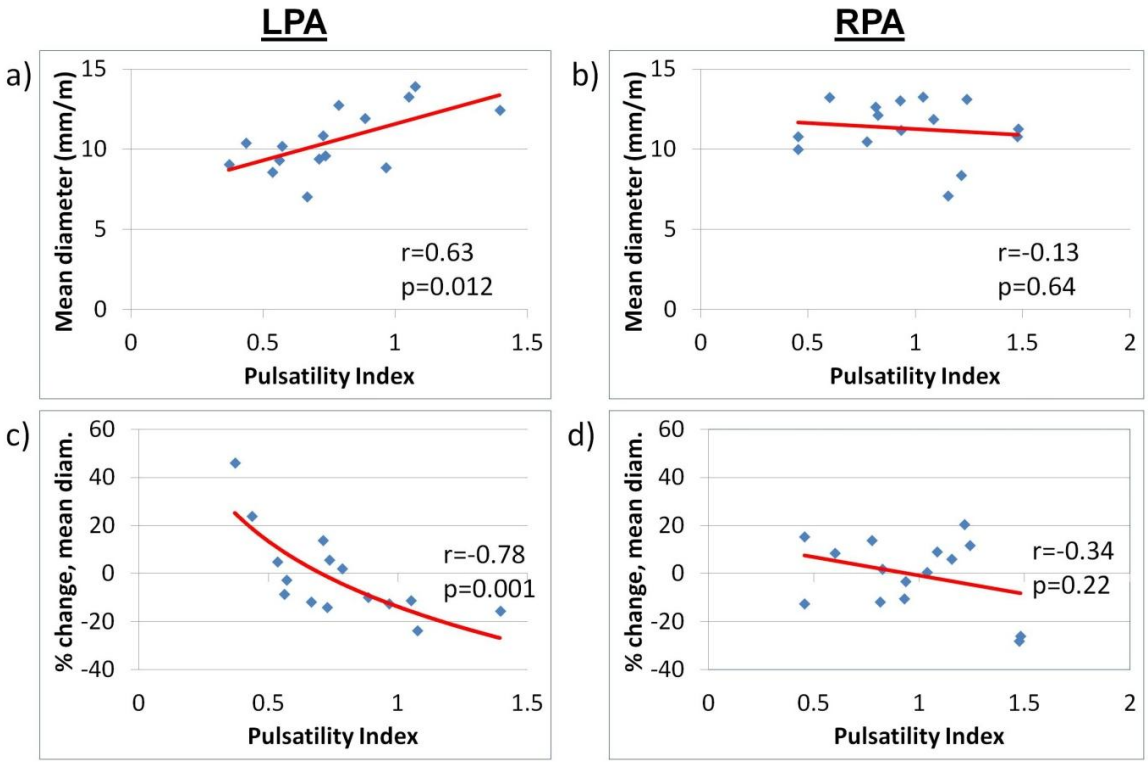


**Figure 9.49** ***Relationship between mean diameter and pulsatility index for the a) LPA and b) RPA, for which only the LPA had a correlation. Also, relationship between the % change in mean diameter vs. PI for c) LPA and d) RPA, for which the LPA correlation was negative and logarithmic while the RPA demonstrated no relationship. See*** **Table 12.24** ***and*** **Table 12.25** ***in Appendix E.***

This LPA % change response (Figure 9.49c) was unexpected and counter-intuitive and therefore deserves additional consideration. First, from a physiologic standpoint, it is important to understand if this trend is 'real' (e.g., are the vessels actually decreasing in size) or if it is an artifact of data normalization. To this end, Figure 9.50 recasts the relationship shown in Figure 9.49c using non-normalized vessel diameters, demonstrating the same negative trend, inclusive of negative diameter changes. Hence, the relationship is 'real', at least with respect to the data available. This finding in

conjunction with the positive correlation noted in Figure 9.49a raises several potential explanations:

1) Varying pulsatility levels may mediate different vessel growth rates such that vessels with high pulsatility reached a 'peak' value quickly, while lower pulsatility vessels grow at a slower rate. This explanation is physiologically sensible, but there was no relationship between age and either pulsatility or LPA diameter to support it.

2) Rather than being linked by an intrinsic mechanism (i.e., the pulsatility directly mediating vessel size), extrinsic factors may be involved. For example, a large over-riding aorta could impact (e.g., increase) pulsatility levels within the LPA while simultaneously impeding its growth[143]. The fact that the LPA and RPA responses were very different supports this possibility.

Further investigation is warranted to determine which of these explanations, or perhaps an entirely different explanation, is correct.

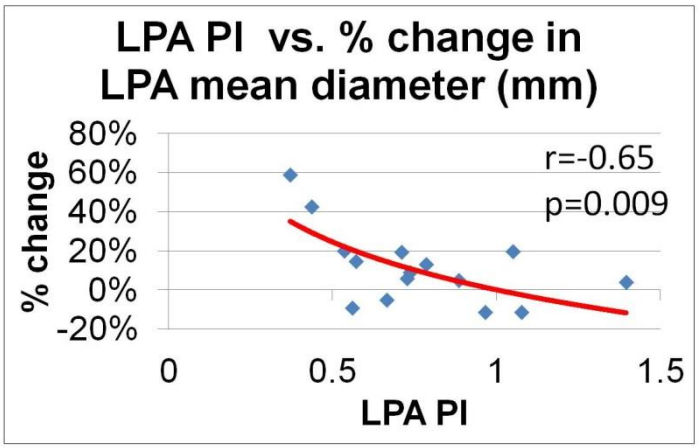


**Figure 9.50 Negative correlation between LPA pulsatility index and raw (non-normalized) LPA diameter serial change. See Table 12.24 in Appendix E.**

## 9.4 Ventricular Function Changes

### 9.4.1 Cardiac Index

While ventricular short axis data were not collected for all patients, phase contrast data were serially collected in the ascending aorta for all cases (N=15) (with one exception: CHOP052E). Table 9.34 provides a summary of the changes with respect to this metric. There was no significant pair-wise difference between the results from the first and second scans (p=0.46). Instead, the number of instances in which the index decreased (8) was nearly equal to the cases in which it increased (7) such that the average absolute change (20%) was much higher than the signed average (-4%). There was one interesting trend with respect to CI changes, and that was with age at first scan. In Figure 9.51, a distinct bi-modal pattern (reminiscent of a $4^{th}$ order polynomial function) can be observed between these variables; yet, with so few data points, it is difficult to

conclusively determine if this is an actual trend or noise in the signal. More patients are certainly needed to better investigate this interesting trend.

**Table 9.34 Summary of Serial Cardiac Index Changes**

| | |
|---|---|
| **Cardiac Index, 1st scan** (L/min/m$^2$) | 3.3 ± 0.9 |
| **Cardiac Index, 2nd scan** (L/min/m$^2$) | 3.1 ± 0.6 |
| **Average change** (%) | -4 |
| **Average absolute change** (%) | 20 |

See Table 12.26 in Appendix E

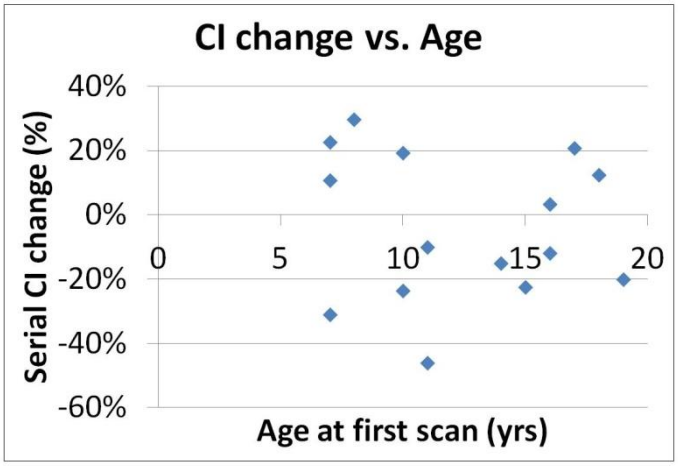


**Figure 9.51 Relationship between serial percent change in cardiac index and age at first scan from the 15 patient subset. A bimodal (i.e., 4th order polynomial) pattern can be observed, but more patients are needed to further evaluate.**

### 9.4.2 Volume Analysis

Serial volume data were available for only seven patients, again underscoring the preliminary nature of this analysis. Table 9.35 summarizes the volume changes and the EDV and ESV results are visually represented in Figure 9.52. As with the cardiac indices in the preceding section, the results were mixed: EDV increased in three cases (average of 27.7%), decreased in three others (average of 8.3%), and was virtually unchanged in one. ESV generally followed the same trends. It is worth noting that in 2 of the 3 cases for which volume increased with time (CHOP019 and CHOP091), more slices were acquired for the short axis stack in the later scan, which may have contributed to the additional volume at that time point if the initial stack did not include the apex.

**Table 9.35 Summary of Ventricular Volume Changes**

| | Slices | EDV (mL/BSA) | ESV (mL/BSA) | StV (mL/BSA) | EF (%) |
|---|---|---|---|---|---|
| CHOP005B | 12 | 92.7 | 46.4 | 45.7 | 50 |
| CHOP005C | 6* | 84.0 | 41.3 | 42.0 | 50 |
| | | -9% | -11% | -8% | |
| CHOP008B | 9 | 75.3 | 41.8 | 33.5 | 45 |
| CHOP008C | 8 | 99.0 | 53.8 | 45.2 | 46 |
| | | 32% | 29% | 35% | |
| CHOP019A | 7 | 45.8 | 17.9 | 28.0 | 61 |
| CHOP019B | 10 | 60.9 | 19.6 | 40.8 | 68 |
| | | 33% | 10% | 46% | |
| CHOP033A | 8 | 75.0 | 39.4 | 35.6 | 47 |
| CHOP033B | 8 | 82.6 | 50.6 | 32.0 | 39 |
| | | 1% | 17% | -10% | |
| CHOP052B | 7 | 87.7 | 37.7 | 50.0 | 57 |
| CHOP052E | 8 | 90.6 | 51.9 | 38.8 | 43 |
| | | -3% | 37% | -23% | |
| CHOP080A | 6 | 58.6 | 22.5 | 36.1 | 61 |
| CHOP080B | 6 | 51.1 | 20.7 | 30.4 | 59 |
| | | -13% | -8% | -16% | |
| CHOP091A | 7 | 41.8 | 19.7 | 21.6 | 52 |
| CHOP091B | 9 | 49.3 | 24.4 | 24.9 | 50 |
| | | 18% | 22% | 15% | |

*Data acquired with different anatomic orientation compared to previous scan.

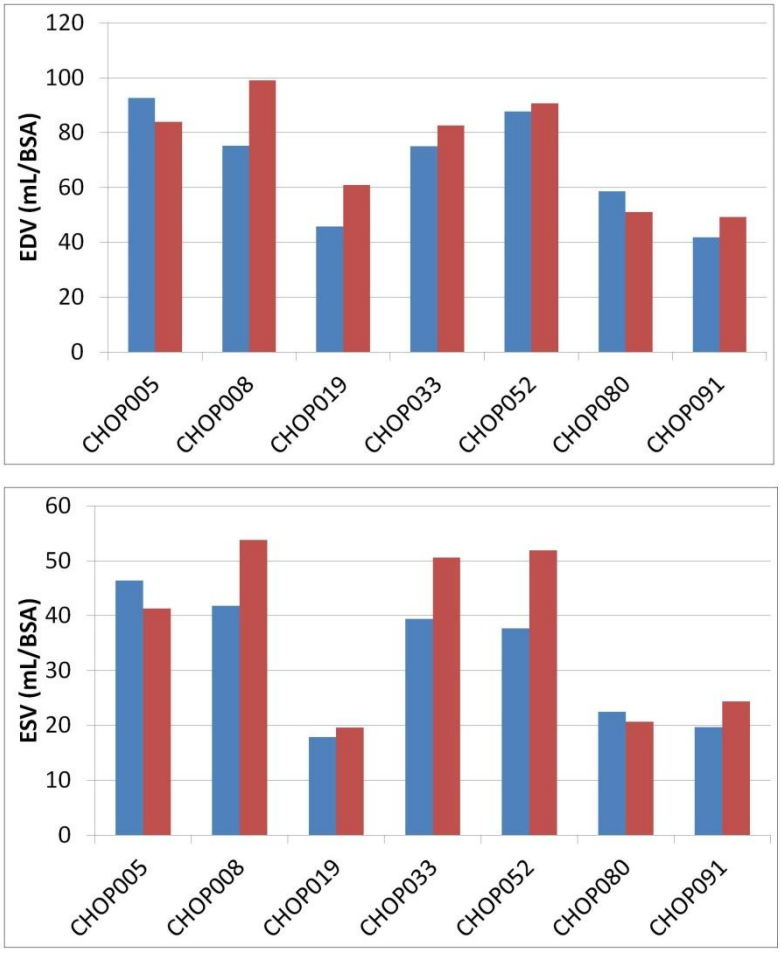


**Figure 9.52 Serial changes in EDV (top) and ESV (bottom) for the 7 patients with VF data from two CMR scans.**

Table 9.36 presents the results for $PER_V$, $PFR_V$, and time ratio to PFR. As for the volume results, responses varied with both increasing and decreasing trends among patient cases. Most interesting was the statistically significant correlation (r=0.86, p=0.013) between the percentage change in $PFR_V$ and the percentage change in EDV, as shown in Figure 9.53A.

**Table 9.36 Summary of Dynamic Volume Measurement Changes**

| | **$PER_V$** [EDV/s] | **$PFR_V$** [EDV/s] | **Time ratio to PFR** |
|---|---|---|---|
| CHOP005B | 2.09 | 2.06 | 0.15 |
| CHOP005C | 2.87 | 1.75 | 0.28 |
| | 37% | -15% | 84% |
| CHOP008B | 2.36 | 1.97 | 0.24 |
| CHOP008C | 2.42 | 2.37 | 0.25 |
| | 3% | 20% | 4% |
| CHOP019A | 3.23 | 2.88 | 0.16 |
| CHOP019B | 4.22 | 3.30 | 0.28 |
| | 31% | 15% | 73% |
| CHOP033A | 2.16 | 2.47 | 0.14 |
| CHOP033B | 1.74 | 2.14 | 0.14 |
| | -19% | -13% | -4% |
| CHOP052B | 3.90 | 3.05 | 0.20 |
| CHOP052E | 2.99 | 3.31 | 0.21 |
| | -23% | 9% | 3% |
| CHOP080A | 3.14 | 1.92 | 0.31 |
| CHOP080B | 2.29 | 1.52 | 0.28 |
| | -27% | -21% | -9% |
| CHOP091A | 2.64 | 2.45 | 0.23 |
| CHOP091B | 2.72 | 2.55 | 0.20 |
| | 3% | 4% | -15% |

As discussed in §6.4.2, $PFR_V$ has previously been described as a surrogate for ventricular relaxation rate, independent of preload[39, 71]. The relationship between serial changes in $PFR_V$ and changes in EDV (a surrogate of preload) would therefore suggest one of two possibilities: 1) normalization by EDV is not sufficient to remove preload

dependence from the measurement of PFR; or 2) the trend reflects a general increase or decrease in ventricular function, likely related to changes in ventricular compliance. The fact that no correlation was observed between the actual values of $PFR_V$ and EDV (see Table 6.5) and was only present between their respective percentage changes suggests that the first point is not accurate. Conversely, the similarly strong correlations between StV/EDV (Figure 9.53C) and CI/EDI (Figure 9.53D) provide strong support for the second conclusion. Serially improving single ventricle function would be surprising given the general understanding of a gradually deteriorating functional state, but such longitudinal VF analyses have not been reported in literature, so clearly more patients are needed.

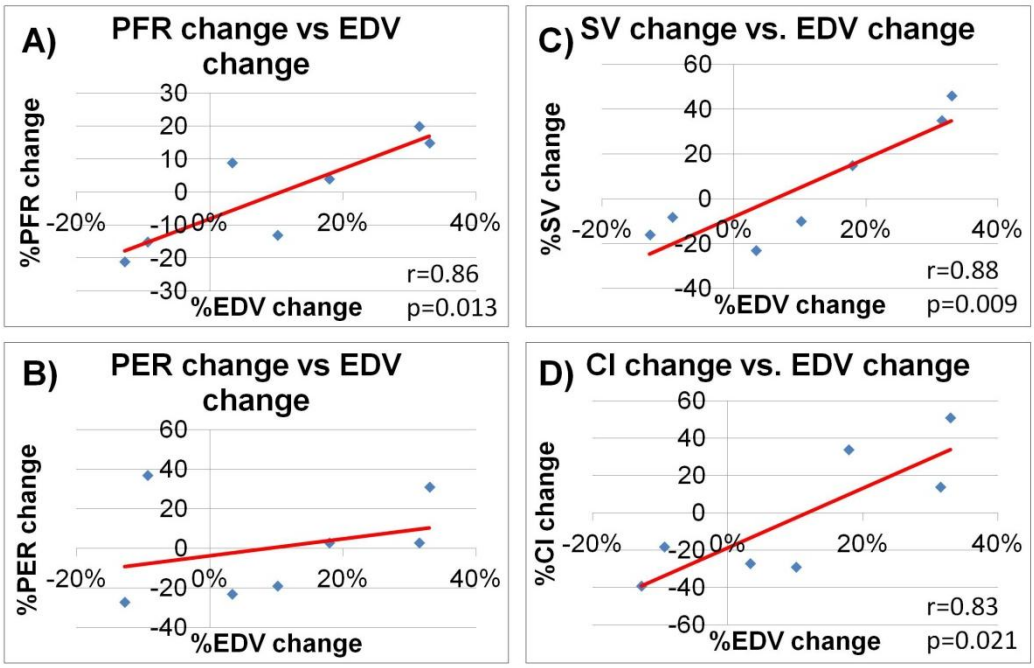


**Figure 9.53 Relationships of percentage changes in $PFR_V$ (A) and $PER_V$ (B) to percentage changes in EDV. The linear PFR/EDV relationship was statistically significant. Similarly strong correlations were observed for stroke volume (SV)/EDV changes and CI/EDV changes. See Table 12.27 in Appendix E.**

## 9.5 Serial TCPC Hemodynamics vs. Ventricular Function

### 9.5.1 Cardiac Index and Systemic Venous Flow

Serial CI and $Q_S$ data are available from PC CMR for all 15 patients included in the serial hemodynamics analysis. Therefore, we will first consider and compare CI vs. power loss and $Q_S$ vs. power loss. There are two questions to consider:

1) Are the relationships between variables consistent from scan to scan?

2) Are the observed changes between variables related (consistent with the analyses performed in the preceding sections)?

Figure 9.54 addresses the first of these points. The left column shows the correlation between CI and TCPC-EDI for the first (top) and last (bottom) scan for each patient; the right column mirrors that comparison for $Q_S$ vs. TCPC-EDI. Two trends are apparent: first, the relationship between TCPC-EDI and $Q_S$ is stronger than that of CI, which is consistent with the findings in Chapter 5. Second, the respective trends were both stronger (based on the $R^2$ values) for the earlier time point than the latter. Since there were no constraints placed on patient age at enrollment or follow-up duration, it is unlikely that this observation has meaningful implications for physiologic evolution in these patients (e.g., that TCPC power loss becomes less important over time). Instead, the result may simply reflect noise present in the small sample size.

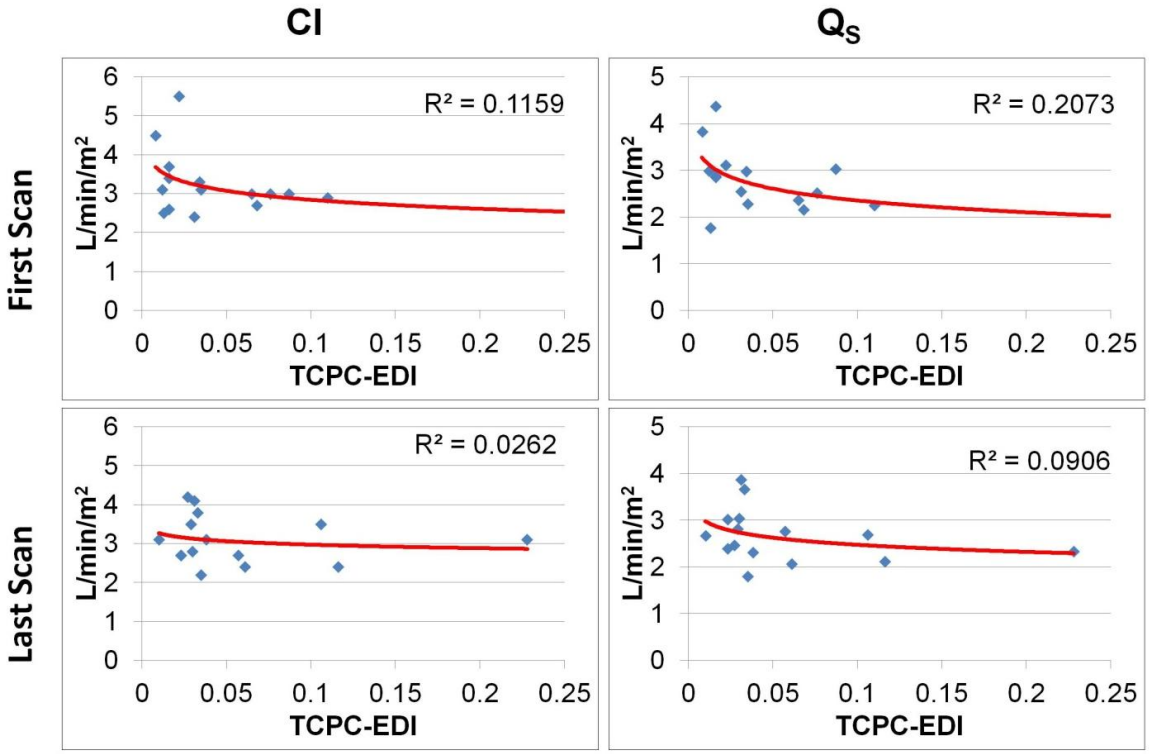


**Figure 9.54 Comparison of CI vs. TCPC-EDI (left column) and $Q_S$ vs. TCPC-EDI (right column) for the first (top row) and last (bottom row) CMR scan for each patient in the serial analysis. All regression lines follow a logarithmic function, as discussed in Chapter 5, with $R^2$ values as shown. None of the correlations were statistically significant. See Table 12.28 in Appendix E.**

Figure 9.55 shows the comparison of TCPC-EDI changes with CI (top) and $Q_S$ (bottom) changes. No correlations were observed in this present data set; however, continued analysis with additional patients is required to conclusively determine potential associations given the numerous underlying variables involved.

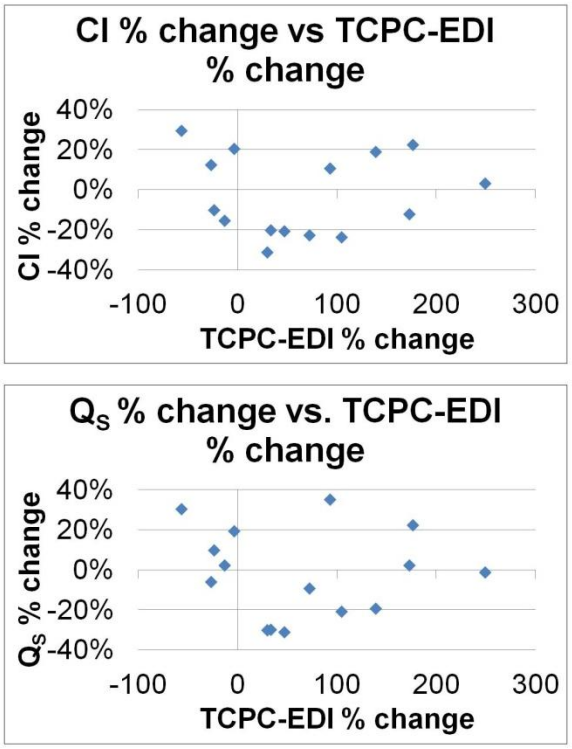


**Figure 9.55 Relationships of % change in TCPC-EDI with change in CI (top) and change in $Q_S$. No correlations were observed in this limited sample; however, a larger sample size is needed. See Table 12.28 in Appendix E.**

### 9.5.2 Ventricular Volumes

Table 9.37 shows a patient-by-patient comparison of the preliminary serial EDV vs. TCPC-EDI data. The '% change' columns are color-coded as either positive (green) or negative (red) to facilitate visual comparison by readily identifying cases that are increasing or decreasing in the respective columns. Based on the working hypothesis, the expected trend from this table is that red values for one measure correspond to green values in the other. This was observed in only three of seven cases, with large changes in TCPC-EDI being again related to un-expected VF changes. Further study will help to better elucidate these relationships.

**Table 9.37 Summary comparison of serial EDV and TCPC-EDI data**

| | $EDV_1$ mL/BSA | $EDV_2$ mL/BSA | % change | TCPC-$EDI_1$ | TCPC-$EDI_2$ | % change |
|---|---|---|---|---|---|---|
| **CHOP005** | 93 | 84 | -9 | 0.087 | 0.116 | 33 |
| **CHOP008** | 75 | 99 | 31 | 0.065 | 0.228 | 251 |
| **CHOP019** | 46 | 61 | 33 | 0.034 | 0.030 | -12 |
| **CHOP033** | 75 | 83 | 10 | 0.016 | 0.038 | 138 |
| **CHOP052** | 88 | 91 | 3 | 0.022 | 0.045 | 105 |
| **CHOP080** | 59 | 51 | -13 | 0.110 | 0.106 | -4 |
| **CHOP091** | 42 | 49 | 18 | 0.031 | 0.023 | -26 |

### 9.5.3 Note about lumped parameter modeling

The original proposal for this SA called for the use of lumped parameter modeling to supplement the trends identified in the serial analysis of patient data to evaluate evolutionary hypotheses for the cause/effect mechanisms underlying the observed trends. However, the findings from these preliminary patient data were lacking in clear trends in many critical areas that are needed to inform such modeling.

There was a non-specific trend toward serially increasing TCPC-EDI that could form the basis for one analysis; however, Sundareswaran *et al*. have already shown the results from a parametric sweep of TCPC resistance in a lumped parameter model[55]. They

reported decreasing cardiac output and ventricular preload as well as increased central venous pressure; repeating such a study would not produce novel findings.

Otherwise, cardiac index, systemic venous flow, and ventricular function results revealed varying responses. This finding should in some sense not be surprising given that patient outcomes have a wide range; however, this variety (coupled with the small patient sample available for analysis) effectively precludes the ability to conduct a meaningful, hypothesis-driven lumped parameter study. Rather than being able to identify a trend from patient data to inform the model (and cross-reference model results back to patient data to check its validity), the selected trends would be arbitrary and without the foundation in clinical experience needed to extrapolate the findings. As such, the lumped parameter modeling study has been excluded from the present analysis in the hope that, with the inclusion of more serial patient data through the ongoing longitudinal patient function/quality of life study, trends might emerge to facilitate a more focused and effective modeling study.

## 9.6 Chapter Summary

### 9.6.1 Major Findings

- Changes in power loss were strongly related (r= -0.80) to average percentage changes in mean normalized PA diameter and, to a lesser extent (r= -0.57), mean normalized Fontan diameter percentage change.
- Ventricular function was seen to both increase and decrease in different cases; percentage changes in EDV were strongly (positively) associated with percentage changes in StV, PFR, and CI.

- Normalized power loss (TCPC-EDI) may tend to increase with time for a given patient (p=0.10).

### 9.6.2 Narrative

A few studies have begun to longitudinally follow and hemodynamically evaluate Fontan patients[178]. Such investigations, while potentially complex in study design, will play a critical role in solving the broader questions of single ventricle physiology. This specific aim represents a preliminary serial analysis of 15 TCPC patients with three objectives: 1) characterize TCPC hemodynamic changes, 2) characterize VF changes, and 3) investigate how TCPC changes relate to VF changes. Importantly, this study represents the first attempt to investigate that third critical component.

Power losses were seen to both increase and decrease on a patient-by-patient basis, with a non-significant trend towards serial increases. Through a detailed analysis of each case, the consistent trend that was found to determine whether power loss went up or down was the change in vessel sizes. This observation was confirmed by a strong correlation (r= -0.80) between changes in mean PA diameters and changes in TCPC-EDI (Figure 9.47).

Beyond simply helping to explain power loss changes, this trend also suggested that PA growth (even on a BSA normalized basis) may be a requirement to maintain consistent levels of indexed power loss. In other words, if the mean PA diameters increase at a rate equal to $BSA^{0.5}$, TCPC-EDI is likely to increase. Instead, a statistically significant decrease in minimum LPA diameter was noted in this data set, with the other PA dimensions not demonstrating any significant change. Furthermore, past studies have shown a confounding influence of a large aortic arch on LPA size[143]. So while no

conclusive trend was observed in power loss in the present patient sample, much of the supporting data and trends (i.e., the mediating effects of PA growth) suggest that, on a general level, biases toward increasing power losses may exist.

For ventricular function, a decrease in metrics such as cardiac index was expected given the gradual nature of Fontan failure; however, no such trend was observed in the present data. It is possible that there were changes in the underlying ventricular compliance based on the generally uniform increase or decrease in all metrics (i.e., EDV, CI, PFR, SV), but imaging methods for tissue characterization (e.g, late gadolinium enhancement or $T_1$ mapping for myocardial fibrosis) would likely be needed to directly assess such questions.

Finally, the comparison that was ultimately sought in this study is the relationship between serial changes in both the TCPC and the single ventricle, which would provide insight into how the TCPC is related to patient functional status over time. There was no evidence of this association from these data (Figure 9.55), but much more work is needed. Based on the correlations between power loss and ventricular function established in Chapter 6 with 40 patients, it is suggested that at least 25 additional patients be added to this study to provide a more detailed sample.

In summary, this chapter detailed one of the first attempts to characterize longitudinal changes in TCPC hemodynamics and ventricular function late after the Fontan procedure. Continued efforts are needed in this regard to sufficiently power the analyses and overcome large patient-to-patient variabilities in the data, especially given the value of what these types of studies can tell us about Fontan failure. What is clear from this preliminary study is that the evolution of TCPC power loss is tightly coupled to growth of the pulmonary arteries. Given the potential role these losses may play in chronic

ventricular preload limitations, there is thus a need to monitor and ensure reasonable growth of the PAs over time.

# Chapter 10. Discussion

The consistent theme of this thesis was the evaluation of TCPC hemodynamics: what are the 'normal' values and ranges (Chapter 5); what are the physiologic implications (Chapters 5 & 6) and serial adaptations (Chapter 9); what are potential engineering tools that can be translated into patient-level improvements (Chapters 7 & 8)? The two end points that were the primary foci of these questions were: 1) power loss and 2) HFD, and the individual chapters have detailed the major findings the respective studies have independently revealed for both end points. However, synthesizing some of these major findings from across study aims will provide additional insights, and a broader picture of the cumulative knowledge gained.

## 10.1 TCPC Power loss and single ventricle physiology (SA1, 2; Chapters 5, 6)

de Leval *et al*. first proposed the TCPC as the successor to the atriopulmonary connection to reduce energy losses in the vascular circuit for single ventricles[17]. Since that time, the TCPC has become the standard for single ventricle palliation, but our understanding of the significance of those energy losses has not advanced appreciably. Some have mistakenly assumed/concluded that energy losses with the TCPC are not a concern[66, 95]. The results presented in this thesis thus represent an important step forward for understanding the role of the TCPC in single ventricle physiology.

The major physiologic findings are as follows:

1. From the largest modeling study of patient-specific Fontan connections to date, we saw that indexed power loss (TCPC-EDI) varied by two orders of magnitude, demonstrating that TCPC hemodynamics are far from uniform.

2. The magnitude of (indexed) power loss (TCPC-EDI) was negatively associated with both the systemic venous flow rate and the cardiac index, such that higher losses corresponded to lower flow rates (Figure 10.1). These relationships were relatively weak, reflective of the large number of variables mediating the dynamics of this pathway; however, the data indicate that the TCPC is indeed one of those factors.
3. There is a significant negative association between TCPC-EDI and ventricular function (particularly EDV), such that higher losses were related to smaller volumes (Figure 10.2).

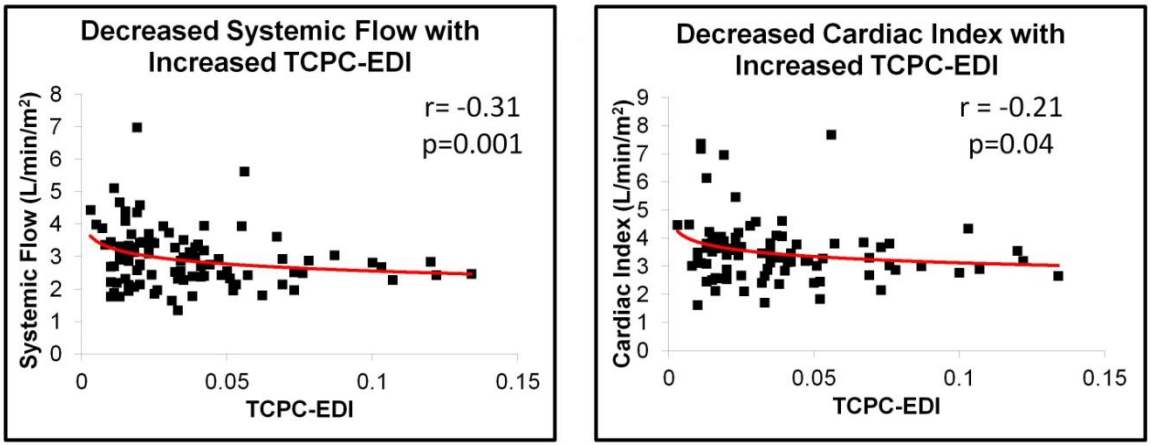


**Figure 10.1 Recreation of Figure 5.14 showing negative relationship between TCPC-EDI and $Q_S$ (left) and CI (right).**

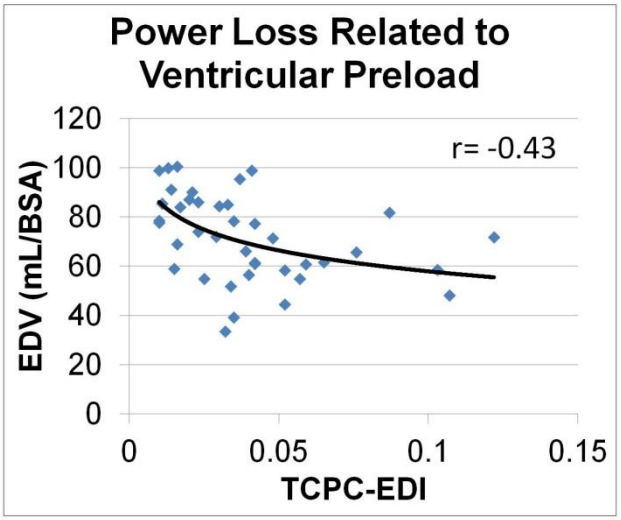


**Figure 10.2 Recreation of Figure 6.5 showing a significant correlation between power loss and end diastolic volume.**

Statistical correlation does not imply mechanistic cause and effect, so further work will be needed to determine the exact nature of these interactions; however, the hypothesized linkage based on our current understanding is as follows. The inherent challenge of Fontan physiology is that, in the absence of a sub-pulmonary pumping chamber, the central venous pressure must provide the driving head pressure for the pulmonary circuit (see Figure 10.3). As the resistance (serial sum of the TCPC and PVR) between this source and the downstream ventricle increases, either the vasculature must compensate by reducing compliance to further increase the driving pressure and maintain constant flow, or the hydrodynamic energy filling the ventricle is reduced[42]. Decreased venous capacitance has been reported in single ventricles[43]; the relationship between power loss and $Q_S$ reported here is evidence of decreased flow. It is likely that both responses occur, perhaps with flow/energy decreasing once the body can no longer continue adapting venous tone to preserve vascular potential energy. These losses

translate to decreased ventricular filling and lower EDV. That is, increased TCPC power loss contributes to the limited ventricular preload and preload reserve that is a known complication of Fontan physiology[39]. Finally, the positive correlation between EDV and CI (in conjunction with the Frank-Starling laws) potentially explains the observed TCPC-EDI/CI correlation as: high power loss contributing to decreased EDV, which in turn suppresses cardiac output. In other words, the negative TCPC-EDI/CI relationship is again reflective of ventricular preload limitations.

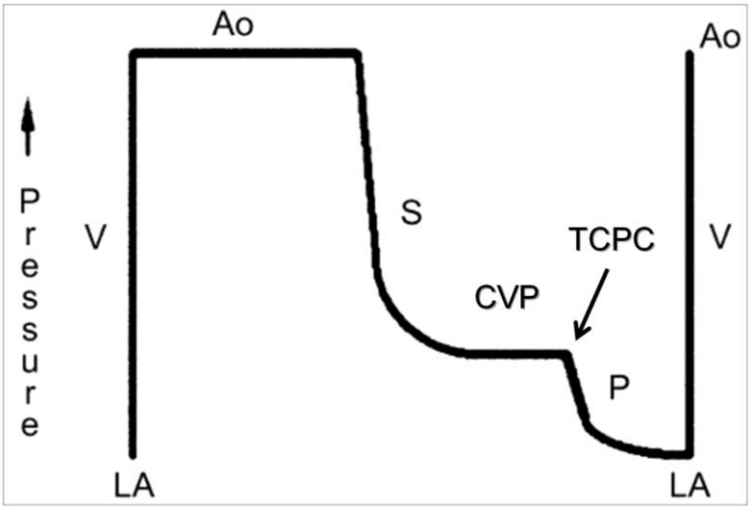


**Figure 10.3 Schematic representation of Fontan physiology with respect to the relative driving pressure through the various cardiovascular compartments. (Adapted from [66]) LA- left atrium; V- ventricle; S- systemic circulation; CVP- central venous pressure; P- pulmonary circulation; Ao- aorta.**

## 10.2 Surgical Planning for HFD (SA1, 3; Chapters 5, 7)

The patients modeled and treated in the surgical planning studies were all (with the exception of CHB_M1) referred on the basis of PAVM and so the primary need was for optimized flow distribution through the Fontan connection. While surgical planning provides a powerful platform for evaluating and treating these patients, it is important to recognize that the technology is not yet widely available outside of three select US centers. Thus, as advocated by de Zelicourt *et al*.[105], the ability to leverage past experience to establish generalizable trends is an equally valuable exercise.

From the cohort geometric analysis (§5.5.2), the primary importance of vessel angles in mediating flow distribution through the connection was noted (Figure 10.4). Such relationships were both expected and intuitively obvious. However, what was not expected was the fact that the SVC connection angles appeared to have a stronger association with the IVC flow distribution than the IVC connection angles did. This finding suggests that the design of the Glenn (or Kawashima) connection can be as important in determining the flow distribution characteristics of the connection as the Fontan. Figure 10.5 aptly demonstrates this point as a favorable (i.e., large) SVC-RPA angle directs all SVC flow to the RPA, thus leaving the IVC flow to make up the balance of LPA flow.

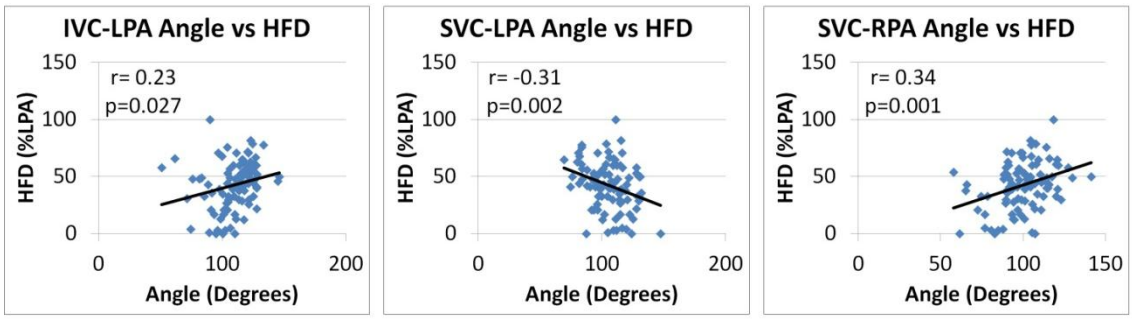


**Figure 10.4 Recreation of Figure 5.33 showing the relationship between TCPC vessel angles and HFD to the LPA.**

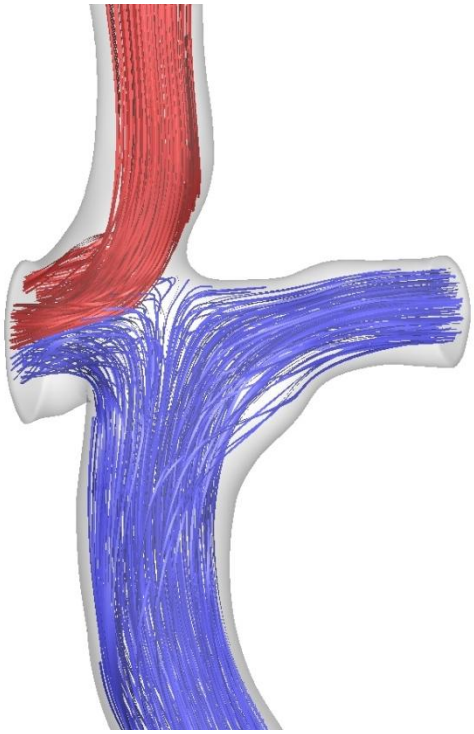

**Figure 10.5 Representative TCPC case showing the potential impact of SVC anastomosis angle in dictating the distribution of IVC flow (blue).**

The surgical planning cases presented in this thesis were generally more anatomically complex than the standard TCPC geometries seen in the cohort analysis. Often they presented 3 or more inlet vessels, which does complicate the application of these geometric relationships. Yet the lessons learned can still be applied: foresight at the time of the Glenn procedure can ultimately help achieve a balanced flow profile, particularly if the approach that will be used for the Fontan is already known.

Using CHOP_M9 as an example (§7.4.3, Figure 10.6), it is seen that the SVC-PA connection for this patient was relatively perpendicular with respect to the PA axis such that there was not a significant bias to either PA as flow entered the connection and the Y-Graft branches were able to span the superior flows with relative ease. It is easy to appreciate that if SVC connection angle had instead been angled toward one side (as with Figure 10.5), the LPA for example, then the ability to direct hepatic flow to that same side may have been compromised. While the introduction of an SVC angle in this instance is viewed as a negative feature, it can alternatively be used as an advantage. In the case of bilateral SVCs, for example, if the right SVC is angled to the RPA (assuming a right-sided IVC), then once the Fontan is completed, the flow through the two SVCs will presumably be unilaterally directed to their respective PAs and the IVC flow will provide the balance to both sides. Focused design studies would likely uncover other such possibilities of leveraging vessel angle relationships, but these examples represent pertinent relationships observed through the present surgical planning/cohort study experiences with easily translatable applications.

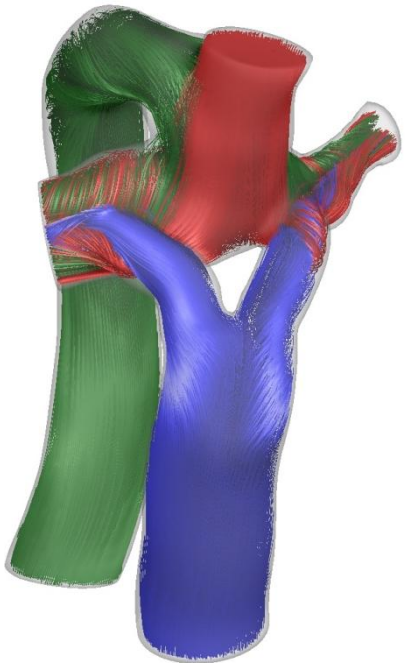

**Figure 10.6 Velocity streamlines from surgical planning Y-Graft model for CHOP_M9.**

### 10.3 Surgical Planning and power loss (SA1, 3; Chapters 5, 7)

The capability to pre-operatively model vessel flow distributions is a demonstrated strength for the surgical planning methodology; however, PAVM is an uncommon pathology for single ventricles, so maintaining a singular focus on that disease will severely limit the patients who stand to benefit from the technology. To ultimately reach a broader population, the ability to optimize other hemodynamic end points will be necessary. Given the potential physiologic significance of TCPC power loss for single ventricle patients, working toward a predictive framework for that metric serves as a logical and important next step. Achieving this goal requires two important questions be addressed: 1) How accurate are pre-operative power loss predictions; 2) How much does power loss vary as a function of surgical design?

The first of these points was addressed, at least in a preliminary fashion, through the analysis of post-operative hemodynamic data for patients who had previously undergone prospective surgical planning (§7.5). Comparing the connection resistances between the prospective pre-operative surgical model and the simulated hemodynamics from the acute post-operative CMR study, it was found that power loss predictions were, on average, within 20% of actual values. However, without the context of how big an improvement in power loss can be realized through surgical planning, the merits of this finding cannot be determined.

While the majority of surgical planning cases were referred for flow distribution optimization, select cases can be used to provide insights into the potential effect and limitations of surgical planning for power loss. Cases with interrupted IVC are not good candidates for such an analysis because the Fontan baffle in those patients carries only low momentum hepatic flow and experience has consistently demonstrated low power loss variance among designed options in those cases[105]. Instead, the patients depicted in Figure 10.7 provide a better basis for comparison as they are generally less anatomically complex than the interrupted IVC cases and power loss as a function of Fontan connection design is expected to vary more. Hence, the surgical planning cases for each of these patients were reviewed to identify the range of power loss among the virtual options investigated. Table 10.1 reports the highest and lowest power loss results recorded for each of these patients at the *in vivo* measured PA splits. The percentage differences ranged from 0-176% with a median of 67%.

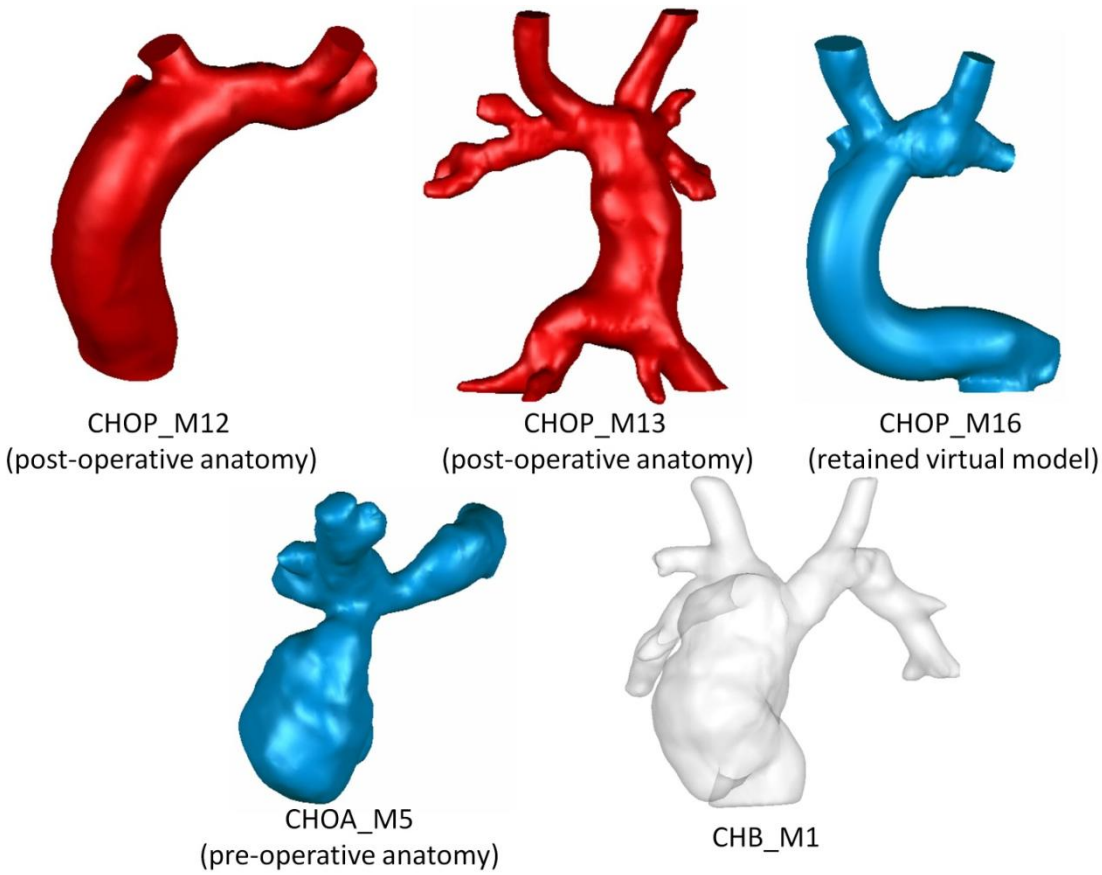


**Figure 10.7 Representative TCPC models for the surgical planning patients retained to evaluate power loss variability.**

**Table 10.1 Range of observed power losses [mW] among virtual models investigated for specified patients. The options that yielded the specified value is provided in each case for reference.**

| | Lowest value | Highest value | % difference |
|---|---|---|---|
| **CHOP_M12** | 2.3 (EC) | 2.5 (Y2) | 9 |
| **CHOP_M13** | 3.3 (option b) | 9.1 (option f) | 176 |
| **CHOP_M16** | 0.9 (right EC) | 1.5 (Y) | 67 |
| **CHOA_M5** | 1.7 (22-11Y) | 2.3 (20-10Y, left medial branch) | 35 |
| **CHB_M1*** | 2.7 | 2.7 | 0 |

*Only 2 options simulated

These values represent the results produced by all of the reasonable surgical alternatives for a given case. However, it cannot be assumed that the surgeon would routinely select the option with the highest losses without surgical planning; thus, this range represents an upper bound (over-estimate) of the surgical planning 'benefit' for power loss. Taking instead a conservative approach to these data (and considering the similar finding from published data[95]), it is estimated that routine surgical planning of the Fontan procedure could help to reduce power loss by 20-30%, on average.

Critically, the low end of this range intersects with the uncertainty in predictive accuracy for power loss, which indicates that the present surgical planning paradigm is not yet sufficient for accurately evaluating power loss. If a given option is predicted to have 20% lower power loss than another, but the implementation of either option may produce a result 20% different from the model predictions, then there may not actually be a

practical difference between the two options. These findings thus provide further motivation for the continued method developments needed to improve power loss predictive accuracy as discussed at length in §7.5.

# Chapter 11. Limitations and Future Directions

This thesis has extensively leveraged the strong foundation of engineering tools developed and validated by past members of the Cardiovascular Fluid Mechanics lab to study TCPC hemodynamics and single ventricle physiology on an unprecedented scale. These tools include medical image segmentation and patient-specific anatomic reconstruction, reconstruction and interpolation of 4D phase contrast CMR data, and computational fluid dynamics simulations. Each of these components has its own associated limitations, which have been discussed at length in their respective development-focused dissertations[119, 124, 179]. However, given the particular use of CFD in these studies, additional attention to that method is presently warranted. Also, as with all research, this thesis has generated as many new questions as answers; some of these potential new investigational avenues are also explored in the following sections.

## 11.1 Reducing CFD assumptions

The primary limitations of the CFD modeling in this thesis were the significant number of assumptions made in performing the simulations. Specifically, most analyses relied on time-averaged flow boundary conditions with flat inlet velocity profiles and (for all cases) rigid vessel walls. Favorable comparisons with 4D CMR (both qualitative and with respect to quantitative flow distribution quantification) demonstrated that these assumptions were generally tolerable. However, as we continue to advance our appreciation for and knowledge of the physiologically relevant magnitudes and thresholds of power loss, the need to refine these models and improve the finer accuracy details will become more important. Incorporating vessel elasticity (either via fluid-structure interaction modeling or imposed wall motion[165]), flow pulsatility, and

patient-specific velocity cross-sectional profiles at the inlets represent the most logical means of accomplishing this objective. Many of these tasks are already under development.

### 11.2 Relating function to patient outcomes

The primary endpoints used in evaluating power losses in this thesis were other functional metrics that could be derived from medical imaging (i.e., VF, CI, $Q_s$). It is implicitly hypothesized that these measures are effective surrogates for patient functional health and long term outcomes; however, these relationships have not been conclusively demonstrated. Ongoing efforts through an NIH-funded R01 should help to explicitly make these connections through exploring correlations between measures such as power loss, ventricular function, and exercise capacity to patient outcome and quality of life. Ultimately, these connections/relationships are needed to begin to establish statistically-based thresholds and surrogates for function, which can be translated to improved guidelines for patient management.

### 11.3 More robust approach to surgical planning boundary condition definition

As discussed in §7.5.2, there is a clear need to refine the means by which boundary conditions are derived and prescribed for surgical planning simulations to improve the fidelity of predicted outcomes. Retention of pre-operative measurements is not a sufficient strategy as there are significant physiologic changes taking place as a result of the surgery, particularly for initial Fontan procedures, which can alter those flows. Reduction of cardiac preload and output, increased resistance downstream of the IVC/hepatic veins, and introduction of a Fontan fenestration are all significant

confounders to consider and address. Lumped parameter modeling provides an excellent first step in the right direction based on the ability to mathematically approximate the physiology response to changing conditions.

Continued follow-up of these early surgical planning cases is also a necessity to determine how the hemodynamics conditions change with time and how those changes impact the desirability of the retained surgical option. To date, the patients have generally been evaluated only in the immediate or acute post-operative period and that has been the basis for assessing model fidelity and utility. In contrast, the surgical connection is intended to last a "lifetime" through dynamic and varying anatomic and physiologic conditions. Thus, the use of a lumped parameter model to predict a singular post-operative state is not advisable either, and more robust protocols may be needed.

### 11.4 The future of the Y-Graft

This thesis was part of a ground-breaking effort to translate the Optiflo concept[106] into clinical practice through the Fontan Y-Graft. Here again, solely considering the acute post-operative period limits the ability to fully evaluate the experience with an appropriate baseline reference state, and so close continuing clinical follow-up of these patients will be crucial.

The other critical question that must be addressed (as discussed in §8.4) is the question of graft sizing *within realistic surgical constraints*. It is clear that, on paper, a larger graft is better, but that may not translate into practice. A parametric study combining virtual surgery expertise and the patient experience to date can provide important insights in this regard: is it energetically preferable to use a smaller graft that can be 'optimally' oriented or a larger graft that may provide lateral separation from the SVC but may not readily allow for streamlined transition to PA flow. If the larger design is found to be

superior under such a scenario, then it will be worth pursuing corporate partnership in manufacturing such a graft.

### 11.5 Mechanical support

Although not directly addressed in this thesis, mechanical cavopulmonary support is becoming a relevant and important topic for single ventricle patients[86, 97, 180] as clinicians and researchers search for answers to address the growing problem of Fontan failure. Ultimately, optimizing TCPC power loss may provide physiologic benefit (as the present work has demonstrated), yet it will not solve Fontan failure in all cases. Thus, continued innovation is needed to ultimately achieve a normal life expectancy for these patients.

Novel devices provide an intuitive answer; however, the difficulty in achieving regulatory approval and commercially manufacturing even a general pediatric ventricular assist device (at present, the Berlin Heart is the only one) should give pause to the long-term viability of that approach. Instead, identifying strategies to make use of existing devices[97] may ultimately provide more practical benefit.

### 11.6 New Approaches to Fontan palliation

Regardless of the upper limit to TCPC efficiency, the systemic venous system and the GI tract in particular will still be subjected to abnormally elevated pressures. As a result, problems associated with liver cirrhosis and failure[181] and portal venous hypertension[182] are becoming more prevalent and may be related to the time since Fontan completion. These issues are beginning to raise the question of whether the current timing of staged palliation is appropriate (i.e., Fontan completion at age 3-4) or if the time between

ventricular unloading (the Glenn procedure) and Fontan could be safely extended to preserve low hepatic pressures for as long as possible. Additionally, some have gone so far as to propose a modification to the Fontan procedure in which only the sub-diaphragmatic IVC is routed to the PAs such that the hepatic veins remain connected to the atrium and GI pressures are kept low (credit: Brian Kogon, MD, Emory University Department of Surgery). Obviously, PAVM may become a problem for a subset of patients[58] in such a scenario, but may be treatable through systemic-to-arterial shunts to route the necessary “hepatic factor” to the lungs. Again, such novel ideas and approaches are needed to continue addressing the complex and multi-faceted nature of Fontan failure.

# Chapter 12. Conclusions

At the beginning of this research endeavor, it was hypothesized that high TCPC power losses restrict preload and ventricular function in SV patients, with both deteriorating with time, and thus surgical planning and novel surgical approaches may improve these hemodynamics. Towards these ends, there are several major findings and conclusions that can be drawn from the studies performed as part of this thesis.

1. TCPC power loss varies widely among patients and is negatively associated with systemic venous flow rate, cardiac index, and end diastolic volume.
    - Relationship between TCPC and SV has not been previously reported and provides strong support for the study hypothesis.
    - Motivates continued research and investigation into means of systematically lowering power losses
    - Strengthens the over-arching hypothesis of ongoing Fontan studies that the TCPC impacts long-term functional health and quality of life.

2. Virtual surgical planning for the Fontan procedure provides a novel platform to prospectively evaluate complex patient cases and potential therapeutic options. Preliminary post-operative verification studies demonstrate promising agreement between model predictions and post-operative hemodynamics.
    - The ability to evaluate and identify desirable hemodynamic characteristics from among the array of potential surgical options fills an otherwise unmet need and has demonstrated potential for therapeutic benefit
    - Continued technological advances in these techniques are needed to improved modeling accuracy

- Efforts should be made to extend this approach to a wider array of end points and procedures to maximize the utility of the paradigm.

3. The Y-Graft Fontan connection is a novel and surgically feasible alternative to standard extracardiac or lateral tunnel TCPCs with the potential to improve connection efficiency.
    - Short-term experience with this approach has been promising with strong modeling evidence to suggest improved hemodynamics (with respect to either power loss or hepatic flow split) in at least four patients
    - More work is needed to pragmatically optimize the surgical implementation of the Y-Graft with respect to graft sizing, and perhaps identifying patients who are anatomically good or bad candidates for this connection scheme.

# A. Appendix A- CFD Cohort Data

## 1. Demographic data for 100 patient cohort

Table 12.1 contains basic demographic details for all 100 patients included in the CFD Cohort analysis. These data include: **Fontan type** (Intra-atrial (IA), Extracardiac (EC), or Atriopulmonary connection (APC)), whether or not the patient was diagnosed with hypoplastic left heart syndrome (HLHS), whether or not the patient has bilateral SVC connections, whether or not the patient has a reconstructed aorta, age, gender, and body surface area (BSA).

**Table 12.1 Patient demographic details**

| | Fontan type | HLHS (H) or Non-HLHS (N) | Bilateral SVC (Y or N) | LV or RV | Recon. aorta (Y or N) | Age | Gender | BSA (m^2) |
|---|---|---|---|---|---|---|---|---|
| CHOP_M10 | EC | N | N | L | N | 3 | F | 0.61 |
| CHOP_M11 | IA | H | N | R | Y | 10 | F | 1.03 |
| CHOP_M12 | EC | N | Y | L | N | 2 | M | 0.46 |
| CHOP_M7 | EC | N | Y | L | N | 11 | M | 1.16 |
| CHOP_M8 | EC | N | Y | R | Y | 6 | M | 0.89 |
| CHOP001B | IA | H | N | R | Y | 16 | F | 1.23 |
| CHOP004B | IA | N | N | L | N | 17 | F | 1.49 |
| CHOP005B | IA | N | N | L | N | 19 | F | 1.51 |
| CHOP007B | IA | N | Y | L | N | 18 | M | 2.01 |
| CHOP008A | IA | H | N | R | Y | 15 | M | 1.94 |
| CHOP010A | IA | H | N | R | Y | 15 | M | 1.62 |
| CHOP013A | EC | N | N | R | N | 16 | M | 1.9 |
| CHOP014A | EC | N | N | L | Y | 9 | M | 1.04 |
| CHOP016A | EC | H | N | R | Y | 6 | M | 0.83 |
| CHOP017B | EC | N | N | L | N | 15 | F | 1.64 |
| CHOP018A | IA | N | N | R | N | 7 | M | 0.68 |
| CHOP019A | IA | H | N | R | Y | 14 | M | 1.68 |

| | | | | | | | | |
|---|---|---|---|---|---|---|---|---|
| CHOP021A | IA | H | N | R | Y | 11 | F | 1.23 |
| CHOP022A | EC | H | Y | R | Y | 7 | M | 0.91 |
| CHOP023A | IA | N | N | R | N | 12 | M | 1.22 |
| CHOP024A | IA | N | N | L | Y | 7 | F | 0.74 |
| CHOP025A | EC | N | Y | M | N | 9 | F | 1.01 |
| CHOP026A | IA | H | N | R | Y | 6 | F | 0.83 |
| CHOP028A | IA | H | N | R | Y | 18 | M | 1.92 |
| CHOP029A | IA | H | N | R | Y | 9 | M | 1.08 |
| CHOP030B | IA | H | N | R | Y | 21 | F | 1.39 |
| CHOP031A | IA | N | N | L | N | 7 | M | 0.89 |
| CHOP032A | IA | N | N | L | N | 18 | F | 1.64 |
| CHOP033A | IA | N | N | L | N | 10 | M | 1.32 |
| CHOP034A | IA | N | N | L | N | 14 | M | 1.89 |
| CHOP035A | EC | N | N | M | Y | 8 | F | 0.69 |
| CHOP036A | IA | N | N | L | N | 11 | M | 1.19 |
| CHOP037A | IA | H | N | R | Y | 10 | M | 1 |
| CHOP038A | EC | N | N | R | N | 18 | M | 1.63 |
| CHOP039A | IA | H | N | R | Y | 10 | F | 1.02 |
| CHOP040A | IA | N | N | R | N | 19 | F | 2.05 |
| CHOP041A | IA | H | N | R | Y | 14 | F | 1.51 |
| CHOP042B | EC | N | Y | M | N | 3 | F | 0.62 |
| CHOP044A | APC | N | N | L | Y | 24 | M | 1.9 |
| CHOP047A | APC | N | N | L | N | 20 | M | 1.84 |
| CHOP049A | IA | N | N | R | N | 19 | M | 1.3 |
| CHOP051B | EC | N | Y | M | N | 4 | M | 0.63 |
| CHOP052B | EC | N | N | L | N | 10 | M | 1.06 |
| CHOP053B | EC | H | N | R | Y | 3 | F | 0.59 |
| CHOP054A | IA | H | N | R | Y | 4 | F | 0.46 |
| CHOP057A | EC | N | N | R | N | 21 | F | 1.6 |
| CHOP061A | IA | H | N | R | Y | 10 | M | 1.13 |
| CHOP062A | IA | N | N | L | N | 12 | F | 1.11 |
| CHOP063A | EC | N | N | L | N | 9 | F | 1.06 |
| CHOP064A | IA | H | N | R | Y | 6 | F | 0.94 |
| CHOP065A | IA | H | N | R | Y | 16 | M | 1.36 |
| CHOP066A | IA | H | N | R | Y | 14 | F | 1.28 |
| CHOP068B | IA | H | N | R | Y | 4 | F | 0.61 |
| CHOP069B | IA | H | N | R | Y | 11 | M | 1.11 |
| CHOP072A | IA | N | N | M | N | 14 | M | 1.65 |
| CHOP073A | IA | N | N | M | N | 20 | F | 1.54 |
| CHOP074A | IA | H | N | R | Y | 12 | M | 1.24 |
| CHOP080A | IA | N | Y | R | N | 17 | F | 1.91 |
| CHOP081A | EC | N | N | L | Y | 3 | F | 0.54 |
| CHOP082A | EC | N | N | L | N | 7 | M | 0.87 |

| | | | | | | | | |
|---|---|---|---|---|---|---|---|---|
| CHOP083A | EC | N | N | L | N | 8 | F | 1.15 |
| CHOP084A | EC | N | N | M | N | 8 | M | 0.99 |
| CHOP085A | IA | H | N | R | Y | 2 | M | 0.5 |
| CHOP086A | IA | N | Y | L | N | 6 | F | 0.81 |
| CHOP087A | IA | N | N | R | Y | 5 | M | 0.81 |
| CHOP088A | EC | N | N | L | N | 8 | F | 1.25 |
| CHOP089A | IA | N | N | L | N | 10 | M | 0.93 |
| CHOP090A | APC | N | N | M | N | 27 | M | 2.02 |
| CHOP091A | IA | N | Y | L | N | 18 | M | 2.08 |
| CHOP094A | IA | N | N | L | Y | 13 | M | 1.2 |
| CHOP097A | IA | H | N | R | Y | 5 | F | 0.67 |
| CHOP100A | IA | N | N | L | N | 19 | M | 1.66 |
| CHOP102A | IA | N | Y | R | N | 25 | F | 1.6 |
| CHOP103A | IA | N | N | R | N | 22 | M | 1.86 |
| CHOP105A | IA | H | N | R | Y | 8 | M | 0.95 |
| CHOP108A | IA | H | N | R | Y | 8 | M | 0.93 |
| CHOP109B | EC | N | N | R | N | 4 | F | 0.65 |
| CHOP114A | IA | H | N | R | Y | 15 | M | 1.75 |
| CHOP118A | EC | N | N | M | Y | 5 | M | 0.77 |
| CHOP119A | IA | N | N | L | N | 4 | F | 0.76 |
| CHOP121A | EC | N | N | M | Y | 5 | M | 0.75 |
| CHOP122A | IA | H | Y | R | Y | 15 | M | 1.51 |
| CHOP128A | IA | N | N | M | N | 10 | F | 0.93 |
| CHOP134A | EC | N | N | L | Y | 4 | F | 0.63 |
| CHOP135A | EC | N | Y | L | N | 6 | M | 0.77 |
| CHOP139A | IA | N | N | L | Y | 9 | M | 1.18 |
| CHOP143A | EC | N | N | M | N | 4 | F | 0.61 |
| CHOP144C | EC | N | Y | M | Y | 4 | F | 0.75 |
| CHOP145A | IA | N | N | L | N | 19 | F | 1.51 |
| CHOP148A | IA | N | N | L | N | 4 | M | 0.73 |
| CHOP152A | IA | N | N | M | N | 17 | M | 1.89 |
| CHOP155A | IA | N | N | M | N | 16 | M | 1.83 |
| CHOP159A | IA | N | N | M | N | 24 | F | 1.9 |
| CHOP161A | EC | N | N | M | N | 14 | F | 1.65 |
| CHOP166A | IA | H | N | R | Y | 15 | M | 1.41 |
| CHOP187A | IA | N | N | L | N | 42 | F | 1.64 |
| CHOP188A | IA | N | N | L | N | 17 | M | 1.51 |
| CHOP191A | EC | N | N | L | N | 16 | F | 1.25 |
| CHOP203A | IA | N | N | R | Y | 16 | M | 1.93 |
| CHOP204A | IA | N | N | L | N | 17 | F | 1.51 |

## 2. PC CMR-derived vessel flow rates for the 100 patient cohort

Table 12.2 presents the flow data derived from PC CMR for all 100 patients. A dash ('-') indicates that no data were acquired for that particular entry while 'N/A' (not applicable) is used when a vessel (LSVC or Az) is not present for a particular patient.

The reported values for collateral flow (Ao-[IVC+SVC+LSVC+Az]) and fenestration flow ([IVC+SVC+Az+LSVC]-[LPA+RPA]) were derived from these values. Thus, when one of these values was represented as a dash, the value could not be calculated for that particular patient.

**Table 12.2 Vessel flow rates (non-normalized) for all 100 patients.**

| | Ao (L/min) | IVC (L/min) | SVC (L/min) | LPA (L/min) | RPA (L/min) | LSVC (L/min) | AZ (L/min) |
|---|---|---|---|---|---|---|---|
| CHOP_M10 | 3.75 | 0.45 | 2.05 | 2.71 | 0.5 | N/A | 0.35 |
| CHOP_M11 | 3.92 | 1.26 | 1.3 | 0.7 | 1.21 | N/A | N/A |
| CHOP_M12 | 1.79 | 0.68 | 0.24 | 0.7 | 0.42 | 0.26 | N/A |
| CHOP_M7 | 4.29 | 0.41 | 1.57 | 2.3 | 1.23 | 0.77 | 1.2 |
| CHOP_M8 | 3.59 | 0.31 | 0.73 | 1.48 | 1.23 | 1.04 | 1.21 |
| CHOP001B | 2 | 1.56 | 0.62 | 0.7 | 1.1 | N/A | N/A |
| CHOP004B | 5.63 | 3.06 | 1.04 | 2.13 | 1.65 | N/A | N/A |
| CHOP005B | 4.54 | 3.59 | 0.98 | 2.55 | - | N/A | N/A |
| CHOP007B | 8.44 | 4.89 | 0.94 | 1.56 | 4.03 | 1.06 | N/A |
| CHOP008A | - | 2.06 | 1.13 | 1.69 | 1.65 | N/A | N/A |
| CHOP010A | - | 3.79 | 1.26 | 4.19 | 3.09 | 1.32 | N/A |
| CHOP013A | - | 2.62 | 0.41 | 1.3 | 1.2 | 0.39 | N/A |
| CHOP014A | - | 1.35 | 0.87 | 1.28 | 1.23 | N/A | N/A |
| CHOP016A | - | 1.85 | 1.42 | 0.83 | - | N/A | N/A |
| CHOP017B | - | 2.48 | 1.26 | 0.6 | 3.11 | N/A | N/A |
| CHOP018A | 3.05 | 1.38 | 1.25 | 0.93 | 1.27 | N/A | N/A |
| CHOP019A | 5.52 | 3.54 | 1.44 | 1.93 | 2.83 | N/A | N/A |
| CHOP021A | 3.73 | 2.17 | 0.93 | 1.18 | - | N/A | N/A |
| CHOP022A | 3.41 | 1.3 | 0.81 | 1.06 | 0.84 | 0.49 | N/A |

| | | | | | | | |
|---|---|---|---|---|---|---|---|
| CHOP023A | 3.89 | 2.1 | 0.38 | 1.38 | 1.93 | N/A | 0.48 |
| CHOP024A | 2.65 | 1.58 | 0.97 | 0.85 | 1.15 | N/A | N/A |
| CHOP025A | 3.23 | 1.75 | 0.58 | 1.46 | 1.07 | 0.62 | N/A |
| CHOP026A | 3.06 | 1.03 | 1.05 | 0.98 | 1.5 | N/A | N/A |
| CHOP028A | 3.53 | 2.83 | 0.91 | 1.11 | 1.94 | N/A | N/A |
| CHOP029A | 3.95 | 2.08 | 1.47 | 0.78 | 1.51 | N/A | N/A |
| CHOP030B | 4.6 | 3.27 | 0.79 | 1.4 | 1.47 | N/A | N/A |
| CHOP031A | 3.25 | 1.43 | 1.3 | 1.04 | 1.55 | N/A | N/A |
| CHOP032A | 5.82 | 3.57 | 1.09 | 1.97 | 2.77 | N/A | N/A |
| CHOP033A | 3.42 | 2.28 | 1.52 | 1.71 | 1.4 | N/A | N/A |
| CHOP034A | 8.22 | 4.15 | 0.89 | 1.67 | 2.24 | N/A | N/A |
| CHOP035A | 5.08 | 2.29 | 1.23 | 2.26 | 1.37 | N/A | N/A |
| CHOP036A | - | 3.31 | 1.93 | 2.27 | 1.85 | N/A | N/A |
| CHOP037A | 3.81 | 1.51 | 0.92 | 0.84 | - | N/A | N/A |
| CHOP038A | - | 2.52 | 1.1 | 1.37 | 2.06 | 0.53 | N/A |
| CHOP039A | 3.94 | 2.7 | 1.75 | 1.02 | 1.1 | N/A | N/A |
| CHOP040A | 5.83 | 4.84 | 2.06 | 1.55 | 1.91 | N/A | N/A |
| CHOP041A | 4.04 | 1.81 | 0.99 | 0.84 | 1.4 | N/A | N/A |
| CHOP042B | 2.15 | 0.3 | 0.16 | 0.98 | 0.3 | 0.54 | 0.49 |
| CHOP044A | 4.43 | 3.64 | 1.81 | 2.65 | 0.72 | N/A | N/A |
| CHOP047A | 3.88 | 2.57 | 1.03 | 1.73 | 2.03 | N/A | N/A |
| CHOP049A | 9.06 | - | 1.8 | - | 3.63 | N/A | N/A |
| CHOP051B | 1.9 | 0.9 | 0.18 | 1.03 | 0.28 | 0.39 | N/A |
| CHOP052B | 5.8 | 2.07 | 1.19 | 1.42 | 1.15 | N/A | N/A |
| CHOP053B | - | 1.05 | 0.79 | 0.86 | 0.73 | N/A | N/A |
| CHOP054A | 2.1 | 1.12 | 0.92 | 0.28 | 1.08 | N/A | N/A |
| CHOP057A | 4.25 | 2.8 | 0.89 | 1.8 | 2.69 | N/A | N/A |
| CHOP061A | 5.02 | 3.15 | 1.29 | 1.53 | 1.07 | N/A | N/A |
| CHOP062A | 2.58 | 1.36 | 0.93 | 0.82 | 1.87 | N/A | N/A |
| CHOP063A | 3.68 | 2.29 | 1.18 | 1.23 | 1.25 | N/A | N/A |
| CHOP064A | 1.6 | 0.78 | 0.48 | 0.61 | 0.51 | N/A | N/A |
| CHOP065A | 3.34 | 1.94 | 0.47 | 0.78 | 1.45 | N/A | N/A |
| CHOP066A | 4.42 | 2.27 | 1.23 | 1.44 | 2.33 | N/A | N/A |
| CHOP068B | 2.33 | 1.14 | 1 | 0.52 | 0.7 | N/A | N/A |
| CHOP069B | 3.21 | 1.93 | 1.13 | 1.43 | 1.7 | N/A | N/A |
| CHOP072A | 4.58 | 3.07 | 1.57 | 2.36 | 2.14 | N/A | N/A |
| CHOP073A | 3.88 | 2.49 | 1.06 | 1.73 | 2.03 | N/A | N/A |
| CHOP074A | - | 1.91 | 0.3 | 0.48 | 0.84 | N/A | N/A |
| CHOP080A | 5.55 | 2.57 | 1.25 | 2.07 | 1.87 | 0.53 | N/A |
| CHOP081A | 3.88 | 0.34 | 1.12 | 0.52 | 0.85 | N/A | N/A |
| CHOP082A | 2.68 | 1.6 | 0.96 | 0.8 | 1.18 | N/A | N/A |
| CHOP083A | 3.8 | 2.38 | 1.06 | 1.8 | 0.78 | N/A | N/A |
| CHOP084A | 2.98 | 2.1 | 1.23 | 1.39 | 1.3 | N/A | N/A |

| | | | | | | | |
|---|---|---|---|---|---|---|---|
| CHOP085A | 1.6 | 0.65 | 0.56 | 0.42 | - | N/A | N/A |
| CHOP086A | 2.94 | 2.27 | 0.24 | 1.34 | - | 1.2 | N/A |
| CHOP087A | 2.69 | 1.22 | 0.71 | 0.68 | 1.24 | N/A | N/A |
| CHOP088A | 3.35 | 1.78 | 0.9 | 1.65 | 1.51 | N/A | N/A |
| CHOP089A | 2.9 | 2.13 | 1.08 | 1.48 | 1.72 | N/A | N/A |
| CHOP090A | - | 3.12 | 1.3 | 2.27 | 2.75 | N/A | N/A |
| CHOP091A | 5.03 | 3.53 | 1.04 | 2.24 | 2.64 | 0.69 | N/A |
| CHOP094A | 5.5 | 2.89 | 1.59 | 1.58 | 2.83 | N/A | N/A |
| CHOP097A | 2.29 | 1.52 | 0.77 | 0.5 | 1.79 | N/A | N/A |
| CHOP100A | 3.53 | 2.04 | 1.18 | 1.4 | 1.89 | N/A | N/A |
| CHOP102A | 4.67 | 3.46 | 0.55 | 2.12 | 2.99 | 0.59 | N/A |
| CHOP103A | 4.93 | 3.12 | 1.45 | 2.78 | 2.57 | N/A | N/A |
| CHOP105A | 3.86 | 1.47 | 1.5 | 0.83 | 1.65 | N/A | N/A |
| CHOP108A | 2.93 | 1.63 | 0.88 | 0.68 | 1.05 | N/A | N/A |
| CHOP109B | 2.64 | 1.07 | 1.59 | 1.15 | 1.13 | N/A | N/A |
| CHOP114A | 5.54 | 3.87 | 1.69 | 2.47 | 1.88 | N/A | N/A |
| CHOP118A | 3.26 | 0.98 | 1.25 | 0.59 | 1.15 | N/A | N/A |
| CHOP119A | 1.44 | 1.45 | 1.35 | 1.02 | 1.78 | N/A | N/A |
| CHOP121A | 2.15 | 0.89 | 1.03 | 0.76 | 0.66 | N/A | N/A |
| CHOP122A | 4.96 | 1.89 | 0.9 | 1.04 | 1.56 | 0.44 | N/A |
| CHOP128A | - | 2.13 | 1.57 | 1.52 | 2.64 | N/A | N/A |
| CHOP134A | 2.34 | 1.09 | 1.01 | 0.61 | 0.99 | N/A | N/A |
| CHOP135A | 3.16 | 1.14 | 0.75 | 0.97 | 0.94 | 0.52 | N/A |
| CHOP139A | 4.49 | 2.3 | 1.6 | 1.11 | 2.46 | N/A | N/A |
| CHOP143A | 4.69 | 0.72 | 1.14 | 2.52 | 1.09 | 0.75 | 0.82 |
| CHOP144C | 1.78 | 0.2 | 0.49 | 0.79 | 0.54 | 0.39 | 0.71 |
| CHOP145A | 3.72 | 2.13 | 0.99 | 1.52 | 2.27 | N/A | N/A |
| CHOP148A | 2.47 | 1.04 | 0.74 | 0.74 | 1.03 | N/A | N/A |
| CHOP152A | 7.69 | 4.61 | 1 | 1.21 | 3.77 | N/A | N/A |
| CHOP155A | 7.51 | 3.75* | 2.59 | 3.44 | 2.9 | N/A | N/A |
| CHOP159A | 4.1 | 2.75 | 0.98 | 1.96 | 2.08 | N/A | N/A |
| CHOP161A | 7.62 | 3.85 | 1.58 | 3.1 | 2.61 | N/A | N/A |
| CHOP166A | 5.25 | 1.42* | 2.43 | 1 | 2.85 | N/A | N/A |
| CHOP187A | 4.17 | 2.45 | 1.06 | 1.26 | 2.42 | N/A | N/A |
| CHOP188A | 5.27 | 2.24 | 1.09 | 1.87 | 1.38 | N/A | N/A |
| CHOP191A | 3.91 | 1.63 | 0.72 | 0.99 | 1.22 | N/A | N/A |
| CHOP203A | 6.65 | 3.75* | 1.45 | 2.66 | 2.95 | N/A | N/A |
| CHOP204A | 5.47 | 3.08* | 1.41 | 1.67 | 2.82 | N/A | N/A |

*Flow measurement taken from phase contrast plane in the Fontan baffle above fenestration

## 3. Time-averaged CFD Results for 100 patient cohort

Table 12.3 provides the time-averaged CFD results from the 100 patient cohort. The cardiac index (CI), indexed systemic venous flow rate ($Q_s$), and global pulmonary flow distribution (GFD) (which are all derived from flow measurements in Table 12.2) were also included since they were frequently used to compare against the CFD data. Simulation end points included hepatic flow distribution (HFD), maximum pressure drop ($\Delta P_{max}$), power loss (PL), TCPC resistance (R), and the TCPC energy dissipation index (TCPC-EDI). The derivations of all of these metrics are covered in Chapter 4.

**Table 12.3 Results from time-averaged CFD simulations for 100 patient cohort**

| | CI ($L/min/m^2$) | Qs ($L/min/m^2$) | GFD (%LPA) | HFD (%LPA) | $\Delta P_{max}$ (mmHg) | PL (mW) | R (WU) | TCPC-EDI |
|---|---|---|---|---|---|---|---|---|
| CHOP_M10 | 6.15 | 4.67 | 85 | 87 | 0.99 | 4.07 | 0.14 | 0.013 |
| CHOP_M11 | 3.81 | 2.49 | 27 | 26 | 3.01 | 5.9 | 0.42 | 0.076 |
| CHOP_M12 | 3.89 | 2.57 | 62 | 54 | 0.41 | 0.72 | 0.18 | 0.019 |
| CHOP_M7 | 3.70 | 3.41 | 65 | 100 | 0.67 | 5.59 | 0.19 | 0.025 |
| CHOP_M8 | 4.03 | 3.7 | 55 | 0 | 1.74 | 5.06 | 0.19 | 0.023 |
| CHOP001B | 1.62 | 1.77 | 39 | 44 | 0.9 | 1.94 | 0.23 | 0.058 |
| CHOP004B | 3.78 | 2.75 | 56 | 71 | 1.26 | 6.69 | 0.27 | 0.044 |
| CHOP005B | 3.01 | 3.03 | 56 | 68 | 3.31 | 17.88 | 0.58 | 0.087 |
| CHOP007B | 4.20 | 3.43 | 28 | 17 | 1.46 | 9.63 | 0.18 | 0.024 |
| CHOP008A | - | 1.64 | 46 | 53 | 0.69 | 1.33 | 0.11 | 0.031 |
| CHOP010A | - | 3.93 | 44 | 33 | 3.32 | 26.55 | 0.47 | 0.055 |
| CHOP013A | - | 1.8 | 52 | 52 | 0.93 | 3.36 | 0.25 | 0.062 |
| CHOP014A | 3.64 | 2.13 | 59 | 33 | 0.38 | 0.77 | 0.07 | 0.016 |
| CHOP016A | - | 3.94 | 25 | 3 | 5.15 | 10.5 | 0.36 | 0.042 |
| CHOP017B | 3.13 | 2.28 | 16 | 0 | 0.76 | 3.38 | 0.18 | 0.035 |

| | | | | | | | | |
|---|---|---|---|---|---|---|---|---|
| CHOP018A | 4.49 | 3.87 | 42 | 67 | 0.38 | 1.41 | 0.06 | 0.007 |
| CHOP019A | 3.29 | 2.96 | 41 | 52 | 1.75 | 7.43 | 0.23 | 0.035 |
| CHOP021A | 3.03 | 2.52 | 41 | 49 | 2.28 | 7.34 | 0.42 | 0.076 |
| CHOP022A | 3.75 | 2.86 | 49 | 33 | 0.81 | 1.7 | 0.1 | 0.016 |
| CHOP023A | 3.19 | 2.43 | 42 | 53 | 2.28 | 10.4 | 0.66 | 0.122 |
| CHOP024A | 3.58 | 3.45 | 43 | 58 | 2.02 | 3.06 | 0.16 | 0.021 |
| CHOP025A | 3.20 | 2.92 | 58 | 50 | 1.95 | 5.78 | 0.31 | 0.047 |
| CHOP026A | 3.69 | 2.51 | 40 | 79 | 2.69 | 4.66 | 0.4 | 0.073 |
| CHOP028A | 1.84 | 1.95 | 36 | 40 | 1.3 | 3.62 | 0.23 | 0.052 |
| CHOP029A | 3.66 | 3.29 | 22 | 40 | 0.93 | 3.17 | 0.12 | 0.017 |
| CHOP030B | 3.31 | 2.92 | 35 | 41 | 3.68 | 11.68 | 0.43 | 0.069 |
| CHOP031A | 3.65 | 3.07 | 40 | 78 | 0.55 | 1.58 | 0.09 | 0.013 |
| CHOP032A | 3.55 | 2.84 | 42 | 43 | 2.96 | 22.2 | 0.76 | 0.12 |
| CHOP033A | 2.59 | 2.88 | 52 | 63 | 0.51 | 2.47 | 0.1 | 0.016 |
| CHOP034A | 4.35 | 2.67 | 43 | 41 | 2.72 | 18.15 | 0.61 | 0.103 |
| CHOP035A | 7.36 | 5.1 | 62 | 21 | 1.37 | 5.08 | 0.13 | 0.011 |
| CHOP036A | 3.53 | 4.4 | 55 | 71 | 1.22 | 7.57 | 0.15 | 0.015 |
| CHOP037A | 3.81 | 2.43 | 35 | 46 | 4.32 | 4.04 | 0.31 | 0.057 |
| CHOP038A | 2.41 | 2.55 | 40 | 22 | 1.46 | 6.57 | 0.27 | 0.05 |
| CHOP039A | 3.86 | 4.36 | 48 | 52 | 3.11 | 7.75 | 0.23 | 0.019 |
| CHOP040A | 2.84 | 3.37 | 37 | 50 | 1.9 | 15.3 | 0.41 | 0.04 |
| CHOP041A | 2.68 | 1.85 | 37 | 21 | 0.34 | 1.17 | 0.1 | 0.025 |
| CHOP042B | 3.47 | 2.4 | 77 | 43 | 2.26 | 1.78 | 0.23 | 0.042 |
| CHOP044A | 2.87 | 2.87 | 49 | 43 | 2.9 | 17.13 | 0.5 | 0.078 |
| CHOP047A | 2.11 | 1.96 | 46 | 45 | 0.49 | 1.77 | 0.11 | 0.026 |
| CHOP049A | 6.97 | 6.97 | 60 | 77 | 4.09 | 40.39 | 0.28 | 0.019 |
| CHOP051B | 3.02 | 2.33 | 78 | 58 | 0.99 | 2 | 0.26 | 0.051 |
| CHOP052B | 5.47 | 3.08 | 44 | 21 | 0.94 | 3.35 | 0.16 | 0.022 |
| CHOP053B | 4.01 | 3.12 | 54 | 38 | 0.97 | 1.33 | 0.09 | 0.015 |
| CHOP054A | 4.48 | 4.43 | 21 | 17 | 0.28 | 0.66 | 0.04 | 0.003 |
| CHOP057A | 2.66 | 2.31 | 40 | 48 | 0.71 | 3.21 | 0.17 | 0.033 |
| CHOP061A | 4.45 | 3.93 | 59 | 52 | 1.84 | 9.56 | 0.24 | 0.028 |
| CHOP062A | 2.57 | 2.06 | 30 | 43 | 0.33 | 0.85 | 0.08 | 0.018 |
| CHOP063A | 3.47 | 3.27 | 50 | 71 | 1.39 | 5.76 | 0.23 | 0.032 |
| CHOP064A | 1.70 | 1.34 | 55 | 82 | 0.28 | 0.37 | 0.1 | 0.033 |
| CHOP065A | 2.46 | 1.77 | 35 | 39 | 0.13 | 0.47 | 0.05 | 0.013 |
| CHOP066A | 3.45 | 2.73 | 38 | 17 | 0.76 | 2.53 | 0.16 | 0.02 |
| CHOP068B | 3.82 | 3.51 | 43 | 41 | 1.96 | 4.57 | 0.28 | 0.035 |
| CHOP069B | 2.90 | 2.76 | 46 | 65 | 1.23 | 2.24 | 0.12 | 0.02 |
| CHOP072A | 2.78 | 2.81 | 52 | 44 | 3.06 | 18.06 | 0.63 | 0.1 |
| CHOP073A | 2.52 | 2.31 | 46 | 60 | 0.27 | 1.39 | 0.08 | 0.015 |
| CHOP074A | - | 1.78 | 37 | 60 | 0.5 | 1.31 | 0.15 | 0.038 |
| CHOP080A | 2.91 | 2.28 | 53 | 29 | 2.4 | 11.8 | 0.54 | 0.107 |

| | | | | | | | | |
|---|---|---|---|---|---|---|---|---|
| CHOP081A | 7.18 | 2.7 | 38 | 3 | 0.22 | 0.58 | 0.06 | 0.011 |
| CHOP082A | 3.08 | 2.94 | 40 | 57 | 0.4 | 1.38 | 0.08 | 0.013 |
| CHOP083A | 3.30 | 2.99 | 70 | 48 | 1.58 | 5.7 | 0.25 | 0.038 |
| CHOP084A | 3.01 | 3.36 | 52 | 72 | 0.63 | 1.41 | 0.06 | 0.008 |
| CHOP085A | 3.20 | 2.42 | 49 | 35 | 1.79 | 1.66 | 0.26 | 0.048 |
| CHOP086A | 3.63 | 4.58 | 36 | 4 | 1.89 | 7.63 | 0.2 | 0.02 |
| CHOP087A | 3.30 | 2.38 | 35 | 39 | 0.86 | 2.19 | 0.22 | 0.041 |
| CHOP088A | 2.68 | 2.14 | 52 | 27 | 1.15 | 4.2 | 0.33 | 0.069 |
| CHOP089A | 3.12 | 3.45 | 46 | 61 | 0.49 | 1.94 | 0.08 | 0.01 |
| CHOP090A | - | 2.19 | 45 | 74 | 0.24 | 1.28 | 0.06 | 0.012 |
| CHOP091A | 2.42 | 2.53 | 46 | 33 | 0.37 | 5.25 | 0.18 | 0.032 |
| CHOP094A | 4.58 | 3.73 | 36 | 45 | 1.69 | 9.09 | 0.24 | 0.03 |
| CHOP097A | 3.41 | 3.42 | 22 | 30 | 3.05 | 2.63 | 0.15 | 0.02 |
| CHOP100A | 2.13 | 1.94 | 43 | 13 | 0.2 | 0.95 | 0.07 | 0.016 |
| CHOP102A | 2.92 | 2.88 | 42 | 31 | 1.09 | 6.32 | 0.22 | 0.034 |
| CHOP103A | 2.65 | 2.46 | 52 | 76 | 2.96 | 18.18 | 0.72 | 0.134 |
| CHOP105A | 4.06 | 3.13 | 33 | 44 | 1.05 | 2.56 | 0.12 | 0.018 |
| CHOP108A | 3.15 | 2.7 | 39 | 42 | 1.34 | 3.7 | 0.25 | 0.041 |
| CHOP109B | 4.06 | 4.09 | 51 | 5 | 1.57 | 3.2 | 0.13 | 0.015 |
| CHOP114A | 3.17 | 3.18 | 44 | 49 | 2.38 | 11.62 | 0.3 | 0.042 |
| CHOP118A | 4.23 | 2.9 | 27 | 44 | 0.45 | 1.26 | 0.09 | 0.014 |
| CHOP119A | 3.68 | 3.68 | 36 | 1 | 1.02 | 3.14 | 0.14 | 0.017 |
| CHOP121A | 2.87 | 2.56 | 53 | 38 | 1.45 | 2.09 | 0.19 | 0.034 |
| CHOP122A | 3.28 | 2.14 | 40 | 30 | 1.61 | 3.88 | 0.34 | 0.053 |
| CHOP128A | - | 3.98 | 37 | 60 | 0.47 | 1.44 | 0.05 | 0.005 |
| CHOP134A | 3.72 | 3.33 | 38 | 28 | 1.03 | 1.84 | 0.12 | 0.016 |
| CHOP135A | 4.10 | 3.13 | 39 | 30 | 1.79 | 4.32 | 0.26 | 0.037 |
| CHOP139A | 3.81 | 3.31 | 29 | 49 | 0.74 | 3.06 | 0.09 | 0.015 |
| CHOP143A | 7.68 | 5.62 | 70 | 12 | 8.6 | 30 | 0.71 | 0.056 |
| CHOP144C | 2.37 | 2.39 | 59 | 0 | 1.07 | 1.88 | 0.2 | 0.038 |
| CHOP145A | 2.46 | 2.07 | 40 | 61 | 0.76 | 3.37 | 0.24 | 0.052 |
| CHOP148A | 3.39 | 2.44 | 42 | 39 | 0.83 | 1.25 | 0.13 | 0.024 |
| CHOP152A | 4.07 | 2.97 | 24 | 36 | 1.23 | 8.82 | 0.25 | 0.036 |
| CHOP155A | 3.85 | 3.85 | 54 | 56 | 0.92 | 30 | 0.55 | 0.059 |
| CHOP159A | 2.16 | 1.96 | 48 | 57 | 1.12 | 5.17 | 0.32 | 0.073 |
| CHOP161A | 4.62 | 3.29 | 54 | 66 | 1.5 | 11.28 | 0.28 | 0.039 |
| CHOP166A | 3.72 | 3.36 | 26 | 13 | 2.45 | 6.12 | 0.17 | 0.023 |
| CHOP187A | 2.54 | 2.14 | 34 | 41 | 0.47 | 1.55 | 0.09 | 0.02 |
| CHOP188A | 3.49 | 2.21 | 58 | 50 | 0.44 | 0.82 | 0.05 | 0.01 |
| CHOP191A | 3.13 | 1.88 | 45 | 65 | 0.2 | 0.45 | 0.05 | 0.011 |
| CHOP203A | 3.45 | 2.69 | 47 | 46 | 0.28 | 1.91 | 0.06 | 0.01 |
| CHOP204A | 3.62 | 2.97 | 37 | 47 | 0.86 | 6.73 | 0.23 | 0.035 |

**Table 12.4 Comparison for single vs. bilateral SVC patients (N=100)**

| | Bilateral SVC (Y or N) | GFD (%LPA) | HFD (%LPA) | $\Delta P_{max}$ (mmHg) | PL (mW) | R (WU) | TCPC-EDI |
|---|---|---|---|---|---|---|---|
| CHOP_M10 | N | 85 | 87 | 0.99 | 4.07 | 0.14 | 0.013 |
| CHOP_M11 | N | 27 | 26 | 3.01 | 5.9 | 0.42 | 0.076 |
| CHOP001B | N | 39 | 48 | 0.4 | 0.35 | 0.04 | 0.01 |
| CHOP004B | N | 56 | 71 | 1.26 | 6.69 | 0.27 | 0.044 |
| CHOP005B | N | 56 | 68 | 3.31 | 17.88 | 0.58 | 0.087 |
| CHOP008A | N | 46 | 53 | 0.69 | 1.33 | 0.11 | 0.031 |
| CHOP010A | N | 44 | 33 | 3.32 | 26.55 | 0.47 | 0.055 |
| CHOP013A | N | 52 | 52 | 0.93 | 3.36 | 0.25 | 0.062 |
| CHOP014A | N | 59 | 33 | 0.38 | 0.77 | 0.07 | 0.016 |
| CHOP016A | N | 25 | 3 | 5.15 | 10.5 | 0.36 | 0.042 |
| CHOP017B | N | 16 | 0 | 0.76 | 3.38 | 0.18 | 0.035 |
| CHOP018A | N | 42 | 67 | 0.38 | 1.41 | 0.06 | 0.007 |
| CHOP019A | N | 41 | 52 | 1.75 | 7.43 | 0.23 | 0.035 |
| CHOP021A | N | 41 | 49 | 2.28 | 7.34 | 0.42 | 0.076 |
| CHOP023A | N | 42 | 53 | 2.28 | 10.4 | 0.66 | 0.122 |
| CHOP024A | N | 43 | 58 | 2.02 | 3.06 | 0.16 | 0.021 |
| CHOP026A | N | 40 | 79 | 2.69 | 4.66 | 0.4 | 0.073 |
| CHOP028A | N | 36 | 40 | 1.3 | 3.62 | 0.23 | 0.052 |
| CHOP029A | N | 22 | 40 | 0.93 | 3.17 | 0.12 | 0.017 |
| CHOP030B | N | 35 | 41 | 3.68 | 11.68 | 0.43 | 0.069 |
| CHOP031A | N | 40 | 78 | 0.55 | 1.58 | 0.09 | 0.013 |
| CHOP032A | N | 42 | 43 | 2.96 | 22.2 | 0.76 | 0.12 |
| CHOP033A | N | 52 | 63 | 0.51 | 2.47 | 0.1 | 0.016 |
| CHOP034A | N | 43 | 41 | 2.72 | 18.15 | 0.61 | 0.103 |
| CHOP035A | N | 62 | 21 | 1.37 | 5.08 | 0.13 | 0.011 |
| CHOP036A | N | 55 | 71 | 1.22 | 7.57 | 0.15 | 0.015 |
| CHOP037A | N | 35 | 46 | 4.32 | 4.04 | 0.31 | 0.057 |
| CHOP038A | N | 40 | 22 | 1.46 | 6.57 | 0.27 | 0.05 |
| CHOP039A | N | 48 | 52 | 3.11 | 7.75 | 0.23 | 0.019 |
| CHOP040A | N | 37 | 50 | 1.9 | 15.3 | 0.41 | 0.04 |
| CHOP041A | N | 37 | 21 | 0.34 | 1.17 | 0.1 | 0.025 |
| CHOP044A | N | 49 | 43 | 2.9 | 17.13 | 0.5 | 0.078 |
| CHOP047A | N | 46 | 45 | 0.49 | 1.77 | 0.11 | 0.026 |
| CHOP049A | N | 60 | 77 | 4.09 | 40.39 | 0.28 | 0.019 |
| CHOP052B | N | 44 | 21 | 0.94 | 3.49 | 0.16 | 0.023 |
| CHOP053B | N | 54 | 38 | 0.97 | 1.33 | 0.09 | 0.015 |

| | | | | | | | |
|---|---|---|---|---|---|---|---|
| CHOP054A | N | 21 | 17 | 0.28 | 0.66 | 0.04 | 3.00E-03 |
| CHOP057A | N | 40 | 48 | 0.71 | 3.21 | 0.17 | 0.033 |
| CHOP061A | N | 59 | 52 | 1.84 | 9.56 | 0.24 | 0.028 |
| CHOP062A | N | 30 | 43 | 0.33 | 0.85 | 0.08 | 0.018 |
| CHOP063A | N | 50 | 71 | 1.39 | 5.76 | 0.23 | 0.032 |
| CHOP064A | N | 55 | 82 | 0.28 | 0.37 | 0.1 | 0.033 |
| CHOP065A | N | 35 | 39 | 0.13 | 0.47 | 0.05 | 0.013 |
| CHOP066A | N | 38 | 17 | 0.76 | 2.53 | 0.16 | 0.02 |
| CHOP068B | N | 43 | 41 | 1.96 | 4.57 | 0.28 | 0.035 |
| CHOP069B | N | 46 | 65 | 1.23 | 2.24 | 0.12 | 0.02 |
| CHOP072A | N | 52 | 44 | 3.06 | 18.06 | 0.63 | 0.1 |
| CHOP073A | N | 46 | 60 | 0.27 | 1.39 | 0.08 | 0.015 |
| CHOP074A | N | 37 | 60 | 0.5 | 1.31 | 0.15 | 0.038 |
| CHOP081A | N | 38 | 3 | 0.22 | 0.58 | 0.06 | 0.011 |
| CHOP082A | N | 40 | 57 | 0.4 | 1.38 | 0.08 | 0.013 |
| CHOP083A | N | 70 | 48 | 1.58 | 5.7 | 0.25 | 0.038 |
| CHOP084A | N | 52 | 72 | 0.63 | 1.41 | 0.06 | 0.008 |
| CHOP085A | N | 49 | 35 | 1.79 | 1.66 | 0.26 | 0.048 |
| CHOP087A | N | 35 | 39 | 0.86 | 2.19 | 0.22 | 0.041 |
| CHOP088A | N | 52 | 27 | 1.15 | 4.2 | 0.33 | 0.069 |
| CHOP089A | N | 46 | 61 | 0.49 | 1.94 | 0.08 | 0.01 |
| CHOP090A | N | 45 | 74 | 0.24 | 1.28 | 0.06 | 0.012 |
| CHOP094A | N | 36 | 45 | 1.69 | 9.09 | 0.24 | 0.03 |
| CHOP097A | N | 22 | 30 | 3.05 | 2.63 | 0.15 | 0.02 |
| CHOP100A | N | 43 | 13 | 0.2 | 0.95 | 0.07 | 0.016 |
| CHOP103A | N | 52 | 76 | 2.96 | 18.18 | 0.72 | 0.134 |
| CHOP105A | N | 33 | 44 | 1.05 | 2.56 | 0.12 | 0.018 |
| CHOP108A | N | 39 | 42 | 1.34 | 3.7 | 0.25 | 0.041 |
| CHOP109B | N | 51 | 5 | 1.57 | 3.2 | 0.13 | 0.015 |
| CHOP114A | N | 44 | 49 | 2.38 | 11.62 | 0.3 | 0.042 |
| CHOP118A | N | 27 | 44 | 0.45 | 1.26 | 0.09 | 0.014 |
| CHOP119A | N | 36 | 1 | 1.02 | 3.14 | 0.14 | 0.017 |
| CHOP121A | N | 53 | 38 | 1.45 | 2.09 | 0.19 | 0.034 |
| CHOP128A | N | 37 | 60 | 0.47 | 1.44 | 0.05 | 0.005 |
| CHOP134A | N | 38 | 28 | 1.03 | 1.84 | 0.12 | 0.016 |
| CHOP139A | N | 29 | 49 | 0.74 | 2.75 | 0.09 | 0.013 |
| CHOP143A | N | 70 | 12.25 | 8.6 | 30 | 0.71 | 0.056 |
| CHOP145A | N | 40 | 61 | 0.76 | 3.37 | 0.24 | 0.052 |
| CHOP148A | N | 42 | 39 | 0.83 | 1.25 | 0.13 | 0.024 |
| CHOP152A | N | 24 | 36 | 1.23 | 9.39 | 0.25 | 0.039 |
| CHOP155A | N | 54 | 56 | 0.92 | 30 | 0.65 | 0.067 |
| CHOP159A | N | 48 | 57 | 1.12 | 5.17 | 0.32 | 0.073 |

| | | | | | | | |
|---|---|---|---|---|---|---|---|
| CHOP161A | N | 54 | 66 | 1.5 | 11.28 | 0.28 | 0.039 |
| CHOP166A | N | 26 | 13 | 2.45 | 6.12 | 0.17 | 0.023 |
| CHOP187A | N | 34 | 41 | 0.47 | 1.55 | 0.09 | 0.02 |
| CHOP188A | N | 58 | 50 | 0.44 | 0.82 | 0.05 | 0.01 |
| CHOP191A | N | 45 | 65 | 0.2 | 0.45 | 0.05 | 0.011 |
| CHOP203A | N | 47 | 46 | 0.28 | 1.91 | 0.06 | 0.01 |
| CHOP204A | N | 37 | 47 | 0.86 | 6.73 | 0.23 | 0.035 |
| CHOP_M12 | Y | 62 | 54 | 0.41 | 0.72 | 0.18 | 0.019 |
| CHOP_M7 | Y | 35 | 0 | 0.67 | 5.59 | 0.19 | 0.025 |
| CHOP_M8 | Y | 55 | 0 | 1.74 | 5.06 | 0.19 | 0.023 |
| CHOP007B | Y | 28 | 17 | 1.46 | 9.63 | 0.18 | 0.024 |
| CHOP022A | Y | 49 | 33 | 0.81 | 1.7 | 0.1 | 0.016 |
| CHOP025A | Y | 58 | 50 | 1.95 | 5.78 | 0.31 | 0.047 |
| CHOP042B | Y | 77 | 43 | 2.26 | 1.78 | 0.23 | 0.042 |
| CHOP051B | Y | 78 | 58 | 0.99 | 2 | 0.26 | 0.051 |
| CHOP080A | Y | 53 | 29 | 2.4 | 11.8 | 0.54 | 0.107 |
| CHOP086A | Y | 36 | 4 | 1.89 | 7.63 | 0.2 | 0.02 |
| CHOP091A | Y | 46 | 33 | 0.37 | 5.25 | 0.18 | 0.032 |
| CHOP102A | Y | 42 | 31 | 1.09 | 6.32 | 0.22 | 0.034 |
| CHOP122A | Y | 40 | 30 | 1.61 | 3.88 | 0.34 | 0.053 |
| CHOP135A | Y | 39 | 30 | 1.79 | 4.32 | 0.26 | 0.037 |
| CHOP144C | Y | 59 | 0 | 1.07 | 1.88 | 0.2 | 0.038 |

*Values reported with respect to the RPA instead of LPA because azygos vein was on the right.

**Table 12.5 TCPC Hemodynamocs for extracardiac and intra-atrial patients (N=97)**

| | EC or IA | Age (yrs) | BSA ($m^2$) | Cardiac Index (L/min /$m^2$) | GFD (%LPA) | HFD (%LPA) | $\Delta P_{max}$ (mmHg) | R (WU) | TCPC-EDI |
|---|---|---|---|---|---|---|---|---|---|
| CHOP_M12 | EC | 2 | 0.46 | 3.89 | 62 | 54 | 0.41 | 0.18 | 0.019 |
| CHOP_M7 | EC | 11 | 1.16 | 3.70 | 65 | 100 | 0.67 | 0.19 | 0.025 |
| CHOP_M8 | EC | 6 | 0.89 | 4.03 | 55 | 0 | 1.74 | 0.19 | 0.023 |
| CHOP051B | EC | 4 | 0.63 | 3.02 | 78 | 58 | 0.99 | 0.26 | 0.051 |
| CHOP053B | EC | 3 | 0.59 | 4.01 | 54 | 38 | 0.97 | 0.09 | 0.015 |
| CHOP118A | EC | 5 | 0.77 | 4.23 | 27 | 44 | 0.45 | 0.09 | 0.014 |
| CHOP143A | EC | 4 | 0.61 | 7.68 | 70 | 12 | 8.6 | 0.71 | 0.056 |
| CHOP144C | EC | 4 | 0.75 | 2.37 | 59 | 0 | 1.07 | 0.2 | 0.038 |
| CHOP161A | EC | 14 | 1.65 | 4.62 | 54 | 66 | 1.5 | 0.28 | 0.039 |
| CHOP191A | EC | 16 | 1.25 | 3.13 | 45 | 65 | 0.2 | 0.05 | 0.011 |
| CHOP013A | EC | 16 | 1.9 | 1.80 | 52 | 52 | 0.93 | 0.25 | 0.062 |
| CHOP014A | EC | 9 | 1.04 | 3.64 | 59 | 33 | 0.38 | 0.07 | 0.016 |
| CHOP016A | EC | 6 | 0.83 | 3.94 | 25 | 3 | 5.15 | 0.36 | 0.042 |
| CHOP017B | EC | 15 | 1.64 | 3.13 | 16 | 0 | 0.76 | 0.18 | 0.035 |
| CHOP022A | EC | 7 | 0.91 | 3.75 | 49 | 33 | 0.81 | 0.1 | 0.016 |
| CHOP025A | EC | 9 | 1.01 | 3.20 | 58 | 50 | 1.95 | 0.31 | 0.047 |
| CHOP035A | EC | 8 | 0.69 | 7.36 | 62 | 21 | 1.37 | 0.13 | 0.011 |
| CHOP038A | EC | 18 | 1.63 | 2.41 | 40 | 22 | 1.46 | 0.27 | 0.05 |
| CHOP042B | EC | 3 | 0.62 | 3.47 | 77 | 43 | 2.26 | 0.23 | 0.042 |
| CHOP057A | EC | 21 | 1.6 | 2.66 | 40 | 48 | 0.71 | 0.17 | 0.033 |
| CHOP063A | EC | 9 | 1.06 | 3.47 | 50 | 71 | 1.39 | 0.23 | 0.032 |
| CHOP109B | EC | 4 | 0.65 | 4.06 | 51 | 5 | 1.57 | 0.13 | 0.015 |
| CHOP121A | EC | 5 | 0.75 | 2.87 | 53 | 38 | 1.45 | 0.19 | 0.034 |
| CHOP134A | EC | 4 | 0.63 | 3.72 | 38 | 28 | 1.03 | 0.12 | 0.016 |
| CHOP135A | EC | 6 | 0.77 | 4.10 | 39 | 30 | 1.79 | 0.26 | 0.037 |
| CHOP052B | EC | 10 | 1.06 | 5.47 | 44 | 21 | 0.94 | 0.16 | 0.023 |
| CHOP081A | EC | 3 | 0.54 | 7.18 | 38 | 3 | 0.22 | 0.06 | 0.011 |
| CHOP082A | EC | 7 | 0.87 | 3.08 | 40 | 57 | 0.4 | 0.08 | 0.013 |
| CHOP083A | EC | 8 | 1.15 | 3.30 | 70 | 48 | 1.58 | 0.25 | 0.038 |
| CHOP084A | EC | 8 | 0.99 | 3.01 | 52 | 72 | 0.63 | 0.06 | 0.008 |
| CHOP086A | EC | 6 | 0.81 | 3.63 | 36 | 4 | 1.89 | 0.2 | 0.02 |
| CHOP088A | EC | 8 | 1.25 | 2.68 | 52 | 27 | 1.15 | 0.33 | 0.069 |
| CHOP_M10 | EC | 3 | 0.61 | 6.15 | 85 | 87 | 0.99 | 0.14 | 0.013 |
| CHOP_M11 | IA | 10 | 1.03 | 3.81 | 27 | 26 | 3.01 | 0.42 | 0.076 |
| CHOP001B | IA | 16 | 1.23 | 1.62 | 39 | 48 | 0.4 | 0.04 | 0.01 |
| CHOP004B | IA | 17 | 1.49 | 3.78 | 56 | 71 | 1.26 | 0.27 | 0.044 |
| CHOP005B | IA | 19 | 1.51 | 3.01 | 56 | 68 | 3.31 | 0.58 | 0.087 |
| CHOP007B | IA | 18 | 2.01 | 4.20 | 28 | 17 | 1.46 | 0.18 | 0.024 |

| | | | | | | | | | |
|---|---|---|---|---|---|---|---|---|---|
| CHOP008A | IA | 15 | 1.94 | 1.64 | 46 | 53 | 0.69 | 0.11 | 0.031 |
| CHOP010A | IA | 15 | 1.62 | 3.93 | 44 | 33 | 3.32 | 0.47 | 0.055 |
| CHOP023A | IA | 12 | 1.22 | 3.19 | 42 | 53 | 2.28 | 0.66 | 0.122 |
| CHOP024A | IA | 7 | 0.74 | 3.58 | 43 | 58 | 2.02 | 0.16 | 0.021 |
| CHOP028A | IA | 18 | 1.92 | 1.84 | 36 | 40 | 1.3 | 0.23 | 0.052 |
| CHOP030B | IA | 21 | 1.39 | 3.31 | 35 | 41 | 3.68 | 0.43 | 0.069 |
| CHOP032A | IA | 18 | 1.64 | 3.55 | 42 | 43 | 2.96 | 0.76 | 0.12 |
| CHOP033A | IA | 10 | 1.32 | 2.59 | 52 | 63 | 0.51 | 0.1 | 0.016 |
| CHOP034A | IA | 14 | 1.89 | 4.35 | 43 | 41 | 2.72 | 0.61 | 0.103 |
| CHOP036A | IA | 11 | 1.19 | 3.53 | 55 | 71 | 1.22 | 0.15 | 0.015 |
| CHOP037A | IA | 10 | 1 | 3.81 | 35 | 46 | 4.32 | 0.31 | 0.057 |
| CHOP041A | IA | 14 | 1.51 | 2.68 | 37 | 21 | 0.34 | 0.1 | 0.025 |
| CHOP064A | IA | 6 | 0.94 | 1.70 | 55 | 82 | 0.28 | 0.1 | 0.033 |
| CHOP065A | IA | 16 | 1.36 | 2.46 | 35 | 39 | 0.13 | 0.05 | 0.013 |
| CHOP073A | IA | 20 | 1.54 | 2.52 | 46 | 60 | 0.27 | 0.08 | 0.015 |
| CHOP091A | IA | 18 | 2.08 | 2.42 | 46 | 33 | 0.37 | 0.18 | 0.032 |
| CHOP100A | IA | 19 | 1.66 | 2.13 | 43 | 13 | 0.2 | 0.07 | 0.016 |
| CHOP102A | IA | 25 | 1.6 | 2.92 | 42 | 31 | 1.09 | 0.22 | 0.034 |
| CHOP103A | IA | 22 | 1.86 | 2.65 | 52 | 76 | 2.96 | 0.72 | 0.134 |
| CHOP128A | IA | 10 | 0.93 | 3.97 | 37 | 60 | 0.47 | 0.05 | 0.005 |
| CHOP145A | IA | 19 | 1.51 | 2.46 | 40 | 61 | 0.76 | 0.24 | 0.052 |
| CHOP148A | IA | 4 | 0.73 | 3.39 | 42 | 39 | 0.83 | 0.13 | 0.024 |
| CHOP152A | IA | 17 | 1.89 | 4.07 | 24 | 36 | 1.23 | 0.25 | 0.039 |
| CHOP155A | IA | 16 | 1.95 | 3.85 | 54 | 56 | 0.92 | 0.65 | 0.067 |
| CHOP159A | IA | 24 | 1.9 | 2.16 | 48 | 57 | 1.12 | 0.32 | 0.073 |
| CHOP166A | IA | 15 | 1.41 | 3.72 | 26 | 13 | 2.45 | 0.17 | 0.023 |
| CHOP187A | IA | 42 | 1.64 | 2.54 | 34 | 41 | 0.47 | 0.09 | 0.02 |
| CHOP188A | IA | 17 | 1.51 | 3.49 | 58 | 50 | 0.44 | 0.05 | 0.01 |
| CHOP203A | IA | 16 | 1.93 | 3.45 | 47 | 46 | 0.28 | 0.06 | 0.01 |
| CHOP204A | IA | 17 | 1.51 | 3.62 | 37 | 47 | 0.86 | 0.23 | 0.035 |
| CHOP019A | IA | 14 | 1.68 | 3.29 | 41 | 52 | 1.75 | 0.23 | 0.035 |
| CHOP021A | IA | 11 | 1.23 | 3.03 | 41 | 49 | 2.28 | 0.42 | 0.076 |
| CHOP018A | IA | 7 | 0.68 | 4.49 | 42 | 67 | 0.38 | 0.06 | 0.007 |
| CHOP026A | IA | 6 | 0.83 | 3.69 | 40 | 79 | 2.69 | 0.4 | 0.073 |
| CHOP029A | IA | 9 | 1.08 | 3.66 | 22 | 40 | 0.93 | 0.12 | 0.017 |
| CHOP031A | IA | 7 | 0.89 | 3.65 | 40 | 78 | 0.55 | 0.09 | 0.013 |
| CHOP039A | IA | 10 | 1.02 | 3.86 | 48 | 52 | 3.11 | 0.23 | 0.019 |
| CHOP040A | IA | 19 | 2.05 | 2.84 | 37 | 50 | 1.9 | 0.41 | 0.04 |
| CHOP049A | IA | 19 | 1.3 | 6.97 | 60 | 77 | 4.09 | 0.28 | 0.019 |
| CHOP054A | IA | 4 | 0.46 | 4.48 | 21 | 17 | 0.28 | 0.04 | 3.00E-03 |
| CHOP061A | IA | 10 | 1.13 | 4.45 | 59 | 52 | 1.84 | 0.24 | 0.028 |
| CHOP062A | IA | 12 | 1.11 | 2.57 | 30 | 43 | 0.33 | 0.08 | 0.018 |

| | | | | | | | | | |
|---|---|---|---|---|---|---|---|---|---|
| CHOP066A | IA | 14 | 1.28 | 3.45 | 38 | 17 | 0.76 | 0.16 | 0.02 |
| CHOP068B | IA | 4 | 0.61 | 3.82 | 43 | 41 | 1.96 | 0.28 | 0.035 |
| CHOP069B | IA | 11 | 1.11 | 2.90 | 46 | 65 | 1.23 | 0.12 | 0.02 |
| CHOP072A | IA | 14 | 1.65 | 2.78 | 52 | 44 | 3.06 | 0.63 | 0.1 |
| CHOP074A | IA | 12 | 1.24 | 1.78 | 37 | 60 | 0.5 | 0.15 | 0.038 |
| CHOP080A | IA | 17 | 1.91 | 2.91 | 53 | 29 | 2.4 | 0.54 | 0.107 |
| CHOP085A | IA | 2 | 0.5 | 3.20 | 49 | 35 | 1.79 | 0.26 | 0.048 |
| CHOP087A | IA | 5 | 0.81 | 3.30 | 35 | 39 | 0.86 | 0.22 | 0.041 |
| CHOP089A | IA | 10 | 0.93 | 3.12 | 46 | 61 | 0.49 | 0.08 | 0.01 |
| CHOP094A | IA | 13 | 1.2 | 4.58 | 36 | 45 | 1.69 | 0.24 | 0.03 |
| CHOP097A | IA | 5 | 0.67 | 3.41 | 22 | 30 | 3.05 | 0.15 | 0.02 |
| CHOP105A | IA | 8 | 0.95 | 4.06 | 33 | 44 | 1.05 | 0.12 | 0.018 |
| CHOP108A | IA | 8 | 0.93 | 3.15 | 39 | 42 | 1.34 | 0.25 | 0.041 |
| CHOP114A | IA | 15 | 1.75 | 3.17 | 44 | 49 | 2.38 | 0.3 | 0.042 |
| CHOP119A | IA | 4 | 0.76 | 3.68 | 36 | 1 | 1.02 | 0.14 | 0.017 |
| CHOP122A | IA | 15 | 1.51 | 3.28 | 40 | 30 | 1.61 | 0.34 | 0.053 |
| CHOP139A | IA | 9 | 1.18 | 3.81 | 29 | 49 | 0.74 | 0.09 | 0.013 |

**Table 12.6 TCPC Hemodynamics for patients with single LV vs. single RV (N=83)**

| | **LV or RV** | **Cardiac Index** (L/min /$m^2$) | **GFD** (%LPA) | **HFD** (%LPA) | **$\Delta P_{max}$** (mmHg) | **R** (WU) | **TCPC-EDI** |
|---|---|---|---|---|---|---|---|
| CHOP_M12 | L | 3.89 | 62 | 54 | 0.41 | 0.18 | 0.019 |
| CHOP_M7 | L | 3.70 | 65 | 100 | 0.67 | 0.19 | 0.025 |
| CHOP004B | L | 3.78 | 56 | 71 | 1.26 | 0.27 | 0.044 |
| CHOP005B | L | 3.01 | 56 | 68 | 3.31 | 0.58 | 0.087 |
| CHOP007B | L | 4.20 | 28 | 17 | 1.46 | 0.18 | 0.024 |
| CHOP014A | L | 3.64 | 59 | 33 | 0.38 | 0.07 | 0.016 |
| CHOP017B | L | 3.13 | 16 | 0 | 0.76 | 0.18 | 0.035 |
| CHOP024A | L | 3.58 | 43 | 58 | 2.02 | 0.16 | 0.021 |
| CHOP031A | L | 3.65 | 40 | 78 | 0.55 | 0.09 | 0.013 |
| CHOP032A | L | 3.55 | 42 | 43 | 2.96 | 0.76 | 0.12 |
| CHOP033A | L | 2.59 | 52 | 63 | 0.51 | 0.1 | 0.016 |
| CHOP034A | L | 4.35 | 43 | 41 | 2.72 | 0.61 | 0.103 |
| CHOP036A | L | 3.53 | 55 | 71 | 1.22 | 0.15 | 0.015 |
| CHOP044A | L | 2.87 | 49 | 43 | 2.9 | 0.5 | 0.078 |
| CHOP047A | L | 2.11 | 46 | 45 | 0.49 | 0.11 | 0.026 |
| CHOP052B | L | 5.47 | 44 | 21 | 0.94 | 0.16 | 0.023 |

| | | | | | | | |
|---|---|---|---|---|---|---|---|
| CHOP062A | L | 2.57 | 30 | 43 | 0.33 | 0.08 | 0.018 |
| CHOP063A | L | 3.47 | 50 | 71 | 1.39 | 0.23 | 0.032 |
| CHOP081A | L | 7.18 | 38 | 3 | 0.22 | 0.06 | 0.011 |
| CHOP082A | L | 3.08 | 40 | 57 | 0.4 | 0.08 | 0.013 |
| CHOP083A | L | 3.30 | 70 | 48 | 1.58 | 0.25 | 0.038 |
| CHOP086A | L | 3.63 | 36 | 4 | 1.89 | 0.2 | 0.02 |
| CHOP088A | L | 2.68 | 52 | 27 | 1.15 | 0.33 | 0.069 |
| CHOP089A | L | 3.12 | 46 | 61 | 0.49 | 0.08 | 0.01 |
| CHOP091A | L | 2.42 | 46 | 33 | 0.37 | 0.18 | 0.032 |
| CHOP094A | L | 4.58 | 36 | 45 | 1.69 | 0.24 | 0.03 |
| CHOP100A | L | 2.13 | 43 | 13 | 0.2 | 0.07 | 0.016 |
| CHOP119A | L | 3.68 | 36 | 1 | 1.02 | 0.14 | 0.017 |
| CHOP134A | L | 3.72 | 38 | 28 | 1.03 | 0.12 | 0.016 |
| CHOP135A | L | 4.10 | 39 | 30 | 1.79 | 0.26 | 0.037 |
| CHOP139A | L | 3.81 | 29 | 49 | 0.74 | 0.09 | 0.013 |
| CHOP145A | L | 2.46 | 40 | 61 | 0.76 | 0.24 | 0.052 |
| CHOP148A | L | 3.39 | 42 | 39 | 0.83 | 0.13 | 0.024 |
| CHOP187A | L | 2.54 | 34 | 41 | 0.47 | 0.09 | 0.02 |
| CHOP188A | L | 3.49 | 58 | 50 | 0.44 | 0.05 | 0.01 |
| CHOP191A | L | 3.13 | 45 | 65 | 0.2 | 0.05 | 0.011 |
| CHOP204A | L | 3.62 | 37 | 47 | 0.86 | 0.23 | 0.035 |
| CHOP_M10 | L | 6.15 | 85 | 87 | 0.99 | 0.14 | 0.013 |
| CHOP_M11 | R | 3.81 | 27 | 26 | 3.01 | 0.42 | 0.076 |
| CHOP_M8 | R | 4.03 | 55 | 0 | 1.74 | 0.19 | 0.023 |
| CHOP001B | R | 1.62 | 39 | 48 | 0.4 | 0.04 | 0.01 |
| CHOP008A | R | 1.64 | 46 | 53 | 0.69 | 0.11 | 0.031 |
| CHOP010A | R | 3.93 | 44 | 33 | 3.32 | 0.47 | 0.055 |
| CHOP013A | R | 1.80 | 52 | 52 | 0.93 | 0.25 | 0.062 |
| CHOP016A | R | 3.94 | 25 | 3 | 5.15 | 0.36 | 0.042 |
| CHOP018A | R | 4.49 | 42 | 67 | 0.38 | 0.06 | 0.007 |
| CHOP019A | R | 3.29 | 41 | 52 | 1.75 | 0.23 | 0.035 |
| CHOP021A | R | 3.03 | 41 | 49 | 2.28 | 0.42 | 0.076 |
| CHOP022A | R | 3.75 | 49 | 33 | 0.81 | 0.1 | 0.016 |
| CHOP023A | R | 3.19 | 42 | 53 | 2.28 | 0.66 | 0.122 |
| CHOP026A | R | 3.69 | 40 | 79 | 2.69 | 0.4 | 0.073 |
| CHOP028A | R | 1.84 | 36 | 40 | 1.3 | 0.23 | 0.052 |
| CHOP029A | R | 3.66 | 22 | 40 | 0.93 | 0.12 | 0.017 |
| CHOP030B | R | 3.31 | 35 | 41 | 3.68 | 0.43 | 0.069 |
| CHOP037A | R | 3.81 | 35 | 46 | 4.32 | 0.31 | 0.057 |
| CHOP038A | R | 2.41 | 40 | 22 | 1.46 | 0.27 | 0.05 |
| CHOP039A | R | 3.86 | 48 | 52 | 3.11 | 0.23 | 0.019 |
| CHOP040A | R | 2.84 | 37 | 50 | 1.9 | 0.41 | 0.04 |
| CHOP041A | R | 2.68 | 37 | 21 | 0.34 | 0.1 | 0.025 |

| | | | | | | | |
|---|---|---|---|---|---|---|---|
| CHOP049A | R | 6.97 | 60 | 77 | 4.09 | 0.28 | 0.019 |
| CHOP053B | R | 4.01 | 54 | 38 | 0.97 | 0.09 | 0.015 |
| CHOP054A | R | 4.48 | 21 | 17 | 0.28 | 0.04 | 3.00E-03 |
| CHOP057A | R | 2.66 | 40 | 48 | 0.71 | 0.17 | 0.033 |
| CHOP061A | R | 4.45 | 59 | 52 | 1.84 | 0.24 | 0.028 |
| CHOP064A | R | 1.70 | 55 | 82 | 0.28 | 0.1 | 0.033 |
| CHOP065A | R | 2.46 | 35 | 39 | 0.13 | 0.05 | 0.013 |
| CHOP066A | R | 3.45 | 38 | 17 | 0.76 | 0.16 | 0.02 |
| CHOP068B | R | 3.82 | 43 | 41 | 1.96 | 0.28 | 0.035 |
| CHOP069B | R | 2.90 | 46 | 65 | 1.23 | 0.12 | 0.02 |
| CHOP074A | R | 1.78 | 37 | 60 | 0.5 | 0.15 | 0.038 |
| CHOP080A | R | 2.91 | 53 | 29 | 2.4 | 0.54 | 0.107 |
| CHOP085A | R | 3.20 | 49 | 35 | 1.79 | 0.26 | 0.048 |
| CHOP087A | R | 3.30 | 35 | 39 | 0.86 | 0.22 | 0.041 |
| CHOP097A | R | 3.41 | 22 | 30 | 3.05 | 0.15 | 0.02 |
| CHOP102A | R | 2.92 | 42 | 31 | 1.09 | 0.22 | 0.034 |
| CHOP103A | R | 2.65 | 52 | 76 | 2.96 | 0.72 | 0.134 |
| CHOP105A | R | 4.06 | 33 | 44 | 1.05 | 0.12 | 0.018 |
| CHOP108A | R | 3.15 | 39 | 42 | 1.34 | 0.25 | 0.041 |
| CHOP109B | R | 4.06 | 51 | 5 | 1.57 | 0.13 | 0.015 |
| CHOP114A | R | 3.17 | 44 | 49 | 2.38 | 0.3 | 0.042 |
| CHOP122A | R | 3.28 | 40 | 30 | 1.61 | 0.34 | 0.053 |
| CHOP166A | R | 3.72 | 26 | 13 | 2.45 | 0.17 | 0.023 |
| CHOP203A | R | 3.45 | 47 | 46 | 0.28 | 0.06 | 0.01 |

**Table 12.7 TCPC Hemodynamics for single LV patients without aortic reconstruction and single RV patients with aortic reconstruction (N=65)**

| | **LV or RV** | **Recon. aorta** (Y or N) | **Cardiac Index** (L/min /$m^2$) | **GFD** (%LPA) | **HFD** (%LPA) | **$\Delta P_{max}$** (mmHg) | **R** (WU) | **TCPC-EDI** |
|---|---|---|---|---|---|---|---|---|
| CHOP_M12 | L | N | 3.89 | 62 | 54 | 0.41 | 0.18 | 0.019 |
| CHOP_M7 | L | N | 3.70 | 65 | 100 | 0.67 | 0.19 | 0.025 |
| CHOP004B | L | N | 3.78 | 56 | 71 | 1.26 | 0.27 | 0.044 |
| CHOP005B | L | N | 3.01 | 56 | 68 | 3.31 | 0.58 | 0.087 |
| CHOP007B | L | N | 4.20 | 28 | 17 | 1.46 | 0.18 | 0.024 |
| CHOP017B | L | N | 3.13 | 16 | 0 | 0.76 | 0.18 | 0.035 |
| CHOP031A | L | N | 3.65 | 40 | 78 | 0.55 | 0.09 | 0.013 |
| CHOP032A | L | N | 3.55 | 42 | 43 | 2.96 | 0.76 | 0.12 |
| CHOP033A | L | N | 2.59 | 52 | 63 | 0.51 | 0.1 | 0.016 |
| CHOP034A | L | N | 4.35 | 43 | 41 | 2.72 | 0.61 | 0.103 |
| CHOP036A | L | N | 3.53 | 55 | 71 | 1.22 | 0.15 | 0.015 |
| CHOP047A | L | N | 2.11 | 46 | 45 | 0.49 | 0.11 | 0.026 |
| CHOP052B | L | N | 5.47 | 44 | 21 | 0.94 | 0.16 | 0.023 |
| CHOP062A | L | N | 2.57 | 30 | 43 | 0.33 | 0.08 | 0.018 |
| CHOP063A | L | N | 3.47 | 50 | 71 | 1.39 | 0.23 | 0.032 |
| CHOP082A | L | N | 3.08 | 40 | 57 | 0.4 | 0.08 | 0.013 |
| CHOP083A | L | N | 3.30 | 70 | 48 | 1.58 | 0.25 | 0.038 |
| CHOP086A | L | N | 3.63 | 36 | 4 | 1.89 | 0.2 | 0.02 |
| CHOP088A | L | N | 2.68 | 52 | 27 | 1.15 | 0.33 | 0.069 |
| CHOP089A | L | N | 3.12 | 46 | 61 | 0.49 | 0.08 | 0.01 |
| CHOP091A | L | N | 2.42 | 46 | 33 | 0.37 | 0.18 | 0.032 |
| CHOP100A | L | N | 2.13 | 43 | 13 | 0.2 | 0.07 | 0.016 |
| CHOP119A | L | N | 3.68 | 36 | 1 | 1.02 | 0.14 | 0.017 |
| CHOP135A | L | N | 4.10 | 39 | 30 | 1.79 | 0.26 | 0.037 |
| CHOP145A | L | N | 2.46 | 40 | 61 | 0.76 | 0.24 | 0.052 |
| CHOP148A | L | N | 3.39 | 42 | 39 | 0.83 | 0.13 | 0.024 |
| CHOP187A | L | N | 2.54 | 34 | 41 | 0.47 | 0.09 | 0.02 |
| CHOP188A | L | N | 3.49 | 58 | 50 | 0.44 | 0.05 | 0.01 |
| CHOP191A | L | N | 3.13 | 45 | 65 | 0.2 | 0.05 | 0.011 |
| CHOP204A | L | N | 3.62 | 37 | 47 | 0.86 | 0.23 | 0.035 |
| CHOP_M10 | L | N | 6.15 | 85 | 87 | 0.99 | 0.14 | 0.013 |
| CHOP_M11 | R | Y | 3.81 | 27 | 26 | 3.01 | 0.42 | 0.076 |
| CHOP_M8 | R | Y | 4.03 | 55 | 0 | 1.74 | 0.19 | 0.023 |
| CHOP001B | R | Y | 1.62 | 39 | 48 | 0.4 | 0.04 | 0.01 |
| CHOP008A | R | Y | 1.64 | 46 | 53 | 0.69 | 0.11 | 0.031 |
| CHOP010A | R | Y | 3.93 | 44 | 33 | 3.32 | 0.47 | 0.055 |
| CHOP016A | R | Y | 3.94 | 25 | 3 | 5.15 | 0.36 | 0.042 |

| | | | | | | | | |
|---|---|---|---|---|---|---|---|---|
| CHOP019A | R | Y | 3.29 | 41 | 52 | 1.75 | 0.23 | 0.035 |
| CHOP021A | R | Y | 3.03 | 41 | 49 | 2.28 | 0.42 | 0.076 |
| CHOP022A | R | Y | 3.75 | 49 | 33 | 0.81 | 0.1 | 0.016 |
| CHOP026A | R | Y | 3.69 | 40 | 79 | 2.69 | 0.4 | 0.073 |
| CHOP028A | R | Y | 1.84 | 36 | 40 | 1.3 | 0.23 | 0.052 |
| CHOP029A | R | Y | 3.66 | 22 | 40 | 0.93 | 0.12 | 0.017 |
| CHOP030B | R | Y | 3.31 | 35 | 41 | 3.68 | 0.43 | 0.069 |
| CHOP037A | R | Y | 3.81 | 35 | 46 | 4.32 | 0.31 | 0.057 |
| CHOP039A | R | Y | 3.86 | 48 | 52 | 3.11 | 0.23 | 0.019 |
| CHOP041A | R | Y | 2.68 | 37 | 21 | 0.34 | 0.1 | 0.025 |
| CHOP053B | R | Y | 4.01 | 54 | 38 | 0.97 | 0.09 | 0.015 |
| CHOP054A | R | Y | 4.48 | 21 | 17 | 0.28 | 0.04 | 3.00E-03 |
| CHOP061A | R | Y | 4.45 | 59 | 52 | 1.84 | 0.24 | 0.028 |
| CHOP064A | R | Y | 1.70 | 55 | 82 | 0.28 | 0.1 | 0.033 |
| CHOP065A | R | Y | 2.46 | 35 | 39 | 0.13 | 0.05 | 0.013 |
| CHOP066A | R | Y | 3.45 | 38 | 17 | 0.76 | 0.16 | 0.02 |
| CHOP068B | R | Y | 3.82 | 43 | 41 | 1.96 | 0.28 | 0.035 |
| CHOP069B | R | Y | 2.90 | 46 | 65 | 1.23 | 0.12 | 0.02 |
| CHOP074A | R | Y | 1.78 | 37 | 60 | 0.5 | 0.15 | 0.038 |
| CHOP085A | R | Y | 3.20 | 49 | 35 | 1.79 | 0.26 | 0.048 |
| CHOP087A | R | Y | 3.30 | 35 | 39 | 0.86 | 0.22 | 0.041 |
| CHOP097A | R | Y | 3.41 | 22 | 30 | 3.05 | 0.15 | 0.02 |
| CHOP105A | R | Y | 4.06 | 33 | 44 | 1.05 | 0.12 | 0.018 |
| CHOP108A | R | Y | 3.15 | 39 | 42 | 1.34 | 0.25 | 0.041 |
| CHOP114A | R | Y | 3.17 | 44 | 49 | 2.38 | 0.3 | 0.042 |
| CHOP122A | R | Y | 3.28 | 40 | 30 | 1.61 | 0.34 | 0.053 |
| CHOP166A | R | Y | 3.72 | 26 | 13 | 2.45 | 0.17 | 0.023 |
| CHOP203A | R | Y | 3.45 | 47 | 46 | 0.28 | 0.06 | 0.01 |

# B. Appendix B- Comparison of Pulsatile and Time-Averaged CFD simulations

**Table 12.8 Comparison of power loss derived from both time-averaged and pulsatile CFD simulations for a subset of 34 patients**

| | Time-averaged PL (mW) | Pulsatile PL (mW) | Time-averaged HFD (%LPA) | Pulsatile HFD (%LPA) |
|---|---|---|---|---|
| CHOP005B | 17.9 | 18.7 | 68 | 72 |
| CHOP008B | 8.2 | 9.9 | 50 | 41 |
| CHOP016A | 10.5 | 11.5 | 3 | 6 |
| CHOP017B | 3.4 | 4 | 0 | 3 |
| CHOP018A | 1.4 | 1.8 | 67 | 61 |
| CHOP019A | 7.4 | 9.1 | 52 | 48 |
| CHOP021A | 7.3 | 7.5 | 49 | 45 |
| CHOP022A | 1.7 | 1.7 | 33 | 33 |
| CHOP024A | 3.1 | 3.6 | 58 | 66 |
| CHOP026A | 4.7 | 5 | 79 | 76 |
| CHOP028A | 3.6 | 5.2 | 40 | 38 |
| CHOP029A | 3.2 | 3.9 | 40 | 35 |
| CHOP034A | 18.2 | 19.1 | 41 | 38 |
| CHOP036A | 7.6 | 7.8 | 71 | 69 |
| CHOP037A | 4 | 4.4 | 46 | 47 |
| CHOP041A | 1.2 | 1.5 | 13 | 11 |
| CHOP042B | 1.8 | 3 | 43 | 48 |
| CHOP052D | 2.7 | 2.6 | 30 | 33 |
| CHOP065A | 0.5 | 0.4 | 39 | 35 |
| CHOP066A | 2.5 | 2.7 | 17 | 25 |
| CHOP080A | 11.8 | 10.2 | 29 | 48 |
| CHOP082B | 10.6 | 15.5 | 51 | 46 |
| CHOP083A | 5.7 | 6.1 | 48 | 48 |
| CHOP085A | 1.7 | 2.2 | 35 | 40 |
| CHOP088A | 4.2 | 5.6 | 27 | 35 |
| CHOP089A | 1.9 | 2.6 | 61 | 66 |
| CHOP091A | 5.3 | 5.7 | 33 | 47 |
| CHOP094A | 9.1 | 11.6 | 45 | 46 |
| CHOP108A | 3.7 | 5.4 | 42 | 37 |
| CHOP114A | 11.6 | 12.7 | 49 | 50 |
| CHOP118A | 1.3 | 2 | 44 | 45 |

| | | | | |
|---|---|---|---|---|
| CHOP122A | 3.9 | 5.9 | 30 | 31 |
| CHOP135A | 5 | 6.8 | 36 | 43 |
| CHOP145A | 3.4 | 3.5 | 61 | 57 |

# C. Appendix C- TCPC geometric parameters from VMTK analysis

This appendix presents the protocol for and data derived from the geometric analysis of the TCPC cohort using VMTK. Patients with an atriopulmonary connection (3) or a Y-Graft (1) connection were excluded leaving N=96.

## 4. VMTK Protocol (Credit: Elaine Tang)

### Outputs from code

| Each vessel |
| --- |
| • Vessel Diameter<br>• Vessel Area<br>• Shape factor<br>• Bifurcation angle<br>• Tortuosity<br>• Vessel length extracted |

| Across vessels (Single SVC) | Across vessels (BilateralSVC) |
| --- | --- |
| • IVC-SVC offsets (projected on AP, RL or PA axis)<br>• VC-PA offset<br>• IVC-SVC angle<br>• LPA-RPA angle<br>• Angle between adjacent vessels (each VC to each PA) | • IVC-LSVC, IVC-SVC, LSVC-SVC offsets (projected on AP, RL or PA axis)<br>• VC-PA offset<br>• Angle between adjacent vessels (each VC to each PA)<br>• IVC-LSVC, IVC-SVC angle, LPA-RPA angle |

**With Azygos Vein (AZY)?**

| Individual vessel | Across vessels |
|---|---|
| • Vessel Diameter<br>• Vessel Area<br>• Shape factor<br>• Bifurcation angle<br>• Tortuosity<br>• Vessel length extracted | • IVC-AZY, AZY-SVC, AZY-LSVC offsets (projected on AP, RL or PA axis)<br>• AZY- PA offset<br>• Angle between AZY and other vessels |

**With Right Upper-lobe Pulmonary Artery (RUPA)?**

| Individual vessel |
|---|
| • Vessel Diameter<br>• Vessel Area<br>• Shape factor<br>• Bifurcation angle<br>• Tortuosity<br>• Vessel length extracted |

The parameters were computed in the following ways:

- Vessel diameter = Maximum Inscribed Radius (r) X 2
- Cross section area = $\pi r^2$
- Shape factor = $d_{min}/d_{max}$
- Bifurcation angle = $cos^{-1}(\frac{b2.b3}{|b2||b3|})$, where b2 and b3 are two vectors coming out from the main branch, and |b2|,|b3| are their respective magnitudes, and b2.b3 is the dot product of the two vectors
- Angle across vessel = angle between specified vectors
- Tortuosity (Curvature) = Length of vessel / (Shortest distance between starting point to ending point of the vessel)
- IVC-SVC offset = distance between IVC and SVC vectors projected on the anterior-posterior (AP) / right-left (RL) / pulmonary artery (PA) axis

- VC-PA offset = closet distance between points on PA line and points on VC line
- AZY-PA offset = closet distance between points on PA line and points on AZY-VCs line

## Protocol Outline

1) **Mesh preparation from GAMBIT**
2) **VMTK code (Centerlines + VC line and PA line)**
3) **Matlab code for automatic computation of parameters**

## Protocol (TCPC)

### 1) Mesh Preparation with GAMBIT

a. With the TCPC geometry prepared in GAMBIT (no flow extension yet), add the following flow extensions:
   - IVC: 10
   - SVC, LPA, RPA: 5 (If RPA is much bigger than LPA, use 8 for RPA)
   - (If present) LSVC, AZY, RUPA: 5

   (The flow extension is necessary as VMTK centerline starts at certain length (~ radius of that vessel) from the edge of the vessel. You can change the extension length if your centerline end-up sticks out too much from the original geometry or vice versa)

b. Mesh the extended TCPC at the only the TCPC wall, the flow extensions but not the end caps, (Triangular mesh, ".FDNEUT" format), mesh size is same as how you prepare the mesh for IB code preprocessing.

### 2) VMTK code

a. Create a new folder for each patient case, copy the following textfiles:
   i. Single SVC: "1TCPC_resamp_geo_bv.txt" and "2VCPAline.txt"
   ii. Bilateral SVC: "1BLSVC_resamp_geo_bv.txt" and "2BLSVC_VCPAline.txt"

   And also the .FDNEUT mesh file inside the folder created

b. Open the first text file ("1TCPC_resamp_geo_bv.txt" or "1BLSVC_resamp_geo_bv.txt"), rename the file in the first line.

```
vmtkmeshtosurface -ifile MESHNAME.FDNEUT -ofile surface.stl \
```

   And save the text file.

c. Run the first part of code by typing "**vmtk --file 1TCPC_resamp_geo_bv.txt**" (Single SVC) or "**vmtk --file 1BLSVC_resamp_geo_bv.txt**" (Bilateral SVC) in the command line

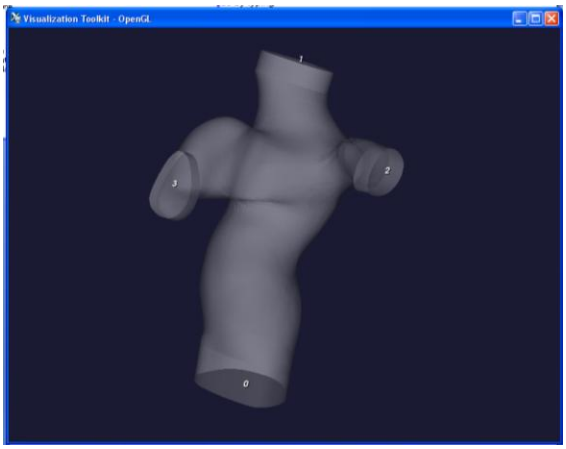


d. Plotting centerlines for IVC
   i. A window with the model will pop up, showing the translucent mesh with numbers denoted on the inlets/outlets. Rotate the model view using left mouse click, zoom in/out using right/middle mouse click, until you can see all vessels and numbers, then press “q” in the new window.
   ii. Go back to the command window, enter the vessel number for inlet (0 for IVC in this case)
   iii. Enter the vessel numbers for outlets (2 [space] 3 for LPA,RPA in this case, don’t put commas in between vessel number as the code does not like it)

e. Repeat step d for other vessels according to this:

**Single SVC**

| Inlet | Outlets |
|---|---|
| SVC | LPA RPA |
| LPA | SVC IVC |
| RPA | SVC IVC |

**Bilateral SVC**

| Inlet | Outlets |
|---|---|
| LSVC | LPA RPA |
| SVC | LPA RPA |
| LPA | SVC IVC |
| RPA | SVC IVC |

Sequence of plotting points for the outlets does not matter, but the sequence of specifying the inlets does matter. The program first saves the IVC centerline first, then SVC, LPA and RPA. So it is important to follow that order to save the centerline with the right name. (You can change the sequence in the text file to accommodate your own preference).

Run the second part of code by typing “vmtk --file 2VCPAline.txt” (Single SVC) or “vmtk --file 2BLSVC_VCPAline” (Bilateral SVC) in the command line

A window with the model will pop up, showing the translucent mesh with numbers denoted on the inlets/outlets. Rotate the model view using left mouse click, zoom in/out using right/middle mouse click, until you can see all vessels and numbers, then press “q” in the new window.

Enter inlets and outlets according to the following:

**Single SVC**

| Inlet | Outlet |
|---|---|
| IVC | SVC |
| LPA | RPA |

**Bilateral SVC**

| Inlet | Outlet |
|---|---|
| IVC | SVC |
| IVC | LSVC |
| LPA | RPA |

### 3) MATLAB code

a. To run the MATLAB code for data processing, you will need the “XXXclgeo.vtk” and “XXXbv.vtk” for each vessel, and also the “IVC_SVCline.vtk” , “LPA_RPAline.vtk” (And “IVC_LSVCline.vtk” and/or “Azy_VCline.vtk”) to reference your offset to the LPA-RPA centerline.

b. Copy the “**TCPCgeo2.m**”, “**compute_vessel2.m**”, “**PAVC_offset.m**”, “**searchPApt.m**” and “**comAngle.m**” MATLAB files to the folder one level above the folder you created. (If they are already there then you don’t need to)

c. In matlab command, type “**TCPCgeo2 ('foldername’,has LSVC?, has AZY?,has_RUPA? export txt? Export excel?) e.g. TCPCgeo2 (‘CHOP051B’,1,0,0,1,1)** “

   i. Single SVC, no AZY, no RUPA: **TCPCgeo2 (‘CHOP057A’,0,0,0,1,1)**
   ii. BilateralSVC, no AZY, no RUPA: **TCPCgeo2 (‘CHOP057A,1,0,0,1,1)**
   iii. Single SVC, has AZY, no RUPA: **TCPCgeo2 (‘CHOP057A,0,1,0,1,1)**
   iv. BilateralSVC, has AZY, no RUPA: **TCPCgeo2 (‘CHOP057A,1,1,0,1,1)**

d. As it finishes running, go into the folder, you will see text files with vessel name and the date and time which the file was created (e.g. “LPA_2011510_151625”). Open the text file you will see the computed results for each vessel:

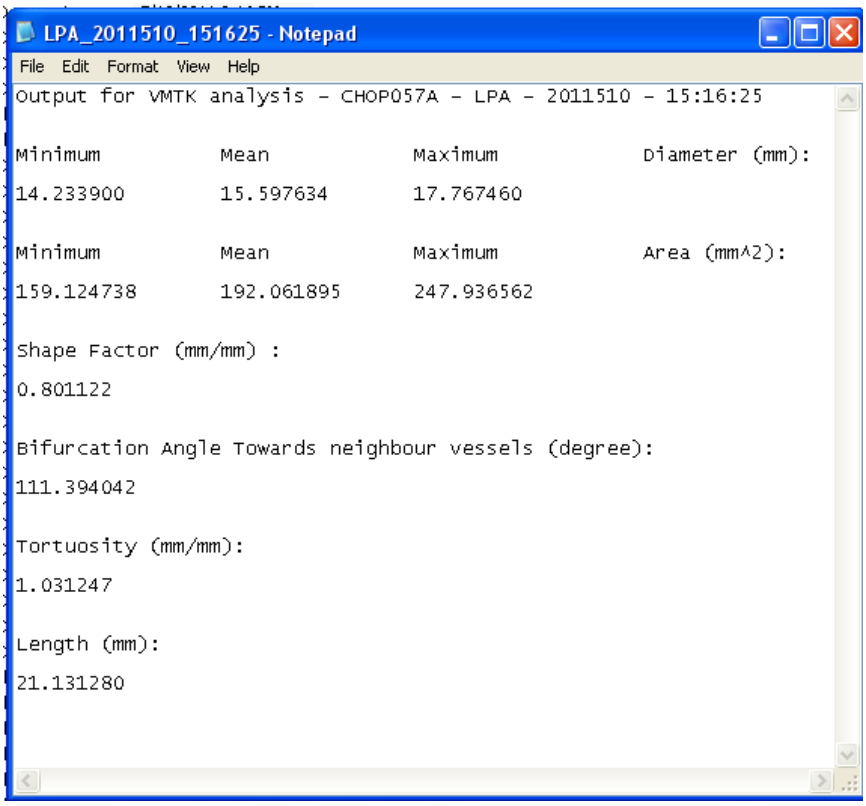


Another text file created “Offsets_2011427_175856” showing vessel offsets

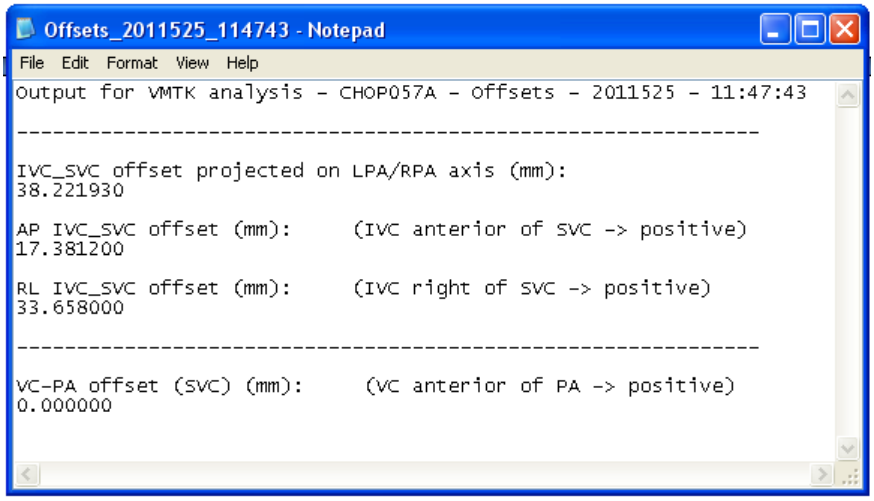


Another text file created “Angles_2011427_175856” showing angles across vessels

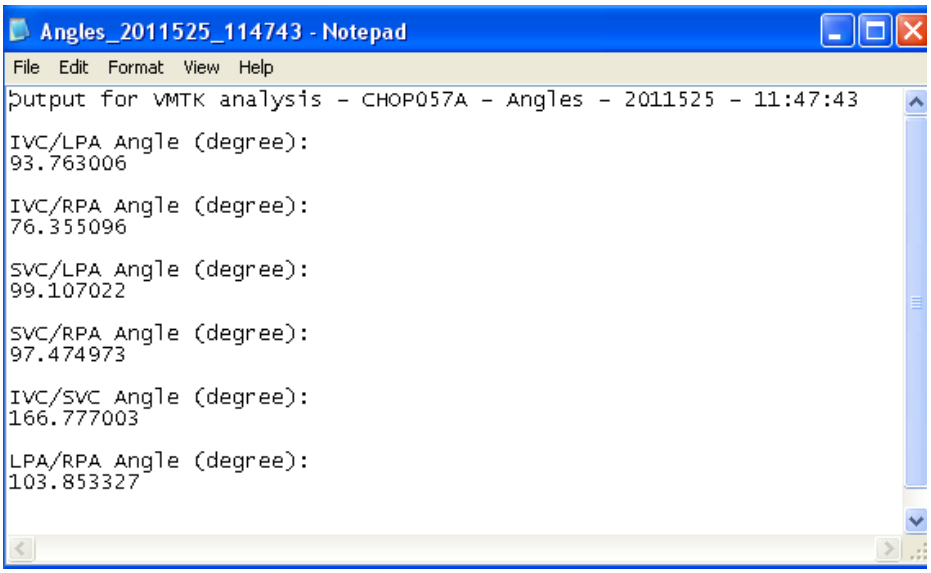


e. You can open the geometry and centerlines files in Paraview in case you have any doubts.

## Sample Results (TCPC)

**CHOP057A**

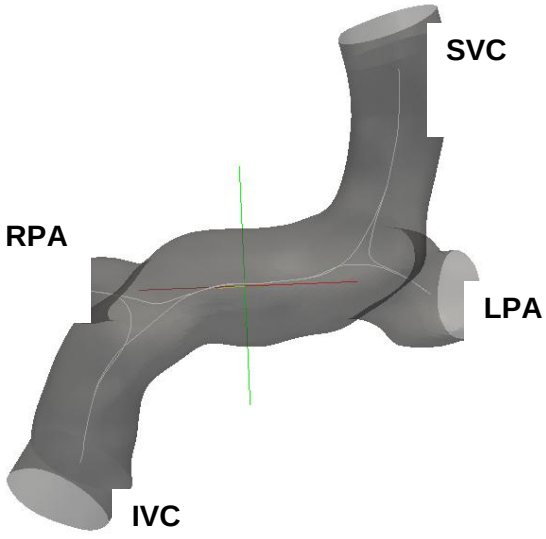

| Vessel | Diameter (mm) | | | Shape Factor (mm/mm) | Tortuosity (mm/mm) | Length (mm) |
|---|---|---|---|---|---|---|
| | Min | Mean | Max | | | |
| IVC | 15.85 | 18.40 | 19.70 | 0.80 | 1.03 | 29.49 |
| SVC | 16.55 | 17.41 | 19.31 | 0.86 | 1.03 | 38.89 |
| LPA | 14.23 | 15.60 | 17.77 | 0.80 | 1.03 | 21.13 |
| RPA | 9.67 | 11.06 | 12.70 | 0.76 | 1.02 | 17.31 |

SVC-IVC offset projected on LPA-RPA axis (mm): 38.22 mm

AP IVC_SVC offset (mm): 17.381200  (IVC anterior of SVC --> positive)

RL IVC_SVC offset (mm): 33.65800  (IVC right of SVC --> positive)

VC-PA offset (mm): 0.000000  (VC anterior of PA --> positive)

IVC-SVC Angle (degree): 166.78

LPA-RPA Angle (degree):  103.85

| Angle between | LPA | RPA |
|---|---|---|

| | | |
|---|---|---|
| (degree) | | |
| IVC | 93.76 | 76.36 |
| SVC | 99.11 | 97.47 |

**Sample Results (Bilateral SVC TCPC)**

**CHOP051B**

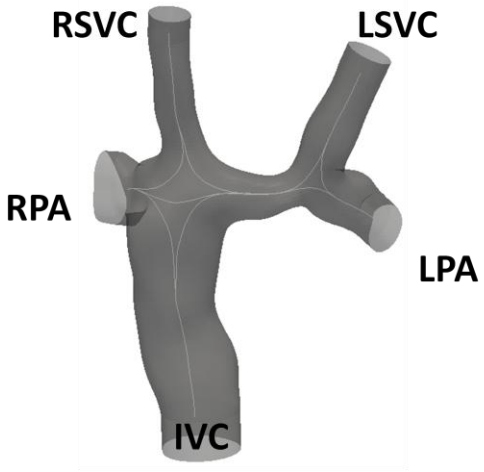

| Vessel | Diameter (mm) | | | Shape Factor (mm/mm) | Tortuosity (mm/mm) | Length (mm) |
|---|---|---|---|---|---|---|
| | Min | Mean | Max | | | |
| IVC | 16.86 | 17.95 | 18.72 | 0.90 | 1.01 | 49.98 |
| LSVC | 9.30 | 10.37 | 11.04 | 0.84 | 1.00 | 23.95 |
| SVC | 8.31 | 8.94 | 11.39 | 0.73 | 1.01 | 31.98 |
| LPA | 9.40 | 10.84 | 11.98 | 0.78 | 1.01 | 23.43 |
| RPA | 10.44 | 11.05 | 11.95 | 0.87 | 1.03 | 9.83 |

**Offsets**

| Offset (mm) | IVC-LSVC | IVC-SVC | LSVC-SVC |
|---|---|---|---|
| Projected on LPA/RPA axis | 30.10 | 0.93 | 29.17 |
| Anterior-posterior (AP) | -2.51 | -0.133 | 2.38 |
| Right-left (RL) | 29.37 | 0.90 | 28.48 |

VC-PA offset (LSVC) (mm): 0.00

VC-PA offset (SVC) (mm): 0.00

**Angles**

**(Inlet VS outlet)**

| Angle between (degree) | LPA | RPA |
|---|---|---|
| IVC | 52.28 | 81.05 |
| LSVC | 115.07 | |
| SVC | | 88.16 |

| **(Inlet VS inlet)** | **(Outlet VS outlet)** |
|---|---|
| LSVC/SVC Angle (degree): 25.13<br>IVC/LSVC Angle (degree): 164.707018<br>IVC/SVC Angle (degree): 169.016106 | LPA/RPA Angle (degree): 90.694991 |

5. **Vessel Diameters**

Table 12.9 includes the diameter values for the IVC and SVC, while

Table 12.10 provides those data for the LPA and RPA. Since the azygos vein and LSVC occur only in a minority of cases, they were not considered in the analysis.

**Table 12.9 Diameter (dimensionless) and Stenosis Index (SI) values for the IVC and SVC**

| | TCPC-EDI | $D_{min}$ IVC | $D_{mean}$ IVC | $D_{max}$ IVC | $SI_{ivc}$ | $D_{min}$ SVC | $D_{mean}$ SVC | $D_{max}$ SVC | $SI_{svc}$ |
|---|---|---|---|---|---|---|---|---|---|
| CHOP_M11 | 0.076 | 15.5 | 20.3 | 23.4 | 0.3 | 12.5 | 13.7 | 14.5 | 0.1 |
| CHOP_M12 | 0.019 | 23.0 | 25.2 | 26.8 | 0.1 | 10.4 | 11.3 | 14.0 | 0.3 |
| CHOP_M7 | 0.025 | 11.0 | 13.6 | 15.8 | 0.3 | 10.4 | 12.0 | 15.6 | 0.3 |
| CHOP_M8 | 0.023 | 13.2 | 14.0 | 16.1 | 0.2 | 8.4 | 8.9 | 9.2 | 0.1 |
| CHOP001B | 0.01 | 15.6 | 19.8 | 22.4 | 0.3 | 10.2 | 13.3 | 18.0 | 0.4 |
| CHOP004B | 0.044 | 12.2 | 15.9 | 20.1 | 0.4 | 9.4 | 11.0 | 13.9 | 0.3 |
| CHOP005B | 0.087 | 15.2 | 21.1 | 26.4 | 0.4 | 8.1 | 10.1 | 11.7 | 0.3 |
| CHOP007B | 0.024 | 13.3 | 16.1 | 18.9 | 0.3 | 7.1 | 9.1 | 13.9 | 0.5 |
| CHOP008A | 0.031 | 14.7 | 17.9 | 23.3 | 0.4 | 11.5 | 14.2 | 19.2 | 0.4 |
| CHOP010A | 0.055 | 15.7 | 19.2 | 20.4 | 0.2 | 7.8 | 8.4 | 12.0 | 0.4 |
| CHOP013A | 0.062 | 10.1 | 17.5 | 25.0 | 0.6 | 6.5 | 8.0 | 15.3 | 0.6 |
| CHOP014A | 0.016 | 16.1 | 18.6 | 22.0 | 0.3 | 12.9 | 14.5 | 20.5 | 0.4 |
| CHOP016A | 0.042 | 14.1 | 17.3 | 20.7 | 0.3 | 14.8 | 15.5 | 16.1 | 0.1 |
| CHOP017B | 0.035 | 11.5 | 13.9 | 19.1 | 0.4 | 11.2 | 12.2 | 12.9 | 0.1 |
| CHOP018A | 0.007 | 20.3 | 21.5 | 23.2 | 0.1 | 14.1 | 14.9 | 16.6 | 0.2 |
| CHOP019A | 0.035 | 12.2 | 16.0 | 19.1 | 0.4 | 9.0 | 11.8 | 16.2 | 0.4 |
| CHOP021A | 0.076 | 12.4 | 15.1 | 18.2 | 0.3 | 9.4 | 10.3 | 12.3 | 0.2 |
| CHOP022A | 0.016 | 15.1 | 16.0 | 17.4 | 0.1 | 11.2 | 13.3 | 17.7 | 0.4 |
| CHOP023A | 0.122 | 7.1 | 11.8 | 20.9 | 0.7 | 12.4 | 14.7 | 17.8 | 0.3 |
| CHOP024A | 0.021 | 17.4 | 19.6 | 23.4 | 0.3 | 15.2 | 17.4 | 19.2 | 0.2 |
| CHOP025A | 0.047 | 9.4 | 10.7 | 13.3 | 0.3 | 7.8 | 8.6 | 10.4 | 0.3 |
| CHOP026A | 0.073 | 20.6 | 21.9 | 23.4 | 0.1 | 12.9 | 15.1 | 15.7 | 0.2 |
| CHOP028A | 0.052 | 11.6 | 14.6 | 18.3 | 0.4 | 9.7 | 11.1 | 14.2 | 0.3 |
| CHOP029A | 0.017 | 15.6 | 19.8 | 23.2 | 0.3 | 14.3 | 15.8 | 17.7 | 0.2 |
| CHOP030B | 0.069 | 15.4 | 18.8 | 21.9 | 0.3 | 7.6 | 8.4 | 10.0 | 0.2 |
| CHOP031A | 0.013 | 18.6 | 20.2 | 23.6 | 0.2 | 12.8 | 13.5 | 14.5 | 0.1 |

| | | | | | | | | | |
|---|---|---|---|---|---|---|---|---|---|
| CHOP032A | 0.12 | 8.3 | 11.4 | 19.2 | 0.6 | 10.8 | 12.4 | 15.4 | 0.3 |
| CHOP033A | 0.016 | 14.1 | 15.2 | 18.1 | 0.2 | 10.4 | 12.7 | 16.7 | 0.4 |
| CHOP034A | 0.103 | 10.1 | 13.8 | 17.0 | 0.4 | 12.0 | 13.9 | 16.7 | 0.3 |
| CHOP035A | 0.011 | 14.0 | 17.8 | 23.0 | 0.4 | 14.6 | 15.5 | 17.0 | 0.1 |
| CHOP036A | 0.015 | 14.0 | 18.0 | 23.6 | 0.4 | 11.4 | 12.7 | 15.4 | 0.3 |
| CHOP037A | 0.057 | 11.8 | 15.1 | 21.4 | 0.4 | 11.6 | 13.6 | 17.8 | 0.3 |
| CHOP038A | 0.05 | 15.7 | 17.6 | 19.9 | 0.2 | 6.7 | 11.0 | 17.7 | 0.6 |
| CHOP039A | 0.019 | 17.1 | 20.1 | 22.2 | 0.2 | 14.2 | 16.4 | 19.3 | 0.3 |
| CHOP040A | 0.04 | 11.5 | 15.0 | 20.1 | 0.4 | 11.1 | 11.9 | 15.1 | 0.3 |
| CHOP041A | 0.025 | 14.6 | 17.1 | 21.6 | 0.3 | 10.1 | 11.0 | 11.7 | 0.1 |
| CHOP042B | 0.042 | 14.0 | 14.5 | 15.8 | 0.1 | 7.4 | 7.8 | 8.0 | 0.1 |
| CHOP051B | 0.051 | 19.5 | 21.4 | 22.7 | 0.1 | 9.3 | 10.4 | 14.3 | 0.3 |
| CHOP052B | 0.023 | 13.6 | 14.7 | 16.0 | 0.2 | 13.4 | 13.5 | 13.7 | 0.0 |
| CHOP053B | 0.015 | 17.8 | 20.0 | 21.2 | 0.2 | 10.5 | 12.0 | 16.1 | 0.3 |
| CHOP054A | 0.003 | 27.6 | 31.2 | 34.0 | 0.2 | 19.9 | 23.5 | 26.2 | 0.2 |
| CHOP057A | 0.033 | 9.8 | 13.1 | 15.4 | 0.4 | 12.4 | 13.1 | 13.6 | 0.1 |
| CHOP061A | 0.028 | 20.6 | 23.8 | 26.1 | 0.2 | 14.6 | 16.7 | 21.5 | 0.3 |
| CHOP062A | 0.018 | 13.7 | 15.7 | 18.3 | 0.2 | 12.2 | 13.4 | 15.5 | 0.2 |
| CHOP063A | 0.032 | 12.0 | 13.6 | 18.9 | 0.4 | 12.8 | 15.4 | 17.5 | 0.3 |
| CHOP064A | 0.033 | 15.7 | 18.1 | 20.3 | 0.2 | 11.5 | 13.6 | 15.8 | 0.3 |
| CHOP065A | 0.013 | 14.8 | 18.1 | 24.2 | 0.4 | 13.8 | 15.7 | 19.9 | 0.3 |
| CHOP066A | 0.02 | 12.5 | 15.1 | 19.2 | 0.3 | 11.0 | 13.5 | 19.2 | 0.4 |
| CHOP068B | 0.035 | 20.2 | 23.2 | 27.0 | 0.3 | 16.8 | 20.2 | 24.6 | 0.3 |
| CHOP069B | 0.02 | 18.4 | 22.7 | 27.3 | 0.3 | 11.6 | 16.4 | 22.8 | 0.5 |
| CHOP072A | 0.1 | 8.9 | 12.9 | 19.2 | 0.5 | 10.0 | 12.9 | 15.3 | 0.3 |
| CHOP073A | 0.015 | 13.2 | 17.2 | 22.7 | 0.4 | 13.7 | 14.8 | 15.3 | 0.1 |
| CHOP074A | 0.038 | 11.7 | 15.0 | 19.4 | 0.4 | 9.4 | 12.5 | 16.1 | 0.4 |
| CHOP080A | 0.107 | 7.5 | 12.0 | 18.2 | 0.6 | 12.7 | 16.3 | 19.5 | 0.3 |
| CHOP081A | 0.011 | 24.5 | 27.3 | 28.7 | 0.1 | 19.1 | 20.5 | 22.2 | 0.1 |
| CHOP082A | 0.013 | 18.6 | 19.7 | 21.2 | 0.1 | 14.7 | 15.8 | 17.1 | 0.1 |

| | | | | | | | | | |
|---|---|---|---|---|---|---|---|---|---|
| CHOP083A | 0.038 | 16.0 | 16.3 | 17.4 | 0.1 | 15.0 | 15.3 | 15.8 | 0.1 |
| CHOP084A | 0.008 | 15.7 | 19.1 | 22.5 | 0.3 | 15.6 | 15.7 | 15.8 | 0.0 |
| CHOP085A | 0.048 | 19.7 | 23.5 | 25.8 | 0.2 | 16.6 | 18.3 | 21.1 | 0.2 |
| CHOP086A | 0.02 | 17.0 | 18.7 | 20.8 | 0.2 | 7.9 | 9.6 | 13.3 | 0.4 |
| CHOP087A | 0.041 | 22.7 | 24.7 | 26.2 | 0.1 | 20.4 | 21.9 | 23.2 | 0.1 |
| CHOP088A | 0.069 | 13.8 | 15.4 | 16.9 | 0.2 | 11.8 | 12.7 | 13.8 | 0.1 |
| CHOP089A | 0.01 | 16.1 | 18.3 | 20.4 | 0.2 | 13.0 | 15.1 | 18.1 | 0.3 |
| CHOP091A | 0.032 | 12.0 | 14.4 | 16.7 | 0.3 | 6.5 | 8.5 | 11.6 | 0.4 |
| CHOP094A | 0.03 | 13.7 | 15.6 | 18.7 | 0.3 | 13.5 | 14.1 | 14.7 | 0.1 |
| CHOP097A | 0.02 | 21.0 | 22.7 | 24.6 | 0.1 | 16.6 | 18.1 | 19.6 | 0.2 |
| CHOP100A | 0.016 | 14.1 | 18.0 | 22.6 | 0.4 | 16.4 | 17.7 | 18.7 | 0.1 |
| CHOP102A | 0.034 | 12.0 | 13.9 | 19.6 | 0.4 | 8.8 | 11.2 | 18.4 | 0.5 |
| CHOP103A | 0.134 | 7.8 | 12.2 | 18.4 | 0.6 | 9.9 | 12.1 | 16.3 | 0.4 |
| CHOP105A | 0.018 | 18.1 | 19.6 | 21.7 | 0.2 | 13.0 | 15.8 | 20.2 | 0.4 |
| CHOP108A | 0.041 | 18.0 | 19.4 | 21.7 | 0.2 | 13.5 | 15.3 | 16.9 | 0.2 |
| CHOP109B | 0.015 | 17.4 | 21.4 | 23.5 | 0.3 | 14.3 | 14.7 | 15.4 | 0.1 |
| CHOP114A | 0.042 | 10.0 | 13.3 | 18.8 | 0.5 | 9.6 | 12.1 | 16.7 | 0.4 |
| CHOP118A | 0.014 | 17.1 | 18.4 | 20.7 | 0.2 | 12.4 | 13.4 | 15.4 | 0.2 |
| CHOP119A | 0.017 | 14.1 | 20.1 | 22.6 | 0.4 | 13.9 | 14.2 | 14.5 | 0.0 |
| CHOP121A | 0.034 | 14.1 | 16.2 | 17.8 | 0.2 | 13.9 | 14.2 | 15.1 | 0.1 |
| CHOP122A | 0.053 | 14.7 | 16.8 | 18.3 | 0.2 | 11.6 | 13.3 | 15.9 | 0.3 |
| CHOP128A | 0.005 | 18.1 | 19.6 | 21.4 | 0.2 | 13.7 | 14.9 | 17.6 | 0.2 |
| CHOP134A | 0.016 | 16.9 | 20.2 | 22.2 | 0.2 | 11.9 | 13.5 | 15.9 | 0.3 |
| CHOP135A | 0.037 | 17.3 | 18.9 | 19.4 | 0.1 | 11.3 | 12.2 | 14.9 | 0.2 |
| CHOP139A | 0.013 | 16.8 | 19.6 | 23.5 | 0.3 | 12.4 | 13.9 | 17.3 | 0.3 |
| CHOP143A | 0.056 | 14.9 | 16.4 | 17.7 | 0.2 | 12.1 | 15.7 | 24.7 | 0.5 |
| CHOP144C | 0.038 | 10.8 | 14.2 | 16.5 | 0.3 | 9.7 | 11.1 | 12.4 | 0.2 |
| CHOP145A | 0.052 | 12.1 | 15.7 | 22.0 | 0.4 | 13.7 | 14.8 | 15.5 | 0.1 |
| CHOP148A | 0.024 | 16.9 | 20.5 | 23.1 | 0.3 | 14.9 | 15.5 | 15.8 | 0.1 |
| CHOP152A | 0.039 | 15.8 | 21.7 | 30.4 | 0.5 | 11.5 | 18.8 | 23.0 | 0.5 |

| | | | | | | | | | |
|---|---|---|---|---|---|---|---|---|---|
| CHOP155A | 0.059 | 11.4 | 14.0 | 17.1 | 0.3 | 13.3 | 14.1 | 15.7 | 0.2 |
| CHOP159A | 0.073 | 12.9 | 18.9 | 28.1 | 0.5 | 10.7 | 13.5 | 18.9 | 0.4 |
| CHOP161A | 0.039 | 10.2 | 11.3 | 16.4 | 0.4 | 13.8 | 14.3 | 14.6 | 0.1 |
| CHOP166A | 0.023 | 16.6 | 19.5 | 22.4 | 0.3 | 9.6 | 12.6 | 18.9 | 0.5 |
| CHOP187A | 0.02 | 23.2 | 28.5 | 33.6 | 0.3 | 13.2 | 15.2 | 17.6 | 0.3 |
| CHOP188A | 0.01 | 17.9 | 20.7 | 25.1 | 0.3 | 12.2 | 13.5 | 16.1 | 0.2 |
| CHOP191A | 0.011 | 16.3 | 17.1 | 18.5 | 0.1 | 10.0 | 11.2 | 13.5 | 0.3 |
| CHOP203A | 0.01 | 15.5 | 17.3 | 21.7 | 0.3 | 12.5 | 14.3 | 15.5 | 0.2 |
| CHOP204A | 0.035 | 10.9 | 13.3 | 18.5 | 0.4 | 11.2 | 12.5 | 15.7 | 0.3 |

**Table 12.10 Diameter (dimensionless) and Stenosis Index (SI) values for the LPA and RPA**

| | TCPC-EDI | $D_{min}$ LPA | $D_{mean}$ LPA | $D_{max}$ LPA | $SI_{lpa}$ | $D_{min}$ RPA | $D_{mean}$ RPA | $D_{max}$ RPA | $SI_{rpa}$ | Min PA | Ave $D_{min}$ |
|---|---|---|---|---|---|---|---|---|---|---|---|
| CHOP_M11 | 0.076 | 4.0 | 8.2 | 14.0 | 0.7 | 8.5 | 10.4 | 13.6 | 0.4 | 4.0 | 6.3 |
| CHOP_M12 | 0.019 | 12.3 | 13.8 | 14.9 | 0.2 | 9.5 | 14.0 | 20.5 | 0.5 | 9.5 | 10.9 |
| CHOP_M7 | 0.025 | 11.0 | 11.6 | 13.2 | 0.2 | 9.7 | 11.5 | 13.6 | 0.3 | 9.7 | 10.4 |
| CHOP_M8 | 0.023 | 11.4 | 12.4 | 15.1 | 0.2 | 10.6 | 10.9 | 11.2 | 0.1 | 10.6 | 11.0 |
| CHOP001B | 0.01 | 6.5 | 8.7 | 15.4 | 0.6 | 9.7 | 11.4 | 15.1 | 0.4 | 6.5 | 8.1 |
| CHOP004B | 0.044 | 9.4 | 11.5 | 14.6 | 0.4 | 5.7 | 7.5 | 11.8 | 0.5 | 5.7 | 7.5 |
| CHOP005B | 0.087 | 6.8 | 9.7 | 13.6 | 0.5 | 10.8 | 11.4 | 12.7 | 0.1 | 6.8 | 8.8 |
| CHOP007B | 0.024 | 6.3 | 7.7 | 9.2 | 0.3 | 9.2 | 10.4 | 11.9 | 0.2 | 6.3 | 7.8 |
| CHOP008A | 0.031 | 5.2 | 9.2 | 17.3 | 0.7 | 9.4 | 12.1 | 16.2 | 0.4 | 5.2 | 7.3 |
| CHOP010A | 0.055 | 5.4 | 7.4 | 12.2 | 0.6 | 9.0 | 10.4 | 12.4 | 0.3 | 5.4 | 7.2 |
| CHOP013A | 0.062 | 8.0 | 12.5 | 17.4 | 0.5 | 7.1 | 9.6 | 17.5 | 0.6 | 7.1 | 7.6 |
| CHOP014A | 0.016 | 8.6 | 12.4 | 19.4 | 0.6 | 11.5 | 13.7 | 19.1 | 0.4 | 8.6 | 10.1 |
| CHOP016A | 0.042 | 5.0 | 7.8 | 15.2 | 0.7 | 11.9 | 12.7 | 14.1 | 0.2 | 5.0 | 8.4 |

| | | | | | | | | | | | |
|---|---|---|---|---|---|---|---|---|---|---|---|
| CHOP017B | 0.035 | 4.3 | 7.5 | 11.6 | 0.6 | 11.5 | 12.4 | 14.2 | 0.2 | 4.3 | 7.9 |
| CHOP018A | 0.007 | 10.6 | 14.1 | 22.6 | 0.5 | 10.4 | 12.2 | 16.3 | 0.4 | 10.4 | 10.5 |
| CHOP019A | 0.035 | 5.9 | 8.8 | 15.9 | 0.6 | 9.0 | 13.4 | 18.1 | 0.5 | 5.9 | 7.5 |
| CHOP021A | 0.076 | 4.7 | 9.3 | 17.8 | 0.7 | 8.4 | 9.3 | 11.8 | 0.3 | 4.7 | 6.5 |
| CHOP022A | 0.016 | 8.0 | 8.4 | 8.5 | 0.1 | 10.0 | 11.5 | 15.2 | 0.3 | 8.0 | 9.0 |
| CHOP023A | 0.122 | 9.2 | 13.6 | 18.6 | 0.5 | 6.9 | 11.6 | 21.0 | 0.7 | 6.9 | 8.1 |
| CHOP024A | 0.021 | 6.7 | 12.5 | 21.8 | 0.7 | 10.3 | 15.2 | 22.9 | 0.6 | 6.7 | 8.5 |
| CHOP025A | 0.047 | 7.0 | 9.5 | 15.0 | 0.5 | 10.5 | 11.8 | 12.5 | 0.2 | 7.0 | 8.7 |
| CHOP026A | 0.073 | 4.9 | 10.3 | 21.4 | 0.8 | 8.5 | 10.1 | 17.2 | 0.5 | 4.9 | 6.7 |
| CHOP028A | 0.052 | 4.8 | 6.6 | 12.4 | 0.6 | 10.0 | 11.9 | 14.0 | 0.3 | 4.8 | 7.4 |
| CHOP029A | 0.017 | 6.8 | 10.9 | 20.9 | 0.7 | 7.8 | 11.4 | 20.0 | 0.6 | 6.8 | 7.3 |
| CHOP030B | 0.069 | 3.9 | 7.9 | 17.6 | 0.8 | 9.8 | 10.2 | 10.7 | 0.1 | 3.9 | 6.8 |
| CHOP031A | 0.013 | 12.3 | 16.0 | 20.5 | 0.4 | 10.8 | 11.7 | 13.3 | 0.2 | 10.8 | 11.6 |
| CHOP032A | 0.12 | 5.7 | 8.6 | 15.5 | 0.6 | 8.6 | 10.8 | 15.1 | 0.4 | 5.7 | 7.2 |
| CHOP033A | 0.016 | 10.3 | 12.6 | 14.9 | 0.3 | 10.5 | 13.0 | 16.8 | 0.4 | 10.3 | 10.4 |
| CHOP034A | 0.103 | 5.7 | 9.2 | 16.1 | 0.6 | 7.4 | 11.0 | 17.3 | 0.6 | 5.7 | 6.5 |
| CHOP035A | 0.011 | 12.7 | 13.5 | 14.3 | 0.1 | 15.1 | 16.2 | 17.4 | 0.1 | 12.7 | 13.9 |
| CHOP036A | 0.015 | 11.1 | 12.6 | 15.5 | 0.3 | 9.0 | 12.0 | 15.6 | 0.4 | 9.0 | 10.1 |
| CHOP037A | 0.057 | 4.2 | 9.5 | 20.0 | 0.8 | 8.4 | 11.3 | 18.4 | 0.5 | 4.2 | 6.3 |
| CHOP038A | 0.05 | 4.4 | 5.7 | 8.3 | 0.5 | 9.2 | 11.3 | 17.3 | 0.5 | 4.4 | 6.8 |
| CHOP039A | 0.019 | 7.8 | 12.5 | 17.6 | 0.6 | 6.6 | 10.0 | 15.9 | 0.6 | 6.6 | 7.2 |
| CHOP040A | 0.04 | 6.0 | 8.8 | 15.2 | 0.6 | 7.9 | 9.8 | 15.7 | 0.5 | 6.0 | 7.0 |
| CHOP041A | 0.025 | 5.2 | 7.4 | 13.7 | 0.6 | 9.1 | 11.2 | 17.6 | 0.5 | 5.2 | 7.2 |
| CHOP042B | 0.042 | 7.6 | 12.5 | 19.0 | 0.6 | 5.4 | 5.5 | 5.7 | 0.0 | 5.4 | 6.5 |
| CHOP051B | 0.051 | 10.1 | 11.6 | 12.7 | 0.2 | 8.8 | 10.5 | 14.9 | 0.4 | 8.8 | 9.5 |
| CHOP052B | 0.023 | 8.7 | 11.8 | 14.8 | 0.4 | 6.4 | 7.5 | 9.8 | 0.3 | 6.4 | 7.5 |
| CHOP053B | 0.015 | 8.6 | 11.3 | 15.8 | 0.5 | 8.8 | 11.8 | 17.2 | 0.5 | 8.6 | 8.7 |
| CHOP054A | 0.003 | 12.6 | 18.0 | 28.0 | 0.5 | 14.8 | 20.1 | 25.2 | 0.4 | 12.6 | 13.7 |
| CHOP057A | 0.033 | 7.1 | 8.3 | 9.3 | 0.2 | 11.1 | 12.1 | 12.9 | 0.1 | 7.1 | 9.1 |
| CHOP061A | 0.028 | 6.4 | 12.1 | 23.5 | 0.7 | 11.8 | 14.8 | 20.9 | 0.4 | 6.4 | 9.1 |

| | | | | | | | | | | | |
|---|---|---|---|---|---|---|---|---|---|---|---|
| CHOP062A | 0.018 | 7.7 | 10.6 | 16.7 | 0.5 | 14.5 | 14.7 | 14.9 | 0.0 | 7.7 | 11.1 |
| CHOP063A | 0.032 | 9.1 | 12.1 | 16.7 | 0.5 | 9.1 | 10.3 | 12.7 | 0.3 | 9.1 | 9.1 |
| CHOP064A | 0.033 | 6.6 | 10.7 | 16.4 | 0.6 | 8.6 | 10.4 | 16.2 | 0.5 | 6.6 | 7.6 |
| CHOP065A | 0.013 | 12.1 | 15.8 | 20.5 | 0.4 | 10.6 | 11.4 | 13.7 | 0.2 | 10.6 | 11.4 |
| CHOP066A | 0.02 | 7.5 | 11.1 | 18.9 | 0.6 | 10.8 | 13.1 | 16.7 | 0.4 | 7.5 | 9.2 |
| CHOP068B | 0.035 | 7.3 | 13.9 | 23.9 | 0.7 | 9.6 | 14.3 | 24.1 | 0.6 | 7.3 | 8.4 |
| CHOP069B | 0.02 | 6.5 | 13.9 | 24.6 | 0.7 | 9.8 | 13.8 | 23.4 | 0.6 | 6.5 | 8.1 |
| CHOP072A | 0.1 | 6.5 | 10.1 | 17.4 | 0.6 | 6.2 | 8.8 | 15.6 | 0.6 | 6.2 | 6.4 |
| CHOP073A | 0.015 | 9.9 | 12.3 | 15.7 | 0.4 | 11.8 | 12.9 | 14.2 | 0.2 | 9.9 | 10.9 |
| CHOP074A | 0.038 | 8.0 | 11.3 | 17.4 | 0.5 | 6.9 | 11.3 | 17.7 | 0.6 | 6.9 | 7.5 |
| CHOP080A | 0.107 | 6.7 | 7.4 | 8.5 | 0.2 | 7.5 | 12.7 | 19.4 | 0.6 | 6.7 | 7.1 |
| CHOP081A | 0.011 | 8.8 | 12.1 | 19.1 | 0.5 | 14.4 | 17.3 | 22.5 | 0.4 | 8.8 | 11.6 |
| CHOP082A | 0.013 | 9.3 | 13.5 | 19.6 | 0.5 | 11.9 | 12.6 | 14.1 | 0.2 | 9.3 | 10.6 |
| CHOP083A | 0.038 | 9.6 | 12.0 | 14.8 | 0.4 | 12.8 | 13.8 | 15.4 | 0.2 | 9.6 | 11.2 |
| CHOP084A | 0.008 | 10.4 | 13.6 | 18.1 | 0.4 | 8.8 | 10.8 | 12.9 | 0.3 | 8.8 | 9.6 |
| CHOP085A | 0.048 | 5.7 | 10.0 | 20.9 | 0.7 | 10.4 | 11.2 | 13.2 | 0.2 | 5.7 | 8.1 |
| CHOP086A | 0.02 | 7.2 | 8.5 | 10.6 | 0.3 | 11.5 | 12.5 | 13.9 | 0.2 | 7.2 | 9.4 |
| CHOP087A | 0.041 | 6.6 | 11.5 | 24.4 | 0.7 | 14.0 | 16.9 | 22.8 | 0.4 | 6.6 | 10.3 |
| CHOP088A | 0.069 | 8.0 | 10.4 | 13.7 | 0.4 | 6.7 | 7.6 | 9.8 | 0.3 | 6.7 | 7.4 |
| CHOP089A | 0.01 | 10.8 | 13.3 | 18.5 | 0.4 | 10.9 | 15.1 | 20.5 | 0.5 | 10.8 | 10.8 |
| CHOP091A | 0.032 | 9.0 | 9.4 | 9.7 | 0.1 | 7.9 | 9.8 | 12.9 | 0.4 | 7.9 | 8.5 |
| CHOP094A | 0.03 | 5.8 | 9.1 | 14.8 | 0.6 | 12.9 | 14.0 | 16.2 | 0.2 | 5.8 | 9.3 |
| CHOP097A | 0.02 | 4.6 | 10.3 | 19.9 | 0.8 | 12.6 | 15.1 | 19.3 | 0.3 | 4.6 | 8.6 |
| CHOP100A | 0.016 | 10.6 | 12.6 | 18.8 | 0.4 | 10.0 | 11.8 | 15.0 | 0.3 | 10.0 | 10.3 |
| CHOP102A | 0.034 | 10.3 | 10.5 | 10.6 | 0.0 | 12.0 | 14.3 | 19.0 | 0.4 | 10.3 | 11.1 |
| CHOP103A | 0.134 | 6.6 | 8.9 | 14.8 | 0.6 | 8.5 | 11.7 | 16.0 | 0.5 | 6.6 | 7.5 |
| CHOP105A | 0.018 | 7.0 | 12.9 | 22.8 | 0.7 | 9.6 | 12.8 | 17.6 | 0.5 | 7.0 | 8.3 |
| CHOP108A | 0.041 | 5.4 | 9.7 | 16.6 | 0.7 | 10.0 | 12.2 | 17.6 | 0.4 | 5.4 | 7.7 |
| CHOP109B | 0.015 | 8.9 | 11.7 | 16.3 | 0.5 | 8.0 | 11.2 | 16.2 | 0.5 | 8.0 | 8.5 |
| CHOP114A | 0.042 | 6.7 | 10.9 | 15.7 | 0.6 | 11.3 | 11.7 | 12.2 | 0.1 | 6.7 | 9.0 |

| | | | | | | | | | | | |
|---|---|---|---|---|---|---|---|---|---|---|---|
| CHOP118A | 0.014 | 6.8 | 10.3 | 16.9 | 0.6 | 9.6 | 12.1 | 16.0 | 0.4 | 6.8 | 8.2 |
| CHOP119A | 0.017 | 8.1 | 10.1 | 12.2 | 0.3 | 10.7 | 12.3 | 13.3 | 0.2 | 8.1 | 9.4 |
| CHOP121A | 0.034 | 7.3 | 9.3 | 14.4 | 0.5 | 11.5 | 12.9 | 14.9 | 0.2 | 7.3 | 9.4 |
| CHOP122A | 0.053 | 5.2 | 5.9 | 6.4 | 0.2 | 8.7 | 10.3 | 16.0 | 0.5 | 5.2 | 7.0 |
| CHOP128A | 0.005 | 13.7 | 16.2 | 18.4 | 0.3 | 13.3 | 14.9 | 18.0 | 0.3 | 13.3 | 13.5 |
| CHOP134A | 0.016 | 7.6 | 12.1 | 17.2 | 0.6 | 10.6 | 11.9 | 15.6 | 0.3 | 7.6 | 9.1 |
| CHOP135A | 0.037 | 6.8 | 7.4 | 9.4 | 0.3 | 7.6 | 10.3 | 14.6 | 0.5 | 6.8 | 7.2 |
| CHOP139A | 0.013 | 7.4 | 11.3 | 17.4 | 0.6 | 12.8 | 14.6 | 17.5 | 0.3 | 7.4 | 10.1 |
| CHOP143A | 0.056 | 8.0 | 10.9 | 16.9 | 0.5 | 9.6 | 10.1 | 11.5 | 0.2 | 8.0 | 8.8 |
| CHOP144C | 0.038 | 12.9 | 13.3 | 14.0 | 0.1 | 7.1 | 8.4 | 11.5 | 0.4 | 7.1 | 10.0 |
| CHOP145A | 0.052 | 10.3 | 14.1 | 20.5 | 0.5 | 11.5 | 12.8 | 15.2 | 0.2 | 10.3 | 10.9 |
| CHOP148A | 0.024 | 7.2 | 9.1 | 13.8 | 0.5 | 7.2 | 9.1 | 12.6 | 0.4 | 7.2 | 7.2 |
| CHOP152A | 0.039 | 6.8 | 7.9 | 10.4 | 0.3 | 8.9 | 10.6 | 12.7 | 0.3 | 6.8 | 7.9 |
| CHOP155A | 0.059 | 10.5 | 12.3 | 16.4 | 0.4 | 7.9 | 9.4 | 13.3 | 0.4 | 7.9 | 9.2 |
| CHOP159A | 0.073 | 6.8 | 10.2 | 19.7 | 0.7 | 7.8 | 11.7 | 20.0 | 0.6 | 6.8 | 7.3 |
| CHOP161A | 0.039 | 9.1 | 9.7 | 10.3 | 0.1 | 6.8 | 9.3 | 12.2 | 0.4 | 6.8 | 8.0 |
| CHOP166A | 0.023 | 4.4 | 9.1 | 17.3 | 0.7 | 11.3 | 13.8 | 16.4 | 0.3 | 4.4 | 7.8 |
| CHOP187A | 0.02 | 7.2 | 11.0 | 21.2 | 0.7 | 13.5 | 14.6 | 17.1 | 0.2 | 7.2 | 10.4 |
| CHOP188A | 0.01 | 8.6 | 12.3 | 15.0 | 0.4 | 8.5 | 9.4 | 9.8 | 0.1 | 8.5 | 8.6 |
| CHOP191A | 0.011 | 8.7 | 10.1 | 12.0 | 0.3 | 12.0 | 12.4 | 12.9 | 0.1 | 8.7 | 10.3 |
| CHOP203A | 0.01 | 11.7 | 13.8 | 17.8 | 0.3 | 13.1 | 13.9 | 16.1 | 0.2 | 11.7 | 12.4 |
| CHOP204A | 0.035 | 10.5 | 12.5 | 16.8 | 0.4 | 13.3 | 14.0 | 14.6 | 0.1 | 10.5 | 11.9 |

## 6. **Angles and Offsets**

Table 12.11 presents the connection angles between indicated the vessels; Table 12.12 shows the offset distances, normalized by IVC diameter.

**Table 12.11 Connection angles between vessels**

| | HFD (%LPA) | IVC-LPA | IVC-RPA | SVC-LPA | SVC-RPA | IVC-SVC | LPA-RPA |
|---|---|---|---|---|---|---|---|
| CHOP_M11 | 26 | 121.5 | 92.9 | 96.1 | 105.7 | 140.1 | 82.1 |
| CHOP_M12 | 54 | 122.6 | 97.6 | 98.6 | 57.8 | 125.7 | 75.0 |
| CHOP_M7 | 100 | 90.1 | 112.4 | 111.3 | 118.5 | 118.3 | 100.7 |
| CHOP_M8 | 0 | 110.4 | 88.9 | 124.0 | 61.5 | 113.2 | 86.5 |
| CHOP001B | 48 | 110.5 | 71.3 | 84.4 | 102.5 | 165.1 | 120.5 |
| CHOP004B | 71 | 121.2 | 95.5 | 96.5 | 93.0 | 115.9 | 132.1 |
| CHOP005B | 68 | 99.8 | 85.6 | 82.0 | 104.9 | 136.4 | 163.6 |
| CHOP007B | 17 | 101.0 | 106.5 | 122.5 | 76.7 | 122.0 | 54.3 |
| CHOP008A | 53 | 115.4 | 63.7 | 128.0 | 96.1 | 114.2 | 119.1 |
| CHOP010A | 33 | 125.2 | 75.1 | 99.8 | 112.3 | 127.8 | 113.9 |
| CHOP013A | 52 | 116.8 | 96.6 | 97.1 | 90.1 | 129.3 | 127.5 |
| CHOP014A | 33 | 109.8 | 83.6 | 104.5 | 120.1 | 121.1 | 117.3 |
| CHOP016A | 3 | 102.2 | 86.6 | 109.4 | 84.8 | 142.7 | 135.1 |
| CHOP017B | 0 | 95.1 | 102.5 | 87.4 | 82.7 | 128.7 | 162.4 |
| CHOP018A | 67 | 127.1 | 78.1 | 105.9 | 99.8 | 122.7 | 115.0 |
| CHOP019A | 52 | 121.5 | 108.4 | 102.4 | 110.5 | 111.1 | 102.5 |
| CHOP021A | 49 | 122.6 | 61.2 | 94.4 | 104.1 | 142.9 | 118.7 |
| CHOP022A | 33 | 85.4 | 92.1 | 128.8 | 74.4 | 145.2 | 106.0 |
| CHOP023A | 53 | 104.5 | 90.2 | 93.5 | 100.7 | 161.0 | 73.3 |
| CHOP024A | 58 | 121.3 | 110.4 | 116.7 | 127.4 | 104.7 | 75.6 |
| CHOP025A | 50 | 146.2 | 118.2 | 130.9 | 104.5 | 82.5 | 64.1 |
| CHOP026A | 79 | 124.7 | 87.6 | 103.6 | 107.8 | 131.1 | 81.7 |
| CHOP028A | 40 | 128.1 | 119.3 | 106.8 | 114.2 | 93.4 | 95.4 |

| | | | | | | | |
|---|---|---|---|---|---|---|---|
| CHOP029A | 40 | 114.0 | 91.7 | 105.8 | 115.0 | 134.1 | 84.0 |
| CHOP030B | 41 | 127.9 | 60.9 | 74.5 | 96.5 | 155.7 | 138.5 |
| CHOP031A | 78 | 133.4 | 79.9 | 83.8 | 104.9 | 140.1 | 107.6 |
| CHOP032A | 43 | 111.1 | 90.9 | 97.8 | 101.3 | 128.4 | 131.2 |
| CHOP033A | 63 | 122.9 | 96.8 | 80.0 | 90.7 | 146.6 | 119.0 |
| CHOP034A | 41 | 115.5 | 88.5 | 108.0 | 91.6 | 135.2 | 103.9 |
| CHOP035A | 21 | 91.0 | 89.6 | 93.4 | 96.7 | 171.9 | 96.4 |
| CHOP036A | 71 | 111.4 | 75.5 | 80.9 | 98.2 | 114.2 | 172.8 |
| CHOP037A | 46 | 114.4 | 98.0 | 107.5 | 113.8 | 112.0 | 111.0 |
| CHOP038A | 22 | 128.0 | 106.9 | 128.0 | 106.9 | 0.0 | 79.8 |
| CHOP039A | 52 | 116.7 | 79.9 | 105.7 | 88.5 | 137.5 | 111.1 |
| CHOP040A | 50 | 112.9 | 109.0 | 130.1 | 117.4 | 97.3 | 89.9 |
| CHOP041A | 21 | 104.3 | 77.0 | 96.6 | 110.8 | 156.5 | 98.5 |
| CHOP042B | 43 | 88.6 | 57.5 | 120.1 | 65.8 | 110.4 | 81.5 |
| CHOP051B | 58 | 51.1 | 77.4 | 128.1 | 89.7 | 166.8 | 74.5 |
| CHOP052B | 21 | 101.4 | 104.1 | 91.7 | 72.3 | 162.4 | 138.4 |
| CHOP053B | 38 | 113.5 | 92.6 | 114.0 | 90.1 | 125.6 | 115.3 |
| CHOP054A | 17 | 93.6 | 75.3 | 102.0 | 93.3 | 162.2 | 100.4 |
| CHOP057A | 48 | 81.5 | 91.8 | 92.2 | 91.7 | 173.4 | 106.6 |
| CHOP061A | 52 | 128.2 | 78.4 | 94.0 | 100.9 | 135.4 | 111.7 |
| CHOP062A | 43 | 115.4 | 110.5 | 101.5 | 115.7 | 91.1 | 119.0 |
| CHOP063A | 71 | 96.8 | 81.9 | 116.3 | 99.4 | 127.0 | 134.3 |
| CHOP064A | 82 | 123.0 | 94.5 | 115.6 | 104.4 | 121.3 | 72.8 |
| CHOP065A | 39 | 112.9 | 81.7 | 115.9 | 100.9 | 126.1 | 110.8 |
| CHOP066A | 17 | 110.3 | 80.1 | 114.7 | 98.2 | 133.1 | 107.3 |
| CHOP068B | 41 | 114.5 | 82.1 | 94.9 | 104.4 | 150.6 | 76.5 |
| CHOP069B | 65 | 116.8 | 99.2 | 110.5 | 109.3 | 114.8 | 104.9 |
| CHOP072A | 44 | 119.0 | 55.0 | 81.6 | 107.1 | 153.8 | 103.1 |
| CHOP073A | 60 | 109.1 | 89.8 | 109.1 | 105.3 | 115.8 | 127.2 |
| CHOP074A | 60 | 113.9 | 95.9 | 112.1 | 121.5 | 124.6 | 79.6 |

| | | | | | | | |
|---|---|---|---|---|---|---|---|
| CHOP080A | 29 | 116.1 | 116.9 | 129.9 | 101.0 | 111.8 | 43.6 |
| CHOP081A | 3 | 96.1 | 91.1 | 111.7 | 80.7 | 148.9 | 132.0 |
| CHOP082A | 57 | 119.1 | 70.2 | 84.1 | 97.4 | 154.5 | 144.6 |
| CHOP083A | 48 | 76.0 | 95.7 | 112.6 | 88.1 | 144.1 | 154.9 |
| CHOP084A | 72 | 120.5 | 60.7 | 105.4 | 90.0 | 133.2 | 140.6 |
| CHOP085A | 35 | 100.6 | 74.8 | 114.4 | 108.5 | 142.6 | 102.1 |
| CHOP086A | 4 | 74.5 | 79.2 | 119.7 | 87.7 | 156.5 | 71.3 |
| CHOP087A | 39 | 108.5 | 90.6 | 98.7 | 120.9 | 137.3 | 92.7 |
| CHOP088A | 27 | 103.7 | 81.7 | 114.8 | 89.2 | 137.7 | 126.0 |
| CHOP089A | 61 | 119.4 | 101.0 | 83.3 | 107.8 | 131.9 | 113.0 |
| CHOP091A | 33 | 105.2 | 86.0 | 97.0 | 78.5 | 152.2 | 87.3 |
| CHOP094A | 45 | 125.0 | 128.9 | 110.4 | 111.1 | 104.1 | 75.1 |
| CHOP097A | 30 | 113.8 | 81.1 | 108.7 | 122.9 | 131.0 | 89.8 |
| CHOP100A | 13 | 111.2 | 89.6 | 111.0 | 93.9 | 122.8 | 127.5 |
| CHOP102A | 31 | 71.4 | 81.4 | 131.3 | 96.8 | 145.5 | 47.8 |
| CHOP103A | 76 | 104.1 | 92.0 | 83.6 | 114.2 | 129.8 | 139.4 |
| CHOP105A | 44 | 104.3 | 83.4 | 108.8 | 92.9 | 146.3 | 107.2 |
| CHOP108A | 42 | 116.7 | 88.0 | 87.9 | 96.8 | 154.8 | 92.3 |
| CHOP109B | 5 | 106.6 | 95.7 | 116.5 | 76.7 | 136.9 | 100.3 |
| CHOP114A | 49 | 83.4 | 68.1 | 92.8 | 129.8 | 158.9 | 121.7 |
| CHOP118A | 44 | 121.4 | 70.9 | 96.7 | 114.9 | 130.6 | 123.7 |
| CHOP119A | 1 | 89.6 | 75.4 | 104.7 | 105.4 | 148.3 | 143.4 |
| CHOP121A | 38 | 117.9 | 116.9 | 119.2 | 65.0 | 121.4 | 99.5 |
| CHOP122A | 30 | 121.5 | 72.6 | 114.2 | 98.9 | 118.5 | 76.0 |
| CHOP128A | 60 | 127.8 | 102.7 | 115.0 | 91.1 | 114.6 | 91.6 |
| CHOP134A | 28 | 104.7 | 85.4 | 115.9 | 94.2 | 132.2 | 120.8 |
| CHOP135A | 30 | 105.0 | 89.4 | 120.5 | 89.6 | 119.7 | 51.9 |
| CHOP139A | 49 | 106.3 | 105.1 | 122.0 | 114.4 | 103.1 | 104.6 |
| CHOP143A | 12.25 | 117.7 | 73.2 | 100.5 | 94.5 | 141.5 | 116.5 |
| CHOP144C | 0 | 100.4 | 103.6 | 147.6 | 107.1 | 111.2 | 56.4 |

| | | | | | | | |
|---|---|---|---|---|---|---|---|
| CHOP145A | 61 | 125.8 | 88.6 | 103.1 | 119.9 | 125.0 | 87.5 |
| CHOP148A | 39 | 97.6 | 101.5 | 109.7 | 93.2 | 131.6 | 126.8 |
| CHOP152A | 36 | 91.6 | 56.8 | 132.0 | 90.2 | 135.1 | 133.2 |
| CHOP155A | 56 | 124.2 | 74.4 | 88.0 | 98.4 | 141.0 | 136.2 |
| CHOP159A | 57 | 106.2 | 90.1 | 101.2 | 97.4 | 144.3 | 117.5 |
| CHOP161A | 66 | 61.7 | 90.8 | 109.4 | 115.9 | 130.6 | 134.4 |
| CHOP166A | 13 | 98.6 | 107.2 | 125.2 | 100.9 | 106.7 | 116.9 |
| CHOP187A | 41 | 108.4 | 72.2 | 90.5 | 92.0 | 160.9 | 138.0 |
| CHOP188A | 50 | 116.1 | 57.7 | 76.2 | 141.3 | 149.5 | 122.7 |
| CHOP191A | 65 | 116.0 | 73.1 | 69.4 | 120.7 | 158.4 | 130.6 |
| CHOP203A | 46 | 145.1 | 90.9 | 93.7 | 104.2 | 119.5 | 90.7 |
| CHOP204A | 47 | 126.0 | 87.9 | 94.3 | 97.6 | 108.3 | 137.8 |

**Table 12.12 Cavopulmonary offset distances normalized by IVC diameter in the Antero-posterior (AP), Right-left (RL), and VC-PA distance (VC).**

| | TCPC-EDI | HFD (%LPA) | AP | RL | VC | abs(RL) |
|---|---|---|---|---|---|---|
| CHOP_M11 | 0.076 | 26 | 0.04 | 0.08 | 0.37 | 0.08 |
| CHOP_M12 | 0.019 | 54 | 0.05 | -0.36 | 0.01 | 0.36 |
| CHOP_M7 | 0.025 | 100 | 0.60 | 1.81 | 0.00 | 1.81 |
| CHOP_M8 | 0.023 | 0 | 0.04 | 0.14 | 0.14 | 0.14 |
| CHOP001B | 0.01 | 48 | 0.03 | 0.24 | -0.01 | 0.24 |
| CHOP004B | 0.044 | 71 | 0.04 | 0.14 | 0.37 | 0.14 |
| CHOP005B | 0.087 | 68 | 0.11 | 0.22 | 0.00 | 0.22 |
| CHOP007B | 0.024 | 17 | 0.06 | 0.13 | 0.32 | 0.13 |
| CHOP008A | 0.031 | 53 | 0.00 | 0.00 | 0.29 | 0.00 |
| CHOP010A | 0.055 | 33 | 0.03 | 0.21 | 0.51 | 0.21 |
| CHOP013A | 0.062 | 52 | 0.02 | 0.04 | 0.25 | 0.04 |
| CHOP014A | 0.016 | 33 | 0.00 | 0.02 | 0.42 | 0.02 |

| | | | | | | |
|---|---|---|---|---|---|---|
| CHOP016A | 0.042 | 3 | -0.04 | -0.19 | 0.05 | 0.19 |
| CHOP017B | 0.035 | 0 | 0.02 | -0.33 | 0.01 | 0.33 |
| CHOP018A | 0.007 | 67 | 0.13 | 0.24 | 0.21 | 0.24 |
| CHOP019A | 0.035 | 52 | 0.00 | 0.09 | 0.43 | 0.09 |
| CHOP021A | 0.076 | 49 | 0.06 | 0.26 | 0.57 | 0.26 |
| CHOP022A | 0.016 | 33 | -0.03 | -0.16 | 0.08 | 0.16 |
| CHOP023A | 0.122 | 53 | 0.00 | 0.00 | 0.56 | 0.00 |
| CHOP024A | 0.021 | 58 | 0.18 | 0.29 | 0.60 | 0.29 |
| CHOP025A | 0.047 | 50 | 0.35 | 1.52 | 0.00 | 1.52 |
| CHOP026A | 0.073 | 79 | 0.19 | 0.23 | 0.35 | 0.23 |
| CHOP028A | 0.052 | 40 | 0.01 | 0.12 | 0.58 | 0.12 |
| CHOP029A | 0.017 | 40 | 0.07 | 0.12 | 0.29 | 0.12 |
| CHOP030B | 0.069 | 41 | 0.41 | 0.38 | 0.01 | 0.38 |
| CHOP031A | 0.013 | 78 | 0.23 | 0.33 | 0.42 | 0.33 |
| CHOP032A | 0.12 | 43 | 0.03 | 0.05 | 0.68 | 0.05 |
| CHOP033A | 0.016 | 63 | 0.04 | 0.18 | 0.34 | 0.18 |
| CHOP034A | 0.103 | 41 | 0.01 | 0.02 | 0.16 | 0.02 |
| CHOP035A | 0.011 | 21 | -0.10 | -2.15 | 0.00 | 2.15 |
| CHOP036A | 0.015 | 71 | 0.01 | 0.22 | 0.17 | 0.22 |
| CHOP037A | 0.057 | 46 | 0.00 | 0.00 | 0.59 | 0.00 |
| CHOP038A | 0.05 | 22 | 0.00 | 0.00 | 0.56 | 0.00 |
| CHOP039A | 0.019 | 52 | 0.00 | 0.00 | 0.24 | 0.00 |
| CHOP040A | 0.04 | 50 | -0.02 | -0.01 | 0.80 | 0.01 |
| CHOP041A | 0.025 | 21 | 0.11 | 0.16 | 0.10 | 0.16 |
| CHOP042B | 0.042 | 43 | 0.35 | 0.67 | 0.00 | 0.67 |
| CHOP051B | 0.051 | 58 | -0.02 | -0.12 | 0.01 | 0.12 |
| CHOP052B | 0.023 | 21 | -0.17 | -0.45 | 0.00 | 0.45 |
| CHOP053B | 0.015 | 38 | 0.01 | 0.03 | 0.21 | 0.03 |
| CHOP054A | 0.003 | 17 | -0.01 | -0.03 | 0.33 | 0.03 |
| CHOP057A | 0.033 | 48 | 0.68 | 1.60 | 0.00 | 1.60 |

| | | | | | | |
|---|---|---|---|---|---|---|
| CHOP061A | 0.028 | 52 | 0.03 | 0.06 | 0.21 | 0.06 |
| CHOP062A | 0.018 | 43 | 0.04 | 0.03 | 0.57 | 0.03 |
| CHOP063A | 0.032 | 71 | -0.03 | -0.08 | 0.17 | 0.08 |
| CHOP064A | 0.033 | 82 | 0.04 | 0.09 | 0.49 | 0.09 |
| CHOP065A | 0.013 | 39 | -0.02 | -0.09 | 0.49 | 0.09 |
| CHOP066A | 0.02 | 17 | 0.05 | 0.06 | 0.08 | 0.06 |
| CHOP068B | 0.035 | 41 | 0.03 | 0.05 | 0.42 | 0.05 |
| CHOP069B | 0.02 | 65 | 0.05 | 0.07 | 0.17 | 0.07 |
| CHOP072A | 0.1 | 44 | 0.27 | 0.33 | 0.85 | 0.33 |
| CHOP073A | 0.015 | 60 | 0.15 | 0.26 | 0.30 | 0.26 |
| CHOP074A | 0.038 | 60 | 0.08 | 0.12 | 0.27 | 0.12 |
| CHOP080A | 0.107 | 29 | 0.11 | 0.30 | 0.81 | 0.30 |
| CHOP081A | 0.011 | 3 | -0.05 | -0.28 | 0.00 | 0.28 |
| CHOP082A | 0.013 | 57 | 0.12 | 0.17 | 0.29 | 0.17 |
| CHOP083A | 0.038 | 48 | -0.19 | -0.42 | 0.00 | 0.42 |
| CHOP084A | 0.008 | 72 | 0.03 | 0.16 | 0.00 | 0.16 |
| CHOP085A | 0.048 | 35 | 0.00 | 0.00 | 0.33 | 0.00 |
| CHOP086A | 0.02 | 4 | 0.08 | 0.20 | 0.00 | 0.20 |
| CHOP087A | 0.041 | 39 | 0.03 | 0.10 | 0.31 | 0.10 |
| CHOP088A | 0.069 | 27 | -0.12 | -0.37 | 0.00 | 0.37 |
| CHOP089A | 0.01 | 61 | 0.11 | 0.20 | 0.57 | 0.20 |
| CHOP091A | 0.032 | 33 | 0.00 | 0.00 | 0.00 | 0.00 |
| CHOP094A | 0.03 | 45 | -0.02 | -0.03 | 0.61 | 0.03 |
| CHOP097A | 0.02 | 30 | 0.03 | 0.20 | 0.32 | 0.20 |
| CHOP100A | 0.016 | 13 | -0.10 | -0.17 | 0.57 | 0.17 |
| CHOP102A | 0.034 | 31 | 0.07 | 0.25 | 0.43 | 0.25 |
| CHOP103A | 0.134 | 76 | 0.01 | 0.02 | 0.09 | 0.02 |
| CHOP105A | 0.018 | 44 | 0.03 | 0.10 | 0.35 | 0.10 |
| CHOP108A | 0.041 | 42 | 0.15 | 0.14 | 0.28 | 0.14 |
| CHOP109B | 0.015 | 5 | -0.02 | -0.16 | 0.31 | 0.16 |

| | | | | | | |
|---|---|---|---|---|---|---|
| CHOP114A | 0.042 | 49 | 0.13 | 0.18 | 0.36 | 0.18 |
| CHOP118A | 0.014 | 44 | 0.10 | 0.22 | 0.10 | 0.22 |
| CHOP119A | 0.017 | 1 | -0.16 | -0.23 | 0.00 | 0.23 |
| CHOP121A | 0.034 | 38 | -0.13 | -0.20 | 0.19 | 0.20 |
| CHOP122A | 0.053 | 30 | 0.06 | 0.07 | 0.49 | 0.07 |
| CHOP128A | 0.005 | 60 | 0.04 | 0.05 | 0.38 | 0.05 |
| CHOP134A | 0.016 | 28 | 0.02 | -0.12 | 0.07 | 0.12 |
| CHOP135A | 0.037 | 30 | 0.00 | 0.00 | 0.28 | 0.00 |
| CHOP139A | 0.013 | 49 | 0.03 | 0.10 | 0.51 | 0.10 |
| CHOP143A | 0.056 | 12.25 | 0.02 | 0.04 | 0.00 | 0.04 |
| CHOP144C | 0.038 | 0 | -0.02 | -0.06 | 0.42 | 0.06 |
| CHOP145A | 0.052 | 61 | 0.20 | 0.30 | 0.49 | 0.30 |
| CHOP148A | 0.024 | 39 | -0.04 | -0.26 | 0.00 | 0.26 |
| CHOP152A | 0.039 | 36 | 0.13 | 0.32 | 0.00 | 0.32 |
| CHOP155A | 0.059 | 56 | 0.12 | 0.21 | 0.39 | 0.21 |
| CHOP159A | 0.073 | 57 | -0.01 | -0.02 | 0.26 | 0.02 |
| CHOP161A | 0.039 | 66 | -0.14 | 0.36 | 0.27 | 0.36 |
| CHOP166A | 0.023 | 13 | 0.01 | 0.02 | 0.50 | 0.02 |
| CHOP187A | 0.02 | 41 | 0.10 | 0.10 | 0.00 | 0.10 |
| CHOP188A | 0.01 | 50 | 0.00 | -0.03 | 0.03 | 0.03 |
| CHOP191A | 0.011 | 65 | 0.11 | 0.50 | 0.00 | 0.50 |
| CHOP203A | 0.01 | 46 | 0.11 | 0.17 | 0.54 | 0.17 |
| CHOP204A | 0.035 | 47 | 0.03 | 0.10 | 0.36 | 0.10 |

# D. Appendix D- Ventricular Function Patients

## 7. Demographic details

**Table 12.13 Demographic details for patients included in ventricular function analysis**

| | Age | Gender | BSA | Ventricle Morphology |
|---|---|---|---|---|
| CHOP004D | 22 | M | 1.58 | L |
| CHOP005B | 19 | F | 1.51 | L |
| CHOP024A | 7 | F | 0.74 | L |
| CHOP033A | 10 | M | 1.32 | L |
| CHOP034A | 14 | M | 1.89 | L |
| CHOP036A | 11 | M | 1.19 | L |
| CHOP052B | 10 | M | 1.06 | L |
| CHOP082B | 22 | F | 1.32 | L |
| CHOP088B | 13 | F | 1.72 | L |
| CHOP089A | 10 | M | 0.93 | L |
| CHOP091A | 18 | M | 2.08 | L |
| CHOP094A | 13 | M | 1.2 | L |
| CHOP135A | 6 | M | 0.77 | L |
| CHOP145A | 19 | F | 1.51 | L |
| CHOP188A | 17 | M | 1.51 | L |
| CHOP204A | 17 | F | 1.51 | L |
| CHOP008B | 16 | M | 1.94 | R |
| CHOP016A | 6 | M | 0.83 | R |
| CHOP019A | 14 | M | 1.68 | R |
| CHOP021A | 11 | F | 1.23 | R |
| CHOP022A | 7 | M | 0.91 | R |
| CHOP023A | 12 | M | 1.22 | R |
| CHOP028A | 18 | M | 1.92 | R |
| CHOP029A | 9 | M | 1.08 | R |
| CHOP037A | 10 | M | 1 | R |
| CHOP041A | 14 | F | 1.51 | R |
| CHOP065A | 16 | M | 1.36 | R |
| CHOP066A | 14 | F | 1.28 | R |
| CHOP080A | 17 | F | 1.91 | R |
| CHOP085A | 2 | M | 0.5 | R |
| CHOP108A | 8 | M | 0.93 | R |
| CHOP114A | 15 | M | 1.75 | R |
| CHOP166A | 15 | M | 1.41 | R |
| CHOP203A | 16 | M | 1.93 | R |

| | | | | |
|---|---|---|---|---|
| CHOP018C | 14 | M | 1.24 | B |
| CHOP040A | 19 | F | 2.05 | B |
| CHOP042B | 3 | F | 0.62 | B |
| CHOP118A | 5 | M | 0.77 | B |
| CHOP155A | 16 | M | 1.83 | B |
| CHOP161A | 14 | F | 1.65 | B |

8. **Imaging details**

**Table 12.14 Ventricular short axis imaging detail by patient**

| | Phases | Slices | dt (in s) | Slice thickness (mm) | Spatial Resolution (mm) |
|---|---|---|---|---|---|
| CHOP004D | 30 | 8 | 0.032 | 8 | 1.56 |
| CHOP005B | 23 | 12 | 0.041 | 10 | 1.46 |
| CHOP024A | 33 | 10 | 0.027 | 5 | 1.88 |
| CHOP033A | 30 | 8 | 0.035 | 9 | 1.46 |
| CHOP034A | 23 | 8 | 0.026 | 10 | 1.67 |
| CHOP036A | 20 | 6 | 0.035 | 8 | 1.95 |
| CHOP052B | 20 | 7 | 0.028 | 10 | 0.57 |
| CHOP082B | 30 | 7 | 0.041 | 10 | 1.17 |
| CHOP088B | 24 | 8 | 0.028 | 10 | 1.77 |
| CHOP089A | 25 | 8 | 0.044 | 9 | 1.04 |
| CHOP091A | 25 | 7 | 0.029 | 10 | 1.82 |
| CHOP094A | 25 | 8 | 0.023 | 8 | 1.35 |
| CHOP135A | 26 | 8 | 0.03 | 8 | 0.6 |
| CHOP145A | 28 | 9 | 0.038 | 8 | 1.77 |
| CHOP188A | 30 | 7 | 0.038 | 10 | 1.37 |
| CHOP204A | 30 | 10 | 0.035 | 8 | 1.25 |
| CHOP008B | 18 | 9 | 0.037 | 9 | 1.56 |
| CHOP016A | 22 | 7 | 0.029 | 6 | 1.41 |
| CHOP019A | 22 | 7 | 0.034 | 8 | 1.46 |
| CHOP021A | 21 | 7 | 0.042 | 7 | 1.46 |
| CHOP022A | 22 | 9 | 0.032 | 7 | 1.56 |
| CHOP023A | 31 | 8 | 0.029 | 7 | 1.72 |
| CHOP028A | 25 | 6 | 0.035 | 10 | 1.67 |
| CHOP029A | 25 | 8 | 0.037 | 7 | 1.36 |
| CHOP037A | 16 | 6 | 0.041 | 8 | 1.15 |
| CHOP041A | 20 | 8 | 0.039 | 8 | 1.3 |
| CHOP065A | 30 | 8 | 0.034 | 10 | 1.56 |
| CHOP066A | 30 | 7 | 0.036 | 8 | 1.46 |
| CHOP080A | 27 | 6 | 0.033 | 10 | 1.77 |

| | | | | | |
|---|---|---|---|---|---|
| CHOP085A | 25 | 9 | 0.024 | 7 | 0.94 |
| CHOP108A | 25 | 8 | 0.032 | 8 | 0.5 |
| CHOP114A | 29 | 8 | 0.034 | 10 | 0.83 |
| CHOP166A | 25 | 9 | 0.03 | 7 | 1.35 |
| CHOP203A | 30 | 8 | 0.032 | 10 | 1.41 |
| CHOP018C | 27 | 7 | 0.028 | 10 | 1.35 |
| CHOP040A | 30 | 8 | 0.033 | 9 | 1.77 |
| CHOP042B | 26 | 8 | 0.023 | 5 | 1.41 |
| CHOP118A | 22 | 7 | 0.03 | 7 | 0.82 |
| CHOP155A | 25 | 8 | 0.026 | 10 | 1.25 |
| CHOP161A | 25 | 8 | 0.029 | 8 | 1.25 |

9. **Functional analysis**

**Table 12.15 Ventricular volume and TCPC-EDI results for each patient**

| | TCPC-EDI | EDV (mL/BSA) | ESV (mL/BSA) | SV (mL/BSA) | EF (%) | CI [L/min/m^2] |
|---|---|---|---|---|---|---|
| CHOP004D | 0.034 | 59.49 | 24.68 | 34.81 | 58 | 2.16 |
| CHOP005B | 0.087 | 92.72 | 46.36 | 45.7 | 50 | 2.92 |
| CHOP024A | 0.021 | 82.43 | 36.49 | 45.95 | 55 | 3.08 |
| CHOP033A | 0.016 | 75 | 39.39 | 35.61 | 47 | 2.03 |
| CHOP034A | 0.103 | 70.9 | 29.63 | 41.27 | 58 | 4.17 |
| CHOP036A | 0.015 | 62.18 | 23.53 | 39.5 | 63 | 3.4 |
| CHOP052B | 0.023 | 87.74 | 37.74 | 50 | 57 | 5.45 |
| CHOP082B | 0.033 | 92.42 | 43.94 | 48.48 | 52 | 2.38 |
| CHOP088B | 0.029 | 84.88 | 40.7 | 43.6 | 52 | 3.84 |
| CHOP089A | 0.01 | 96.77 | 48.39 | 48.39 | 50 | 2.66 |
| CHOP091A | 0.032 | 41.83 | 19.71 | 21.63 | 52 | 1.82 |
| CHOP094A | 0.03 | 89.17 | 36.67 | 52.5 | 59 | 5.41 |
| CHOP135A | 0.037 | 88.31 | 22.08 | 66.23 | 75 | 5.1 |
| CHOP145A | 0.052 | 66.23 | 20.53 | 45.7 | 69 | 2.56 |
| CHOP188A | 0.01 | 88.08 | 26.49 | 61.59 | 70 | 3.2 |
| CHOP204A | 0.035 | 88.74 | 42.38 | 46.36 | 48 | 2.64 |
| CHOP008B | 0.065 | 75.26 | 41.75 | 33.51 | 45 | 2.98 |
| CHOP016A | 0.042 | 57.83 | 25.3 | 32.53 | 57 | 3.09 |
| CHOP019A | 0.035 | 45.83 | 17.86 | 27.98 | 61 | 2.27 |
| CHOP021A | 0.076 | 77.24 | 34.15 | 43.09 | 55 | 2.93 |
| CHOP022A | 0.016 | 97.8 | 67.03 | 31.87 | 32 | 2.74 |

| | | | | | | |
|---|---|---|---|---|---|---|
| CHOP023A | 0.122 | 76.23 | 27.87 | 48.36 | 64 | 3.19 |
| CHOP028A | 0.052 | 54.17 | 21.35 | 32.29 | 60 | 2.23 |
| CHOP029A | 0.017 | 86.11 | 32.41 | 53.7 | 62 | 3.49 |
| CHOP037A | 0.057 | 55 | 30 | 25 | 46 | 2.28 |
| CHOP041A | 0.025 | 62.25 | 19.21 | 42.38 | 69 | 3.26 |
| CHOP065A | 0.013 | 109.56 | 55.88 | 52.94 | 49 | 3.12 |
| CHOP066A | 0.02 | 93.75 | 38.28 | 55.47 | 59 | 3.05 |
| CHOP080A | 0.107 | 58.64 | 22.51 | 36.13 | 61 | 2.46 |
| CHOP085A | 0.048 | 58 | 24 | 34 | 59 | 3.33 |
| CHOP108A | 0.041 | 96.77 | 47.31 | 48.39 | 51 | 3.63 |
| CHOP114A | 0.042 | 91.43 | 49.14 | 42.29 | 46 | 2.58 |
| CHOP166A | 0.023 | 82.27 | 33.33 | 48.94 | 59 | 3.87 |
| CHOP203A | 0.01 | 95.85 | 42.49 | 53.37 | 55 | 3.36 |
| CHOP018C | 0.011 | 91.13 | 47.58 | 43.55 | 48 | 3.4 |
| CHOP040A | 0.04 | 70.24 | 34.63 | 35.61 | 50 | 2.17 |
| CHOP042B | 0.042 | 53.23 | 32.26 | 20.97 | 40 | 2.12 |
| CHOP118A | 0.014 | 84.42 | 50.65 | 33.77 | 40 | 3.07 |
| CHOP155A | 0.059 | 74.36 | 38.97 | 35.9 | 48 | 3.27 |
| CHOP161A | 0.039 | 76.97 | 35.76 | 40.61 | 53 | 3.41 |

**Table 12.16 Dynamic volume and temporal VF data**

| | $PER_B$ ($mL/s/m^2$) | $PER_V$ (EDV/s) | $PFR_B$ ($mL/s/m^2$) | $PFR_V$ (EDV/s) | Time ratio to PFR | HR (bpm) |
|---|---|---|---|---|---|---|
| CHOP004D | -189.87 | -3.19 | 146.84 | 2.47 | 0.17 | 62 |
| CHOP005B | -194.04 | -2.09 | 190.73 | 2.06 | 0.15 | 64 |
| CHOP024A | -227.03 | -2.75 | 310.81 | 3.77 | 0.19 | 67 |
| CHOP033A | -162.12 | -2.16 | 185.61 | 2.47 | 0.14 | 57 |
| CHOP034A | -288.36 | -4.07 | 197.35 | 2.78 | 0.29 | 101 |
| CHOP036A | -208.4 | -3.35 | 241.18 | 3.88 | 0.19 | 86 |
| CHOP052B | -342.45 | -3.9 | 267.92 | 3.05 | 0.2 | 109 |
| CHOP082B | -228.03 | -2.47 | 229.55 | 2.48 | 0.13 | 49 |
| CHOP088B | -233.14 | -2.75 | 220.93 | 2.6 | 0.17 | 88 |
| CHOP089A | -229.03 | -2.37 | 208.6 | 2.16 | 0.12 | 55 |
| CHOP091A | -110.58 | -2.64 | 102.4 | 2.45 | 0.24 | 84 |
| CHOP094A | -289.17 | -3.24 | 408.33 | 4.58 | 0.24 | 103 |
| CHOP135A | -402.6 | -4.56 | 331.17 | 3.75 | 0.22 | 77 |
| CHOP145A | -235.76 | -3.56 | 217.88 | 3.29 | 0.27 | 56 |
| CHOP188A | -284.11 | -3.23 | 288.08 | 3.27 | 0.16 | 52 |
| CHOP204A | -218.54 | -2.46 | 139.74 | 1.57 | 0.09 | 57 |
| CHOP008B | -177.32 | -2.36 | 148.45 | 1.97 | 0.24 | 89 |

| | | | | | | |
|---|---|---|---|---|---|---|
| CHOP016A | -191.57 | -3.31 | 212.05 | 3.67 | 0.25 | 95 |
| CHOP019A | -148.21 | -3.23 | 132.14 | 2.88 | 0.16 | 81 |
| CHOP021A | -168.29 | -2.18 | 144.72 | 1.87 | 0.19 | 68 |
| CHOP022A | -141.76 | -1.45 | 253.85 | 2.6 | 0.2 | 86 |
| CHOP023A | -266.39 | -3.49 | 263.11 | 3.45 | 0.18 | 66 |
| CHOP028A | -170.83 | -3.15 | 163.02 | 3.01 | 0.23 | 69 |
| CHOP029A | -254.63 | -2.96 | 271.3 | 3.15 | 0.2 | 65 |
| CHOP037A | -119 | -2.16 | 118 | 2.15 | 0.32 | 91 |
| CHOP041A | -203.31 | -3.27 | 191.39 | 3.07 | 0.26 | 77 |
| CHOP065A | -243.38 | -2.22 | 172.79 | 1.58 | 0.24 | 59 |
| CHOP066A | -227.34 | -2.43 | 175 | 1.87 | 0.14 | 55 |
| CHOP080A | -184.29 | -3.14 | 112.57 | 1.92 | 0.31 | 68 |
| CHOP085A | -230 | -3.97 | 206 | 3.55 | 0.25 | 98 |
| CHOP108A | -252.69 | -2.61 | 210.75 | 2.18 | 0.16 | 75 |
| CHOP114A | -229.14 | -2.51 | 176 | 1.93 | 0.07 | 61 |
| CHOP166A | -214.89 | -2.61 | 261.7 | 3.18 | 0.2 | 79 |
| CHOP203A | -308.81 | -3.22 | 267.88 | 2.79 | 0.17 | 63 |
| CHOP018C | -257.26 | -2.82 | 272.58 | 2.99 | 0.26 | 78 |
| CHOP040A | -140 | -1.99 | 119.51 | 1.7 | 0.23 | 61 |
| CHOP042B | -154.84 | -2.91 | 170.97 | 3.21 | 0.2 | 101 |
| CHOP118A | -179.22 | -2.12 | 187.01 | 2.22 | 0.18 | 91 |
| CHOP155A | -245.9 | -3.1 | 271.04 | 3.42 | 0.24 | 91 |
| CHOP161A | -228.48 | -2.97 | 165.45 | 2.15 | 0.15 | 84 |

## 10. Comparison of Single LV and Single RV Volumes

**Table 12.17 Volume Data for Single LV and Single RV comparison**

| | Ventricle Morphology | EDV (mL/BSA) | ESV (mL/BSA) | SV (mL/BSA) | EF (%) |
|---|---|---|---|---|---|
| CHOP004D | L | 59.49 | 24.68 | 34.81 | 58 |
| CHOP005B | L | 92.72 | 46.36 | 45.7 | 50 |
| CHOP024A | L | 82.43 | 36.49 | 45.95 | 55 |
| CHOP033A | L | 75 | 39.39 | 35.61 | 47 |
| CHOP034A | L | 70.9 | 29.63 | 41.27 | 58 |
| CHOP036A | L | 62.18 | 23.53 | 39.5 | 63 |
| CHOP052B | L | 87.74 | 37.74 | 50 | 57 |
| CHOP082B | L | 92.42 | 43.94 | 48.48 | 52 |

| | | | | | |
|---|---|---|---|---|---|
| CHOP088B | L | 84.88 | 40.7 | 43.6 | 52 |
| CHOP089A | L | 96.77 | 48.39 | 48.39 | 50 |
| CHOP091A | L | 41.83 | 19.71 | 21.63 | 52 |
| CHOP094A | L | 89.17 | 36.67 | 52.5 | 59 |
| CHOP135A | L | 88.31 | 22.08 | 66.23 | 75 |
| CHOP145A | L | 66.23 | 20.53 | 45.7 | 69 |
| CHOP188A | L | 88.08 | 26.49 | 61.59 | 70 |
| CHOP204A | L | 88.74 | 42.38 | 46.36 | 48 |
| CHOP008B | R | 75.26 | 41.75 | 33.51 | 45 |
| CHOP016A | R | 57.83 | 25.3 | 32.53 | 57 |
| CHOP019A | R | 45.83 | 17.86 | 27.98 | 61 |
| CHOP021A | R | 77.24 | 34.15 | 43.09 | 55 |
| CHOP022A | R | 97.8 | 67.03 | 31.87 | 32 |
| CHOP023A | R | 76.23 | 27.87 | 48.36 | 64 |
| CHOP028A | R | 54.17 | 21.35 | 32.29 | 60 |
| CHOP029A | R | 86.11 | 32.41 | 53.7 | 62 |
| CHOP037A | R | 55 | 30 | 25 | 46 |
| CHOP041A | R | 62.25 | 19.21 | 42.38 | 69 |
| CHOP065A | R | 109.56 | 55.88 | 52.94 | 49 |
| CHOP066A | R | 93.75 | 38.28 | 55.47 | 59 |
| CHOP080A | R | 58.64 | 22.51 | 36.13 | 61 |
| CHOP085A | R | 58 | 24 | 34 | 59 |
| CHOP108A | R | 96.77 | 47.31 | 48.39 | 51 |
| CHOP114A | R | 91.43 | 49.14 | 42.29 | 46 |
| CHOP166A | R | 82.27 | 33.33 | 48.94 | 59 |
| CHOP203A | R | 95.85 | 42.49 | 53.37 | 55 |

11. **Inter-user variability**

To evaluate user-dependence on the derived values, results were compared between my segmentations and those of Kartik Sundareswaran with the volume data presented in Table 12.18.

**Table 12.18 Comparison of derived volumes for 8 patients from separate segmentations of Kartik Sundareswaran (KS) and Christopher Haggerty (CH)**

| | | EDV (mL) | ESV (mL) | SV (mL) |
|---|---|---|---|---|
| **CHOP108A** | CH | 100.4 | 49.1 | 50.2 |
| | KS | 88.3 | 45.6 | 42.7 |

| | | | | |
|---|---|---|---|---|
| **CHOP114A** | CH | 69.1 | 37.2 | 32.0 |
| | KS | 70.4 | 30.7 | 39.7 |
| **CHOP033A** | CH | 65.3 | 34.3 | 31.0 |
| | KS | 52.3 | 25.8 | 26.4 |
| **CHOP036A** | CH | 57.0 | 21.6 | 36.2 |
| | KS | 50.2 | 21.2 | 29.0 |
| **CHOP052B** | CH | 85.2 | 36.7 | 48.6 |
| | KS | 64.9 | 30.7 | 34.1 |
| **CHOP065A** | CH | 94.0 | 47.9 | 45.4 |
| | KS | 99.6 | 59.9 | 39.7 |
| **CHOP066A** | CH | 82.9 | 33.8 | 49.0 |
| | KS | 96.0 | 38.7 | 58.0 |
| **CHOP085A** | CH | 82.0 | 33.9 | 48.1 |
| | KS | 80.9 | 34.8 | 46.1 |

12. **Intra-User variability**

To evaluate the repeatability of the analysis, 5 cases were selected at random for repeat segmentations 7-8 months removed from the original analysis with the volume results provided in Table 12.19.

**Table 12.19 Volume results from repeat segmentations of 5 patients by the same user (CH). The second evaluation is denoted by '-2'**

| | EDV (mL) | ESV (mL) | SV (mL) |
|---|---|---|---|
| CHOP036A | 74 | 28 | 47 |
| CHOP036A-2 | 67 | 31 | 35 |
| CHOP089A | 90 | 45 | 45 |
| CHOP089A-2 | 87 | 45 | 42 |
| CHOP008B | 146 | 81 | 65 |
| CHOP008B-2 | 151 | 81 | 70 |
| CHOP021A | 95 | 42 | 53 |
| CHOP021A-2 | 98 | 47 | 51 |
| CHOP028A | 104 | 41 | 62 |
| CHOP028A-2 | 107 | 49 | 58 |

# E. Appendix E- Serial Patient Studies

## 13. Evaluating BSA normalization scheme

**Table 12.20 Relationship of ascending aortic diameter to BSA**

| | **Ao Diameter** (mm) | **BSA** ($m^2$) | **BSA$^{0.5}$** (m) |
|---|---|---|---|
| CHOP019A | 31 | 1.68 | 1.30 |
| CHOP019B | 37.1 | 1.84 | 1.36 |
| CHOP005B | 37.4 | 1.51 | 1.23 |
| CHOP005C | 44.6 | 1.5 | 1.22 |
| CHOP018A | 20.3 | 0.68 | 0.82 |
| CHOP018B | 26.9 | 0.93 | 0.96 |
| CHOP018C | 36.3 | 1.24 | 1.11 |
| CHOP021A | 31.3 | 1.23 | 1.11 |
| CHOP021B | 33.5 | 1.63 | 1.28 |
| CHOP022A | 32.3 | 0.91 | 0.95 |
| CHOP022B | 32.4 | 1.19 | 1.09 |
| CHOP033A | 23 | 1.32 | 1.15 |
| CHOP033B | 33.2 | 1.78 | 1.33 |
| CHOP036A | 29.9 | 1.19 | 1.09 |
| CHOP036B | 27.5 | 1.46 | 1.21 |
| CHOP065A | 35.5 | 1.36 | 1.17 |
| CHOP065B | 43.7 | 1.83 | 1.35 |
| CHOP080A | 40.5 | 1.91 | 1.38 |
| CHOP080B | 38.4 | 2.27 | 1.51 |
| CHOP082A | 29.3 | 0.87 | 0.93 |
| CHOP082B | 32.4 | 1.32 | 1.15 |
| CHOP088A | 32 | 1.25 | 1.12 |
| CHOP088B | 36.6 | 1.74 | 1.32 |
| CHOP091A | 41.6 | 2.08 | 1.44 |
| CHOP091B | 37.3 | 2.21 | 1.49 |

## 14. Flow changes

**Table 12.21 Changes in systemic venous flow rates**

| | | $Q_{IVC}$ (L/min) | $Q_{SVC}$ (L/min) | $Q_{IVC}$ (L/min/m$^2$) | $Q_{SVC}$ (L/min/m$^2$) | $Q_S$ (L/min/m$^2$) |
|---|---|---|---|---|---|---|
| CHOP005 | Scan 2 | 3.6 | 1 | 2.4 | 0.7 | 3.1 |
| | Scan 3 | 1.2 | 1.1 | 0.8 | 0.7 | 1.5 |
| CHOP008 | Scan 2 | 3.8 | 0.8 | 2 | 0.4 | 2.4 |
| | Scan 3 | 3.5 | 1.1 | 1.8 | 0.6 | 2.4 |
| CHOP017 | Scan 2 | 2.5 | 1.3 | 1.5 | 0.8 | 2.3 |
| | Scan 3 | 3 | 1 | 1.6 | 0.5 | 2.1 |
| CHOP018 | Scan 1 | 1.4 | 1.3 | 2.1 | 1.9 | 4 |
| | Scan 3 | 2.3 | 1 | 1.9 | 0.8 | 2.7 |
| CHOP019 | Scan 1 | 3.5 | 1.4 | 2.1 | 0.8 | 2.9 |
| | Scan 2 | 3.8 | 1.8 | 2.1 | 1 | 3.1 |
| CHOP021 | Scan 1 | 2.2 | 0.9 | 1.8 | 0.7 | 2.5 |
| | Scan 2 | 3.2 | 1.3 | 2 | 0.8 | 2.8 |
| CHOP022 | Scan 1 | 1.3 | 1.3 | 1.4 | 1.4 | 2.8 |
| | Scan 2 | 2.7 | 1.9 | 2.3 | 1.6 | 3.9 |
| CHOP033 | Scan 1 | 2.3 | 1.5 | 1.7 | 1.1 | 2.8 |
| | Scan 2 | 2.9 | 1.2 | 1.6 | 0.7 | 2.3 |
| CHOP036 | Scan 1 | 3.3 | 1.9 | 2.8 | 1.6 | 4.4 |
| | Scan 2 | 2.4 | 2 | 1.6 | 1.4 | 3 |
| CHOP052 | Scan 2 | 2.1 | 1.2 | 2 | 1.1 | 3.1 |
| | Scan 5 | 2.4 | 1.6 | 1.5 | 1 | 2.5 |
| CHOP065 | Scan 1 | 1.9 | 0.5 | 1.4 | 0.4 | 1.8 |
| | Scan 2 | 2.2 | 1.1 | 1.2 | 0.6 | 1.8 |
| CHOP080 | Scan 1 | 2.6 | 1.8 | 1.4 | 0.9 | 2.3 |
| | Scan 2 | 4.2 | 1.9 | 1.9 | 0.8 | 2.7 |
| CHOP082 | Scan 1 | 1.6 | 1 | 1.8 | 1.1 | 2.9 |
| | Scan 2 | 3.2 | 1.6 | 2.4 | 1.2 | 3.6 |
| CHOP088 | Scan 1 | 1.8 | 0.9 | 1.4 | 0.7 | 2.1 |
| | Scan 2 | 3.6 | 1.3 | 2.1 | 0.7 | 2.8 |
| CHOP091 | Scan 1 | 3.5 | 1.7 | 1.7 | 0.8 | 2.5 |
| | Scan 2 | 3.7 | 1.6 | 1.7 | 0.7 | 2.4 |

**Table 12.22 Respective differences in global pulmonary flow distribution (GFD) and HFD across serial patient scans**

| | %GFD difference | %HFD difference |
|---|---|---|
| CHOP005 | 2 | 25 |
| CHOP008 | -9 | -8 |
| CHOP017 | -1 | 2 |
| CHOP018* | -2 | -8 |
| CHOP019 | 1 | 8 |
| CHOP021 | -8 | -11 |
| CHOP022 | -11 | -2 |
| CHOP033 | 0 | 2 |
| CHOP036 | 7 | 19 |
| CHOP052* | 8 | 11 |
| CHOP065 | 20 | 19 |
| CHOP080 | -4 | 0 |
| CHOP082 | -7 | -6 |
| CHOP088 | -9 | 23 |
| CHOP091 | 9 | 3 |

*Difference taken between earliest and latest time points

## 15. Relating change in vessel size to change in power loss

**Table 12.23 Percentage change in normalized vessel diameters and TCPC-EDI**

| | % Change $D_{mean}$ LPA | % Change $D_{mean}$ RPA (%) | Ave % Change $D_{mean}$ both PAs | % Change $D_{mean}$ IVC | % Change TCPC-EDI |
|---|---|---|---|---|---|
| CHOP005 | -8.55 | 9.1 | 0.25 | 3.40 | 33 |
| CHOP008 | -12.5 | -10.5 | -12.00 | -7.50 | 249 |
| CHOP017 | -11.7 | 11.7 | 0.10 | -13.40 | 71.8 |
| CHOP018* | -11.20 | 0.50 | -5.00 | 8.00 | 29.2 |
| CHOP019 | 13.80 | -11.70 | 1.00 | 7.20 | -13.5 |
| CHOP021 | 23.90 | 15.30 | 20.00 | -1.00 | -24.3 |
| CHOP022 | 5.00 | -12.50 | -4.00 | -10.80 | 92.5 |
| CHOP033 | -9.90 | -26.10 | -18.00 | 1.50 | 138.4 |
| CHOP036 | 2.10 | 1.90 | 2.00 | -10.60 | 46.7 |

| | | | | | |
|---|---|---|---|---|---|
| CHOP052* | -14.00 | 6.00 | -4.00 | -17.80 | 104.4 |
| CHOP065 | -23.80 | -3.30 | -14.00 | -16.60 | 172.7 |
| CHOP080 | 46.00 | 8.60 | 27.00 | -5.80 | -4 |
| CHOP082 | -15.50 | -28.10 | -22.00 | -29.90 | 175.8 |
| CHOP088 | -2.60 | 20.50 | 9.00 | -11.70 | -57.1 |
| CHOP091 | 5.70 | 13.90 | 10.00 | 14.30 | -27.1 |

*Difference taken between earliest and latest time points

16. **Flow rate and pulsatility related to PA sizes**

Table 12.24 and Table 12.25 provide serially averaged (i.e., [value @ time 1+value @ time 2]/2) flow, diameter, and pulsatility data for the LPA and RPA, respectively. Additionally, the entry labeled '$\Delta D_{mean}$' provides the percentage difference between the serial values.

**Table 12.24 Serially averaged diameter, flow, and pulsatility data for the LPA**

| | **LPA $D_{mean}$ (mm/m)** | **$\Delta D_{mean}$ LPA (%)** | **LPA $D_{mean}$ (mm)** | **$\Delta D_{mean}$ LPA (%mm)** | **$Q_{avg}$ LPA (L/min)** | **$Q_{avg}$ LPA (L/min/m$^2$)** | **LPA PI** |
|---|---|---|---|---|---|---|---|
| CHOP005 | 9.3 | -8.6 | 11.5 | -9.2 | 2.2 | 1.46 | 0.56 |
| CHOP008 | 8.9 | -12.5 | 12.5 | -11.4 | 1.7 | 0.86 | 0.965 |
| CHOP017 | 7.0 | -11.7 | 9.4 | -5.2 | 0.6 | 0.33 | 0.665 |
| CHOP018* | 13.3 | -11.2 | 12.8 | 19.8 | 1.1 | 1.14 | 1.05 |
| CHOP019 | 9.4 | 13.8 | 12.5 | 19.5 | 2.2 | 1.22 | 0.71 |
| CHOP021 | 10.4 | 23.9 | 12.5 | 42.7 | 1.3 | 0.94 | 0.435 |
| CHOP022 | 8.6 | 5 | 8.8 | 20.0 | 1.4 | 1.30 | 0.535 |
| CHOP033 | 11.9 | -9.9 | 10.1 | 4.9 | 1.9 | 1.25 | 0.885 |
| CHOP036 | 12.8 | 2.1 | 14.7 | 13.0 | 2.2 | 1.67 | 0.785 |
| CHOP052* | 10.9 | -14 | 12.5 | 5.8 | 1.6 | 1.25 | 0.73 |
| CHOP065 | 13.9 | -23.8 | 17.4 | -11.4 | 1.3 | 0.77 | 1.075 |
| CHOP080 | 9.1 | 46 | 13.2 | 58.8 | 3.1 | 1.45 | 0.37 |
| CHOP082 | 12.4 | -15.5 | 12.9 | 4.0 | 1.2 | 1.05 | 1.395 |
| CHOP088 | 10.2 | -2.6 | 12.5 | 14.7 | 2.3 | 1.52 | 0.57 |
| CHOP091 | 9.6 | 5.7 | 14.1 | 8.9 | 2.6 | 1.22 | 0.735 |

*Difference taken between earliest and latest time points

**Table 12.25 Serially averaged diameter, flow, and pulsatility data for the RPA**

| | RPA $D_{mean}$ (mm/m) | $\Delta D_{mean}$_RPA (%) | $Q_{avg}$ RPA (L/min) | $Q_{avg}$ RPA (L/min/m$^2$) | RPA PI |
|---|---|---|---|---|---|
| CHOP005 | 11.90 | 9.10 | N/A | N/A | 1.09 |
| CHOP008 | 13.06 | -10.50 | 2.4 | 1.23 | 0.93 |
| CHOP017 | 13.14 | 11.70 | 3.1 | 1.77 | 1.24 |
| CHOP018* | 13.30 | 0.50 | 1.4 | 1.47 | 1.04 |
| CHOP019 | 12.66 | -11.70 | 3.1 | 1.74 | 0.82 |
| CHOP021 | 10.02 | 15.30 | 3.5 | 2.15 | 0.46 |
| CHOP022 | 10.80 | -12.50 | 1.3 | 1.18 | 0.46 |
| CHOP033 | 11.29 | -26.10 | 1.7 | 1.09 | 1.48 |
| CHOP036 | 12.14 | 1.90 | 1.6 | 1.22 | 0.83 |
| CHOP052* | 7.10 | 6.00 | 1.6 | 1.23 | 1.15 |
| CHOP065 | 11.20 | -3.30 | 1.5 | 0.93 | 0.94 |
| CHOP080 | 13.26 | 8.60 | 3.1 | 1.43 | 0.60 |
| CHOP082 | 10.82 | -28.10 | 1.7 | 1.54 | 1.48 |
| CHOP088 | 8.39 | 20.50 | 1.7 | 1.14 | 1.22 |
| CHOP091 | 10.49 | 13.90 | 2.6 | 1.20 | 0.78 |

*Difference taken between earliest and latest time points

17. **Change in Cardiac Index with Age**

**Table 12.26 Relationship between serial cardiac index change and age at first CMR evaluation**

| | Age (yrs) at first CMR | CI scan 1 (L/min/m$^2$) | CI scan 2 (L/min/m$^2$) | %CI |
|---|---|---|---|---|
| CHOP005 | 19 | 3 | 2.4 | -20% |
| CHOP008 | 16 | 3 | 3.1 | 3% |
| CHOP017 | 15 | 3.1 | 2.4 | -23% |
| CHOP018* | 7 | 4.5 | 3.1 | -31% |
| CHOP019 | 14 | 3.3 | 2.8 | -15% |
| CHOP021 | 11 | 3 | 2.7 | -10% |
| CHOP022 | 7 | 3.7 | 4.1 | 11% |

| | | | | |
|---|---|---|---|---|
| CHOP033 | 10 | 2.6 | 3.1 | 19% |
| CHOP036 | 11 | 4.7 | 2.7 | -43% |
| CHOP052* | 10 | 5.5 | 4.2 | -24% |
| CHOP065 | 16 | 2.5 | 2.2 | -12% |
| CHOP080 | 17 | 2.9 | 3.5 | 21% |
| CHOP082 | 7 | 3.1 | 3.8 | 23% |
| CHOP088 | 8 | 2.7 | 3.5 | 30% |
| CHOP091 | 18 | 2.4 | 2.7 | 13% |

*Difference taken between earliest and latest time points

18. **Serial Ventricular Function Changes**

**Table 12.27 Percentage changes in serial ventricular function measures**

| | EDV% | SV% | ESV% | PER% | PFR% | CI% | TCPC-EDI% |
|---|---|---|---|---|---|---|---|
| CHOP005 | -9% | -8 | -11% | 37 | -15 | -18 | 33% |
| CHOP008 | 31% | 35 | 29% | 3 | 20 | 14 | 251% |
| CHOP019 | 33% | 46 | 9% | 31 | 15 | 51 | -12% |
| CHOP033 | 10% | -10 | 28% | -19 | -13 | -29 | 138% |
| CHOP052 | 3% | -23 | 38% | -23 | 9 | -27 | 105% |
| CHOP080 | -13% | -16 | -8% | -27 | -21 | -39 | -4% |
| CHOP091 | 18% | 15 | 24% | 3 | 4 | 34 | -26% |

**Table 12.28 Serial measures of $Q_s$, cardiac index, and TCPC-EDI**

| | $Q_s$ scan 1 (L/min/m$^2$) | $Q_s$ scan 2 (L/min/m$^2$) | CI scan 1 (L/min/m$^2$) | CI scan 2 (L/min/m$^2$) | EDI scan 1 | EDI scan 2 |
|---|---|---|---|---|---|---|
| CHOP005 | 3.0 | 2.1 | 3.0 | 2.4 | 0.087 | 0.116 |
| CHOP008 | 2.4 | 2.3 | 3.0 | 3.1 | 0.065 | 0.228 |
| CHOP017 | 2.3 | 2.1 | 3.1 | 2.4 | 0.035 | 0.061 |
| CHOP018* | 3.8 | 2.7 | 4.5 | 3.1 | 0.008 | 0.01 |
| CHOP019 | 3.0 | 3.0 | 3.3 | 2.8 | 0.034 | 0.03 |
| CHOP021 | 2.5 | 2.8 | 3.0 | 2.7 | 0.076 | 0.057 |
| CHOP022 | 2.9 | 3.9 | 3.7 | 4.1 | 0.016 | 0.031 |
| CHOP033 | 2.9 | 2.3 | 2.6 | 3.1 | 0.016 | 0.038 |
| CHOP036 | 4.4 | 3.0 | 3.4 | 2.7 | 0.016 | 0.023 |
| CHOP052* | 3.1 | 2.5 | 5.5 | 4.2 | 0.022 | 0.027 |
| CHOP065 | 1.8 | 1.8 | 2.5 | 2.2 | 0.013 | 0.035 |
| CHOP080 | 2.3 | 2.7 | 2.9 | 3.5 | 0.11 | 0.106 |
| CHOP082 | 3.0 | 3.7 | 3.1 | 3.8 | 0.012 | 0.033 |
| CHOP088 | 2.2 | 2.8 | 2.7 | 3.5 | 0.068 | 0.029 |
| CHOP091 | 2.5 | 2.4 | 2.4 | 2.7 | 0.031 | 0.023 |

*Difference taken between earliest and latest time points

# F. Appendix F- List of Codes and Programs Used

19. **MRI Data Sorting**

- **"DICOM-sort.py"** (Credit: Jonathan Suever)- Reads in the raw dicom files for a patient scan (which usually have arbitrary numbers as file names) and can sort and organize by information provided in the dicom headers ("Series Description" for example).

20. **Axial Interpolation**

- **Adaptive Control Grid Interpolation (ACGI)** (Credit: David Frakes)- all sub-routines entirely contained within the 'ACGI' directory and driven by "acgi_driver.m"

21. **TCPC Segmentation**

- **"Bouncing Ball" Algorithm** (Credit: David Frakes)- all sub-routines entirely contained within the "Segmentation Code" directory and driven by "runit.m"

- **3D Level Set** (Credit Kartik Sundareswaran)- creates 3D point cloud by reading in segmentation masks from bouncing ball. Consists of 4 files: "LevelSetSegmentation_3D_Phasic_v3.m" (driver file); "levelsetEvolution_3D.m"; "MRI_Coord_Transform_3D_axial.m"; and "Image_To_MRI_Coord_Transform.m"

22. **Phase contrast velocity segmentation**

- **"flow_chop.m"-** read in, segment, and export velocity and flow data for through plane PC data

- **“auto_noise_fuzzy_resegm_specific_dataset.m” –**(credit Kartik Sundareswaran) post-processing step for velocity data that filters results with fuzzy rules

23. **Divergence Free Interpolation** (credit: Kartik Sundareswaran)

- **“SegmentationCoronal.m”-** registers coronal velocity data to axial anatomic data
- **“Interpolation_Driver_Pulsatile.m”** – interpolation driver file
- **“ErrorAnalysis.m”** – optional step to compare interpolated results for a given slice to the measured velocity on that slice

24. **CFD Solver** (credit: Diane de Zélicourt)

- **PreProcessor (IBUns_Li_MPI_PreProcess)**
- **Solver (FS_MPI_Solver)**
- **PostProcessor (GetFlowField)** (note- I added a second version of the post-processor “GetFlowField-s” that does not write the tecplot flow fields, which helps to speed up post-processing for pulsatile runs)
- **Auxillary-** input_MPI.txt; control.txt; GetFlowField_input.txt; pulseBC_forCode.f90 (reads in BC_input.txt and creates BC.txt input for pulse simulations); makeBC_input_forCFD.m (reads in output from velocity segmentation and creates the BC_input file for pulse simulations).

25. **CFD Data Analysis**

- **Steady power loss calculation**- done using spreadsheets (see "Template.xls" in CFD code backup
- **Pulsatile power loss calculation- "CFDpulsatile_powerloss_compute.m"** (reads in "GetDvol.m")

26. **HFD Quantification**

- **Steady streamtraces**- (credit: Diane de Zélicourt) "compute_IVC_split.f90" and "exact_streamtraces.f90" (require tecplot)
- **Pulsatile particle tracking-** (credit: Diane de Zélicourt) "all_data.f", "main.f", Makefile
- **From DFI data-** (credit: Lucia Mirabella)- "HFDfromParticles.m", "pointIsInBox.m" (require Paraview, see protocol in methods chapter)

27. **VF Analysis**

- **"SV_Segment.m"-** driver file for semi-automatic ventricular short axis segmentation
- **"VF_analysis.m"** – reads in results of segmentation and outputs results

28. **Miscellaneous Tecplot Macros**

- **"PlotQ.mcr"** (credit- Min Yun)- calculates Q-criterion
- **"anatomy_rotate.mcr"-** creates a movie of a rotating body

- **“image_setup.mcr”** – expedites figure creation from steady CFD results after loading flow field and body file into tecplot

- **“make_streamtraces.f90”** – derived from “extract_streamtraces.f90” but creates volume ribbons and does not create individual zones

- **“StreamtraceMovieMaker.mcr”** – writes an avi by consecutively cycling through zones of a pulsatile data series with streamtraces already drawn in.

- **“PT_presentation.mcr”-** like the streamtrace file, but designed for particle tracking data sets

- **“Jpg-movie.mcr” –** tecplot writes avi files using a broken windows codec making it non-compatible with linux or adobe players, my work-around for this (to insert movies into the thesis pdf, for example) was to export individual frames as jpg files (with this macro) and stitch them together with ffmpeg into an mpeg movie.

# REFERENCES


1. O'Leary PW. Prevalence, clinical presentation and natural history of patients with single ventricle. *Progress in Pediatric Cardiology*. 2002;16:31-38
2. Sonnenblick E. Implications of muscle mechanics in the heart. *Federation Proceedings*. 1962;21:975-990
3. Vasan RS, Levy D. Defining diastolic heart failure: A call for standardized diagnostic criteria. *Circulation*. 2000;101:2118-2121
4. Fogel MA. *Ventricular function and blood flow in congenital heart disease*. Malden, Mass.: Blackwell Futura; 2005.
5. National Heart Lung and Blood Institute. What are congenital heart defects? <http://www.nhlbi.nih.gov/health/health-topics/topics/chd/> July, 2012.
6. Hoffman JI, Kaplan S. The incidence of congenital heart disease. *Journal of the American College of Cardiology*. 2002;39:1890-1900
7. The Children's Heart Foundation. About chf: Fact sheets. <http://www.childrensheartfoundation.org/about-chf/fact-sheets> July, 2012.
8. Williams RG, Pearson GD, Barst RJ, Child JS, del Nido P, Gersony WM, Kuehl KS, Landzberg MJ, Myerson M, Neish SR, Sahn DJ, Verstappen A, Warnes CA, Webb CL. Report of the national heart, lung, and blood institute working group on research in adult congenital heart disease. *J Am Coll Cardiol*. 2006:j.jacc.2005.2008.2074
9. Morris Cd MVD. 25-year mortality after surgical repair of congenital heart defect in childhood: A population-based cohort study. *JAMA: The Journal of the American Medical Association*. 1991;266:3447-3452

10. Norwood W, Lang P, Castaneda AR, Campbell D. Experience with operations for hypoplastic left heart syndrome. *Journal of Thoracic and Cardiovascular Surgery*. 1981;82:511-519

11. Sano S, Ishino K, Kado H, Shiokawa Y, Sakamoto K, Yokota M, Kawada M. Outcome of right ventricle–to–pulmonary artery shunt in first-stage palliation of hypoplastic left heart syndrome: A multi-institutional study. *The Annals of Thoracic Surgery*. 2004;78:1951-1958

12. Ohye RG, Sleeper LA, Mahony L, Newburger JW, Pearson GD, Lu M, Goldberg CS, Tabbutt S, Frommelt PC, Ghanayem NS, Laussen PC, Rhodes JF, Lewis AB, Mital S, Ravishankar C, Williams IA, Dunbar-Masterson C, Atz AM, Colan S, Minich L, Pizarro C, Kanter K, Jaggers J, Jacobs JP, Krawczeski CD, Pike NA, McCrindle BW, Virzi L, Gaynor JW. Comparison of shunt types in the norwood procedure for single-ventricle lesions. *New England Journal of Medicine*. 2010;362:1980-1992

13. Fontan F, Baudet E. Surgical repair of tricuspid atresia. *Thorax*. 1971;26:240-248

14. Kreutzer G, Galíndez E, Bono H, De Palma C, Laura JP. An operation for the correction of tricuspid atresia. *The Journal of thoracic and cardiovascular surgery*. 1973;66:613-621

15. Mair DD, Puga FJ, Danielson GK. Late functional status of survivors of the fontan procedure performed during the 1970s. *Circulation*. 1992;86:II106-109

16. Dobell ARC, Trusler GA, Smallhorn JF, Williams WG. Atrial thrombi after the fontan operation. *The Annals of Thoracic Surgery*. 1986;42:664-667

17. de Leval MR, Kilner P, Gewillig M, Bull C. Total cavopulmonary connection: A logical alternative to atriopulmonary connection for complex fontan operations. *Journal of Thoracic and Cardiovascular Surgery*. 1988;96:682-695

18. Balaji S, Gewillig M, Bull C, de Leval MR, Deanfield J. Arrhythmias after the fontan procedure. Comparison of total cavopulmonary connection and atriopulmonary connection. *Circulation*. 1991;84:III162-167

19. Marcelletti C, Corno A, Giannico S, Marino B. Inferior vena cava-pulmonary artery extracardiac conduit. A new form of right heary bypass. *Journal of Thoracic and Cardiovascular Surgery*. 1990;100:228-232

20. Stewart RD, Pasquali SK, Jacobs JP, Benjamin DK, Jaggers J, Cheng J, Mavroudis C, Jacobs M. Contemporary fontan operation: Association between early outcome and type of cavopulmonary connection. *Annals of Thoracic Surgery*. 2012;93:1254-1261

21. Rodefeld MD, Boyd JH, Myers CD, Robert G. Presson J, Wiltz W. Wagner J, Brown JW. Cavopulmonary assist in the neonate; an alternative strategy for single-ventricle palliation. *Journal of Thoracic and Cardiovascular Surgery*. 2004;127:705-711

22. Mair DD, Puga FJ, Danielson GK. The fontan procedure for tricuspid atresia: Early and late results of a 25-year experience with 216 patients. *J Am Coll Cardiol*. 2001;37:933-939

23. Gaynor JW, Bridges ND, Cohen MI, Mahle WT, DeCampli WM, Steven JM, Nicolson SC, Spray TL. Predictors of outcome after the fontan operation: Is hypoplastic left heart syndrome still a risk factor? *Journal of Thoracic and Cardiovascular Surgery*. 2002;123:237-245

24. Huddleston CB. The failing fontan: Options for surgical therapy. *Pediatric Cardiology*. 2007;28:472-476

25. Mayer JE, Bridges ND, Lock JE, Hanley FL, Jonas RA, Castaneda AR. Factors associated with marked reduction in mortality for fontan operations in patients

with single ventricle. *The Journal of thoracic and cardiovascular surgery*. 1992;103:444-451; discussion 451-442

26. Gewillig M. The fontan circulation. *Heart*. 2005;91:839-846

27. Khairy P, Fernandes SM, John E. Mayer J, Triedman JK, Walsh EP, Lock JE, Landzberg MJ. Long-term survival, modes of death, and predictors of martality in patients with fontan surgery. *Circulation*. 2008;117:85-92

28. Rychik J, Goldberg D, Dodds K. Long-term results and consequences of single ventricle palliation. *Progress in Pediatric Cardiology*. 2010;29:19-23

29. Gersony DR, Gersony WM. Management of the postoperative fontan patient. *Progress in Pediatric Cardiology*. 2003;17:73-79

30. Anderson PAW, Sleeper LA, Mahony L, Colan SD, Atz AM, Breitbart RE, Gersony WM, Gallagher D, Geva T, Margossian R, McCrindle BW, Paridon SM, Schwartz M, Stylianou M, Williams RV, III BJC. Contemporary outcomes after the fontan procedure. *Journal of the American College of Cardiology*. 2008;52:85-98

31. Jayakumar KA, Addonizio LJ, Kichuk-Chrisant MR, Galantowicz ME, Lamour JM, Quaegebeur JM, Hsu DT. Cardiac transplantation after the fontan or glenn procedure. *Journal of the American College of Cardiology*. 2004;44:2065-2072

32. Kirklin J, Blackstone E, Kirklin J, Pacifico A, Bargeron L. The fontan operation. Ventricular hypertrophy, age and date of operation as risk factors. *Journal of Thoracic and Cardiovascular Surgery*. 1986;92:1049-1064

33. Fogel M, Weinberg PM, Chin AJ, Fellows KE, Hoffman EA. Late ventricular geometry and performance changes of functional single ventricle throughout staged fontan reconstruction assessed by magnetic resonance imaging. *Journal of the American College of Cardiology*. 1996;28:212-221

34. Cavalcanti S, Gnudi G, Mesetti P, Ussia G, Macelletti C. Analysis by mathematical model of haemodynamic data in the failing fontan circulation. *Physiological Measurement*. 2001;22:209-222

35. Eicken A, Fratz S, Gutfried C, Balling G, Schwaiger M, Lange R, Busch R, Hess J, Stern H. Hearts late after fontan operation have normal mass, normal volume, and reduced systolic function. *Journal of the American College of Cardiology*. 2003;42:1061-1065

36. Piran S, veldtman GR, Siu S, Webb GD, Liu PP. Heart failure and ventricular dysfunction in patients with single or systemic right ventricles. *Circulation*. 2002;105:1189-1194

37. Cheung Y, Penny D, Redington A. Serial assessment of left ventricular diastolic function after fontan procedure. *Heart*. 2000;83:420-424

38. Senzaki H, Masutani S, Kobayashi J, Kobayashi T, Sasaki N, Asano H, Kyo S, Yokote Y, Ishizawa A. Ventricular afterload and ventricular work in fontan circulation: Comparison with normal two-ventricle circulation and single-ventricle circulation with blalock-taussig shunts. *Circulation*. 2002;105:2885-2892

39. Senzaki H, Masutani S, Ishido H, Taketazu M, Kobayashi T, Saski N, Asano H, Katogi TK, Shunei, Yokote Y. Cardiac rest and reserve function in patients with fontan circulation. *Journal of the American College of Cardiology*. 2006;47:2528-2535

40. Szabo G, Buhmann V, Graf A, Melnitschuk S, Bahrle S, Vahl CF, Hagl S. Ventricular energetics after the fontan operation: Contractility-afterload mismatch. *J Thorac Cardiovasc Surg*. 2003;125:1061-1069

41. Sundareswaran K, Kanter KR, Kitajima HD, KrishnankuttyRema R, Sabatier JF, Parks WJ, Sharma S, Yoganathan AP, Fogel MA. Impaired power output and

cardiac index with hypoplastic left heart syndrome: A magnetic resonance imaging study. *Annals of Thoracic Surgery*. 2006;82

42. Guyton A, Abernathy B, Langston J, Kaufmann B, Fairchild H. Relative importance of venous and arterial resistances in controlling venous return and cardiac output. *American Journal of Physiology*. 1959;196:1008-1014

43. Kelly J, Mack G, Fahey J. Diminished venous vascular capacitance in patients with univentricular hearts after the fontan operation. *American Journal of Cardiology*. 1995;76:158-163

44. Krishnan US, Taneja I, Gewitz M, Young R, Stewart J. Peripheral vascular adaptation and orthostatic tolerance in fontan physiology. *Circulation*. 2009;120:1775-1783

45. de Leval MR. The fontan circulation: What have we learned? What to expect? *Pediatric Cardiology*. 1998;19:316-320

46. Rychik J. Protein-losing enteropathy after fontan operation. *Congenital Heart Disease*. 2007;2:288-300

47. Kendall TJ, Stedman B, Hacking N, Haw M, Vettukattill JJ, Salmon AP, Cope R, Sheron N, Millward-Sadler H, Veldtman GR, Iredale JP. Hepatic fibrosis and cirrhosis in the fontan circulation: A detailed morphological study. *Journal of Clinical Pathology*. 2008;61:504-508

48. Kiesewetter CH, Sheron N, Vettukattill JJ, Hacking N, Stedman B, Millward-Sadler H, Haw M, Cope R, Salmon AP, Sivaprakasam MC, Kendall T, Keeton BR, Iredale JP, Veldtman GR. Hepatic changes in the failing fontan circulation. *Heart*. 2007;93:579-584

49. Goldberg D, French B, McBridge MG, Marino BS, Mirarchi N, Hanna BD, Wernovsky G, Paridon SM, Rychik J. Impact of oral sildenafil on exercise

performance in children and young adults after the fontan operation. *Circulation*. 2011;123:1185-1193

50. Reinhardt Z, Uzun O, Bhole V, Ofoe V, Wilson D, Onuzo O, Wright J, Stumper O. Sildenafil in the management of the failing fontan circulation. *Cardiology in the Young*. 2010;20:522-525

51. Uzun O, Wong JK, Bhole V, Stumper O. Resolution of protein-losing enteropathy and normalization of mesenteric doppler flow with sildenafil after fontan. *Annals of Thoracic Surgery*. 2006;82:e39-e40

52. Mertens L, Hagler D, Sauer U, Somerville J, Gewillig M. Protein-losing eneropathy after the fontan operation: An international multicenter study. Ple study group. *Journal of Thoracic and Cardiovascular Surgery*. 1998;115:1063-1073

53. Sharma S, Goudy S, Walker P, Panchal S, Ensley A, Kanter K, Tam V, Fyfe D, Yoganathan AP. In vitro flow experiments for determination of optimal geometry of total cavopulmonary connection for surgical repair of children with functional single ventricle. *Journal of the American College of Cardiology*. 1996;27:1264-1269

54. DeGroff CG. Modeling the fontan circulation: Where we are and where we need to go. *Pediatric Cardiology*. 2008;29:3-12

55. Sundareswaran KS, Pekkan K, Dasi LP, Whitehead K, Sharma S, Kanter K, Fogel M, Yoganathan AP. The total cavopulmonary connection resistance: A significant impact on single ventricle hemodynamics at rest and exercise. *American Journal of Physiology Heart and Circulatory Physiology*. 2008;295:H2427-H2435

56. Whitehead KK, Pekkan K, Kitajima HD, Paridon SM, Yoganathan AP, Fogel MA. Nonlinear power loss during exercise in single-ventricle patients after the fontan: Insights from computational fluid dynamics. *Circulation*. 2007;116:I-165-I-171

57. Bendien C, Bossina KK, Buurma AE, Gerding AM, Kuipers JRG, Landsman MLJ, Mook GA, Zijlstra WG. Hemodynamic effects of dynamic exercise in children and adolescents with moderate-to-small ventricular septal defects. *Circulation*. 1984;70:929-934

58. Duncan B, Desai S. Pulmonary arteriovenous malformations after cavopulmonary anastomosis. *Annals of Thoracic Surgery*. 2003;76:1759-1766

59. Pandurangi UM, Shah MJ, Murali R, Cherian KM. Rapid onset of pulmonary arteriovenous malformations after cavopulmonary anastomosis. *Annals of Thoracic Surgery*. 1999;68:237-239

60. Pike NA, Vricella LA, Feinstein JA, Black MD, Reitz BA. Regression of severe pulmonary arteriovenous malformations after fontan revision and "hepatic factor" rerouting. *Annals of Thoracic Surgery*. 2004;78:697-699

61. Sundareswaran KS, de Zelicourt D, Sharma S, Kanter K, Spray TL, Rossignac J, Sotiropoulos F, Fogel M, Yoganathan AP. Correction of pulmonary arteriovenous malformation using image-based surgical planning. *Journal of the American College of Cardiology: Cardiovascular Imaging*. 2009;2:1024-1030

62. McElhinney DB, Marx GR, Marshall AC, Mayer JEJ, del Nido P. Cavopulmonary pathway modification in patients with heterotaxy and newly diagnosed or persistent pulmonary arteriovenous malformations after a modified fontan operation. *Journal of Thoracic and Cardiovascular Surgery*. 2011;131:1362-1370

63. Akagi T, Benson LN, Green M, Ash J, Gilday DL, Williams WG, Freedom RM. Ventricular performance before and after fontan repair for univentricular

atrioventricular connection: Angiographic and radionuclide assessment. *J Am Coll Cardiol*. 1992;20:920-926

64. Akagi T, Benson LN, Gilday DL, Ash J, Green M, Williams WG, Freedom RM. Influence of ventricular morphology on diastolic filling performance in double-inlet ventricle after the fontan procedure. *Journal of the American College of Cardiology*. 1993;22:1948-1952

65. Parikh SR, Hurwitz RA, Caldwell RL, Girod DA. Ventricular function in the single ventricle before and after fontan surgery. *The American Journal of Cardiology*. 1991;67:1390-1395

66. Gewillig M, Brown SC, Eyskens B, Heying R, Ganame J, Budts W, Gerche AL, Gorenflo M. The fontan circulation: Who controls cardiac output? *Interactive CardioVascular and Thoracic Surgery*. 2010;10:428-433

67. Rathod RH, Prakash A, Powell AJ, Geva T. Myocardial fibrosis identified by cardiac magnetic resonance late gadolinium enhancement is associated with adverse ventricular mechanics and ventricular tachycardia late after fontan operation. *Journal of the American College of Cardiology*. 2010;55:1721-1728

68. Gledhill N, Cox D, Jamnik R. Endurance athletes' stroke volume does not plateau: Major advantage is diastolic function. *Medicine and science in sports and exercise*. 1994;26:1116-1121

69. Milanesi O, Stellin G, Colan S, Facchin P, Crepaz R, Biffanti R, Zacchello F. Systolic and diastolic performance late after the fontan procedure for a single ventricle and comparison of those undergoing operation at <12 months of age and at >12 months of age. *American Journal of Cardiology*. 2002;89:276-280

70. Frommelt PC, Snider R, Meliones JN, Vermilion RP. Doppler assessment of pulmonary artery flow patterns and ventricular function after the fontan operation. *American Journal of Cardiology*. 1991;68:1211-1215

71. Ishida Y, Meisner J, Tsujioka K, Gallo J, Yoran C, Frater R, Yellin E. Left ventricular filling dynamics: Influence of left ventricular relaxation and left atrial pressure *Circulation*. 1986;74:187-196

72. Penny D, Rigby M, Redington A. Abnormal patterns of intraventricular flow and diastolic filling after the fotan operation: Evidence for incoordinate ventricular wall motion. *British Heart Journal*. 1991;66:375-278

73. Khunatorn Y, Shandas R, DeGroff C, Mahalingam S. Comparison of in vitro velocity measurements in a scaled total cavopulmonary connection with computational predictions. *Annals of Biomedical Engineering*. 2003;31:810-822

74. Gerdes A, Kunze J, Pfister G, Sievers HH. Addition of a small curvature reduces power losses across total cavopulmonary connections. *Annals of Thoracic Surgery*. 1999;67:1760-1764

75. Ensley A, Lynch P, Chatzimavroudis GP, Lucas CL, Sharma S, Yoganathan AP. Toward designing the optimal total cavopulmonary connection: An in vitro study. *Annals of Thoracic Surgery*. 1999;68:1384-1390

76. DeGroff CG, Birnbaum B, Shandas R, Orlando W, Hertzberg J. Computational simulations of the total cavo-pulmonary connection: Insights in optimizing numerical solutions. *Medical Engineering & Physics*. 2005;27:135-146

77. Wang C, Pekkan K, Zelicourt DD, Horner M, Parihar A, Kulkarni A, Yoganathan AP. Progress in the cfd modeling of flow instabilities in anatomical total cavopulmonary connections. *Annals of Biomedical Engineering*. 2007;35:1840-1856

78. DeGroff CG, Carlton JD, Weinberg CE, Ellison MC, Shandas R, Valdes-Cruz L. Effect of vessel size on the flow efficiency of the total cavopulmonary connection: In vitro studies. *Pediatr Cardiol*. 2002;23:171-177

79. Ryu K, Healy T, Ensley A, Sharma S, Lucas C, Yoganathan AP. Importance of accurate geometry in the study of the total cavopulmonary connection: Computational studies and in vitro experiments. *Annals of Biomedical Engineering*. 2001;29:844-853

80. de Zelicourt D, Pekkan K, Wills L, Kanter K, Forbess J, Sharma S, Fogel M, Yoganathan AP. In vitro flow analysis of a patient-specific intraatrial total cavopulmonary connection. *Annals of Thoracic Surgery*. 2005;79:2094-2102

81. de Zelicourt D, Pekkan K, Parks WJ, Kanter K, Fogel M, Yoganathan AP. Flow study of an extracardiac connection with persistent left superior vena cava. *Journal of Thoracic and Cardiovascular Surgery*. 2006;131:785-791

82. Migliavacca F, Dubini G, Bove E, De Leval MR. Computational fluid dynamics simulations in realistic 3-d geometries of the total cavopulmonary anastomosis: The influence of the inferior caval anastomosis. *Journal of Biomechanical Engineering*. 2003;125:805-813

83. Pekkan K, Kitajima HD, de Zelicourt D, Forbess JM, Parks WJ, Fogel MA, Sharma S, Kanter KR, Frakes D, Yoganathan AP. Total cavopulmonary connection flow with functional left pulmonary artery stenosis: Angioplasty and fenestration in vitro. *Circulation*. 2005;112:3264-3271

84. Hsia T-Y, Migliavacca F, Pittaccio S, Radaelli A, Dubini G, Pennati G, De Leval MC. Computational fluid dynamic study of flow optimization in realistic models of the total cavopulmonary connections. *Journal of Surgical Research*. 2004;116:305-313

85. Marsden AL, Vignon-Clementel IE, Chan FP, Feinstein JA, Taylor CA. Effects of exercise and respiration on hemodynamic efficiency in cfd simulations of the total cavopulmonary connection. *Annals of Biomedical Engineering*. 2007;35:250-263

86. Throckmorton AL, Kapadia JY, Chopski SG, Bhavsar SS, Moskowitz WB, Gullquist SD, Gangemi JJ, Haggerty CM, Yoganathan AP. Numerical, hydraulic, and hemolytic evaluation of an intravascular axial flow blood pump to mechanically support fontan patients. *Annals of Biomedical Engineering*. 2011;39:324-336

87. Rodefeld M, Coats B, Fisher T, Giridharan GA, Chen J, Brown J, Frankel SH. Cavopulmonary assist for the univentricular fontan circulation: Von karman viscous impeller pump. *Journal of Thoracic and Cardiovascular Surgery*. 2010;140:529-536

88. Lacour-Gayet FG, Lanning CJ, Stoica S, Wang R, Rech B, Goldberg S, Shandas R. An artificial right ventricle for failing fontan: In vitro and computational study. *Annals of Thoracic Surgery*. 2009;88:170-176

89. Be'eri E, Maier SE, Landzberg MJ, Chung T, Geva T. *In vivo* evaluation of fontan pathway flow dynamics by multidimensional phase-velocity magnetic resonance imaging. *Circulation*. 1998;98:2873-2882

90. Sharma S, Ensley A, Hopkins K, Chatzimavroudis GP, Healy T, Tam V, Kanter K, Yoganathan AP. *In vivo* flow dynamics of the total cavopulmonary connection from three-dimensional multislice magnetic resonance imaging. *The Annals of Thoracic Surgery*. 2001;71:889-898

91. Markl M, Geiger J, Kilner PJ, Foll D, Stiller B, Beyersdorf F, Arnold R, Frydrychowicz A. Time-resolved three-dimensional magnetic resonance velocity mapping of cardiovascular flow paths in volunteers and patients with fontan circualation. *European Journal of Cardio-Thoracic Surgery*. 2011;39:206-212

92. Sundareswaran KS, Haggerty CM, de Zelicourt D, Dasi LP, Pekkan K, Frakes D, Powell AJ, Kanter KR, Fogel MA, Yoganathan AP. Visualization of flow structures

in fontan patients using three-dimensional phase contrast magnetic resonance imaging. *Journal of Thoracic and Cardiovascular Surgery*. 2012;143:1108-1116

93. Migliavacca F, Balossino R, Pennati G, Dubini G, Hsia T-Y, De Leval MR, Bove E. Multiscale modelling in biofluidynamics: Application to reconstructive paediatric cardiac surgery. *Journal of Biomechanics*. 2006;39:1010-1020

94. Pennati G, Corsini C, Cosentino D, Hsia T-Y, Luisi VS, Dubini G, Migliavacca F. Boundary conditions of patient-specific fluid dynamics modelling of cavopulmonary connections: Possible adaptation of pulmonary resistances results is a critical issue for virtual surgical planning. *Interface Focus*. 2011;1:297-307

95. Baretta A, Corsini C, Yang W, Vignon-Clementel I, Marsden AL, Feinstein JA, Hsia T-Y, Dubini G, Migliavacca F, Pennati G. Virtual surgeries in patients with congenital heart disease: A multi-scale modelling test case. *Philosophical Transactions of the Royal Society A*. 2011;369:4316-4330

96. Pekkan K, Frakes D, Zelicourt DD, Lucas C, Parks WJ, Yoganathan AP. Coupling pediatric ventricle assist devices to the fontan circulation: Simulations with a lumped-parameter model. *ASAIO Journal*. 2005;51:618-628

97. Haggerty CM, Fynn-Thompson F, McElhinney DB, Valente AM, Saikrishnan N, del Nido PJ, Yoganathan AP. Experimental and numeric investigation of impella pumps as cavopulmonary assistance for a failing fontan. *The Journal of thoracic and cardiovascular surgery*. 2012;144:563-569

98. Vannier M, Marsh J. Three dimensional ct reconstruction images for craniofacial surgical planning and evaluation. *Radiology*. 1984;150:179-184

99. Foroglou N, Zamani A, Black P. Intra-operative mri (iop-mri) for brain tumour surgery. *British Journal of Neurosurgery*. 2009;23:14-22

100. Kikinis R, Gleason PL, Moriarty T, Moore MR, Alexander EI, Stieg PE, Matsumae M, Lorensen WE, Cline HE, Black P, Jolesz F. Computer-assisted interactive three-dimensional planning for neurosurgical procedures. *Neurosurgery*. 1996;38:640-651

101. Schlenzka D, Laine T, Lund T. Computer-assisted spine surgery. *European Spine Journal*. 2000;9:S57-S64

102. Nghiem H, Dimas C, McVicar J, Perkins J, Luna J, Winter TI, Harris A, Freeny P. Impact of double helical ct and three-dimensional ct arteriography on surgical planning for hepatic transplantation. *Abdominal Imaging*. 1999;24:278-284

103. Razavi R, Hill D, Keevil S, Miquel M, Muthurangu V, Hegde S, Rhode K, Barnett M, van Vaals J, Hawkes D, Baker E. Cardiac catheterisation guided by mri in children and adults with congenital heart disease. *Lancet*. 2003;362:1877-1882

104. Dutton AQ, Yeo S-J, Yang K-Y, Lo N-N, Chia K-U, Chong H-C. Computer-assisted minimally invasive total knee arthroplasty compared with standard total knee arthroplasty. A prospective, randomized study. *J Bone Joint Surg Am*. 2008;90:2-9

105. De Zelicourt D, Haggerty CM, Sundareswaran KS, Whited B, Rossignac J, Kanter K, Gaynor JW, Spray TL, Sotiropoulos F, Fogel MA, Yoganathan AP. Individualized computer-based surgical planning to address pulmonary ateriovenous malformations in patients with a single ventricle with an interrupted inferior vena cava and azygous continuation. *Journal of Thoracic and Cardiovascular Surgery*. 2011;141:1170-1177

106. Soerensen DD, Pekkan K, de Zelicourt D, Sharma S, Kanter K, Fogel M, Yoganathan AP. Introduction of a new optimized total cavopulmonary connection. *Annals of Thoracic Surgery*. 2007;83:2182-2190

107. Marsden AL, Bernstein AJ, Reddy VM, Shadden SC, Spilker RL, Chan FP, Taylor CA, Feinstein JA. Evaluation of a novel y-shaped extracardiac fontan baffle using computational fluid dynamics. *Journal of Thoracic and Cardiovascular Surgery*. 2009;137:394-403

108. Brickner ME, Hillis LD, Lange RA. Congenital heart disease in adults: First of two parts. *New England Journal of Medicine*. 2000;342:256-263

109. Somerville J. Management of adults with congenital heart disease: An increasing problem. *Annual Review of Medicine*. 1997;48:283-293

110. Pekkan K, Whited B, Kanter K, Sharma S, de Zelicourt D, Sundareswaran KS, Frakes D, Rossignac J, Yoganathan AP. Patient-specific surgical planning and hemodynamic computational fluid dynamics optimization through free-form haptic anatomy editing tool (surgem). *Medical and Biological Engineering and Computing*. 2008;46:1139-1152

111. McRobbie DW, Moore EA, Graves MJ, Prince MR. *Mri: From picture to proton*. New York: Cambridge University Press; 2006.

112. Atkinson DJ, Edelman R. Cineangiography of the heart in a single breath hold with a segmented turboflash sequence. *Radiology*. 1991;178:357-360

113. Simonetti OP, Cook S. Technical aspects of pediatric cmr. *Journal of Cardiovascular Magnetic Resonance*. 2006;8:581-593

114. Frakes D, Conrad C, Healy T, Monaco J, Fogel MA, Sharma S, Smith M, Yoganathan AP. Application of an adaptive control grid interpolation technique to morphological vascular reconstruction. *IEEE Transactions in Biomedical Engineering*. 2003;50:197-206

115. Frakes D, Smith M, Parks WJ, Sharma S, Fogel M, Yoganathan AP. New techniques for the reconstruction of complex vascular anatomies from mri images. *Journal of Cardiovascular Magnetic Resonance*. 2005;7:425-432

116. Sundareswaran KS, Frakes D, Fogel MA, Soerensen DD, Oshinski JN, Yoganathan AP. Optimum fuzzy filters for phase-contrast magnetic resonance imaging segmentation. *Journal of Magnetic Resonance Imaging*. 2009;29:155-165

117. Kass M, Witkin A, Terzopoulos D. Snakes: Active contour models. *International Journal of Computer Vision*. 1988;1:321-331

118. Xu C, Prince J. Snakes, shapes, and gradient vector flow. *IEEE Transactions on Image Processing*. 1998;7:359-369

119. Sundareswaran KS. Characterizing single ventricle hemodynamics using phase contrast magnetic resonance imaging. *School of Biomedical Engineering*. 2008;Doctor of Philosophy:393

120. Li C, Xu C, Gui C, Fox MD. Level set evolution without re-initialization: A new variational formulation. *Proceedings of the 2005 IEEE Computer Society Conference on Computer Vision and Pattern Recognition*. 2005;1:430-436

121. Sundareswaran KS, Frakes D, Fogel M, Skrinjar O, Yoganathan AP. Four dimensional velocity field reconstruction from pc mri using adaptive divergence free radial basis functions. *Journal of Cardiovascular Magnetic Resonance*. 2008;10:A90

122. Narcowich F, Ward J. Generalized hermite interpolation via matrix valued conditionally positive definite functions. *Mathematics of Computation*. 1994;63:661-687

123. Lowitzch S. A density theorem for matrix-valued radial basis functions. *Numerical Algorithms*. 2005;39:253-256

124. de Zelicourt D. Pulsatile fontan hemodynamics and patient-specific surgical planning: A numerical investigation. *Biomedical Engineering*. 2010;PhD

125. Gilmanov A, Sotiropoulos F. A hybrid cartesian/immersed boundary method for simulating flows with 3d, geometrically complex, moving bodies. *Journal of Computational Physics*. 2005;207:457-492

126. de Zelicourt D, Ge L, Wang C, Sotiropoulos F, Gilmanov A, Yoganathan AP. Flow simulations in arbitrarily complex cardiovascular anatomies- an unstructured cartesian grid approach. *Computers & Fluids*. 2009;38:1749-1762

127. Harlow FH, Welch JE. Numerical calculation of time-dependent viscous incompressible flow of fluid with free surface. *Physics of Fluids*. 1965;8:2182-2189

128. Ge L, Sotiropoulos F. A numerical method for solving the 3d unsteady incompressible navier-stokes equations in curviliniear domains with complex immersed boundaries. *Journal of Computational Physics*. 2007;225:1782-1809

129. Dasi LP, Pekkan K, de Zelicourt D, Sundareswaran KS, KrishnankuttyRema R, Del Nido P, Yoganathan AP. Hemodynamic energy dissipation in the cardiovascular system: Generalized theoretical analysis on disease states. *Annals of Biomedical Engineering*. 2009;37:661-673

130. Dasi LP, Pekkan K, Kitajima HD, Yoganathan AP. Functional analysis of fontan energy dissipation. *Journal of Biomechanics*. 2008;41:2246-2252

131. Piccinelli M, Veneziani A, Steinman DA, Remuzzi A, Antiga L. A framework for geometric analysis of vascular structures: Application to cerebral aneurysms. *Medical Imaging, IEEE Transactions on*. 2009;28:1141-1155

132. Marsden AL, Feinstein JA, Taylor CA. A computational framework for derivative-free optimization of cardiovascular geometries. *Computer Methods in Applied Mechanics and Engineering*. 2008;197:1890-1905

133. Gaynor JW, Bridges ND, Cohen MI, Mahle WT, Decampli WM, Steven JM, Nicolson SC, Spray TL. Predictors of outcome after the fontan operation: Is

hypoplastic left heart syndrome still a risk factor? *J Thorac Cardiovasc Surg*. 2002;123:237-245

134. Whitehead KK, Pekkan K, Kitajima HD, Paridon SM, Yoganathan AP, Fogel MA. Nonlinear power loss during exercise in single-ventricle patients after the fontan: Insights from computational fluid dynamics. *Circulation*. 2007;116:I165-171

135. Sharma S, Goudy S, Walker P, Panchal S, Ensley A, Kanter K, Tam V, Fyfe D, Yoganathan A. In vitro flow experiments for determination of optimal geometry of total cavopulmonary connection for surgical repair of children with functional single ventricle. *J Am Coll Cardiol*. 1996;27:1264-1269

136. de Leval MR, Dubini G, Migliavacca F, Jalali H, Camporini G, Redington A, Pietrabissa R. Use of computational fluid dynamics in the design of surgical procedures: Application to the study of competitive flows in cavopulmonary connections. *Journal of Thoracic and Cardiovascular Surgery*. 1996;111:502-513

137. Dubini G, de Leval MR, Pietrabissa R, Montevecchi FM, Fumero R. A numerical fluid mechanical study of repaired congenital heart defects. Application to the total cavopulmonary connection. *Journal of Biomechanics*. 1996;29:111-121

138. Pekkan K, Kitajima HD, de Zelicourt D, Forbess JM, Parks WJ, Fogel MA, Sharma S, Kanter KR, Frakes D, Yoganathan AP. Total cavopulmonary connection flow with functional left pulmonary artery stenosis: Angioplasty and fenestration in vitro. *Circulation*. 2005;112:3264-3271

139. Haggerty CM, Kanter KR, Restrepo M, de Zelicourt D, Parks WJ, Rossignac J, Fogel MA, Yoganathan AP. Simulating hemodynamics of the fontan y-graft based on patient-specific in vivo connections. *Journal of Thoracic and Cardiovascular Surgery*. 2012;(in press)

140. Dasi LP, Krishnankutty R, Kitajima H, Pekkan K, Sundareswaran K, Fogel M, Sharma S, Whitehead K, Kanter K, Yoganathan AP. Fontan hemodynamics:

Importance of pulmonary artery diameter. *Journal of Thoracic and Cardiovascular Surgery.* 2009;137:560-564

141. Kitajima HD. In vitro fluid dynamics of stereolithographic single ventricle congenital heart defects from in vivo magnetic resonance imaging. *Biomedical Engineering*. 2007;PhD

142. Whitehead KKS, Kartik S., Parks WJ, Harris MA, Yoganathan AP, Fogel M. Blood flow distribution in a large series of patients having the fontan operation: A cardiac magnetic resonance velocity mapping study. *Journal of Thoracic and Cardiovascular Surgery*. 2009;138:96-102

143. Dasi LP, Sundareswaran KS, Sherwin C, de Zelicourt D, Kanter KR, Fogel MA, Yoganathan AP. Larger aortic reconstruction corresponds to diminished left pulmonary artery size in patients with single ventricle phyisology. *Journal of Thoracic and Cardiovascular Surgery*. 2010;139:557-561

144. Dasi LP, Whitehead K, Pekkan K, de Zelicourt D, Sundareswaran K, Kanter K, Fogel MA, Yoganathan AP. Pulmonary hepatic flow distribution in total cavopulmonary connections: Extracardiac versus intracardiac. *The Journal of thoracic and cardiovascular surgery*. 2011;141:207-214

145. Pekkan K, Dasi LP, de Zelicourt D, Sundareswaran KS, Fogel MA, Kanter KR, Yoganathan AP. Hemodynamic performance of stage-2 univentricular reconstruction: Glenn vs. Hemi-fontan templates. *Ann Biomed Eng*. 2009;37:50-63

146. Fiore AC, Turrentine M, Rodefeld M, Vijay P, Schwartz T, Virgo K, Fischer L, Brown J. Fontan operation: A comparison of lateral tunnel with extracardiac conduit. *Annals of Thoracic Surgery*. 2007;83:622-630

147. Lardo AC, Webber S, Friehs I, del Nido P, Cape EG. Fluid dynamic comparison of intra-atrial and extracardiac total cavopulmonary connections. *Journal of Thoracic and Cardiovascular Surgery*. 1999;117:697-704

148. Kumar SP, Rubinstein CS, Simsic JM, Taylor AB, Saul JP, Bradley SM. Lateral tunnel versus extracardiac conduit fontan procedure: A concurrent comparison. *Annals of Thoracic Surgery*. 2003;76:1389-1397

149. Hunt JCR, Wray AA, Moin P. Eddies, stream, and convergence zones in turbulent flows. *Center for Turbulence Research Report CTR-S88*. 1988:193

150. Senzaki H, Masutani S, Ishido H, Taketazu M, Kobayashi T, Saski N, Asano H, Katogi T, Kyo S, Yokote Y. Cardiac rest and reserve function in patients with fontan circulation. *Journal of the American College of Cardiology*. 2006;47:2528-2535

151. Ingul CB, Tjonna AE, Stolen TO, Stoylen A, Wisloff U. Impaired cardiac function among obese adolescents: Effect of aerobic interval training. *Archives of Pediatrics and Adolescent Medicine*. 2010;164:852-859

152. Laird WP, Fixler DE, Huffines FD. Cardiovascular response to isometric exercise in normal adolescents. *Circulation*. 1979;59:651-654

153. Fogel M, Weinberg PM, Fellows KE, Hoffman EA. A study in ventricular-ventricular interaction: Single right ventricles compared with systemic right ventricles in a dual-chamber circulation. *Circulation*. 1995;92:219-230

154. Fogel M, Weinberg PM, Gupta KB, Rychik J, Hubbard AM, Hoffman EA, Haselgrove J. Mechanics of the single left ventricle: A study in ventricular-ventricular interaction ii. *Circulation*. 1998;98:330-338

155. Beyar R, Yin F, Hausknecht M, Weisfeldt ML, Kass DA. Dependence of left ventricular twist-radial shortening relations on cardiac cycle phase. *American Journal of Physiology-Heart and Circulatory Physiology*. 1989;257:H1119-H1126

156. Hansen DE, Daughters G, Alderman E, Stinson E, Baldwin J, Miller DC. Effect of acute human cardiac allograft rejection on left ventricular systolic torsion and diastolic recoil measured by intramyocardial markers. *Circulation*. 1987;76:998-1008

157. Shachar G, Fuhrman B, Wang Y, Lucas RJ, Lock J. Rest and exercise hemodynamics after the fontan procedure. *Circulation*. 1982;65:1043-1048

158. Rosenthal M, Bush A, Deanfield J, Redington A. Comparison of cardiopulmonary adaptation during exercise in children after the atriopulmonary and total cavopulmonary connection fontan procedures. *Circulation*. 1995;91:372-378

159. Sundareswaran K, de Zélicourt D, Sharma S, Kanter K, Spray T, Rossignac JR, Sotiropoulos F, Fogel M, Yoganathan AP. Correction of pulmonary arteriovenous malformation using image based surgical planning. *JACC Imaging*. 2009;2:1024-1030

160. Peskin CS, Tu C. Hemodynamics in congenital heart disease. *Computers in Biology and Medicine*. 1986;16:331-359

161. Cilliers A, Gewillig M. Fontan procedure for univentricular hearts: Have changes in design improved outcome? *Cardiovascular Journal of South Africa*. 2002;13:111-116

162. Myers CD, Ballman K, Riegle LE, Mattix KD, Litwak K, Rodefeld M. Mechanisms of systemic adaptation to univentricular fontan conversion. *Journal of Thoracic and Cardiovascular Surgery*. 2010;140:850-856

163. Senzaki H, Masutani S, Ishido H, Taketazu M, Kobayashi T, Sasaki N, Asano H, Katogi T, Kyo S, Yokote Y. Cardiac rest and reserve function in patients with fontan circulation. *J Am Coll Cardiol*. 2006;47:2528-2535

164. Vignon-Clementel IE, Alberto Figueroa C, Jansen KE, Taylor CA. Outflow boundary conditions for three-dimensional finite element modeling of blood flow

and pressure in arteries. *Computer Methods in Applied Mechanics and Engineering*. 2006;195:3776-3796

165. Mirabella L, Haggerty CM, Passerini T, Piccinelli M, Powell AJ, Del Nido PJ, Veneziani A, Yoganathan AP. Treatment planning for a tcpc test case: A numerical investigation under rigid and moving wall assumptions. *International Journal for Numerical Methods in Biomedical Engineering*. 2012:n/a-n/a

166. Haggerty CM, de Zelicourt D, Restrepo M, Rossignac J, Spray TL, Kanter KR, Fogel MA, Yoganathan AP. Comparing pre- and post-operative fontan hemodynamic simulations: Implications for the reliability of surgical planning. *Annals of Biomedical Engineering*. 2012;40:2639-2651

167. Sankaran S, Marsden AL. A stochastic collocation method for uncertainty quantification and propagation in cardiovascular simulations. *Journal of Biomechanical Engineering*. 2011;133:031001

168. de Leval MR, Dubini G, Migliavacca F, Jalali H, Camporini G, Redington A, Pietrabissa R. Use of computational fluid dynamics in the design of surgical procedures: Application to the study of competitive flows in cavopulmonary connections. *The Journal of Thoracic and Cardiovascular Surgery*. 1996;111:502-513

169. Yang W, Feinstein JA, Marsden AL. Constrained optimization of an idealized y-shaped baffle for the fontan surgery at rest and exercise. *Computer Methods in Applied Mechanics and Engineering*. 2010;199:2135-2149

170. Kanter KR, Haggerty CM, Restrepo M, De Zelicourt D, Rossignac J, Parks WJ, Yoganathan AP. Preliminary clinical experience with a bifurcated y-graft fontan procedure- a feasibility study. *Journal of Thoracic and Cardiovascular Surgery*. 2012;(accepted)

171. Pedersen EM, Stenbog EV, Frund T, Houlind K, Kromann O, Sorensen KE, Emmertsen K, Hjortdal VE. Flow during exercise in the total cavopulmonary connection measured by magnetic resonance velocity mapping. *Heart*. 2002;87:554-558

172. Soerensen DD. Optimization and analysis of the total cavo-pulmonary connection. *Bioengineering*. 2006;MS

173. Sluysmans T, Colan SD. Theoretical and empirical derivation of cardiovascular allometric relationships in children. *Journal of Applied Physiology*. 2005;99:445-457

174. Jarmakani JMM, Graham JTP, Benson DWJ, Canent RVJ, Greenfield JCJ. In vivo pressure-radius relationships of the pulmonary artery in children with congenital heart disease. *Circulation*. 1971;43:858-592

175. Lim DS, Peeler BB, Matherne GP, Kramer CM. Cardiovascular magnetic resonance of pulmonary artery growth and ventricular function after norwood procedure with sano modification. *Journal of Cardiovascular Magnetic Resonance*. 2008;10

176. Reddy VM, McElhinney DB, Moore P, Petrossian E, Hanley FL. Pulmonary artery growth after bidirectional cavopulmonary shunt: Is there a cause for concern? *Journal of Thoracic and Cardiovascular Surgery*. 1996;112:1180-1192

177. Fogel MA, Weinberg PM, Hoydu A, Hubbard AM, Rychik J, Jacobs M, Fellows KE, Haselgrove J. The nature of flow in the systemic venous pathway measured by magnetic resonance blood tagging in patients having the fontan operation. *Journal of Thoracic and Cardiovascular Surgery*. 1997;114:1032-1041

178. Restrepo M, Mirabella L, Tang E, Haggerty CM, Fogel MA, Valente AM, McElhinney DB, Yoganathan AP. Growth of the inferior cavopulmonary pathway in patients with a lateral tunnel fontan connection: Quantification from serial

magnetic resonance images. *Journal of Cardiovascular Magnetic Resonance*. 2012;14:1-2

179. Frakes D. An adaptive control grid interpolation technique for the three-dimensional reconstruction of mri data. *Biomedical Engineering*. 2003;PhD

180. Rodefeld M, Frankel SH, Giridharan GA. Cavopulmonary assist: (em)powering the univentricular fontan circulation. *Seminars in Thoracic and Cardiovascular Surgery: Pediatric Cardiac Surgery Annual*. 2011;14:45-54

181. Ghaferi AA, Hutchins GM. Progression of liver pathology in patients undergoing the fontan procedure: Chronic passive congestion, cardiac cirrhosis, hepatic adenoma, and hepatocellular carcinoma. *The Journal of thoracic and cardiovascular surgery*. 2005;129:1348-1352

182. McCabe NM, Veledar E, Romero R, Hebson C, Jokhadar M, Sahu A, McConnell ME, Kogon BE, Book WM. Clinical portal hypertension is related to major adverse outcomes in adolescents and adults with congenital heart disease after fontan procedure. *American Heart Association Scientific Sessions*. 2012